Bobo Bai

**Multicomponent diffusion in natural silicate melts:
Toward a universal eigenvector matrix**

submitted in partial fulfillment of the requirements for the degree of
Master of Science in Earth and Environmental Sciences
Department of Earth and Environmental Sciences
The University of Michigan

Accepted by:

Youxue Zhang	Youxue Zhang	4/4/2023
Signature	Name	Date
Jie Li Digitally signed by Jie Li Date: 2023.04.04 13:53:39 -04'00'	Jie (Jackie) Li	4/4/2023
Signature	Name	Date
	Julia Cole	5/4/2023
Department Chair Signature	Name	Date

I hereby grant the University of Michigan, its heirs and assigns, the non-exclusive right to reproduce and distribute single copies of my thesis, in whole or in part, in any format. I represent and warrant to the University of Michigan that the thesis is an original work, does not infringe or violate any rights of others, and that I make these grants as the sole owner of the rights to my thesis. I understand that I will not receive royalties for any reproduction of this thesis.

☑ Permission granted.

☐ Permission granted to copy after: _____

☐ Permission declined.

_____
Author Signature

Earth and Environmental Sciences
M UNIVERSITY OF MICHIGAN

ABSTRACT

Diffusion is due to thermally activated random motion of particles on the atomic scale and it is one of the two ways of mass transport (the other one is convection). In a multicomponent system, the different components interact with each other. Therefore, the concentration gradient of one component can affect not only its own motion, but also the motion of other components, leading to cross effects. As a result, diffusion in an N-component system is described by an $N-1$ square matrix called diffusion matrix ($[D]$). Natural silicate melt usually contains 6-10 major components (defined to be more than 1 wt% oxide), thus diffusion in natural silicate melt is always multicomponent diffusion. Previous studies show that eigenvectors of $[D]$ are roughly independent of temperature, whereas eigenvalues of $[D]$ follow an Arrhenius relation with temperature. In this study, whether the diffusion eigenvectors depend on melt composition was evaluated. MATLAB codes were written to obtain a universal eigenvector matrix by simultaneously fitting concentration profiles from 27 diffusion couple experiments in basaltic melts (Guo and Zhang, 2018, 2020). Using the MATLAB codes, the diffusion profiles of 27 diffusion couple experiments were fitted twice—using mass fraction and mole fractions as concentration, respectively—and two different eigenvector matrices $[P_w]$ and $[P_X]$ were obtained. The eigenvector matrix $[P_w]$ is significantly different from that of Guo and Zhang (2020), and our fitting more rigorously proved that diffusion eigenvectors are independent of temperature. Using both eigenvector matrices, the oxide concentrations were transformed to eigen-component "concentrations", which were plotted as a function of distance. Then, literature diffusion profiles in diffusion couple and mineral dissolution experiments of rhyolitic to andesitic to haplo-basaltic melts were examined in our new eigen-component plots to evaluate whether the profiles are monotonic. If the eigenvector matrix from the 27 experiments is

composition-invariant, then all eigen-component "concentration" plots should be monotonic.

Most eigen-component "concentration" plots are monotonic (no obvious uphill diffusion). Only about 3% of the >1000 eigen-component "concentrations" plots display obvious non-monotonic profiles, showing that we are getting close to a universal eigenvector matrix.

ACKNOWLEDGEMENT

Table of Contents

LIST OF FIGURES

LIST OF TABLES

LIST OF APPENDICES

I. Introduction

Natural silicate melt usually contains 6-10 major components (defined to be more than 1 wt% oxide, e.g., SiO_2-TiO_2-Al_2O_3-FeO-MgO-CaO-Na_2O-K_2O) and diffusion in natural silicate melt is always multicomponent diffusion. In nature, many geological processes involving mass transport are essentially multicomponent diffusion, e.g., magma mixing and contamination (Sato, 1975; Watson, 1982; Koyaguchi, 1985, 1989; Oldenburg et al., 1989), and mineral growth and dissolution (Watson, 1982; Zhang et al., 1989). To quantitatively predict mass transport requires an in-depth understanding of multicomponent diffusion in natural silicate melts.

A classic treatment for diffusion in natural silicate melts is effective binary diffusion (EBD) model (e.g., Cooper, 1968), which treats diffusant i of interest as one component and all other components as one "component" m (stands for mixture). Then the flux of component of interest is assumed to be:

$$J_i = -D_{im}\nabla C_i \tag{1}$$

where J_i is the flux of component i, D_{im} is the effective binary diffusion coefficient (EBDC) and ∇C_i is the concentration gradient of component i. Due to its simplicity, the method has been extensively used for monotonic profiles (e.g., Zhang et al., 1989; Chen and Zhang, 2008, 2009). However, the method fails when it comes to uphill diffusion, which is often encountered in natural systems and experiments. In addition, the effective binary diffusion diffusivities depend strongly on thermodynamic condition, melt composition and the direction of diffusion in composition space, which restricts the applications of EBDCs to interdiffusion under a different thermodynamic condition and in melt systems with a different composition (Cooper, 1968; Zhang et al., 1989; Liang et al., 1996; Zhang, 2010; Chen and Zhang, 2008, 2009; Guo and Zhang, 2016, 2018, 2020).

To treat non-monotonic diffusion profiles, Zhang (1993) proposed a modified effective binary diffusion model, which assumes the diffusive flux of a component is proportional to its activity gradient (instead of concentration gradient).

$$J_i = -\frac{\mathcal{D}_i}{\gamma_i}\nabla a_i \qquad (2)$$

where J_i, $\mathcal{D}_i$, a_i and γ_i are the flux, activity based EBDC (a.k.a. intrinsic EBDC), activity and activity coefficient of component i, respectively. Even though the model has some values of fitting non-monotonic diffusion profiles, due the complexity of the model and lack of activity data for silicate melts, it has not been widely applied. In addition, both the EBD model and the modified EBD model neglect interactions among diffusants, making it difficult to decipher the diffusion mechanism in natural silicate melts.

To solve diffusion problems in a multicomponent system more rigorously, there is a critical need for a multicomponent treatment (Onsager, 1945; Liang, 2010; Zhang, 2010, 2022), in which the flux of the component i is a linear combination of the concentration gradients of independent components:

$$J_i = -\sum_j D_{ij}\nabla C_j \qquad (3)$$

where J_i is the flux of component i, D_{ij} is diffusion coefficient, which characterizes the cross effect of the concentration gradients of the component j on the flux of component i, and ∇C_j is the concentration gradient of component j. The $n \times n$ square matrix whose (i, j) entry is D_{ij} is called the diffusivity matrix and denoted by $[D]$. Enormous efforts have been made to determine the diffusivity matrix at desired compositions, e.g., SiO_2-Al_2O_3-CaO (Sugawara et al., 1977; Oishi et al., 1982; Liang et al., 1996), SiO_2-Al_2O_3-MgO (Kress and Ghiorso, 1993; Richter et al., 1998), SiO_2-Al_2O_3-K_2O (Chakraborty et al., 1995a), SiO_2-B_2O_3-Na_2O (Pablo et al., 2017), SiO_2-Al_2O_3-MgO-CaO (Kress and Ghiorso, 1993), SiO_2-Al_2O_3-Na_2O-K_2O-H_2O (Mungall et al., 1998),

2

SiO$_2$-TiO$_2$-Al$_2$O$_3$-MgO-CaO-Na$_2$O-K$_2$O (Guo and Zhang, 2016) and SiO$_2$-TiO$_2$-Al$_2$O$_3$-FeO-MgO-CaO-Na$_2$O-K$_2$O (Guo and Zhang, 2018, 2020).

Among those studies, Guo and Zhang (2018, 2020) conducted numerous experiments to extract diffusivity matrices in an 8-component system (SiO$_2$-TiO$_2$-Al$_2$O$_3$-FeO-MgO-CaO-Na$_2$O-K$_2$O) at 1260 °C, 1350 °C and 1500 °C. Their success of using diffusivity matrix to predict mass transport during mineral dissolution shows the validity and utility of multicomponent treatment in diffusion in natural silicate melts. In addition, they found that eigenvectors of $[D]$ are roughly independent of temperature and eigenvalues of $[D]$ follows an Arrhenius relation with temperature. With these observations, we can hence calculate diffusion matrix in basaltic melt at temperatures within the studied range. Furthermore, the calculated diffusion matrix can be used to predict diffusion behavior in magma mixing and mineral dissolution. However, if the diffusion involves a large difference in melt composition (i.e., from basalt to rhyolite), it would be necessary to first assess the compositional effect on the diffusion matrix.

In this study, we focus on an 8-component melt system (SiO$_2$-TiO$_2$-Al$_2$O$_3$-FeO-MgO-CaO-Na$_2$O-K$_2$O) and evaluate whether diffusion eigenvectors depend on composition. Diffusion profiles from previous studies (e.g., Guo and Zhang 2018, 2020) were collected and fitted by assuming a constant eigenvector matrix. Then the best two eigenvector matrices—obtained by fitting diffusion profiles using mass fraction and mole fraction as concentration, respectively— were used to calculate profiles of eigen-components. Finally, the profiles of eigen-components were plotted to check whether they show uphill diffusion features.

II. Theoretical background

2.1 Diffusivity matrices, eigenvectors, and eigenvalues

In an N-component melt system with a barycentric (mass-fixed) frame of reference, without bulk motion, sink and source, there are only $n = N - 1$ independent components (Kirkwood et al., 1960; Miller et al., 1986). As a generalization of Fick's first law (Onsager, 1945), the flux of the component i is a linear combination of the concentration gradients of independent components, i.e.,

$$J_i = -\sum_{j=1}^{n} D_{ij}^N \nabla C_j \qquad (4)$$

Here J_i is mass-unit flow. D_{ij}^N is the coefficient characterizing the cross effect of the concentration gradient of the component j on the flux of component i, where the superscript N means we choose the Nth component as the dependent component. And C_j is the concentration of component j expressed as mass per unit volume, usually with a unit of g/cm³. Accordingly, the vector form of Fick's first law is given by:

$$J = \begin{bmatrix} J_1 \\ J_2 \\ \vdots \\ J_n \end{bmatrix} = \begin{bmatrix} -\sum_{j=1}^{n} D_{1j}^N \nabla C_j \\ -\sum_{j=1}^{n} D_{2j}^N \nabla C_j \\ \vdots \\ -\sum_{j=1}^{n} D_{nj}^N \nabla C_j \end{bmatrix} = -\begin{bmatrix} D_{11}^N & D_{12}^N & \cdots & D_{1n}^N \\ D_{21}^N & D_{22}^N & & D_{2n}^N \\ \vdots & & \ddots & \vdots \\ D_{n1}^N & D_{n2}^N & \cdots & D_{nn}^N \end{bmatrix} \times \nabla \begin{bmatrix} C_1 \\ C_2 \\ \vdots \\ C_n \end{bmatrix} = -[D^N]\nabla C \qquad (5)$$

where $[D^N]$ is the diffusivity matrix.

It has been shown that in a thermodynamically stable region $[D^N]$ is positive-definite (e.g., Gupta and Cooper, 1971), namely, having positive eigenvalues, and hence the diagonal terms of $[D^N]$ are always positive. However, the off-diagonal terms of $[D^N]$ can be either positive or negative, and sometimes has large absolute values, which enables a component to diffuse against its concentration gradient, leading to uphill diffusion. Mathematically, $[D^N]$ can be diagonalized:

$$[D^N] = [P][\Lambda][P^{-1}] \qquad (6)$$

where $[P]$ is an $n \times n$ matrix whose columns $\boldsymbol{v_i}$ are eigenvectors of $[D^N]$, $[P^{-1}]$ is the inverse of $[P]$ and $[\Lambda]$ is an $n \times n$ diagonal matrix whose diagonal terms λ_i are eigenvalues of $[D^N]$, such that:

$$[D^N]\boldsymbol{v_i} = \lambda_i \boldsymbol{v_i} \tag{7}$$

The eigenvectors of $[D^N]$ describe interactions among components and are commonly used to infer exchange mechanisms and the eigenvalues of $[D^N]$ characterize the exchange rates in the melt system (Varshneya and Cooper, 1972; Liang et al., 1996; Guo and Zhang, 2016, 2018, 2020).

2.2 Eigen-components and eigen-space

Combining Fick's first law and mass conservation gives Fick's second law:

$$\frac{\partial \boldsymbol{C}}{\partial t} = \nabla \cdot ([D^N]\nabla \boldsymbol{C}) \tag{8}$$

where t is time.

Diffusion problems are usually studied in one dimension; thus Eq. (8) is often simplified to the expression:

$$\frac{\partial \boldsymbol{C}}{\partial t} = \frac{\partial}{\partial x}\left([D^N]\frac{\partial \boldsymbol{C}}{\partial x}\right) \tag{9}$$

Plugging Eq. (6) into Eq. (9), leads to

$$\frac{\partial \boldsymbol{C}}{\partial t} = \frac{\partial}{\partial x}\left([P][\Lambda][P^{-1}]\frac{\partial \boldsymbol{C}}{\partial x}\right) \tag{10}$$

If eigenvector matrix $[P]$ is independent of melt composition, then Eq. (10) can be converted into the following expression:

$$\frac{\partial [P^{-1}]\boldsymbol{C}}{\partial t} = \frac{\partial}{\partial x}\left([\Lambda]\frac{\partial [P^{-1}]\boldsymbol{C}}{\partial x}\right) \tag{11}$$

Denoting $[P^{-1}]\boldsymbol{C}$ by $\boldsymbol{Z}$, namely,

$$\mathbf{Z} = \begin{bmatrix} Z_1 \\ Z_2 \\ \vdots \\ Z_n \end{bmatrix} = [P^{-1}] \begin{bmatrix} C_1 \\ C_2 \\ \vdots \\ C_n \end{bmatrix} = [P^{-1}]\mathbf{C} \tag{12}$$

then Eq. (11) can be converted into the following equation:

$$\frac{\partial \mathbf{Z}}{\partial t} = \frac{\partial}{\partial x}\left([\Lambda]\frac{\partial \mathbf{Z}}{\partial x}\right) \tag{13}$$

Eq. (13) contains n independent equations:

$$\frac{\partial Z_i}{\partial t} = \frac{\partial}{\partial x}\left(\lambda_i \frac{\partial Z_i}{\partial x}\right) \tag{14}$$

To distinguish $\mathbf{C}$ from $\mathbf{Z}$, we name each term C_i in $\mathbf{C}$ an oxide component and each term Z_i in $\mathbf{Z}$ an eigen-component. Accordingly, the compositional space composed of Z_i is referred to as eigen-space. Note that since λ_i is always positive, profiles of eigen-components should always be monotonic as long as the initial concentration profile is monotonic. Since Eq. (14) is obtained based on a constant eigenvector matrix $[P]$, the monotonicity of profiles of eigen-components is a necessary condition of the universality of eigenvector matrix $[P]$.

2.3 Analytical solutions to multicomponent diffusion

For multicomponent diffusion in an infinite diffusion couple, assuming that $[D^N]$ is constant within the studied range and the interface position is at $x = 0$, the analytical solution can be easily obtained (Lasaga, 1979; Morgan et al., 2006; Guo and Zhang, 2016):

$$\mathbf{C} = \frac{\mathbf{C_R} + \mathbf{C_L}}{2} + [P][E][P^{-1}]\frac{\mathbf{C_R} - \mathbf{C_L}}{2} \tag{15}$$

where $\mathbf{C_L}$ and $\mathbf{C_R}$ are initial melt concentration vectors at $x < 0$ and $x > 0$, $[P]$ is eigenvector matrix, $[E]$ is a diagonal matrix whose diagonal terms are:

$$E_{ii} = \mathrm{erf}\left(\frac{x}{\sqrt{4\lambda_i t}}\right) \tag{16}$$

in which x is distance from the interface and t is time.

6

2.4 Diffusivity matrices when other units of concentration are used

The diffusivity matrix $[D^N]$ depends on many factors, e.g., thermodynamic state (e.g., Liang and Davis, 2002; Guo and Zhang, 2020), melt composition (e.g., Liang et al., 1996), the choice of the dependent component (e.g., Liang et al., 1996; Guo and Zhang, 2016, 2018, 2020), the choice of reference frame (e.g., Kirkwood et al., 1960; Miller et al., 1986), and the choice of concentration unit. Among them, the effect of choice of concentration unit hasn't been studied. Here we derive how diffusivity matrix varies when cation mole concentration, mass fraction and cation mole fraction are used.

First, one may substitute the vector $\boldsymbol{C}$ of mass concentration (kg/m^3) by the vector $\widetilde{\boldsymbol{C}}$ of cation molar concentration (mol/m^3), using the following expression:

$$\boldsymbol{C} = \begin{bmatrix} C_1 \\ C_2 \\ \vdots \\ C_n \end{bmatrix} = \begin{bmatrix} M_1 \tilde{C}_1 \\ M_2 \tilde{C}_2 \\ \vdots \\ M_n \tilde{C}_n \end{bmatrix} = [M^N]\widetilde{\boldsymbol{C}} \tag{17}$$

where $\tilde{C}_i$ is molar concentration of the ith cation and $[M^N]$ is a diagonal matrix with the diagonal term M_i as the molar mass of the ith oxide component, namely,

$$[M^N] = \begin{bmatrix} M_1 & & & \\ & M_2 & & \\ & & \ddots & \\ & & & M_n \end{bmatrix} \tag{18}$$

Plugging Eq. (17) into Eq. (8), leads to

$$\frac{\partial \widetilde{\boldsymbol{C}}}{\partial t} = \nabla \cdot \left([M^{N^{-1}}][D^N][M^N]\nabla\widetilde{\boldsymbol{C}} \right) \tag{19}$$

where $[M^{N^{-1}}]$ is the inverse of $[M^N]$. We see from Eq. (19) that the diffusivity matrix $[\widetilde{D}^N]$, when cation mole concentration is used, is related to $[D^N]$ by the following expression:

$$[\widetilde{D}^N] = [M^{N^{-1}}][D^N][M^N] \tag{20}$$

Plugging Eq. (6) into Eq. (20), leads to:

$$[\tilde{D}^N] = \left[M^{N^{-1}}\right][P][\Lambda][P^{-1}][M^N] = \left(\left[M^{N^{-1}}\right][P]\right)[\Lambda]\left(\left[M^{N^{-1}}\right][P]\right)^{-1} \tag{21}$$

From Eq. (21) we see that the eigenvector matrix $[\tilde{P}]$ obtained from $\tilde{C}$ would be:

$$[\tilde{P}] = \left[M^{N^{-1}}\right][P] \tag{22}$$

and the eigenvalue matrix obtained from $\tilde{C}$ should be the same as that of $[D^N]$.

For convenience, concentration data are often expressed as mass fraction or mole fraction. In the former case, the concentration vector is often substituted by the mass fraction vector $\boldsymbol{w}$ using the equation:

$$\boldsymbol{C} = \begin{bmatrix} C_1 \\ C_2 \\ \vdots \\ C_n \end{bmatrix} = \begin{bmatrix} \rho w_1 \\ \rho w_2 \\ \vdots \\ \rho w_n \end{bmatrix} = \rho \boldsymbol{w} \tag{23}$$

where ρ is the mass density of the melt and w_i is the mass fraction of the ith oxide component. Plugging Eq. (23) into Eq. (8) and assuming ρ doesn't change much within the studied composition range, then we obtain the following expression:

$$\frac{\partial \boldsymbol{w}}{\partial t} = \nabla \cdot ([D^N]\nabla \boldsymbol{w}) \tag{24}$$

Eq. (24) shows that the diffusivity matrix $[D_w^N]$ obtained from $\boldsymbol{w}$ is the same as $[D^N]$, and hence has the same eigenvector matrix $[P_w]$, namely,

$$[D_w^N] = [D^N] \tag{25}$$

and

$$[P_w] = [P] \tag{26}$$

Alternatively, the concentration vector $\boldsymbol{C}$ can be replaced by vector $\boldsymbol{X}$ of cation mole fraction using the expression:

$$\boldsymbol{C} = \begin{bmatrix} C_1 \\ C_2 \\ \vdots \\ C_n \end{bmatrix} = \begin{bmatrix} \tilde{\rho} M_1 X_1 \\ \tilde{\rho} M_1 X_2 \\ \vdots \\ \tilde{\rho} M_n X_n \end{bmatrix} = \tilde{\rho}[M^N]\boldsymbol{X} \tag{27}$$

If we assume $\tilde{\rho}$ is nearly constant within the studied composition range, plugging Eq. (27) into Eq. (8) leads to:

$$\frac{\partial \boldsymbol{X}}{\partial t} = \nabla \cdot \left([M^{N^{-1}}][D^N][M^N] \nabla \boldsymbol{X} \right) \tag{28}$$

Thus, according to Eq. (28), the diffusivity matrix $[D_X^N]$ obtained from $\boldsymbol{X}$ is:

$$[D_X^N] = [M^{N^{-1}}][D^N][M^N] \tag{29}$$

By comparing Eq. (20) and Eq. (29), we see that:

$$[D_X^N] = [\tilde{D}^N] = \left(\left[M^{N^{-1}} \right][P] \right) [\Lambda] \left(\left[M^{N^{-1}} \right][P] \right)^{-1} \tag{30}$$

Therefore, the eigenvector matrix $[P_X]$ obtained from $\boldsymbol{X}$ would be:

$$[P_X] = [\tilde{P}] = \left[M^{N^{-1}} \right][P] \tag{31}$$

and the eigenvalue matrix obtained from $\boldsymbol{X}$ should be the same as those of $[D^N]$.

III. Methods

3.1 Data collection and processing

Eigenvectors and eigenvalues in desired melt composition can be obtained by simultaneously fitting diffusion profiles of all oxides from diffusion experiments. Diffusion profiles in the 8-component melt system (SiO_2-TiO_2-Al_2O_3-FeO-MgO-CaO-Na_2O-K_2O) were collected from previous studies (Zhang et al., 1989; Chen and Zhang, 2008, 2009; Yu et al., 2016; Yu et al., 2019; Guo and Zhang, 2016, 2018, 2020; González -Garcia et al., 2017; Wang et al., 2020). The studied melt compositions vary from basaltic melt to rhyolitic melt. The oxide concentrations from those studies were all reported as mass fraction in weight percent (wt%). Original concentration profiles were first plotted to check data quality. Then points that apparently deviate from diffusion trend or show a significant quench effect in mineral dissolution experiments were removed. After that, mass fraction concentrations w_i were converted into mole fraction concentrations X_i using the expression:

$$X_i = \frac{\frac{w_i}{M_i}}{\sum_{j=1}^{N} \frac{w_j}{M_j}} * 100 \, mole\% \tag{32}$$

where w_i is the mass fraction of component i, X_i is the mole fraction of component i, M_i is the molar mass of component i on a single cation basis, and N is the total number of components. In our calculation, we replaced SiO_2 with $SiO_2^* = SiO_2 - (total - 100)$ and treated SiO_2^* as the dependent component following the studies of Guo and Zhang (2016, 2018, 2020).

Only the experimental data from Guo and Zhang (2018, 2020) were incorporated in the fitting process, as those data show small concentration variations (typically less than 3 wt%) across the diffusion profiles. Those data are from diffusion couple experiments in a basaltic melt at three different temperatures, 1260 °C, 1350 °C and 1500 °C. For simplicity of experiment

naming, the three temperatures were represented by the letters C, A and B, respectively. For example, "BS1&2C" denotes a diffusion couple experiment conducted at 1260 °C. The selected experimental data were fitted using mass fraction as concentration and mole fraction as concentration separately, generating two eigenvector matrices $[P_w]$ and $[P_X]$. After the fitting process, all collected experimental data were used to verify the universality of the extracted eigenvector matrices. Since the monotonicity of profiles of eigen-components is a necessary condition of the universality of eigenvector matrix, a natural next step is to plot profiles of eigen-components. Concentration vector w (or X) of oxide components was converted into concentration vector Z_w (or Z_X) of eigen-components using the equation:

$$Z_w = [P_w{}^{-1}]w \tag{33}$$

or

$$Z_X = [P_X{}^{-1}]X \tag{34}$$

If profiles of eigen-components are indeed monotonic, then our hypothesis is consistent with experimental data. The hypothesis can be further tested by more experimental data, but there is no straightforward proof of the hypothesis.

3.2 Numerical method

In this part, we do not distinguish between the fitting using mass fraction as concentration and that using mole fraction as concentration, since they are essentially the same in terms of computation. The selected diffusion couple data were fitted using one eigenvector matrix $[P]$ and three sets of eigenvalue matrices $[\Lambda^{1260}]$, $[\Lambda^{1350}]$ and $[\Lambda^{1500}]$ where the superscripts 1260, 1350 and 1500 represent temperature in °C. To optimize eigenvectors and eigenvalues, we follow the procedure in the studies of Guo and Zhang (2016, 2018, 2020) to minimize χ^2:

$$\chi^2 = \frac{1}{2} \sum_{k=1}^{N_e} \sum_{j=1}^{Np_k} \sum_{i=1}^{N_c} \left(\frac{w_{ijk}{}^{meas} - w_{ijk}{}^{calc}}{\sigma_{ik}} \right)^2 \tag{35}$$

where N_c is the number of components ($N_c = 8$), Np_k is the number of points in the kth experiments, N_e is number of experiments incorporated in the fitting process ($N_e = 27$), $w_{ijk}{}^{meas}$ is the measured concentration of oxide i at position j in experiment k, $w_{ijk}{}^{calc}$ is the calculated concentration using Eq. (15) and Eq. (16), σ_{ik} is 1-σ error on $w_{ijk}{}^{meas}$.

Denoting $\frac{w_{ijk}{}^{meas} - w_{ijk}{}^{calc}}{\sigma_{ik}}$ in Eq. (35) by r_{ijk} and putting all r_{ijk} in a column vector $\boldsymbol{r}$ in ascending order of (i, j, k) with k as primary index, j as secondary index and i as tertiary index, namely,

$$r = (r_{111}, r_{211}, ..., r_{N_c11}, r_{121}, r_{221} ..., r_{N_c21}, ..., r_{N_cN_{p_1}1}, r_{112}, r_{212} ... ... r_{N_cN_{p_{N_e}}N_e})^T \tag{36}$$

then Eq. (35) can be converted into the expression:

$$\chi^2 = \frac{1}{2} r^T r \tag{37}$$

Our fitting parameters include 49 elements in the 7×7 eigenvector matrix $[P]$ and 21 eigenvalues in 3 diagonal eigenvalue matrices at three different temperatures. One complexity is that all eigenvalues λ must be positive. However, if we take $\theta = \ln \lambda$, then θ can be any real values. Therefore, θ is treated as the fitting parameter in place of λ. For simplicity, we put our 70 fitting parameters into a column vector β, in which the first 49 elements are the vectorized eigenvector matrix and the remaining 21 elements are θ values, namely,

$$\beta = (P_{11}, P_{21}, ..., P_{67}, P_{77}, \theta_1^{1260}, ..., \theta_7^{1260}, \theta_1^{1350}, ..., \theta_7^{1350}, \theta_1^{1500}, ..., \theta_7^{1500})^T \tag{38}$$

For the iterative algorithm, we used the Broyden–Fletcher–Goldfarb–Shanno method (independently proposed by Broyden, Fletcher, Goldfarb and Shanno, 1970) with the Armijo-type line search and a cautious update (Donghui and Masao, 2001b). The Broyden–Fletcher–Goldfarb–Shanno (BFGS hereafter) method is one of the most popular Quasi-Newton methods

for solving unconstrained nonlinear optimization problems. Conventional Newton method involves the calculation of Hessian matrix $[H]$—a square matrix of second-order partial derivatives of the loss function—and the inversion of $[H]$, which is very computationally expensive. In addition, to make sure the algorithm converges to a minimum, $[H]$ is required to be positive definite. When the loss function is non-convex, however, the positive definiteness of $[H]$ cannot be guaranteed. In contrast to Newton method, Quasi-Newton methods approximate $[H]$ with a positive definite matrix $[B]$, which is updated iteratively using the information calculated from previous steps. Quasi-Newton methods differ in the way they construct $[B]$, but all of them satisfy the Quasi-Newton condition. Among various Quasi-Newton methods, the BFGS method is currently regarded as the most efficient method (Donghui and Masao, 2001a) and has been widely used to solve unconstrained nonlinear optimization problems.

Generally, consider the unconstrained nonlinear optimization problem: $\min f(\beta)$, $\beta \in R^m$, where $f: R^m \to R$ is a continuously differentiable function (in this study $f = \chi^2$ and $m = 70$). The BFGS method begins with an initial guess for the optimal value β_0 and an initial symmetric and positive definite matrix $B_0 \in R^{m \times m}$ and updates β using the expression:

$$\beta_{k+1} = \beta_k + \gamma_k p_k, \qquad k = 0, 1, 2 \dots \tag{39}$$

where γ_k is the step size at step k and p_k is the search direction at step k.

The search direction p_k is given by the equation:

$$p_k = -B_k^{-1} g_k \tag{40}$$

where g_k is the gradient of f at $\beta = \beta_k$, namely,

$$g_k = \nabla f(\beta_k) \tag{41}$$

The step size γ_k can be obtained by the backtracking line search which looks for the largest value γ_k in the set $\{\rho^i | i = 0,1 \dots\}$ that satisfies the inequality:

13

$$f(\beta_k + \gamma_k p_k) \leq f(\beta_k) + \sigma\gamma_k g_k{}^T p_k \tag{42}$$

where ρ and σ are control parameters so that $\rho, \sigma \in (0, 1)$.

The original BFGS method updates B_k using the following equation:

$$B_{k+1} = B_k - \frac{B_k s_k s_k^T B_k}{s_k^T B_k s_k} + \frac{y_k y_k^T}{y_k^T s_k} \tag{43}$$

where $s_k = \beta_{k+1} - \beta_k$ and $y_k = g_{k+1} - g_k$. Eq. (43) conserves the symmetry of the matrix $[B]$ and as long as $y_k^T s_k > 0$, B_{k+1} is also positive definite. However, the backtracking method cannot guarantee that $y_k^T s_k > 0$. To make sure B_{k+1} is positive definite, Donghui and Masao (2001b) proposed a cautious update that determines B_{k+1} by the following condition:

$$B_{k+1} = \begin{cases} B_k - \dfrac{B_k s_k s_k^T B_k}{s_k^T B_k s_k} + \dfrac{y_k y_k^T}{y_k^T s_k}, & \text{if } \dfrac{y_k^T s_k}{||s_k||^2} \geq \varepsilon ||g_k||^\alpha \\ B_k & , \quad \text{otherwise} \end{cases} \tag{44}$$

where ε and α are positive constants.

The inverse of B_{k+1} can be obtained by applying the Sherman–Morrison formula:

$$B_{k+1}^{-1} = B_k^{-1} + \frac{(y_k^T s_k + y_k^T B_k^{-1} y_k)(s_k s_k^T)}{(y_k^T s_k)^2} - \frac{B_k^{-1} y_k s_k^T + s_k y_k^T B_k^{-1}}{y_k^T s_k} \tag{45}$$

In practical applications, to avoid any matrix inversion, the inverse of Hessian matrix instead of the Hessian matrix itself is approximated. Denoting B_k^{-1} by H_k, then Eq. (40) and Eq. (45) become:

$$p_k = -H_k g_k \tag{46}$$

and

$$H_{k+1} = H_k + \frac{(y_k^T s_k + y_k^T H_k y_k)(s_k s_k^T)}{(y_k^T s_k)^2} - \frac{H_k y_k s_k^T + s_k y_k^T H_k}{y_k^T s_k} \tag{47}$$

respectively. Accordingly, H_{k+1} will be determined using the criteria:

$$H_{k+1} = \begin{cases} H_k + \dfrac{(y_k^T s_k + y_k^T H_k y_k)(s_k s_k^T)}{(y_k^T s_k)^2} - \dfrac{H_k y_k s_k^T + s_k y_k^T H_k}{y_k^T s_k}, & \text{if } \dfrac{y_k^T s_k}{||s_k||^2} \geq \varepsilon ||g_k||^\alpha \\ H_{k+1} & , \quad \text{otherwise} \end{cases} \tag{48}$$

In general, the BFGS method with a cautious update is summarized as follows:

Step 1:	Choose an initial $\beta_0 \in R^m$, an initial inverse Hessian approximation $H_0 \in R^{m \times m}$, a convergence tolerance $\kappa > 0$, constants $\rho, \sigma \in (0,1)$ and $\varepsilon, \alpha > 0$. Let $k := 0$;
Step 2:	Terminate the iteration if $||g_k||^2 < \kappa$;
Step 3:	Compute search direction p_k using Eq. (46);
Step 4:	Determine step size γ_k that that satisfies Eq. (42);
Step 5:	Compute β_{k+1} using Eq. (39);
Step 6:	Determine H_{k+1} using Eq. (48);
Step 7:	Let $k := k + 1$ and go to step 2;

In our case of minimizing χ^2, the gradient of χ^2 can be calculated using the equation:

$$\nabla \chi^2 = J^T r \tag{49}$$

where J is the Jacobian matrix with J_{ij} being:

$$J_{ij} = \frac{\partial r_i}{\partial \beta_j} \tag{50}$$

J can be analytically solved in our problem, and the solution is given in **Appendix A**.

Once the parameters β_i are optimized, the 1-σ error on β_i can be obtained. The asymptotic standard parameter errors $\boldsymbol{\sigma}$ are given by the equation (Clifford, 1973):

$$\boldsymbol{\sigma} = \sqrt{\text{diag}([J^T J]^{-1})} \tag{51}$$

And the 1-σ error on β_i is given by:

$$\sigma(\beta_i) = \boldsymbol{\sigma_{ii}} \tag{52}$$

IV. Results

4.1 Fitting diffusion profiles with mass fraction as concentration

Optimized eigenvector matrix $[P_w]$ and eigenvalues obtained by fitting mass fraction data together with the 1-σ errors are shown in Table 4.1. Generally, eigenvalues are listed in ascending order. All features of the diffusion profiles from the diffusion couple experiments are well reproduced by the optimal parameters (e.g., Figs. 4.2-4.4).

Table 4.1. Eigenvalues at different temperatures and eigenvector matrix $[P_w]$ fitted by mass fraction data.

Eigenvalues	λ_1	λ_2	λ_3	λ_4	λ_5	λ_6	λ_7
1260 °C	1.95±0.04	1.98±0.09	3.60±0.11	20.35±0.50	22.16±0.51	27.1±0.44	168.98±1.90
1350 °C	6.88±0.22	4.72±0.24	13.11±0.38	34.41±0.95	31.47±0.94	47.46±1.03	207.27±3.64
1500 °C	17.76±0.61	18.5±0.76	37.07±0.88	101.35±1.73	104.2±1.83	147.53±2.41	456.17±9.14
Eigenvectors	v_1	v_2	v_3	v_4	v_5	v_6	v_7
SiO₂	-1.45	-0.78	-0.59	**0.25**	-0.38	-0.04	-0.19
TiO₂	**0.64**±0.04	-0.08±0.09	-0.34±0.03	**0.03**±0.01	-0.06±0.01	**0.02**±0.01	-0.01±0.00
Al₂O₃	-0.01±0.14	**0.98**±0.55	-0.20±0.03	**0.01**±0.02	-0.09±0.02	-0.03±0.01	-0.1±0.02
FeO	**0.55**±0.03	-0.07±0.08	**0.64**±0.02	-0.56±0.12	**0.88**±0.1	-0.63±0.06	-0.39±0.07
MgO	**0.28**±0.02	-0.11±0.08	**0.43**±0.02	-0.23±0.11	-0.17±0.09	-0.05±0.02	-0.16±0.03
CaO	**0.38**±0.01	**0.09**±0.03	**0.43**±0.01	**0.76**±0.11	-0.37±0.09	**0.69**±0.05	-0.07±0.01
Na₂O	-0.19±0.01	-0.01±0.01	-0.17±0.01	-0.02±0.02	-0.05±0.02	-0.23±0.01	**0.90**±0.16
K₂O	-0.19	-0.03	-0.20	-0.25	**0.23**	**0.26**	**0.02**

Note: λ is in $\mu m^2/s$. The "SiO₂" term in each eigenvector was obtained by taking the inverse of the sum of all elements in that eigenvector. In the eigenvector matrix, all positive elements are shown in bold and errors greater than 0.20 are highlighted in red.

The obtained eigenvalues at different temperatures were fitted by the Arrhenius relation:

$\ln \lambda = \ln \lambda_0 - \frac{E_a}{RT}$, where λ_0 is the pre-exponential factor in $\mu m^2/s$, E_a is activation energy in kJ/mol, R is the universal gas constant (8.31447 J mol^{-1} K^{-1}), and T is temperature in K. The fitted dependence of λ on temperature is listed in Table 4.2 and plotted in Fig. 4.1. All eigenvalues roughly follow the Arrhenius relation with temperature, but some eigenvalues are close to each other (e.g., λ_1 and λ_2; λ_4, λ_5 and λ_6), a phenomenon defined to be near degeneracy

by Guo and Zhang (2020). Mathematically, an eigenvalue is said to be degenerate if corresponding eigenspace has dimension greater than one. In this case, any vector in that eigenspace will be an eigenvector corresponding to the eigenvalue. The near degeneracy of our eigenvalues means that our eigenvectors may not be well constrained, and hence more constrains are needed to improve our eigenvector matrix.

Table 4.2. Temperature dependence of eigenvalues listed in Table 4.1 and corresponding activation energies.

Eigenvalues	Arrhenius relation	Activation Energy (kJ/mol)
λ_1	$\ln \lambda_1 = 16.820 - 24552/T$	204
λ_2	$\ln \lambda_2 = 17.225 - 25390/T$	211
λ_3	$\ln \lambda_3 = 18.337 - 25947/T$	216
λ_4	$\ln \lambda_4 = 14.940 - 18366/T$	153
λ_5	$\ln \lambda_5 = 14.675 - 17917/T$	149
λ_6	$\ln \lambda_6 = 15.884 - 19374/T$	161
λ_7	$\ln \lambda_7 = 12.566 - 11522/T$	96

Notes: λ_i is in $\mu m^2/s$ and T is temperature in K.
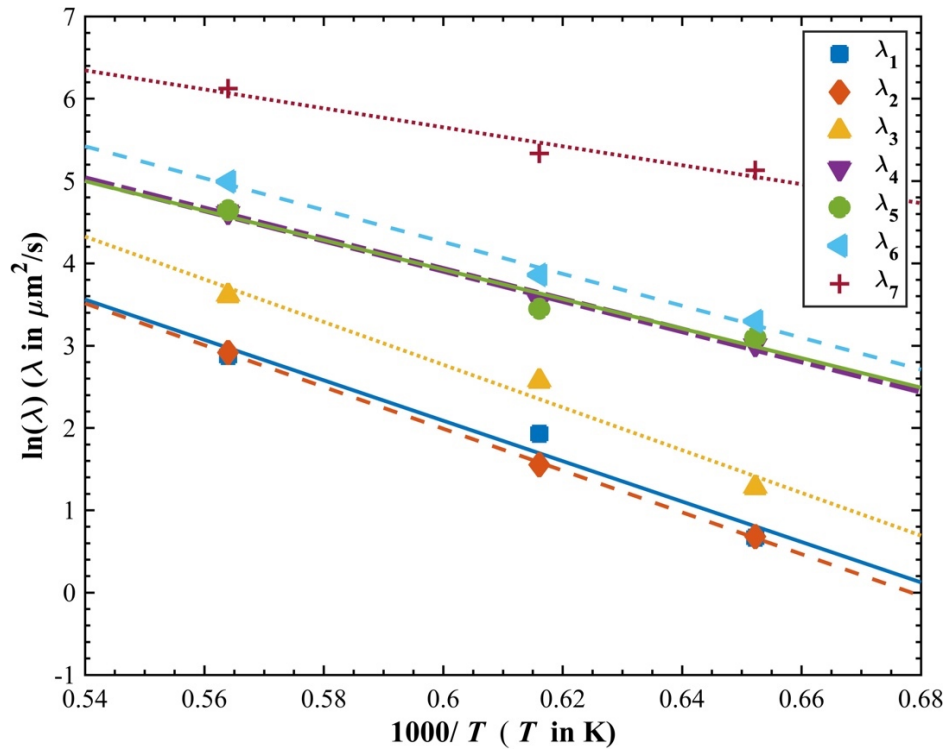
Figure 4.1. Temperature dependence of eigenvalues listed in Table 4.1. The straight lines are fits by Arrhenius relation.
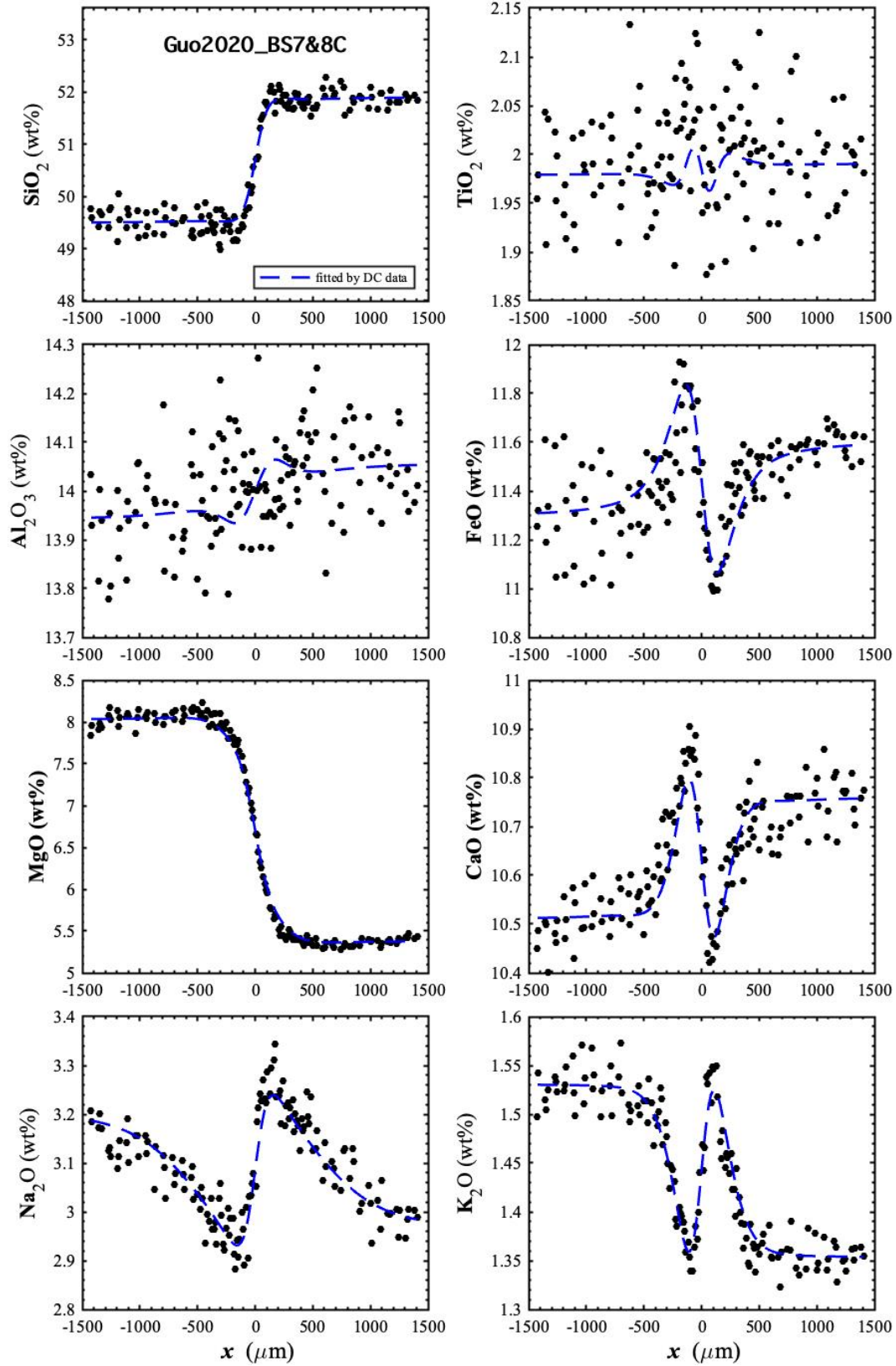
Figure 4.2. Diffusion profiles of oxide components in wt% of BS7&8C (Guo and Zhang, 2020) with fits. The dash curves are fits by the parameters in Table 4.1.

18
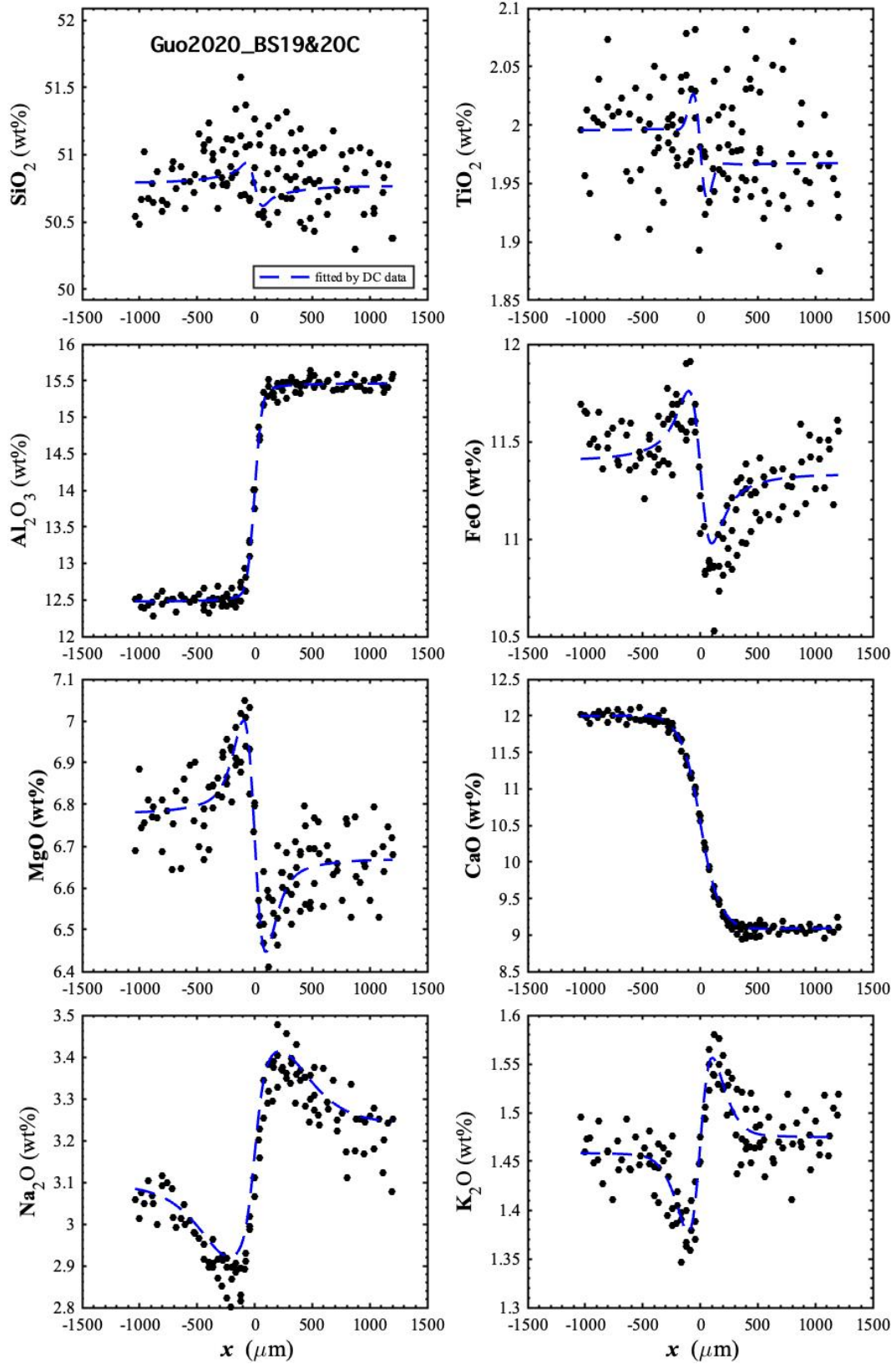
Figure 4.3. Diffusion profiles of oxide components in wt% of BS19&20C (Guo and Zhang, 2020) with fits. The dash curves are fits by the parameters in Table 4.1.

19
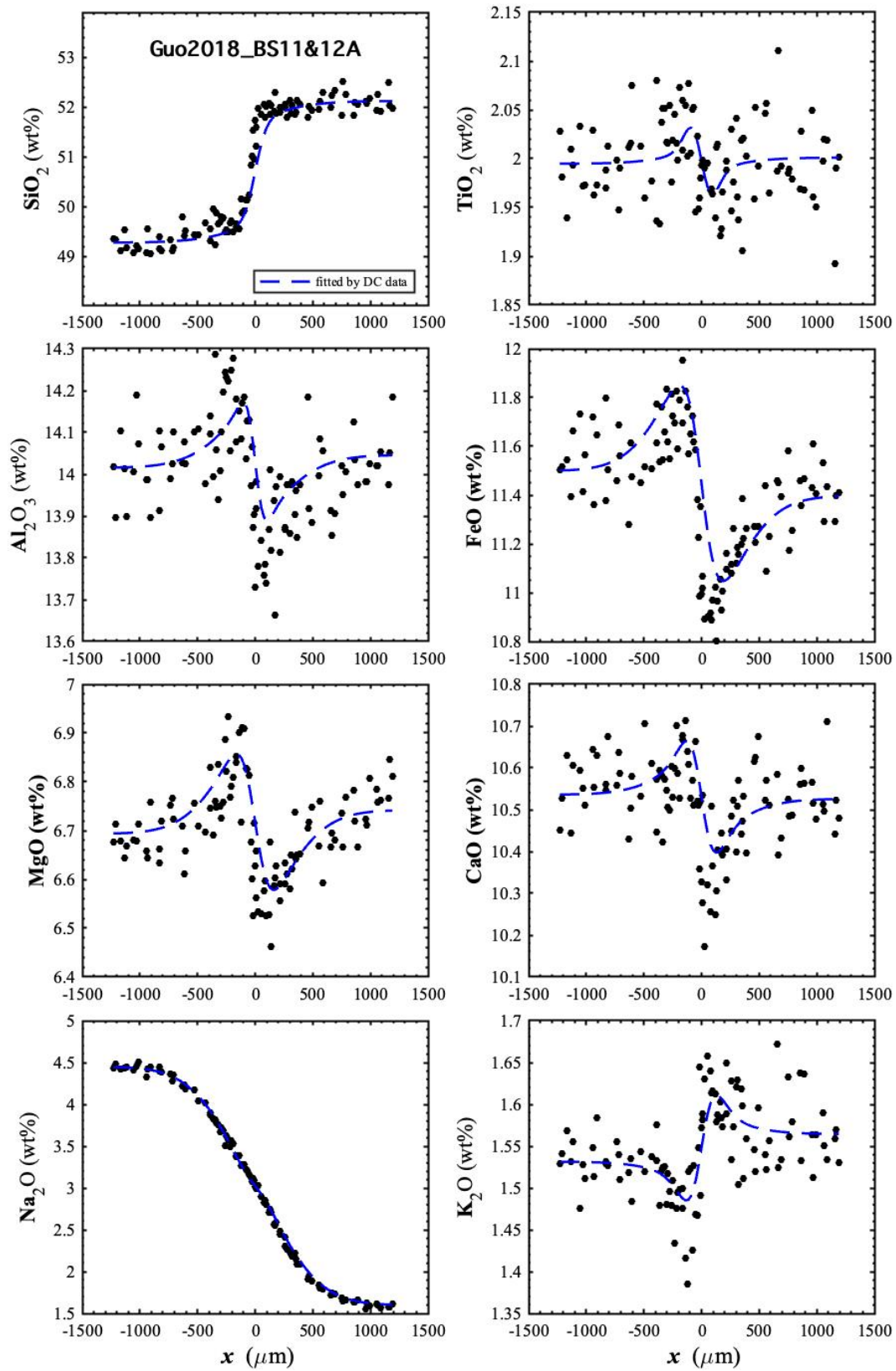
Figure 4.4. Diffusion profiles of oxide components in wt% of BS11&12A (Guo and Zhang, 2018) with fits. The dash curves are fits by the parameters in Table 4.1.

20

4.2 Fitting diffusion profiles with mole fraction as concentration

Optimized eigenvector matrix $[P_X]$ and eigenvalues obtained by fitting mole fraction data together with the 1-σ errors are shown in Table 4.3. Eigenvalues are listed generally in ascending order. All features of the diffusion profiles from the diffusion couple experiments are well reproduced by the optimal parameters (e.g., Figs. 4.6-4.8).

Table 4.3. Eigenvalues at different temperatures and eigenvector matrix $[P_X]$ fitted by mole fraction data.

Eigenvalues	λ_1	λ_2	λ_3	λ_4	λ_5	λ_6	λ_7
1260 °C	1.92±0.08	1.95±0.04	3.57±0.10	19.70±0.46	22.12±0.45	27.30±0.45	168.56±1.86
1350 °C	4.71±0.21	6.99±0.22	13.57±0.38	35.46±0.94	31.27±0.86	48.00±1.02	205.40±3.44
1500 °C	18.36±0.68	17.39±0.56	37.28±0.87	102.11±1.64	103.63±1.74	148.44±2.37	459.07±8.42
Eigenvectors	v_1	v_2	v_3	v_4	v_5	v_6	v_7
SiO$_2$	0.73	-1.33	-0.55	-0.24	0.29	-0.03	-0.33
TiO$_2$	-0.06±0.06	0.47±0.03	-0.23±0.02	0.02±0.01	-0.04±0.01	0.01±0.00	-0.01±0.01
Al$_2$O$_3$	0.98±0.48	0.12±0.15	-0.19±0.03	0.01±0.02	-0.07±0.01	-0.04±0.01	-0.13±0.07
FeO	-0.07±0.06	0.47±0.02	0.49±0.02	-0.28±0.09	0.80±0.08	-0.47±0.05	-0.22±0.12
MgO	-0.15±0.10	0.42±0.04	0.59±0.02	-0.44±0.13	-0.23±0.10	-0.07±0.03	-0.17±0.09
CaO	0.07±0.01	0.43±0.01	0.42±0.01	0.80±0.11	-0.42±0.08	0.70±0.05	-0.09±0.05
Na$_2$O	-0.02±0.01	-0.35±0.01	-0.30±0.01	-0.06±0.03	-0.09±0.02	-0.42±0.02	0.95±0.50
K$_2$O	-0.03	-0.24	-0.23	-0.28	0.34	0.32	0.00

Note: λ is in $\mu m^2/s$. The "SiO$_2$" term in each eigenvector was obtained by taking the inverse of the sum of all elements in that eigenvector. In the eigenvector matrix, all positive elements are shown in bold and errors greater than 0.20 are highlighted in red.

As an analogy to Part 4.1, the obtained eigenvalues at different temperatures were also fitted using the Arrhenius relation (see Table 4.4) and then plotted in Fig. 4.5. It can be observed that all eigenvalues listed in Table 4.3 roughly follow the Arrhenius relation with temperature. However, despite using mole fraction as concentration, the near degeneracies of λ_1 and λ_2 and of λ_4, λ_5 and λ_6 still exist.

Table 4.4. Temperature dependence of eigenvalues listed in Table 4.3 and corresponding activation energies.

Eigenvalues	Arrhenius relation	Activation Energy (kJ/mol)
$\ln \lambda_1$	$17.337 - 25595/T$	213
$\ln \lambda_2$	$16.650 - 24276/T$	202
$\ln \lambda_3$	$18.420 - 26065/T$	217
$\ln \lambda_4$	$15.180 - 18755/T$	156
$\ln \lambda_5$	$14.647 - 17879/T$	149
$\ln \lambda_6$	$15.880 - 19353/T$	161
$\ln \lambda_7$	$12.634 - 11636/T$	97

Notes: λ_i is in $\mu m^2/s$ and T is temperature in K.
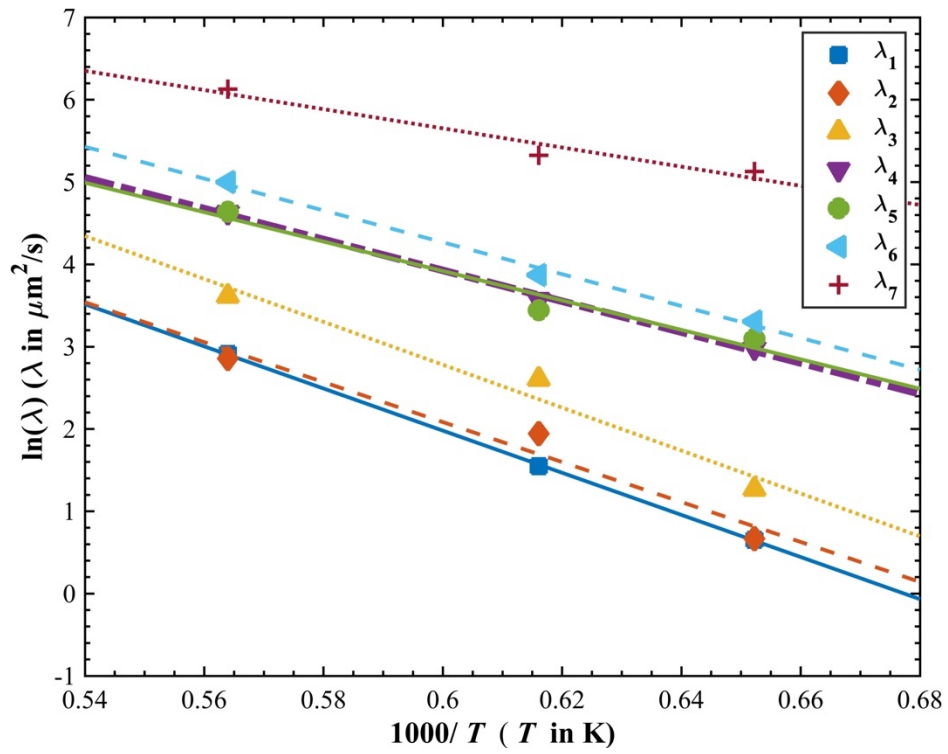
Figure 4.5. Temperature dependence of eigenvalues listed in Table 4.3. The straight lines are fits by Arrhenius relation.
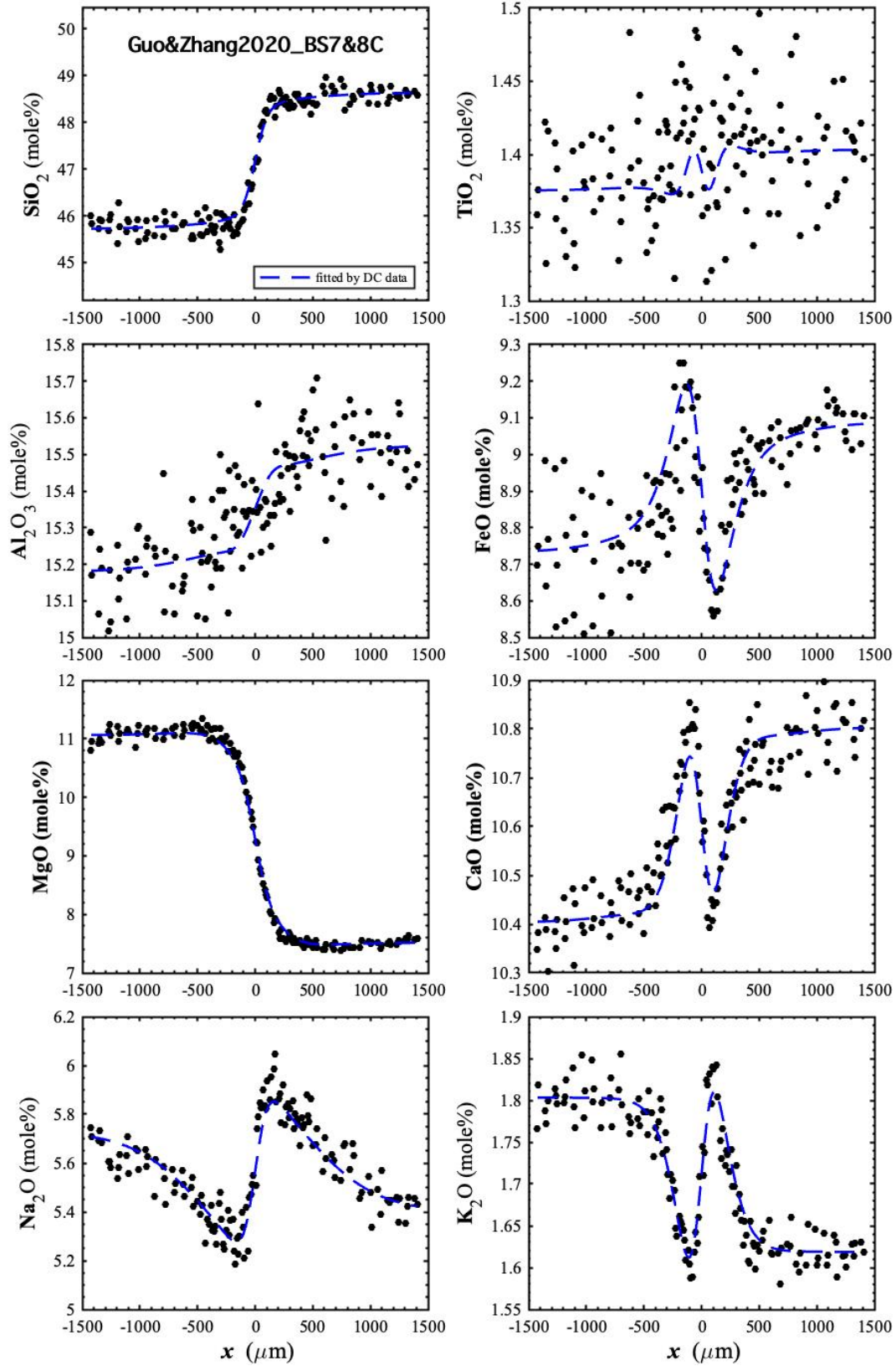
Figure 4.6. Diffusion profiles of oxide components in mole% of BS7&8C (Guo and Zhang, 2020) with fits. The dash curves are fits by the parameters in Table 4.3.
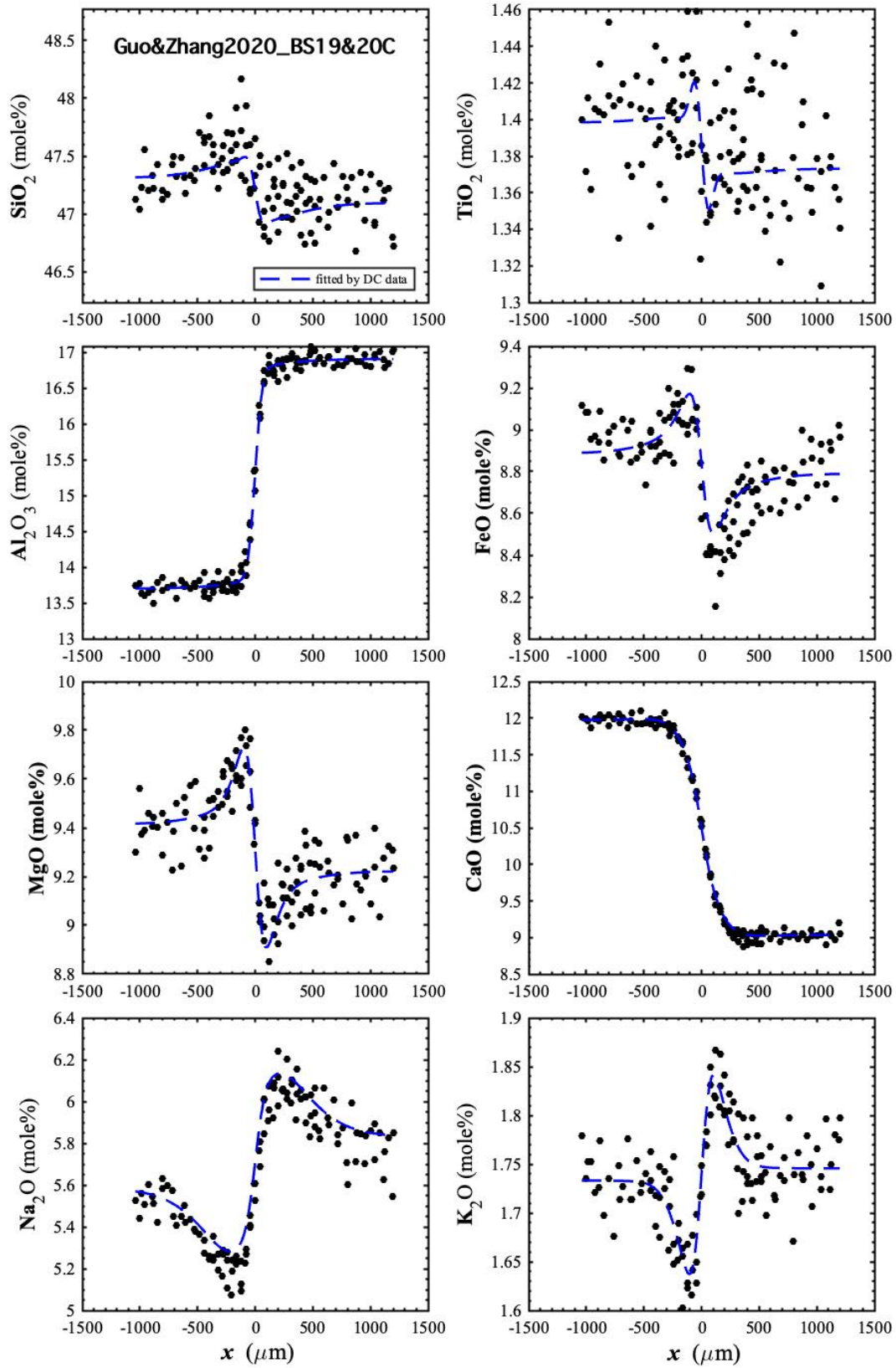
Figure 4.7. Diffusion profiles of oxide components in mole% of BS19&20C (Guo and Zhang, 2020) with fits. The dash curves are fits by the parameters in Table 4.3.
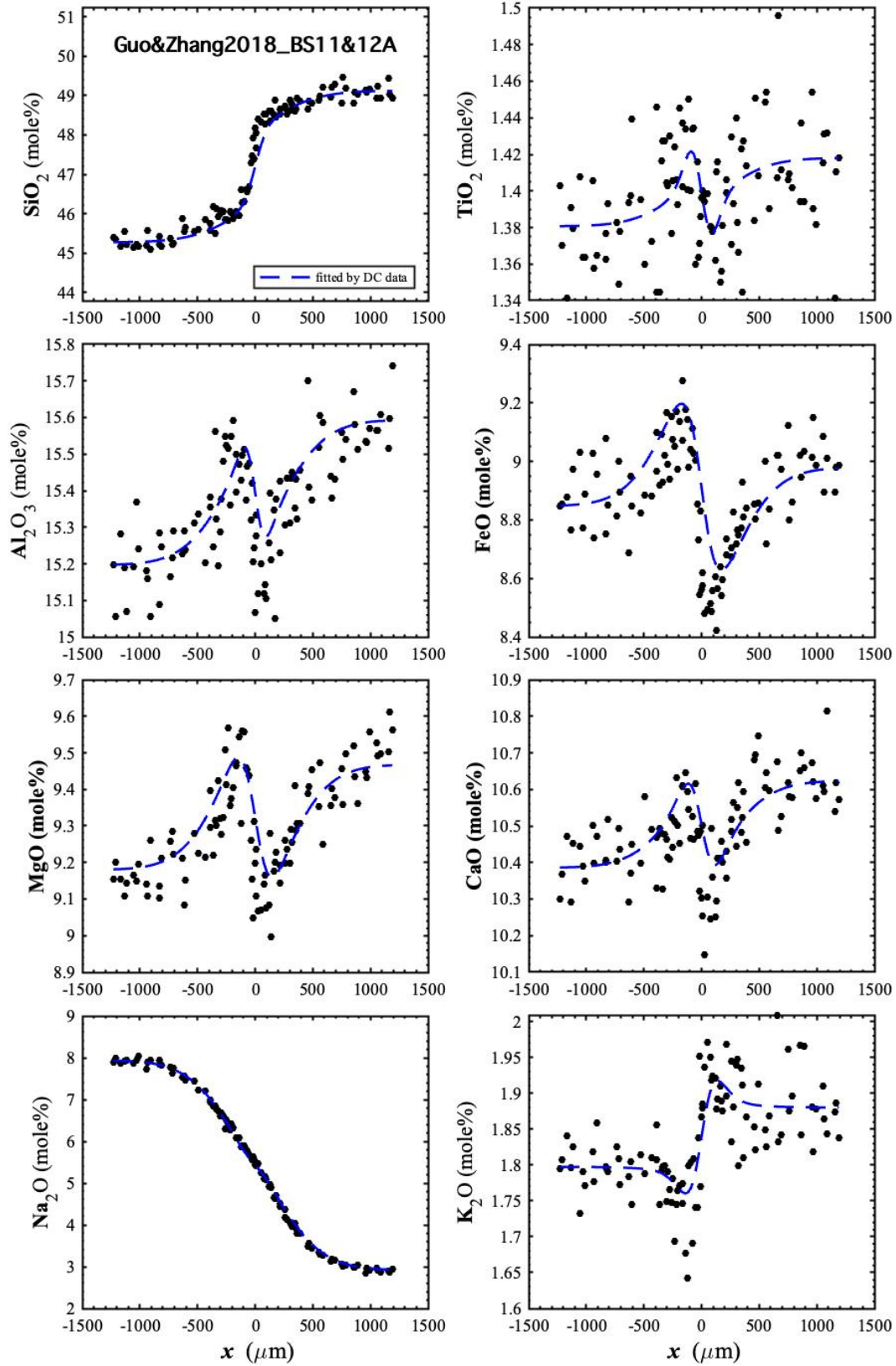
Figure 4.8. Diffusion profiles of oxide components in mole% of BS11&12A (Guo and Zhang, 2018) with fits. The dash curves are fits by the parameters in Table 4.3.

V. Discussion

5.1 Comparison to eigenvector matrices from previous studies

Guo and Zhang (2018, 2020) fit the three sets of diffusion couple data using mass fraction as concentration at different temperatures separately and obtained three similar eigenvector matrices, indicating that the diffusion eigenvectors in basaltic melts do not depend much on temperature. Our fitting results show that one eigenvector matrix with three sets of eigenvalues fit all concentration profiles well, more rigorously demonstrating that the diffusion eigenvectors are invariant with temperature. In addition, Guo and Zhang (2020) have estimated a constant eigenvector matrix (referred to as $[P_0]$ hereafter) by taking the weighted average of eigenvectors at three different temperatures. The $[P_0]$ matrix together with our $[P_w]$ matrix are given in Table 5.1. It is readily seen that two matrices are pretty much similar in terms of v_2, v_3, v_5, v_6 and v_7, but still show apparent differences in v_1 and v_4.

Table 5.1. The constant eigenvector matrix $[P_0]$ obtained by Guo and Zhang (2020) and $[P_w]$ obtained in this study.

$[P_0]$	v_1	v_2	v_3	v_4	v_5	v_6	v_7
TiO_2	**0.76**	-0.20	-0.18	**0.02**	-0.02	-0.02	-0.02
Al_2O_3	**0.18**	**0.97**	-0.47	**0.01**	-0.15	-0.07	-0.10
FeO	**0.51**	**0.00**	**0.66**	-0.06	**0.86**	-0.41	-0.36
MgO	**0.17**	-0.03	**0.41**	**0.71**	-0.14	-0.32	-0.15
CaO	**0.22**	**0.12**	**0.33**	-0.70	-0.33	**0.79**	-0.08
Na_2O	-0.17	-0.04	-0.18	**0.04**	-0.12	-0.19	**0.91**
K_2O	-0.13	-0.02	-0.09	**0.10**	**0.32**	**0.25**	**0.06**
$[P_w]$	v_1	v_2	v_3	v_4	v_5	v_6	v_7
TiO_2	**0.64**	-0.08	-0.34	**0.03**	-0.06	**0.02**	-0.01
Al_2O_3	-0.01	**0.98**	-0.20	**0.01**	-0.09	-0.03	-0.10
FeO	**0.55**	-0.07	**0.64**	-0.56	**0.88**	-0.63	-0.39
MgO	**0.28**	-0.11	**0.43**	-0.23	-0.17	-0.05	-0.16
CaO	**0.38**	**0.09**	**0.43**	**0.76**	-0.37	**0.69**	-0.07
Na_2O	-0.19	-0.01	-0.17	-0.02	-0.05	-0.23	**0.90**
K_2O	-0.19	-0.03	-0.20	-0.25	**0.23**	**0.26**	**0.02**

Note: All positive elements are shown in bold.

5.2 Comparison of $[P_w]$ and $[P_X]$

The eigenvector matrix $[P_w]$ is obtained based on the assumption that the mass density ρ is roughly constant across the diffusion profiles, whereas the eigenvector matrix $[P_X]$ is obtained based on the assumption that the single cation molar density $\tilde{\rho}$ is roughly constant across the diffusion profiles. Even though theoretically these two conditions cannot be satisfied simultaneously, we see that the experimental data from Guo and Zhang (2018, 2020) show small compositional variations across the diffusion profiles and hence we are inclined to neglect both density variations. If both conditions roughly hold, it can be seen from Eq. (26) and Eq. (31) that the two eigenvector matrices should satisfy the equation:

$$[P_X] = \left[M^{N-1}\right][P_w] \tag{53}$$

where in our case,

$$[M^N] = \begin{bmatrix} M_{TiO_2} & & & & & & \\ & M_{AlO_{1.5}} & & & & & \\ & & M_{FeO} & & & & \\ & & & M_{MgO} & & & \\ & & & & M_{CaO} & & \\ & & & & & M_{NaO_{0.5}} & \\ & & & & & & M_{KO_{0.5}} \end{bmatrix} \tag{54}$$

Using Eqs. (53)-(54) and the eigenvector matrix $[P_w]$ listed in Table 4.1, the matrix $\left[M^{N-1}\right][P_w]$ was calculated. To make it comparable to the eigenvector matrix $[P_X]$ listed in Table 4.3, each column vector of $\left[M^{N-1}\right][P_w]$ was normalized so that its 2-norm equals to 1. The normalized $\left[M^{N-1}\right][P_w]$, denoted as $[P_X^*]$, as well as $[P_X]$ are given in Table 5.2. We tested whether matrices $[P_X^*]$ and $[P_X]$ are different by calculating $T_{ij} = \left(P_{X,ij}^* - P_{X,ij}\right)/\sqrt{\sigma_{ij}^{*2} + \sigma_{ij}^2}$. If $[P_X^*]$ and $[P_X]$ agree with each other within error, then the absolute values of T_{ij} would be less

than 2 at 95% probability assuming a standard normal distribution. Our calculation shows that all

T_{ij} values have an absolute value less than 2, thus $[P_X^*]$ and $[P_X]$ are the same within errors.

Nevertheless, it can be clearly seen that some elements in $[P_X^*]$ and $[P_X]$ are quite different, e.g.,

the (2,2), (3,4) and (4,4) entries in both matrices. The discrepancy can be attributed to the two

assumptions we made about mass density ρ and molar density $\tilde{\rho}$, both of which cannot be

rigorously constant when composition varies across diffusion profiles.

Table 5.2. Eigenvector matrix $[P_X^*]$ and eigenvector matrix $[P_X]$.

$[P_X^*]$	v_1	v_2	v_3	v_4	v_5	v_6	v_7
TiO_2	-0.05±0.06	**0.49±0.03**	-0.23±0.02	**0.02±0.01**	-0.04±0.01	**0.01±0.00**	0.00±0.00
Al_2O_3	**0.98±0.55**	-0.01±0.17	-0.21±0.04	**0.02±0.03**	-0.11±0.03	-0.03±0.01	-0.07±0.01
FeO	-0.05±0.06	**0.47±0.02**	**0.49±0.02**	-0.45±0.10	**0.79±0.09**	-0.49±0.05	-0.18±0.03
MgO	-0.14±0.1	**0.42±0.04**	**0.58±0.02**	-0.32±0.15	-0.28±0.14	-0.06±0.03	-0.13±0.02
CaO	**0.09±0.02**	**0.41±0.01**	**0.42±0.01**	**0.78±0.11**	-0.42±0.10	**0.70±0.05**	-0.04±0.01
Na_2O	-0.01±0.02	-0.38±0.01	-0.30±0.01	-0.04±0.04	-0.10±0.03	-0.42±0.02	**0.97±0.17**
K_2O	-0.03	-0.25	-0.23	-0.31	**0.32**	**0.31**	**0.01**
$[P_X]$	v_1	v_2	v_3	v_4	v_5	v_6	v_7
TiO_2	-0.06±0.06	**0.47±0.03**	-0.23±0.02	**0.02±0.01**	-0.04±0.01	**0.01±0.00**	-0.01±0.01
Al_2O_3	**0.98±0.48**	**0.12±0.15**	-0.19±0.03	**0.01±0.02**	-0.07±0.01	-0.04±0.01	-0.13±0.07
FeO	-0.07±0.06	**0.47±0.02**	**0.49±0.02**	-0.28±0.09	**0.80±0.08**	-0.47±0.05	-0.22±0.12
MgO	-0.15±0.10	**0.42±0.04**	**0.59±0.02**	-0.44±0.13	-0.23±0.10	-0.07±0.03	-0.17±0.09
CaO	**0.07±0.01**	**0.43±0.01**	**0.42±0.01**	**0.80±0.11**	-0.42±0.08	**0.70±0.05**	-0.09±0.05
Na_2O	-0.02±0.01	-0.35±0.01	-0.30±0.01	-0.06±0.03	-0.09±0.02	-0.42±0.02	**0.95±0.50**
K_2O	-0.03	-0.24	-0.23	-0.28	**0.34**	**0.32**	0.00

Note: All positive elements are shown in bold and errors greater than 0.20 are highlighted in red.

5.3 Verification of the universality of eigenvector matrix

To test our hypothesis that eigenvector matrix is invariant with composition in natural

silicate melts, we transformed the oxide concentrations into eigen-component "concentrations"

and plotted the profiles of eigen-components as a function of distance using data from earlier

diffusion experiments (Zhang et al., 1989; Chen and Zhang, 2008, 2009; Yu et al., 2016; Guo

and Zhang, 2016; González -Garcia et al., 2017; Yu et al., 2019; Guo and Zhang, 2018, 2020;

Wang et al., 2020). In total, there are 171 experiments and 1197 concentration profiles. The two eigenvector matrices $[P_w]$ and $[P_X]$ were tested separately. Profiles of eigen-components using mass fraction as concentration were calculated using Eq. (33) to test the universality of $[P_w]$, whereas profiles of eigen-components using mole fraction as concentration were calculated using Eq. (34) to test the universality of $[P_X]$. In the former case, about 3% (35 out of 1197) profiles are non-monotonic (Table 5.3), of which 23% are from crystal dissolution experiments in andesite (Zhang et al., 1989), 20% are from plagioclase dissolution experiments in basalt (Yu et al., 2016) and 29% are from diffusion couple experiments in haplo-basalt (Guo and Zhang, 2016). In the latter case, roughly 2% (28 out of 1197) profiles are non-monotonic (Table 5.4), of which 32% are from crystal dissolution experiments in andesite (Zhang et al., 1989), 25% are from diffusion couple experiments in haplo-basalt (Guo and Zhang, 2016) and 18% are from shoshonite-rhyolite diffusion couple experiments (González -Garcia et al., 2017). In both cases, all diffusion profiles of quartz dissolution experiments in basalt and rhyolite are monotonic, even though the compositional variations are large across the profiles. Overall, most profiles (e.g., Figs. 5.1-5.6) are monotonic and show no oblivious uphill diffusion, supporting our hypothesis that the matrix is independent of melt composition.

Table 5.3. Summary of the 35 $[P_w]$-converted concentration profiles of eigen-components that show obvious uphill diffusion, along with the corresponding experimental conditions. The remaining 1162 profiles of eigen-components are monotonic.

Exp	Melt comp	Type	Z_1	Z_2	Z_3	Z_4	Z_5	Z_6	Z_7
Zhang1989_Exp#225[a]	Andesite	DiDisAn	×						×
Zhang1989_Exp#236RU [a]	Andesite	RuDisAn		×			×	×	×
Zhang1989_Exp#259PL [a]	Andesite	PlDisAn						×	×
Chen2008_Exp#44 [b]	JDF Basalt	OlDisBa						×	
Chen2009_Exp#5 [c]	JDF Basalt	CpxDisBa							×
Yu2016_PlDisBa202 [d]	JDF Basalt	PlDisBa					×		
Yu2016_PlDisBa210 [d]	JDF Basalt	PlDisBa					×		
Yu2016_PlDisBa211 [d]	JDF Basalt	PlDisBa					×		
Yu2016_PlDisBa214 [d]	JDF Basalt	PlDisBa					×		
Yu2016_PlDisBa216 [d]	JDF Basalt	PlDisBa					×		
Yu2016_PlDisBa233 [d]	JDF Basalt	PlDisBa					×		
Yu2016_PlDisBa230 [d]	JDF Basalt	PlDisBa					×		
Guo2016_HB2&4A [e]	Haplobasalt	DC		×					
Guo2016_HB3&4A [e]	Haplobasalt	DC		×		×	×		
Guo2016_HB5&6A [e]	Haplobasalt	DC				×			
Guo2016_HB7&8B [e]	Haplobasalt	DC		×					

Exp	Base comp	Type							
Guo2016_HB11&12F [e]	Haplobasalt	DC		×					
Guo2016_HB15&16A [e]	Haplobasalt	DC	×		×		×		
Guo2020_BS11&12C [f]	Basalt	DC			×		×		
Guo2020_BS17&18C [f]	Basalt	DC		×					
González2017_P050-H0-4 [g]	Shoshonite & Rhyolite	DC				×			
González2017_P300-H0-4 [g]	Shoshonite & Rhyolite	DC	×	×	×				
González2017_P300-H2-4 [g]	Shoshonite & Rhyolite	DC		×					

Notes: 1. [a] Experiments from Zhang et al. (1989); [b] Experiments from Chen and Zhang (2008); [c] Experiments from Chen and Zhang (2009); [d] Experiments from Yu et al. (2016); [e] Experiments from Guo and Zhang (2016); [f] Experiments from Guo and Zhang (2020); [g] Experiments from González -Garcia et al. (2017).

2. "OlDisAn" means olivine dissolution in andesite; "DiDisAn" means diopside dissolution in andesite; "QzDisAn" means quartz dissolution in andesite; "RuDisAn" means rutile dissolution in andesite; "PlDisAn" means plagioclase dissolution in andesite; "OlDisBa" means olivine dissolution in basalt; "CpxDisBa" means clinopyroxene dissolution in basalt; "PlDisBa" means plagioclase dissolution in basalt; "DC" means diffusion couple.

Table 5.4. Summary of the 28 $[P_X]$-converted concentration profiles of eigen-components that show obvious uphill diffusion, along with the corresponding experimental conditions. The remaining 1169 profiles of eigen-components are monotonic.

Exp	Base comp	Type	Z_1	Z_2	Z_3	Z_4	Z_5	Z_6	Z_7
Zhang1989_Exp#220 [a]	Andesite	OlDisAn							×
Zhang1989_Exp#225 [a]	Andesite	DiDisAn		×					×
Zhang1989_Exp#234 [a]	Andesite	QzDisAn					×		
Zhang1989_Exp#236RU [a]	Andesite	RuDisAn				×	×	×	
Zhang1989_Exp#259PL [a]	Andesite	PlDisAn						×	×
Yu2016_PlDisBa202 [d]	JDF Basalt	PlDisBa					×		
Yu2016_PlDisBa211 [d]	JDF Basalt	PlDisBa		×			×		
Guo2016_HB3&4A [e]	Haplobasalt	DC	×	×		×			
Guo2016_HB5&6A [e]	Haplobasalt	DC					×		
Guo2016_HB7&8B [e]	Haplobasalt	DC	×						
Guo2016_HB15&16A [e]	Haplobasalt	DC		×	×				
Guo2020_BS11&12C [f]	Basalt	DC		×	×				
Guo2020_BS17&18C [f]	Basalt	DC	×			×			
González2017_P050-H0-4 [g]	Shoshonite & Rhyolite	DC					×		
González2017_P300-H0-4 [g]	Shoshonite & Rhyolite	DC	×	×	×				
González2017_P300-H2-4 [g]	Shoshonite & Rhyolite	DC	×						

Note: see notes in Table 5.3.

5.4 Diffusion mechanism in natural silicate melts

Eigenvector matrix characterizes the diffusion mechanism in natural silicate melts. Previous studies interpreted the diffusion mechanism by directly checking the terms in each eigenvector, with the assumption that the oxide components corresponding to the terms with large absolute values contribute more during diffusion and the oxide components corresponding to the terms with different signs diffuse against each other (e.g., Guo and Zhang, 2018, 2020). However, we note in Eqs. (33)- (34) that it is the terms in the inverse of the eigenvector matrix that comprise the "stoichiometric" coefficients in the formula of eigen-components expressed by oxide components. Instead, the terms in the eigenvector matrix are basically the "stoichiometric"

coefficients to express oxide components by eigen-components. Furthermore, the way of looking at the components in eigenvectors only works for interpreting the exchange mechanism among eigen-components instead of oxide components. As a result, to truly interpret the exchange mechanism among oxide components, it is necessary to first calculate the inverse of the eigenvector matrix. Furthermore, to better understand the diffusion exchange mechanism in natural silicate melts, the eigenvector matrix $[P_X]$ instead of $[P_W]$ should be used.

Table 5.5. The inverse of the eigenvector matrix $[P_X]$.

	SiO_2	TiO_2	$AlO_{1.5}$	FeO	MgO	CaO	$NaO_{0.5}$	$KO_{0.5}$
Z_1	-1.46	-0.42	**1.02**	**0.13**	**0.11**	**0.20**	**0.21**	**0.21**
Z_2	-2.72	**1.45**	**0.14**	**0.30**	**0.29**	**0.28**	**0.18**	**0.09**
Z_3	-0.54	-1.26	**0.02**	**0.42**	**0.61**	**0.52**	**0.25**	-0.02
Z_4	**1.84**	-0.18	-0.22	**0.27**	-1.08	**0.42**	-0.12	-0.93
Z_5	-1.32	-0.09	-0.03	**0.89**	-0.61	**0.26**	**0.12**	**0.78**
Z_6	-2.66	**0.07**	**0.05**	-0.18	**0.37**	**0.69**	**0.09**	**1.57**
Z_7	-3.46	**0.13**	**0.08**	**0.27**	**0.34**	**0.63**	**1.25**	**0.75**

Note: All positive elements are shown in bold. The "SiO_2" term in each row was obtained by the sum of all elements in that row multiplied by -1.

The inverse of $[P_X]$ was calculated and shown in Table 5.5. We see that the Z_1 (one of the two slowest diffusing eigen-components) is due to the exchange between $SiO_2 + TiO_2$ and Al_2O_3 + everything else; Z_2 (the other one of the two slowest diffusing eigen-components) is due to the exchange between SiO_2 and TiO_2 + everything else; Z_3 (the third slowest diffusing eigen-component) is mostly due to the exchange between $TiO_2 + SiO_2$ and divalent cations; Z_4 and Z_5 (the fourth and the third fastest diffusing eigen-components) are mostly due to the exchange between SiO_2 and $MgO + K_2O$, and the exchange between $SiO_2 + MgO$ and $FeO + K_2O$, respectively; Z_6 (the second fastest diffusing eigen-component) are mostly due to the exchange between SiO_2 and $MgO + CaO + K_2O$; Z_7 (the fastest diffusing eigen-component) are mostly due to the exchange between SiO_2 and all alkalis.
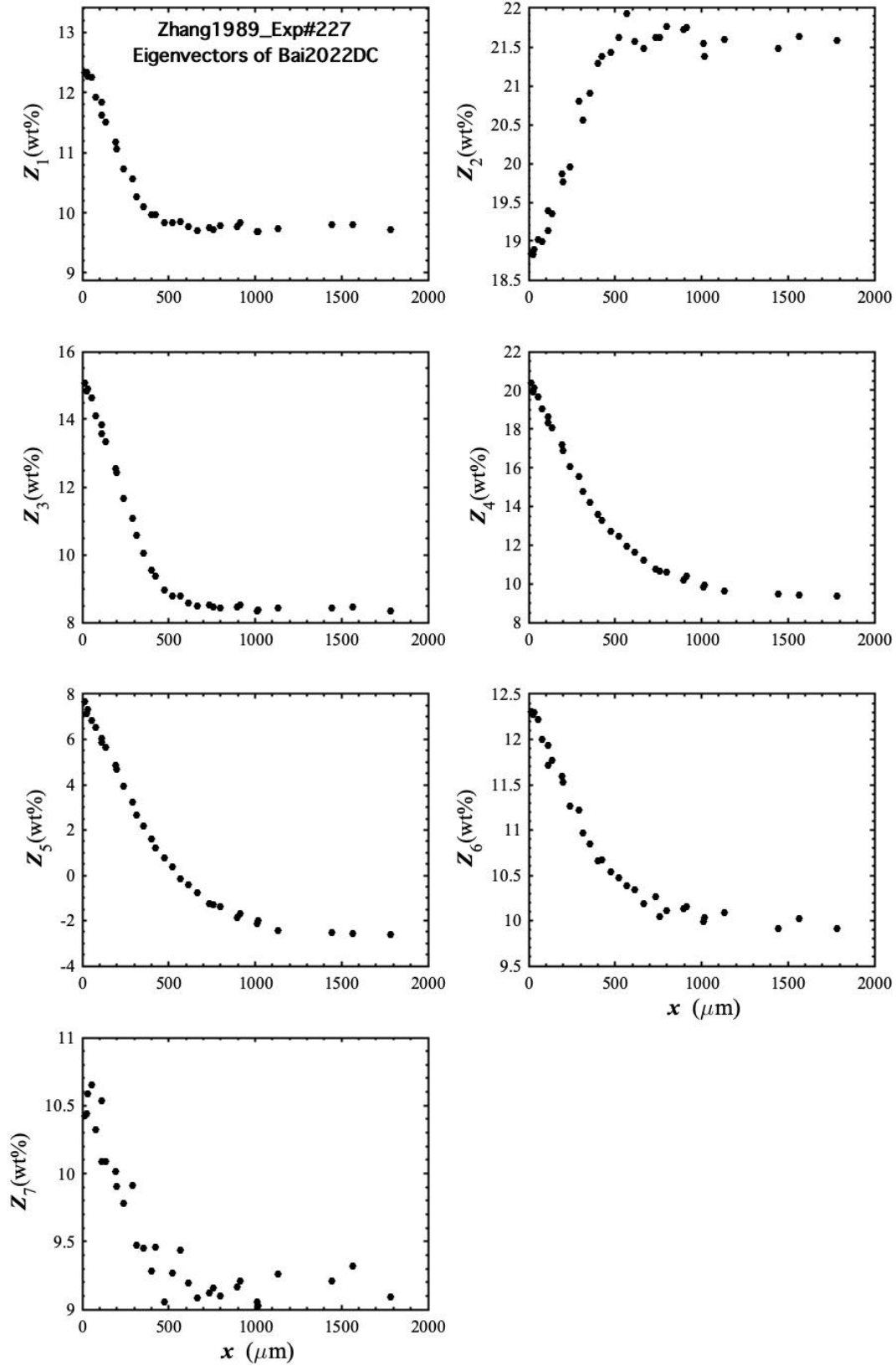
Figure 5.1. $[P_w]$-converted concentration profiles of eigen-components of Exp#227 (Zhang et al., 1989). Exp#227 is a forsterite dissolution experiment in andesite.
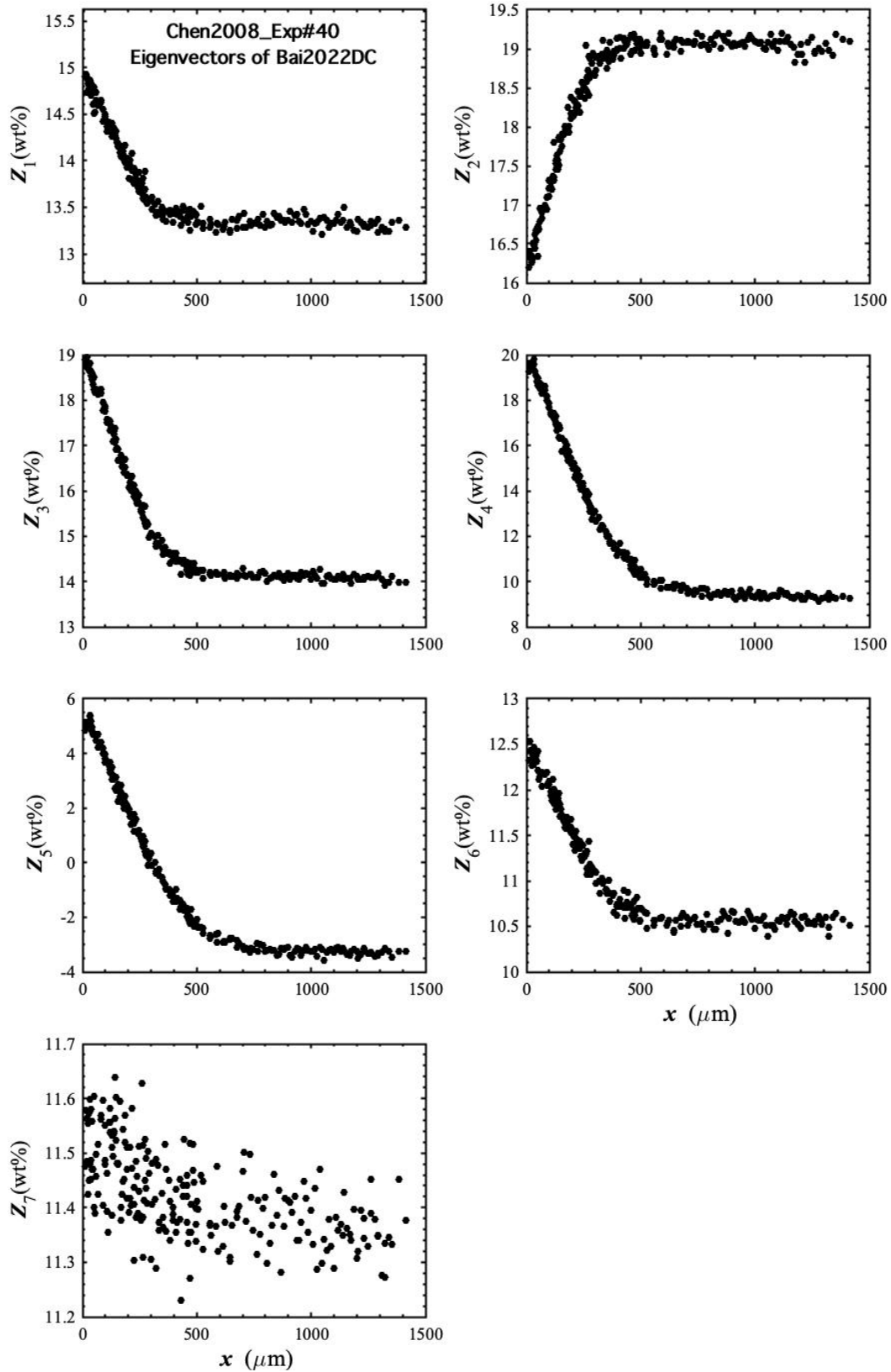
Figure 5.2. $[P_w]$-converted concentration profiles of eigen-components of Exp#40 (Chen and Zhang, 2008). Exp#40 is an olivine dissolution experiment in basalt.
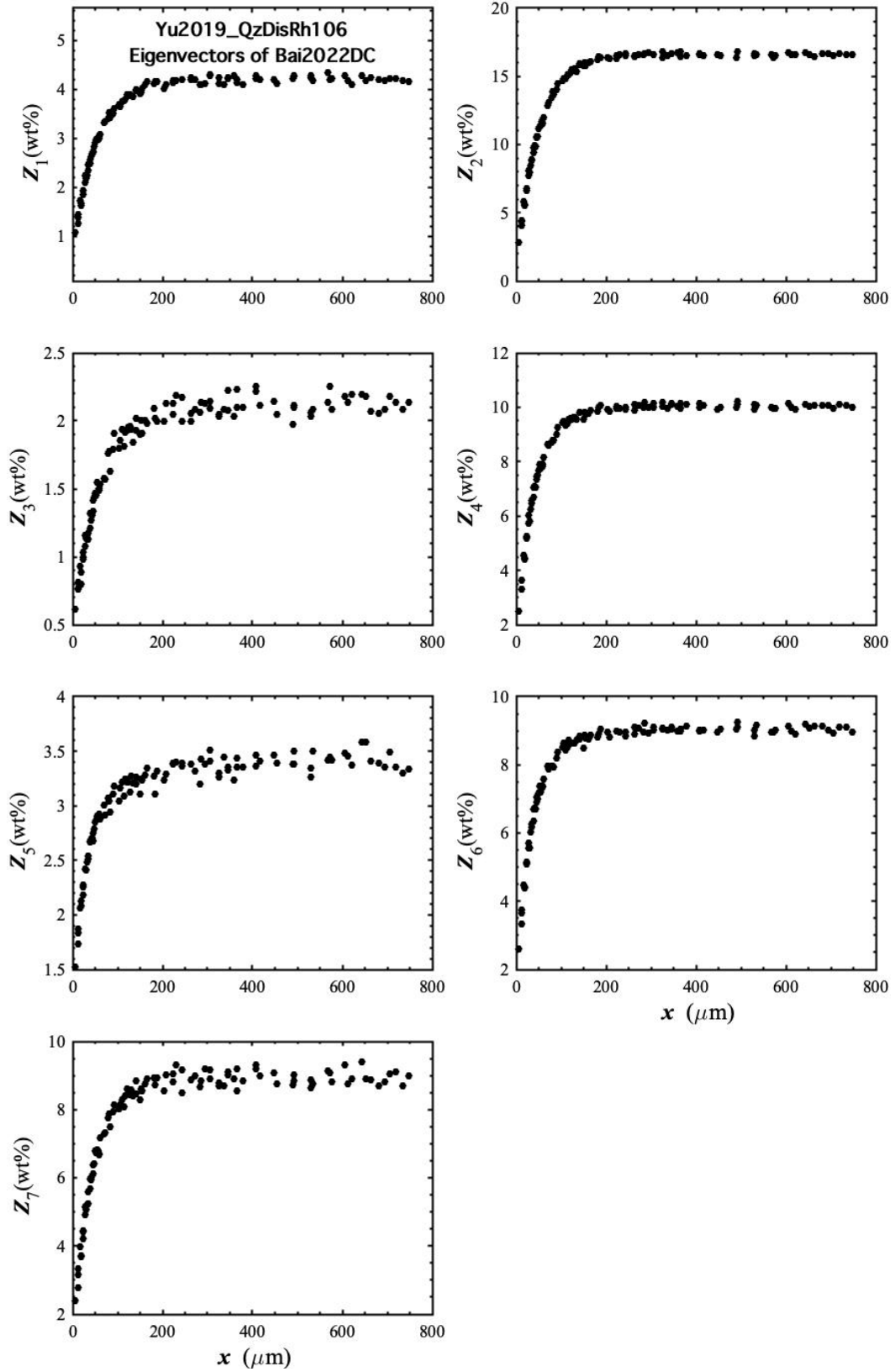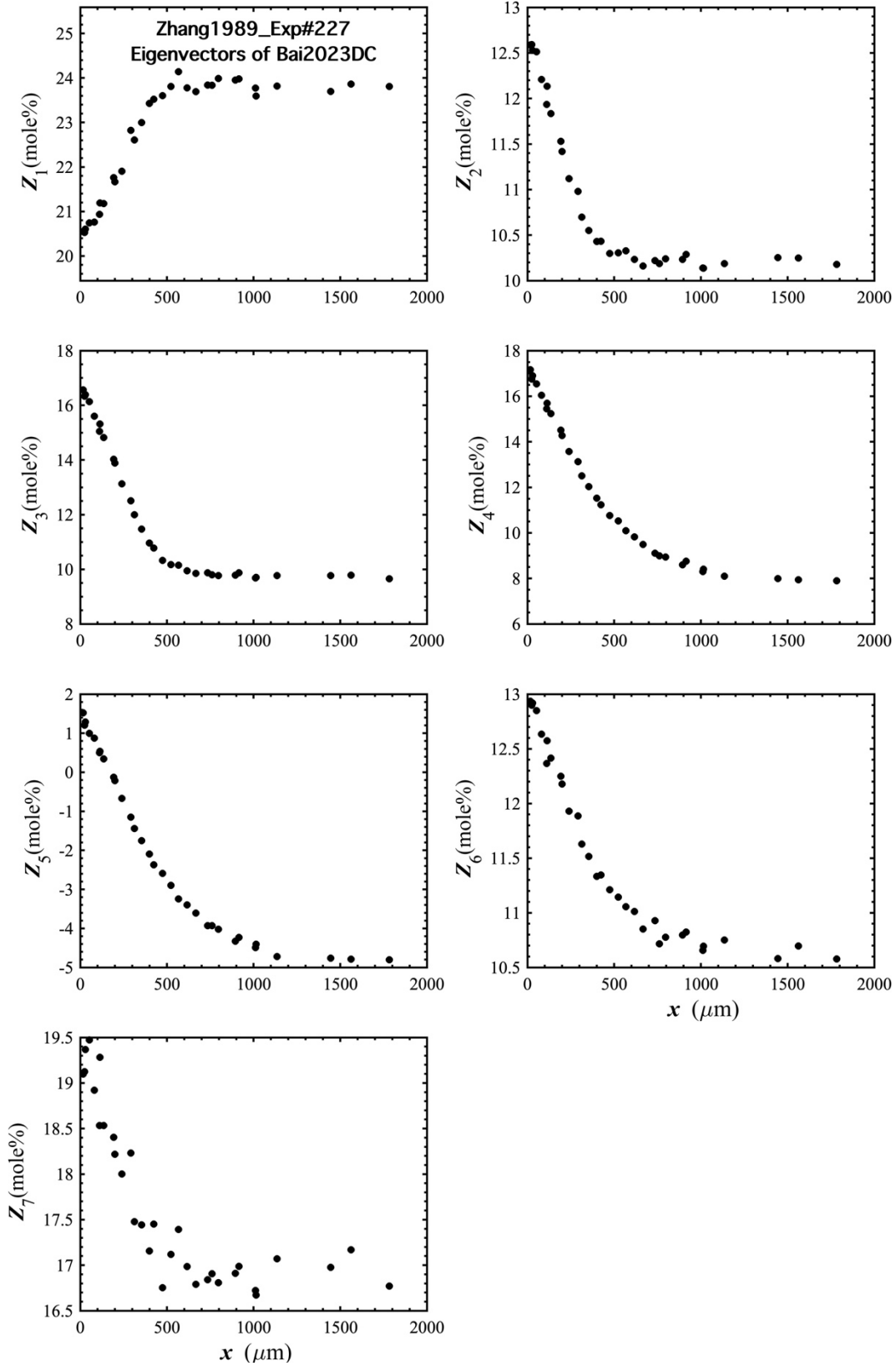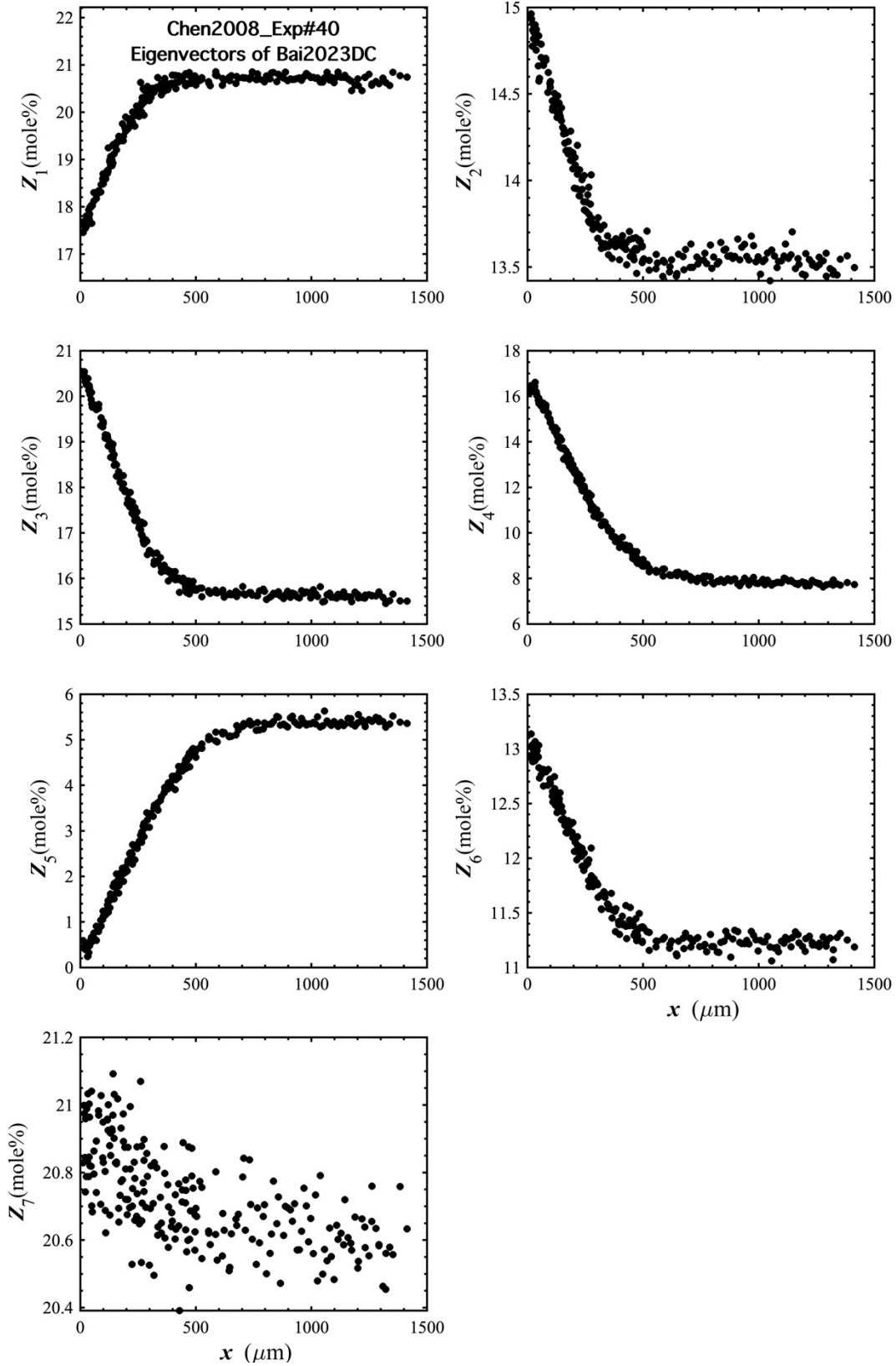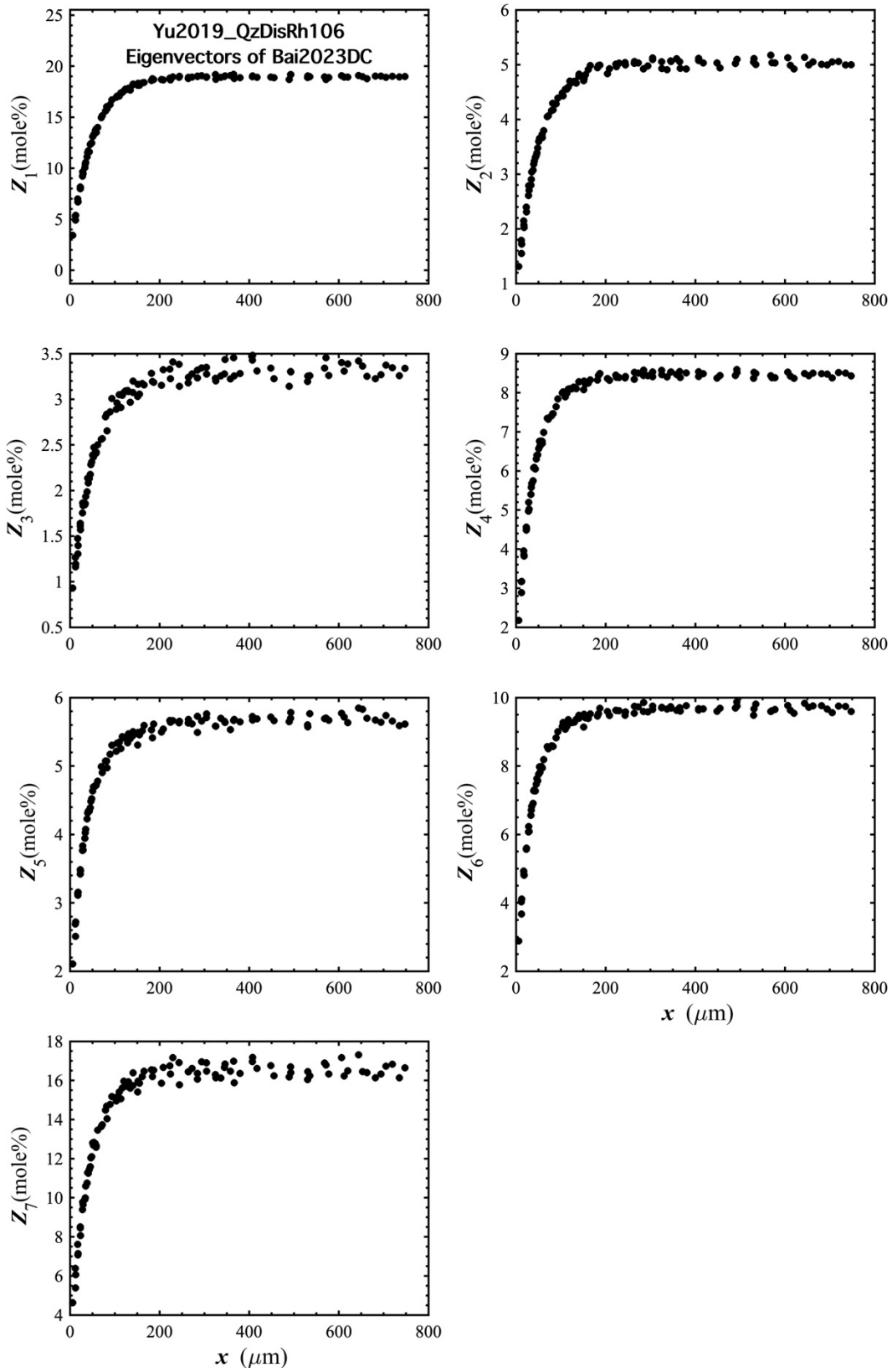
Figure 5.3. $[P_w]$-converted concentration profiles of eigen-components of QzDisRh106 (Yu et al., 2019). QzDisRh106 is a quartz dissolution experiment in rhyolite.

Figure 5.4. [P_X]-converted concentration profiles of eigen-components of Exp#227 (Zhang et al., 1989). Exp#227 is a forsterite dissolution experiment in andesite.

35

Figure 5.5. [P_X]-converted concentration profiles of eigen-components of Exp#40 (Chen and Zhang, 2008). Exp#40 is an olivine dissolution experiment in basalt.

Figure 5.6. [P_X]-converted concentration profiles of eigen-components of QzDisRh106 (Yu et al., 2019). QzDisRh106 is a quartz dissolution experiment in rhyolite.

VI. Summary and Implications

In this study, we hypothesize that there exists a universal diffusion eigenvector matrix in natural silicate melts. The eigenvector matrix and eigenvalue matrices were obtained by simultaneously fitting diffusion profiles from 27 diffusion couple experiments from previous studies (Guo and Zhang, 2018, 2020). Using both mass fraction as concentration and mole fraction as concentration, we obtained two eigenvector matrices, $[P_w]$ and $[P_X]$, respectively. Both eigenvector matrices were used to examine the "concentration" profiles of eigen components. Most profiles of eigen-components from numerous diffusion experiments including diffusion-couple and mineral-dissolution experiments are monotonic and show no obvious uphill diffusion, supporting that the matrix of eigenvectors is invariable with composition. Finally, diffusion mechanism were interpreted from the eigenvector matrix $[P_X]$.

With the universal eigenvector matrix, investigations, and applications of multicomponent diffusion in natural silicate melts would be greatly simplified in different aspects. Theoretically, the diffusion mechanism in natural silicate melts, which is interpreted from the eigenvector matrix, would also be independent of melt composition. And the eigen-components will also be invariable with melt composition. Experimentally, to accurately extract a diffusivity matrix at selected melt composition typically need at least N-1 experiments for an N-component system (e.g., Trial and Spera, 1994). With an accurate eigenvector matrix, however, only a couple experiment may be needed to extract N-1 unknown eigenvalues. In addition, since the eigen-components are universal, characterization of the compositional dependence of eigenvalues would be viable.

Multicomponent diffusion is also key to understanding magma mixing processes, in which two or more magmas come into contact and form a new magma with a different composition. In the absence of convection or other fluid dynamic processes, multicomponent diffusion can be the

exclusive mechanism to account for the complicated compositional variations at the interface of two melts (Chakraborty et al., 1995b). With the universal eigenvector matrix, modeling and prediction of melt composition at the diffusive interface will be simplified. Here we give an example to show compositional variations along the diffusive interface of dacite and basalt at 1500 °C. We did the calculation using our universal eigenvector matrix $[P_X]$, and assuming eigenvalues are 2 times smaller than our optimal eigenvalues at 1500 °C listed in Table 4.3. The calculated profiles are shown in Fig. 6.1. TiO_2, Al_2O_3, FeO, Na_2O and K_2O show clear uphill diffusion features. Specifically, TiO_2, Al_2O_3, and FeO are depleted at $x \approx -400 \ \mu m$, but enriched at $x \approx 400 \ \mu m$, while Na_2O and K_2O exhibit complementary patterns. The melt compositions at $x \approx \pm 400 \ \mu m$ may be captured as inclusions in other melts or early formed crystals. If these melt inclusions reach the surface and are collected as research samples, however, the chemical compositions will be difficult to explain exclusively by a binary mixing model. Therefore, in future studies of magma mixing, the kinetic control of multicomponent diffusion must be considered to explain the potential composition anomalies in melt inclusions.
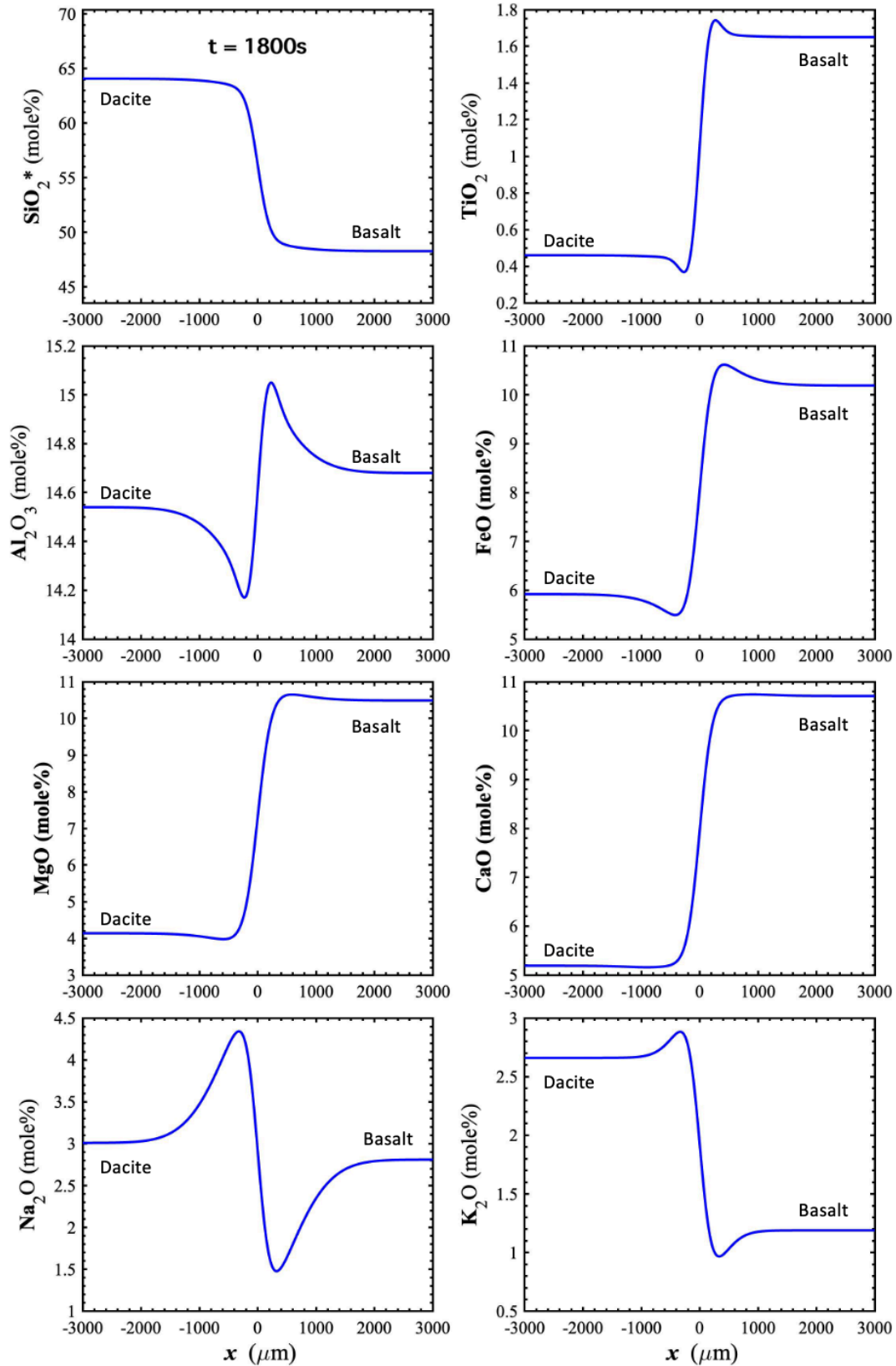
Figure 6.1. Calculated concentration profiles resulting from magma mixing between dacite and basalt at 1500 °C, using the eigenvector matrix $[P_X]$ and assuming eigenvalues are 2 times smaller than our optimal eigenvalues at 1500 °C listed in Table 4.3.

References

Broyden, C.G. (1970) The Convergence of a Class of Double-rank Minimization Algorithms. *J. Inst. Maths Applies* 6, 76-90, 222-231.

Chakraborty, S., Dingwell, D.B., Rubie, D.C. (1995a) Multicomponent diffusion in ternary silicate melts in the system K2O-Al2O3-SiO2: I. Experimental measurements. *Geochim. Cosmochim. Acta* 59, 255–264.

Chakraborty, S., Dingwell, D.B., Rubie, D.C. (1995b) Multicomponent diffusion in ternary silicate melts in the system K2O-Al2O3-SiO2: II. Mechanisms, systematics, and geological applications. *Geochim. Cosmochim. Acta* 59, 265–277.

Chen, Y., Zhang, Y. (2008) Olivine dissolution in basaltic melt. *Geochim. Cosmochim. Acta* 72, 4756–4777.

Chen, Y., Zhang, Y. (2009) Clinopyroxene dissolution in basaltic melt. *Geochim. Cosmochim. Acta* 73, 5730–5747.

Clifford, A.A. (1973) Multivariate error analysis: a handbook of error propagation and calculation in many-parameter system. Wiley, NY.

Cooper, A.R. (1968) The use and limitations of the concept of an effective binary diffusion coefficient for multi-component diffusion. In: Wachman, J.B., Franklin, A.D. (Eds.), Mass Transport in Oxides. *Nat. Bur. Stand. Spec. Publ*, pp. 79–84.

Fletcher, R. (1970) A new approach to variable metric algorithms. *The Computer Journal* 13, 317-322.

Goldfarb, D. (1970) A Family of Variable-Metric Methods Derived by Variational Means. *Mathematics of Computation* 24, 23-26.

González-Garcia, D., Behrens, H., Petrelli, M., Vetere, F., Morgavi, D., Zhang, C., Perugini, D. (2017) Water-enhanced interdiffusion of major elements between natural shoshonite and high-K rhyolite melts. *Chem. Geol.* 466, 86–101.

Guo, C., Zhang, Y. (2016) Multicomponent diffusion in silicate melts: SiO_2-TiO_2-Al_2O_3-MgO-CaO-Na_2O-K_2O system. *Geochim. Cosmochim. Acta* 195, 126–141.

Guo, C., Zhang, Y. (2018) Multicomponent diffusion in basaltic melts at 1350°C. *Geochim. Cosmochim. Acta* 228, 190–204.

Guo, C., Zhang, Y. (2020) Multicomponent diffusion in a basaltic melt: Temperature dependence. *Chem. Geol.* 549, 119700.

Gupta P.K., Cooper A.R. (1971) The [D] matrix for multicomponent diffusion. *Physica* 54, 39-59.

Kirkwood, J.G. (1960) Flow Equations and Frames of Reference for Isothermal Diffusion in Liquids. *J. Chem. Phys.* 33, 1505-1513.

Koyaguchi, T. (1985) Magma mixing in a conduit. *J. Volcanol. Geotherm. Res.* 25, 365–369.

Koyaguchi, T. (1989) Chemical gradient at diffusive interfaces in magma chambers. *Contrib. Mineral. Petrol.* 103, 143–152.

Kress, V.C., Ghiorso, M.S. (1993) Multicomponent diffusion in $MgO-Al_2O_3-SiO_2$ and $CaO-MgO-Al_2O_3-SiO_2$ melts. *Geochim. Cosmochim. Acta* 57, 4453–4466.

Lasaga, A.C. (1979) Multicomponent exchange and diffusion in silicates. *Geochim. Cosmochim. Acta* 54, 2709–2715.

Li, D., Fukushima., M. (2001a) A modified BFGS method and its global convergence in nonconvex minimization. *J. Comput. Appl. Math.* 129, 15–35.

Li, D., Fukushima., M. (2001b) On the global convergence of the BFGS method for nonconvex unconstrained optimization problems. *Siam J. Optim.* Vol. 11, No. 4, 1054–1064.

Liang, Y., Davis, A.M. (2002) Energetics of multicomponent diffusion in molten $CaO-Al_2O_3-SiO_2$. *Geochim. Cosmochim. Acta* 66, 635–646.

Liang, Y., Richter, F.M., Watson, E.B. (1996) Diffusion in silicate melts, II: multicomponent diffusion in $CaO-Al_2O_3-SiO_2$ at 1500°C and 1 GPa. *Geochim. Cosmochim. Acta* 60, 5021–5035.

Liang, Y. (2010) Multicomponent diffusion in molten silicates: theory, experiments, and geological application. *Rev. Mineral. Geochem.* 72, 409–446.

Miller, D.G., Vitagliano, V., Sartorio, R. (1986) Some comments on multicomponent diffusion: Negative main term diffusion coefficients, second law constrains, solvent choices, and reference frame. *J. Phys. Chem.* 90, 1509-1519.

Morgan, Z.T., Liang, Y., Hess., P.C. (2006) An experimental study of the kinetics of anorthite dissolution in lunar picritic magmas with applications to lunar crustal assimilation processes. *Geochim. Cosmochim. Acta* 70, 3477–3491.

Mungall, J.E., Romano, C., Dingwell, D.B. (1998) Multicomponent diffusion in the molten system K_2O-Na_2O-Al_2O_3-SiO_2-H_2O. *Am. Mineral.* 83, 685–699.

Oldenburg, C.M., Spera, F.J., Yuen, D.A., Sewell, G. (1989) Dynamic mixing in magma bodies: theory, simulations, and implications. *J. Geophys. Res.* 94, 9215–9236.

Onsager, L. (1945) Theories and problems of liquid diffusion. *Ann. New York Acad. Sci.* 46, 241–265.

Oishi, Y., Nanba, M., Pask, J. A. (1982) Analysis of liquid-state interdiffusion in the system CaO–Al_2O_3–SiO_2 using multiatomic ion models. J. Am. Ceram. Soc. 65, 247–253.

Pablo, H., Schuller, S., Toplis, M.J., Gouillart, E., Mostefaoui, S., Charpetier, T., Roskosz, M. (2017) Multicomponent diffusion in sodium borosilicate glasses. *J. Non-Cryst. Sol.* 478, 29–40.

Richter, F., Liang, Y., Minarik, W.G. (1998) Multicomponent diffusion and convection in molten MgO-Al_2O_3-SiO_2. *Geochim. Cosmochim. Acta* 62, 1985–1991.

Sato, H. (1975) Diffusion coronas around quartz xenocrysts in andesite and basalt from Tertiary volcanic region in northeastern Shikoku, Japan. *Contrib. Mineral. Petrol.* 50, 49–64.

Shanno, D.F. (1970) Conditioning of Quasi-Newton Methods for Function Minimization. *Mathematics of Computation* 24, 647-656.

Sugawara, H., Nagata, K., Goto, K.S. (1977) Interdiffusivities matrix of CaO-Al_2O_3-SiO_2 melt at 1723 K to 1823 K. *Metall. Trans. A.* 8B, 605–612.

Varshneya, A.K., Cooper, A.R. (1972) Diffusion in the system K_2O-SrO-SiO_2: III, Interdiffusion coefficients. *J. Amer. Ceram. Soc.* 55, 312-317.

Wang, C., Cascio, M.L., Liang, Y., Xu., W. (2020) An experimental study of peridotite dissolution in eclogite-derived melts: Implications for styles of melt-rock interaction in lithospheric mantle beneath the North China Craton. *Geochim. Cosmochim. Acta* 278, 157-176.

Watson, E.B. (1982) Basalt contamination by continental crust: some experiments and models. *Contrib. Mineral. Petrol.* 80, 73–87.

Yu, Y., Zhang, Y., Chen, Y., Xu, Z. (2016) Kinetics of anorthite dissolution in basaltic melt. *Geochim. Cosmochim. Acta* 179, 257–274.

Yu, Y., Zhang, Y., Yang, Y. (2019) Kinetics of quartz dissolution in natural silicate melts and dependence of SiO_2 diffusivity on melt composition. *ACS Earth Space Chem.* 3, 599–616.

Zhang, Y. (1993) A modified effective binary diffusion model. *J. Geophys. Res.* 98, 11901–11920.

Zhang, Y. (2010) Diffusion in Minerals and Melts: Theoretical Background. *Rev. Mineral. Geochem.* 72, 311–408.

Zhang, Y., Walker, D., Lesher, C.E. (1989) Diffusive crystal dissolution. *Contrib. Mineral. Petrol.* 102, 492–513.

Zhang, Y., Gan, T. (2010) Diffusion in Melts and Magmas. *Rev. Mineral. Geochem.* 87, 283–337.

Appendix A

Derivation of an explicit expression of Jacobian matrix

The Jacobian matrix, which is defined in Eq. (50), is a key parameter in the fitting process. It determines both the search direction (see Eq. (40)) and the 1-σ error of optimal fitting parameters (see Eq. (51)). The Jacobian matrix can be easily obtained using a "universal" numerical method. One disadvantage of the method is that the calculated matrix may not be accurate. Thus, if there is a high demand for data accuracy and the function is not too complicated, one may try to derive an explicit expression of Jacobian matrix. We see that the Jacobian matrix in our case is essentially the partial derivatives of oxide concentrations with respect to eigenvector matrix and eigenvalues. Thus, once such partial derivatives are explicitly expressed, the Jacobian matrix can be accurately obtained.

In an N-component melt system, choose the Nth oxide component as the dependent component. Let $n = N - 1$ and w_i be the mass fraction of the ith oxide component. Then according to mass conservation, we have

$$w_N = 100\% - \sum_{i=1}^{n} w_i \tag{A1}$$

Define the concentration vector $\boldsymbol{w}$ as follows:

$$\boldsymbol{w} = \begin{pmatrix} w_1 \\ w_2 \\ \vdots \\ w_n \end{pmatrix} \tag{A2}$$

Assuming a constant diffusivity matrix, the analytical solution to an infinite diffusion couple is given by:

$$\boldsymbol{w} = \frac{\boldsymbol{w_2} + \boldsymbol{w_1}}{2} + [P] \times [E] \times [P^{-1}] \times \frac{\boldsymbol{w_2} - \boldsymbol{w_1}}{2} \tag{A3}$$

where w_1 and w_2 are initial melt concentration vectors at $x < 0$ and $x > 0$, $[P]$ is eigenvector matrix and $[E]$ is a diagonal matrix:

$$[E] = \begin{bmatrix} \mathrm{erf}\left(\frac{x-x_0}{\sqrt{4e^{\theta_1}t}}\right) & & \\ & \ddots & \\ & & \mathrm{erf}\left(\frac{x-x_0}{\sqrt{4e^{\theta_n}t}}\right) \end{bmatrix}$$

$$= \begin{bmatrix} \mathrm{erf}\left(\frac{x-x_0}{\sqrt{4t}}e^{-\frac{\theta_1}{2}}\right) & & \\ & \ddots & \\ & & \mathrm{erf}\left(\frac{x-x_0}{\sqrt{4t}}e^{-\frac{\theta_n}{2}}\right) \end{bmatrix} \tag{A4}$$

Define $\boldsymbol{\theta}$ vector as follows:

$$\boldsymbol{\theta} = \begin{pmatrix} \theta_1 \\ \vdots \\ \theta_n \end{pmatrix} \tag{A5}$$

Now let's derive the partial derivative of $\boldsymbol{w}$ with respect to $[P]$ and $\boldsymbol{\theta}$.

Define $\boldsymbol{Y}$ vector as follows:

$$\boldsymbol{Y} = \begin{pmatrix} \frac{x-x_0}{\sqrt{4t}}e^{-\frac{\theta_1}{2}} \\ \vdots \\ \frac{x-x_0}{\sqrt{4t}}e^{-\frac{\theta_n}{2}} \end{pmatrix} = \frac{x-x_0}{\sqrt{4t}}e^{-\frac{\boldsymbol{\theta}}{2}} \tag{A6}$$

Then $[E]$ matrix can be expressed by $\boldsymbol{Y}$:

$$[E] = \mathrm{diag}\begin{pmatrix} \mathrm{erf}\left(\frac{x-x_0}{\sqrt{4t}}e^{-\frac{\theta_1}{2}}\right) \\ \vdots \\ \mathrm{erf}\left(\frac{x-x_0}{\sqrt{4t}}e^{-\frac{\theta_n}{2}}\right) \end{pmatrix} = \mathrm{diag}\big(\mathrm{erf}\,(\boldsymbol{Y})\big) \tag{A7}$$

where diag is a function so that $\mathrm{diag}(v)$ returns a square diagonal matrix with the elements of vector v on the main diagonal and $\mathrm{diag}([A])$ returns a column vector of the main diagonal elements of matrix $[A]$.

In Eq. (A3), take the total differential of $\boldsymbol{w}$:

$$\mathbf{d}\,w = \mathbf{d}\,[P] \times [E] \times [P^{-1}] \times \frac{w_2 - w_1}{2} + [P] \times \mathbf{d}\,[E] \times [P^{-1}] \times \frac{w_2 - w_1}{2}$$

$$+ [P] \times [E] \times \mathbf{d}\,[P^{-1}] \times \frac{w_2 - w_1}{2} \tag{A8}$$

Our next step is to express the total differential of w by the total differential of $[P]$ and $\boldsymbol{\theta}$. There are three terms on the right-hand side (RHS) of Eq. (A8), but only the first term is a desired form. Now let's calculate $\mathbf{d}\,[E]$ in the second term and $\mathbf{d}\,[P^{-1}]$ in the third term on the RHS of Eq. (A8). In the following part, we use the symbol $\odot$ to denote the entry wise product of two vectors (or two matrices) of the same size and use the symbol $\otimes$ to denote Kronecker product of two matrices.

In Eq. (A7), take the total differential of $[E]$:

$$\mathbf{d}\,[E] = \mathbf{d}\,\mathrm{diag}(\mathrm{erf}(Y)) = \mathrm{diag}(\mathbf{d}\,\mathrm{erf}(Y))$$

$$= \mathrm{diag}\left(\frac{2}{\sqrt{\pi}} e^{-Y \odot Y} \odot \mathbf{d}\,Y\right)$$

$$= \mathrm{diag}\left(\frac{2}{\sqrt{\pi}} e^{-Y \odot Y} \odot \mathbf{d}\left(\frac{x - x_0}{\sqrt{4t}} e^{-\frac{\theta}{2}}\right)\right)$$

$$= \mathrm{diag}\left(\frac{2}{\sqrt{\pi}} e^{-Y \odot Y} \odot \left(\frac{x - x_0}{\sqrt{4t}} * \left(-\frac{1}{2}\right) * e^{-\frac{\theta}{2}} \odot \mathbf{d}\,\boldsymbol{\theta}\right)\right)$$

$$= \mathrm{diag}\left(\frac{-(x - x_0)}{\sqrt{4\pi t}} e^{-Y \odot Y} \odot e^{-\frac{\theta}{2}} \odot \mathbf{d}\,\boldsymbol{\theta}\right)$$

$$= \mathrm{diag}\left(\frac{-(x - x_0)}{\sqrt{4\pi t}} e^{-Y \odot Y} \odot e^{-\frac{\theta}{2}}\right) \odot \mathbf{d}\,(\mathrm{diag}\,\boldsymbol{\theta})$$

$$= [dE] \odot \mathbf{d}\,(\mathrm{diag}\,\boldsymbol{\theta}) \tag{A9}$$

where the matrix $[dE]$ is defined as:

$$[dE] = \mathrm{diag}\left(\frac{-(x - x_0)}{\sqrt{4\pi t}} e^{-Y \odot Y} \odot e^{-\frac{\theta}{2}}\right) \tag{A10}$$

Therefore, the second term on the RHS of Eq. (A8) can be expressed as follows:

$$[P] \times \mathbf{d}\,[E] \times [P^{-1}] \times \frac{w_2 - w_1}{2}$$

$$= [P] \times \left([dE] \odot \mathbf{d}\,(\mathrm{diag}\,\boldsymbol{\theta})\right) \times [P^{-1}] \times \frac{w_2 - w_1}{2} \tag{A11}$$

$\mathbf{d}\,[P^{-1}]$ in the third term on the RHS of Eq. (A8) can be calculated as follows:

$$\mathbf{d}\,[P^{-1}] = -[P^{-1}] \times \mathbf{d}\,[P] \times [P^{-1}] \tag{A12}$$

Plugging Eq. (A11) and Eq. (A12) into Eq. (A8), leads to:

$$\mathbf{d}\,w = \mathbf{d}\,[P] \times [E] \times [P^{-1}] \times \frac{w_2 - w_1}{2}$$

$$+ [P] \times \left([dE] \odot \mathbf{d}\,(\mathrm{diag}\,\boldsymbol{\theta})\right) \times [P^{-1}] \times \frac{w_2 - w_1}{2} \tag{A13}$$

$$- [P] \times [E] \times [P^{-1}] \times \mathbf{d}\,[P] \times [P^{-1}] \times \frac{w_2 - w_1}{2}$$

Now we have expressed the total differential of $\boldsymbol{w}$ by the total differentials of $[P]$ and diag $\boldsymbol{\theta}$. To make sure that the partial derivative of $\boldsymbol{w}$ with respect with respect to $[P]$ and diag $\boldsymbol{\theta}$ is a 2-dimensional matrix, we need to convert $[P]$ and diag $\boldsymbol{\theta}$ into 1-dimenal column vectors.

Taking the vectorization of first term on the RHS of Eq. (A13), leads to

$$\mathrm{vec}\left(\mathbf{d}\,[P] \times [E] \times [P^{-1}] \times \frac{w_2 - w_1}{2}\right)$$

$$= \left(\left([E] \times [P^{-1}] \times \frac{w_2 - w_1}{2}\right)^{\mathrm{T}} \otimes [I_n]\right) \times \mathrm{vec}(\mathbf{d}\,[P]) \tag{A14}$$

where $[I_n]$ is an n square identity matrix.

Taking the vectorization of second term on the RHS of Eq. (A13), leads to

$$\mathrm{vec}\left([P] \times \left([dE] \odot \mathbf{d}\,(\mathrm{diag}\,\boldsymbol{\theta})\right) \times [P^{-1}] \times \frac{w_2 - w_1}{2}\right)$$

$$= \left(\left([P^{-1}] \times \frac{w_2 - w_1}{2}\right)^{T} \otimes [P]\right) \times vec\left([dE] \odot \mathbf{d}\,(\mathrm{diag}\,\boldsymbol{\theta})\right)$$

$$= \left(\left([P^{-1}] \times \frac{w_2 - w_1}{2}\right)^{T} \otimes [P]\right) \times \mathrm{diag}\left(\mathrm{vec}([dE])\right) \times \mathrm{vec}\left(\mathbf{d}\,(\mathrm{diag}\,\boldsymbol{\theta})\right) \tag{A15}$$

And taking the vectorization of last term on the RHS of Eq. (A13), we have

$$\text{vec}\left(-[P] \times [E] \times [P^{-1}] \times \mathbf{d}\,[P] \times [P^{-1}] \times \frac{\mathbf{w_2} - \mathbf{w_1}}{2}\right)$$

$$= -\left(\left([P^{-1}] \times \frac{\mathbf{w_2} - \mathbf{w_1}}{2}\right)^T \otimes ([P] \times [E] \times [P^{-1}])\right) \times \text{vec}(\mathbf{d}\,[P]) \tag{A16}$$

According to Eqs. (A14) -(A16), the vectorization of $\mathbf{d}\,\mathbf{w}$ is as following:

$$\text{vec}(\mathbf{d}\,\mathbf{w})$$

$$= \left\{\left(\left([E] \times [P^{-1}] \times \frac{\mathbf{w_2} - \mathbf{w_1}}{2}\right)^T \otimes [I_n]\right) - \left(\left([P^{-1}] \times \frac{\mathbf{w_2} - \mathbf{w_1}}{2}\right)^T \otimes ([P] \times [E] \times [P^{-1}])\right)\right\} \times vec(\mathbf{d}\,[P])$$

$$+ \left(\left([P^{-1}] \times \frac{\mathbf{w_2} - \mathbf{w_1}}{2}\right)^T \otimes [P]\right) \times \text{diag}(\text{vec}([dE])) \times \text{vec}(\mathbf{d}\,(\text{diag}\,\boldsymbol{\theta})) \tag{A17}$$

Therefore, the partial derivative of $\mathbf{w}$ with respect to $[P]$ can be expressed as:

$$[w_P] = \frac{\partial \mathbf{w}}{\partial [P]} = \left\{\left(\left([E] \times [P^{-1}] \times \frac{\mathbf{w_2} - \mathbf{w_1}}{2}\right)^T \otimes [I_n]\right) - \left(\left([P^{-1}] \times \frac{\mathbf{w_2} - \mathbf{w_1}}{2}\right)^T \otimes ([P] \times [E] \times [P^{-1}])\right)\right\}^T$$

$$= \left(\left([E] \times [P^{-1}] \times \frac{\mathbf{w_2} - \mathbf{w_1}}{2}\right)^T \otimes [I_n]\right) - \left(\left([P^{-1}] \times \frac{\mathbf{w_2} - \mathbf{w_1}}{2}\right) \otimes ([P] \times [E] \times [P^{-1}])^T\right) \tag{A18}$$

And the partial derivative of $\mathbf{w}$ with respect to $[\text{diag}\,\boldsymbol{\theta}]$ can be expressed as:

$$[w_{\text{diag}\,\theta}] = \frac{\partial \mathbf{w}}{\partial [\text{diag}\,\boldsymbol{\theta}]} = \left\{\left(\left([P^{-1}] \times \frac{\mathbf{w_2} - \mathbf{w_1}}{2}\right)^T \otimes [P]\right) \times \text{diag}(\text{vec}([dE]))\right\}^T$$

$$= \text{diag}(\text{vec}([dE])) \times \left(\left([P^{-1}] \times \frac{\mathbf{w_2} - \mathbf{w_1}}{2}\right) \otimes [P^T]\right) \tag{A19}$$

According to Eq. (A1), we have:

$$\mathbf{d}\,w_N = -\sum_{i=1}^{n} \mathbf{d}\,w_i \tag{A20}$$

Therefore, the partial derivatives of w_N with respect to $[P]$ and $[\text{diag}\,\boldsymbol{\theta}]$ are as follows:

$$\frac{\partial w_N}{\partial [P]} = -\sum_{i=1}^{n} [w_P](:,i) \tag{A21}$$

and

49

$$\frac{\partial w_N}{\partial [\text{diag } \boldsymbol{\theta}]} = -\sum_{i}^{n} [w_{\text{diag } \theta}](:, i) \tag{A22}$$

where $[w_P](:, i)$ is the ith column of matrix $[w_P]$ and $[w_{\text{diag } \theta}](:, i)$ is the ith column of matrix $[w_{\text{diag } \theta}]$.

If we use the symbol $\oslash$ to express the element-wise division of two vectors of the same size, then the vector of residual difference can be expressed by the formula:

$$\boldsymbol{r} = (\boldsymbol{w_0} - \boldsymbol{w}) \oslash \boldsymbol{\sigma} \tag{A23}$$

where $\boldsymbol{w_0}$ is the vector of measured concentrations of n independent oxide components, $\boldsymbol{\sigma}$ is the 1-σ error on $\boldsymbol{w_0}$.

Then the partial derivatives of $\boldsymbol{r}$ with respect to $[P]$ and $[\text{diag } \boldsymbol{\theta}]$ are given by:

$$[r_P] = \frac{\partial \boldsymbol{r}}{\partial [P]} = -\frac{\partial \boldsymbol{w}}{\partial [P]} \oslash \boldsymbol{\sigma} = -[w_P] \oslash \boldsymbol{\sigma} \tag{A24}$$

and

$$[r_{\text{diag } \theta}] = \frac{\partial \boldsymbol{r}}{\partial [\text{diag } \boldsymbol{\theta}]} = -\frac{\partial \boldsymbol{w}}{\partial [\text{diag } \boldsymbol{\theta}]} \oslash \boldsymbol{\sigma} = -[w_{\text{diag } \theta}] \oslash \boldsymbol{\sigma} \tag{A25}$$

where $[w_P]$ and $[w_{\text{diag } \theta}]$ can be obtained by Eq. (A18) and Eq. (A19), respectively.

Finally, the partial derivative of the residual difference r_N of the Nth components are given by:

$$\frac{\partial r_N}{\partial [P]} = \frac{\partial \dfrac{(w_{0,N} - w_N)}{\sigma_N}}{\partial [P]} = -\frac{1}{\sigma_N} \frac{\partial w_N}{\partial [P]} \tag{A26}$$

and

$$\frac{\partial r_N}{\partial [\text{diag } \boldsymbol{\theta}]} = \frac{\partial \dfrac{(w_{0,N} - w_N)}{\sigma_N}}{\partial [\text{diag } \boldsymbol{\theta}]} = -\frac{1}{\sigma_N} \frac{\partial w_N}{\partial [\text{diag } \boldsymbol{\theta}]} \tag{A27}$$

where $\frac{\partial w_N}{\partial [P]}$ and $\frac{\partial w_N}{\partial [\mathrm{diag}\,\boldsymbol{\theta}]}$ can be obtained by Eq. (A21) and Eq. (A22).

Once all derivatives of all residual differences are calculated, according to Eq. (50), the Jacobian

matrix can be obtained.

Appendix B

MATLAB codes for fitting diffusion profiles

B1. Main program "BFGS_Main.m"

```
%% this program uses the BFGS method to obtain eigenvectors and eigenvalues
by simultaneously fitting diffusion profiles.

% Input parameters are stored in the files: "Initial_beta.xlsx"
% Input parameters should be a 10×7 matrix, with the last 7 rows
% being eigenvector matrix and the first 3 rows being eigenvalues.

% Once the program ends, the reduced chi-square is stored as the variable
% "S_DF", fitted parameters are stored as "trans_beta" and the 1-sigma errors
% are sorted as "error_trans_beta".


close all;
clear all;
start_time = clock();

%% ---------------------------define a structure---------------------------
data.temp= 1260; %1260, 1350,1500
data.type= 1;% 1:diffusion couple(DC); 2:mineral dissolution(MD)
data.np = 100; % number of points for each exp
data.dist = 1;
% for DC: data.dist is the location of the interface ; for MD: data.dist is
the growth thickness of the melt
data.time = 1000;% exp duration
data.boundary = [];%boundary condition; size:[8,2]
data.x = [];% x-coordinate;[np,1]
data.w = [];% concentration;[np,8]
data.w_calc = []; % predicted concentration;[np,8];
data.error=[]; % error of concentration measured by EMPA


%% ----------------------------initialization---------------------------
T = [1260,1350,1500];%exp temp

% exp duration at different temp
t1 = [1826.0, 1809.6, 1325.5, 1269.2, 950.8, 579.5, 740.0, 577.4, 599.9,...
    335.4, 1981.2, 395.3]; % exp duration at 1260
t2 = [1492.4, 1243.2, 899.0, 974.4, 563.9, 393.6, 522.0, 335.7, 346.3, ...
         298, 1163, 601, 742, 1611, 395, 3087, 121, 2138]; % at 1350
t3 = [276.1, 223.6, 247.8, 213.7, 158.5, 157.1, 154.8, 184.9, 221.4]; % at
1500
t=[t1,t2,t3];

% num of points of each exp
Np1 = [112,121,128,140,97,146,123,128,120,146,54,102];
% number of points of exp at 1260
Np2 = [116,84,100,109,105,101,64,122,123,191,226,183,191,152,136,166,91,160];
% number of points at 1350
```

```matlab
Np3 = [92,124,116,118,120,141,131,141,166];
% number of points at 1500
Np=[Np1,Np2,Np3];

Ndm = [12,18,9]; % number of exp at 1260, 1350 and 1500
threshold = [0,12,30]; % no actual meaning, just for reading data

% x0 and L of each exp
% for diffusion couple exp, we have already adjusted x0 to be 0
A1 = [0.158, 0.12, 0.295];
% constant alpha in mineral dissolution exp at 1260
L1 = 2*A1.*sqrt(t1(10:12));
% growth thickness of the melt in mineral dissolution exp at 1260
A2 = [0.5174, 0.5174, 0.5174, 1.1961, 0.9985, 0.9985, 0.9985, 0.9985,
0.9985];
%constant alpha at 1350

L2 = 2*A2.*sqrt(t2(10:18)); % growth thickness of the melt at 1350
L = [zeros(1,9),L1,zeros(1,9),L2,zeros(1,9)];

Nexp = 39; % total number of exp

%read data
for i=1:3
    T_str = string(T(i));
    realdata = xlsread(strcat(T_str,"_RealData_8Comp.xlsx"));
    realerror = xlsread(strcat(T_str,"_RealError_8Comp.xlsx"));
    realboundary = xlsread(strcat(T_str,"_RealBoundary_8Comp.xlsx"));

    for j=1:Ndm(i)
        j1 = j+threshold(i);
        data(j1).temp = T(i);

        if j<10
            data(j1).type = 1;
        else
            data(j1).type = 2;
        end

        data(j1).np= Np(j1);
        data(j1).dist = L(j1);
        data(j1).time= t(j1);
        data(j1).boundary = realboundary(1:8,(3*j-2):(3*j-1));
        data(j1).x = realdata(1:Np(j1),12*j-11);
        data(j1).w = realdata(1:Np(j1),(12*j-10):(12*j-3));
        data(j1).error=realerror(:,j);

    end
end

% read initial beta
read_b = xlsread("Initial_beta.xlsx");

%% --------------------Choose data to fit--------------------------------
data_d =[data(1:9),data(13:21),data(31:39)];   %only DC data
% data_d =[data(10:12),data(22:30)];%only MD data
% data_d = data; %all data

[~,m]=size(data_d); % number of exp involved in fitting
```

```matlab
Nc = 7; %7 independent components;

%% ---------------- claculate degree of freedom--------------------------
Npoint = 0;
for i = 1:m
    Npoint = Npoint + data_d(i).np;
end

% DF = Nc*Npoint - 49; % only one temperature included
% DF = Nc*Npoint - 56; % two temperatures included
DF = Nc*Npoint - 63; % three temperatures included

%% ------------------------initialize error---------------------------
error =[];
for i = 1:m
    Np_i = data_d(i).np;
    error_i = kron(ones(Np_i,1),data_d(i).error);
    error = [error;error_i];
end

P = read_b(4:10,1:7);% matrix of eigenvector of D
Beta1 = read_b(1,1:7)';% initial log of eigenvalue at 1260 C
Beta2 = read_b(2,1:7)';% initial log of eigenvalue at 1350 C
Beta3 = read_b(3,1:7)';% initial log of eigenvalue at 1500 C


%% ---------------------start of BFGS method----------------------------
% x, y1, y2 are used for plotting
x = [];
y1 = [];
y2 = [];

n_loop1= 0; % number of outer loops
n_loop2= 0; % number of inner loops

beta =[reshape(P,Nc^2,1);Beta1;Beta2;Beta3];% parameters to be fitted;[70,1]

% Normalize eigenvectors
Num_Max = [1,2,3,5,3,5,6];
% the positions of the largest terms in each eigenvector; only for DC
% Num_Max = [2,2,3,3,3,5,6];
% the positions of the largest terms in each eigenvector; all data
for i =1:7
    Max = beta(7*i-7+Num_Max(i));
    beta(7*i-6:7*i) = beta(7*i-6:7*i) / norm(beta(7*i-6:7*i)) *
( Max/abs(Max));
end

[n,~] = size(beta);

w0=[]; % initial concentration
for i=1:m
    transform_w = reshape((data_d(i).w)',[],1);
    w0 = [w0;transform_w];
end
w = con(data_d,beta); %calculate concentration
r = (w0-w)./error; % calculate residue difference
S = r'*r; % sum of square error
```

```matlab
S_DF = S/DF/2;    % reduced chi-square
J = calculate_J(data_d,beta); % calculate Jacobian matrix
g = 2*J'*r; %gradient of S
H = eye(70); % H matrix

x = [x;n_loop1];
y1 = [y1;S_DF];
y2 = [y2;n_loop2];
yyaxis left
plot(x,y1,'-b');
xlabel('num of loop1');
ylabel('reduced chi-square');
yyaxis right
plot(x,y2,'-*r');
ylabel('num of loop2');
drawnow;

max1 = 800;
max2 = 50;
sigma = 0.5;
% control parameter used in Armijo-type line search
rho = 0.5;
% control parameter used in Armijo-type line search
n_loop1 = 1;
while n_loop1 < max1 && norm(g)/DF/2 > 1E-6
% when n_loop1 exceeds max1 or ||S_DF|| > 1E-6, iteration ends

    p = -H*g;
    % the BFGS direction obtained by solving the linear equation: p=-H*g
    step=1;
    n_loop2 = 0;

    % search for proper step using Armijo-type line search.
    while n_loop2 < max2
        beta1 = beta + step*p;
        w1 = con(data_d,beta1);
        r1 = (w0-w1)./error;
        S1 = r1'*r1;
        l= S + sigma*step*g'*p; % parameter used in Armijo-type line search

    % if S1<l, the step is OK, otherwise, reduce the step by a factor of rho
        if S1 < l
            break;
        end
        step = rho*step;
        n_loop2 = n_loop2+1;
    end

    if n_loop2==max2
        fprintf("n_loop2 = %d \n",max2);
        break;
    end

    s = beta1 - beta; % increase in beta
    % update beta
    beta = beta1;
    % normalize eigenvectors
    for i =1:7
        Max = beta( 7*i - 7 + Num_Max(i));
```

```matlab
        beta(7*i-6:7*i) = beta(7*i-6:7*i) / norm(beta(7*i-6:7*i)) *
( Max/abs(Max));
    end

    % update w,r,S,S_DF,J and y
    w = w1;
    r = r1;
    S = S1;
    S_DF = S/DF/2;
    J = calculate_J(data_d,beta);
    y = 2*J'*r - g;

    % update H matrix to guarantee the positive definiteness of H
    if norm(g)>1
        if (y'*s)/(s'*s)>= 10^-6*norm(g)^0.01
            H = H + (y'*s + y'*H*y)*(s*s')/(y'*s)^2 - (H*y*s'+s*y'*H)/(y'*s);
        end
    else
        if (y'*s)/(s'*s)>= 10^-6*norm(g)^3
            H = H + (y'*s + y'*H*y)*(s*s')/(y'*s)^2 - (H*y*s'+s*y'*H)/(y'*s);
        end
    end

    % update g
    g = 2*J'*r;

    x = [x;n_loop1];
    y1 = [y1;S_DF];
    y2 = [y2;n_loop2];
    yyaxis left
    plot(x,y1,'-b');
    xlabel('num of loop1');
    ylabel('reduced chi-square');
    yyaxis right
    plot(x,y2,'-*r');
    ylabel('num of loop2');
    drawnow;

    n_loop1 = n_loop1 +1;
end

% Normalize eigenvectors
for i =1:7
    Max = beta(7*i-7+Num_Max(i));
    beta(7*i-6:7*i) = beta(7*i-6:7*i) / norm(beta(7*i-6:7*i)) *
( Max/abs(Max));
end

%% ----------------------end of BFGS method------------------------------

transform_w = reshape(w,8,[])';
j=0;

%% store calculated concentration
for i=1:m
    data_d(i).w_calc = transform_w(j+1:j+data_d(i).np,:);
    j = j + data_d(i).np;
end
```

```matlab
%% using obtained beta to predict concentration profiles of all exp
w_predict = con(data,beta);
transform_w = reshape(w_predict,8,[])';
j=0;
for i=1:Nexp
    data(i).w_calc = transform_w(j+1:j+data(i).np,:);
    j = j + data(i).np;
end

%% calculate eigenvalues
%trans_beta is a 10 by 7 matrix.
% First row: log of eigenvalues at 1260
% Second row: log of eigenvalues at 1350
% Third row: log of eigenvalues at 1500
% The rest: matrix of eigenvector

trans_beta = zeros(10,7);   % change dimensions of beta
trans_beta(1:3,:) = reshape(beta(50:70) ,7,3)'; % calculate lambda of each
exp
trans_beta(4:10,:) = reshape(beta(1:49),7,7);

%% sequence eigenvalues using bubble sort
for i = 1:6
    for j = 1:7-i
        if trans_beta(1,j)>trans_beta(1,j+1)
            store = trans_beta(:,j+1);
            trans_beta(:,j+1)=trans_beta(:,j);
            trans_beta(:,j)= store;
        end
    end
end

%% calculate D matrix at each temperature
D1 = trans_beta(4:10,:)*diag(exp(trans_beta(1,:)))/trans_beta(4:10,:); %1260
D2 = trans_beta(4:10,:)*diag(exp(trans_beta(2,:)))/trans_beta(4:10,:); %1350
D3 = trans_beta(4:10,:)*diag(exp(trans_beta(3,:)))/trans_beta(4:10,:); %1500

%% calculate error of trans_beta
beta(1:49) = reshape(trans_beta(4:10,:),49,1);
beta(50:70)= reshape(trans_beta(1:3,:)',21,1);
J7 = calculate_J7(data_d,beta);
A = J7'*J7;
inv_A = (diag(inv(A))).^0.5;

error_beta = zeros(70,1);
for i = 0:6
    error_beta(7*i+1:7*i+6)= inv_A(6*i+1:6*i+6);
end
error_beta(50:70) = inv_A(43:63);

error_trans_beta = zeros(10,7);
error_trans_beta(1:3,:) = reshape( error_beta(50:70) , 7,3)';
error_trans_beta(4:10,:) = reshape( error_beta(1:49), 7,7);

elapsed_time = etime(clock(),start_time);
```

B2. Subroutine "con.m"

```matlab
%% Calculate concentration using assumed eigenvector matrix and eigenvalues.

function ww = con(data_d,beta)
    [~,m]=size(data_d);
    P = reshape(beta(1:49),7,7);
    ww = [];

    for i=1:m
        w1 = data_d(i).boundary(2:8,1);
        w2 = data_d(i).boundary(2:8,2);
        %for DC, w1 = w_left, w2 = w_right
        %for MD, w1 = w_interface, w2 = w_initial

        x0 = data_d(i).dist;
        t = data_d(i).time;

        if data_d(i).temp == 1260
            Beta = beta(50:56);
        elseif data_d(i).temp == 1350
            Beta = beta(57:63);
        else
            Beta = beta(64:70);
        end

        if data_d(i).type==1
            for j=1:data_d(i).np
                x = data_d(i).x(j);
                Y = (x-x0)*exp(-Beta/2)/(sqrt(4*t));
                E = diag( erf(Y) );
                ww1 = (w2 + w1)/2 +P * E *P^-1*(w2-w1)/2;
                %concentration of independent components
                ww2 = 100-sum(ww1,"all");
                %concentration of the dependent component,i.e.,SiO2
                ww = [ww;ww2;ww1];
            end

        elseif data_d(i).type==2
            for j=1:data_d(i).np
                x = data_d(i).x(j);
                Y = (x-x0)*exp(-Beta/2)/(sqrt(4*t));
                Y0 = -x0*exp(-Beta/2)/(sqrt(4*t));
                E =  diag( erfc(Y)./erfc(Y0) );
                ww1 = w2 +P * E *P^-1*(w1-w2);
                %concentration of independent components
                ww2 = 100-sum(ww1,"all");
                %concentration of the dependent component,i.e.,SiO2
                ww = [ww;ww2;ww1];
            end
        end
    end
end
```

B3. Subroutine "calculate_J.m"

```
% Calculate and return the derivates of r with respect to P (matrix of
eigenvector) and beta (log of eigenvalue)

function J=calculate_J(data_d,beta)
    [~,m]=size(data_d); %number of experiments included
    P = reshape(beta(1:49),7,7); % matrix of eigenvector
    num = 0;
    n_start = 0;
    n_end = 0;
    JT=[];

    for i=1:m
        w1 = data_d(i).boundary(2:8,1);
        w2 = data_d(i).boundary(2:8,2);
        %for DC, w1 = w_left, w2 = w_right
        %for MD, w1 = w_interface, w2 = w_initial

        x0 = data_d(i).dist;
        t = data_d(i).time;
        error1 = data_d(i).error(2:8);
        error2 = data_d(i).error(1);

        if data_d(i).temp == 1260
            num = 0;
            Beta = beta(50:56);
        elseif data_d(i).temp == 1350
            num = 1;
            Beta = beta(57:63);
        else
            num = 2;
            Beta = beta(64:70);
        end

        n_start = num*7+1;
        n_end = (num+1)*7;

        if data_d(i).type==1    %for diffusion couple

            for j=1:data_d(i).np
                x= data_d(i).x(j);
                Y= (x-x0)*exp(-Beta/2)/(sqrt(4*t));
                E = diag( erf(Y) ); %  Eq.(7) in "derivation1.pdf"
                dE = diag( -(x-x0)/sqrt(4*pi*t) * exp(-Y.*Y).*exp(-Beta/2) );
                wp = kron( (E *P^-1*(w2-w1)/2), eye(7))-...
                    kron((P^-1*(w2-w1)/2),(P*E*P^-1)');
                % wp is the partial derivative of concentration of
                % independent components with respect to P

                wBeta =diag(reshape(dE,49,1))...
                    *kron((P^-1*(w2-w1)/2),P');
                % wBeta is the partial derivative of concentration of
                % independent components with respect to Beta

                rp1 = -wp/diag(error1);
```

```matlab
        % partial derivative of residue error of independent
        % components with respect with to P

        rBeta1= -wBeta/diag(error1);
        % partial derivative of residue error of independent
        % components with respect with to Beta

        rp2 = sum(wp,2)/error2;
        % partial derivative of residue error of the dependent
        % components with respect with to P

        rBeta2 = sum(wBeta,2)/error2;
        % partial derivative of residue error of the dependent
        % components with respect with to Beta

        rp = [rp2,rp1];
        % partial derivative of residue error of all
        % components with respect with to P

        rBeta3=[rBeta2,rBeta1];%49*8
        % partial derivative of residue error of all
        % components with respect with to Beta

        rBeta=zeros(21,8);
        for k=1:8
            rBeta(n_start:n_end,k)= diag(reshape(rBeta3(:,k),7,7));
        end
        JT =[JT,[rp;rBeta]];
    end

elseif data_d(i).type==2  % for mineral dissolution

    for j=1:data_d(i).np
        x= data_d(i).x(j);
        Y= (x-x0)*exp(-Beta/2)/(sqrt(4*t));
        Y0 = -x0*exp(-Beta/2)/(sqrt(4*t));

        E = erfc(Y);
        E0 = erfc(Y0);
        E_ratio = diag (E./E0);

        dE = (x-x0)/(sqrt(4*pi*t))*exp(-Y.*Y).*exp(-Beta/2);
        dE0 = -x0/(sqrt(4*pi*t))*exp(-Y0.*Y0).*exp(-Beta/2);

        dE_ratio = diag( ( dE.*E0 - dE0.*E )./(E0.^2) );

        wp = kron( (E_ratio*P^-1*(w1-w2)), eye(7))-...
            kron((P^-1*(w1-w2)),(P*E_ratio*P^-1)');
        % wp is the partial derivative of concentration of
        % independent components with respect to P

        wBeta = diag(reshape(dE_ratio,49,1))...
            *kron((P^-1*(w1-w2)),P');
        % wBeta is the partial derivative of concentration of
        % independent components with respect to Beta
```

```matlab
                rp1 = -wp/diag(error1);
                % partial derivative of residue error of independent
                % components with respect with to P

                rBeta1= -wBeta/diag(error1);
                % partial derivative of residue error of independent
                % components with respect with to Beta


                rp2 = sum(wp,2)/error2;
                % partial derivative of residue error of the dependent
                % components with respect with to P

                rBeta2 = sum(wBeta,2)/error2;
                % partial derivative of residue error of the dependent
                % components with respect with to Beta

                rp = [rp2,rp1];
                % partial derivative of residue error of all
                % components with respect with to P

                rBeta3=[rBeta2,rBeta1];%49*8
                % partial derivative of residue error of all
                % components with respect with to Beta

                rBeta=zeros(21,8);
                for k=1:8
                    rBeta(n_start:n_end,k)= diag(reshape(rBeta3(:,k),7,7));
                end
                JT =[JT,[rp;rBeta]];
            end
        end
    end
    J = JT';
end
```

B4. Subroutine "calculate_J7.m"

```matlab
% Calculate the derivates of r with respect to P (matrix of eigenvector) and
% beta.

% J7 differs from J in that J7 doesn't return the derivatives
% of r with respect to the 7th terms of each eigenvector. Therefore, J7 is
% only used to calculate the error while assuming that the errors of the 7th
% terms of each eigenvector is zero.

function J=calculate_J7(data_d,beta)
    [~,m]=size(data_d); %number of experiments included
    P = reshape(beta(1:49),7,7); % matrix of eigenvector
    num = 0;
    n_start = 0;
    n_end = 0;
    JT=[];

    for i=1:m
        w1 = data_d(i).boundary(2:8,1);
        w2 = data_d(i).boundary(2:8,2);
        %for DC, w1 = w_left, w2 = w_right
        %for MD, w1 = w_interface, w2 = w_initial

        x0 = data_d(i).dist;
        t = data_d(i).time;
        error1 = data_d(i).error(2:8);
        error2 = data_d(i).error(1);

        if data_d(i).temp == 1260
            num = 0;
            Beta = beta(50:56);
        elseif data_d(i).temp == 1350
            num = 1;
            Beta = beta(57:63);
        else
            num = 2;
            Beta = beta(64:70);
        end

        n_start = num*7+1;
        n_end = (num+1)*7;

        if data_d(i).type==1    %for diffusion couple

            for j=1:data_d(i).np
                x= data_d(i).x(j);
                Y= (x-x0)*exp(-Beta/2)/(sqrt(4*t));
                E = diag( erf(Y) );
                dE = diag( -(x-x0)/sqrt(4*pi*t) * exp(-Y.*Y).*exp(-Beta/2) );
                wp = kron( (E *P^-1*(w2-w1)/2), eye(7))-...
                    kron((P^-1*(w2-w1)/2),(P*E*P^-1)');
                % wp is the partial derivative of concentration of
                % independent components with respect to P

                wBeta =diag(reshape(dE,49,1))...
```

62

```matlab
                *kron((P^-1*(w2-w1)/2),P');
            % wBeta is the partial derivative of concentration of
            % independent components with respect to Beta

            rp1 = -wp/diag(error1);
            % partial derivative of residue error of independent
            % components with respect with to P

            rBeta1= -wBeta/diag(error1);
            % partial derivative of residue error of independent
            % components with respect with to Beta

            rp2 = sum(wp,2)/error2;
            % partial derivative of residue error of the dependent
            % components with respect with to P

            rBeta2 = sum(wBeta,2)/error2;
            % partial derivative of residue error of the dependent
            % components with respect with to Beta

            rp = [rp2,rp1];
            % partial derivative of residue error of all
            % components with respect with to P

            rBeta3=[rBeta2,rBeta1];%49*8
            % partial derivative of residue error of all
            % components with respect with to Beta

            rBeta=zeros(21,8);
            for k=1:8
                rBeta(n_start:n_end,k)= diag(reshape(rBeta3(:,k),7,7));
            end
            JT =[JT,[rp;rBeta]];
        end

    elseif data_d(i).type==2  % for mineral dissolution

        for j=1:data_d(i).np
            x= data_d(i).x(j);
            Y= (x-x0)*exp(-Beta/2)/(sqrt(4*t));
            Y0 = -x0*exp(-Beta/2)/(sqrt(4*t));

            E = erfc(Y);
            E0 = erfc(Y0);
            E_ratio = diag (E./E0);

            dE = (x-x0)/(sqrt(4*pi*t))*exp(-Y.*Y).*exp(-Beta/2);
            dE0 = -x0/(sqrt(4*pi*t))*exp(-Y0.*Y0).*exp(-Beta/2);

            dE_ratio = diag( ( dE.*E0 - dE0.*E )./(E0.^2) );

            wp = kron( (E_ratio*P^-1*(w1-w2)), eye(7))-...
                kron((P^-1*(w1-w2)),(P*E_ratio*P^-1)');
            % wp is the partial derivative of concentration of
            % independent components with respect to P
```

```matlab
                wBeta = diag(reshape(dE_ratio,49,1))...
                    *kron((P^-1*(w1-w2)),P');
                % wBeta is the partial derivative of concentration of
                % independent components with respect to Beta

                rp1 = -wp/diag(error1);
                % partial derivative of residue error of independent
                % components with respect with to P

                rBeta1= -wBeta/diag(error1);
                % partial derivative of residue error of independent
                % components with respect with to Beta


                rp2 = sum(wp,2)/error2;
                % partial derivative of residue error of the dependent
                % components with respect with to P

                rBeta2 = sum(wBeta,2)/error2;
                % partial derivative of residue error of the dependent
                % components with respect with to Beta

                rp = [rp2,rp1];
                % partial derivative of residue error of all
                % components with respect with to P

                rBeta3=[rBeta2,rBeta1];%49*8
                % partial derivative of residue error of all
                % components with respect with to Beta

                rBeta=zeros(21,8);
                for k=1:8
                    rBeta(n_start:n_end,k)= diag(reshape(rBeta3(:,k),7,7));
                end
                JT =[JT,[rp;rBeta]];
            end
        end
    end
    J1 = JT';

    [n,~]=size(J1);
    J=zeros(n,63);
    for i=0:6
        J(:,6*i+1:6*i+6)=J1(:,7*i+1:7*i+6);
    end
    J(:,43:63)=J1(:,50:70);
end
```

Appendix C

Fits for 27 diffusion couple experiments from Guo and Zhang (2018, 2020)

The diffusion profiles of oxide components obtained from 27 diffusion couple experiments conducted by Guo and Zhang (2018, 2020) were fitted twice using two different concentration units, namely mass fraction, and mole fraction. The fits in the former case are shown in Appendix C1, and the fits in the latter case are shown in Appendix C2.

C1. Fits of diffusion profiles using mass fraction as concentration
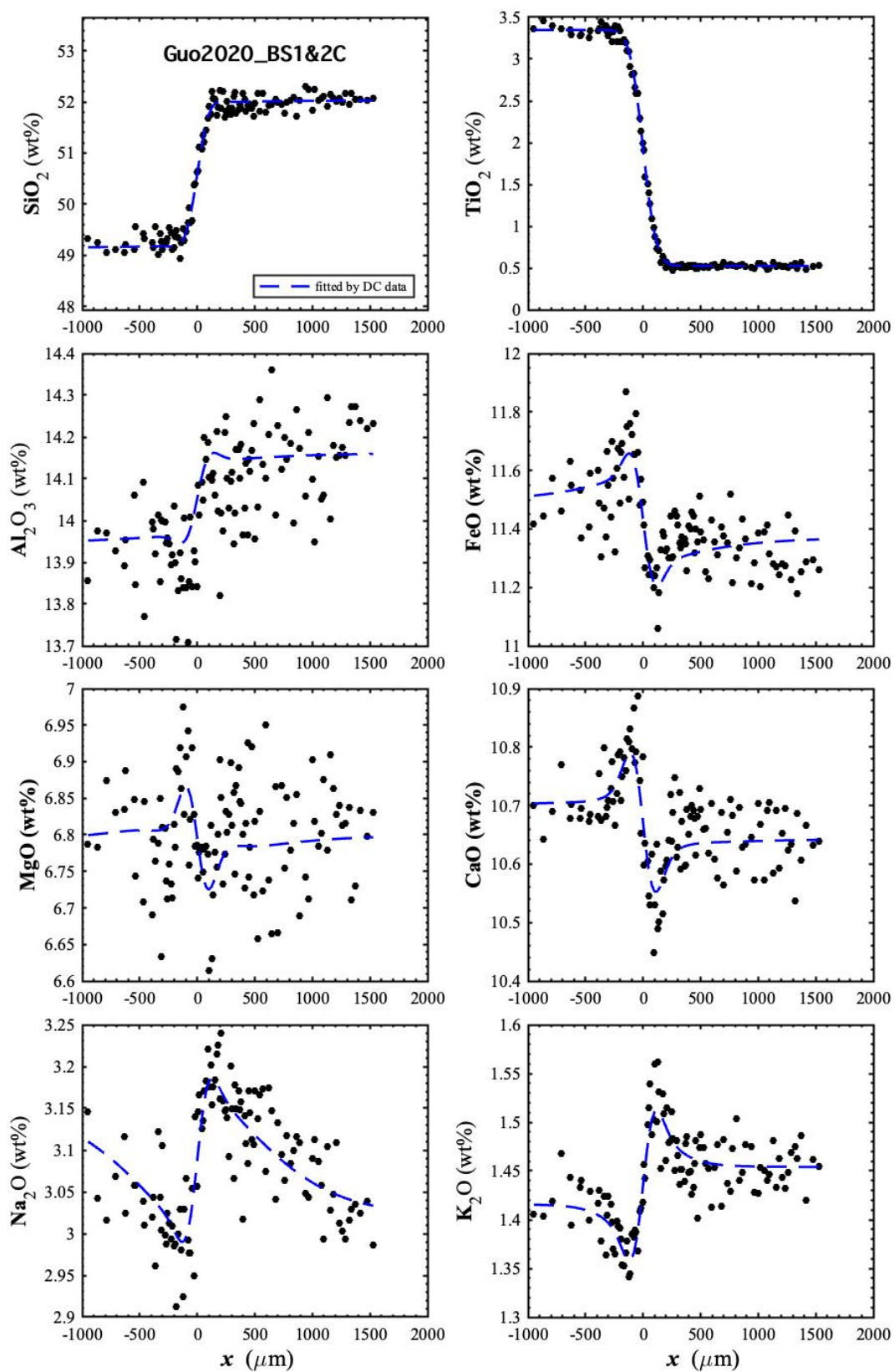
Figure C1.1. Diffusion profiles of oxide components in wt% of BS1&2C (Guo and Zhang, 2020) with fits. The dash curves are fits by the parameters in Table 4.1.
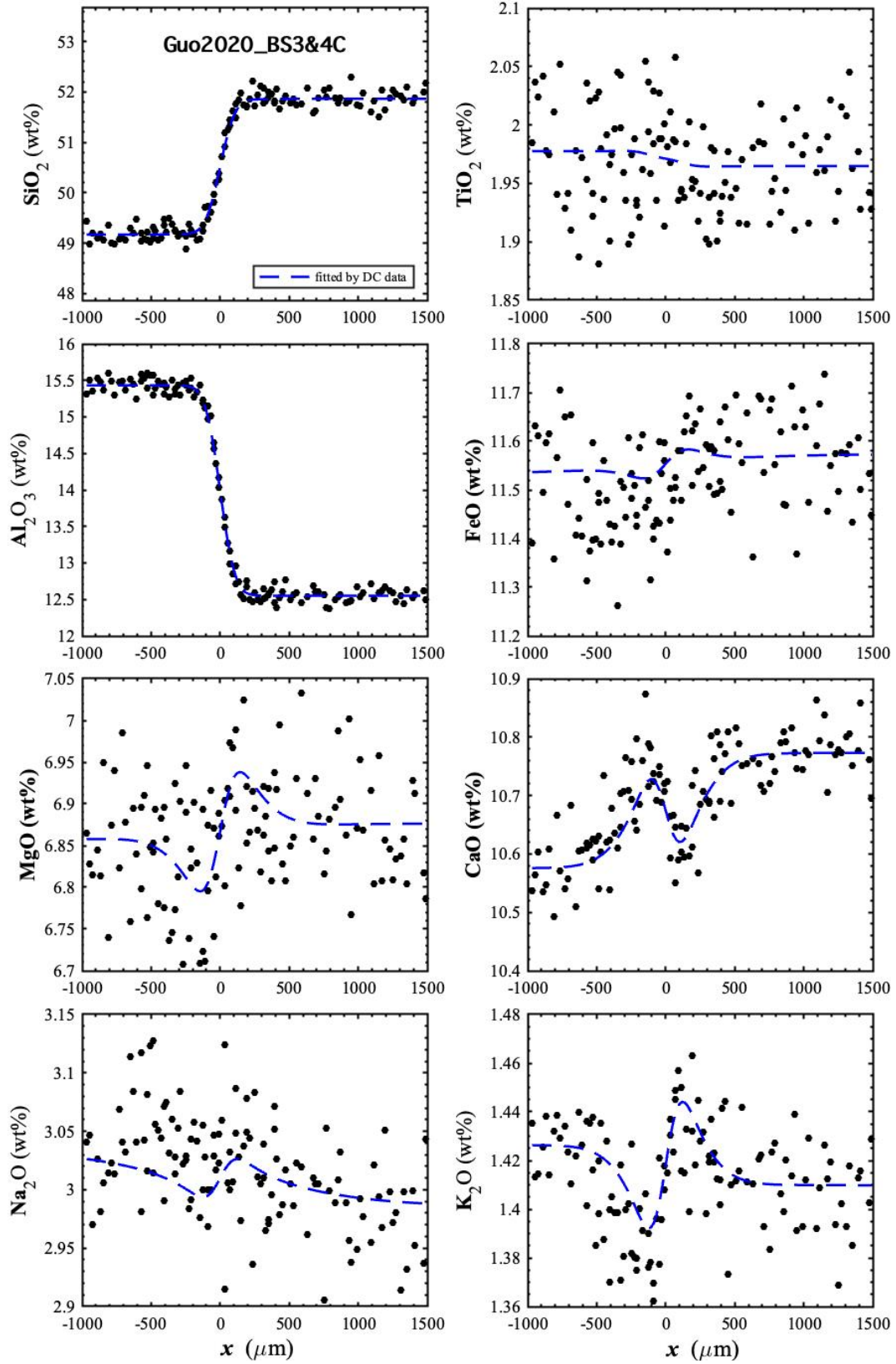
Figure C1.2. Diffusion profiles of oxide components in wt% of BS3&4C (Guo and Zhang, 2020) with fits. The dash curves are fits by the parameters in Table 4.1.
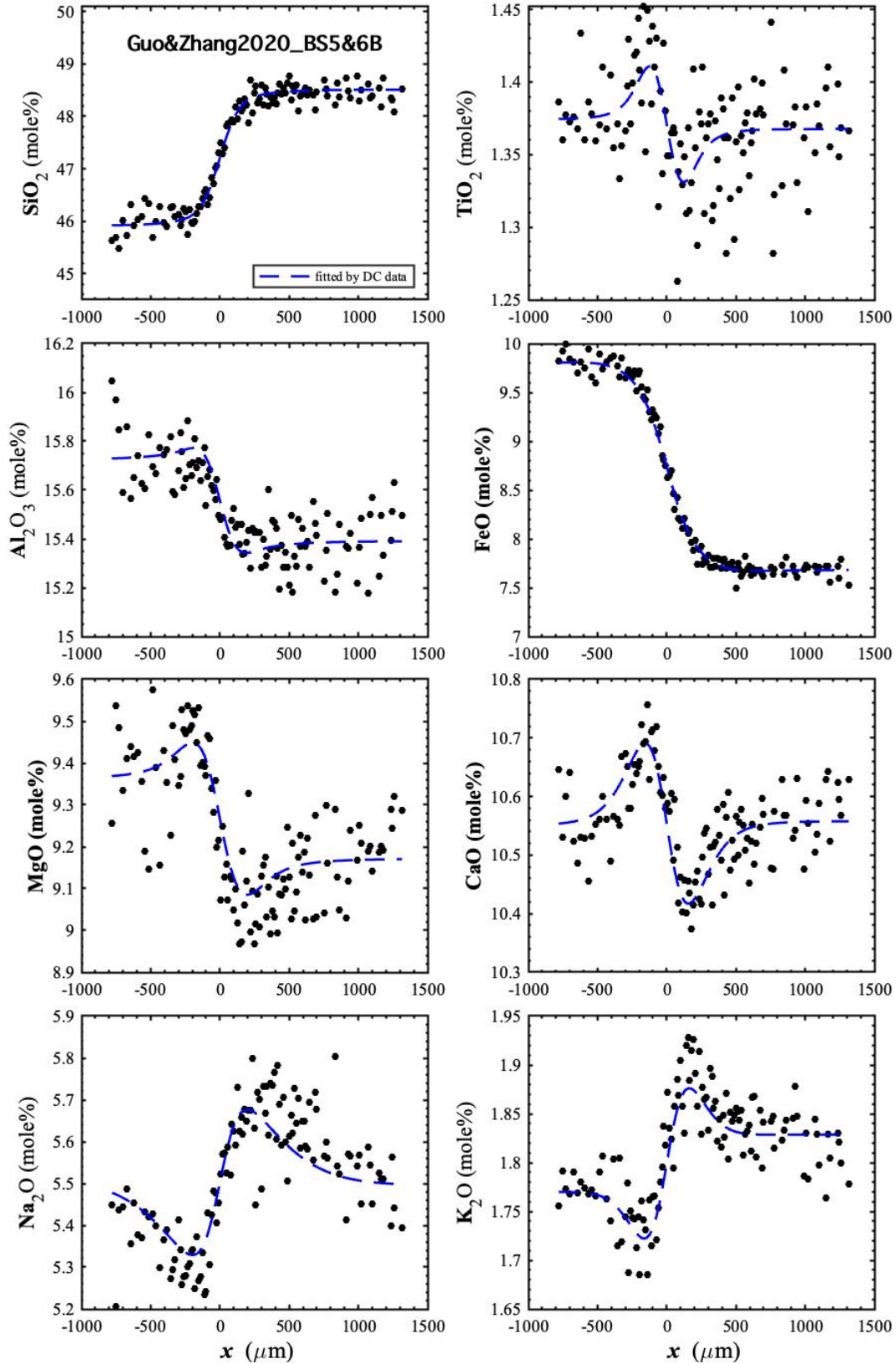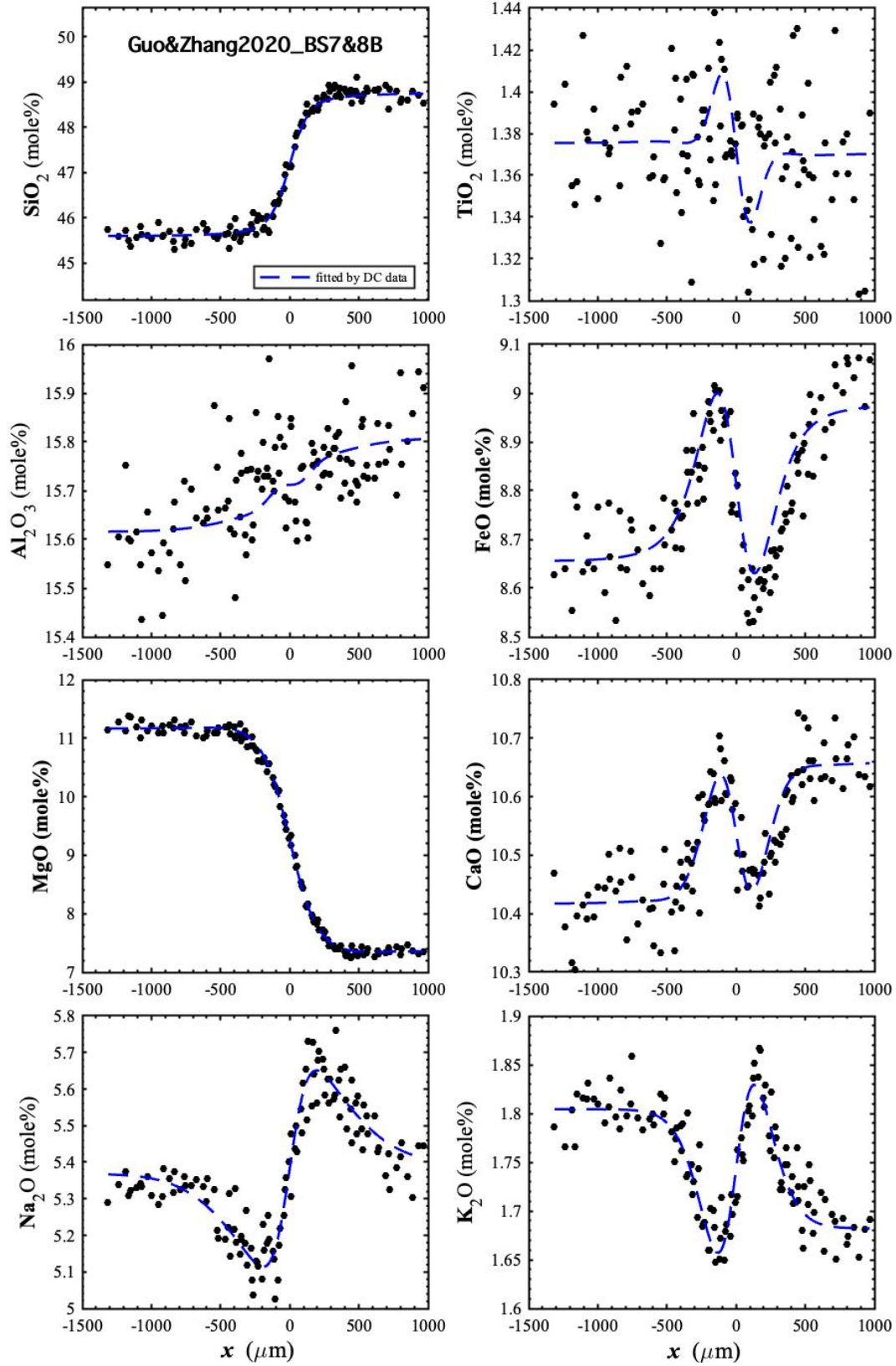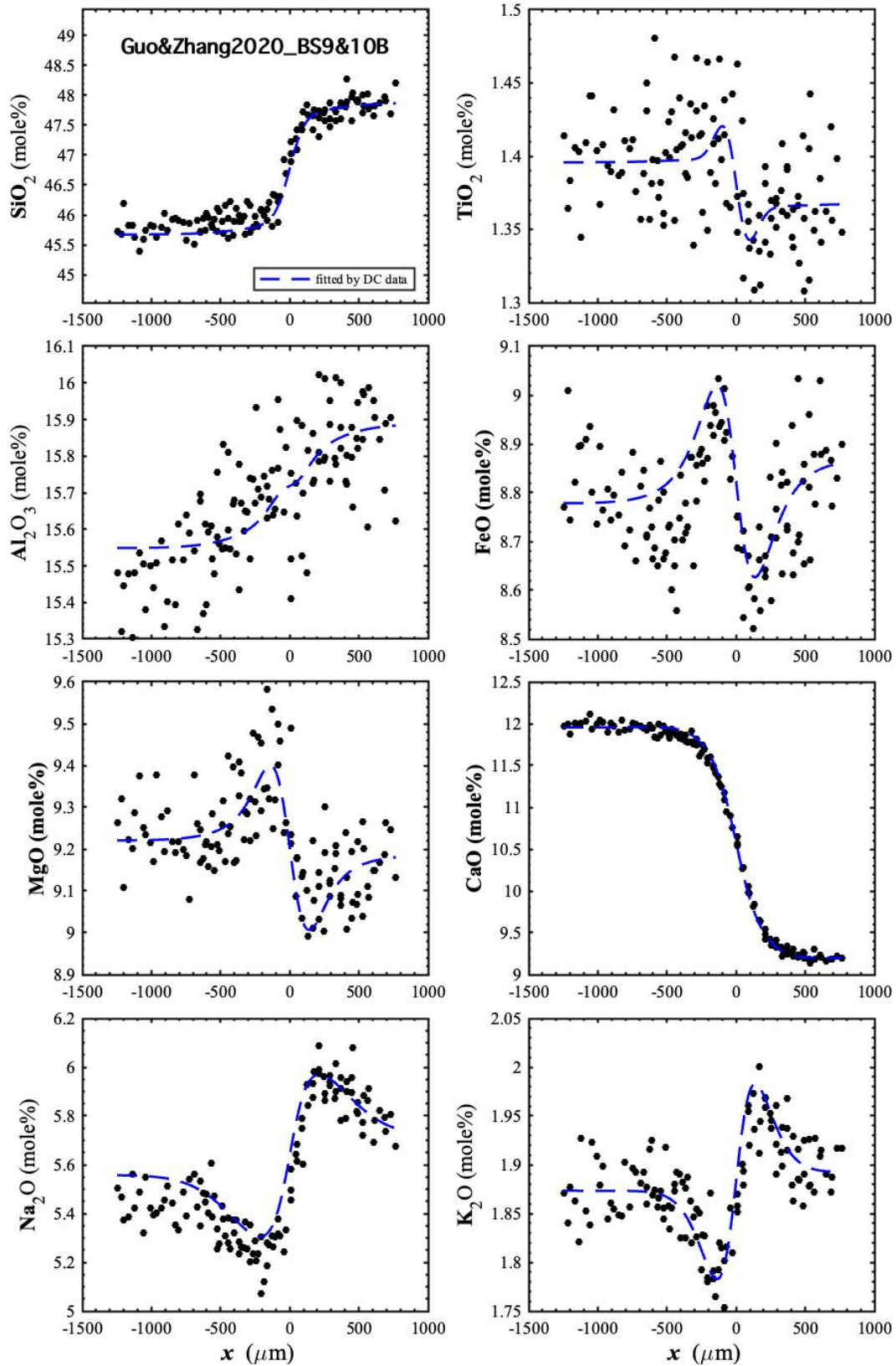
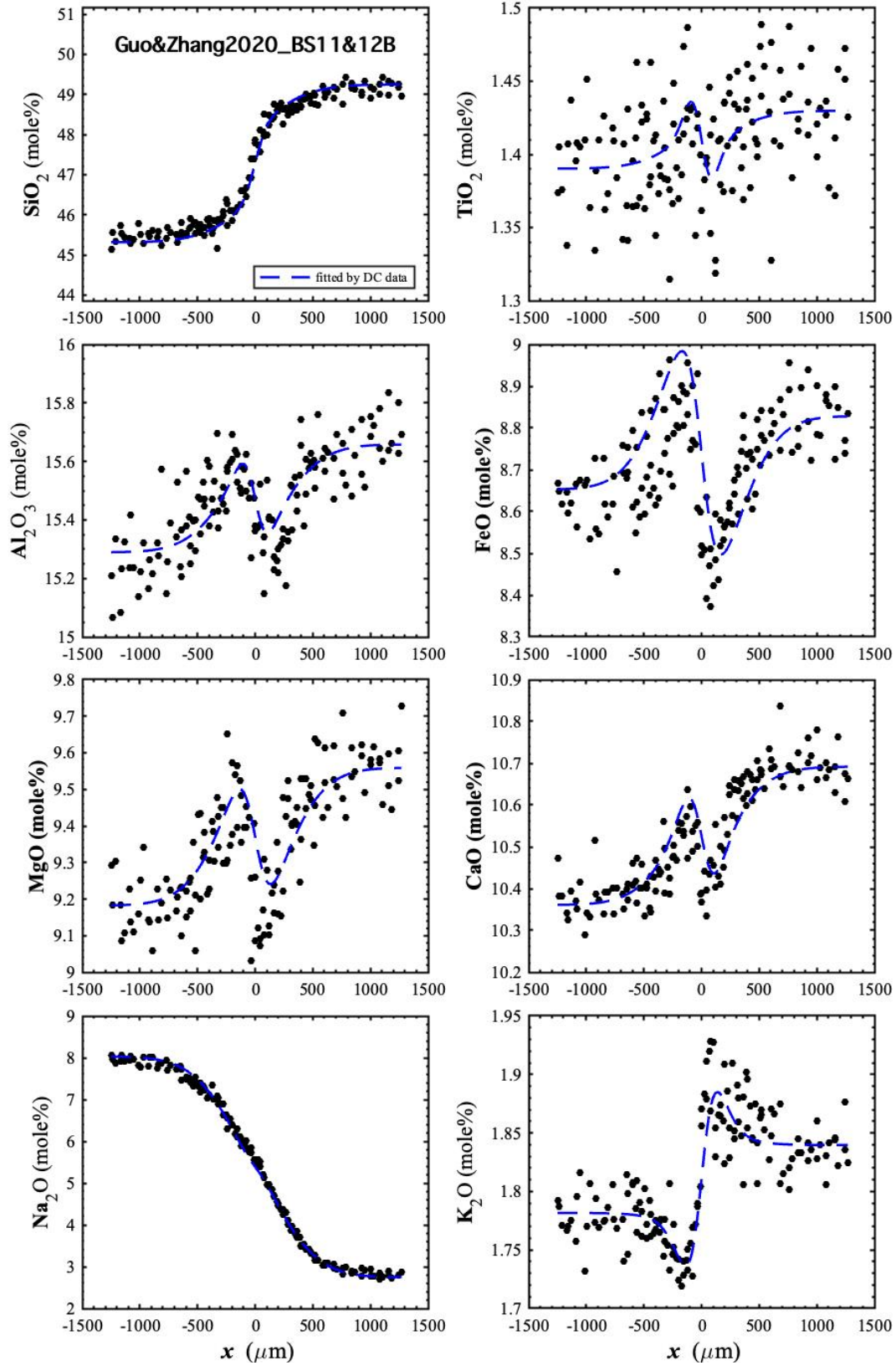67
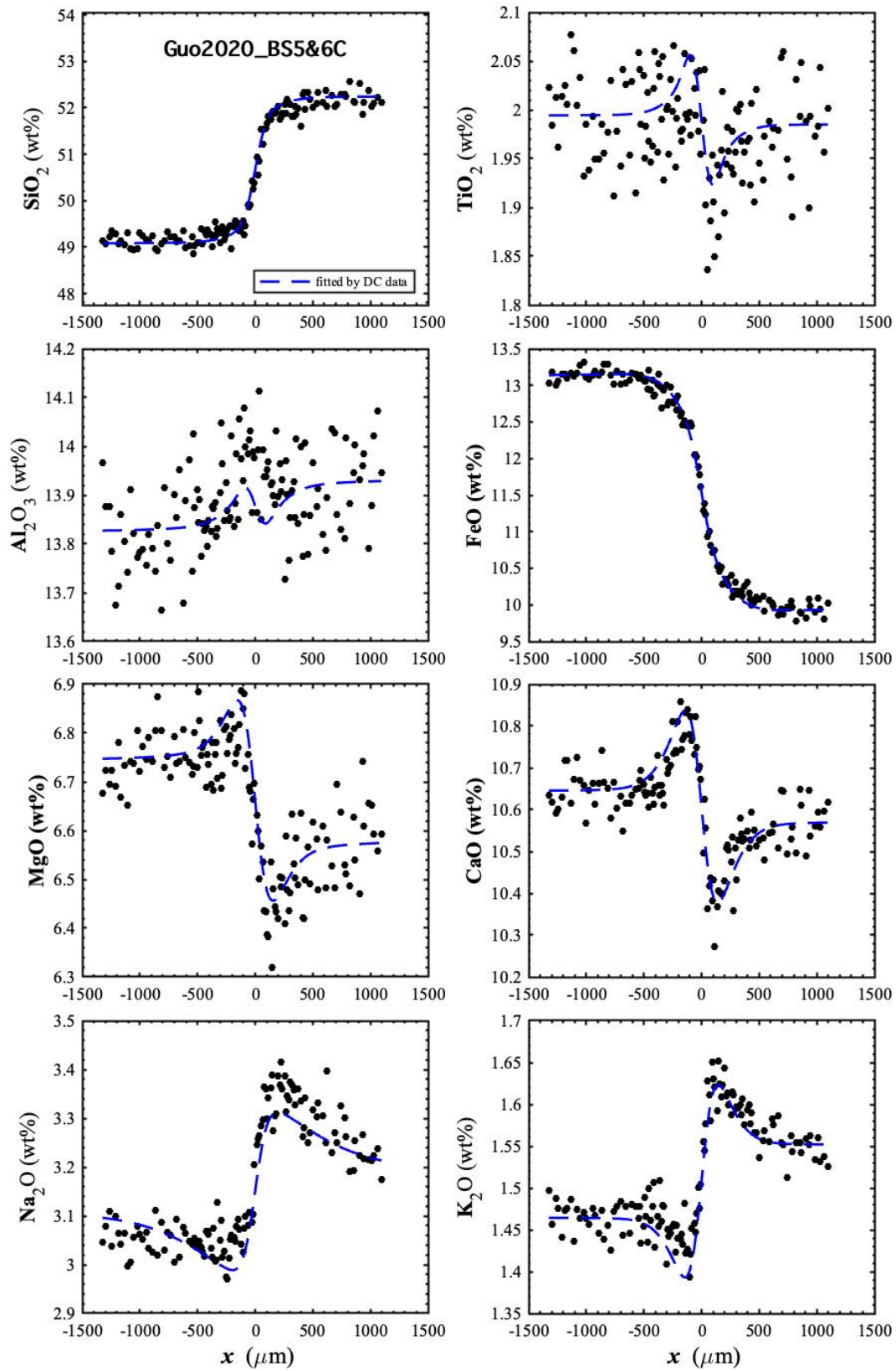
Figure C1.3. Diffusion profiles of oxide components in wt% of BS5&6C (Guo and Zhang, 2020) with fits. The dash curves are fits by the parameters in Table 4.1.
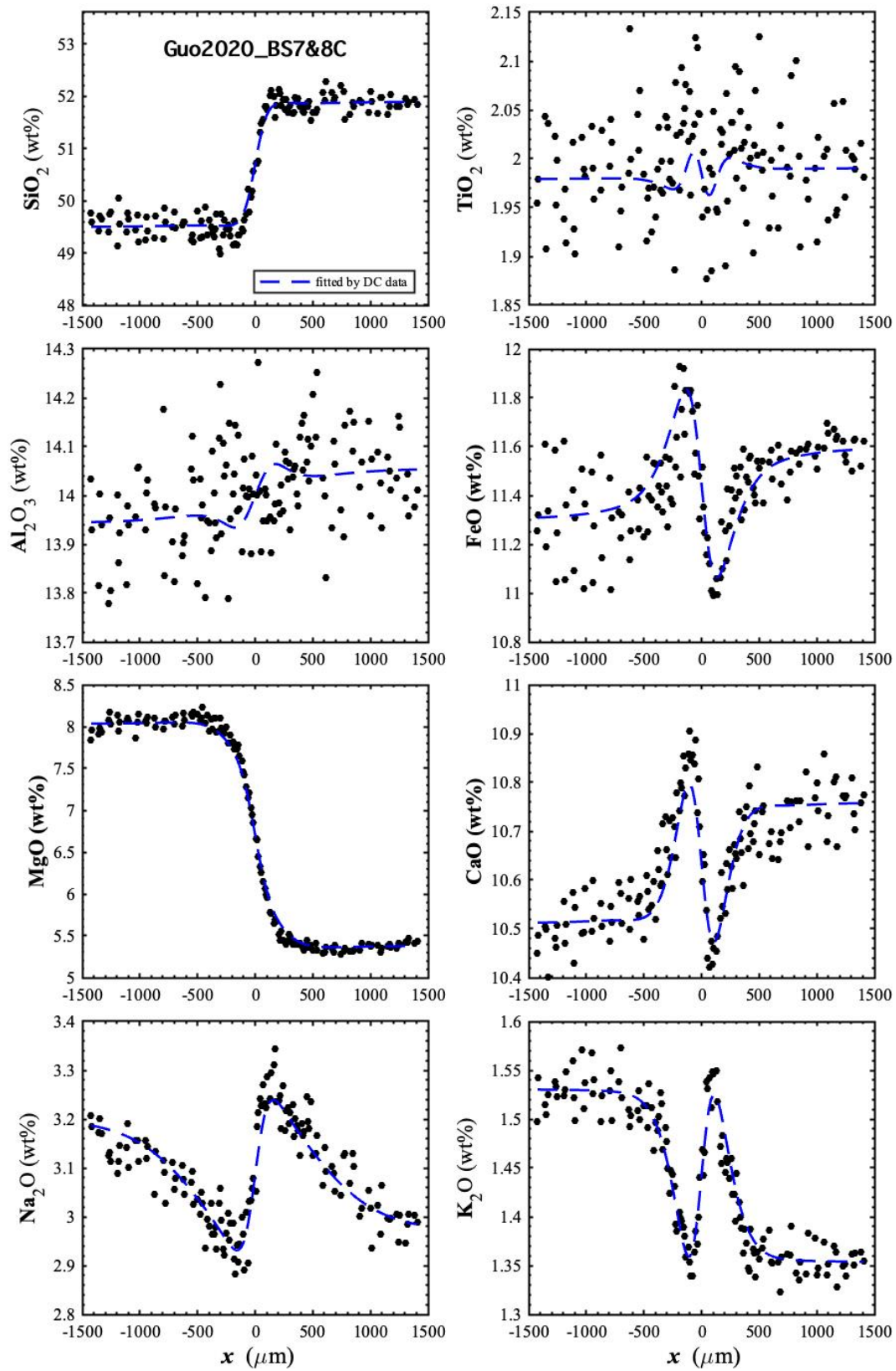
Figure C1.4. Diffusion profiles of oxide components in wt% of BS7&8C (Guo and Zhang, 2020) with fits. The dash curves are fits by the parameters in Table 4.1.
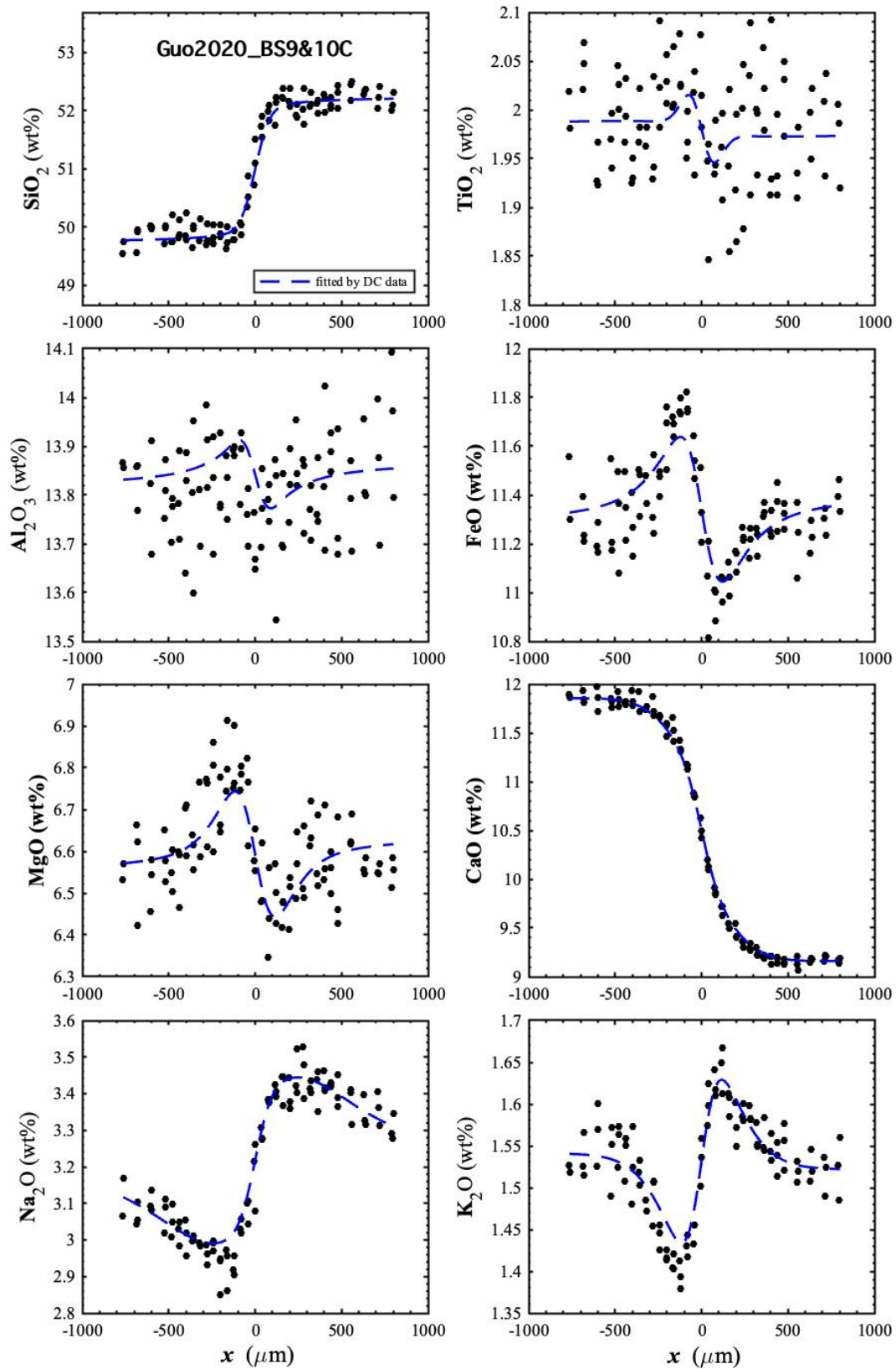
Figure C1.5. Diffusion profiles of oxide components in wt% of BS9&10C (Guo and Zhang, 2020) with fits. The dash curves are fits by the parameters in Table 4.1.

70
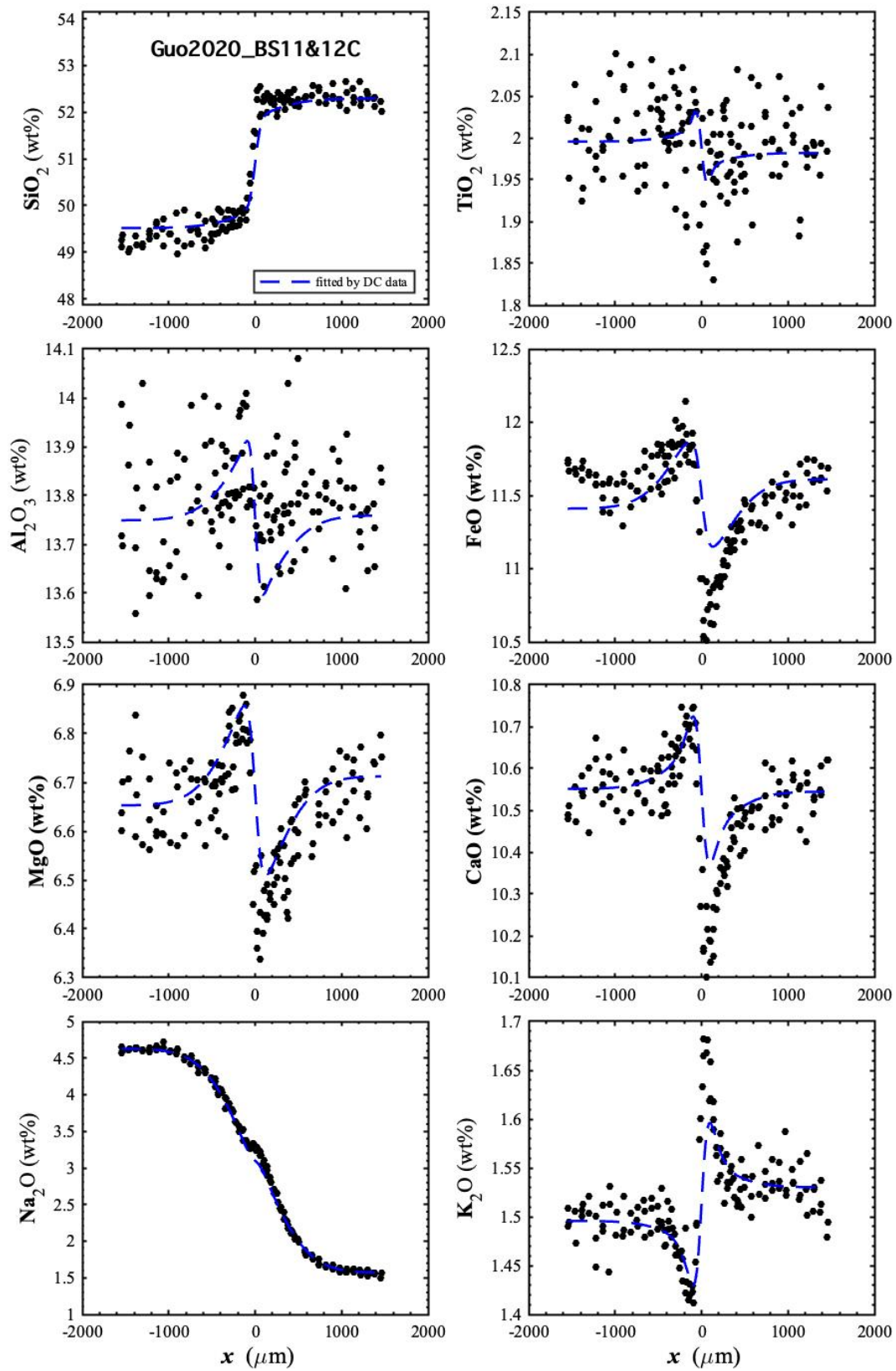
Figure C1.6. Diffusion profiles of oxide components in wt% of BS11&12C (Guo and Zhang, 2020) with fits. The dash curves are fits by the parameters in Table 4.1.
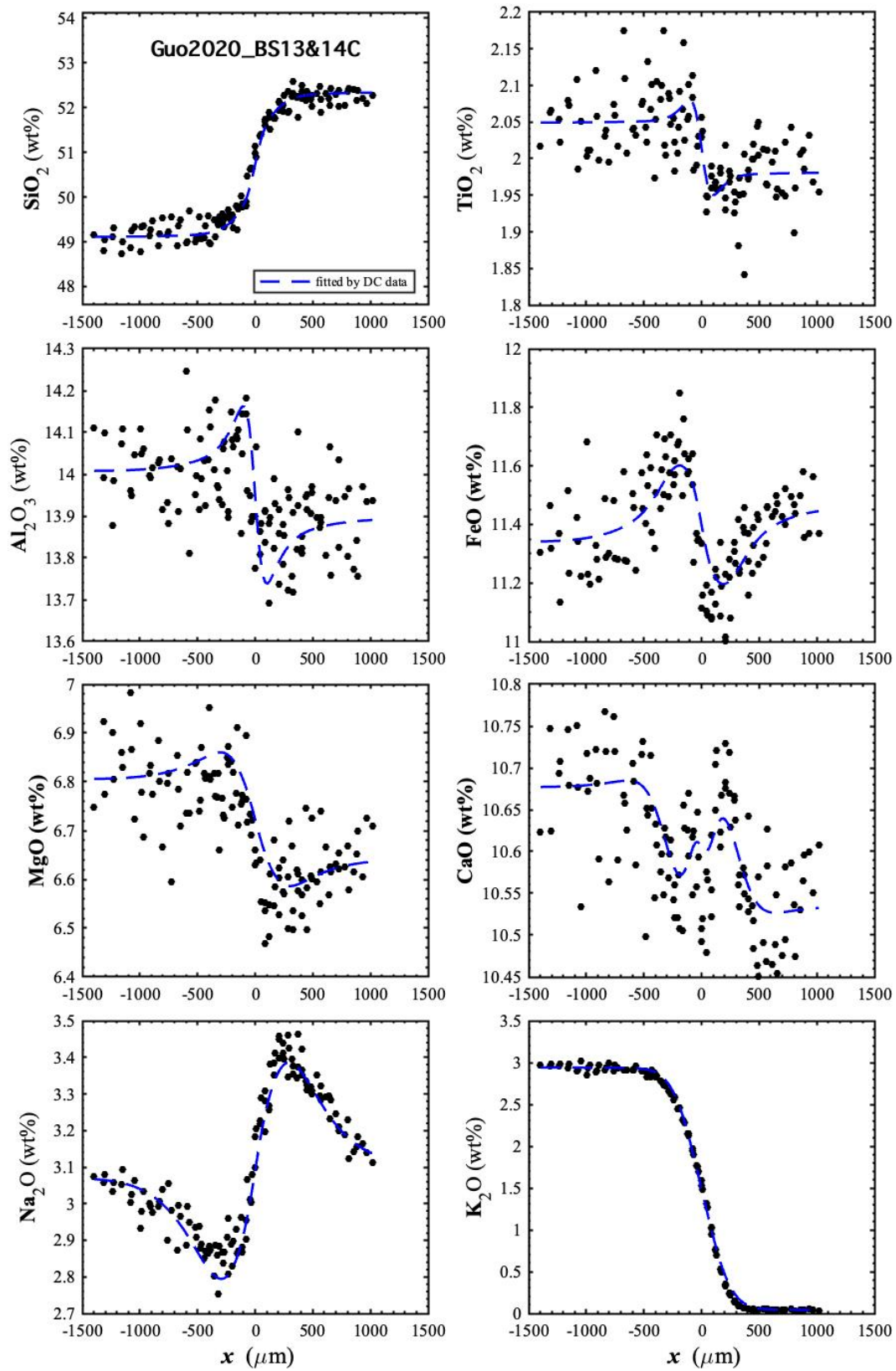
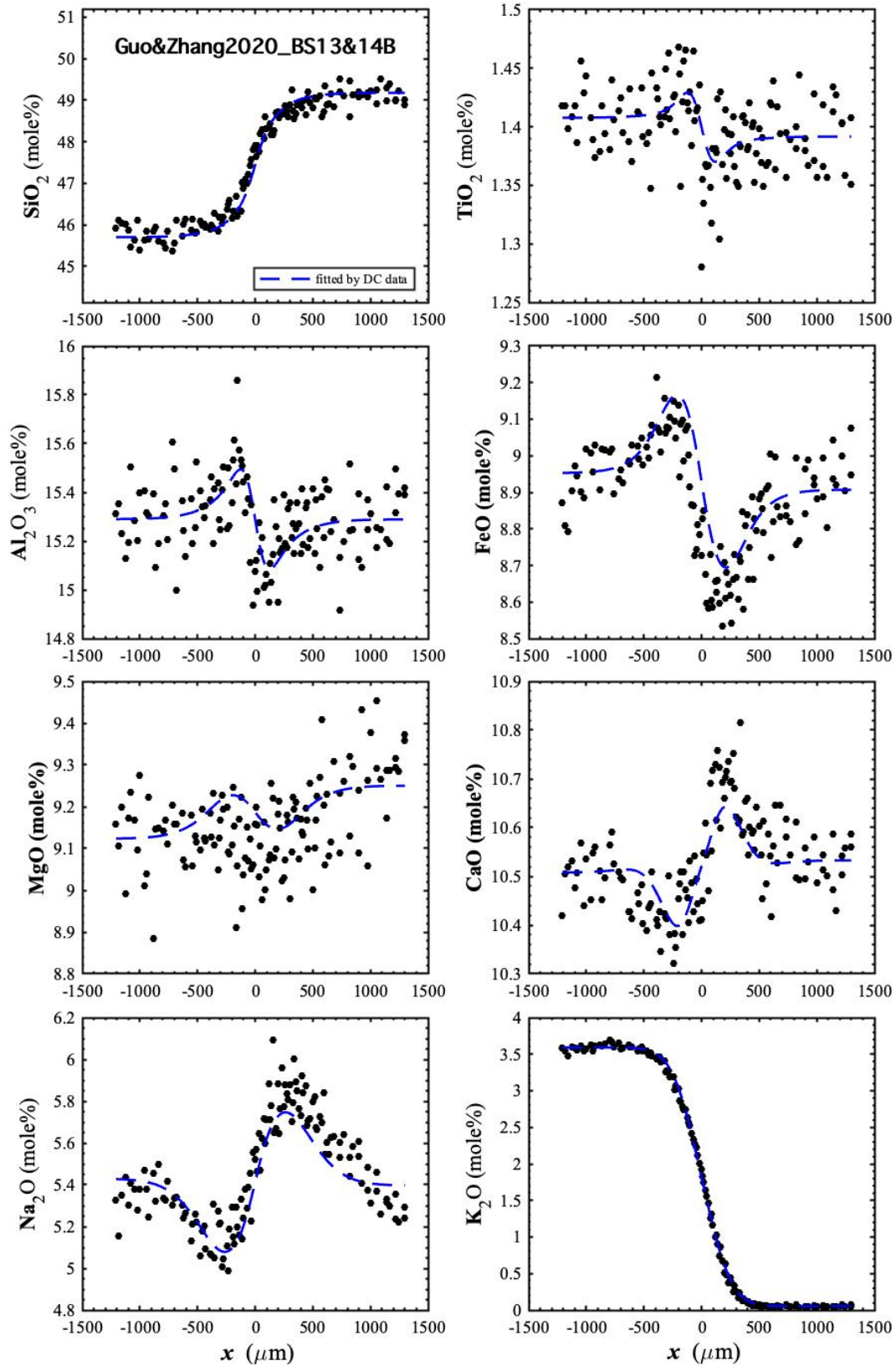**Figure C1.7.** Diffusion profiles of oxide components in wt% of BS13&14C (Guo and Zhang, 2020) with fits. The dash curves are fits by the parameters in Table 4.1.
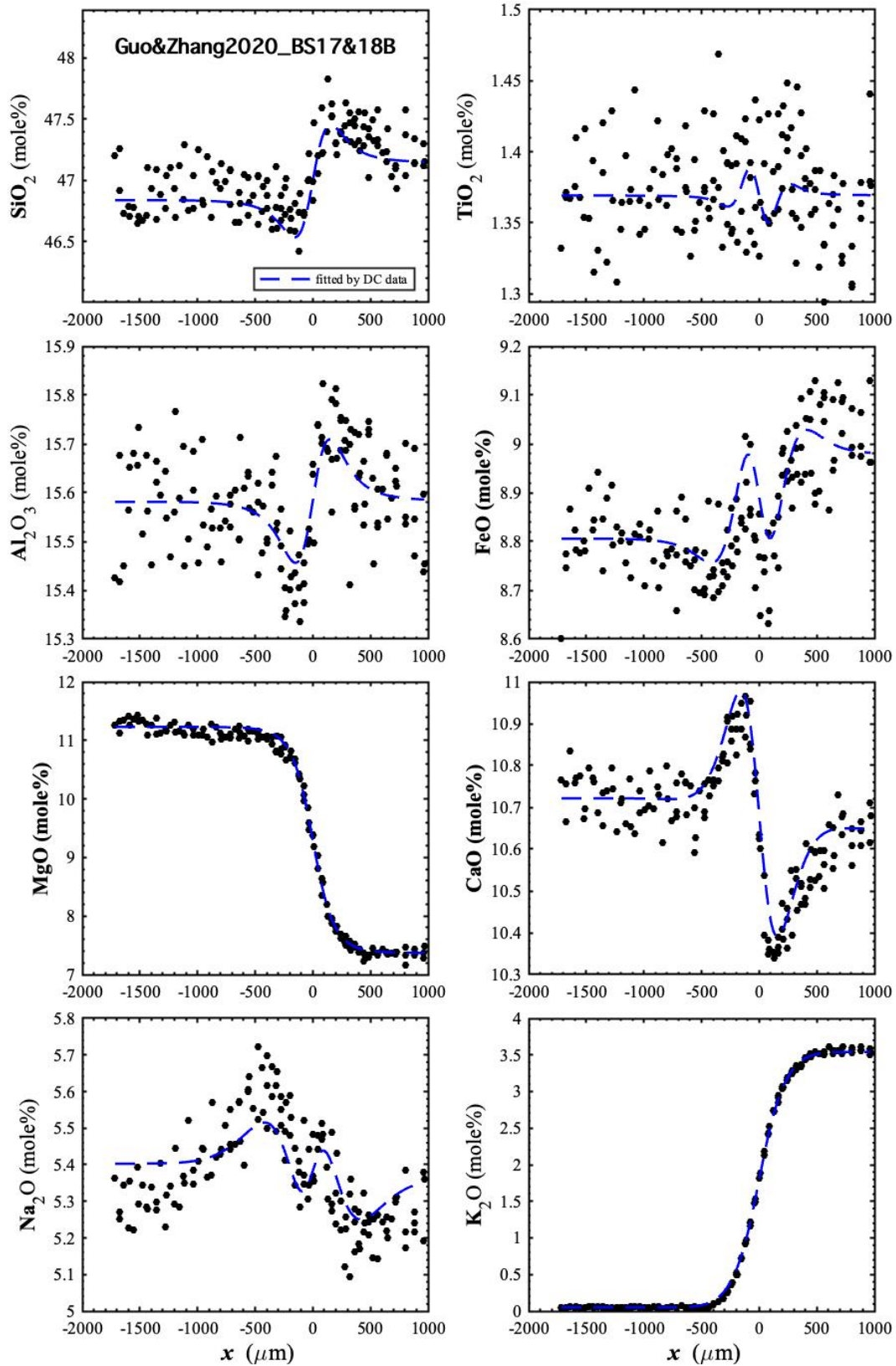
72
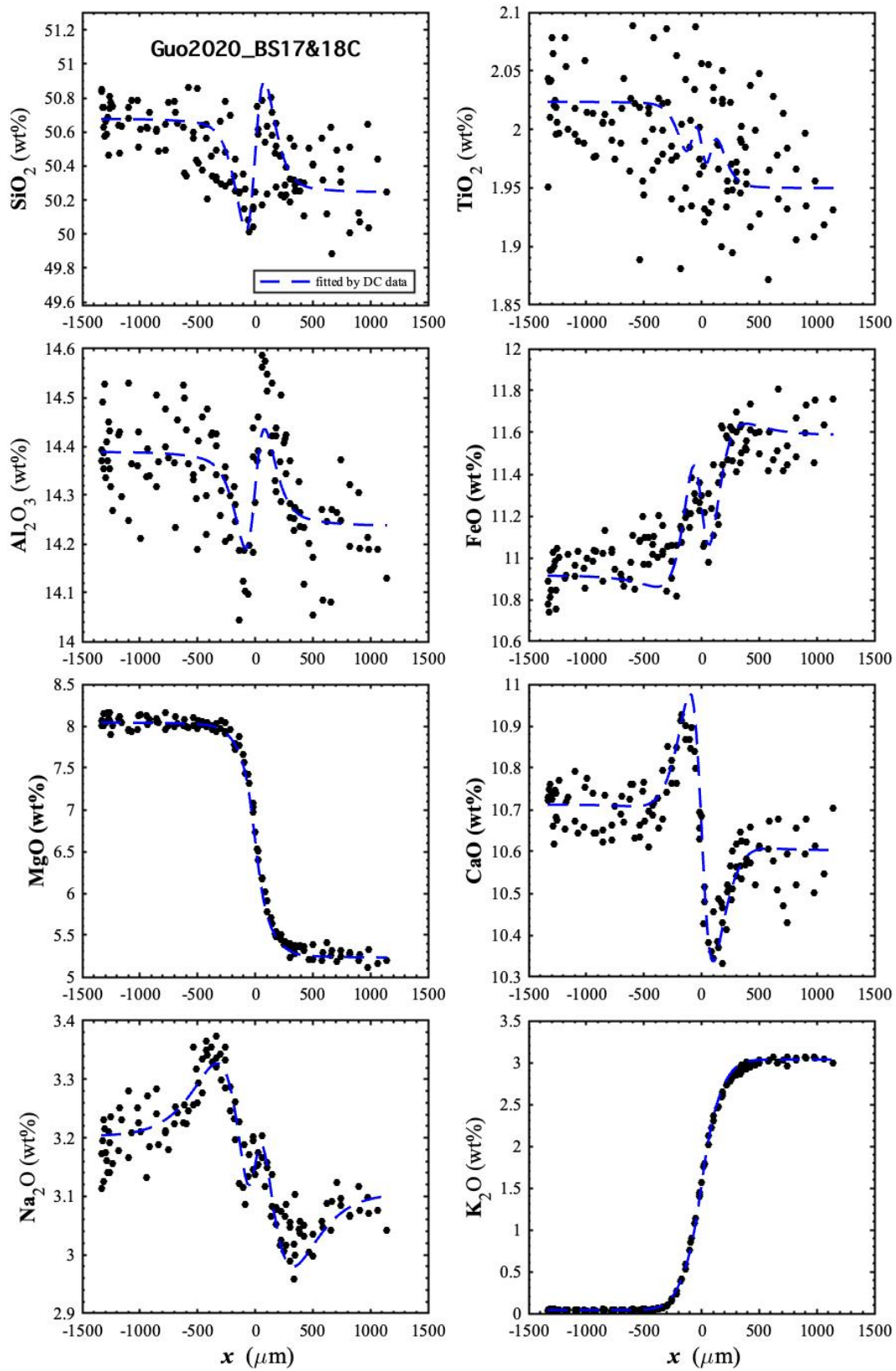
Figure C1.8. Diffusion profiles of oxide components in wt% of BS17&18C (Guo and Zhang, 2020) with fits. The dash curves are fits by the parameters in Table 4.1.
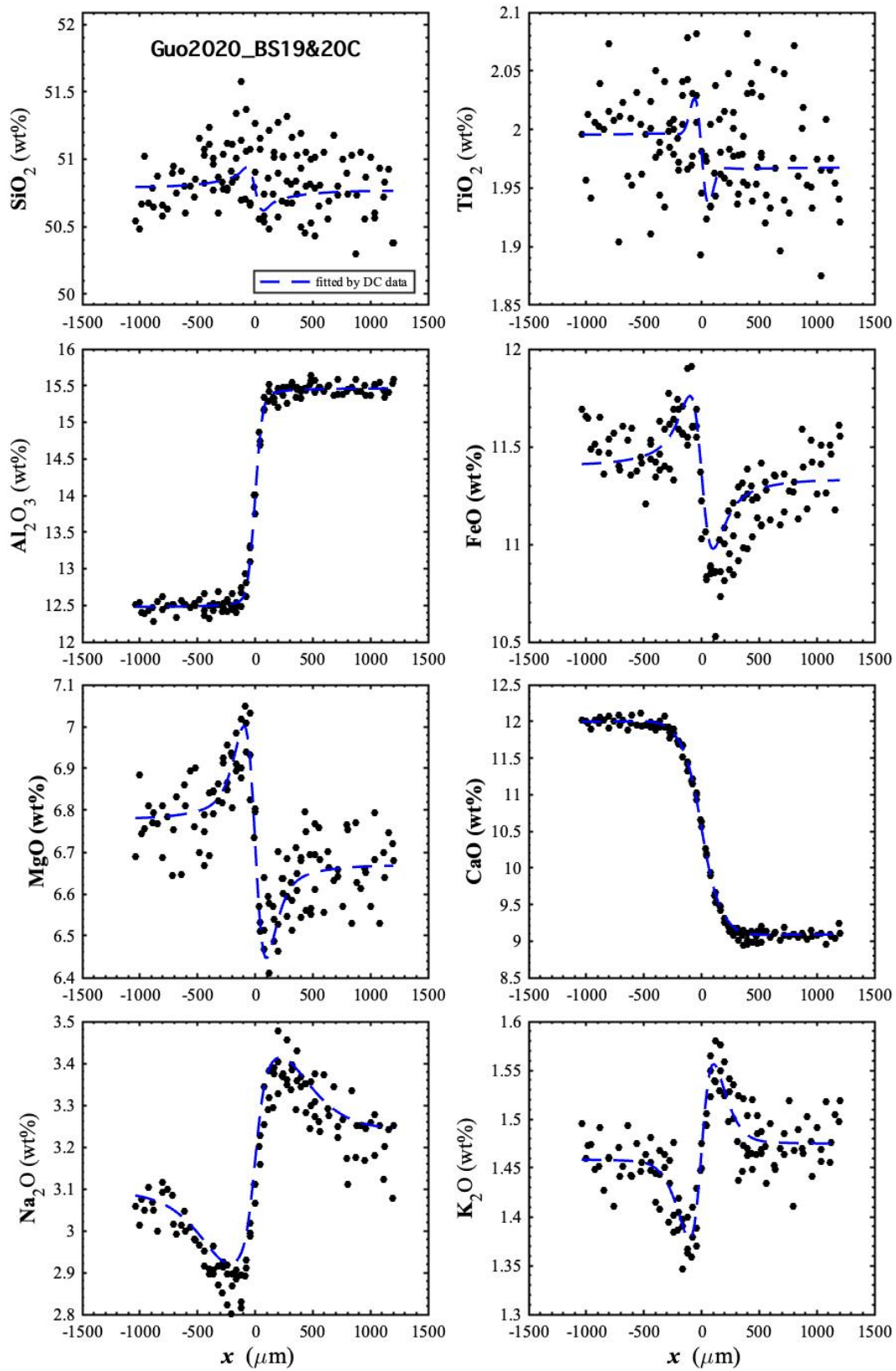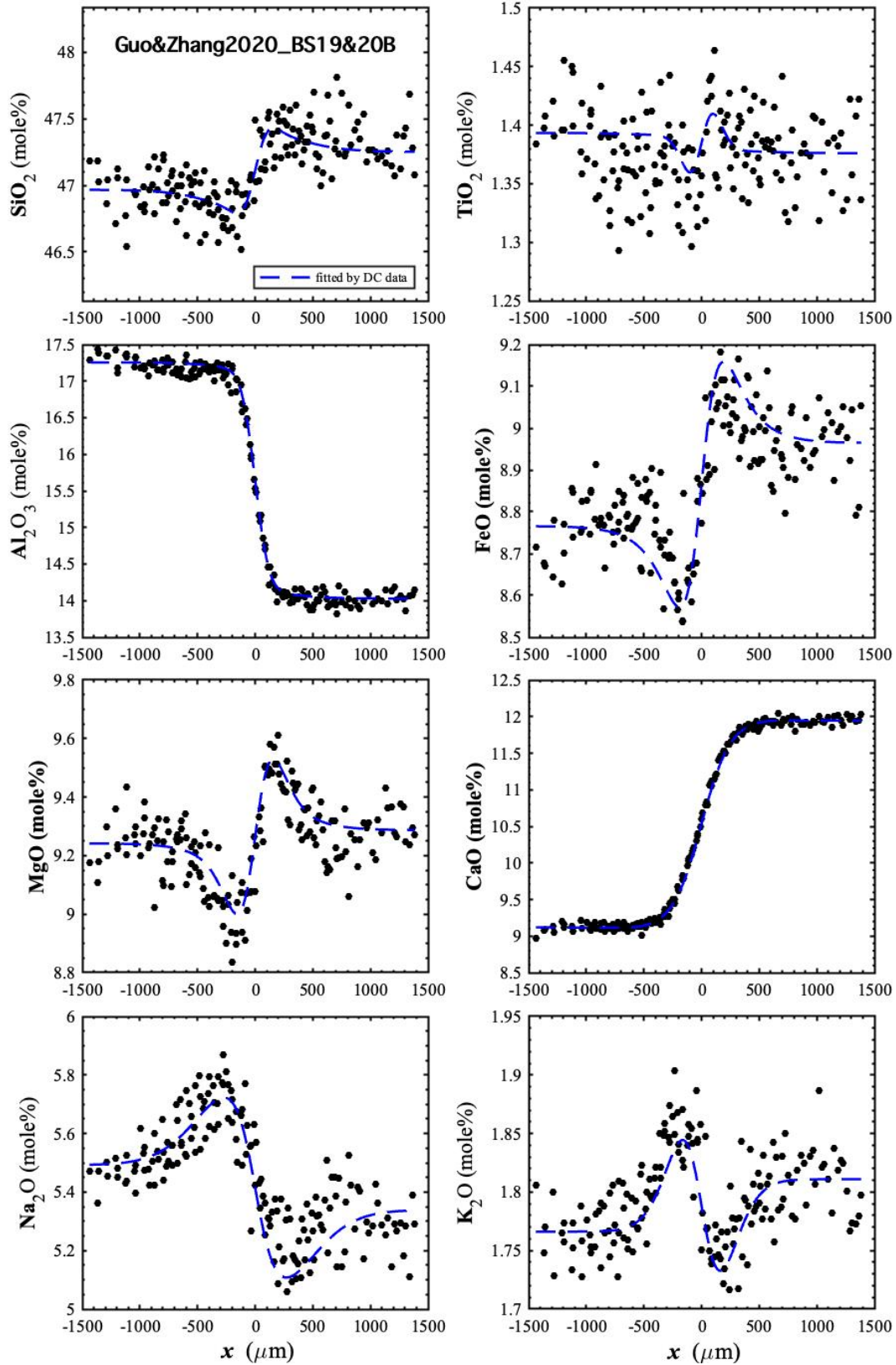
Figure C1.9. Diffusion profiles of oxide components in wt% of BS19&20C (Guo and Zhang, 2020) with fits. The dash curves are fits by the parameters in Table 4.1.
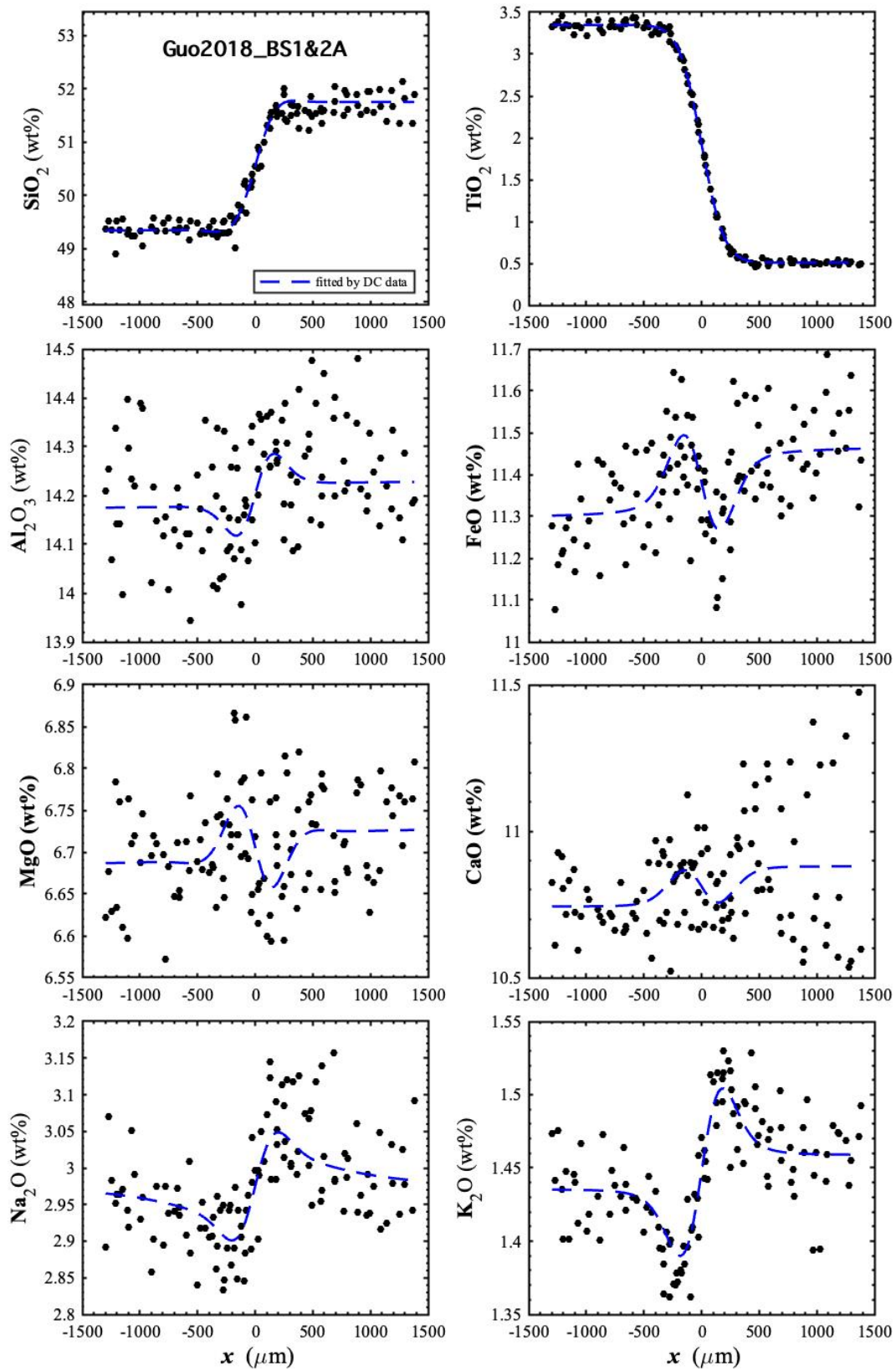
Figure C1.10. Diffusion profiles of oxide components in wt% of BS1&2A (Guo and Zhang, 2018) with fits. The dash curves are fits by the parameters in Table 4.1.

75
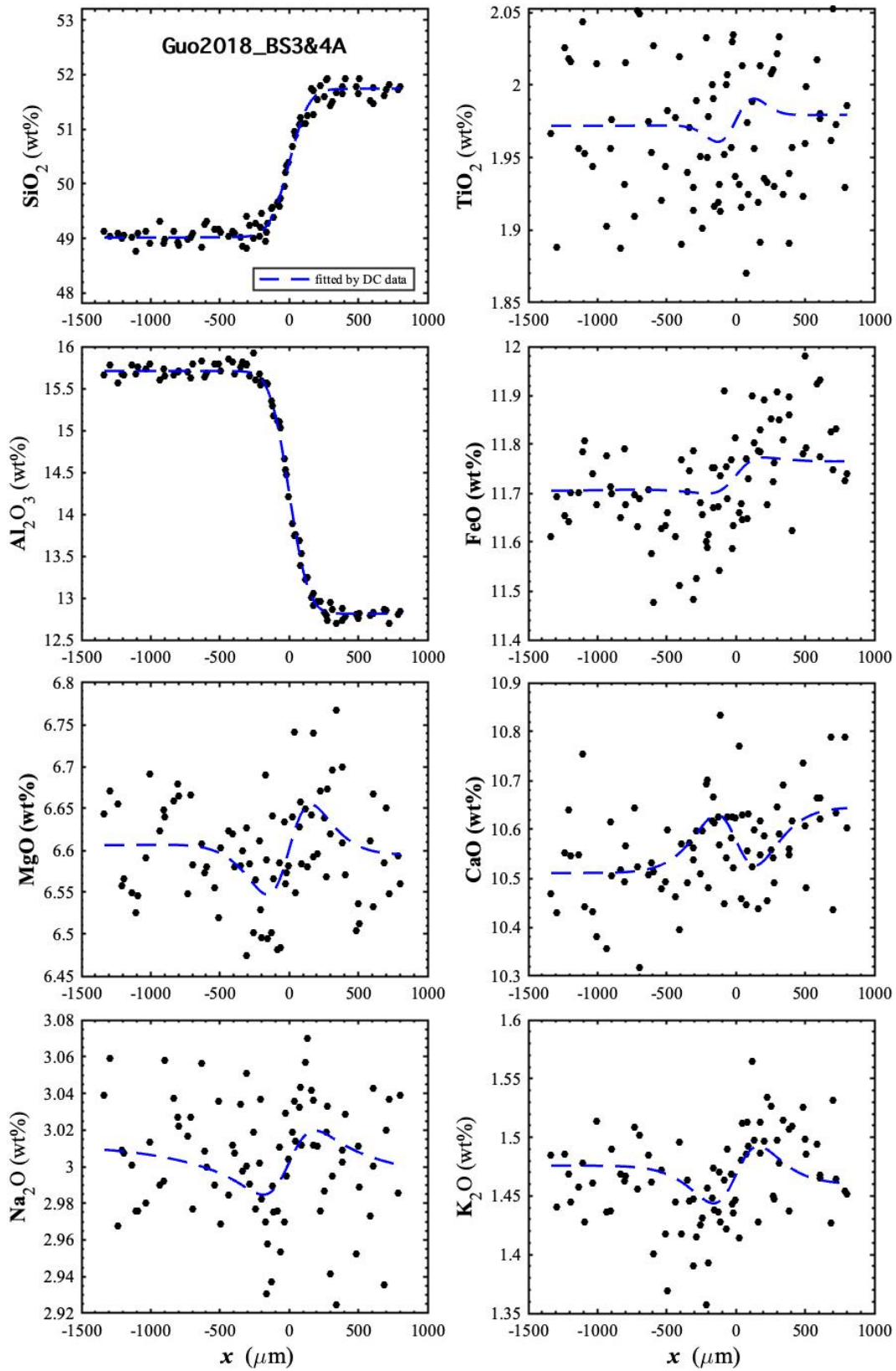
Figure C1.11. Diffusion profiles of oxide components in wt% of BS3&4A (Guo and Zhang, 2018) with fits. The dash curves are fits by the parameters in Table 4.1.
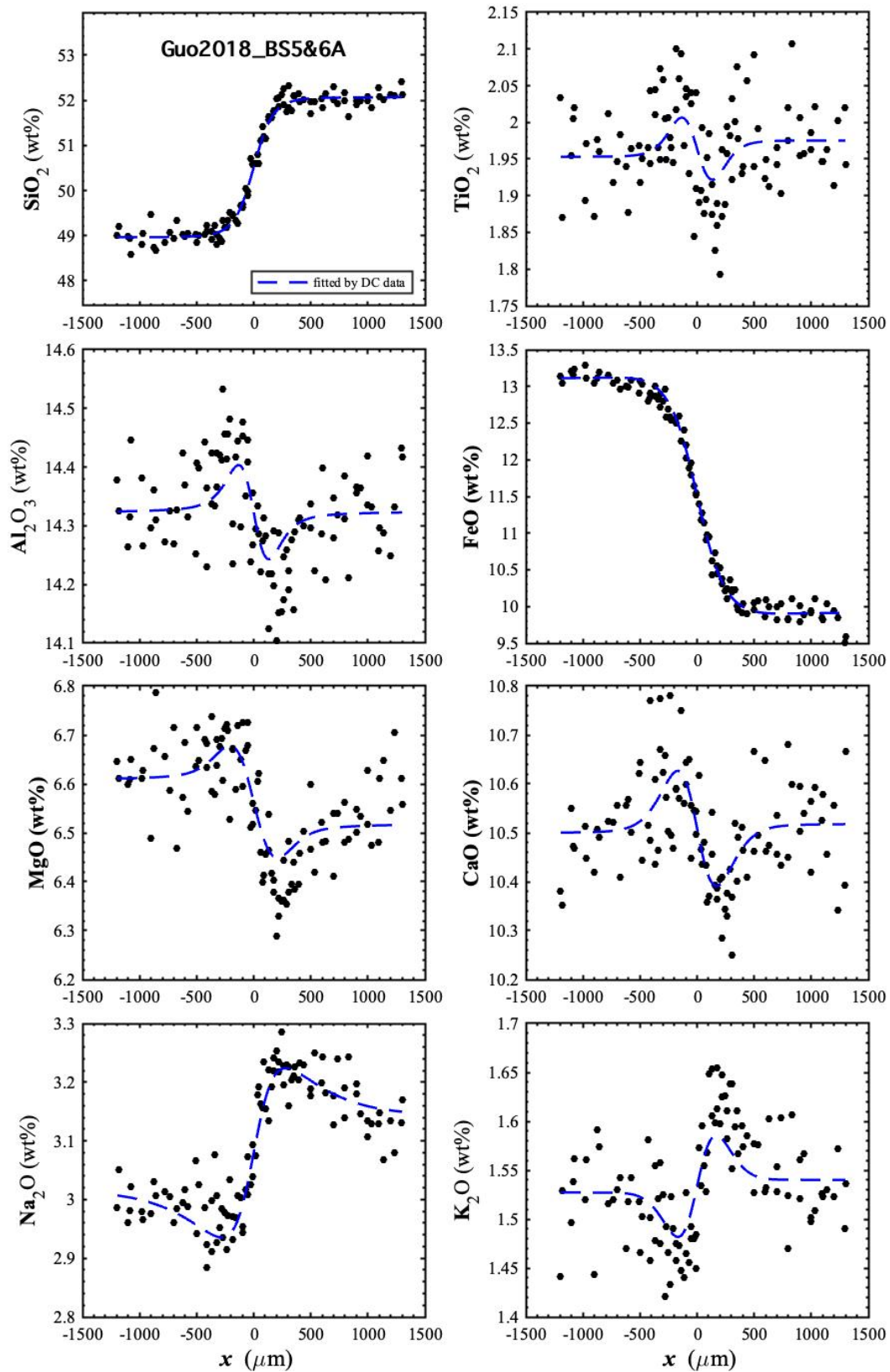
Figure C1.12. Diffusion profiles of oxide components in wt% of BS5&6A (Guo and Zhang, 2018) with fits. The dash curves are fits by the parameters in Table 4.1.
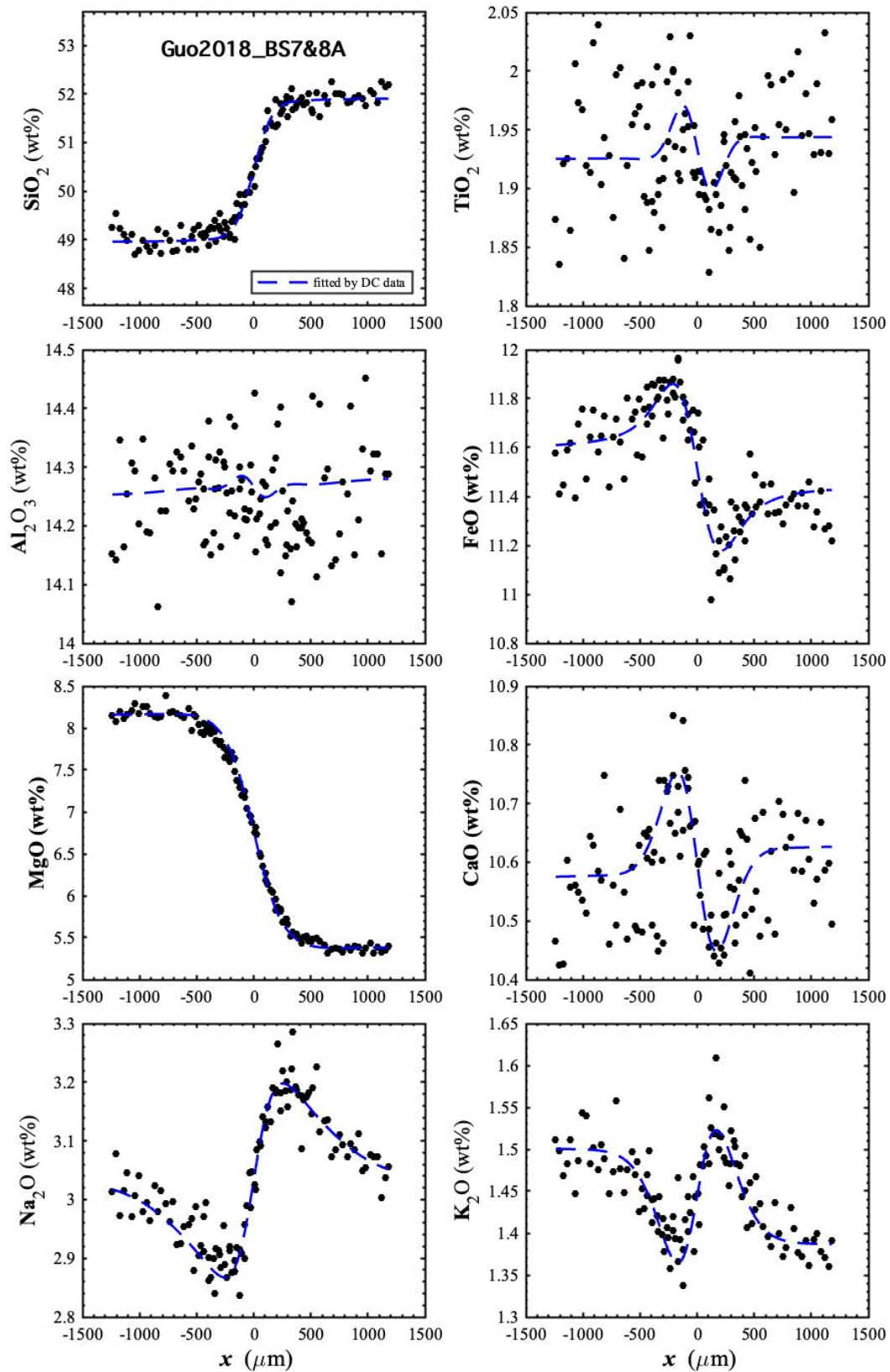
Figure C1.13. Diffusion profiles of oxide components in wt% of BS7&8A (Guo and Zhang, 2018) with fits. The dash curves are fits by the parameters in Table 4.1.

78
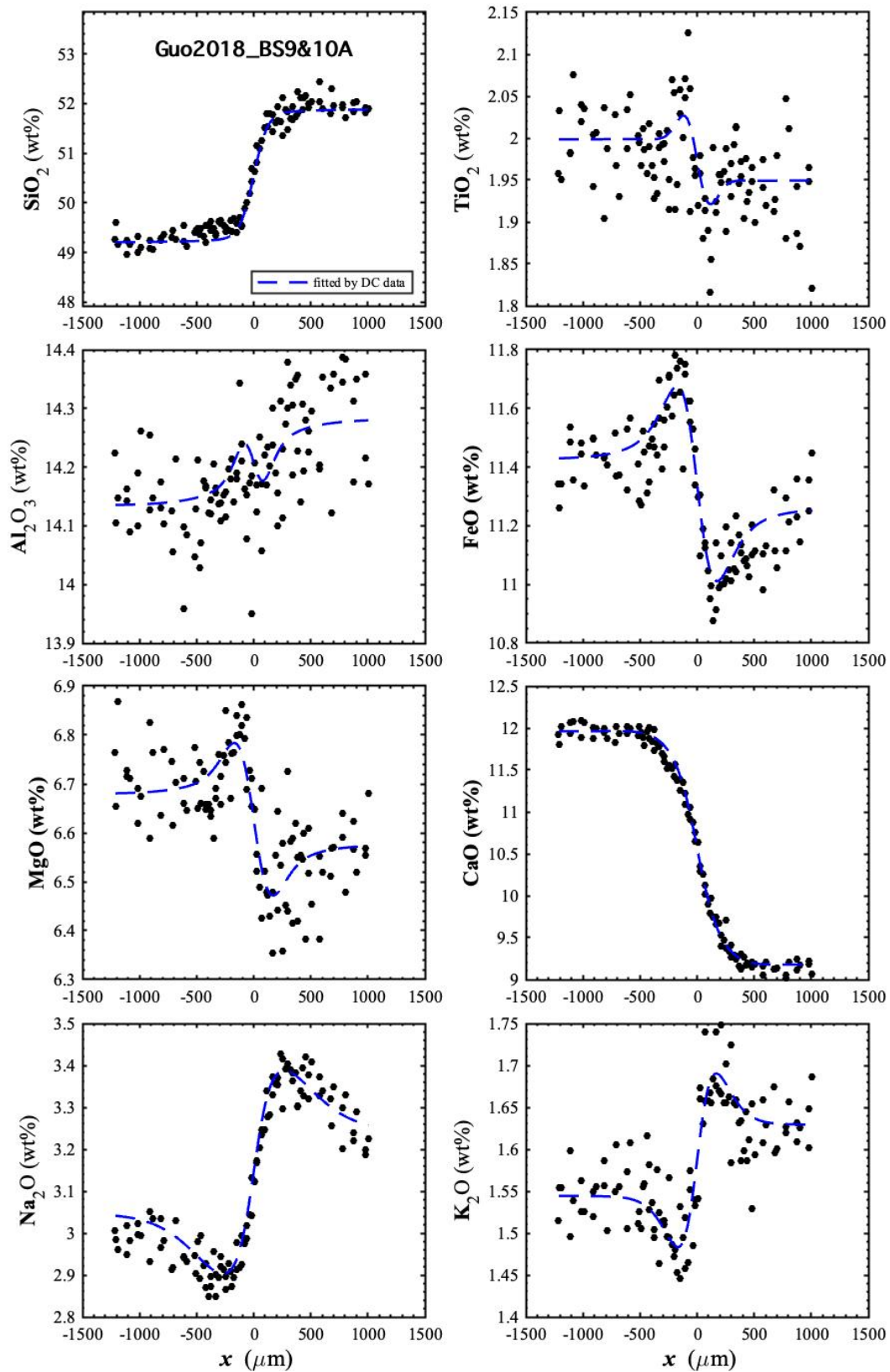
Figure C1.14. Diffusion profiles of oxide components in wt% of BS9&10A (Guo and Zhang, 2018) with fits. The dash curves are fits by the parameters in Table 4.1.

79
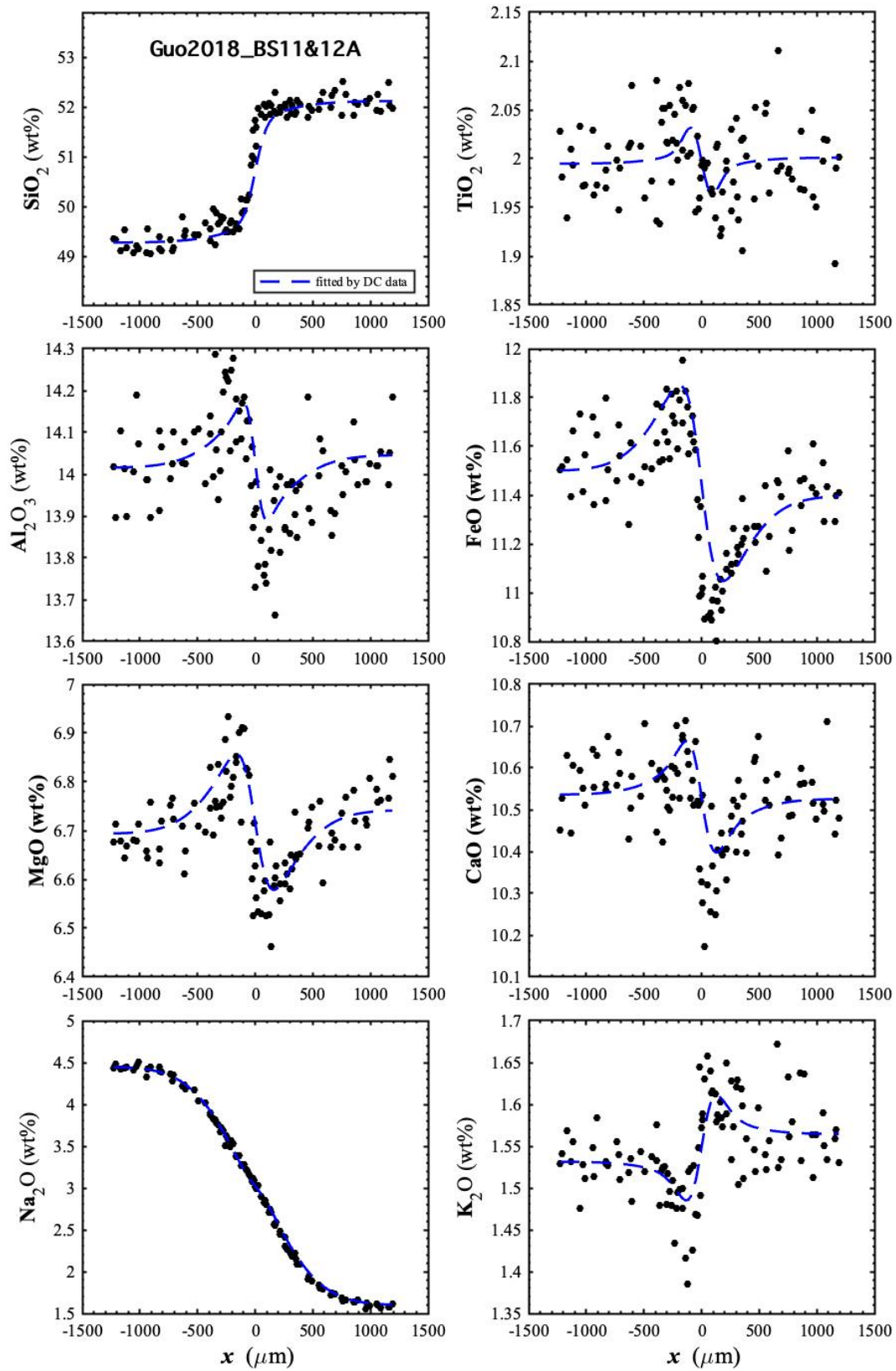
Figure C1.15. Diffusion profiles of oxide components in wt% of BS11&12C (Guo and Zhang, 2018) with fits. The dash curves are fits by the parameters in Table 4.1.

80
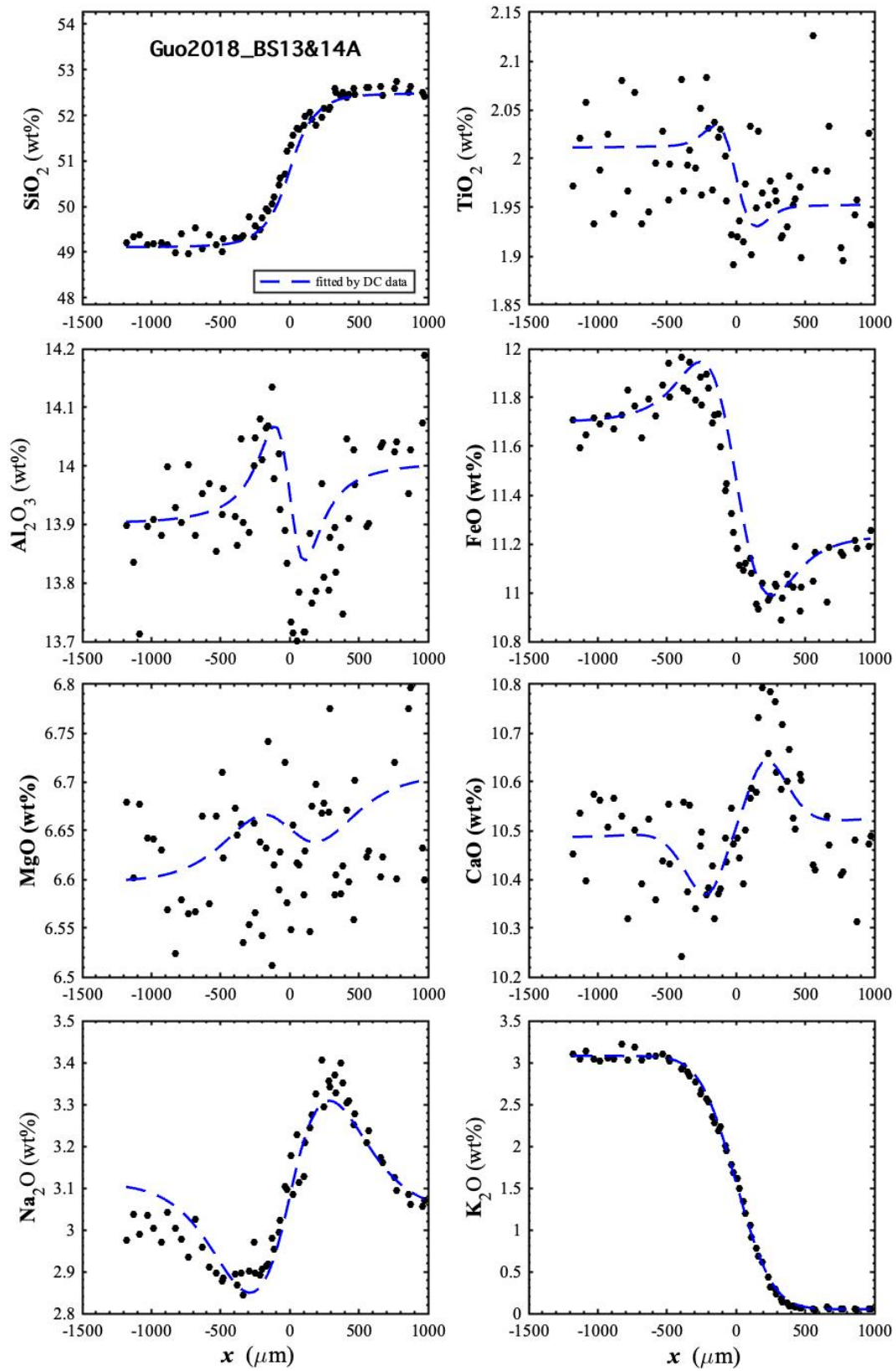
Figure C1.16. Diffusion profiles of oxide components in wt% of BS13&14A (Guo and Zhang, 2018) with fits. The dash curves are fits by the parameters in Table 4.1.

81
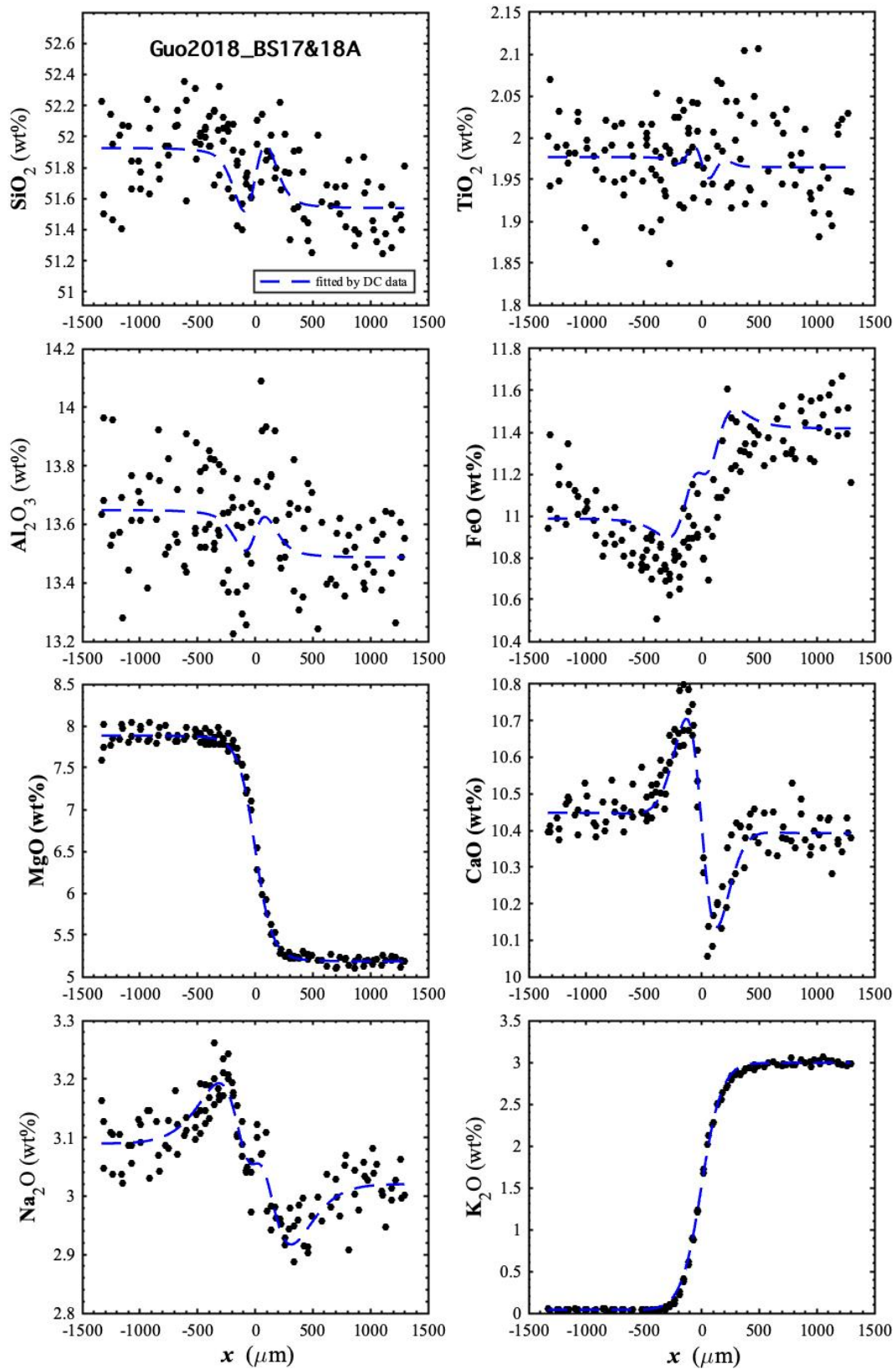
Figure C1.17. Diffusion profiles of oxide components in wt% of BS17&18A (Guo and Zhang, 2018) with fits. The dash curves are fits by the parameters in Table 4.1.
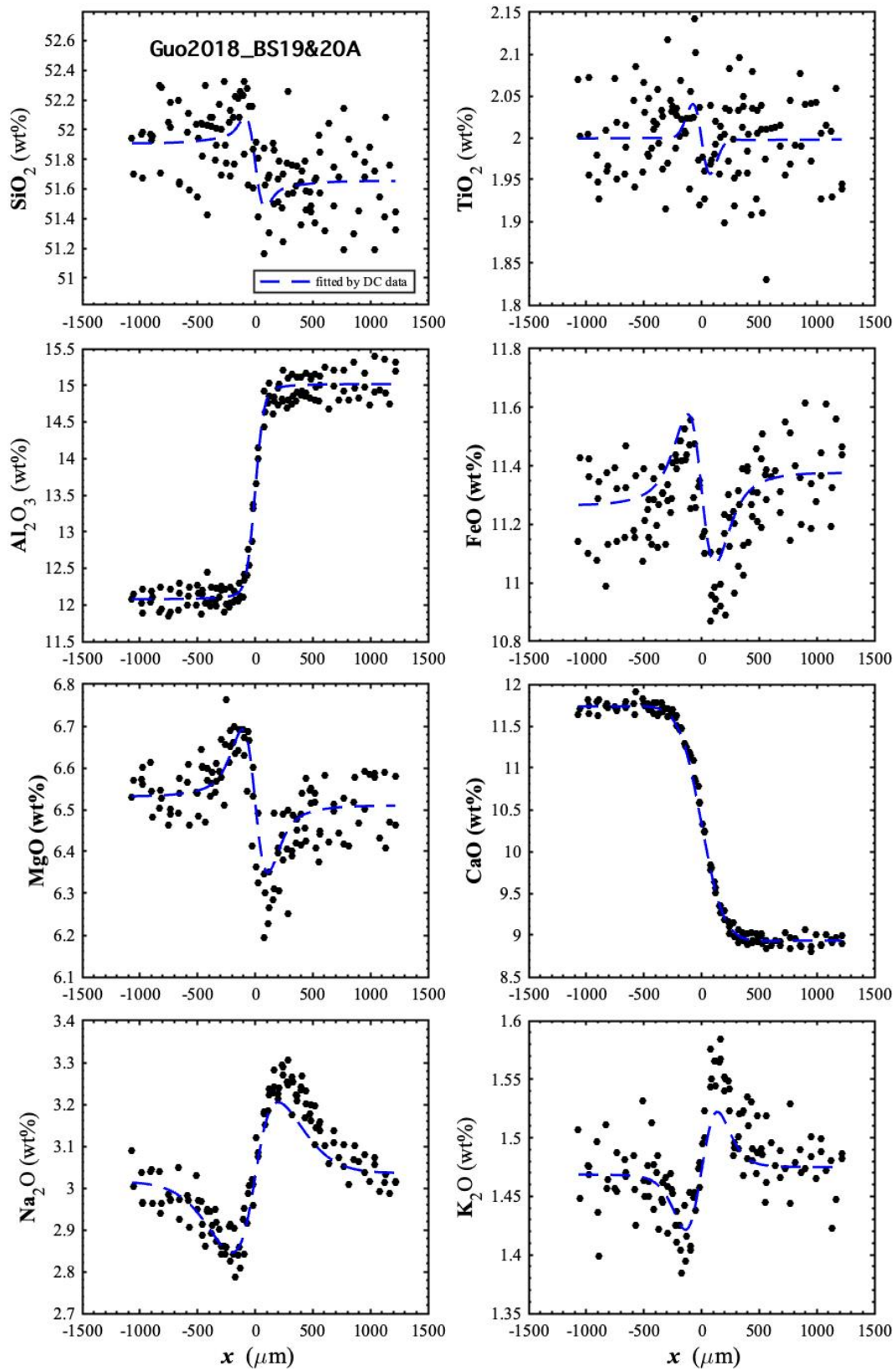
Figure C1.18. Diffusion profiles of oxide components in wt% of BS19&20C (Guo and Zhang, 2018) with fits. The dash curves are fits by the parameters in Table 4.1.
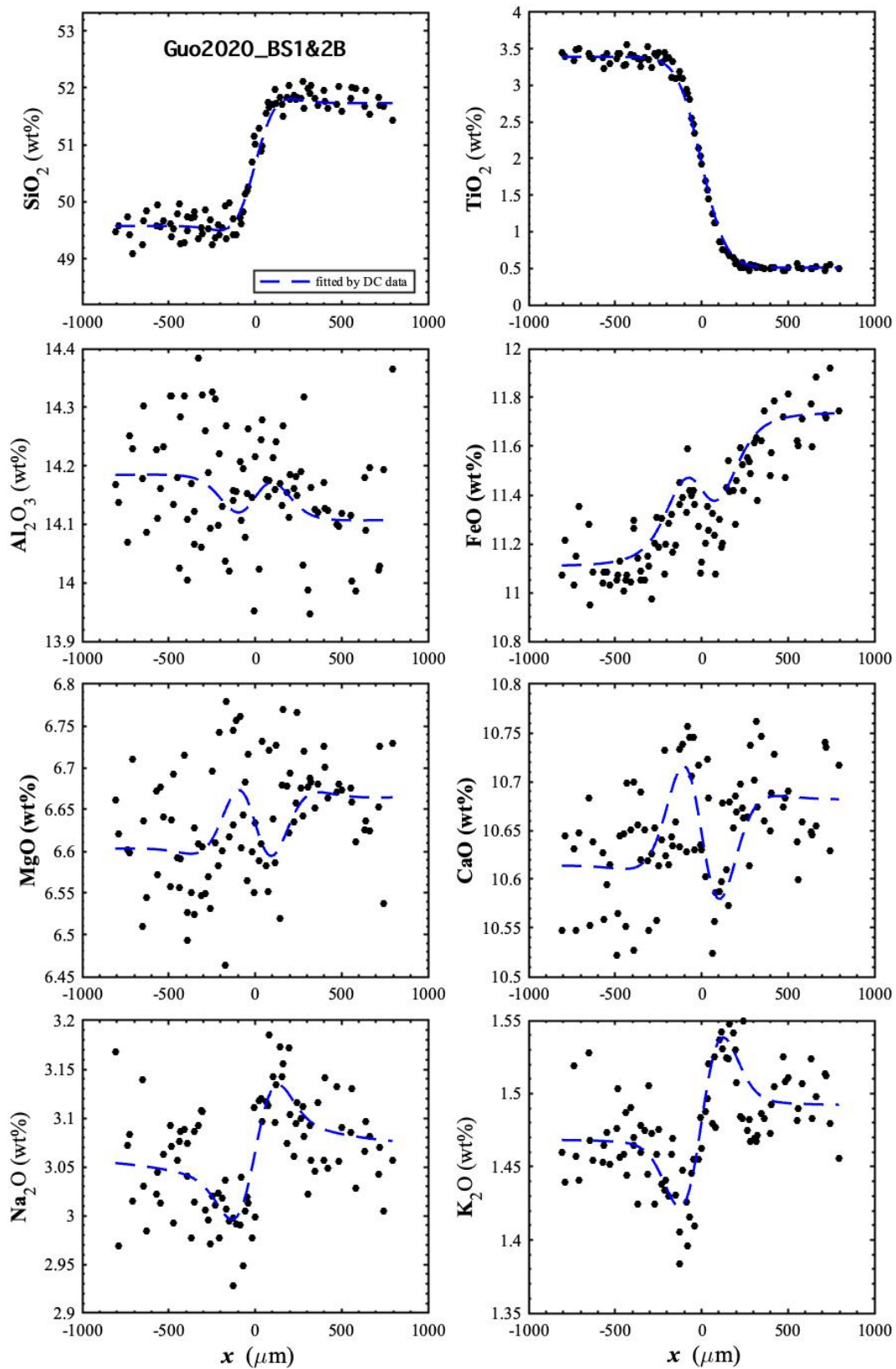
Figure C1.19. Diffusion profiles of oxide components in wt% of BS1&2B (Guo and Zhang, 2020) with fits. The dash curves are fits by the parameters in Table 4.1.

84
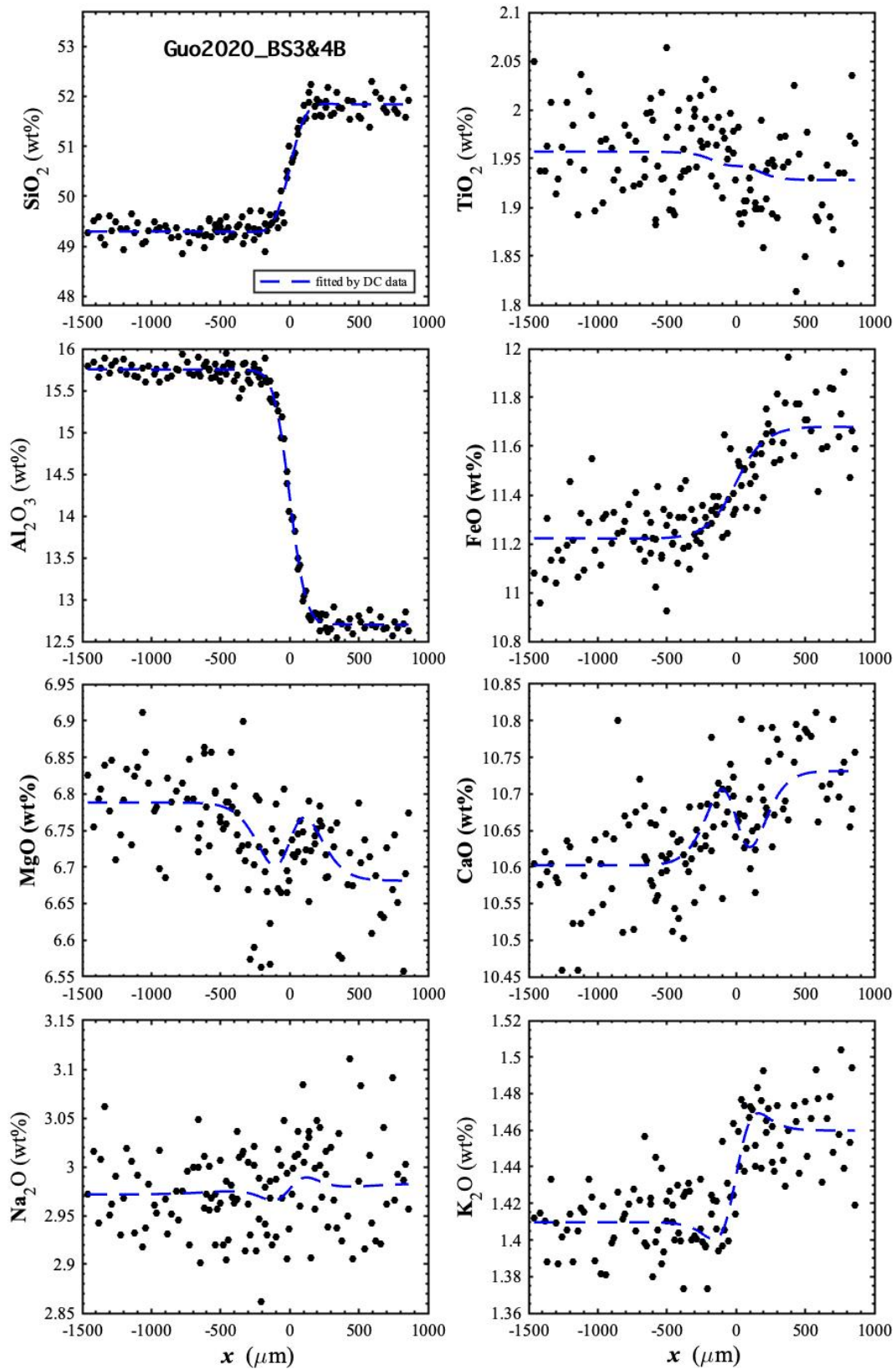
Figure C1.20. Diffusion profiles of oxide components in wt% of BS3&4B (Guo and Zhang, 2020) with fits. The dash curves are fits by the parameters in Table 4.1.
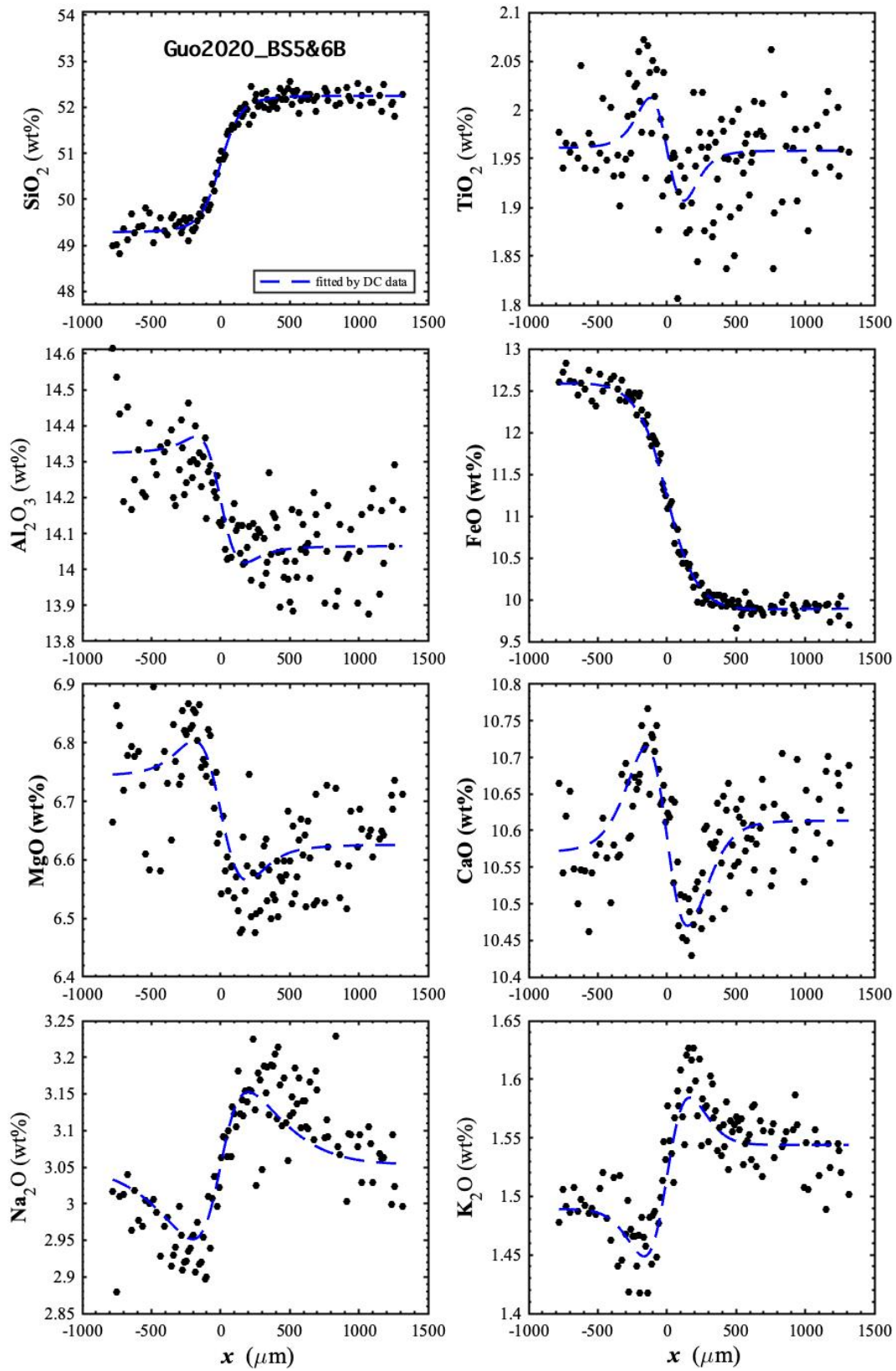
Figure C1.21. Diffusion profiles of oxide components in wt% of BS5&6B (Guo and Zhang, 2020) with fits. The dash curves are fits by the parameters in Table 4.1.

86
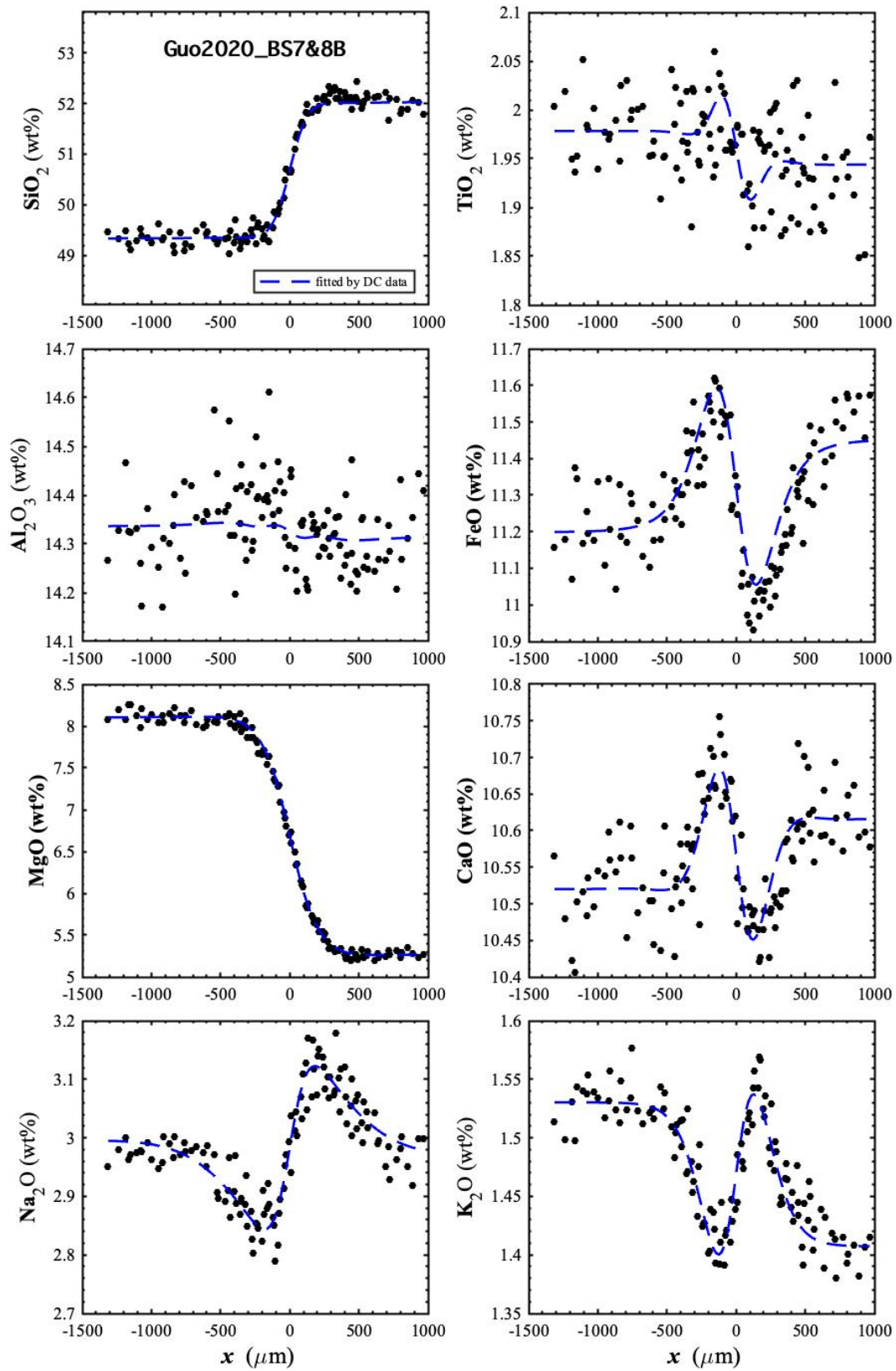
Figure C1.22. Diffusion profiles of oxide components in wt% of BS7&8B (Guo and Zhang, 2020) with fits. The dash curves are fits by the parameters in Table 4.1.
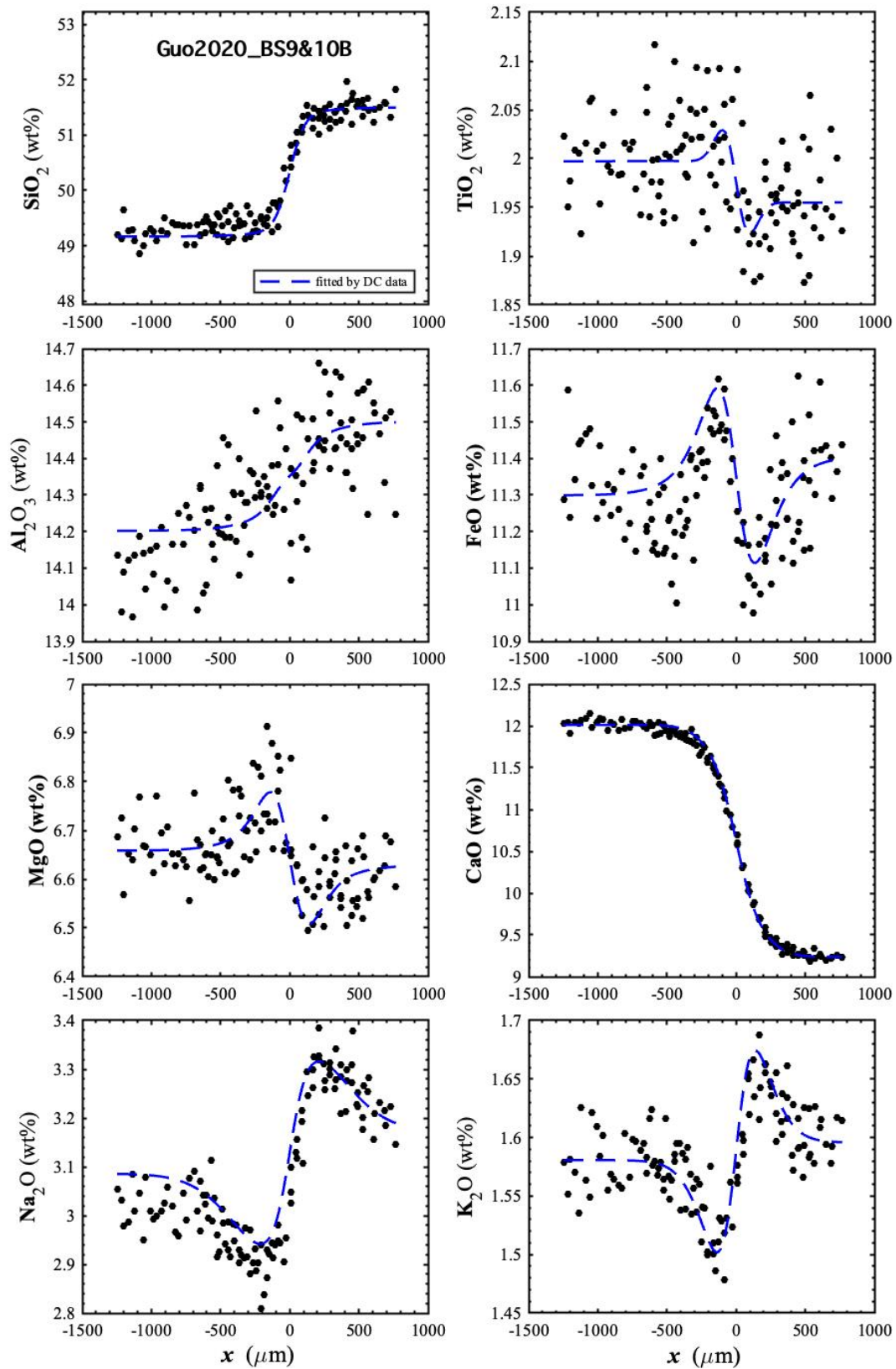
Figure C1.23. Diffusion profiles of oxide components in wt% of BS9&10B (Guo and Zhang, 2020) with fits. The dash curves are fits by the parameters in Table 4.1.
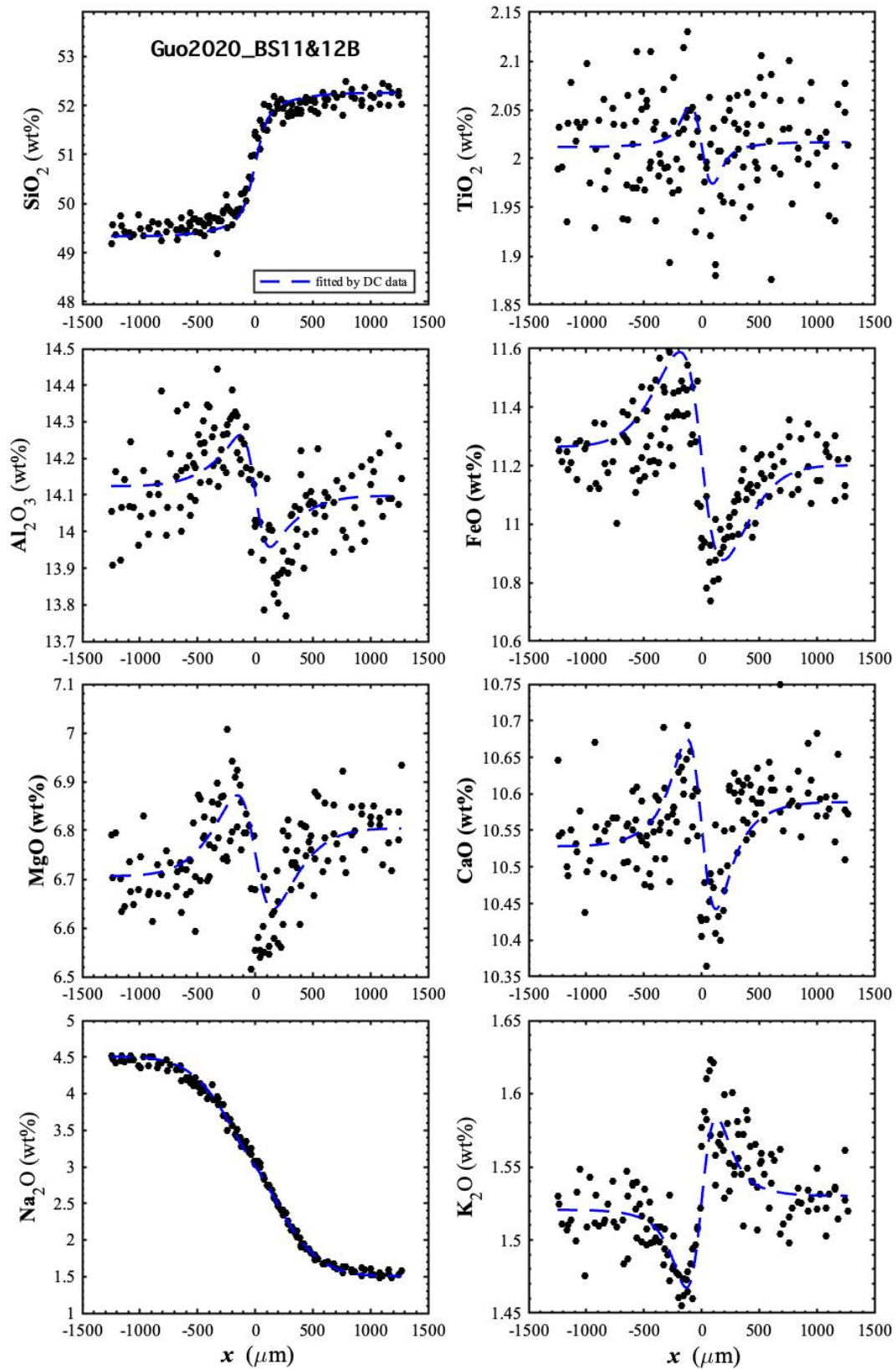
Figure C1.24. Diffusion profiles of oxide components in wt% of BS11&12B (Guo and Zhang, 2020) with fits. The dash curves are fits by the parameters in Table 4.1.

89
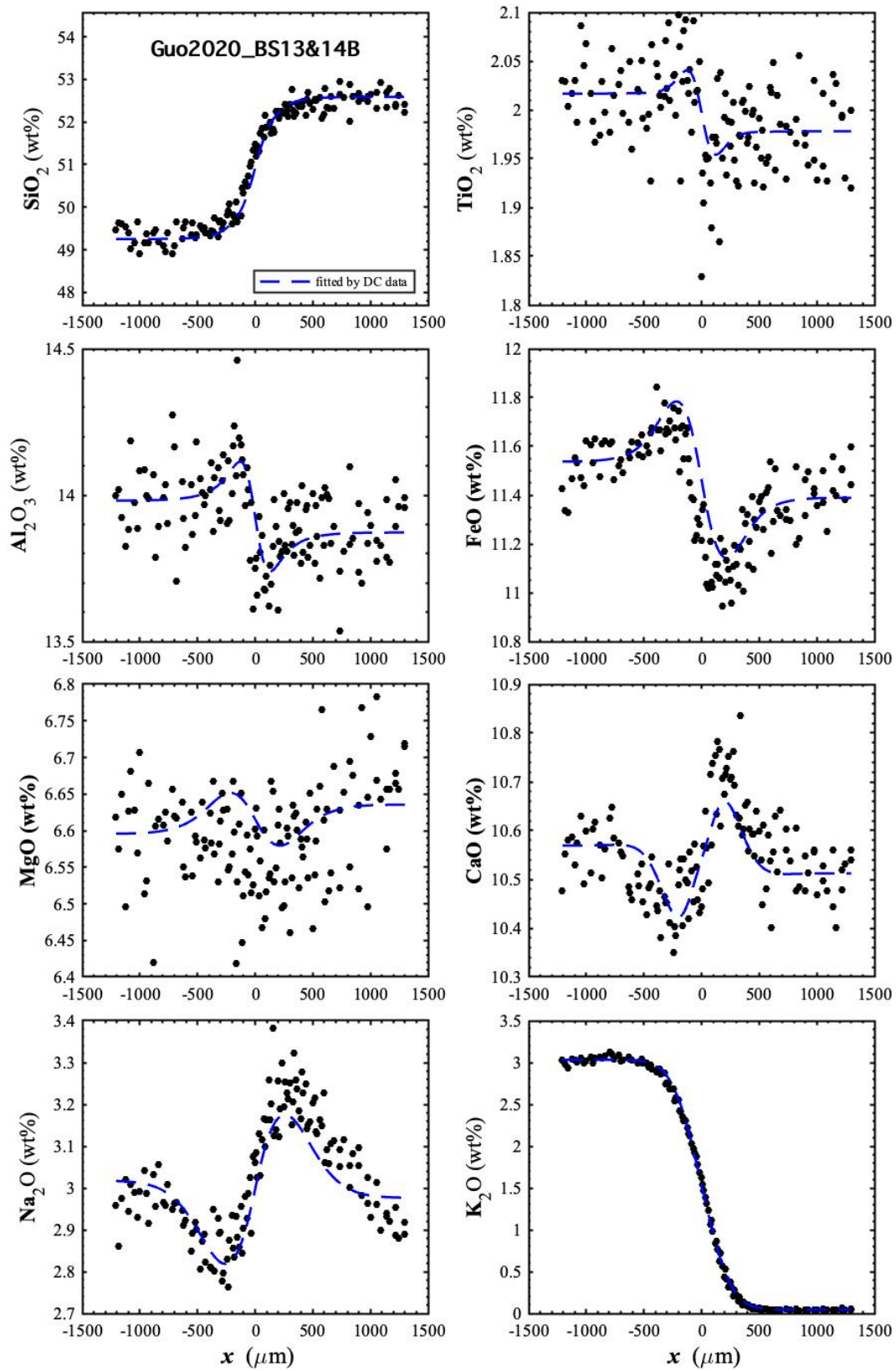
Figure C1.25. Diffusion profiles of oxide components in wt% of BS13&14B (Guo and Zhang, 2020) with fits. The dash curves are fits by the parameters in Table 4.1.

90
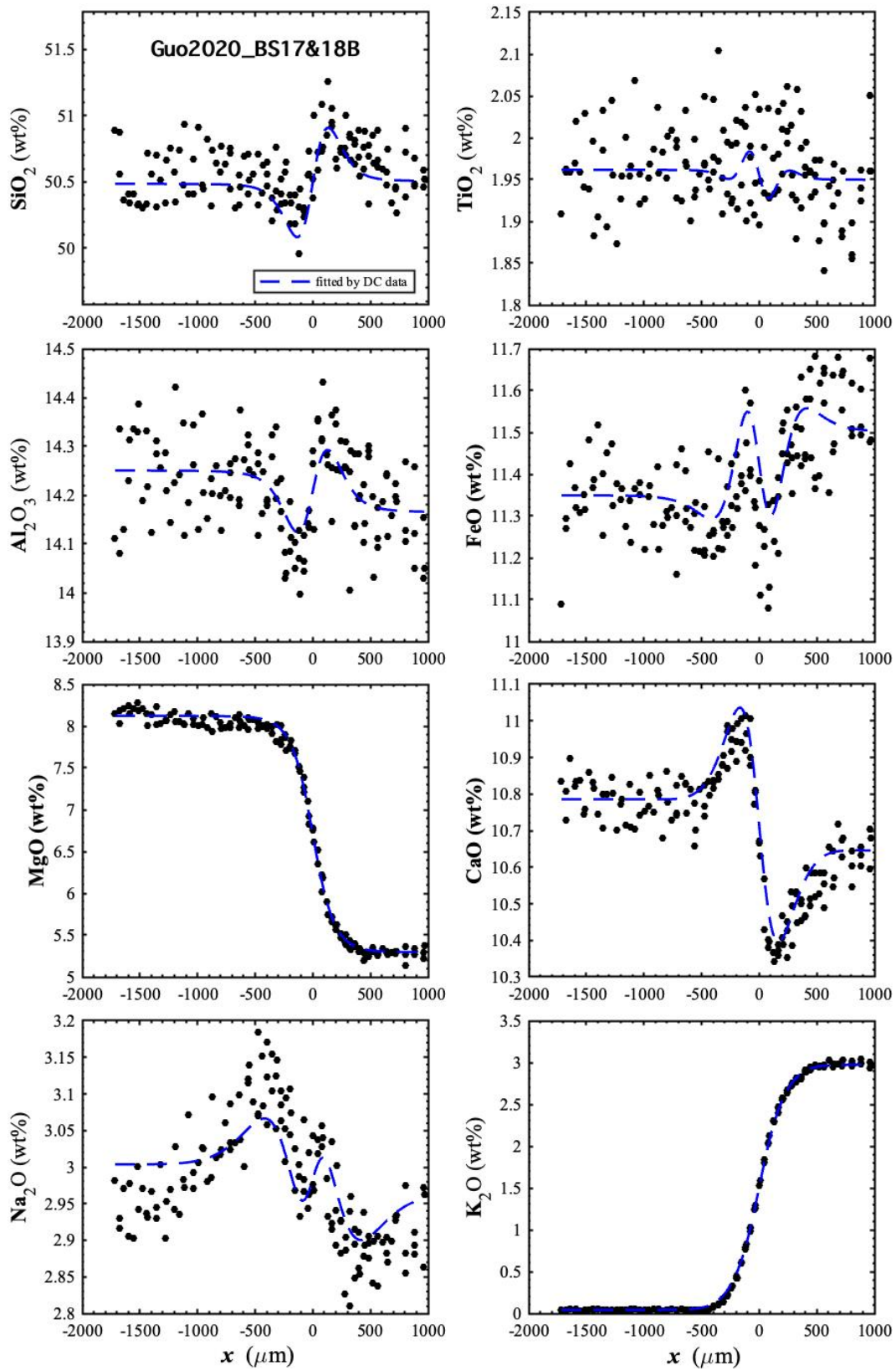
Figure C1.26. Diffusion profiles of oxide components in wt% of BS17&18B (Guo and Zhang, 2020) with fits. The dash curves are fits by the parameters in Table 4.1.

91
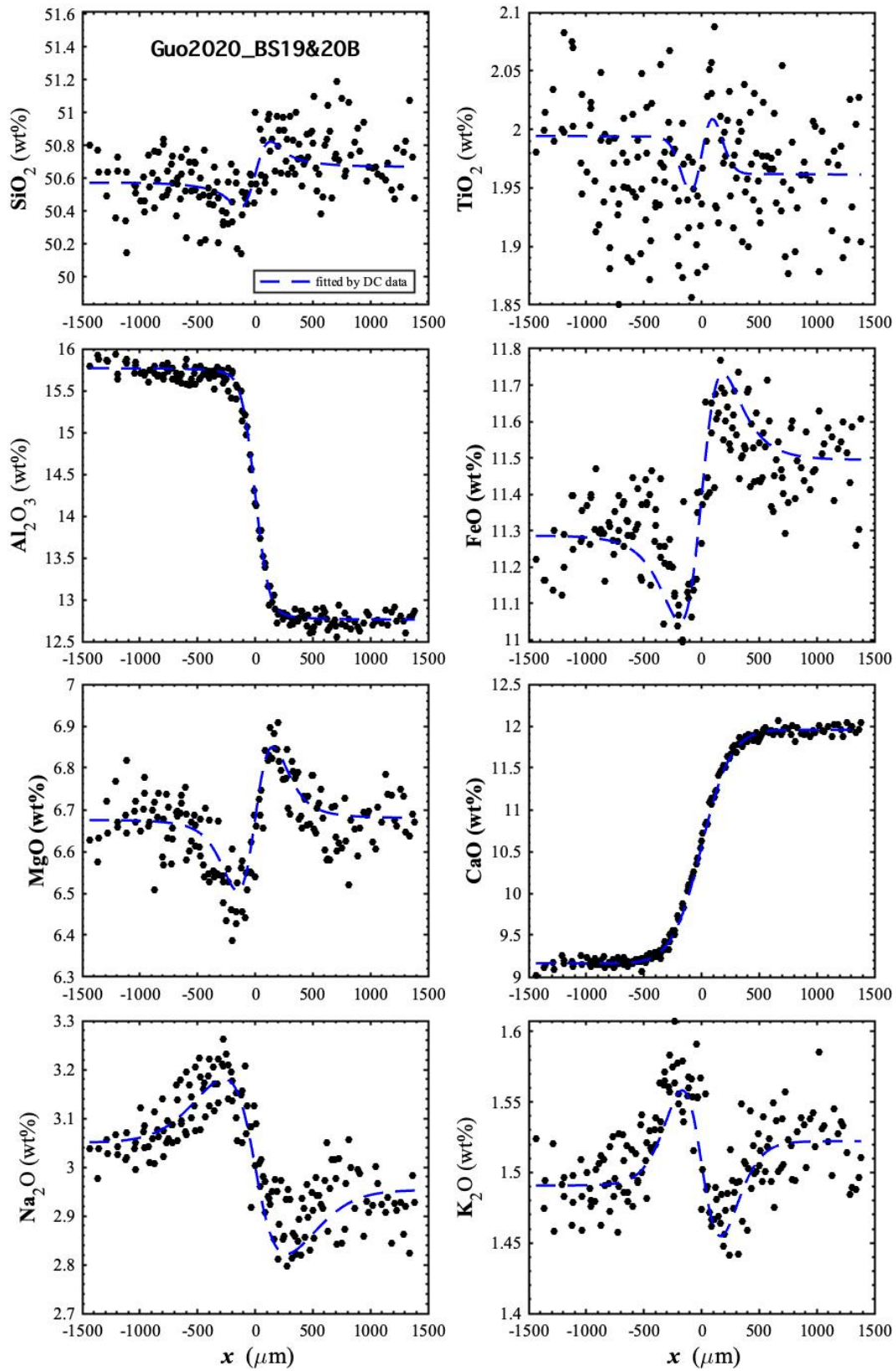
Figure C1.27. Diffusion profiles of oxide components in wt% of BS19&20B (Guo and Zhang, 2020) with fits. The dash curves are fits by the parameters in Table 4.1.

C2. Fits of diffusion profiles using mole fraction as concentration
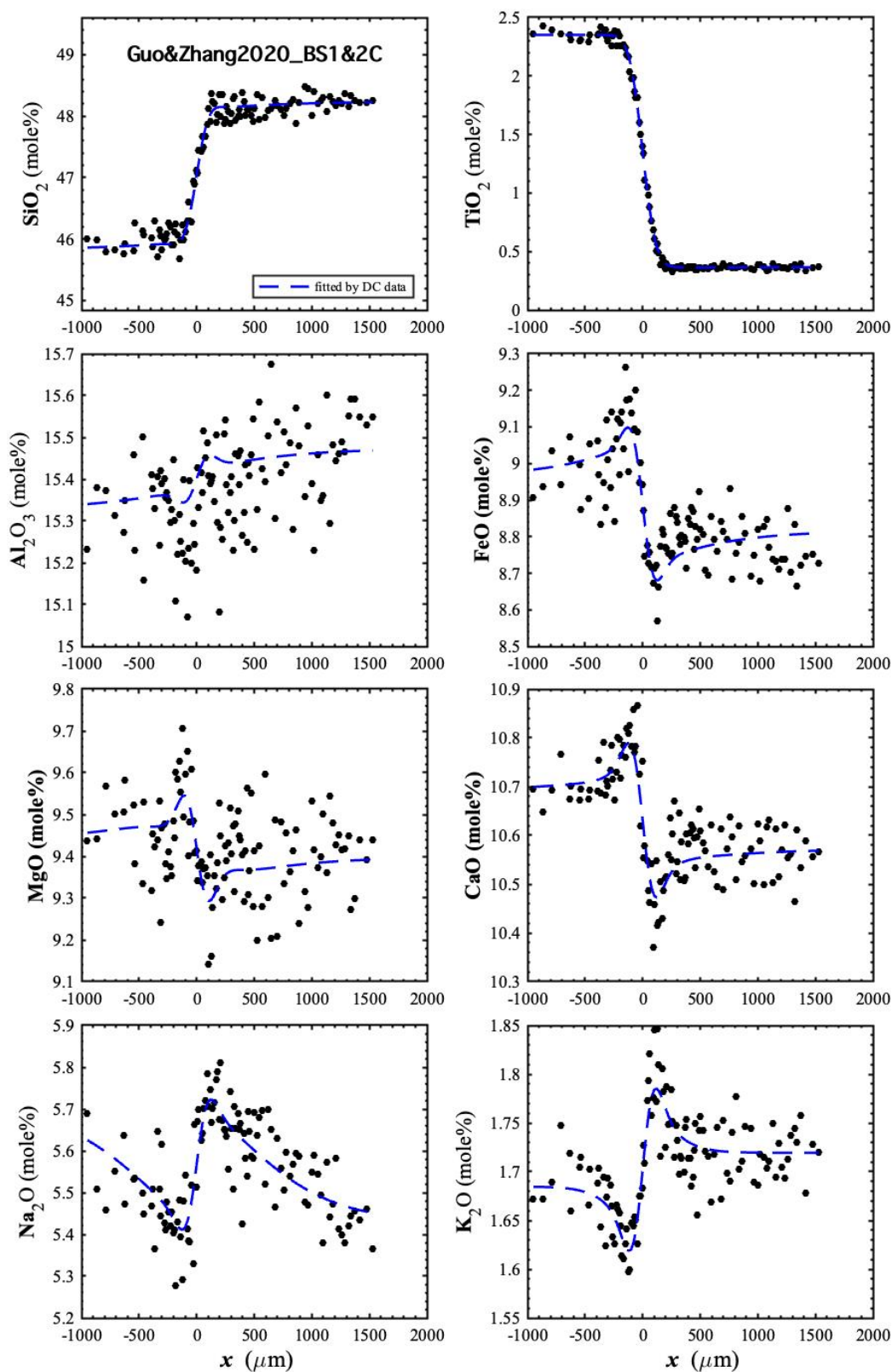
Figure C2.1. Diffusion profiles of oxide components in mole% of BS1&2C (Guo and Zhang, 2020) with fits. The dash curves are fits by the parameters in Table 4.3.
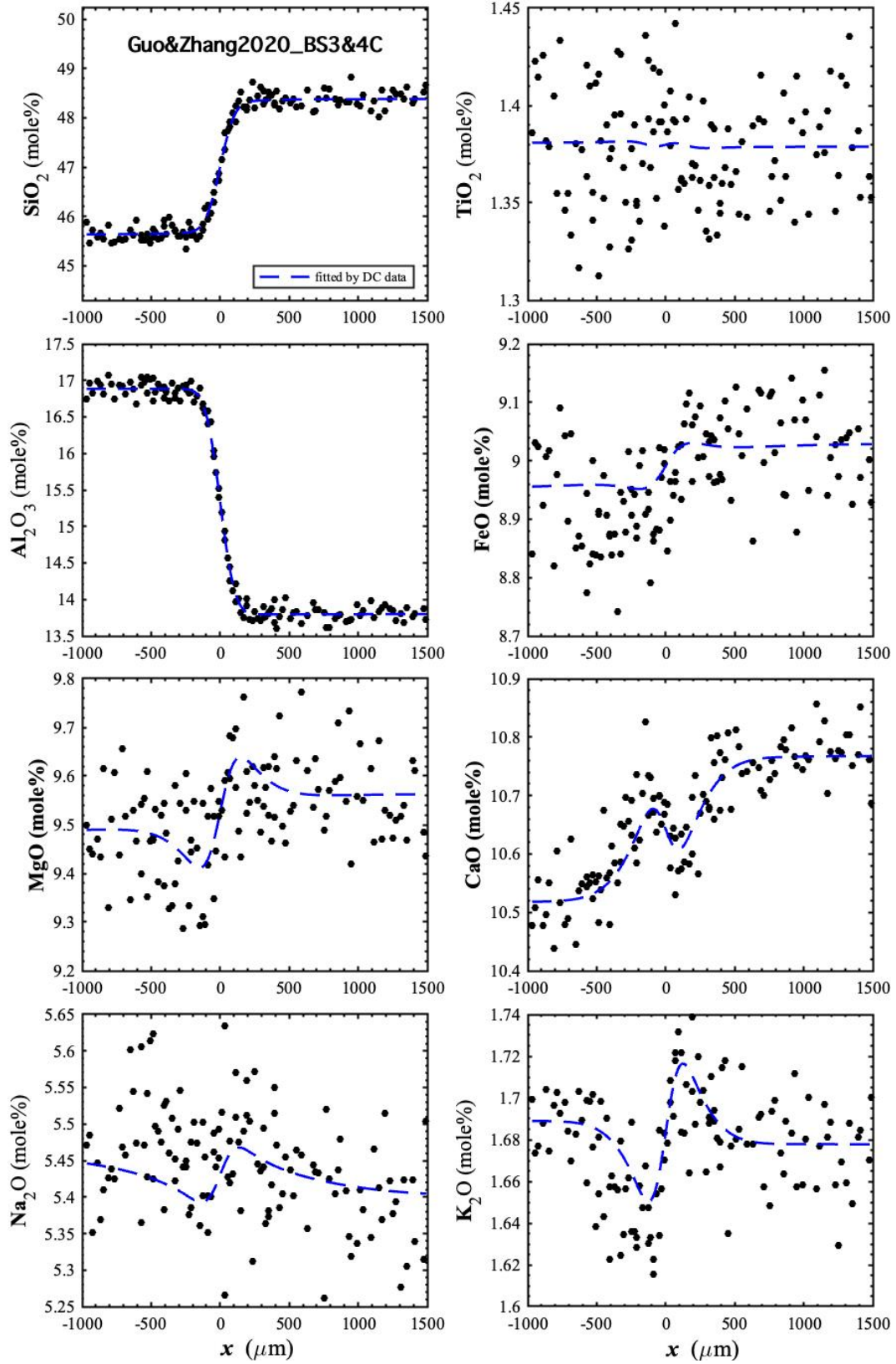
Figure C2.2. Diffusion profiles of oxide components in mole% of BS3&4C (Guo and Zhang, 2020) with fits. The dash curves are fits by the parameters in Table 4.3.
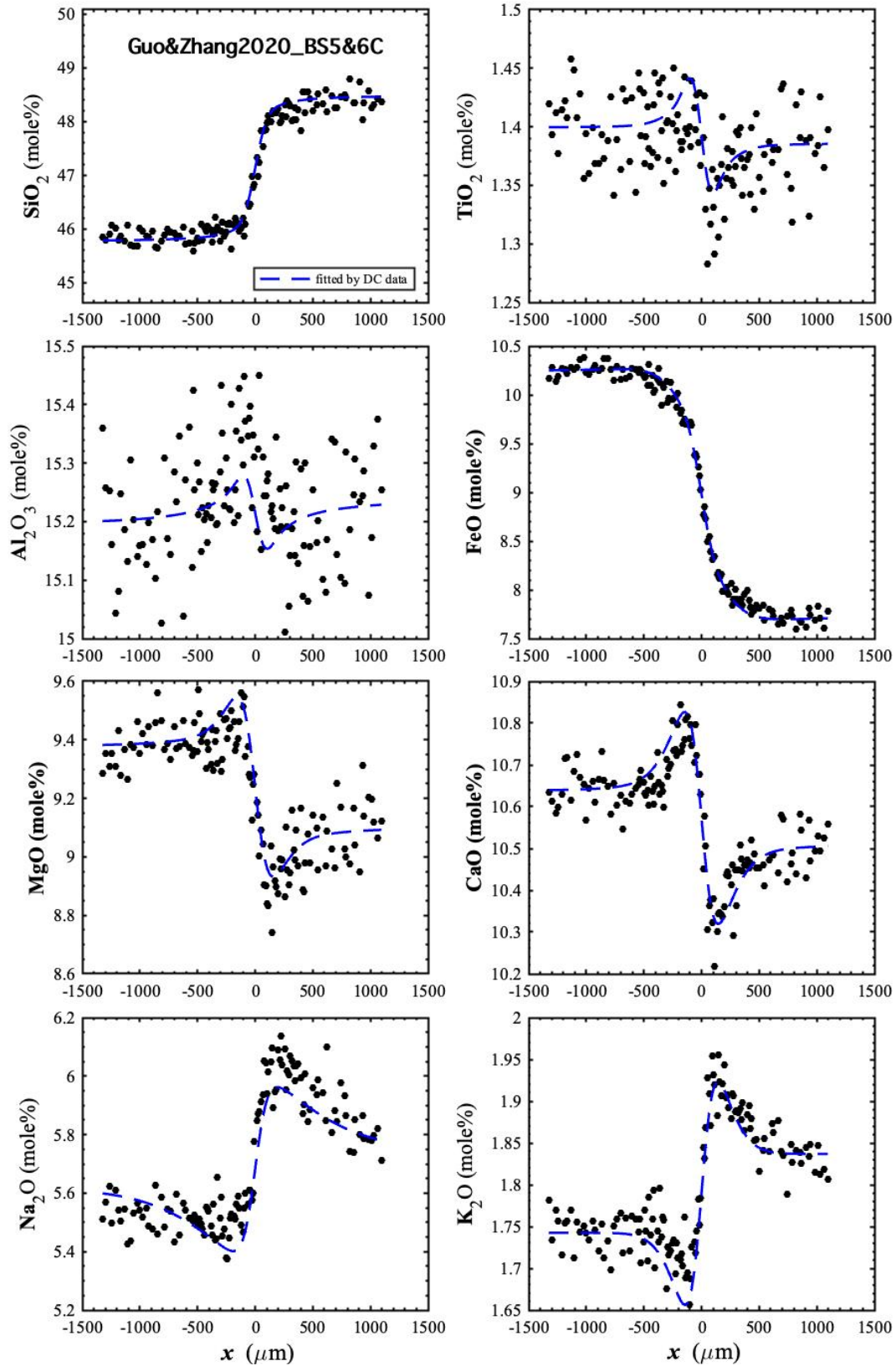
Figure C2.3. Diffusion profiles of oxide components in mole% of BS5&6C (Guo and Zhang, 2020) with fits. The dash curves are fits by the parameters in Table 4.3.
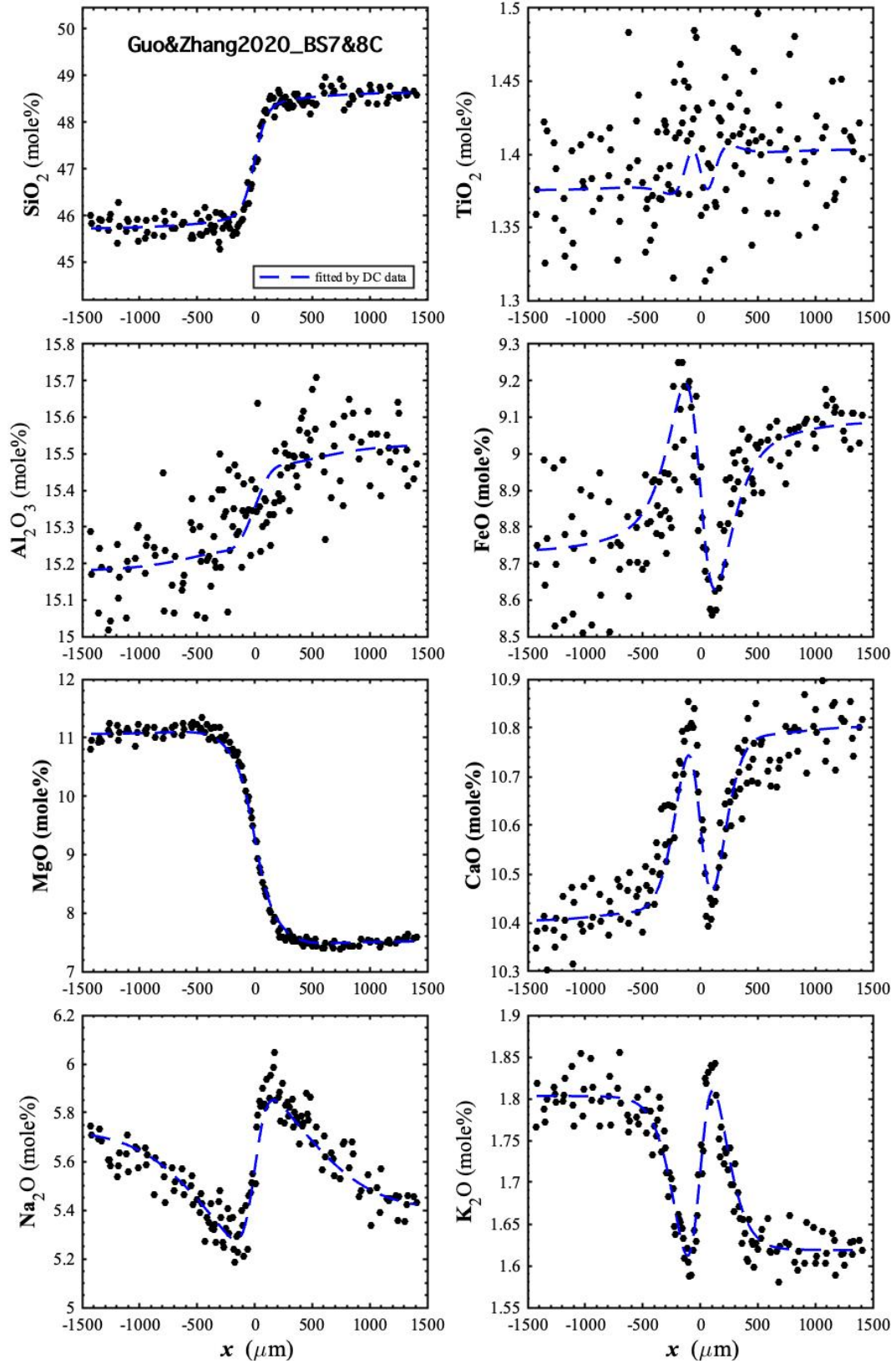
Figure C2.4. Diffusion profiles of oxide components in mole% of BS7&8C (Guo and Zhang, 2020) with fits. The dash curves are fits by the parameters in Table 4.3.

96
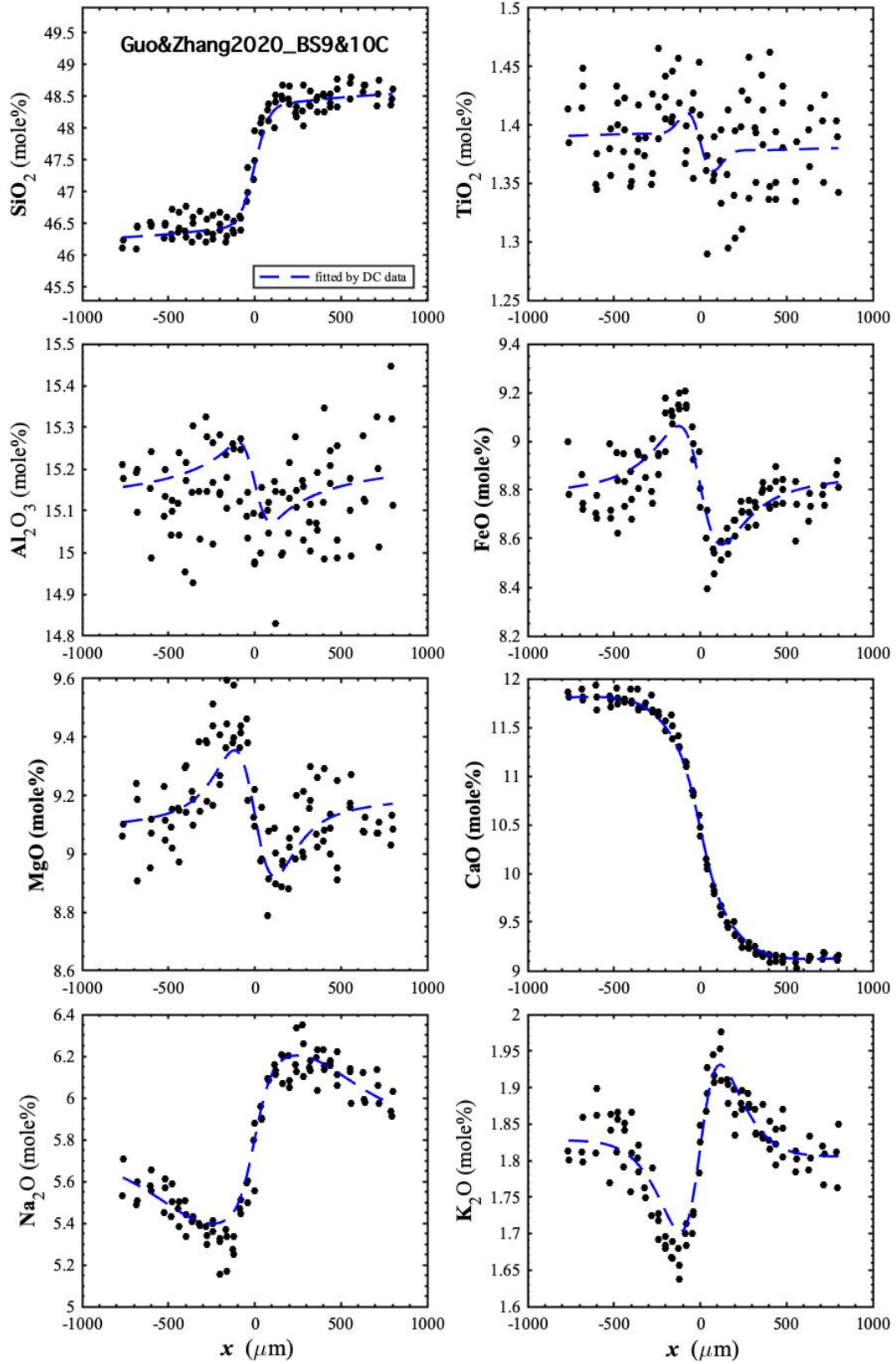
Figure C2.5. Diffusion profiles of oxide components in mole% of BS9&10C (Guo and Zhang, 2020) with fits. The dash curves are fits by the parameters in Table 4.3.
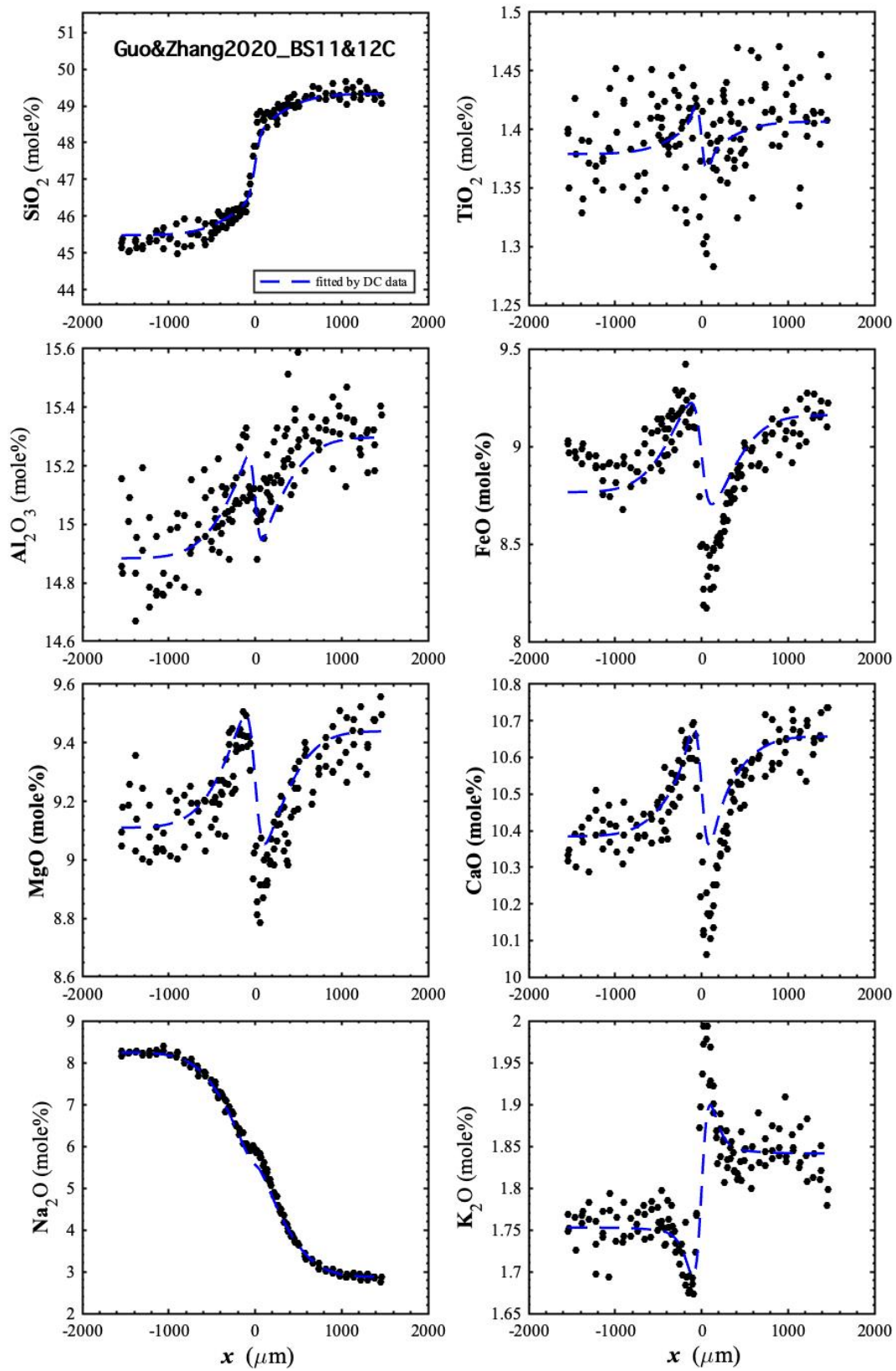
Figure C2.6. Diffusion profiles of oxide components in mole% of BS11&12C (Guo and Zhang, 2020) with fits. The dash curves are fits by the parameters in Table 4.3.
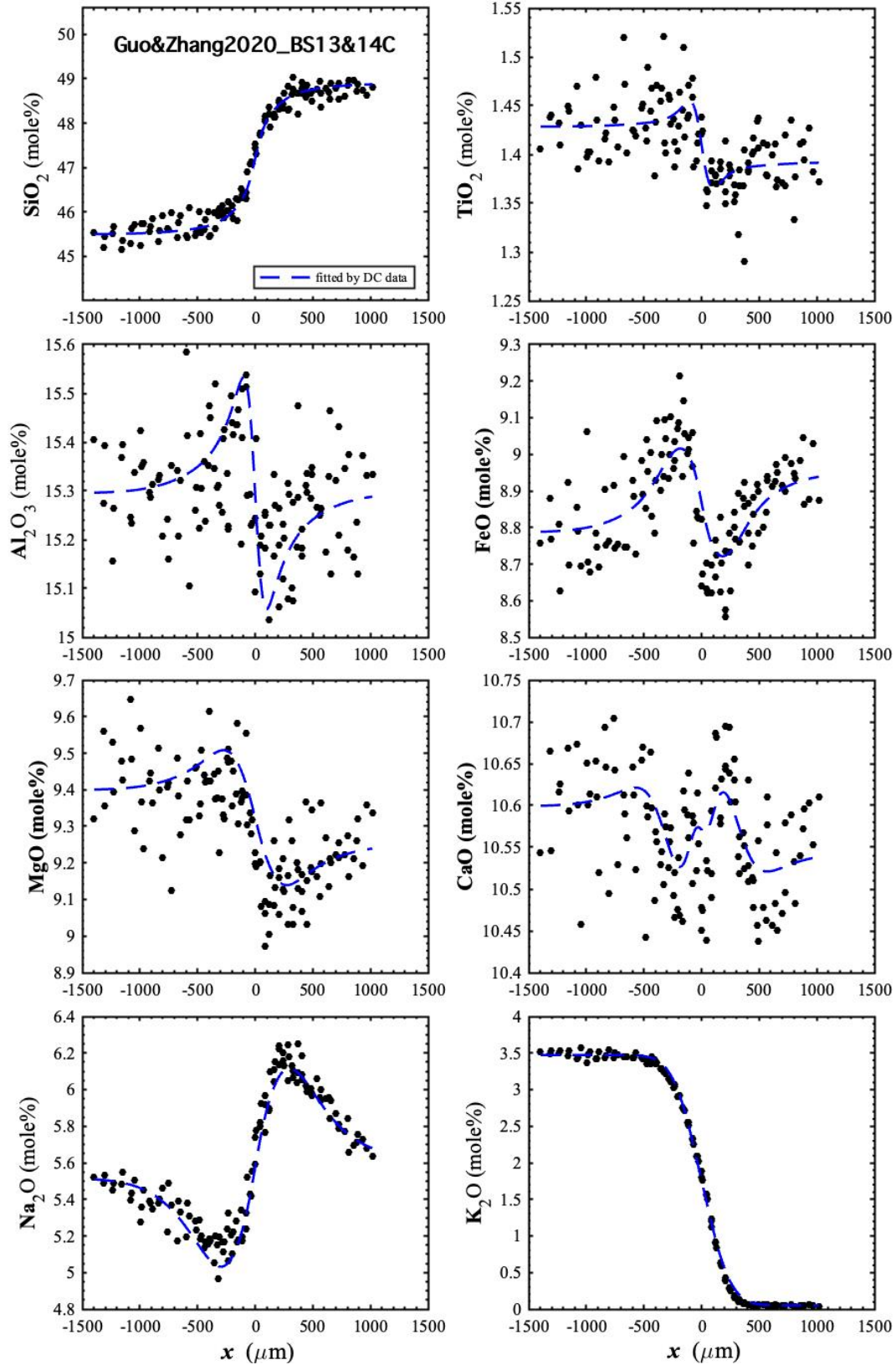
Figure C2.7. Diffusion profiles of oxide components in mole% of BS13&14C (Guo and Zhang, 2020) with fits. The dash curves are fits by the parameters in Table 4.3.
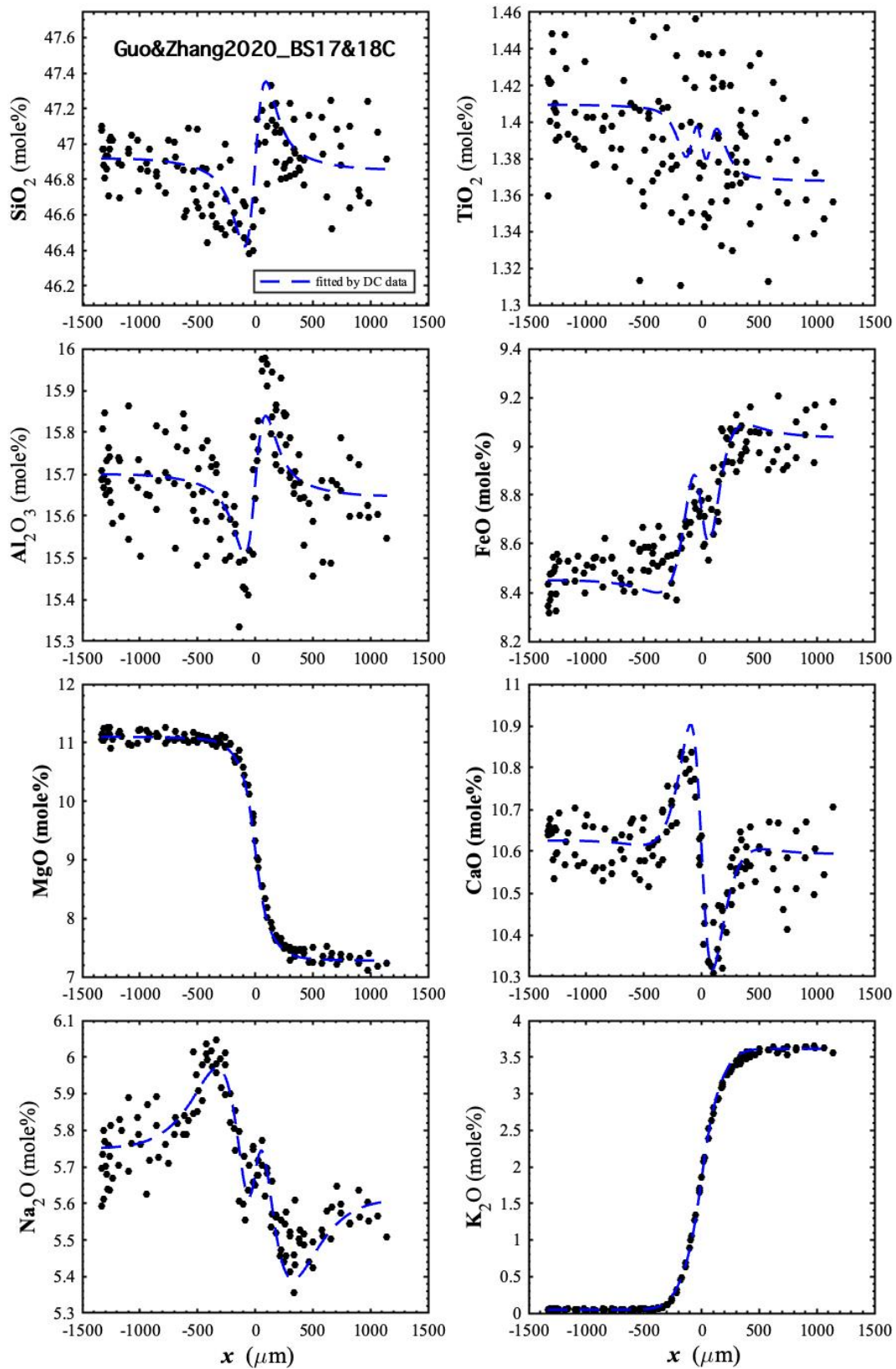
Figure C2.8. Diffusion profiles of oxide components in mole% of BS17&18C (Guo and Zhang, 2020) with fits. The dash curves are fits by the parameters in Table 4.3.
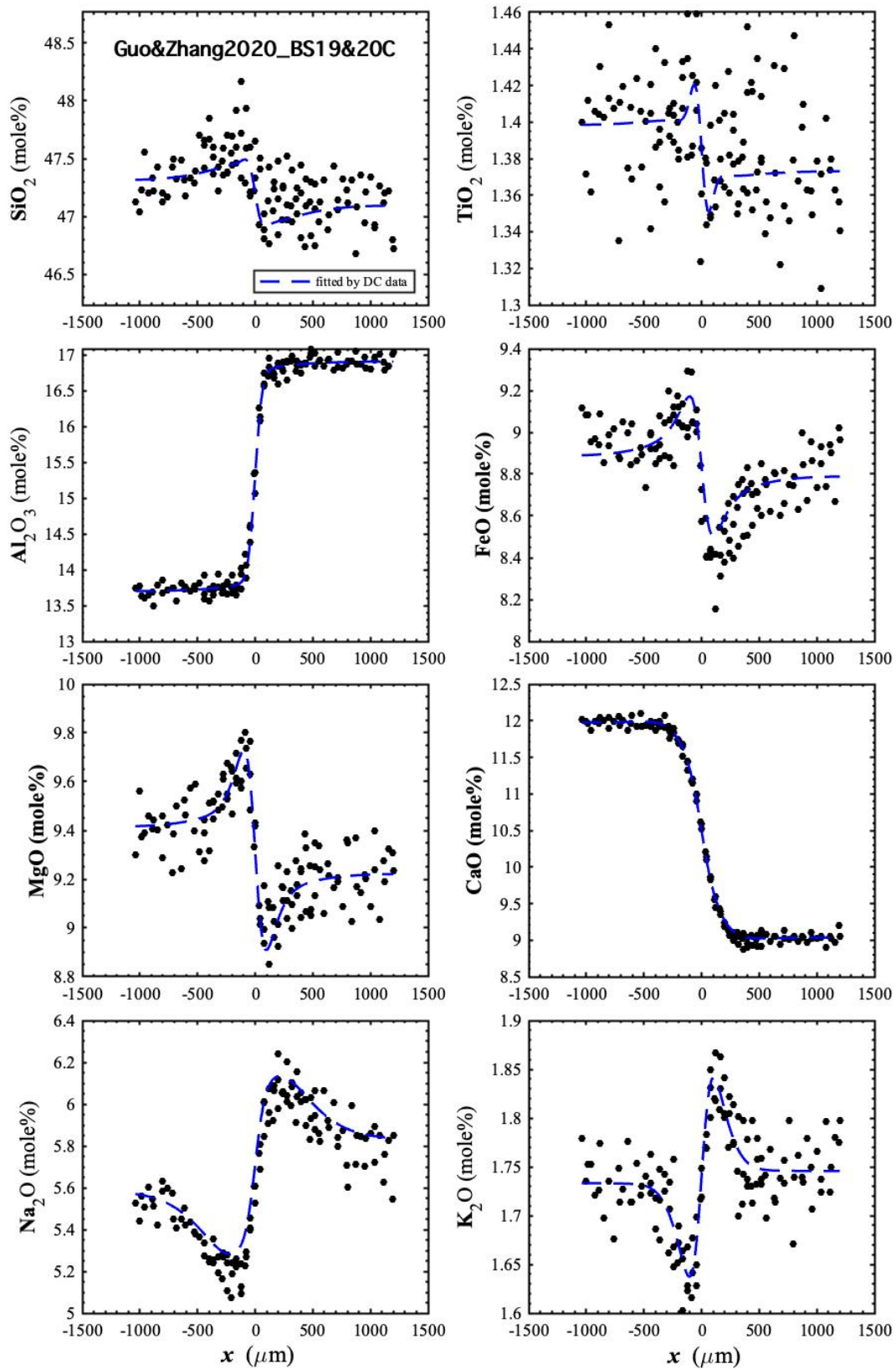
Figure C2.9. Diffusion profiles of oxide components in mole% of BS19&20C (Guo and Zhang, 2020) with fits. The dash curves are fits by the parameters in Table 4.3.

101
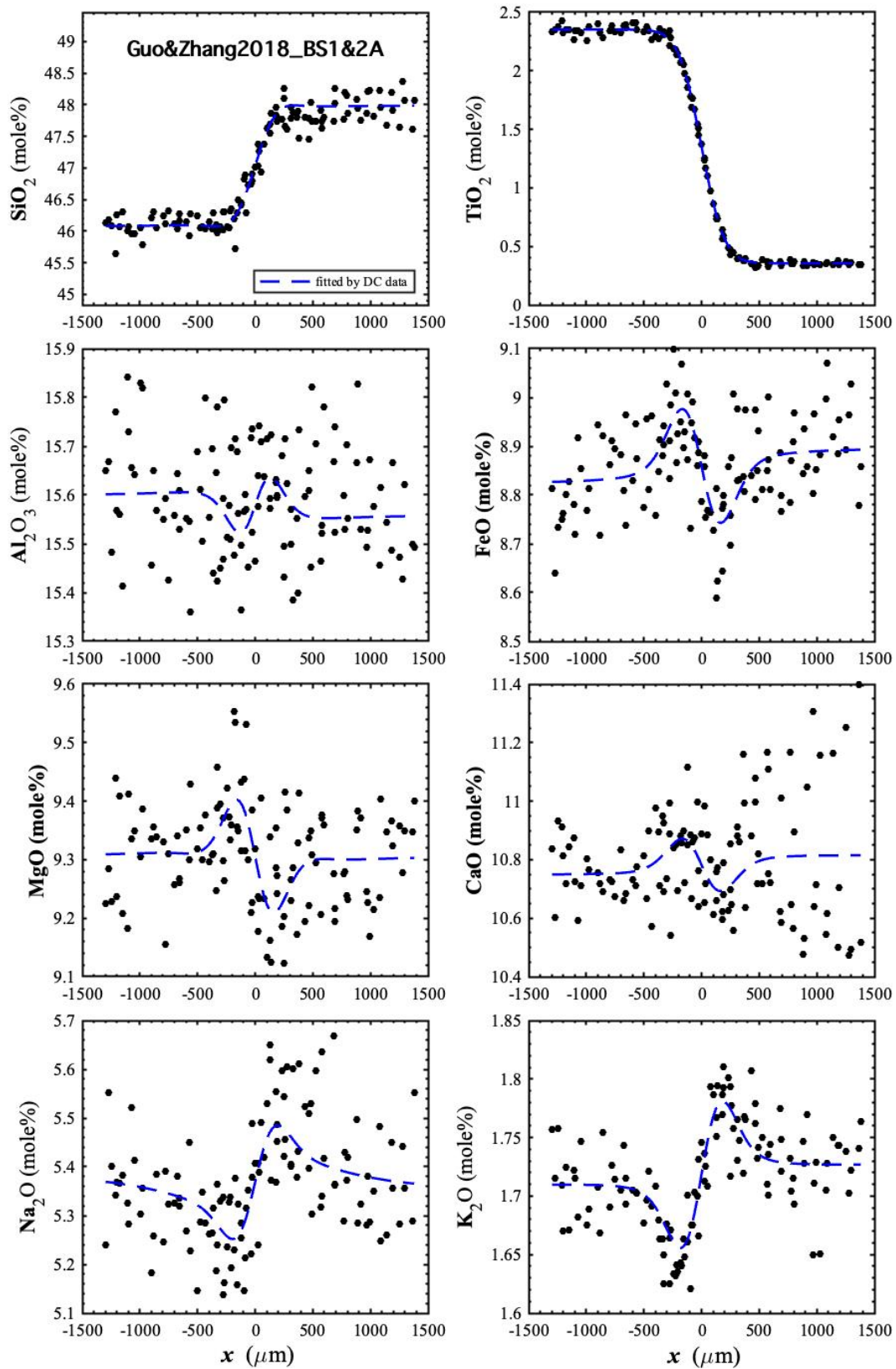
Figure C2.10. Diffusion profiles of oxide components in mole% of BS1&2A (Guo and Zhang, 2018) with fits. The dash curves are fits by the parameters in Table 4.3.
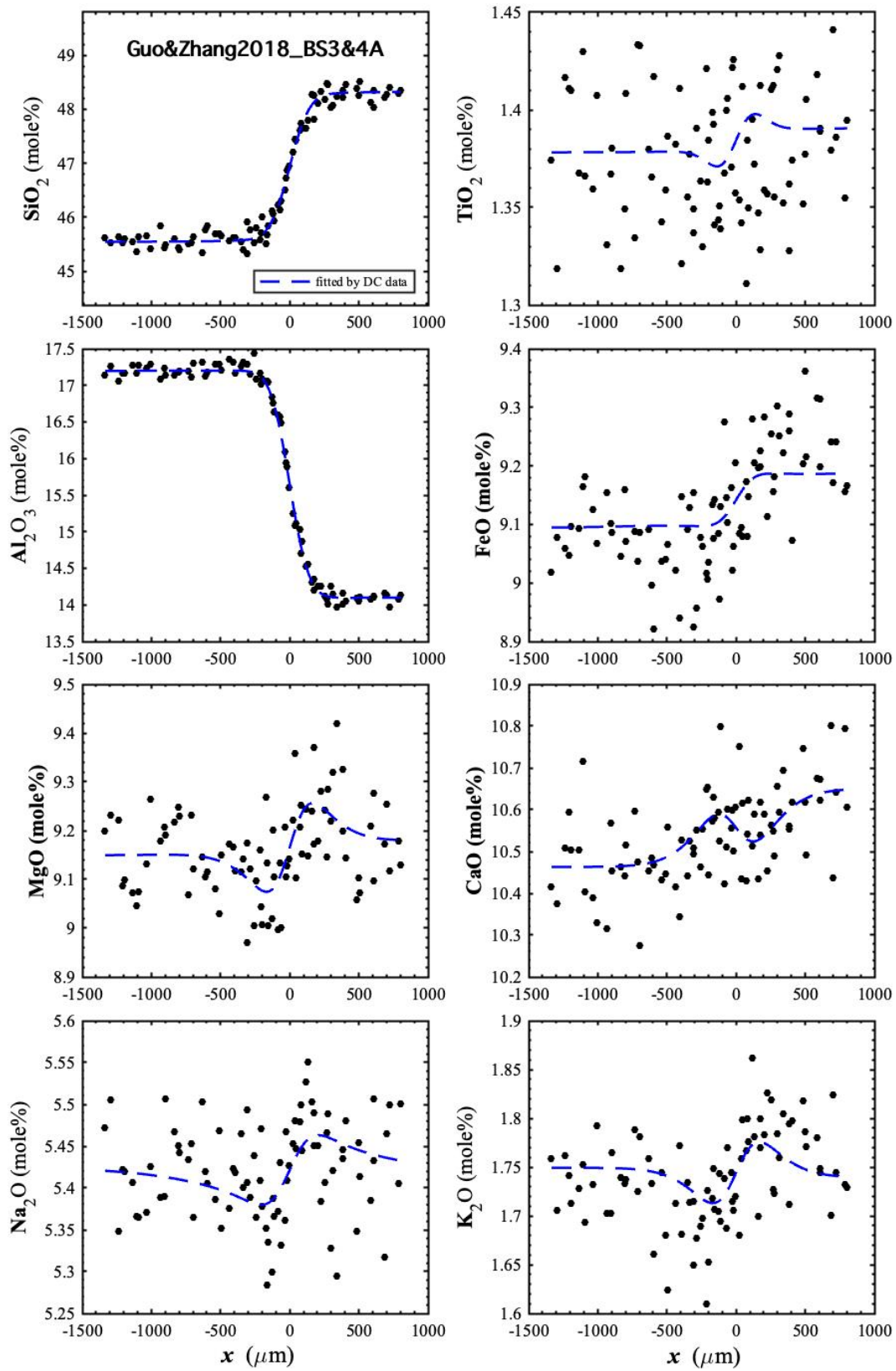
Figure C2.11. Diffusion profiles of oxide components in mole% of BS3&4A (Guo and Zhang, 2018) with fits. The dash curves are fits by the parameters in Table 4.3.
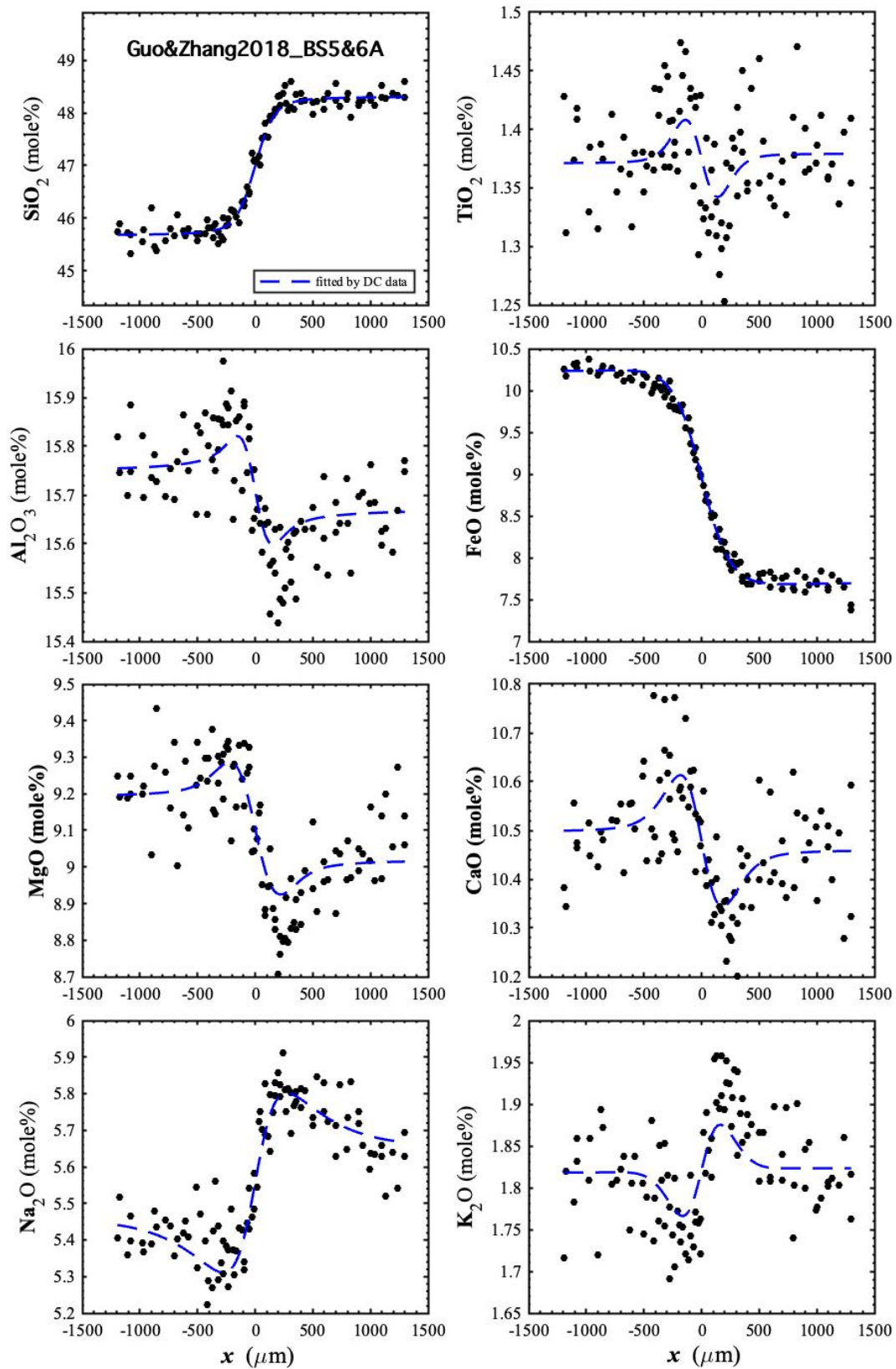
Figure C2.12. Diffusion profiles of oxide components in mole% of BS5&6A (Guo and Zhang, 2018) with fits. The dash curves are fits by the parameters in Table 4.3.
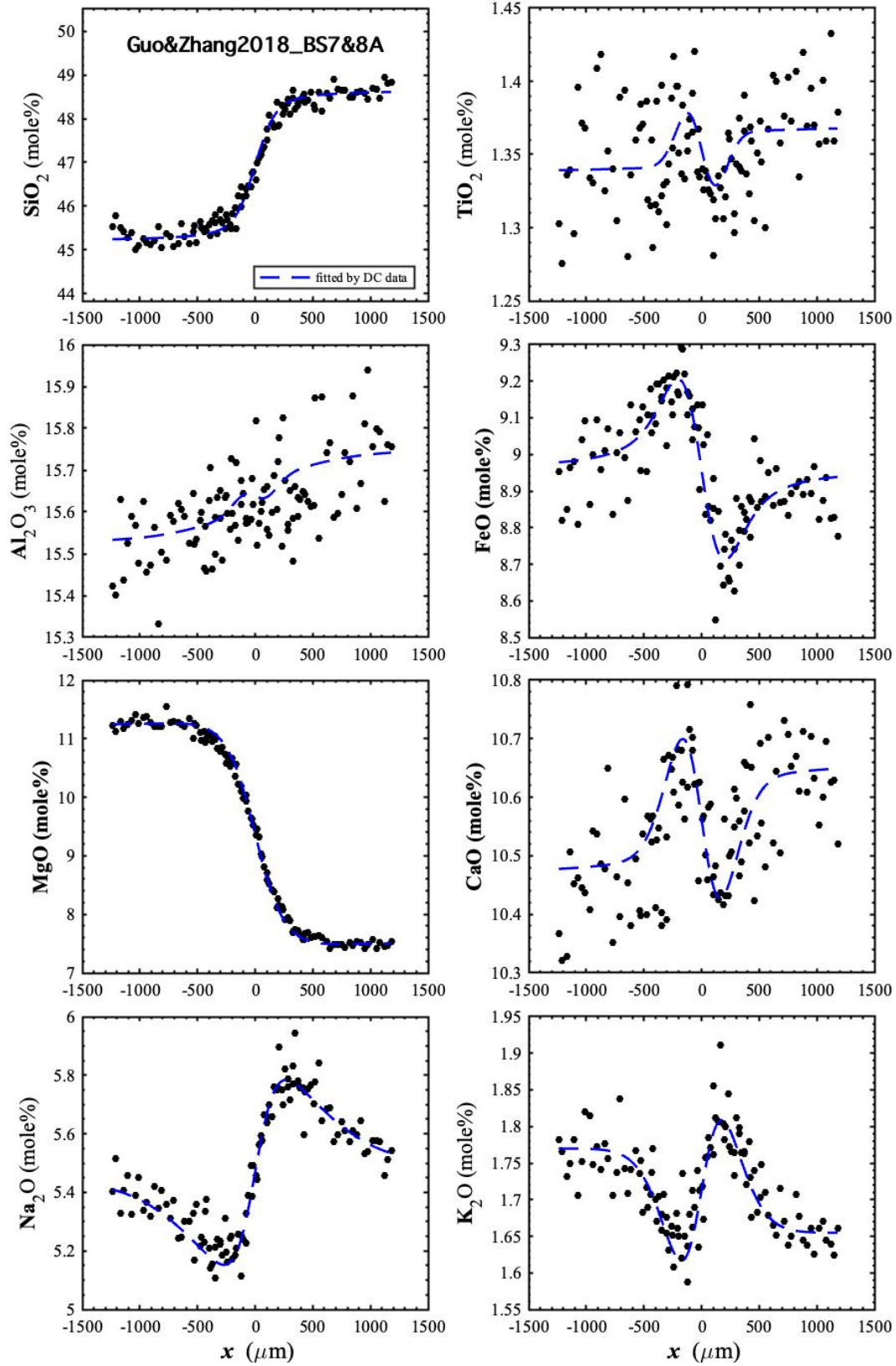
Figure C2.13. Diffusion profiles of oxide components in mole% of BS7&8A (Guo and Zhang, 2018) with fits. The dash curves are fits by the parameters in Table 4.3.
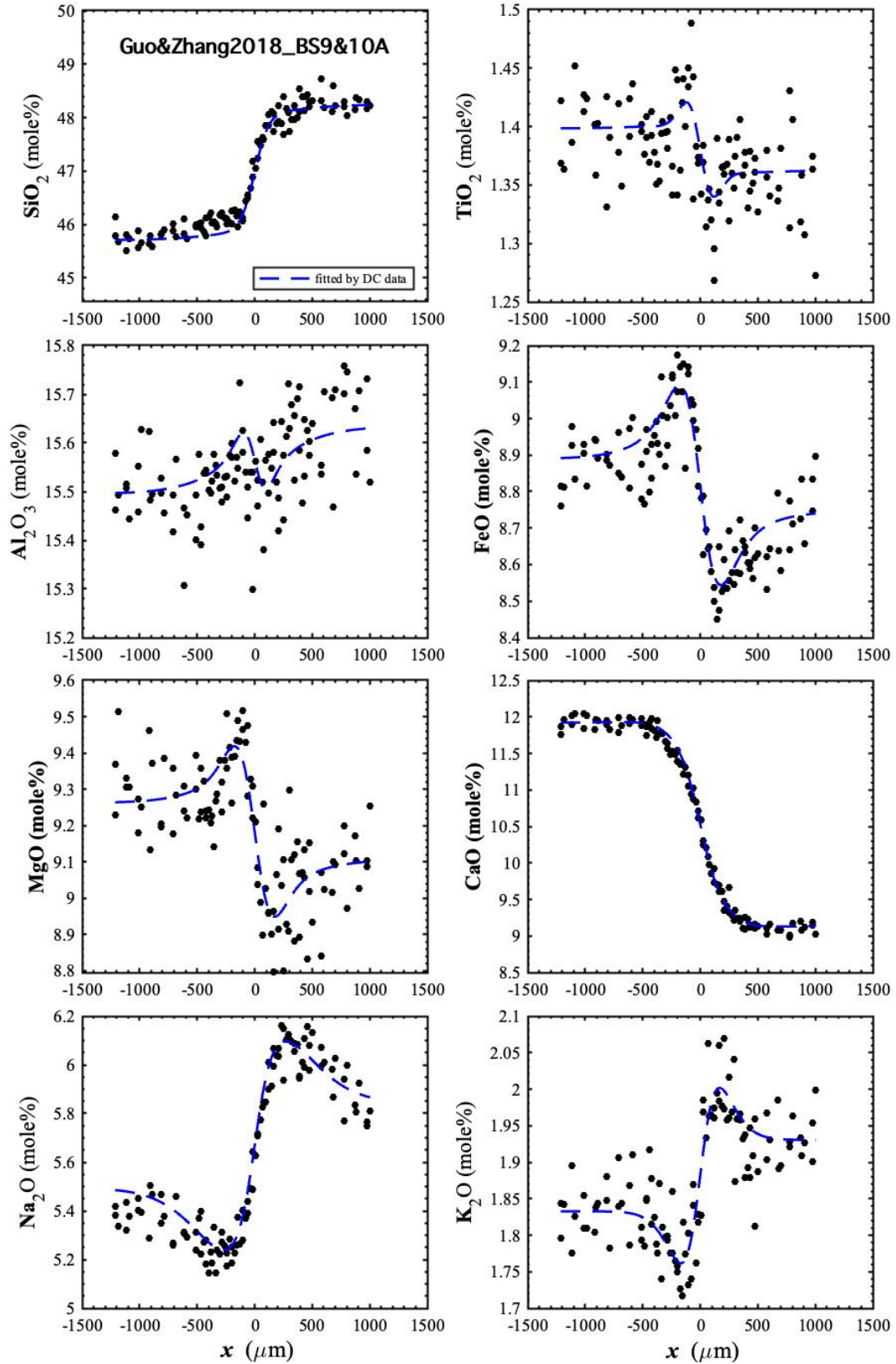
Figure C2.14. Diffusion profiles of oxide components in mole% of BS9&10A (Guo and Zhang, 2018) with fits. The dash curves are fits by the parameters in Table 4.3.

106
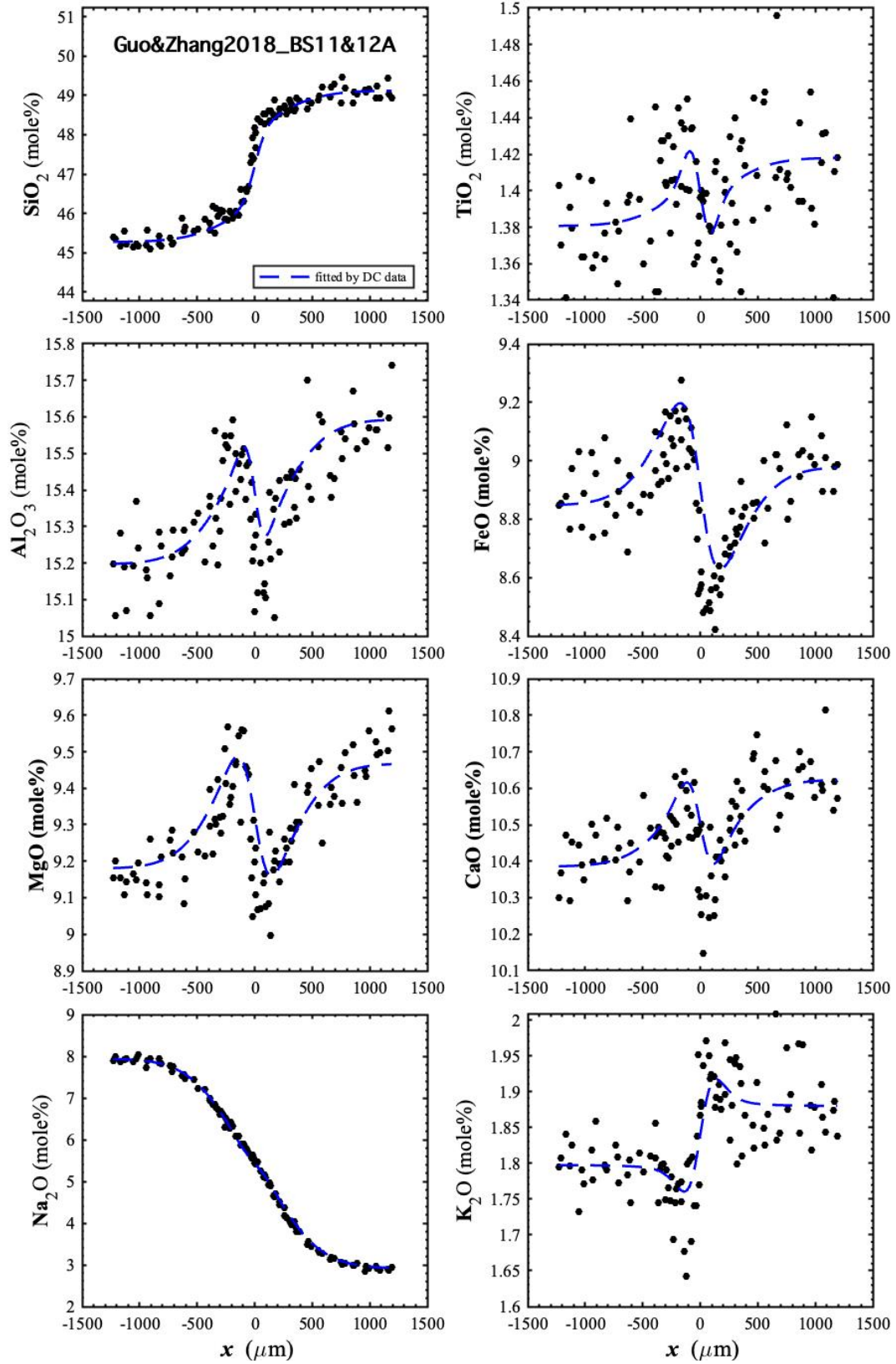
Figure C2.15. Diffusion profiles of oxide components in mole% of BS11&12A (Guo and Zhang, 2018) with fits. The dash curves are fits by the parameters in Table 4.3.
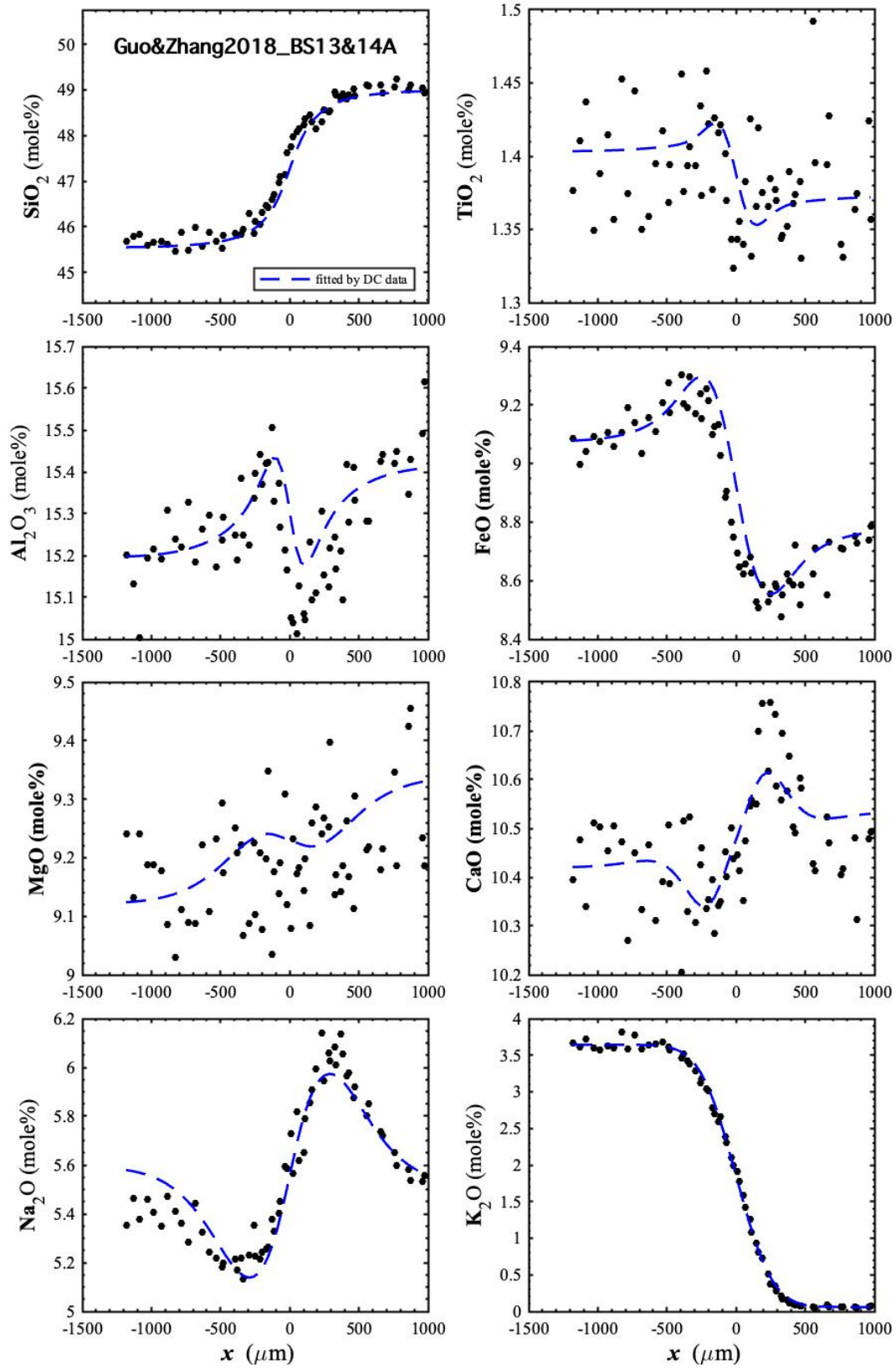
Figure C2.16. Diffusion profiles of oxide components in mole% of BS13&14A (Guo and Zhang, 2018) with fits. The dash curves are fits by the parameters in Table 4.3.

108
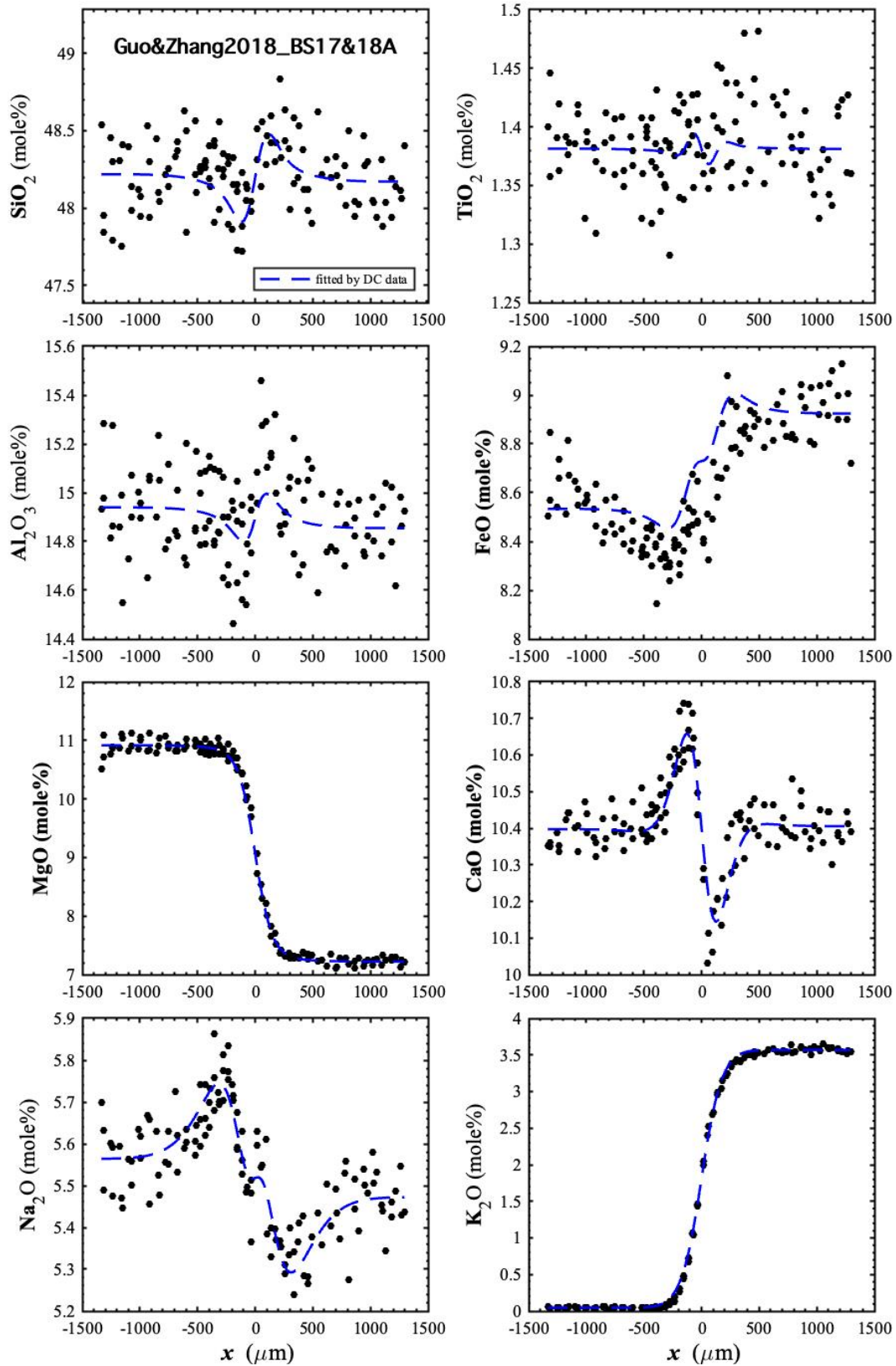
Figure C2.17. Diffusion profiles of oxide components in mole% of BS17&18A (Guo and Zhang, 2018) with fits. The dash curves are fits by the parameters in Table 4.3.
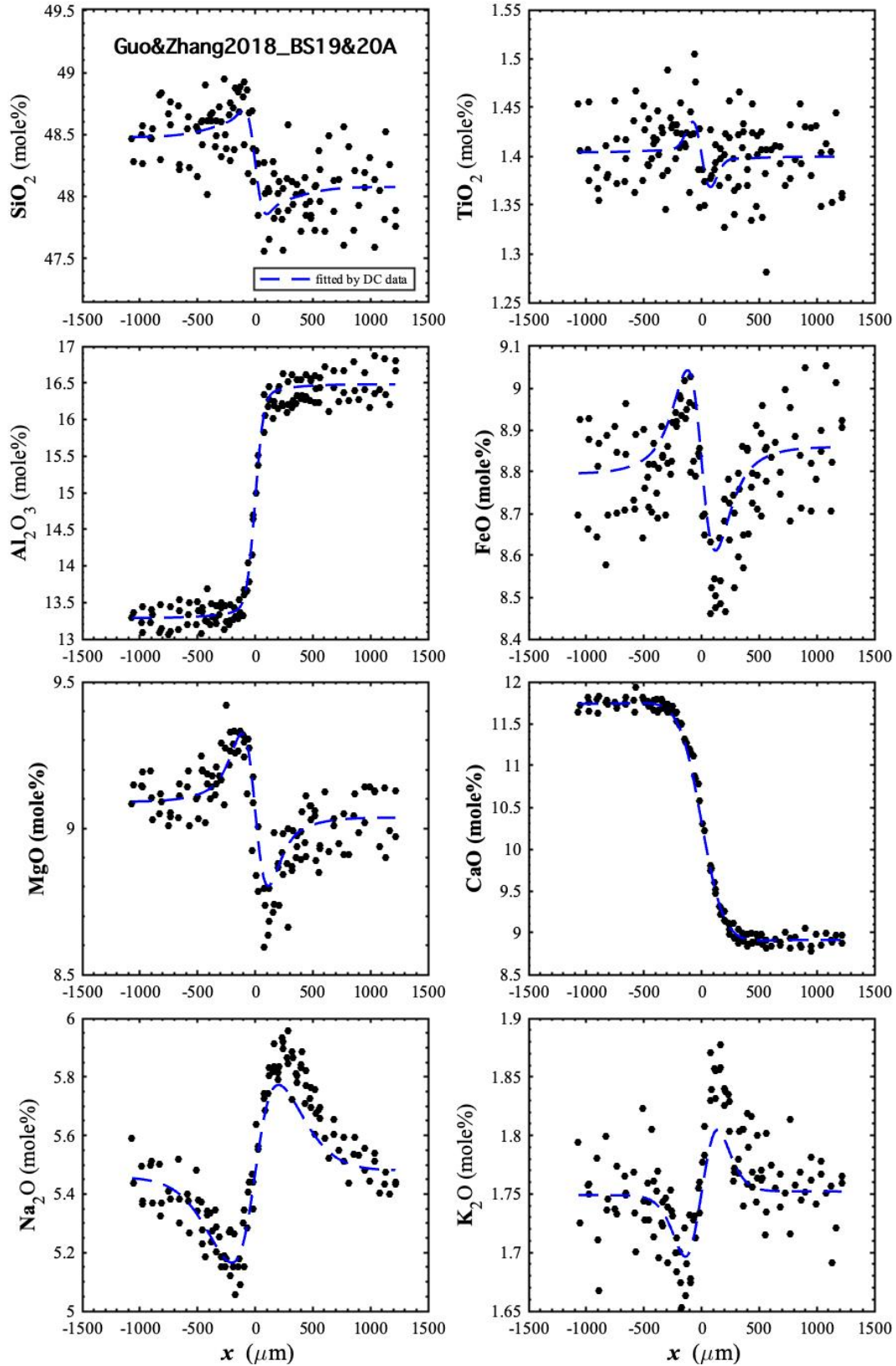
Figure C2.18. Diffusion profiles of oxide components in mole% of BS19&20A (Guo and Zhang, 2018) with fits. The dash curves are fits by the parameters in Table 4.3.
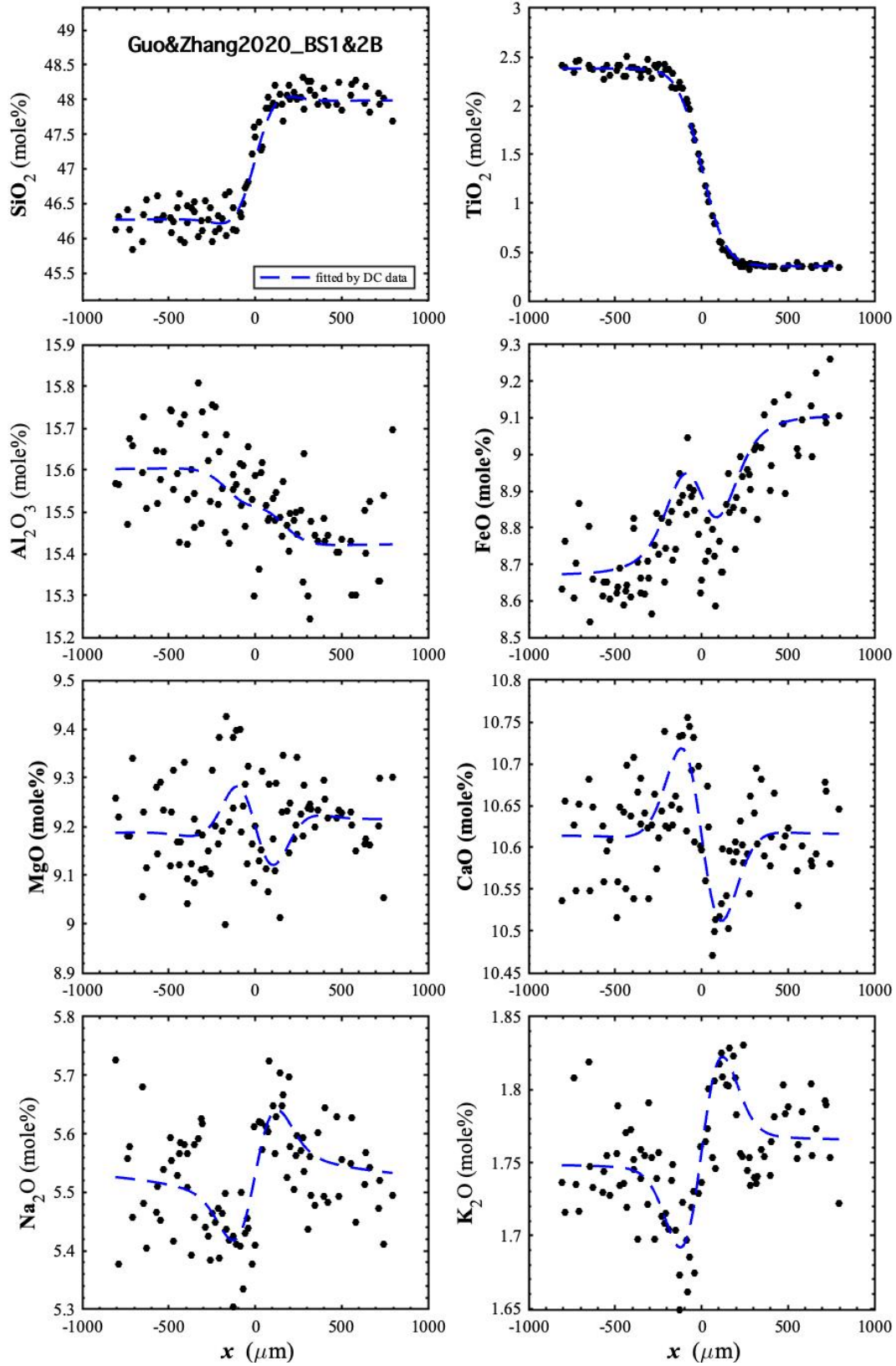
Figure C2.19. Diffusion profiles of oxide components in mole% of BS1&2B (Guo and Zhang, 2020) with fits. The dash curves are fits by the parameters in Table 4.3.

111
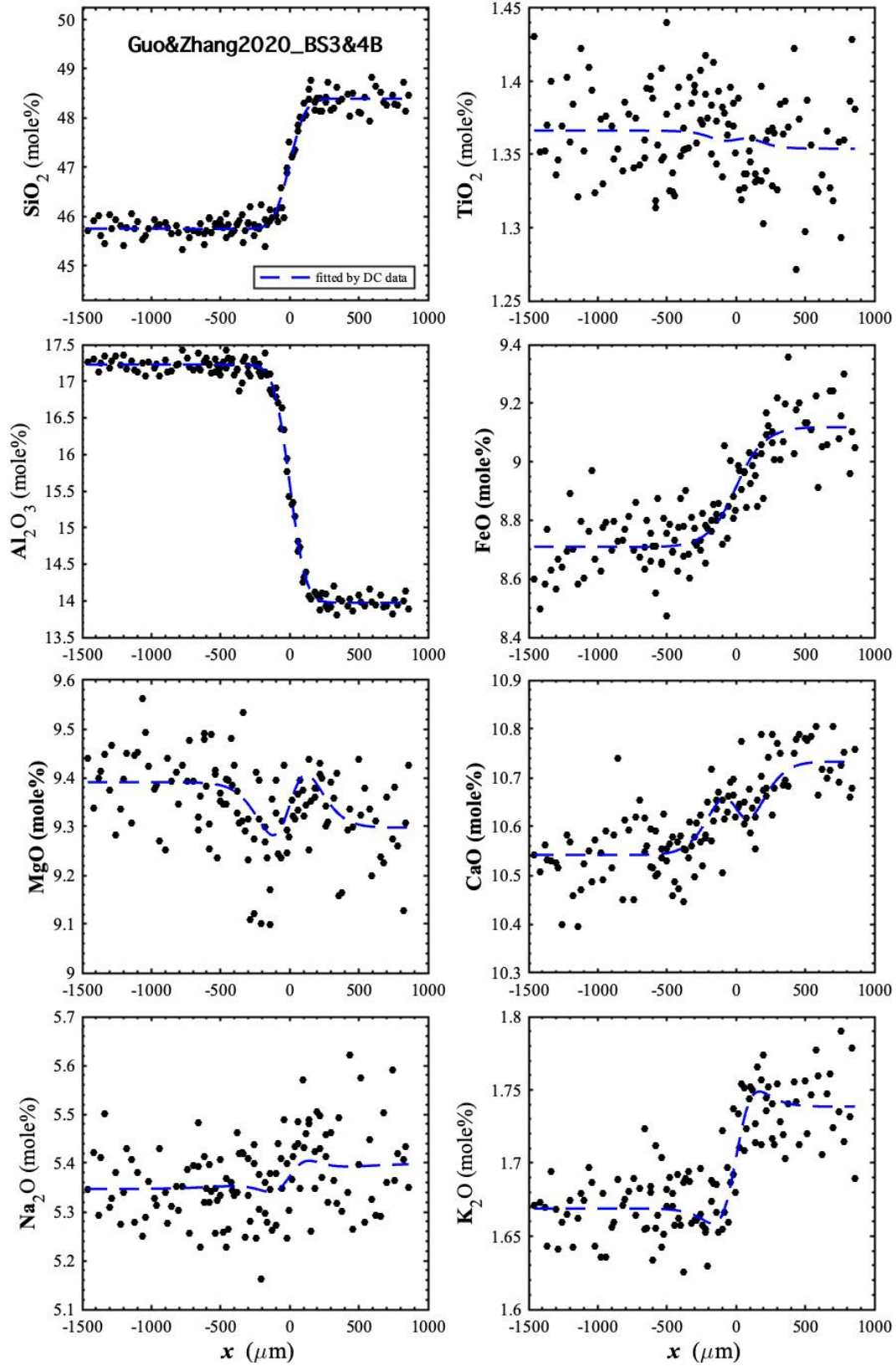
Figure C2.20. Diffusion profiles of oxide components in mole% of BS3&4B (Guo and Zhang, 2020) with fits. The dash curves are fits by the parameters in Table 4.3.

Figure C2.21. Diffusion profiles of oxide components in mole% of BS5&6B (Guo and Zhang, 2020) with fits. The dash curves are fits by the parameters in Table 4.3.

Figure C2.22. Diffusion profiles of oxide components in mole% of BS7&8B (Guo and Zhang, 2020) with fits. The dash curves are fits by the parameters in Table 4.3.

114

Figure C2.23. Diffusion profiles of oxide components in mole% of BS9&10B (Guo and Zhang, 2020) with fits. The dash curves are fits by the parameters in Table 4.3.

Figure C2.24. Diffusion profiles of oxide components in mole% of BS11&12B (Guo and Zhang, 2020) with fits. The dash curves are fits by the parameters in Table 4.3.

Figure C2.25. Diffusion profiles of oxide components in mole% of BS13&14B (Guo and Zhang, 2020) with fits. The dash curves are fits by the parameters in Table 4.3.

117

Figure C2.26. Diffusion profiles of oxide components in mole% of BS17&18B (Guo and Zhang, 2020) with fits. The dash curves are fits by the parameters in Table 4.3.

118

Figure C2.27. Diffusion profiles of oxide components in mole% of BS19&20B (Guo and Zhang, 2020) with fits. The dash curves are fits by the parameters in Table 4.3.

119

Appendix D

Concentration profiles of oxide components and eigen-components

To facilitate observation, concentration profiles of oxide components in weight percent (wt%), oxide components in mole percent (mole%), [P_w]-converted eigen-components and [P_X]-converted eigen-components of the same experiment are plotted together. The concentration profiles of 171 experiments, conducted by Zhang et al. (1989), Chen and Zhang (2008, 2009), Yu et al. (2016, 2019), Guo and Zhang (2016, 2018, 2020), González -Garcia et al. (2017), and Wang et al. (2020), are shown in Figs. D1-D171.
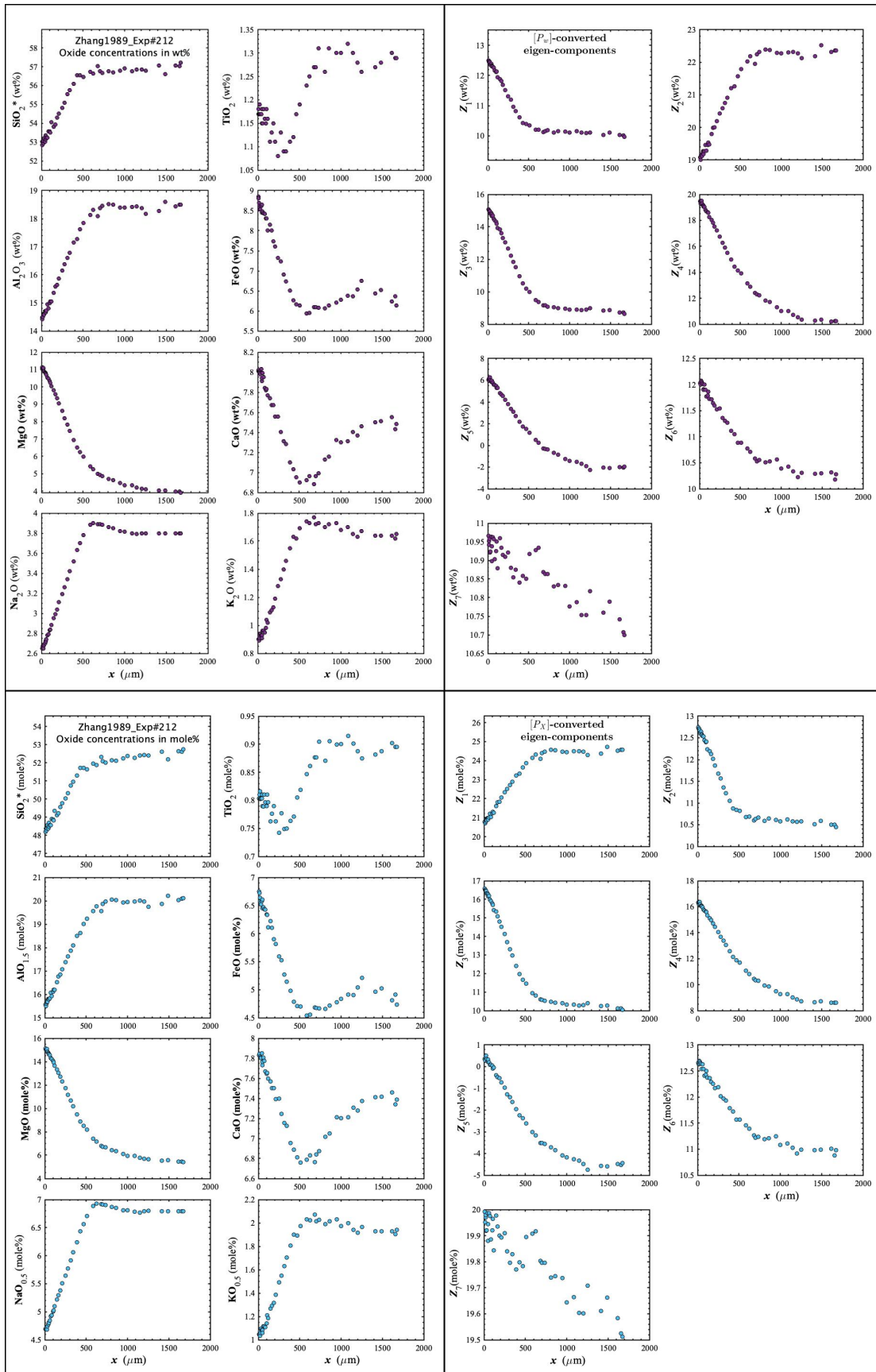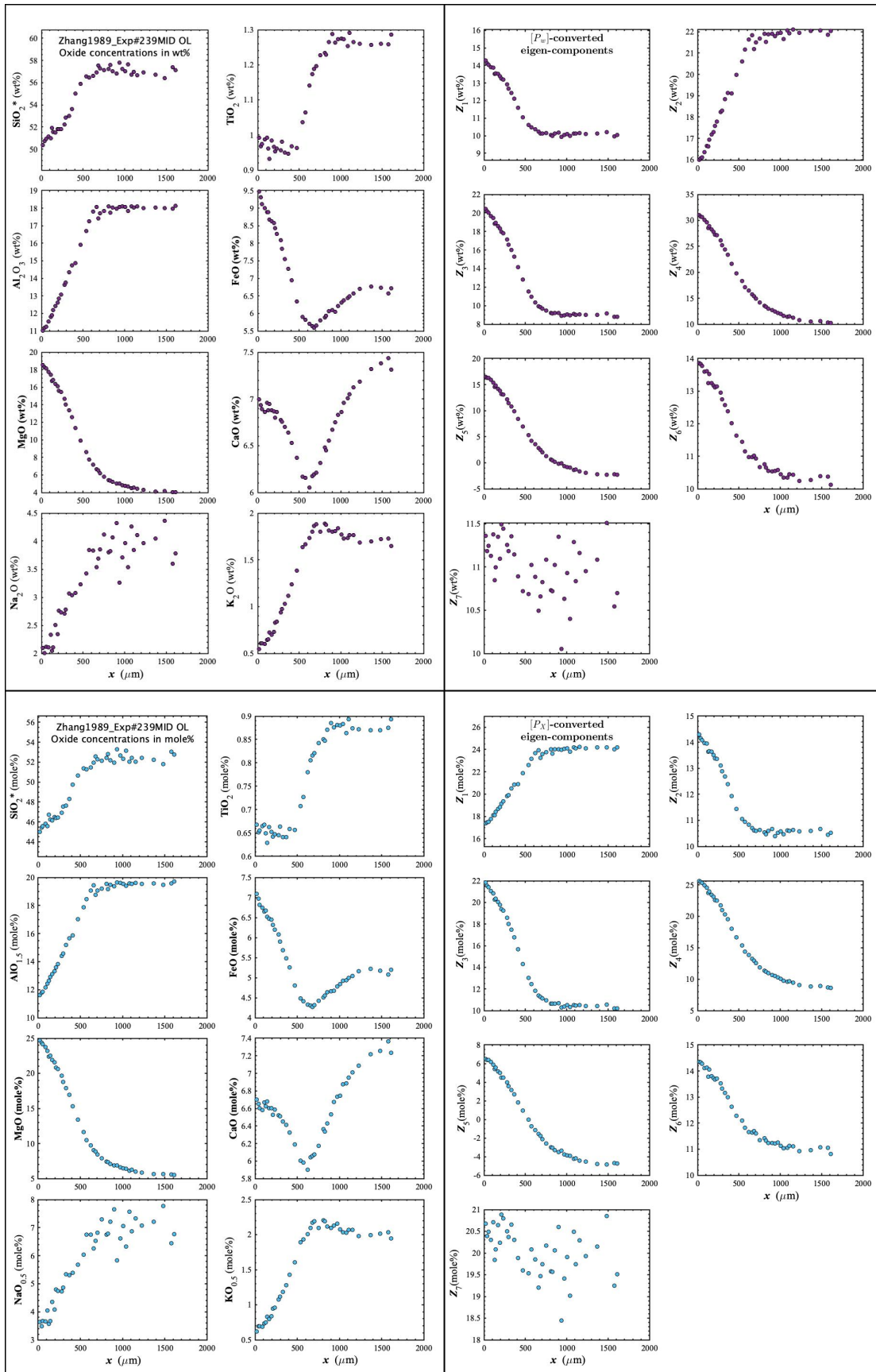
Figure D1. Concentration profiles of oxide components in wt% (upper left panel), oxide components in mole% (lower left panel), [P_w]-converted eigen-components (upper right panel), and [P_X]-converted eigen-components (lower right panel) of Zhang1989_Exp#212, which is an olivine dissolution experiment in andesite (Zhang et al., 1989).
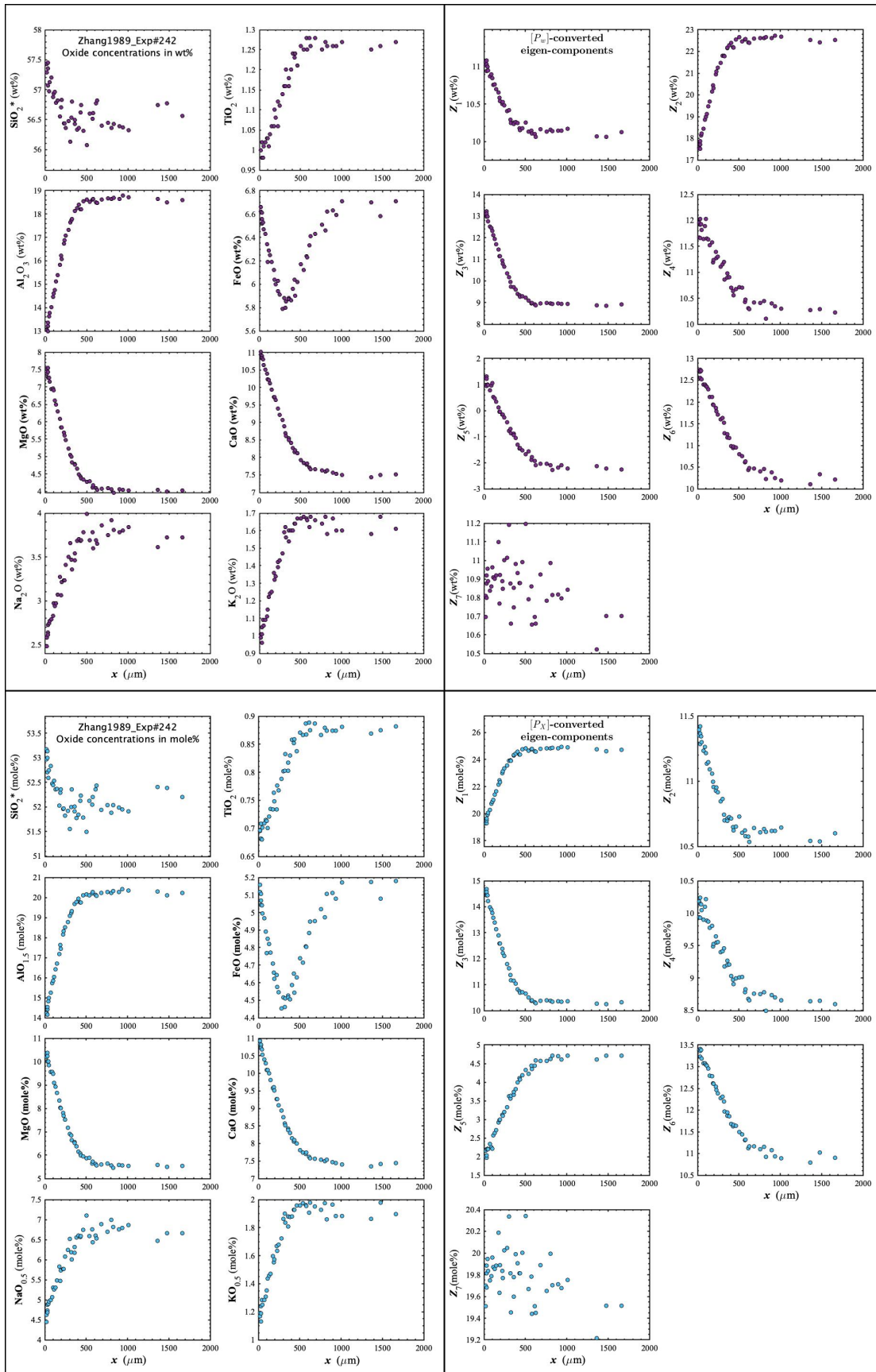
121
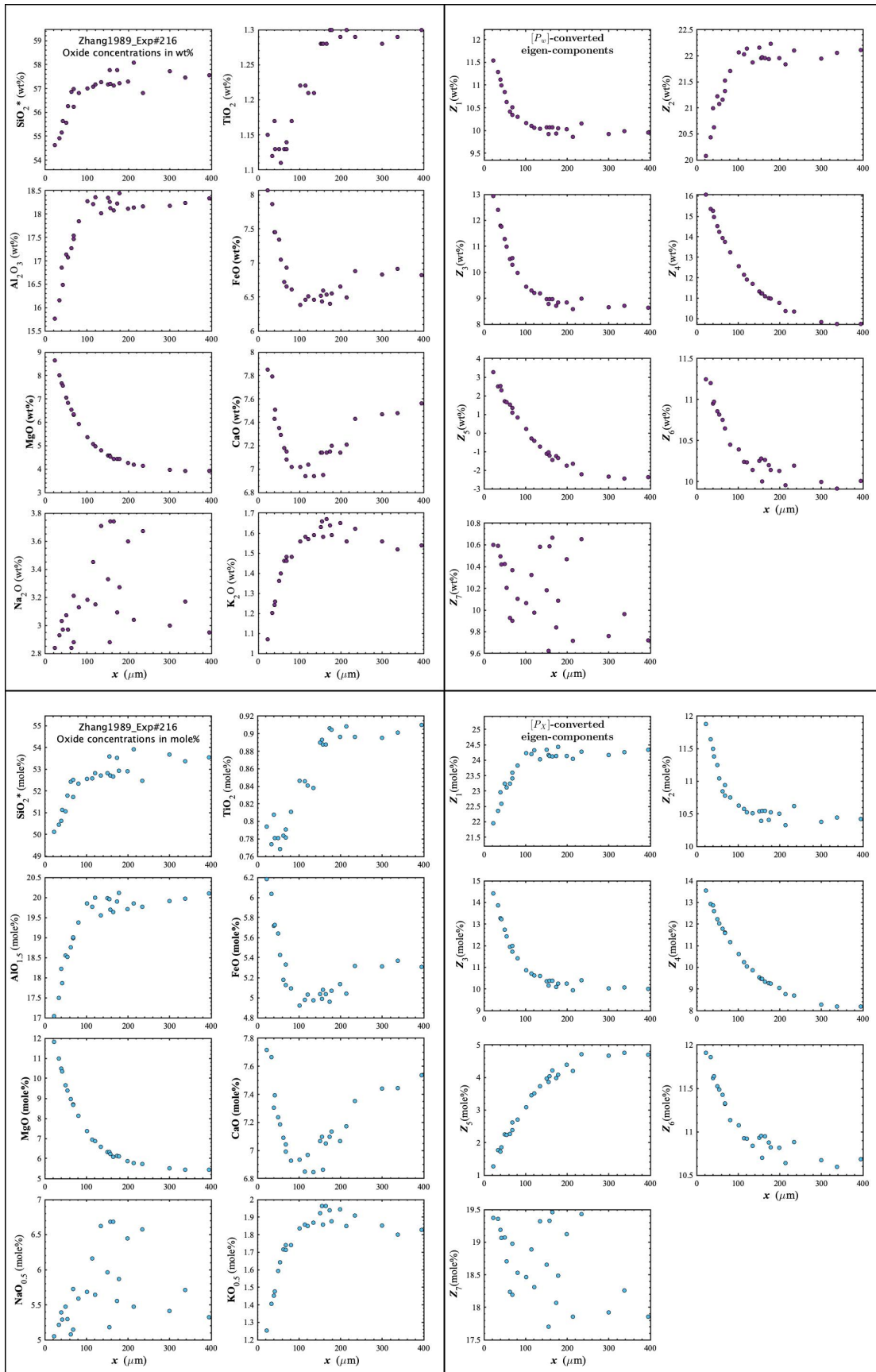
Figure D2. Concentration profiles of oxide components in wt% (upper left panel), oxide components in mole% (lower left panel), [P_w]-converted eigen-components (upper right panel), and [P_X]-converted eigen-components (lower right panel) of Zhang1989_Exp#216, which is an olivine dissolution experiment in andesite (Zhang et al., 1989).
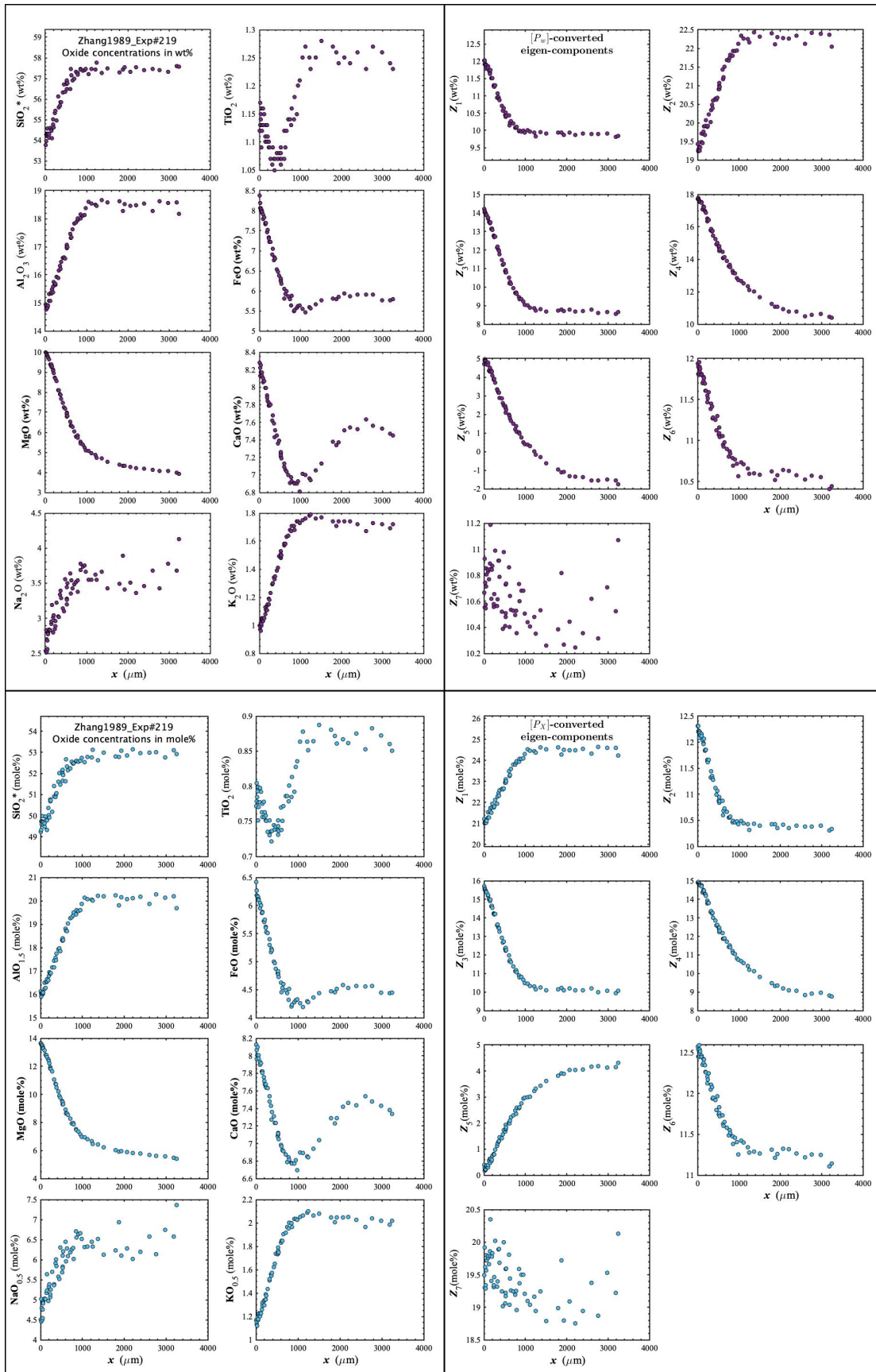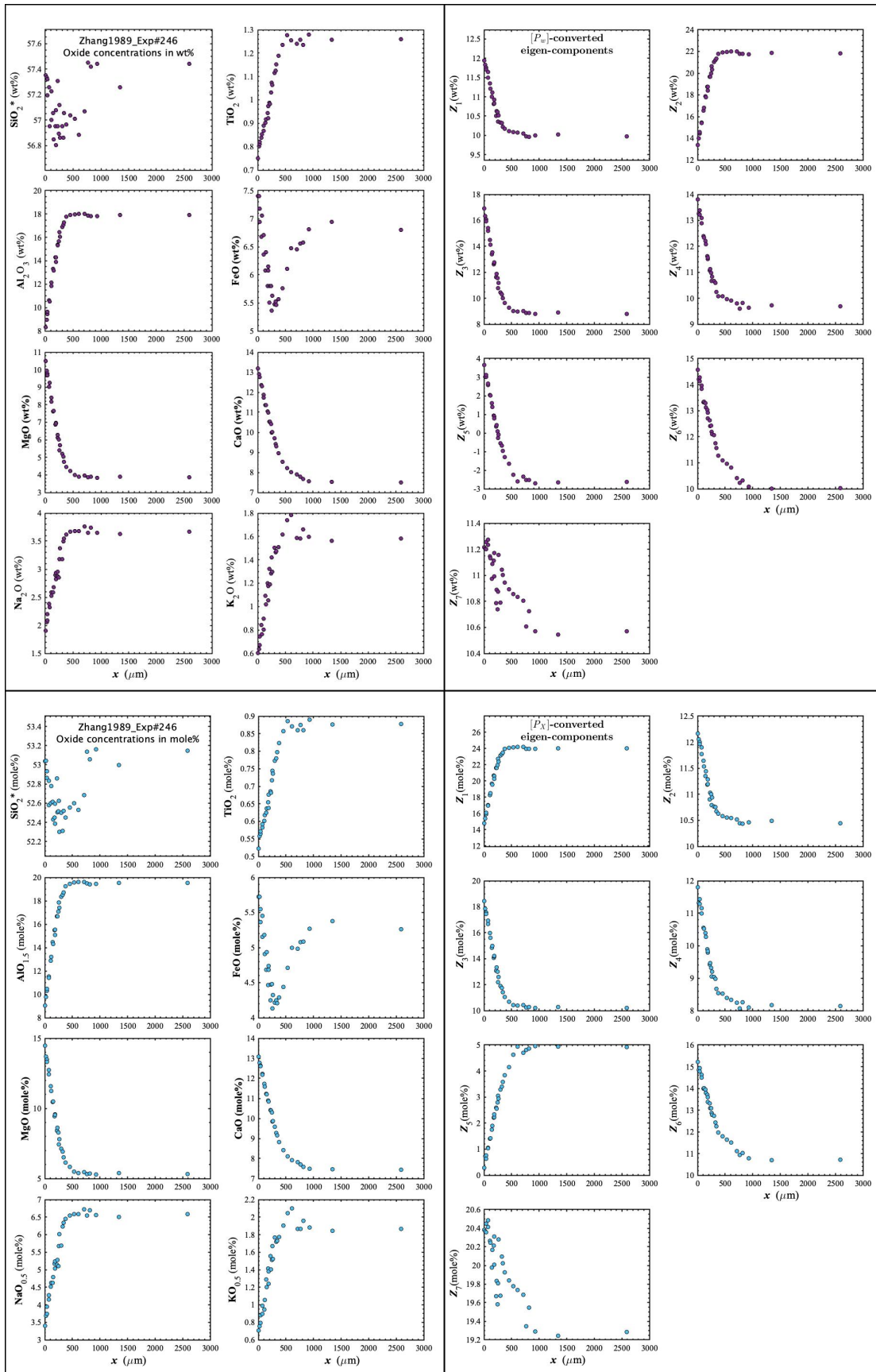
Figure D3. Concentration profiles of oxide components in wt% (upper left panel), oxide components in mole% (lower left panel), [P_w]-converted eigen-components (upper right panel), and [P_X]-converted eigen-components (lower right panel) of Zhang1989_Exp#219, which is an olivine dissolution experiment in andesite (Zhang et al., 1989).
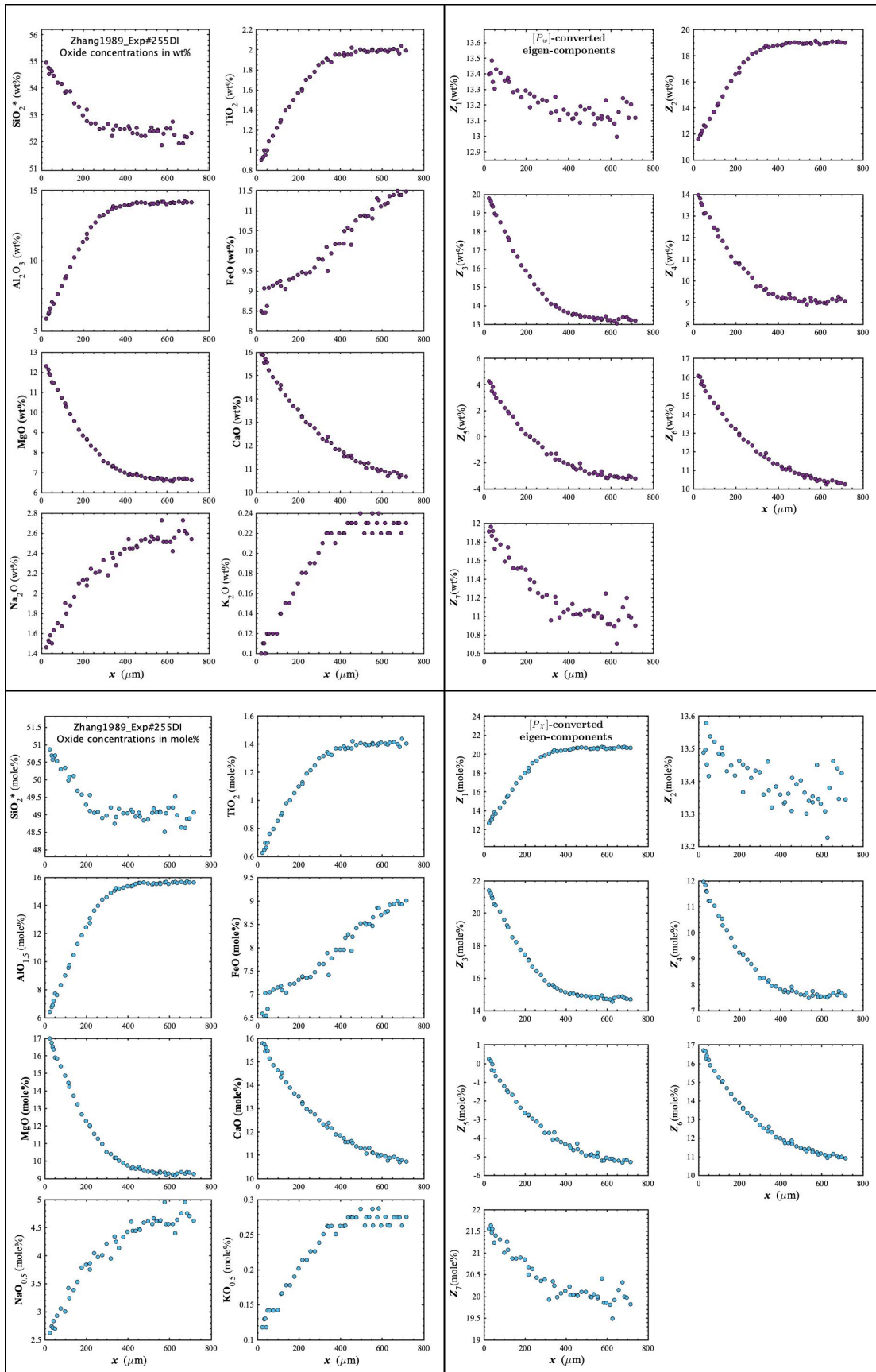
123
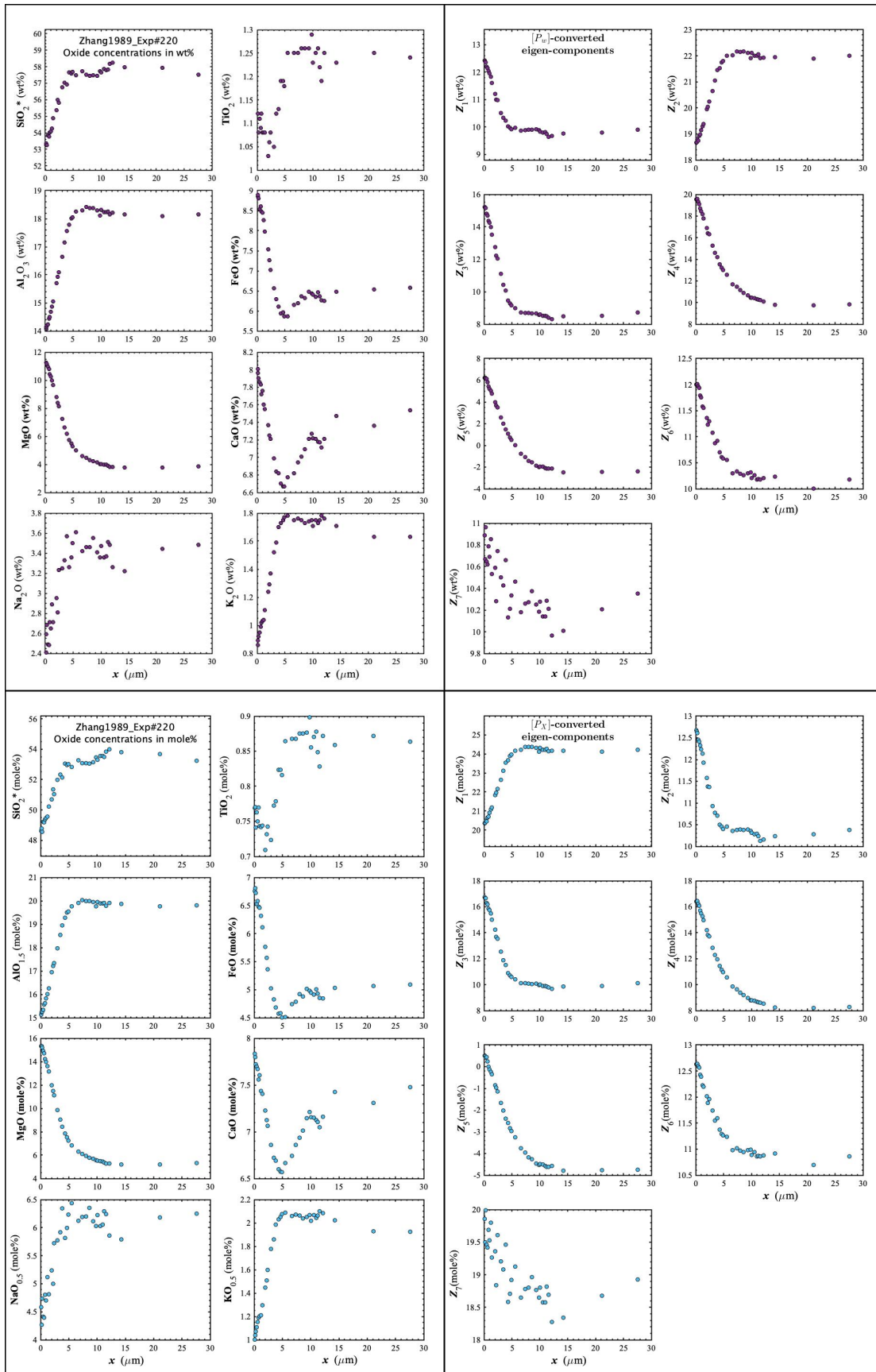
Figure D4. Concentration profiles of oxide components in wt% (upper left panel), oxide components in mole% (lower left panel), $[P_w]$-converted eigen-components (upper right panel), and $[P_X]$-converted eigen-components (lower right panel) of Zhang1989_Exp#220, which is an olivine dissolution experiment in andesite (Zhang et al., 1989). Note that the duration of the experiment is unknown. Therefore, the x-coordinates were calculated based on $x/2\sqrt{t}$, assuming a value of 1s for t.
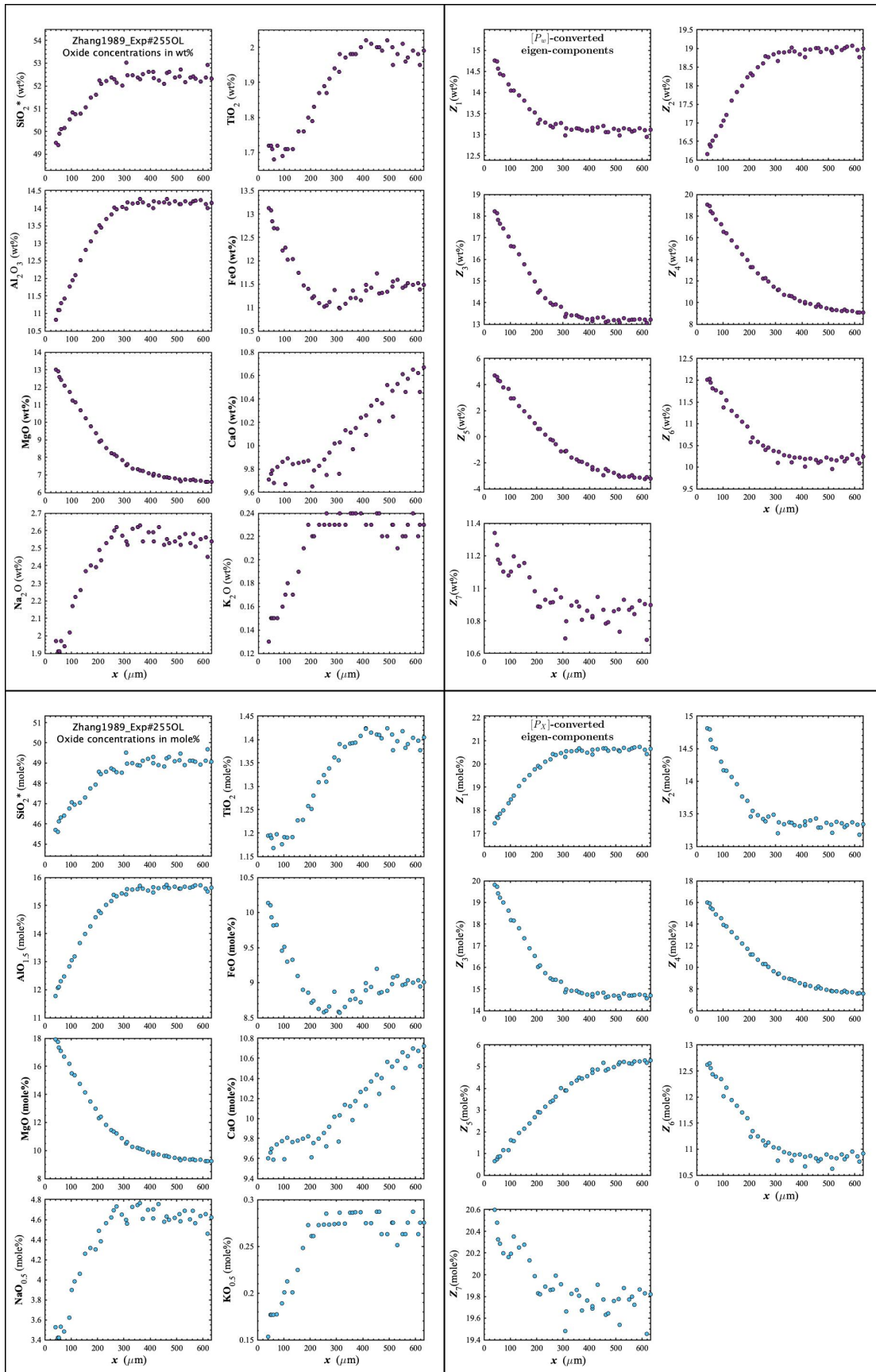
124
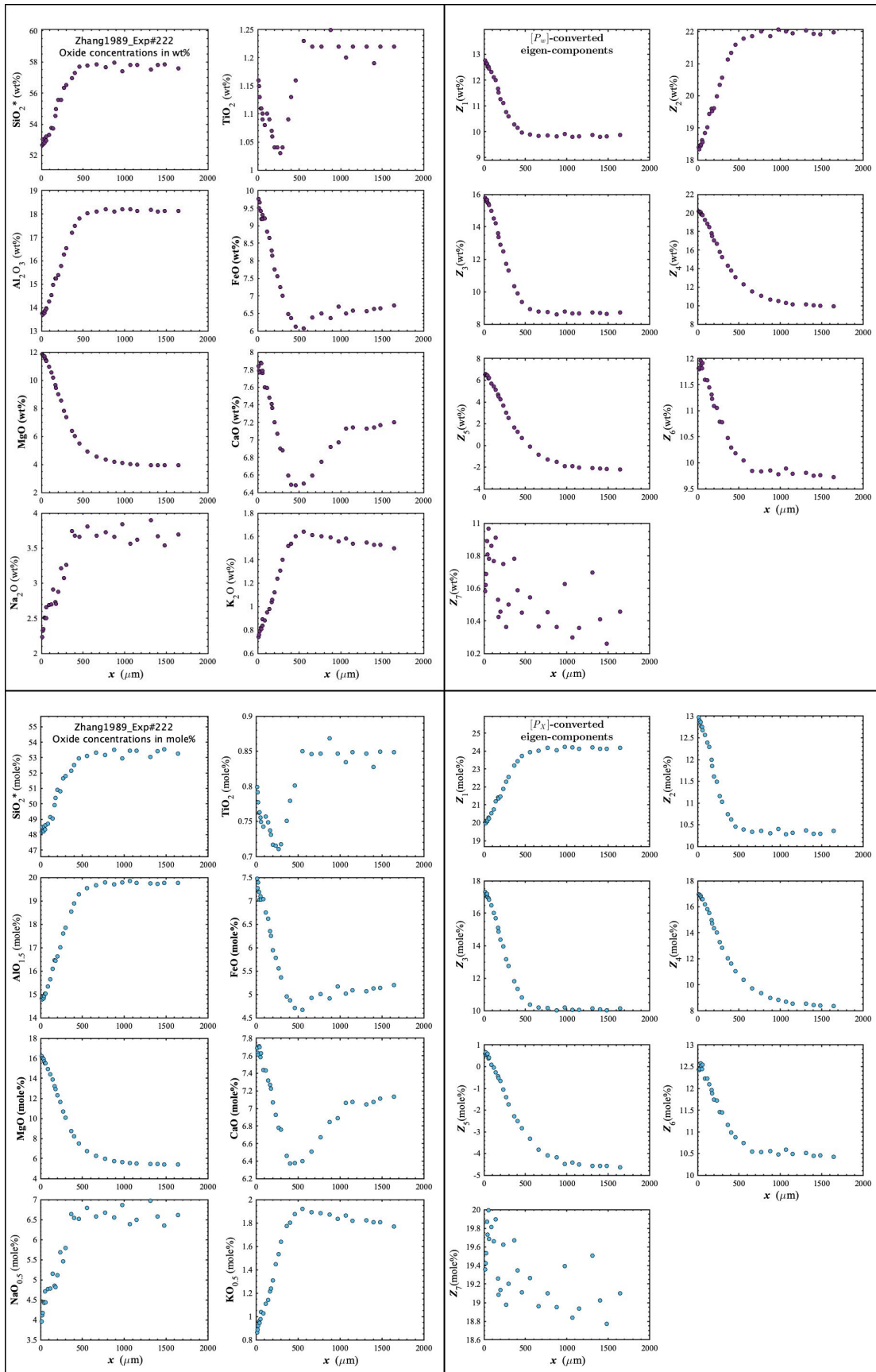
Figure D5. Concentration profiles of oxide components in wt% (upper left panel), oxide components in mole% (lower left panel), $[P_w]$-converted eigen-components (upper right panel), and $[P_X]$-converted eigen-components (lower right panel) of Zhang1989_Exp#222, which is an olivine dissolution experiment in andesite (Zhang et al., 1989).
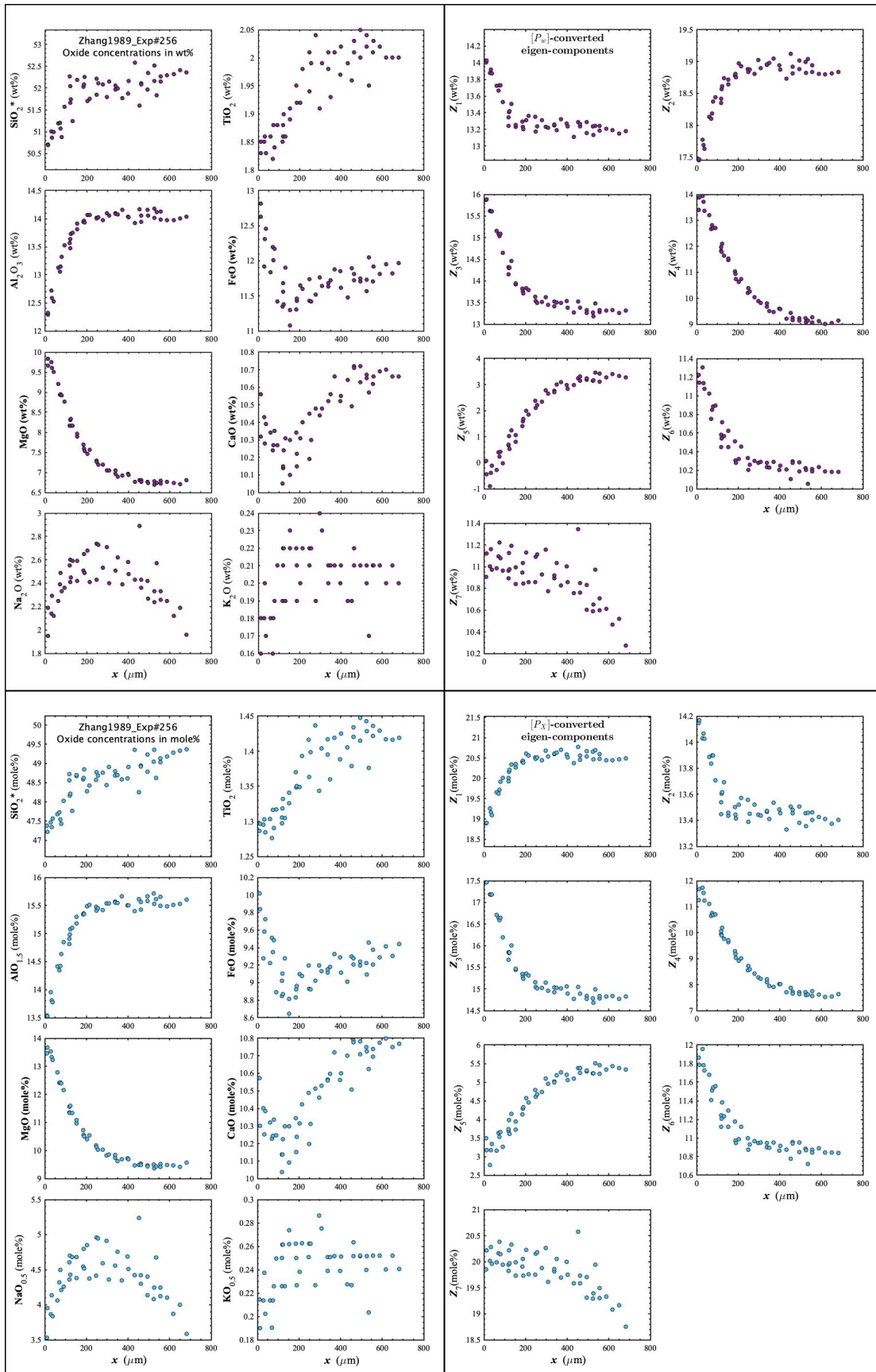
125
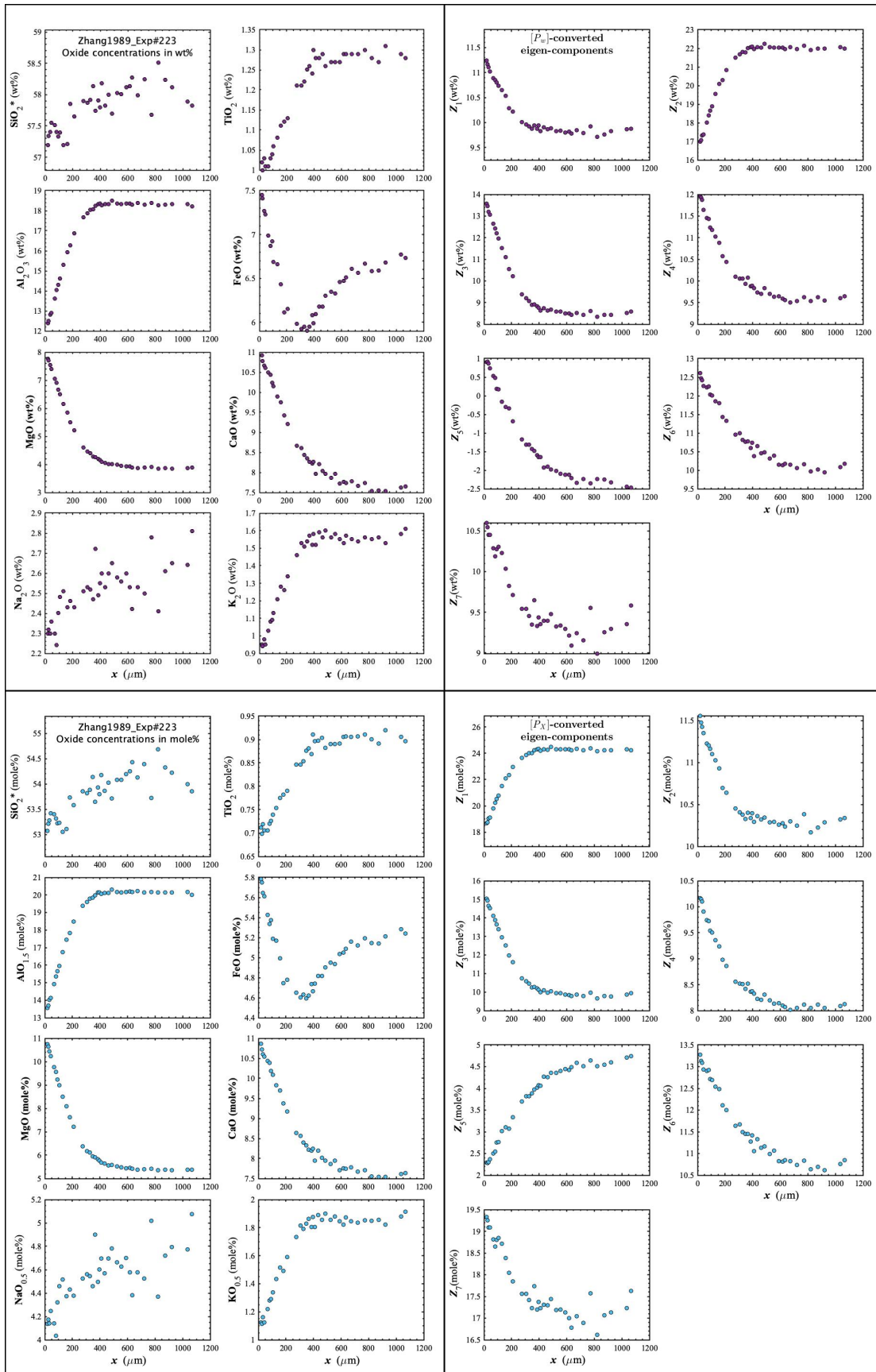
Figure D6. Concentration profiles of oxide components in wt% (upper left panel), oxide components in mole% (lower left panel), [P_w]-converted eigen-components (upper right panel), and [P_X]-converted eigen-components (lower right panel) of Zhang1989_Exp#223, which is a diopside dissolution experiment in andesite (Zhang et al., 1989).
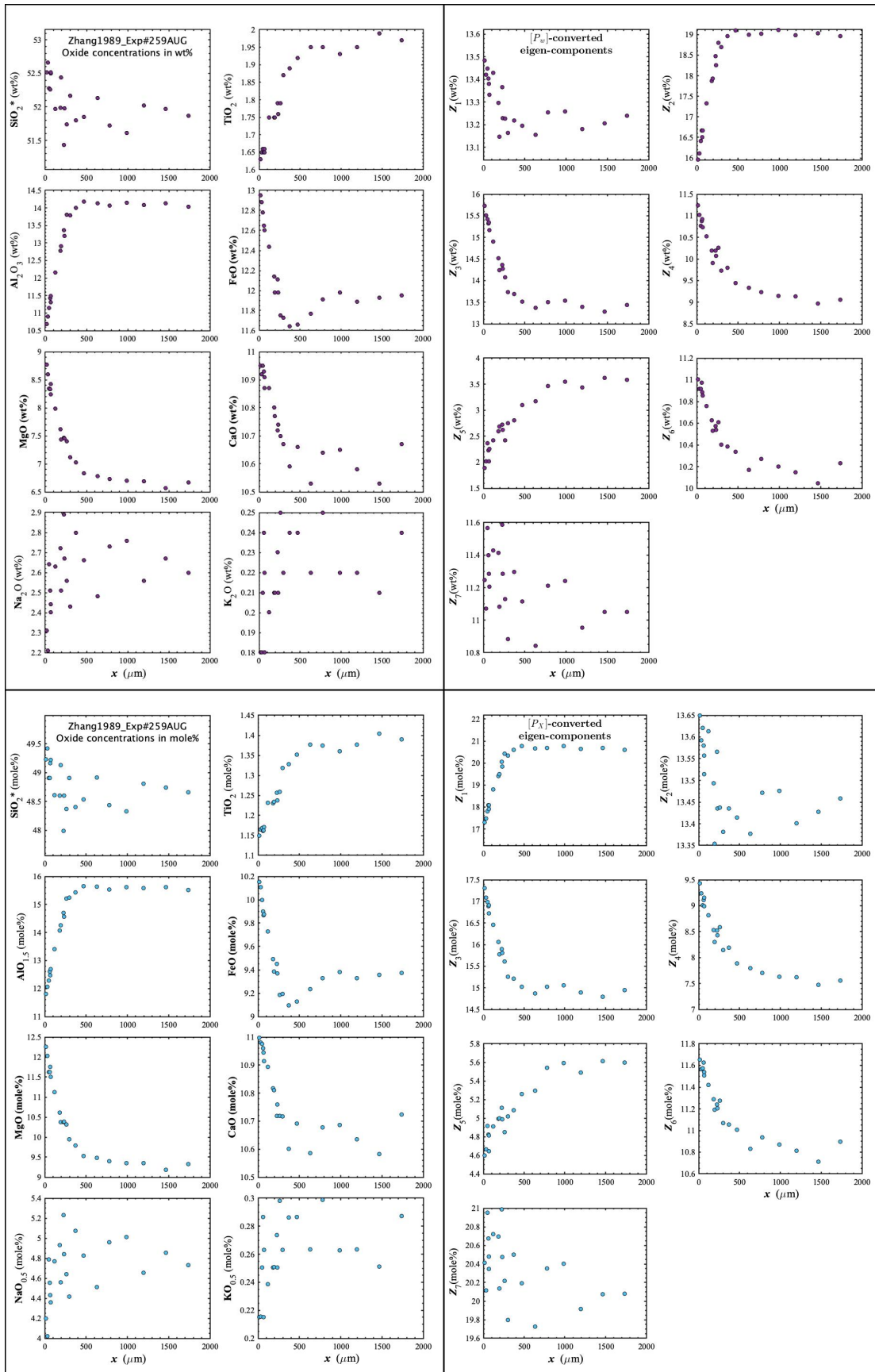
126
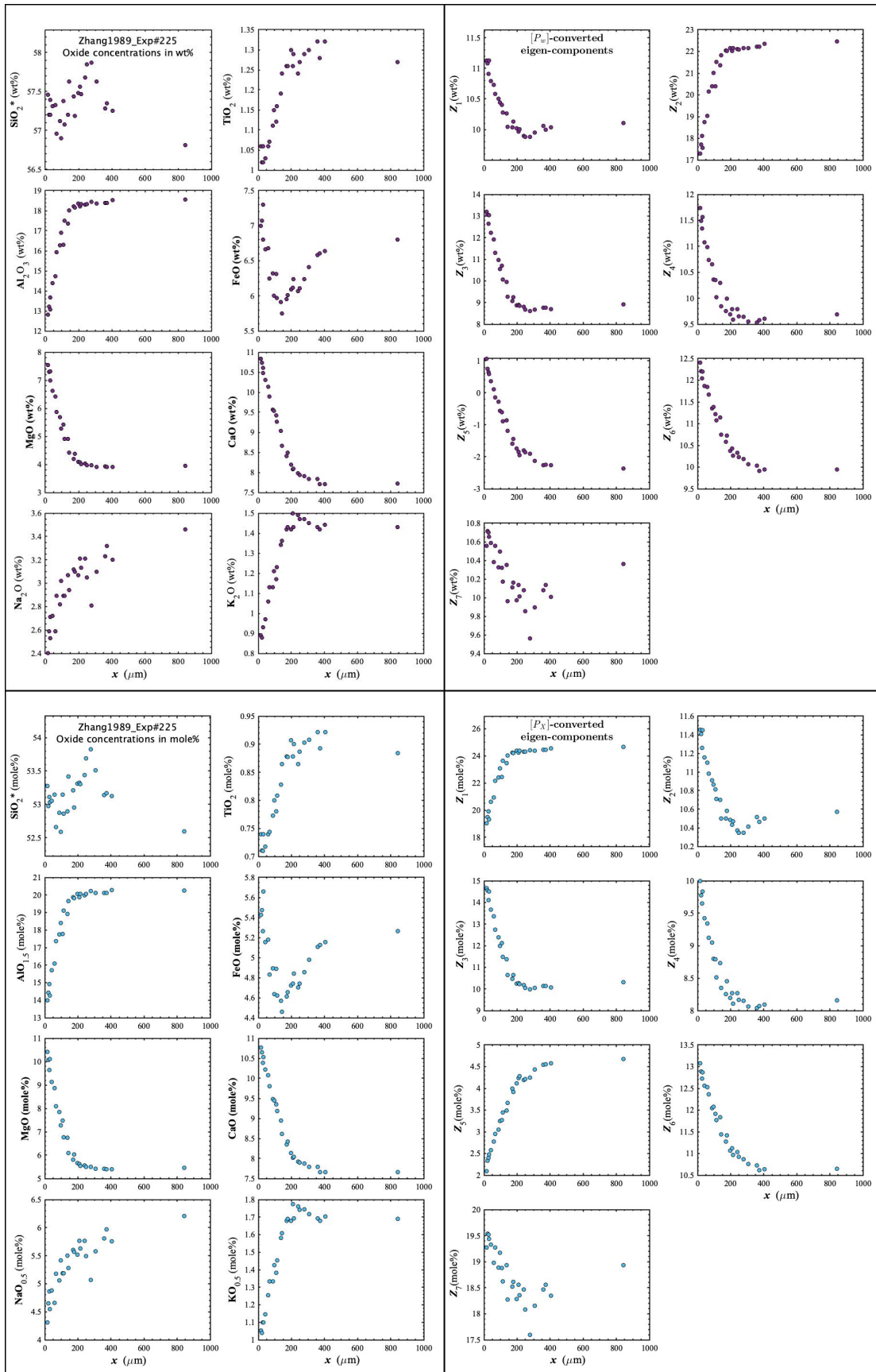
Figure D7. Concentration profiles of oxide components in wt% (upper left panel), oxide components in mole% (lower left panel), $[P_w]$-converted eigen-components (upper right panel), and $[P_X]$-converted eigen-components (lower right panel) of Zhang1989_Exp#225, which is a diopside dissolution experiment in andesite (Zhang et al., 1989).
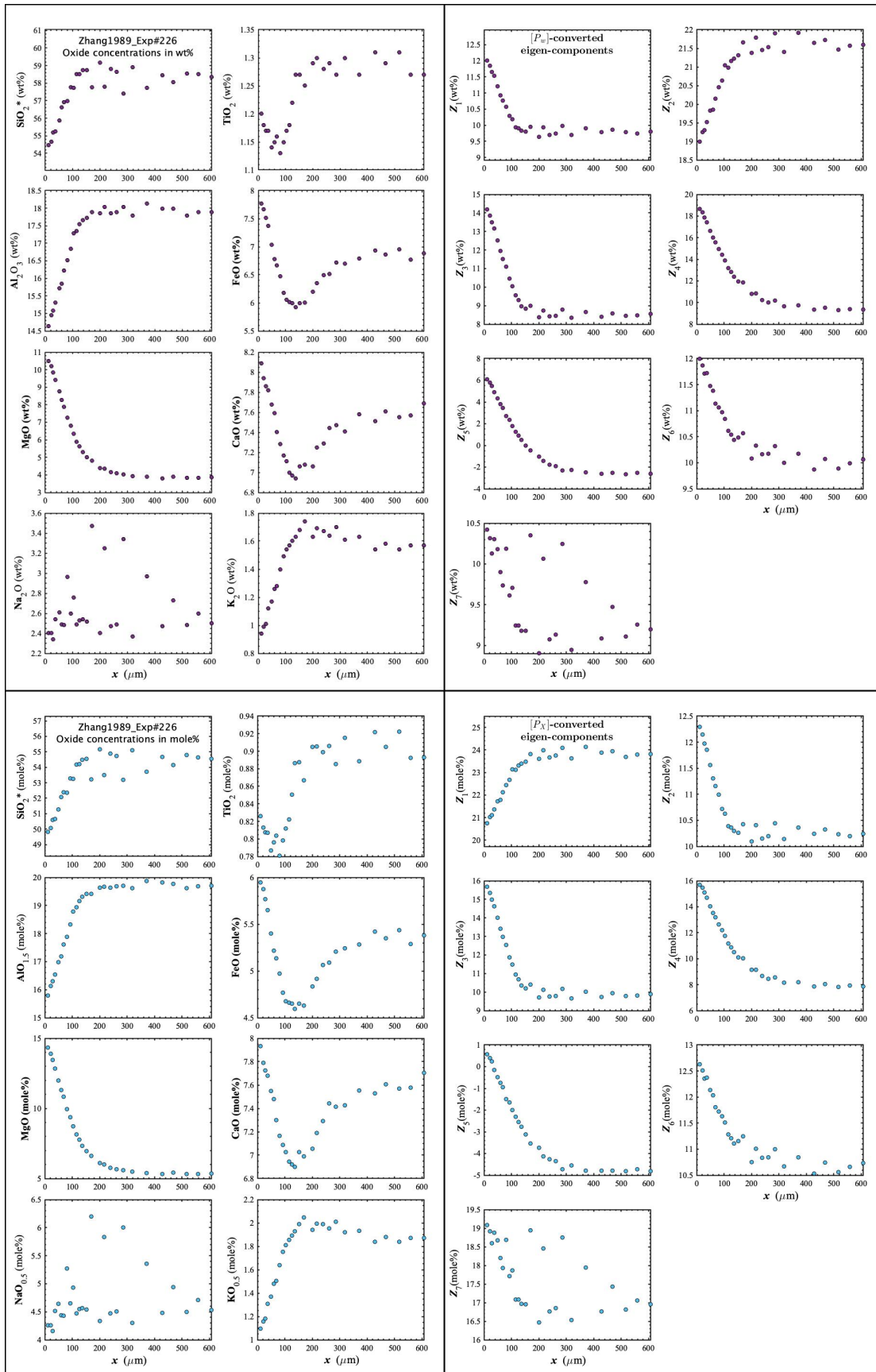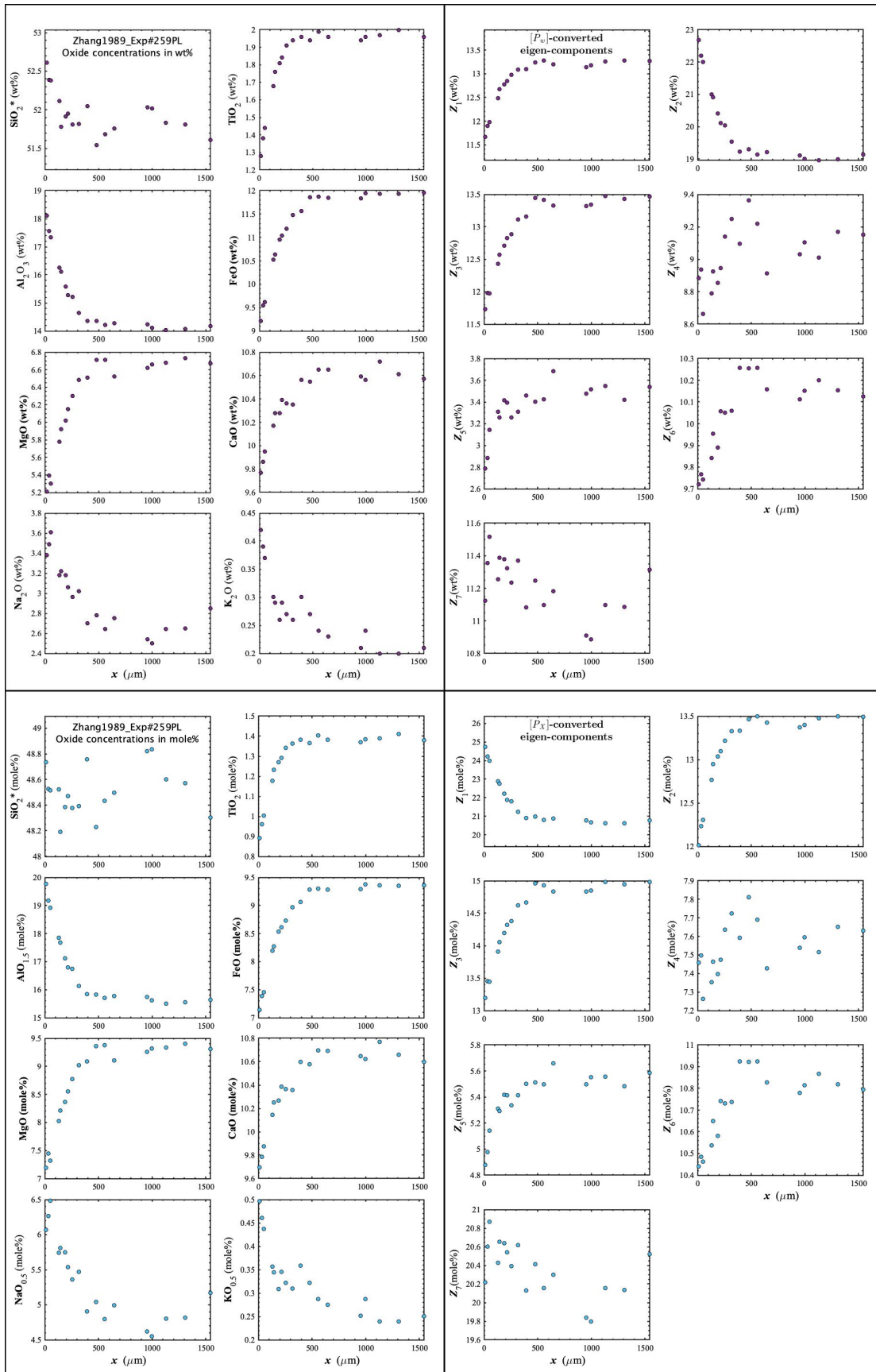
Figure D8. Concentration profiles of oxide components in wt% (upper left panel), oxide components in mole% (lower left panel), [P_w]-converted eigen-components (upper right panel), and [P_X]-converted eigen-components (lower right panel) of Zhang1989_Exp#226, which is a forsterite dissolution experiment in andesite (Zhang et al., 1989).
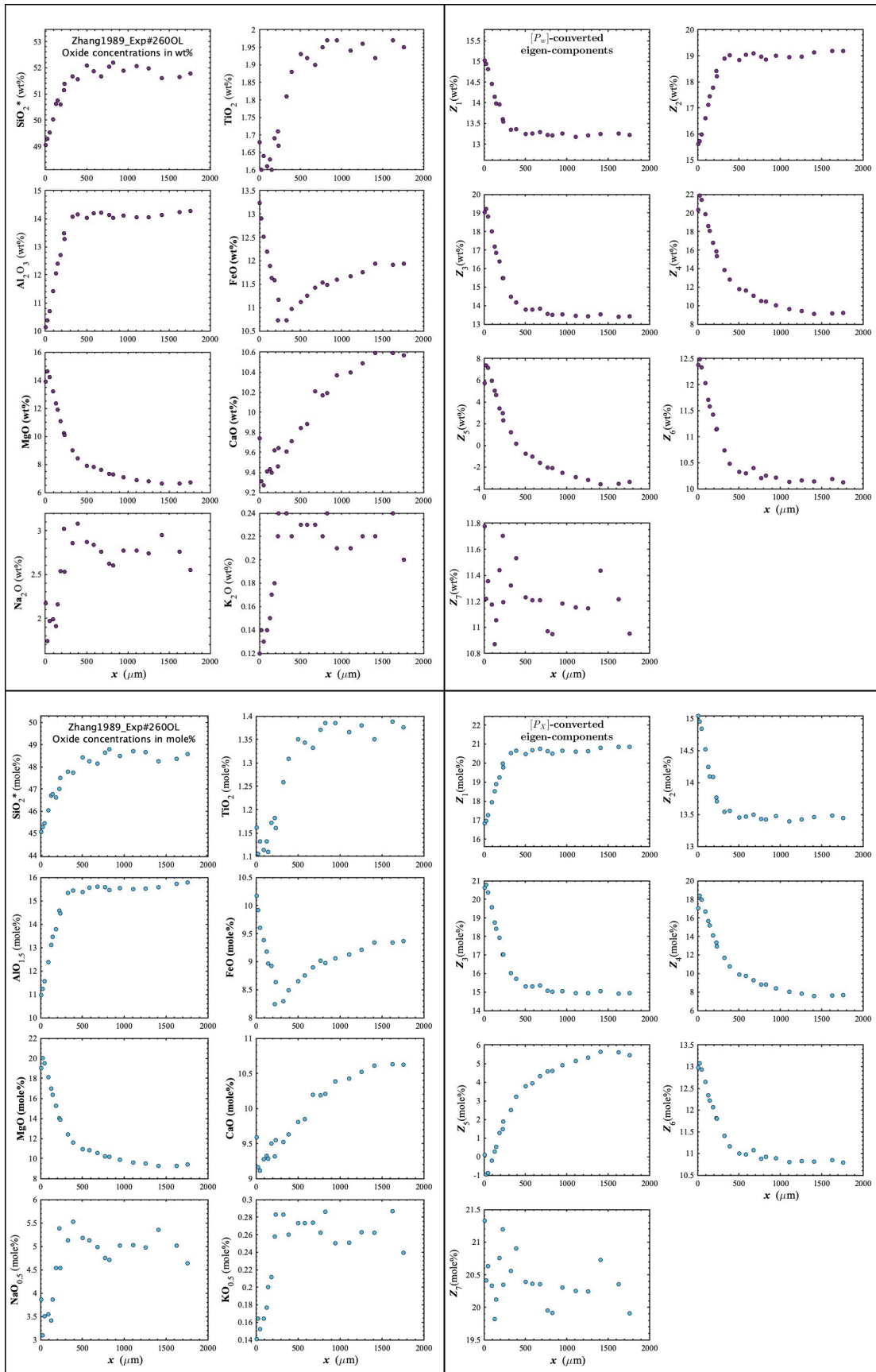
128
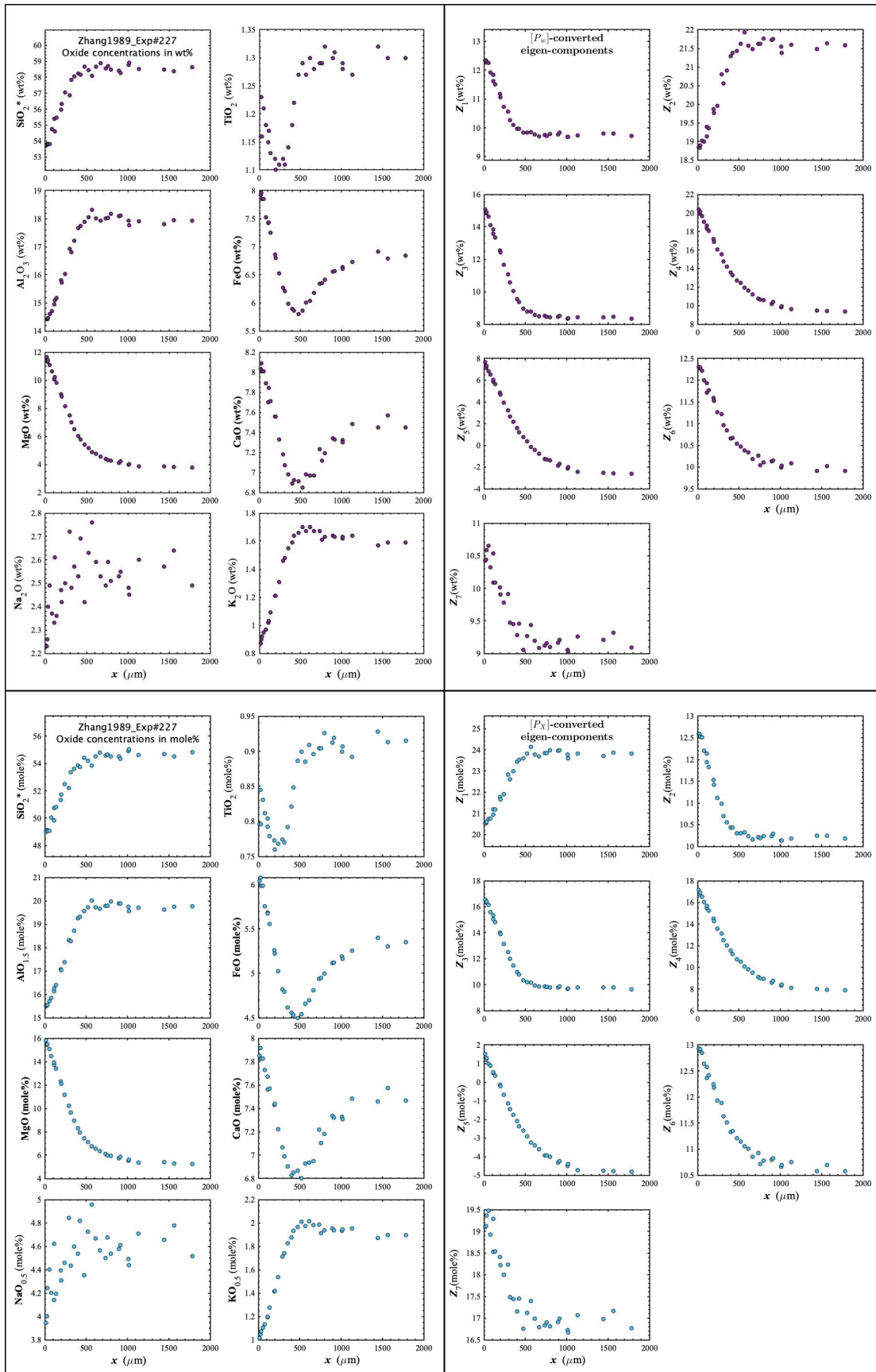
Figure D9. Concentration profiles of oxide components in wt% (upper left panel), oxide components in mole% (lower left panel), [P_w]-converted eigen-components (upper right panel), and [P_X]-converted eigen-components (lower right panel) of Zhang1989_Exp#227, which is a forsterite dissolution experiment in andesite (Zhang et al., 1989).
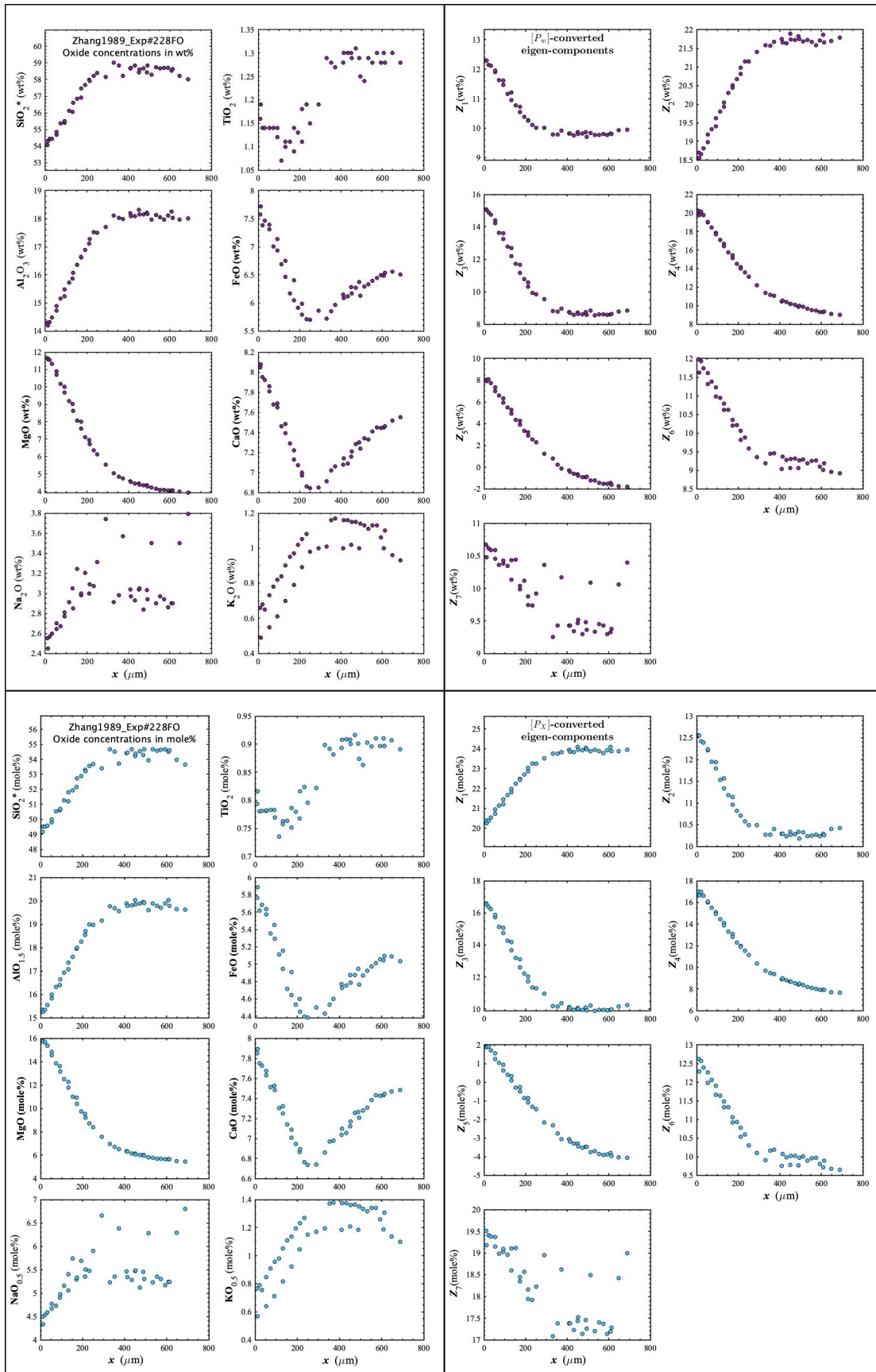
Figure D10. Concentration profiles of oxide components in wt% (upper left panel), oxide components in mole% (lower left panel), [P_w]-converted eigen-components (upper right panel), and [P_X]-converted eigen-components (lower right panel) of Zhang1989_Exp#228FO, which is a forsterite dissolution experiment in andesite (Zhang et al., 1989).

130
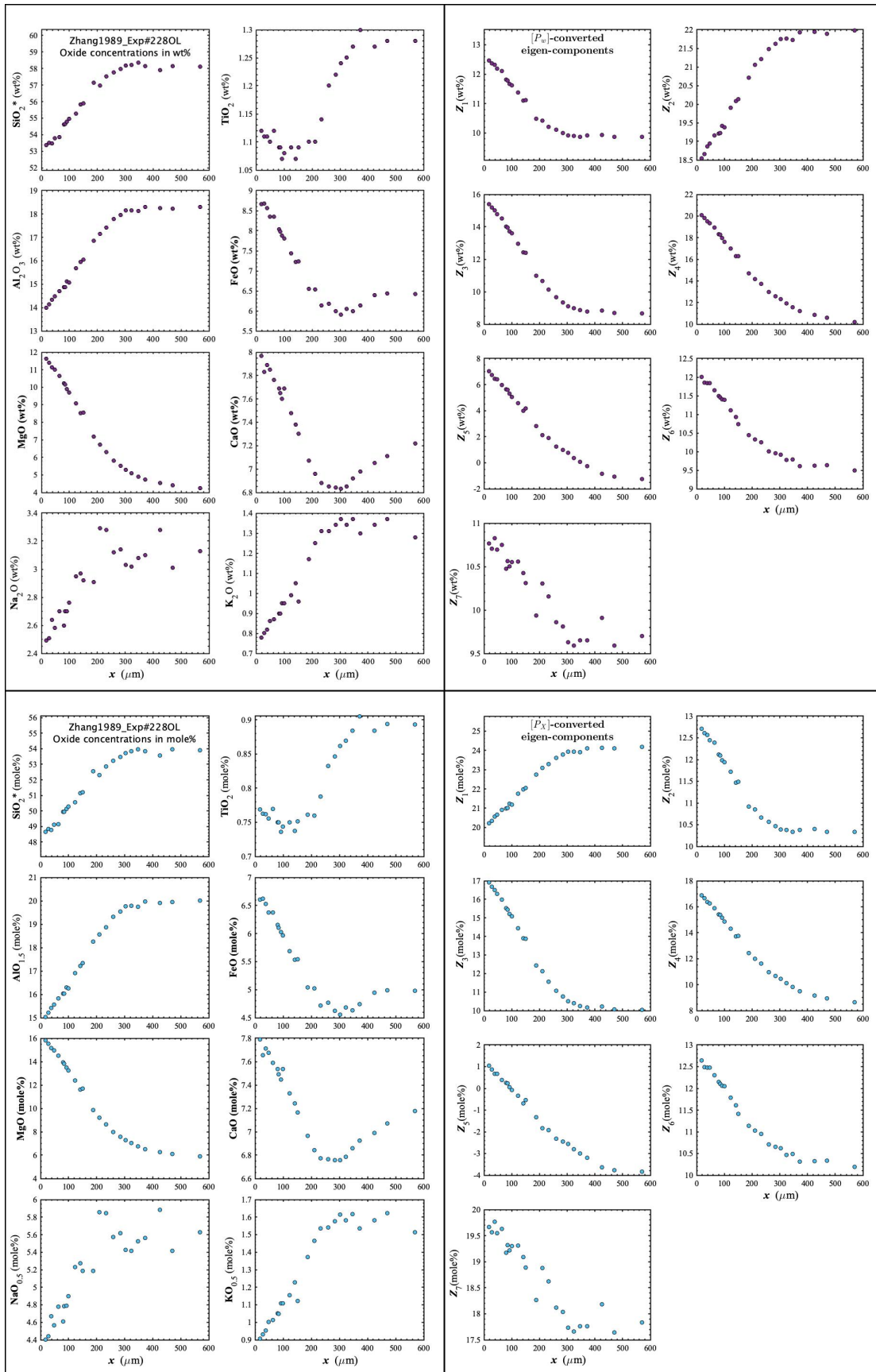
Figure D11. Concentration profiles of oxide components in wt% (upper left panel), oxide components in mole% (lower left panel), [P_w]-converted eigen-components (upper right panel), and [P_X]-converted eigen-components (lower right panel) of Zhang1989_Exp#228OL, which is an olivine dissolution experiment in andesite (Zhang et al., 1989).
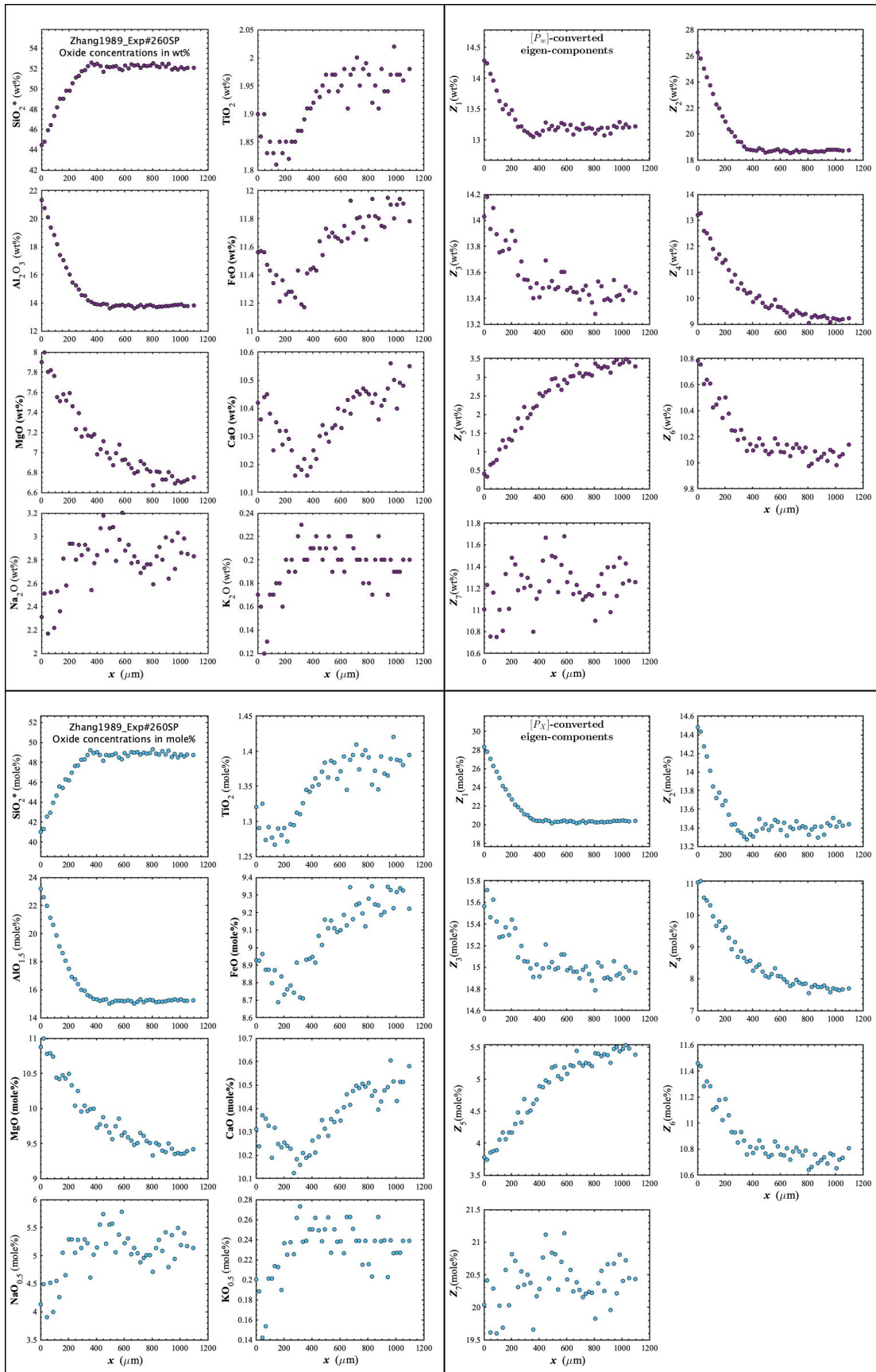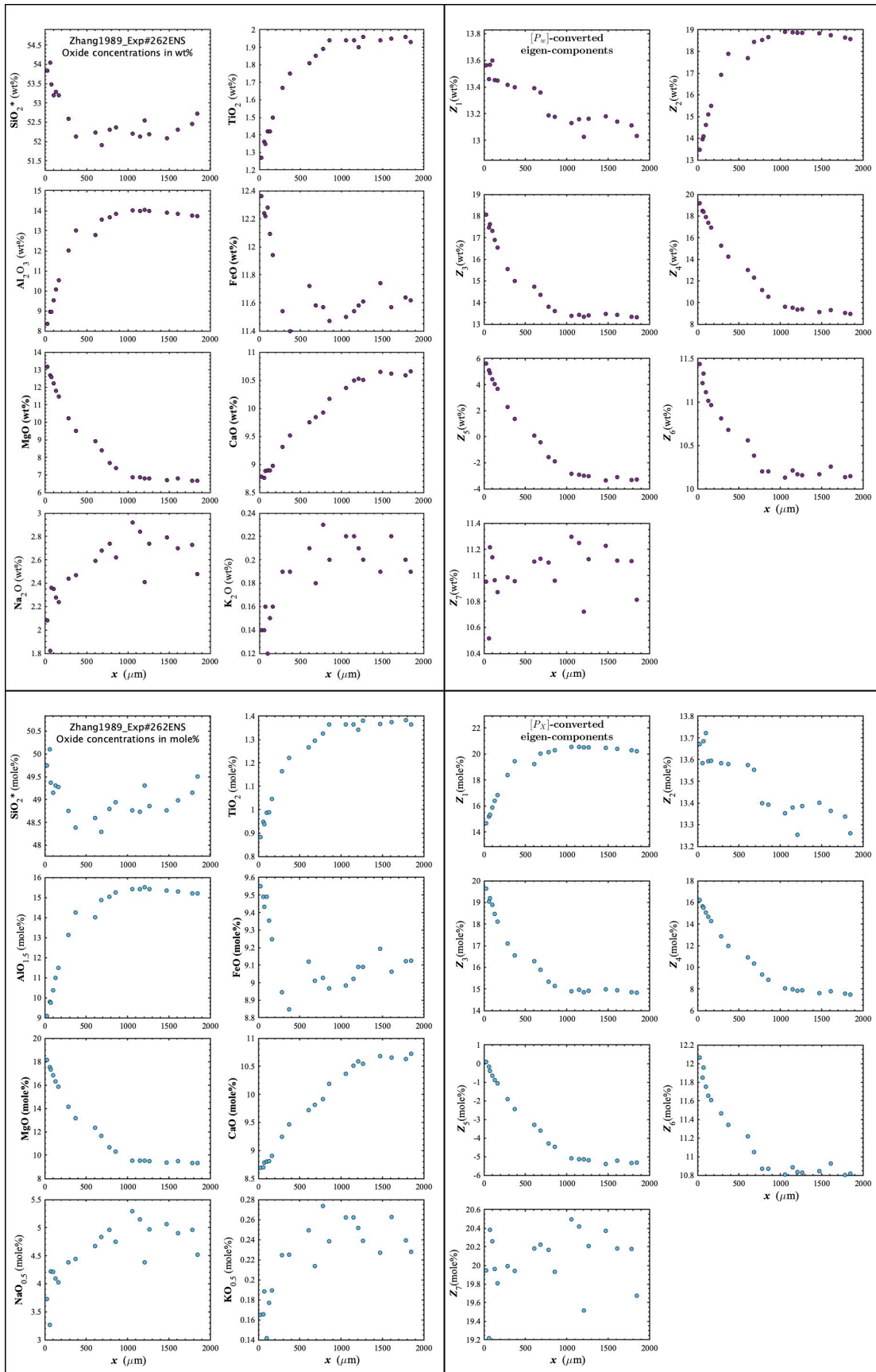
131
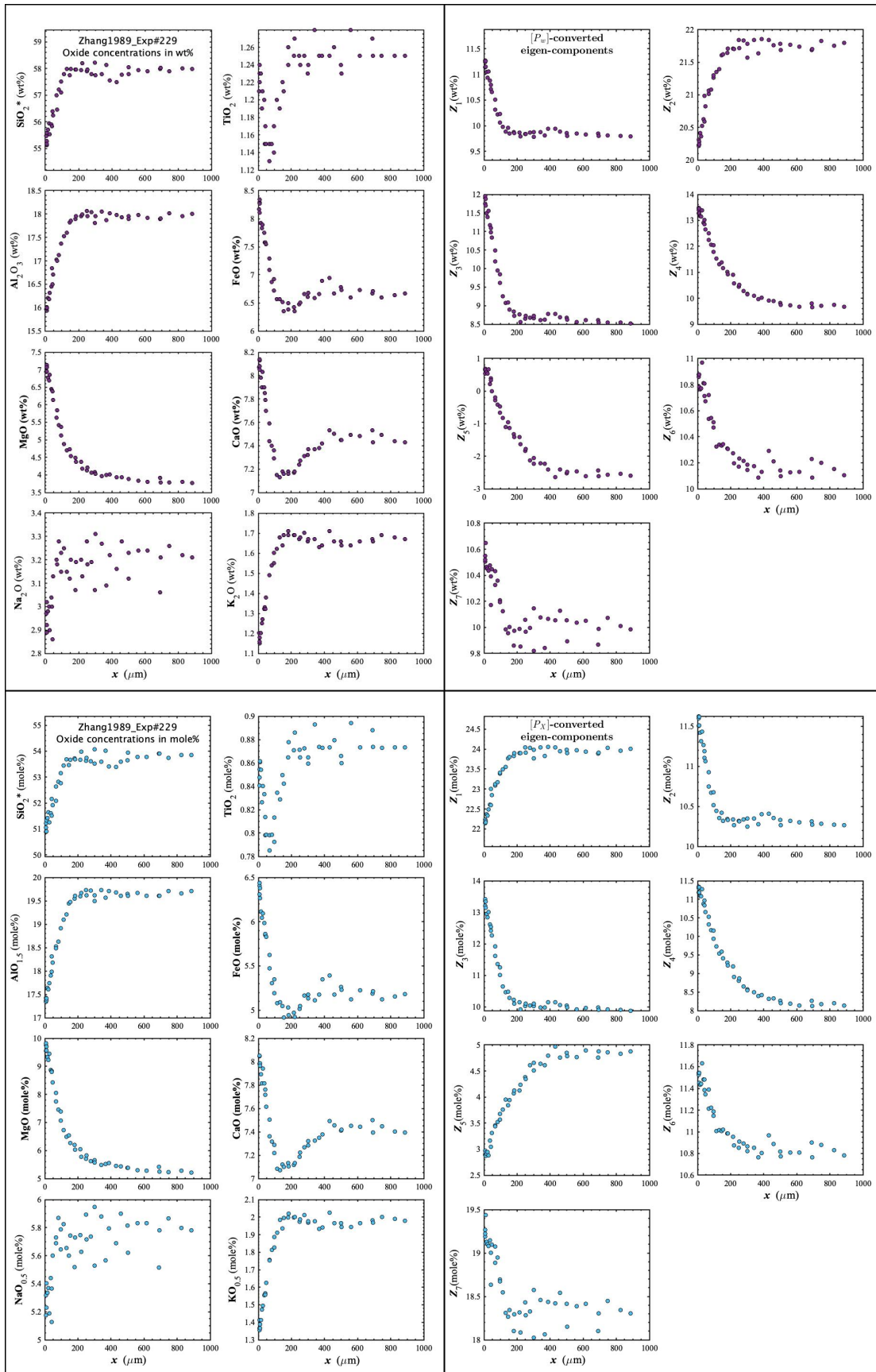
Figure D12. Concentration profiles of oxide components in wt% (upper left panel), oxide components in mole% (lower left panel), [P_w]-converted eigen-components (upper right panel), and [P_X]-converted eigen-components (lower right panel) of Zhang1989_Exp#229, which is an olivine dissolution experiment in andesite (Zhang et al., 1989).
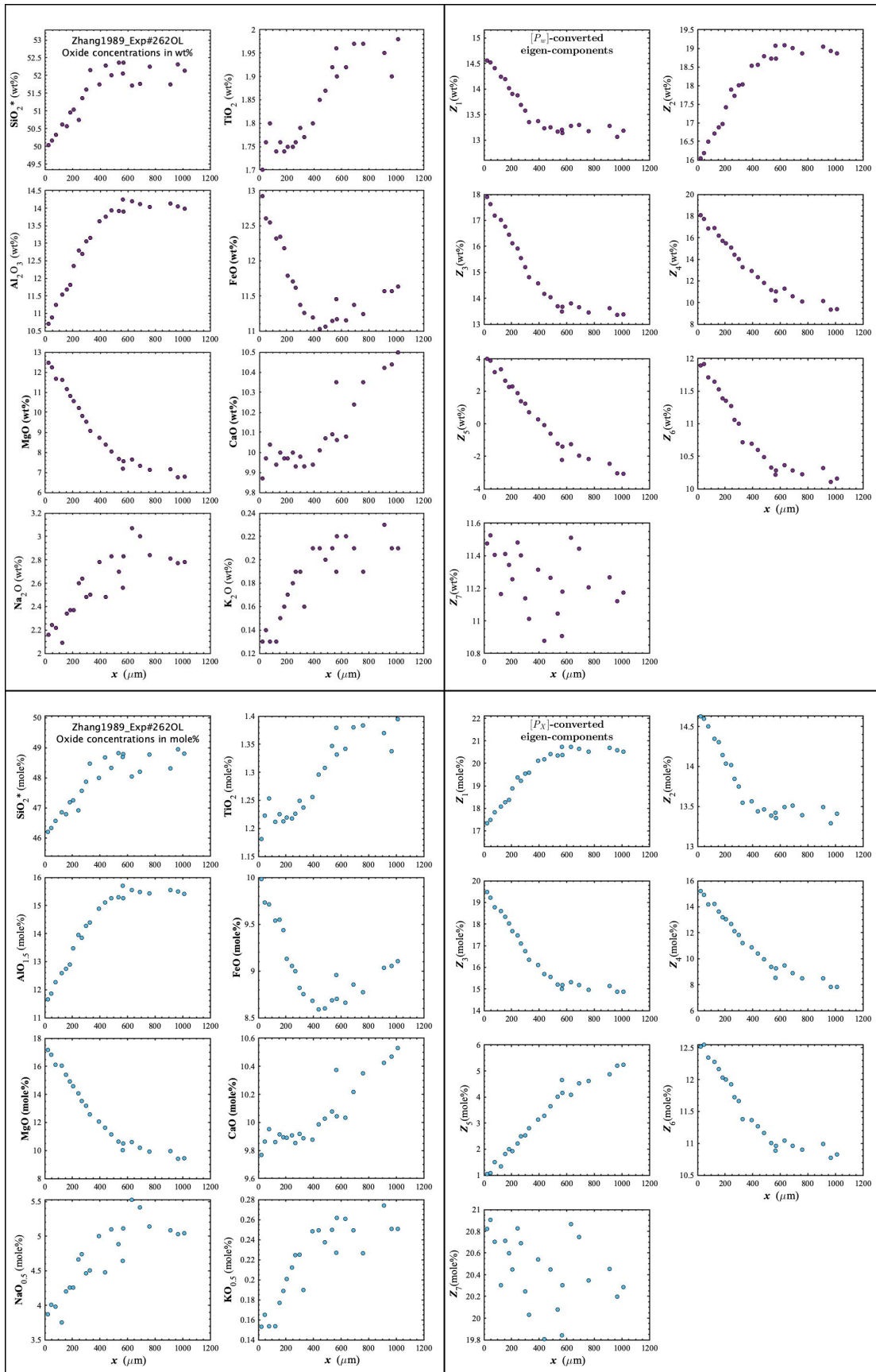
132
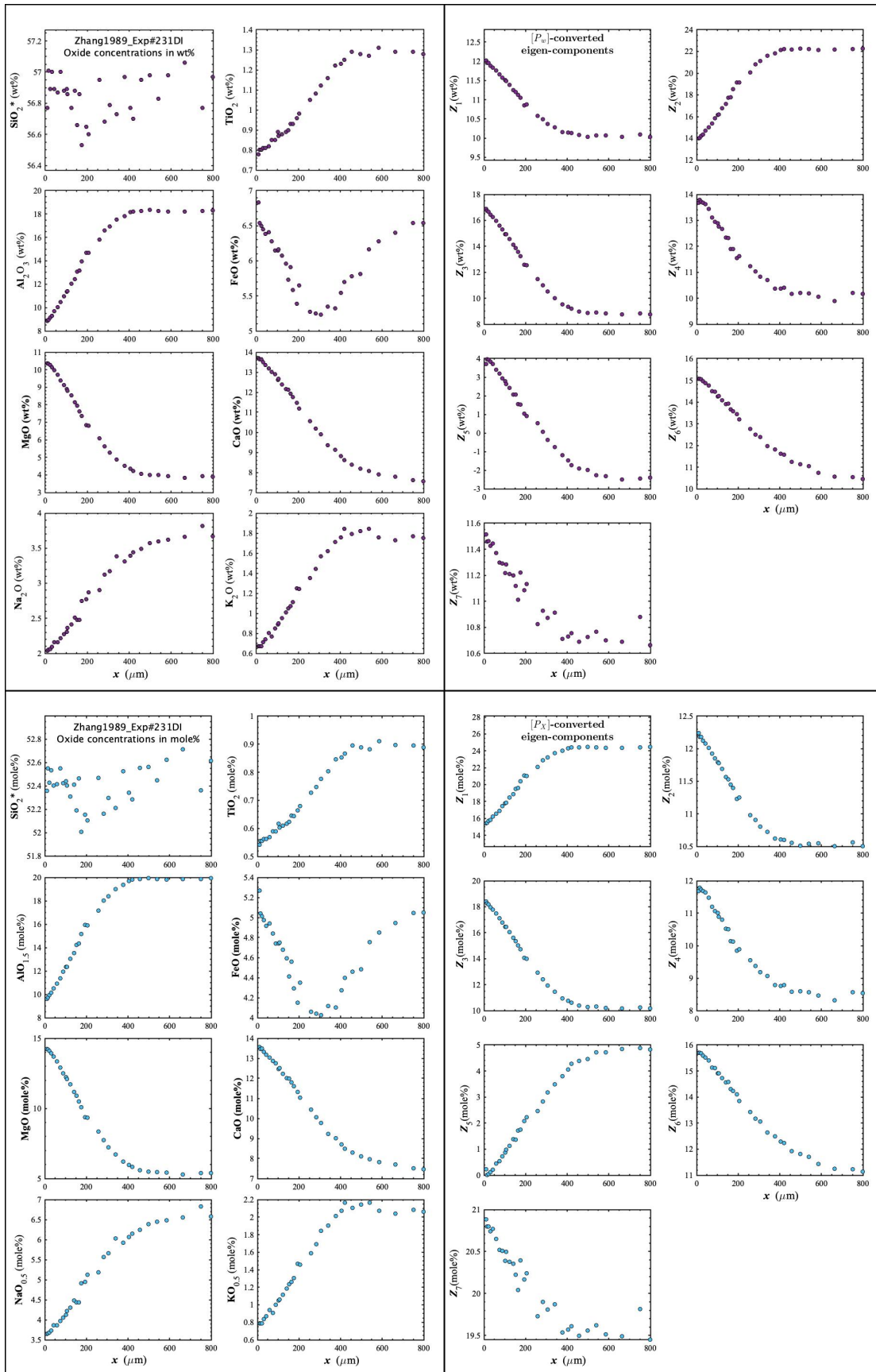
Figure D13. Concentration profiles of oxide components in wt% (upper left panel), oxide components in mole% (lower left panel), [P_w]-converted eigen-components (upper right panel), and [P_X]-converted eigen-components (lower right panel) of Zhang1989_Exp#231DI, which is a diopside dissolution experiment in andesite (Zhang et al., 1989).
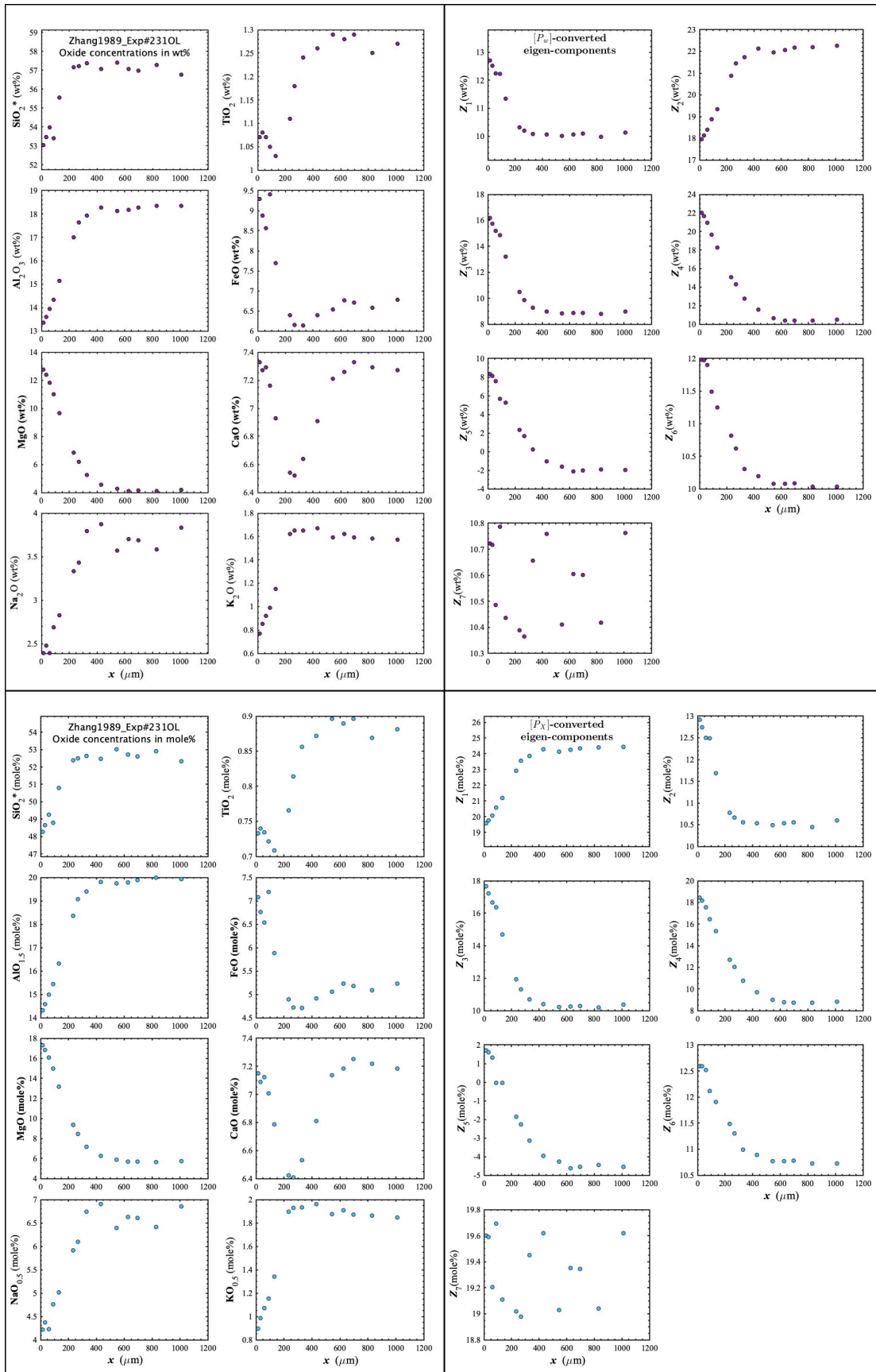
Figure D14. Concentration profiles of oxide components in wt% (upper left panel), oxide components in mole% (lower left panel), [P_w]-converted eigen-components (upper right panel), and [P_X]-converted eigen-components (lower right panel) of Zhang1989_Exp#231OL, which is an olivine dissolution experiment in andesite (Zhang et al., 1989).
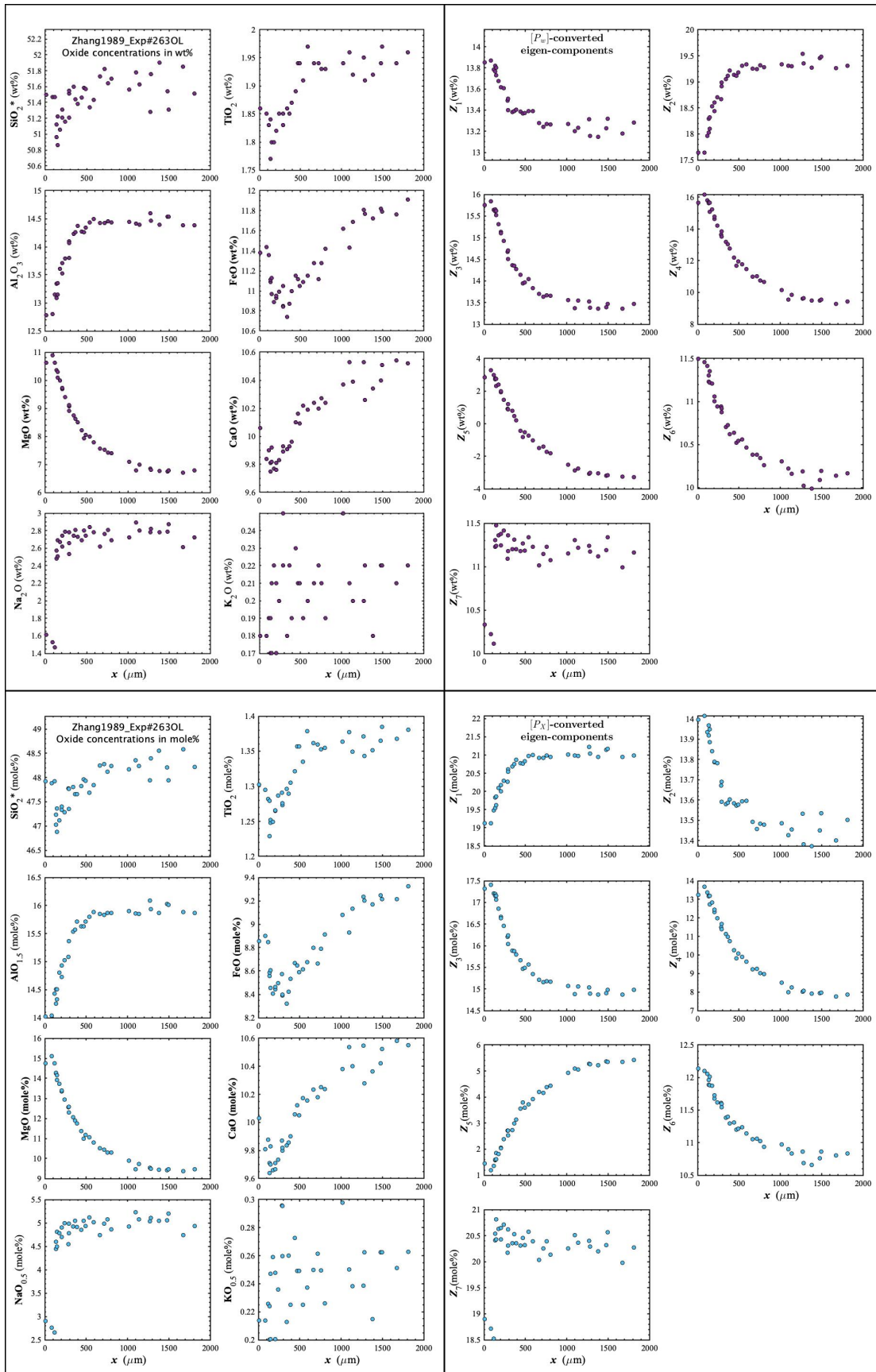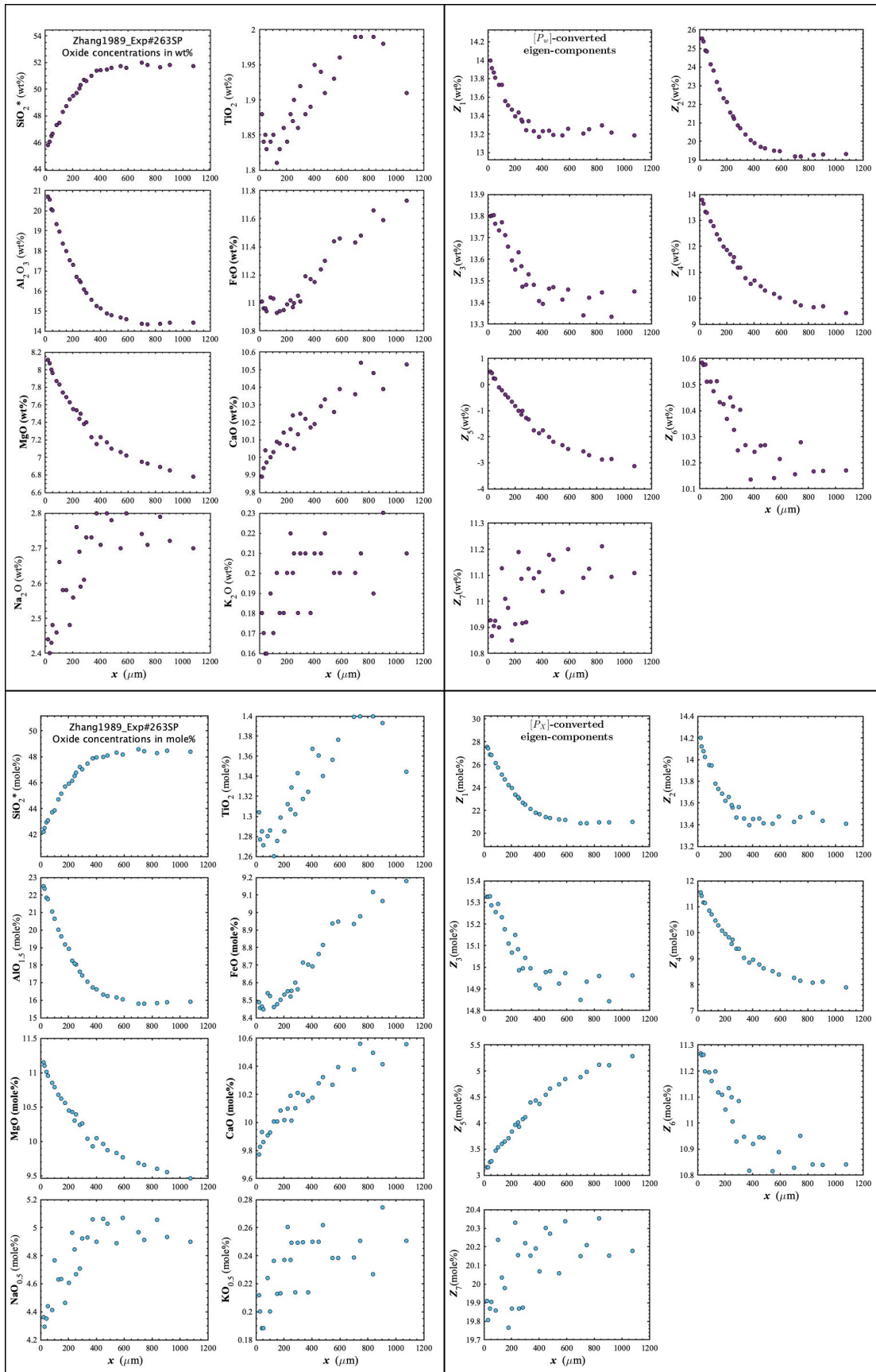
134
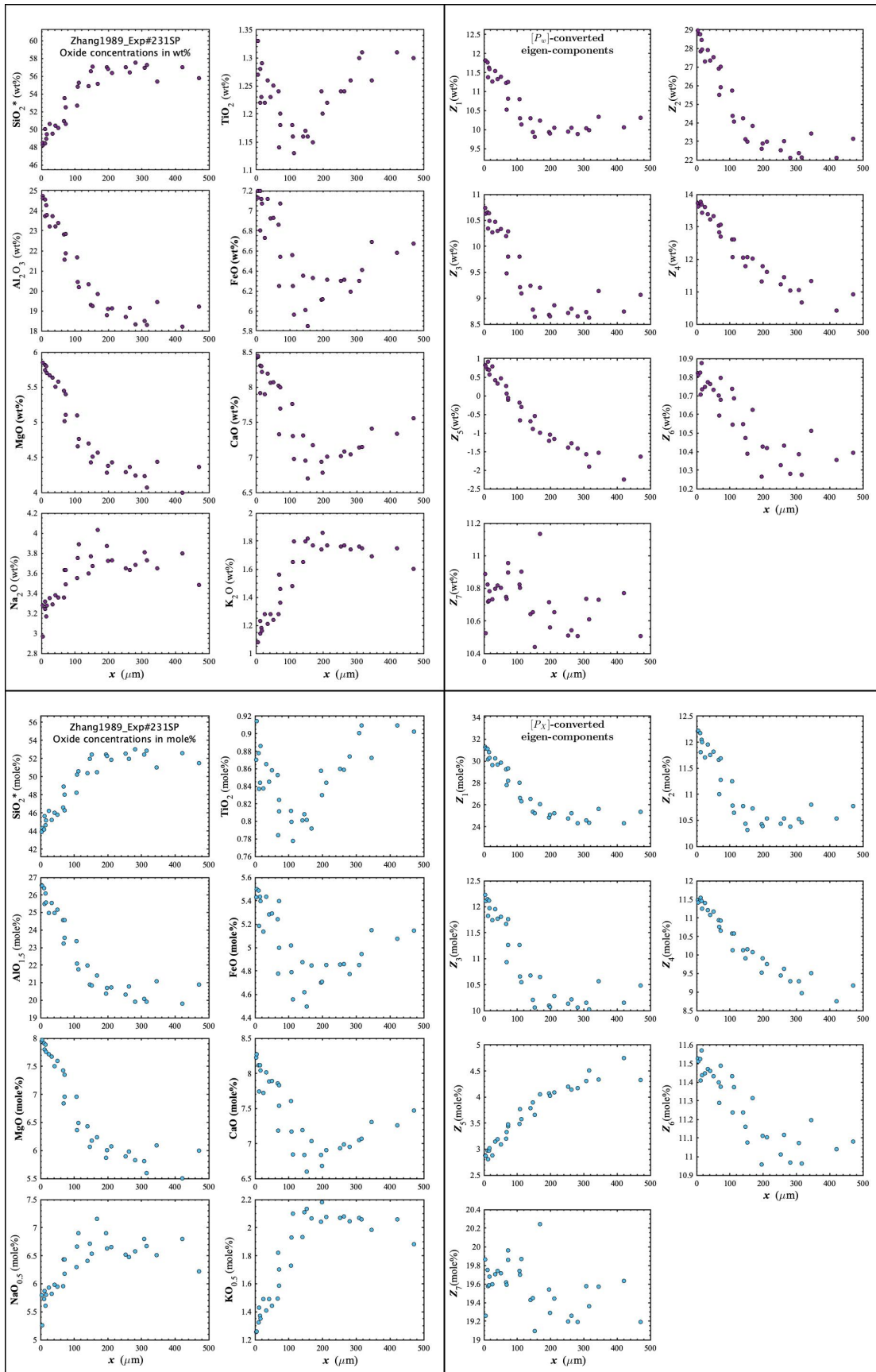
Figure D15. Concentration profiles of oxide components in wt% (upper left panel), oxide components in mole% (lower left panel), [P_w]-converted eigen-components (upper right panel), and [P_X]-converted eigen-components (lower right panel) of Zhang1989_Exp#231SP, which is a spinel dissolution experiment in andesite (Zhang et al., 1989).
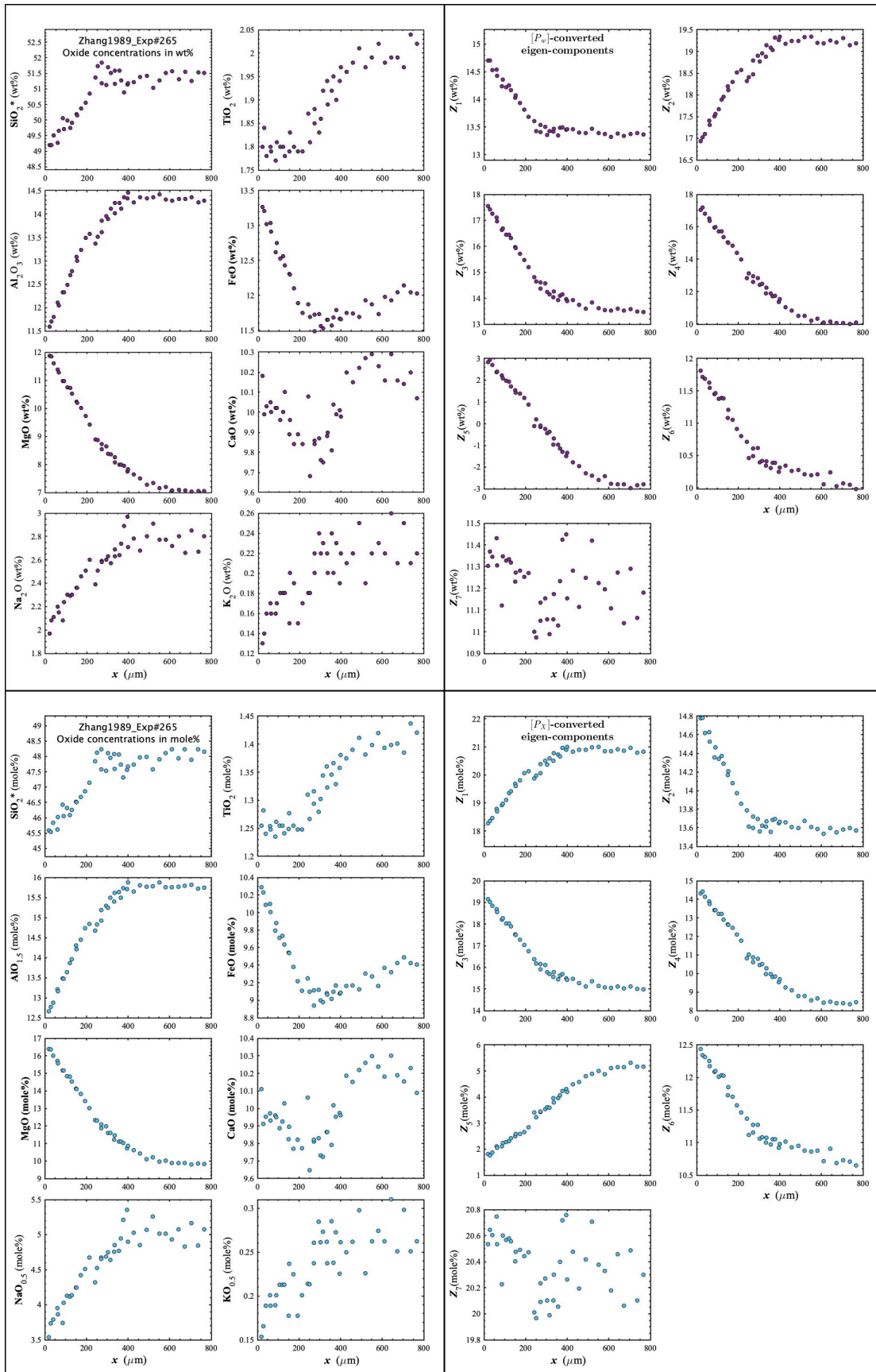
135
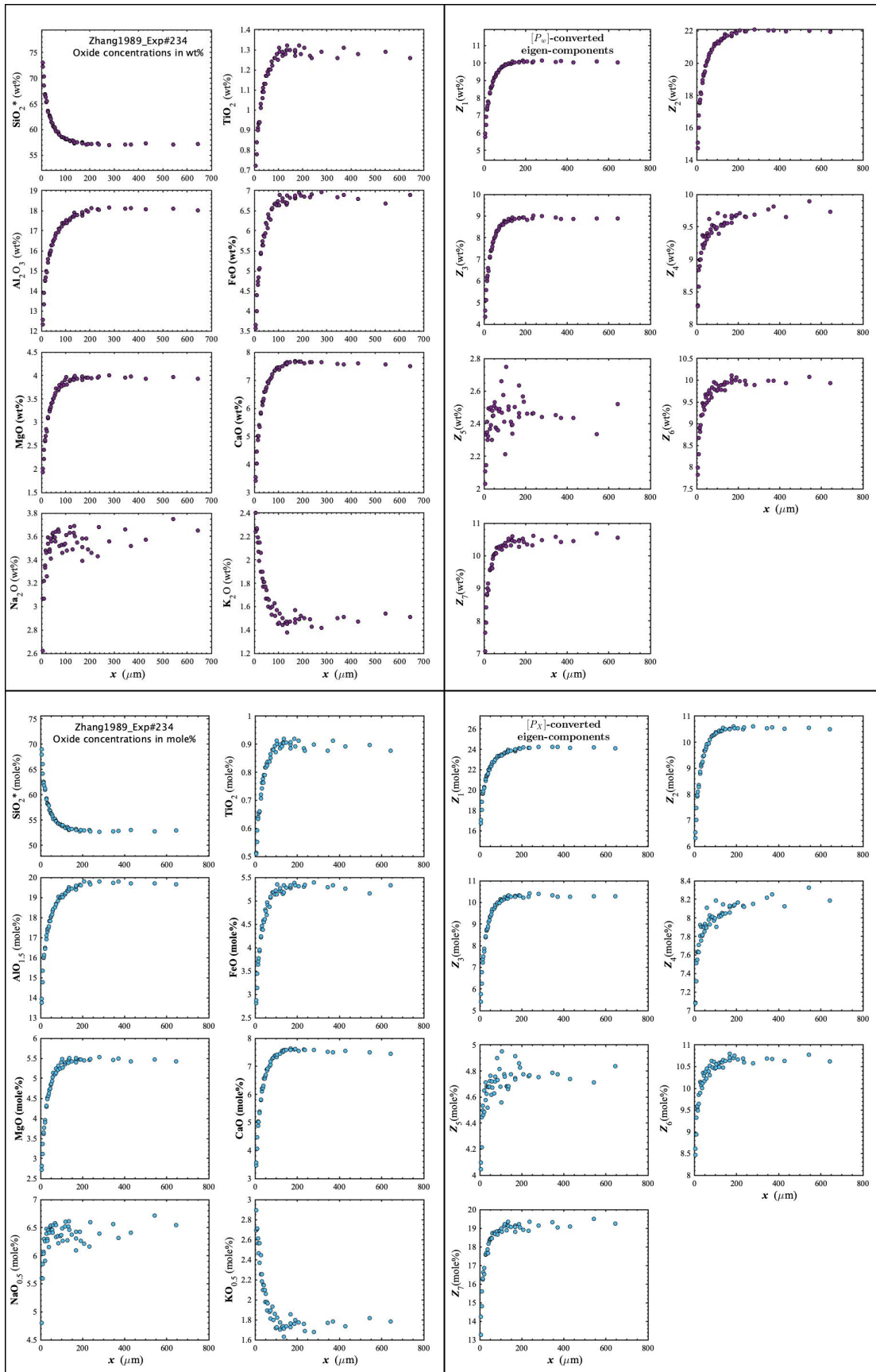
Figure D16. Concentration profiles of oxide components in wt% (upper left panel), oxide components in mole% (lower left panel), $[P_w]$-converted eigen-components (upper right panel), and $[P_X]$-converted eigen-components (lower right panel) of Zhang1989_Exp#234, which is a quartz dissolution experiment in andesite (Zhang et al., 1989).

136
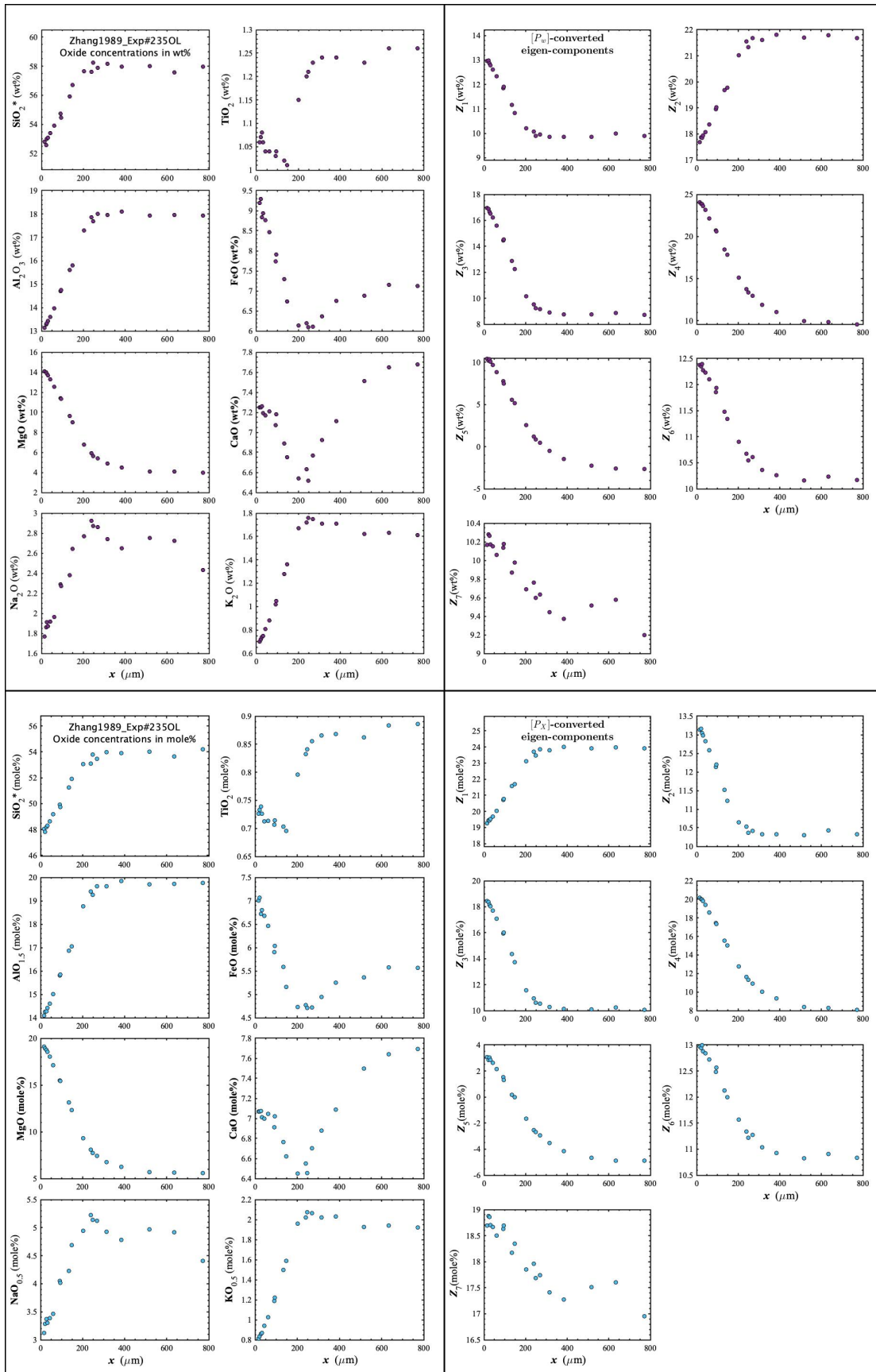
Figure D17. Concentration profiles of oxide components in wt% (upper left panel), oxide components in mole% (lower left panel), [P_w]-converted eigen-components (upper right panel), and [P_X]-converted eigen-components (lower right panel) of Zhang1989_Exp#235OL, which is an olivine dissolution experiment in andesite (Zhang et al., 1989).
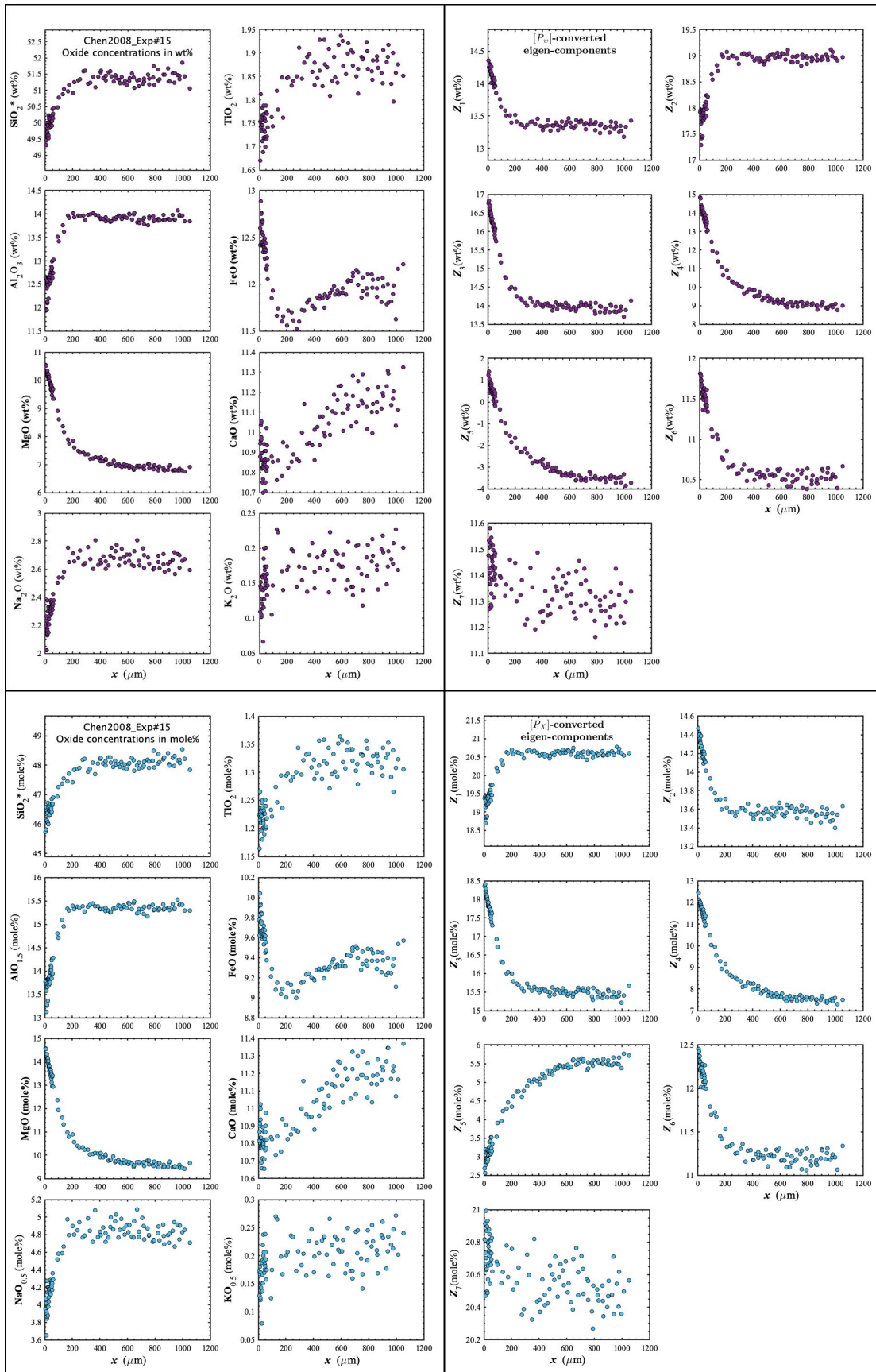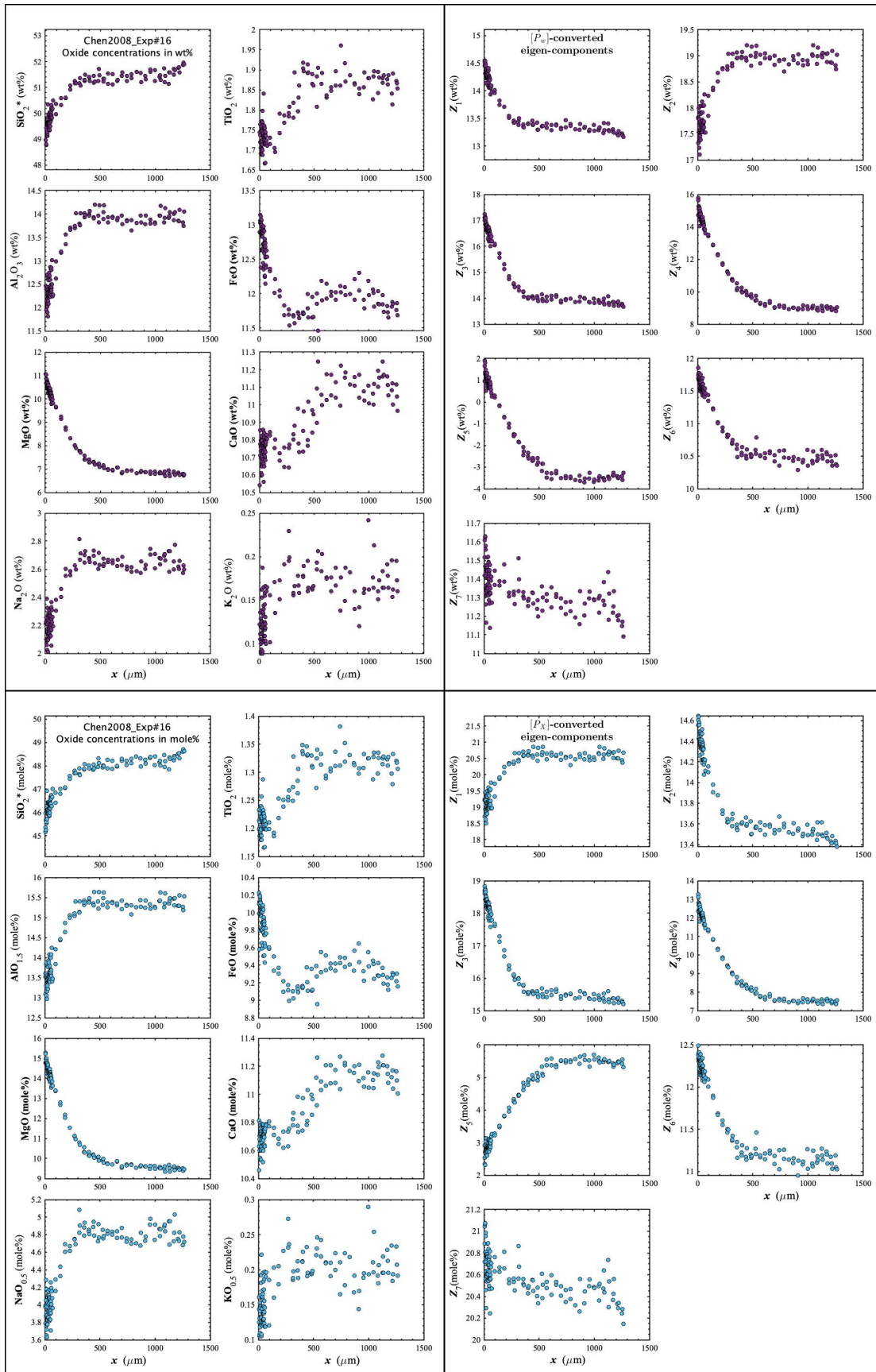
137
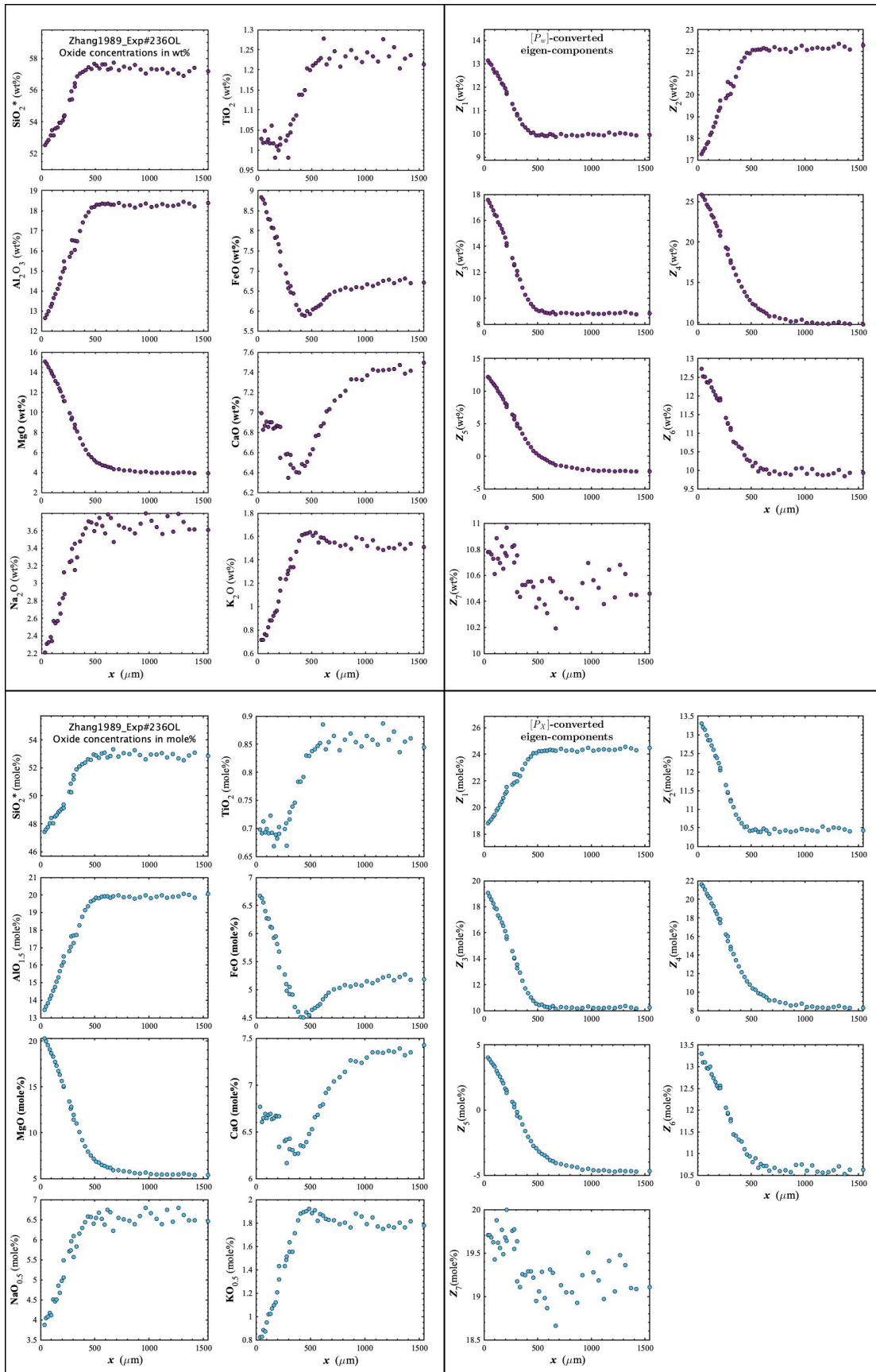
Figure D18. Concentration profiles of oxide components in wt% (upper left panel), oxide components in mole% (lower left panel), [P_w]-converted eigen-components (upper right panel), and [P_X]-converted eigen-components (lower right panel) of Zhang1989_Exp#236OL, which is an olivine dissolution experiment in andesite (Zhang et al., 1989).
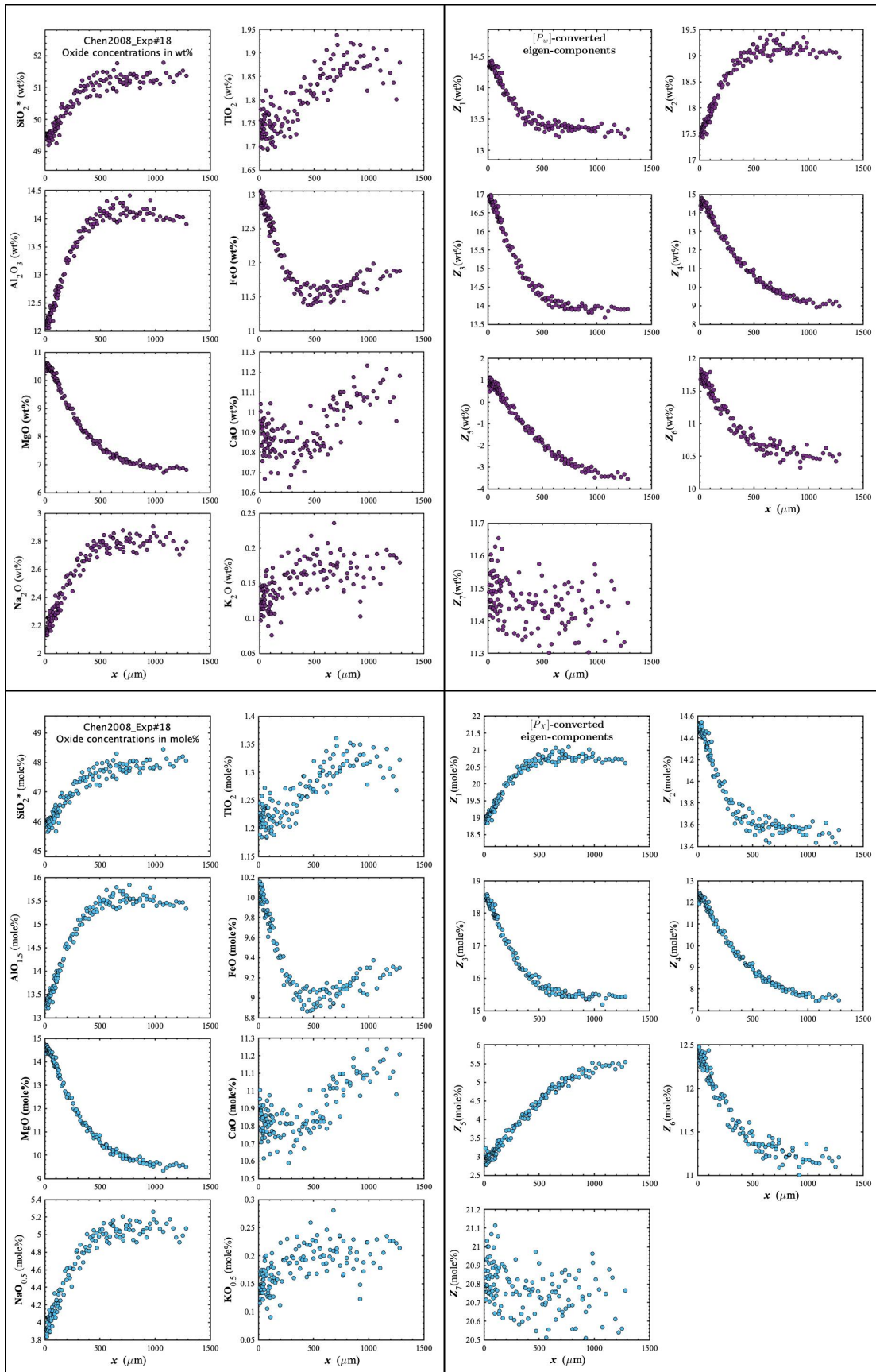
138
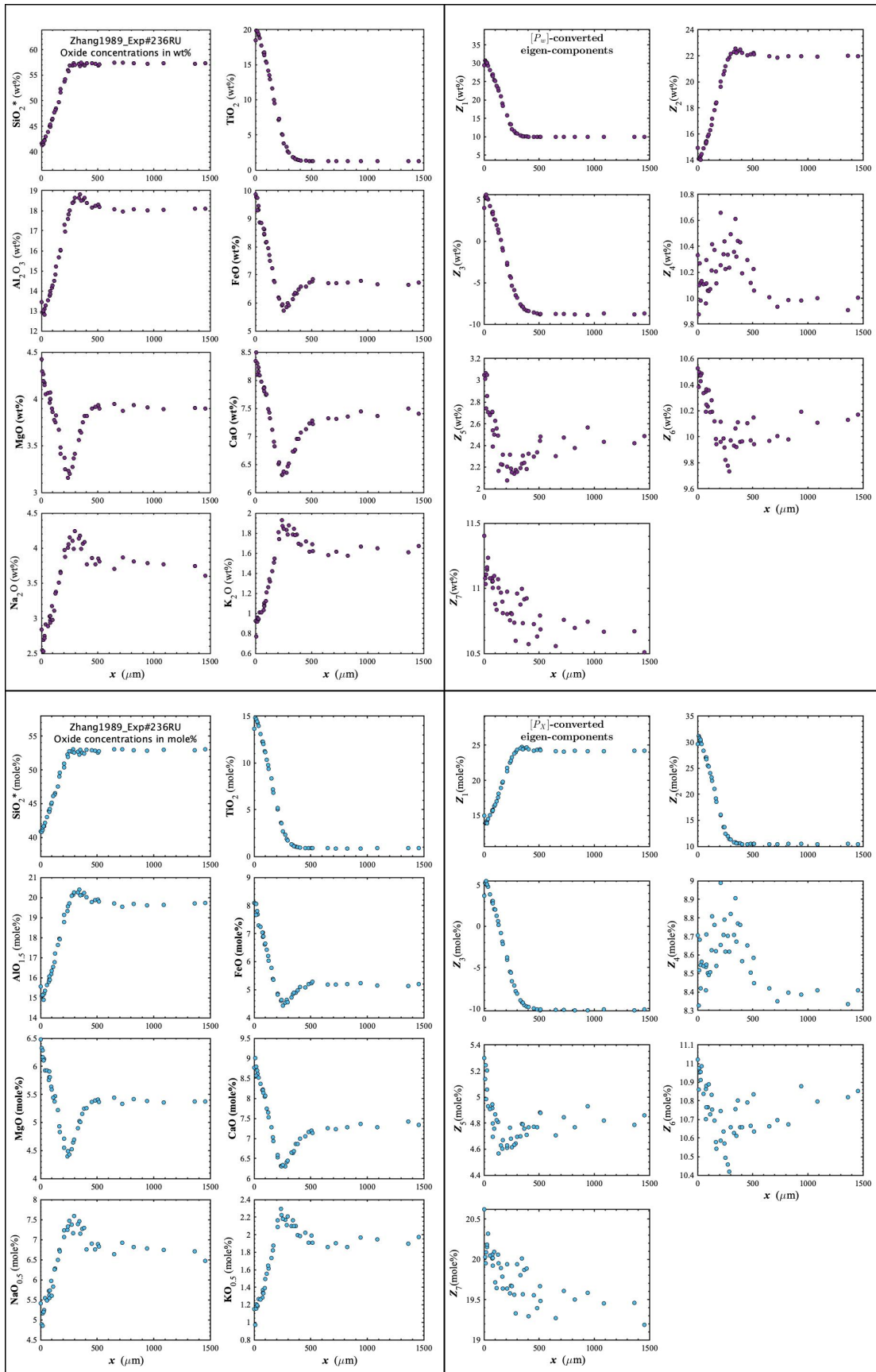
Figure D19. Concentration profiles of oxide components in wt% (upper left panel), oxide components in mole% (lower left panel), [P_w]-converted eigen-components (upper right panel), and [P_X]-converted eigen-components (lower right panel) of Zhang1989_Exp#236RU, which is a rutile dissolution experiment in andesite (Zhang et al., 1989).
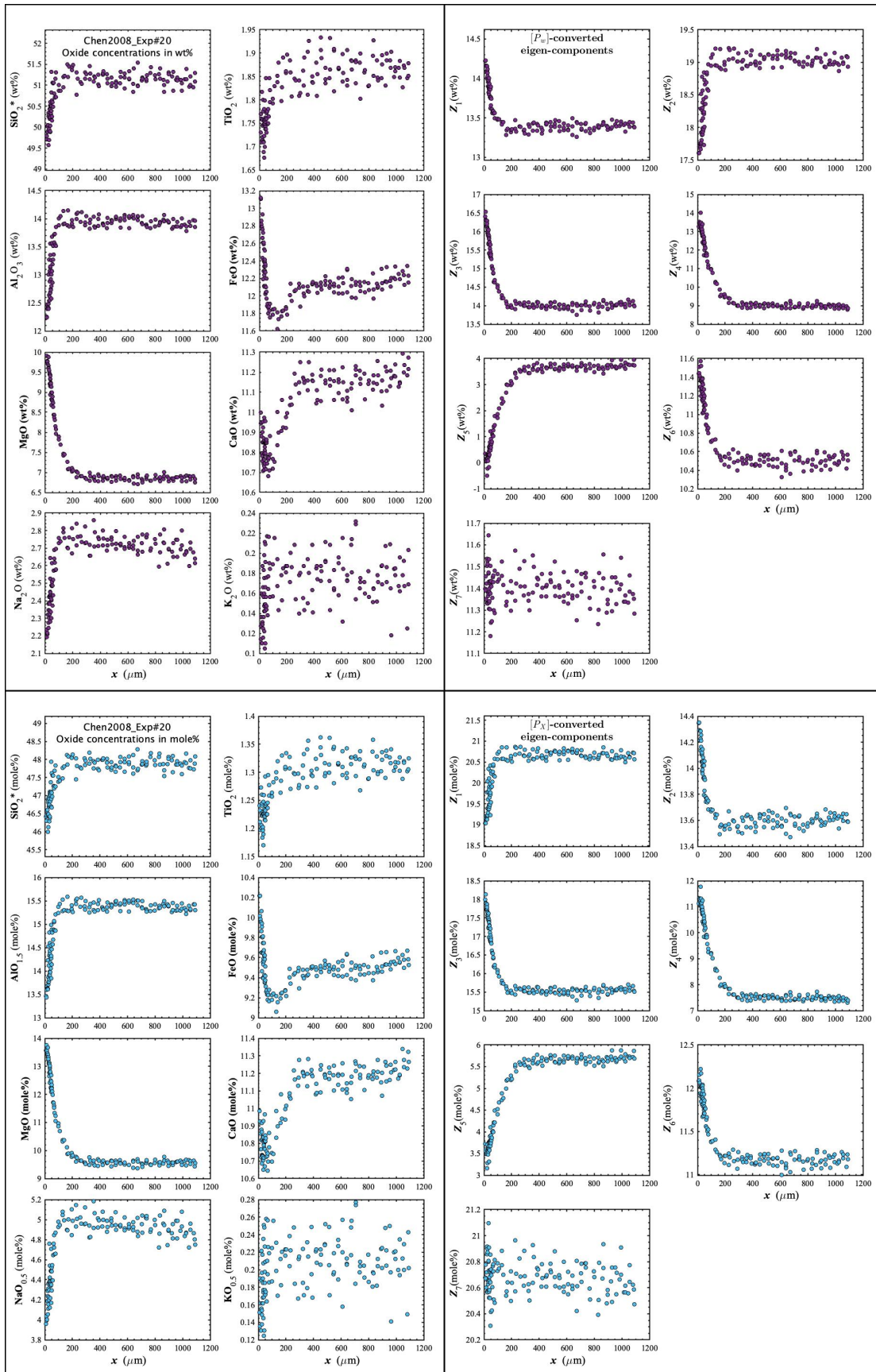
Figure D20. Concentration profiles of oxide components in wt% (upper left panel), oxide components in mole% (lower left panel), $[P_w]$-converted eigen-components (upper right panel), and $[P_X]$-converted eigen-components (lower right panel) of Zhang1989_Exp#239MID OL, which is an olivine dissolution experiment in andesite (Zhang et al., 1989).

Figure D21. Concentration profiles of oxide components in wt% (upper left panel), oxide components in mole% (lower left panel), [P_w]-converted eigen-components (upper right panel), and [P_X]-converted eigen-components (lower right panel) of Zhang1989_Exp#242, which is a diopside dissolution experiment in andesite (Zhang et al., 1989).
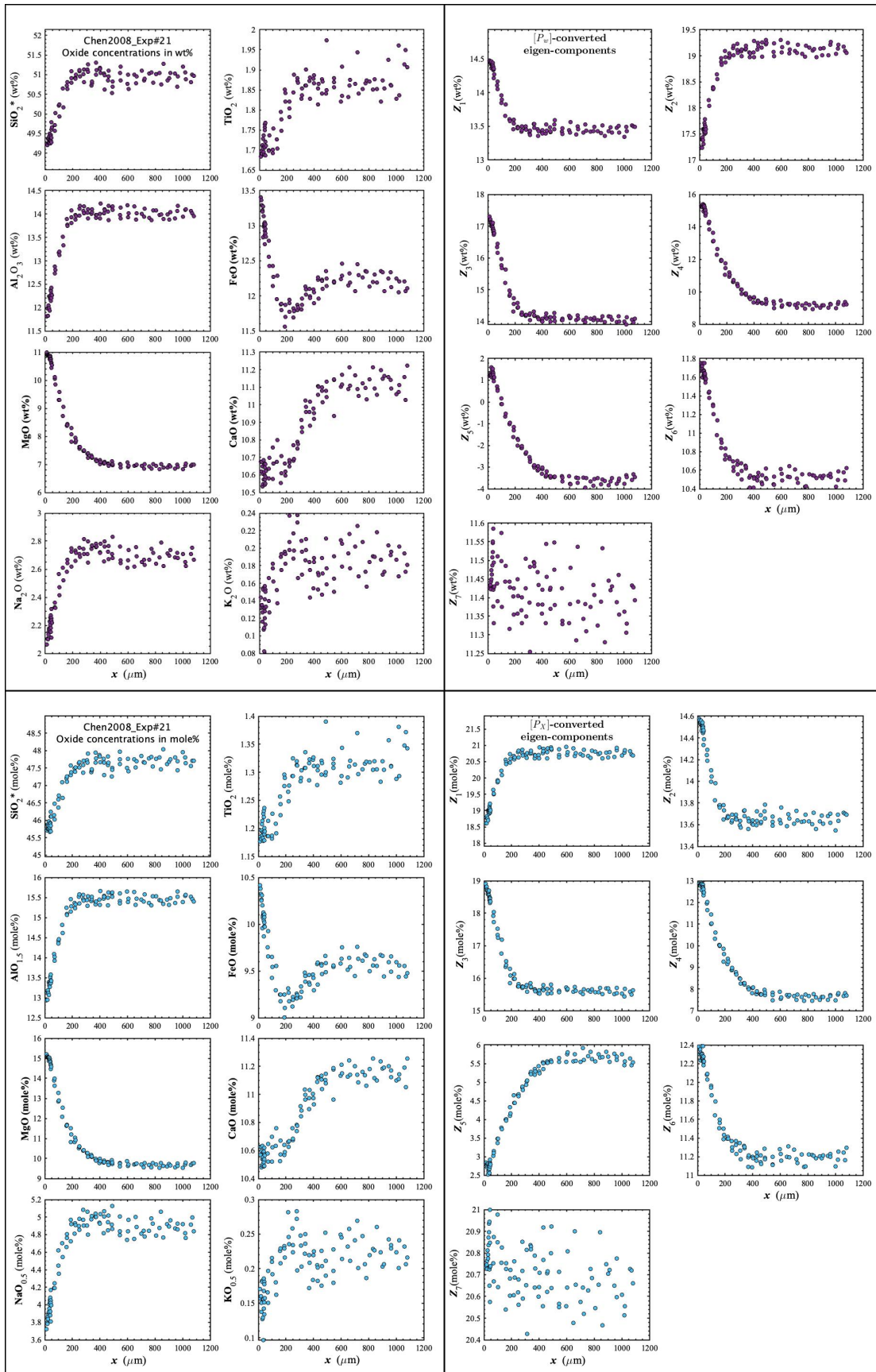
141

Figure D22. Concentration profiles of oxide components in wt% (upper left panel), oxide components in mole% (lower left panel), [P_w]-converted eigen-components (upper right panel), and [P_X]-converted eigen-components (lower right panel) of Zhang1989_Exp#246, which is an unknow crystal dissolution experiment in andesite (Zhang et al., 1989).
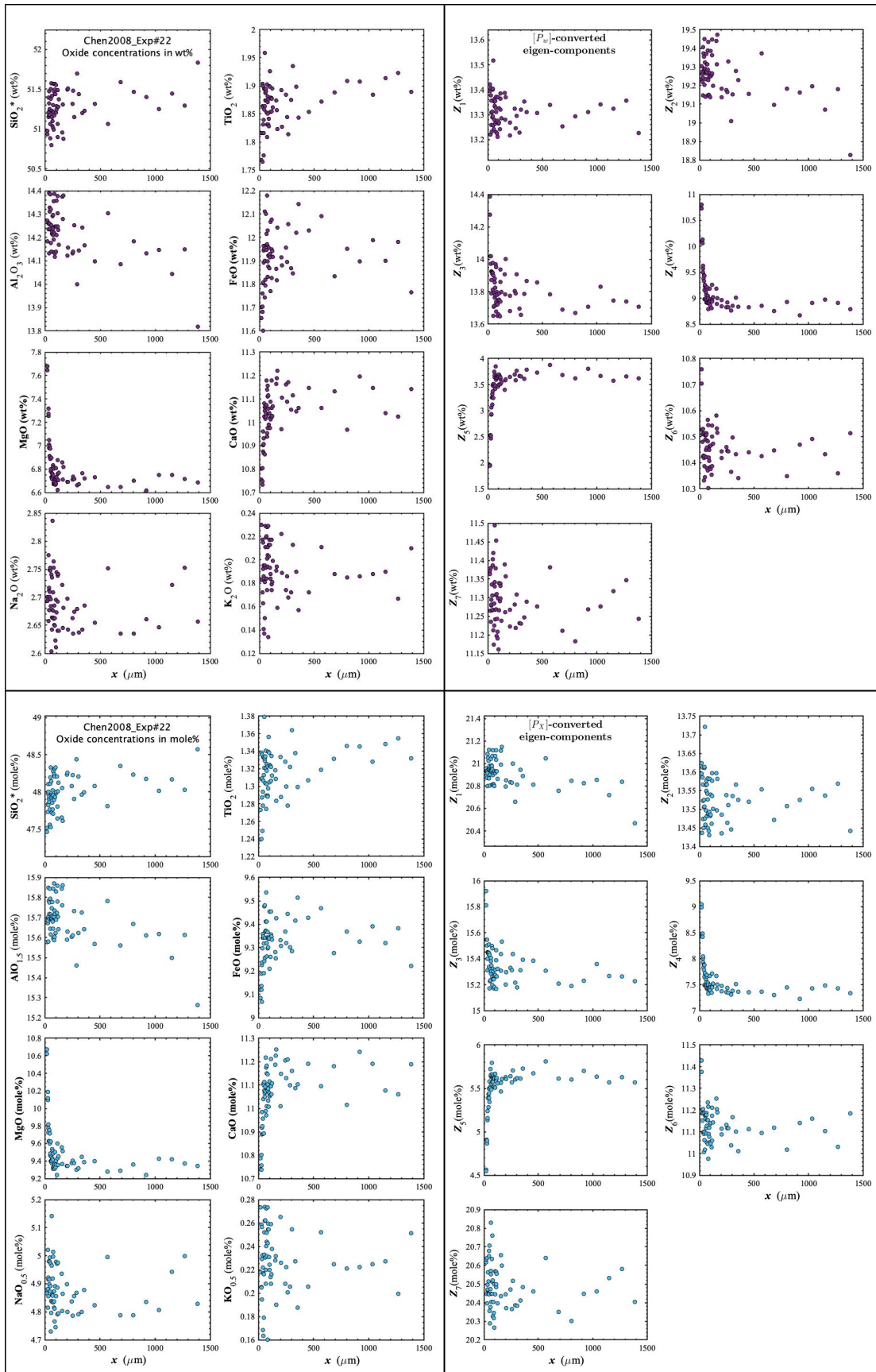
Figure D23. Concentration profiles of oxide components in wt% (upper left panel), oxide components in mole% (lower left panel), [P_w]-converted eigen-components (upper right panel), and [P_X]-converted eigen-components (lower right panel) of Zhang1989_Exp#255DI, which is a diopside dissolution experiment in andesite (Zhang et al., 1989).
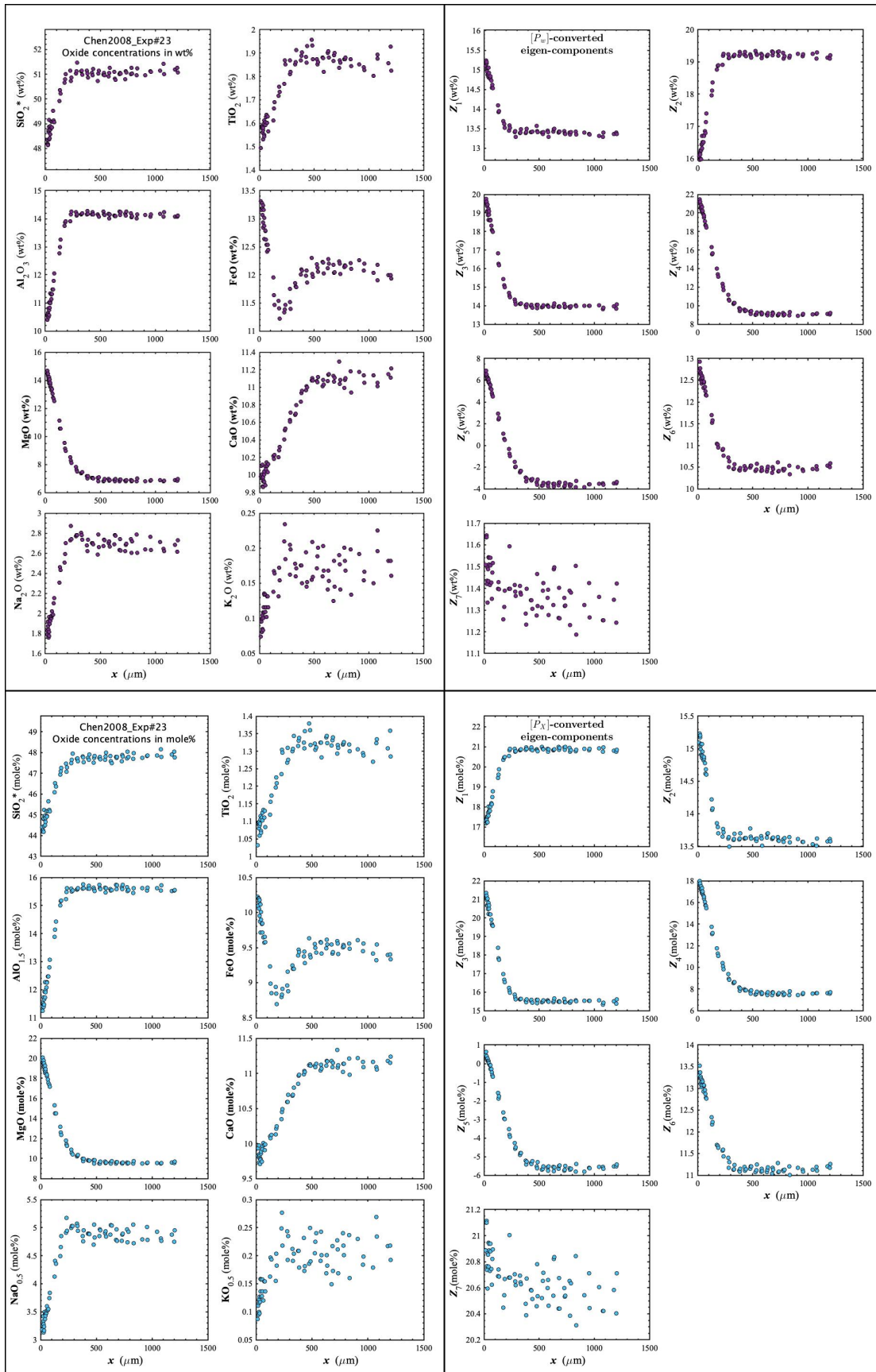
143

Figure D24. Concentration profiles of oxide components in wt% (upper left panel), oxide components in mole% (lower left panel), [P_w]-converted eigen-components (upper right panel), and [P_X]-converted eigen-components (lower right panel) of Zhang1989_Exp#255OL, which is an olivine dissolution experiment in andesite (Zhang et al., 1989).
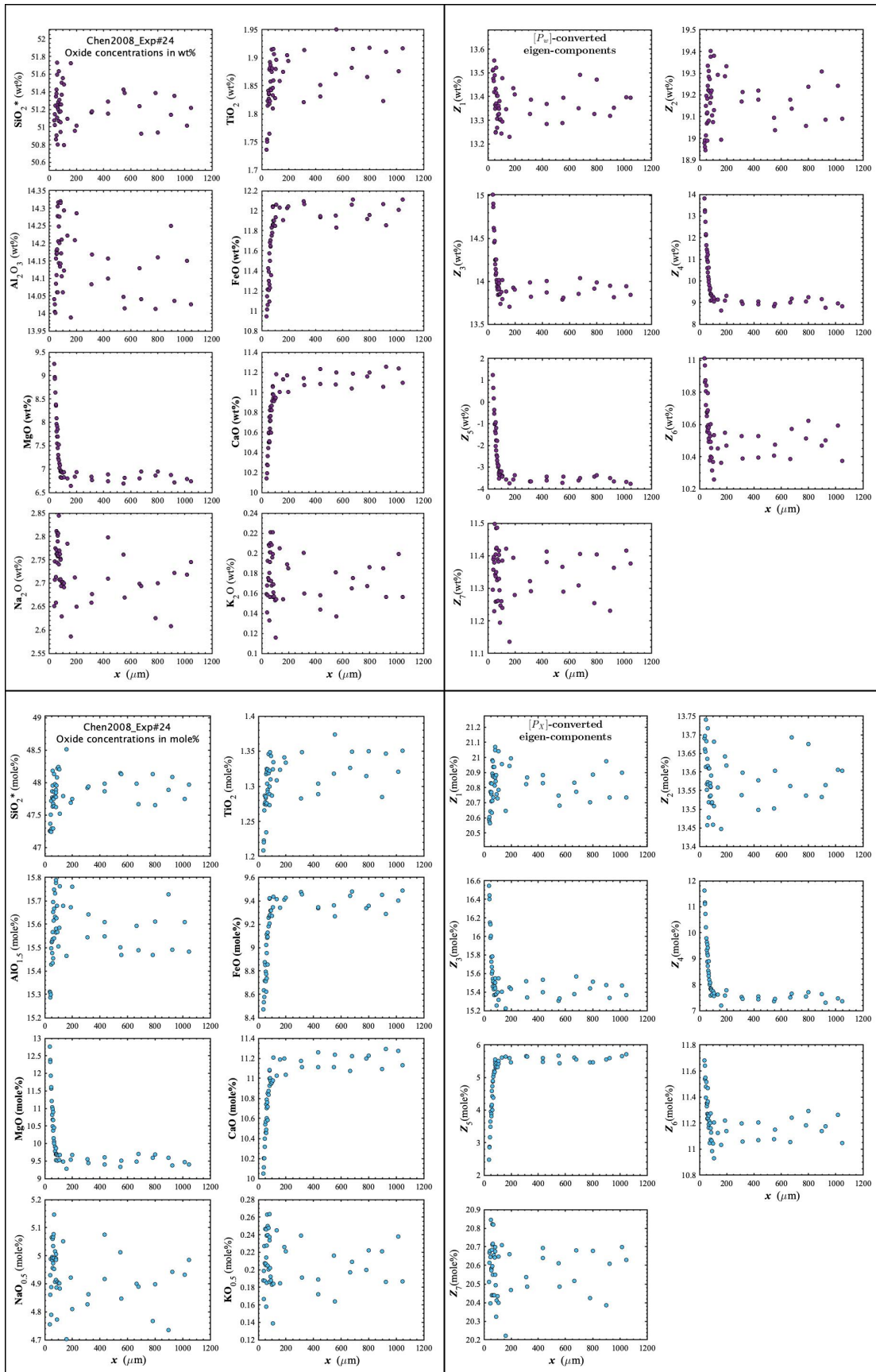
144

Figure D25. Concentration profiles of oxide components in wt% (upper left panel), oxide components in mole% (lower left panel), [P_w]-converted eigen-components (upper right panel), and [P_X]-converted eigen-components (lower right panel) of Zhang1989_Exp#256, which is an olivine dissolution experiment in andesite (Zhang et al., 1989).
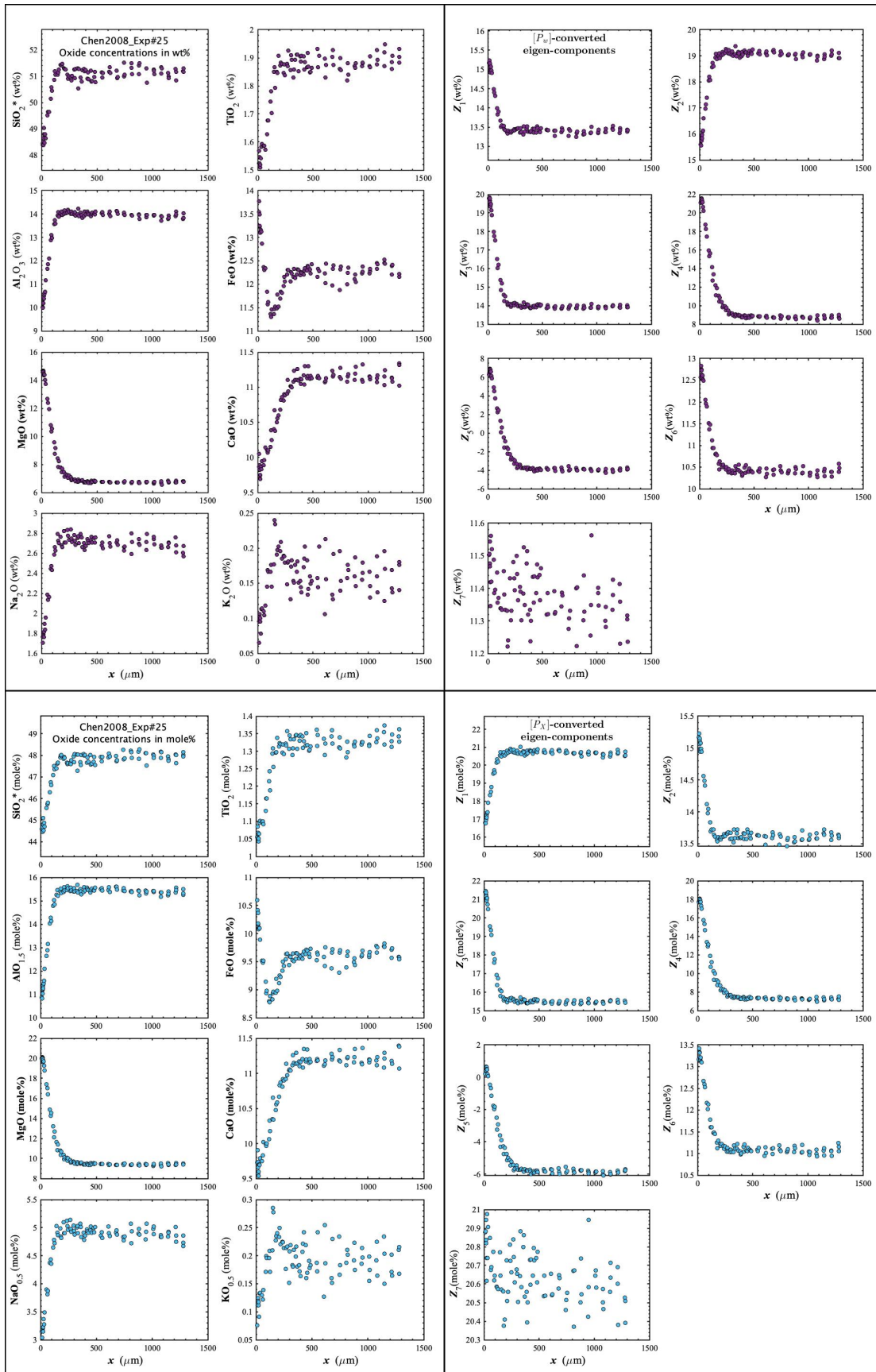
145

Figure D26. Concentration profiles of oxide components in wt% (upper left panel), oxide components in mole% (lower left panel), $[P_w]$-converted eigen-components (upper right panel), and $[P_X]$-converted eigen-components (lower right panel) of Zhang1989_Exp#259AUG, which is an augite dissolution experiment in andesite (Zhang et al., 1989).
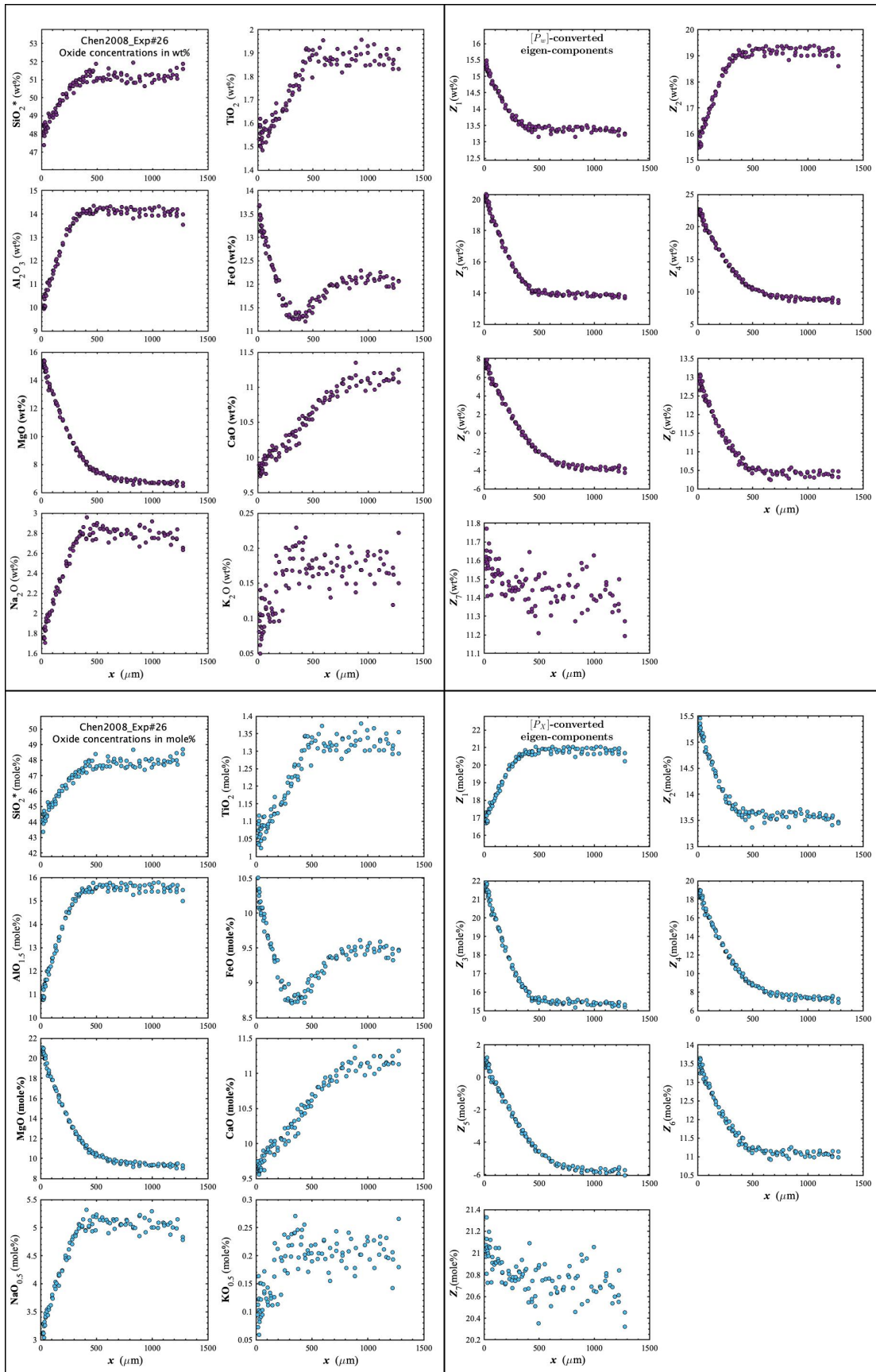
146

Figure D27. Concentration profiles of oxide components in wt% (upper left panel), oxide components in mole% (lower left panel), $[P_w]$-converted eigen-components (upper right panel), and $[P_X]$-converted eigen-components (lower right panel) of Zhang1989_Exp#259PL, which is a plagioclase dissolution experiment in andesite (Zhang et al., 1989).
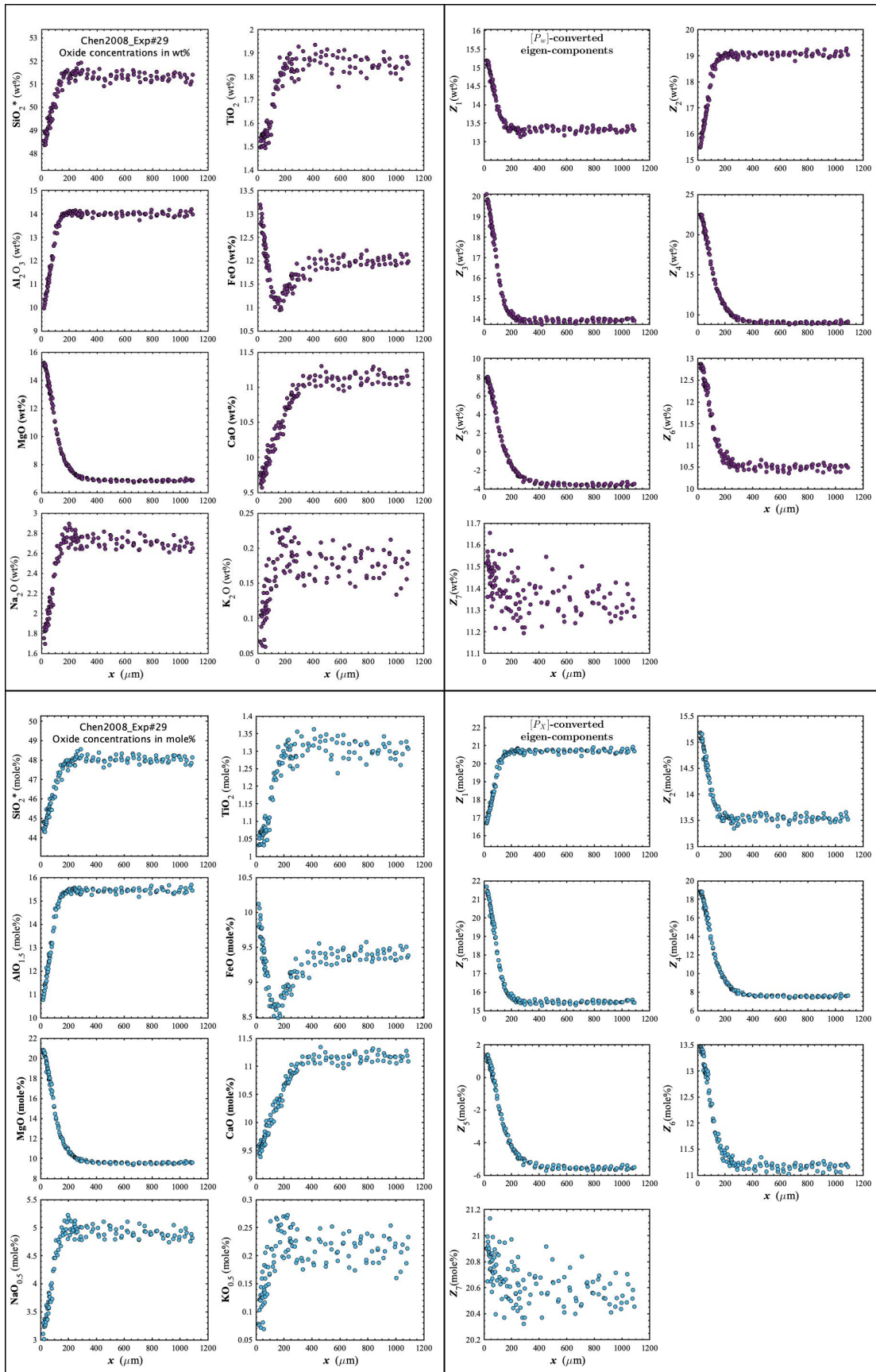
Figure D28. Concentration profiles of oxide components in wt% (upper left panel), oxide components in mole% (lower left panel), [P_w]-converted eigen-components (upper right panel), and [P_X]-converted eigen-components (lower right panel) of Zhang1989_Exp#260OL, which is an olivine dissolution experiment in andesite (Zhang et al., 1989).
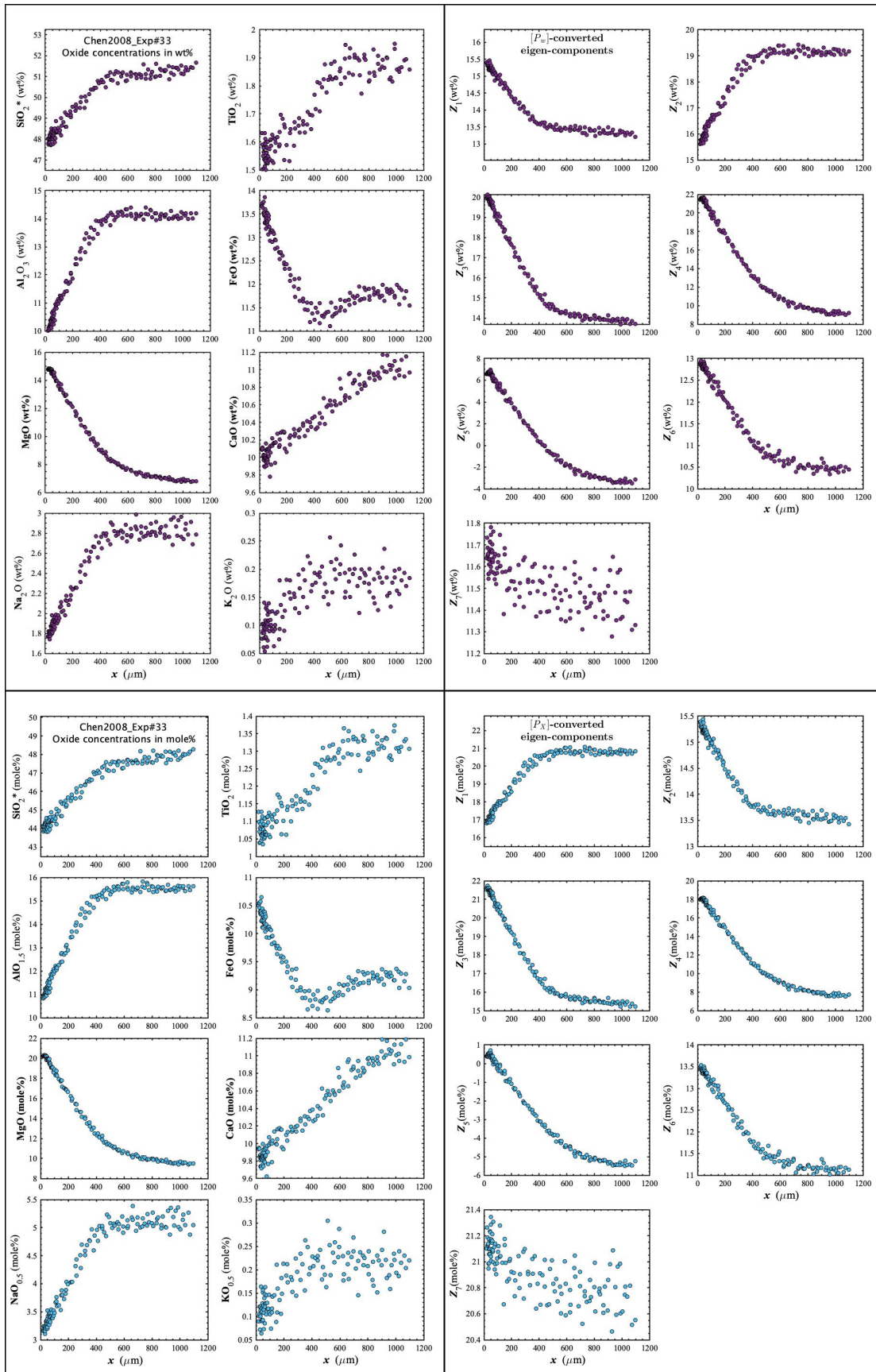
148

Figure D29. Concentration profiles of oxide components in wt% (upper left panel), oxide components in mole% (lower left panel), [P_w]-converted eigen-components (upper right panel), and [P_X]-converted eigen-components (lower right panel) of Zhang1989_Exp#260SP, which is a spinel dissolution experiment in andesite (Zhang et al., 1989).

Figure D30. Concentration profiles of oxide components in wt% (upper left panel), oxide components in mole% (lower left panel), [P_w]-converted eigen-components (upper right panel), and [P_X]-converted eigen-components (lower right panel) of Zhang1989_Exp#262ENS, which is an enstatite dissolution experiment in andesite (Zhang et al., 1989).
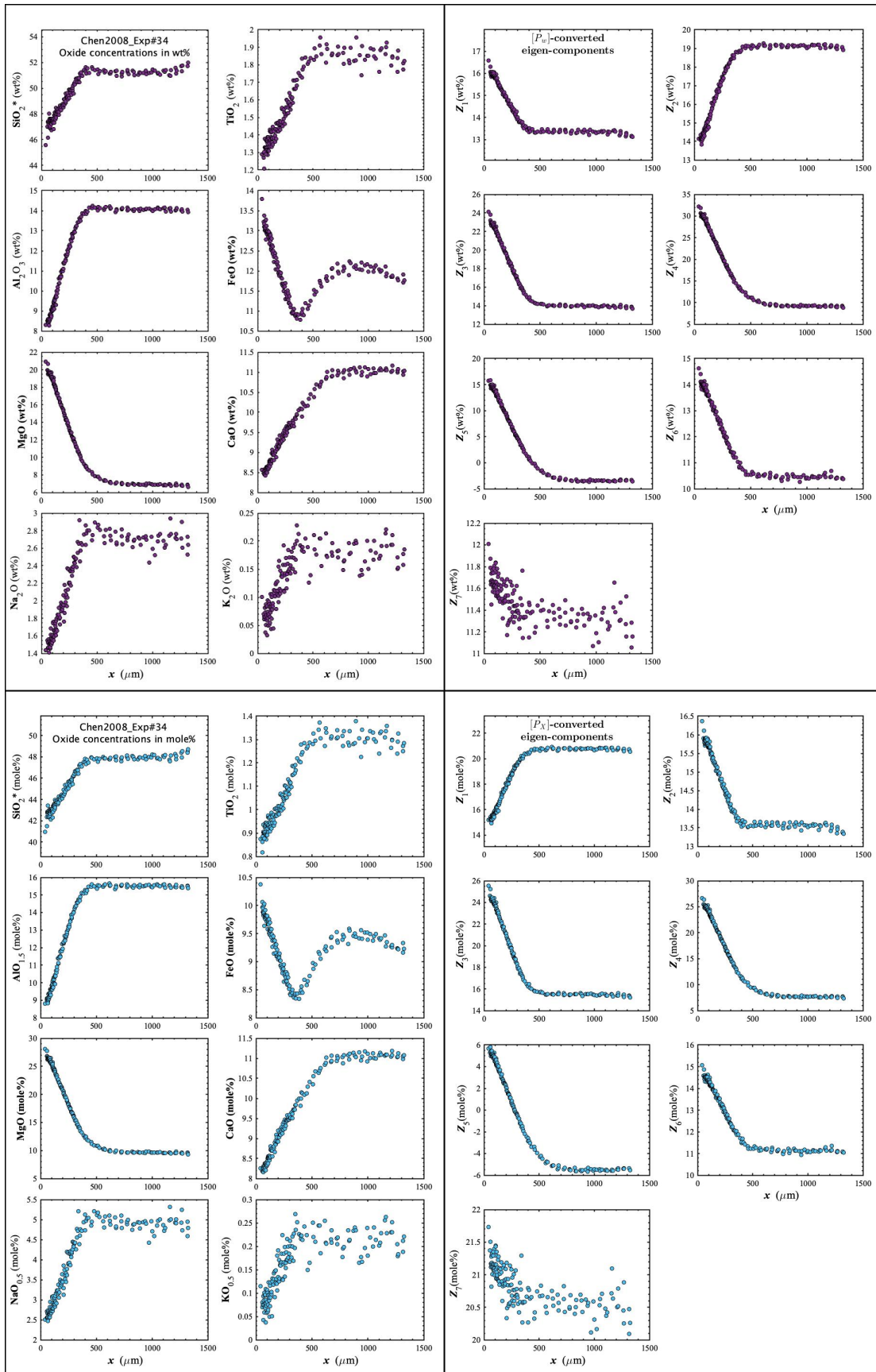
150

Figure D31. Concentration profiles of oxide components in wt% (upper left panel), oxide components in mole% (lower left panel), $[P_w]$-converted eigen-components (upper right panel), and $[P_X]$-converted eigen-components (lower right panel) of Zhang1989_Exp#262OL, which is an olivine dissolution experiment in andesite (Zhang et al., 1989).
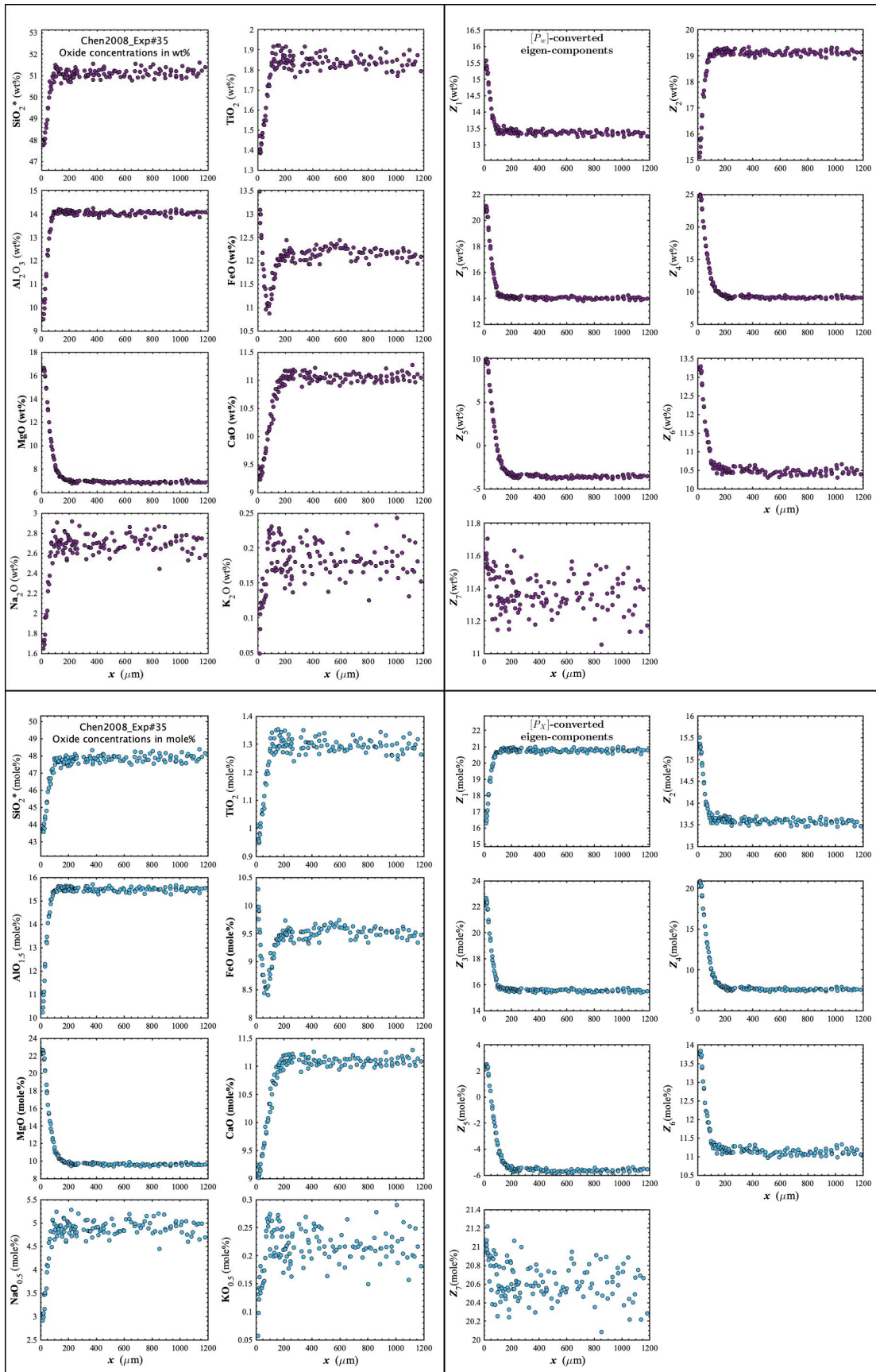
151

Figure D32. Concentration profiles of oxide components in wt% (upper left panel), oxide components in mole% (lower left panel), $[P_w]$-converted eigen-components (upper right panel), and $[P_X]$-converted eigen-components (lower right panel) of Zhang1989_Exp#263OL, which is an olivine dissolution experiment in andesite (Zhang et al., 1989).
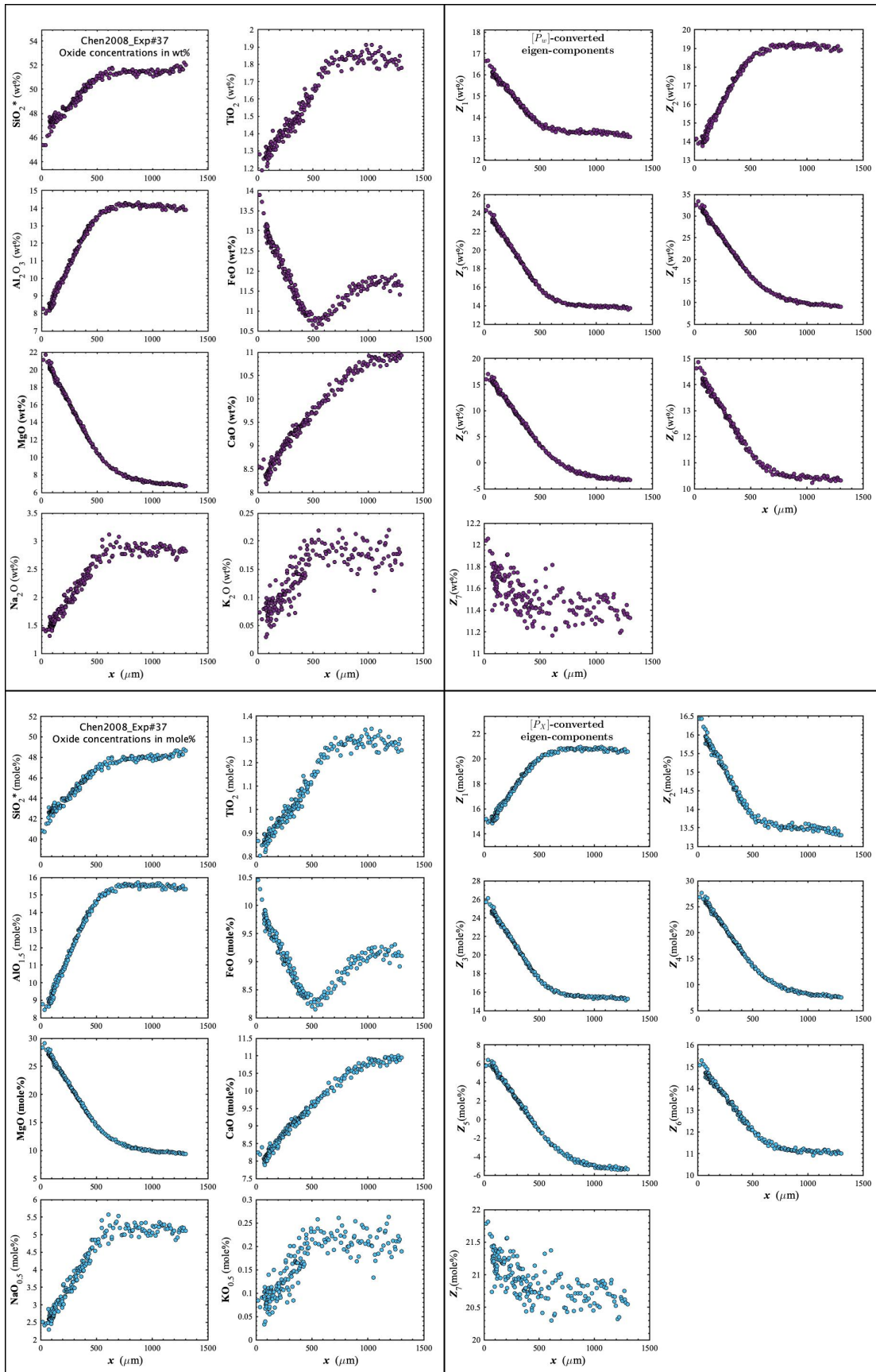
152

Figure D33. Concentration profiles of oxide components in wt% (upper left panel), oxide components in mole% (lower left panel), [P_w]-converted eigen-components (upper right panel), and [P_X]-converted eigen-components (lower right panel) of Zhang1989_Exp#263SP, which is a spinel dissolution experiment in andesite (Zhang et al., 1989).
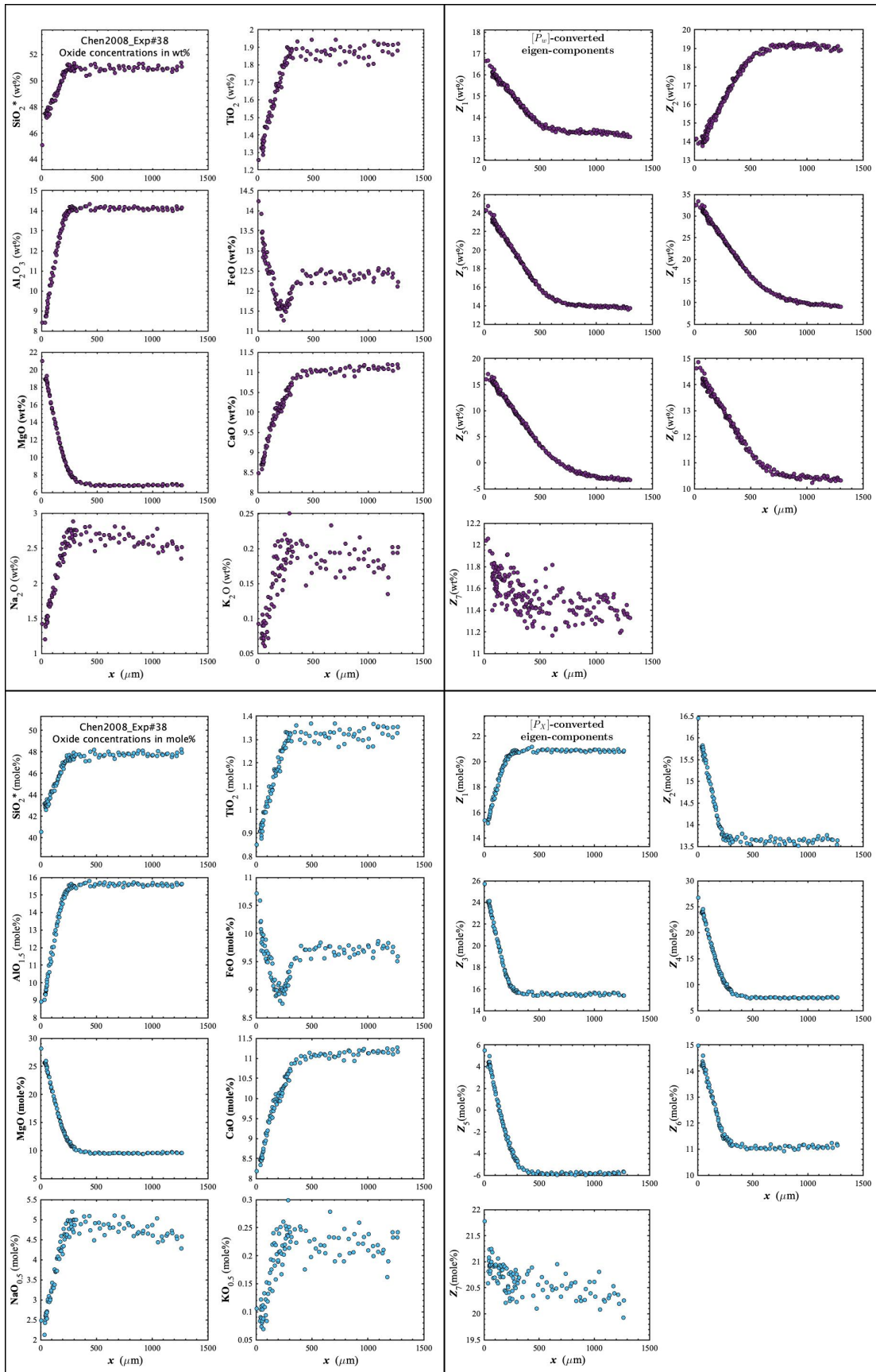
Figure D34. Concentration profiles of oxide components in wt% (upper left panel), oxide components in mole% (lower left panel), [P_w]-converted eigen-components (upper right panel), and [P_X]-converted eigen-components (lower right panel) of Zhang1989_Exp#265, which is an olivine dissolution experiment in andesite (Zhang et al., 1989).

154

Figure D35. Concentration profiles of oxide components in wt% (upper left panel), oxide components in mole% (lower left panel), [P_w]-converted eigen-components (upper right panel), and [P_X]-converted eigen-components (lower right panel) of Chen2008_Exp#15, which is an olivine dissolution experiment in basalt (Chen and Zhang, 2008).
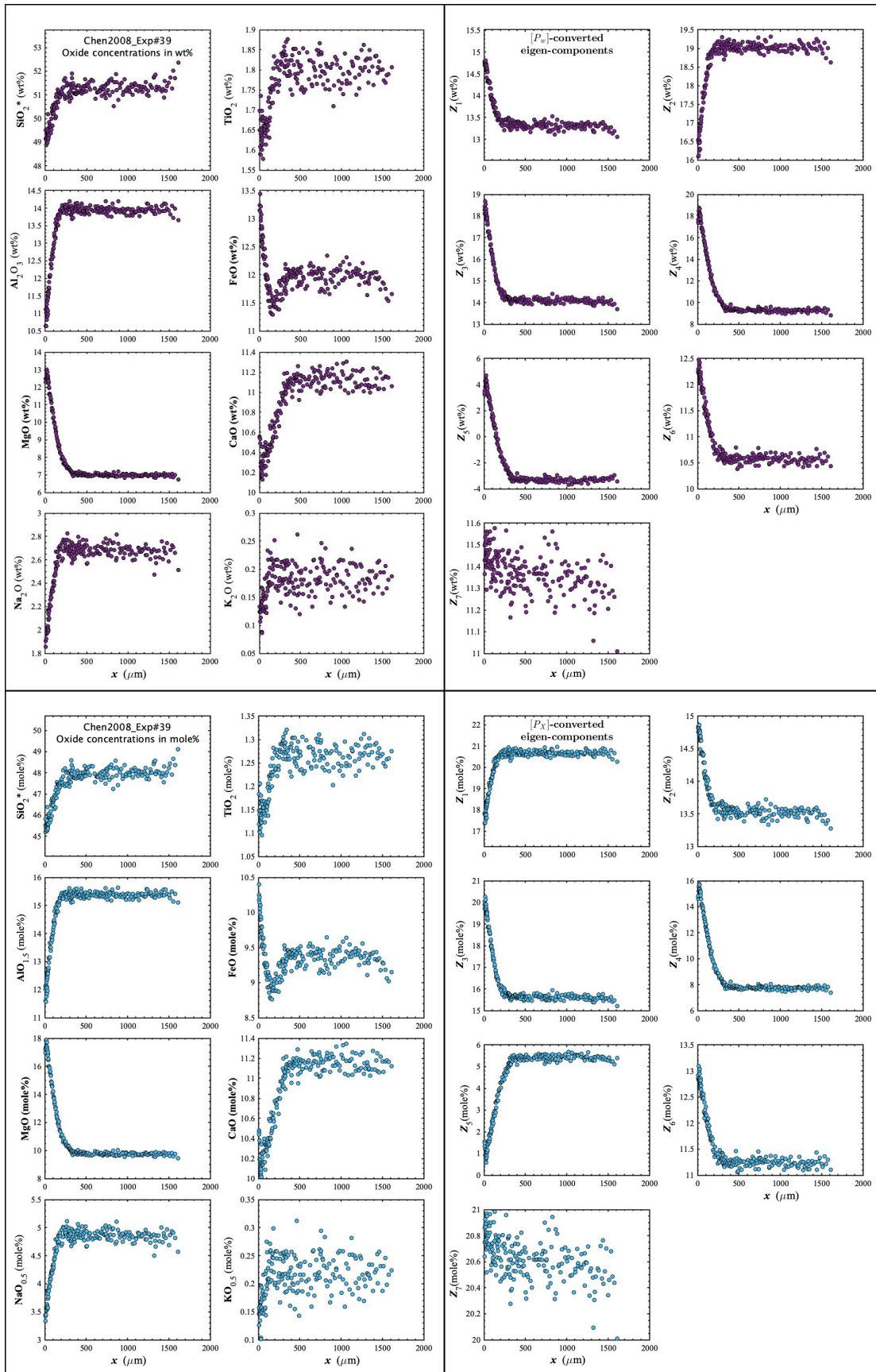
155

Figure D36. Concentration profiles of oxide components in wt% (upper left panel), oxide components in mole% (lower left panel), $[P_w]$-converted eigen-components (upper right panel), and $[P_X]$-converted eigen-components (lower right panel) of Chen2008_Exp#16, which is an olivine dissolution experiment in basalt (Chen and Zhang, 2008).
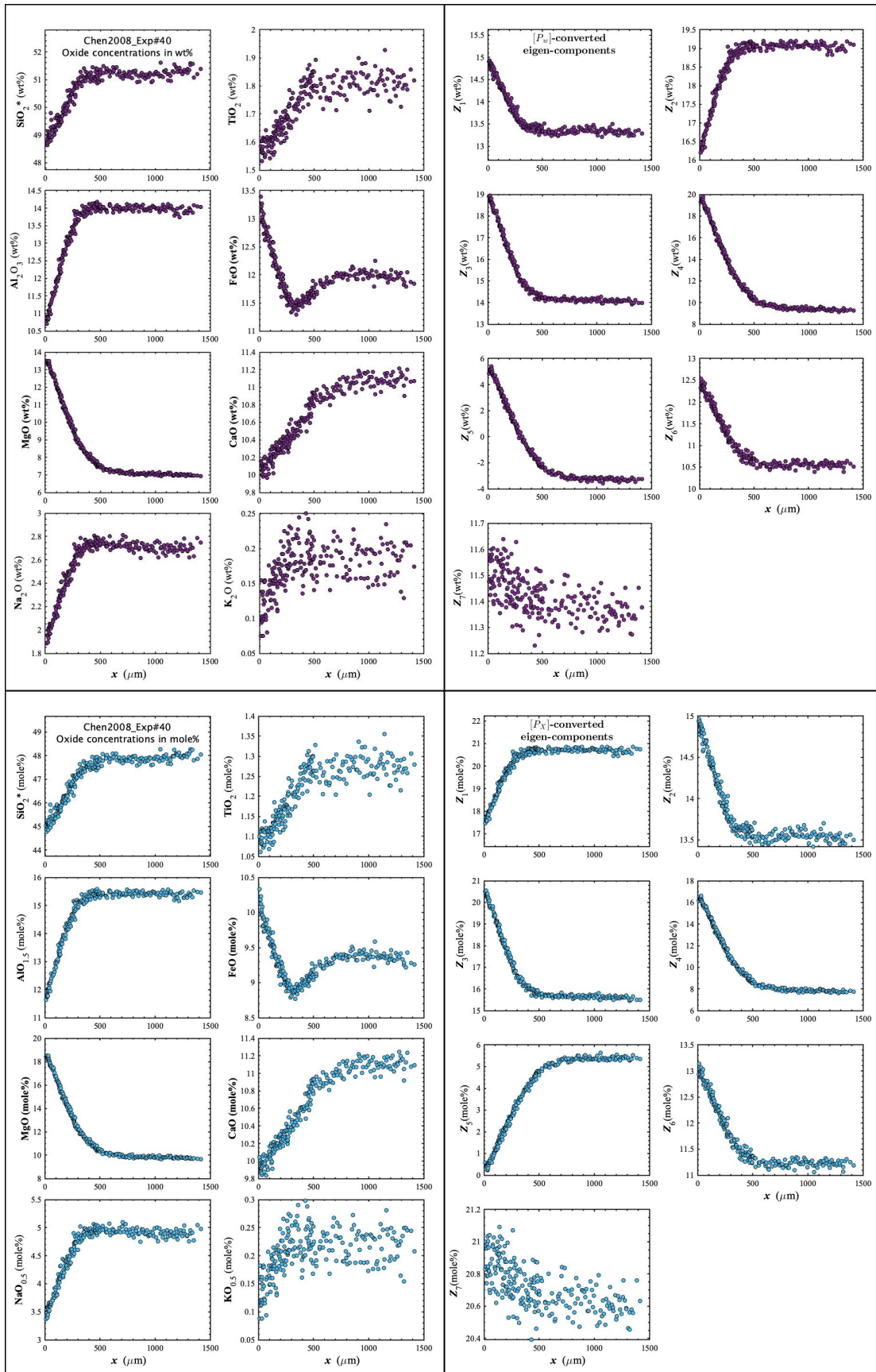
156

Figure D37. Concentration profiles of oxide components in wt% (upper left panel), oxide components in mole% (lower left panel), [P_w]-converted eigen-components (upper right panel), and [P_X]-converted eigen-components (lower right panel) of Chen2008_Exp#18, which is an olivine dissolution experiment in basalt (Chen and Zhang, 2008).
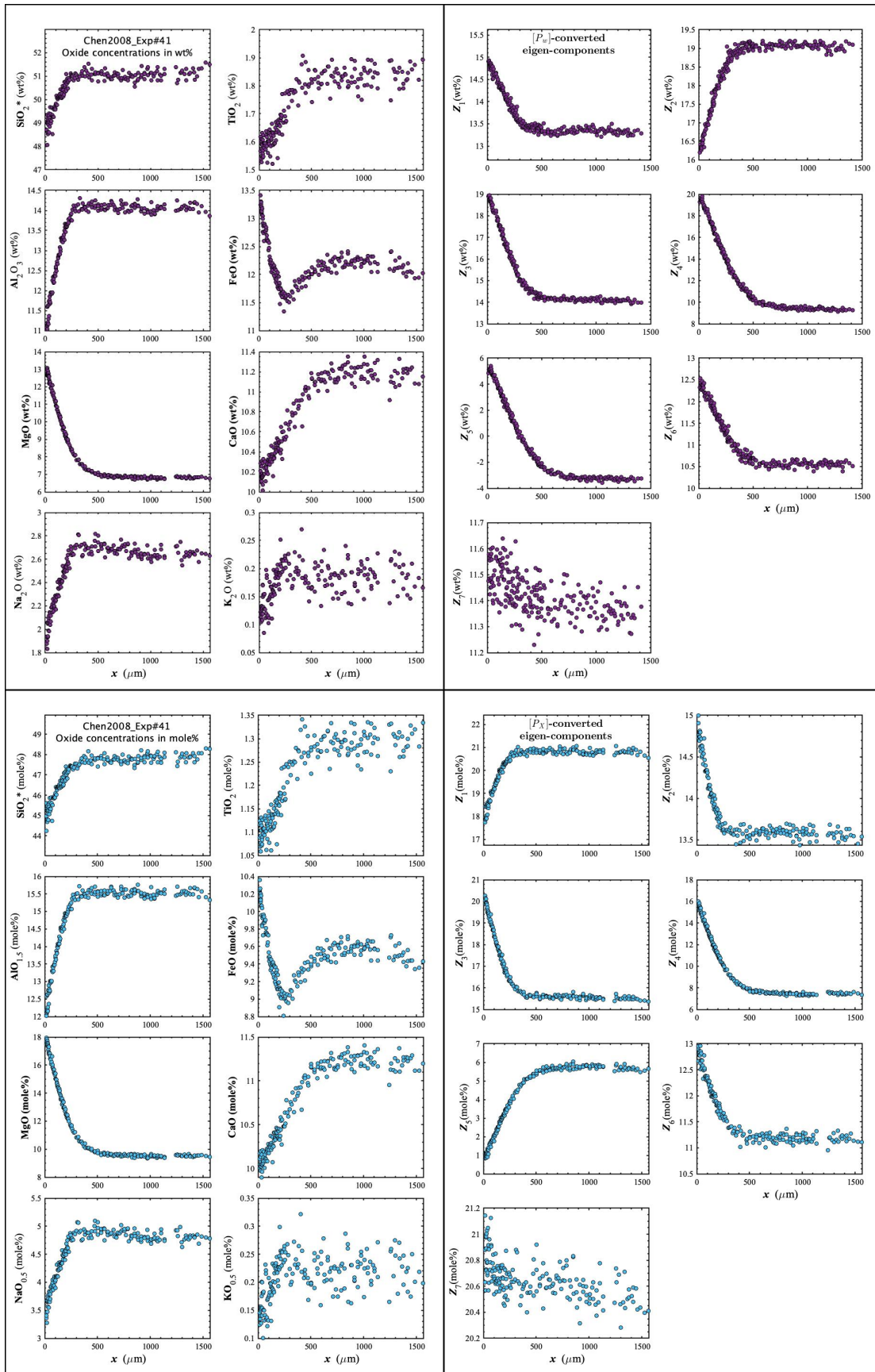
157

Figure D38. Concentration profiles of oxide components in wt% (upper left panel), oxide components in mole% (lower left panel), [P_w]-converted eigen-components (upper right panel), and [P_X]-converted eigen-components (lower right panel) of Chen2008_Exp#20, which is an olivine dissolution experiment in basalt (Chen and Zhang, 2008).
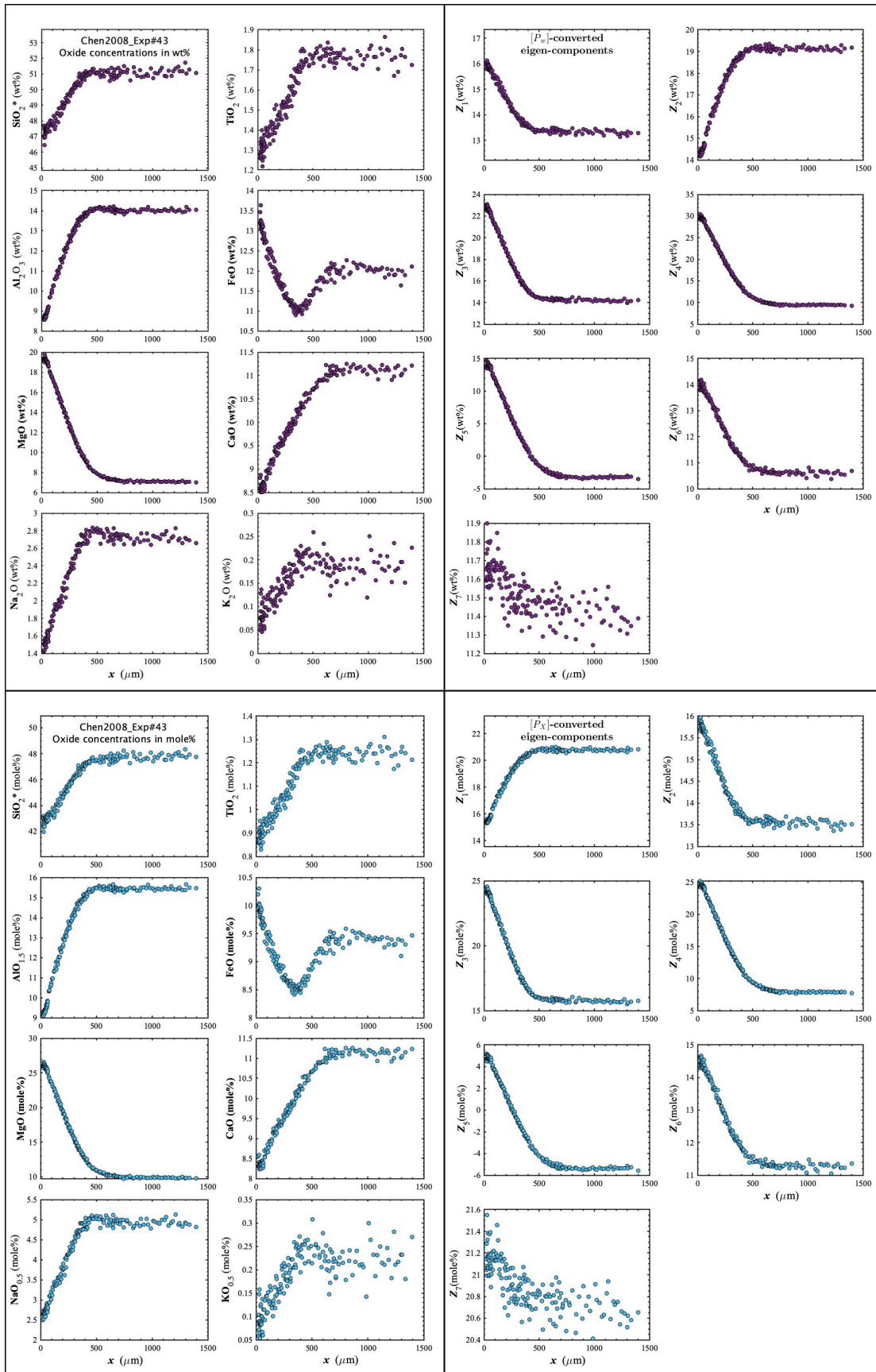
158

Figure D39. Concentration profiles of oxide components in wt% (upper left panel), oxide components in mole% (lower left panel), [P_w]-converted eigen-components (upper right panel), and [P_X]-converted eigen-components (lower right panel) of Chen2008_Exp#21, which is an olivine dissolution experiment in basalt (Chen and Zhang, 2008).
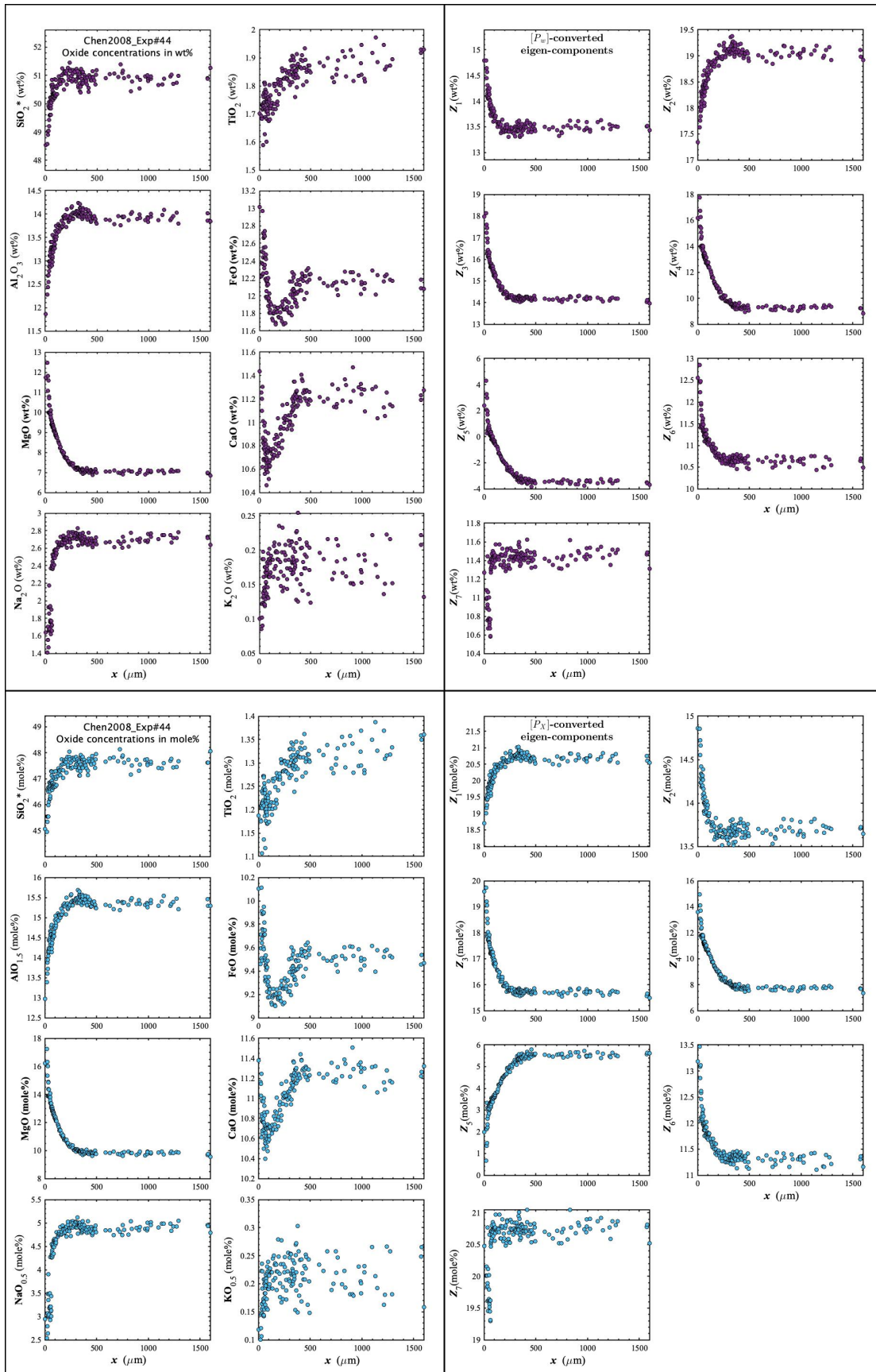
159

Figure D40. Concentration profiles of oxide components in wt% (upper left panel), oxide components in mole% (lower left panel), $[P_w]$-converted eigen-components (upper right panel), and $[P_X]$-converted eigen-components (lower right panel) of Chen2008_Exp#22, which is an olivine dissolution experiment in basalt (Chen and Zhang, 2008).
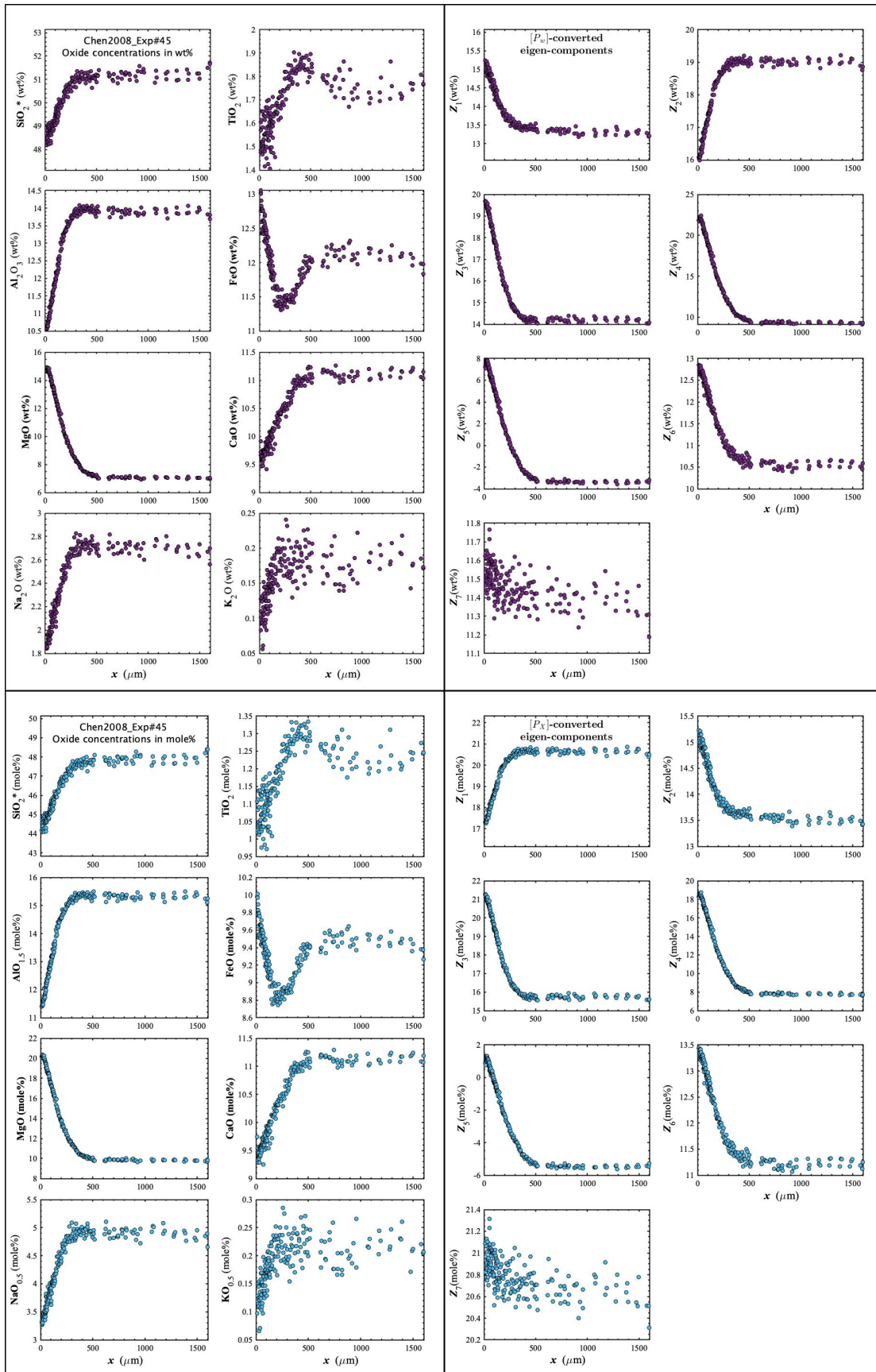
160

Figure D41. Concentration profiles of oxide components in wt% (upper left panel), oxide components in mole% (lower left panel), [*P_w*]-converted eigen-components (upper right panel), and [*P_X*]-converted eigen-components (lower right panel) of Chen2008_Exp#23, which is an olivine dissolution experiment in basalt (Chen and Zhang, 2008).
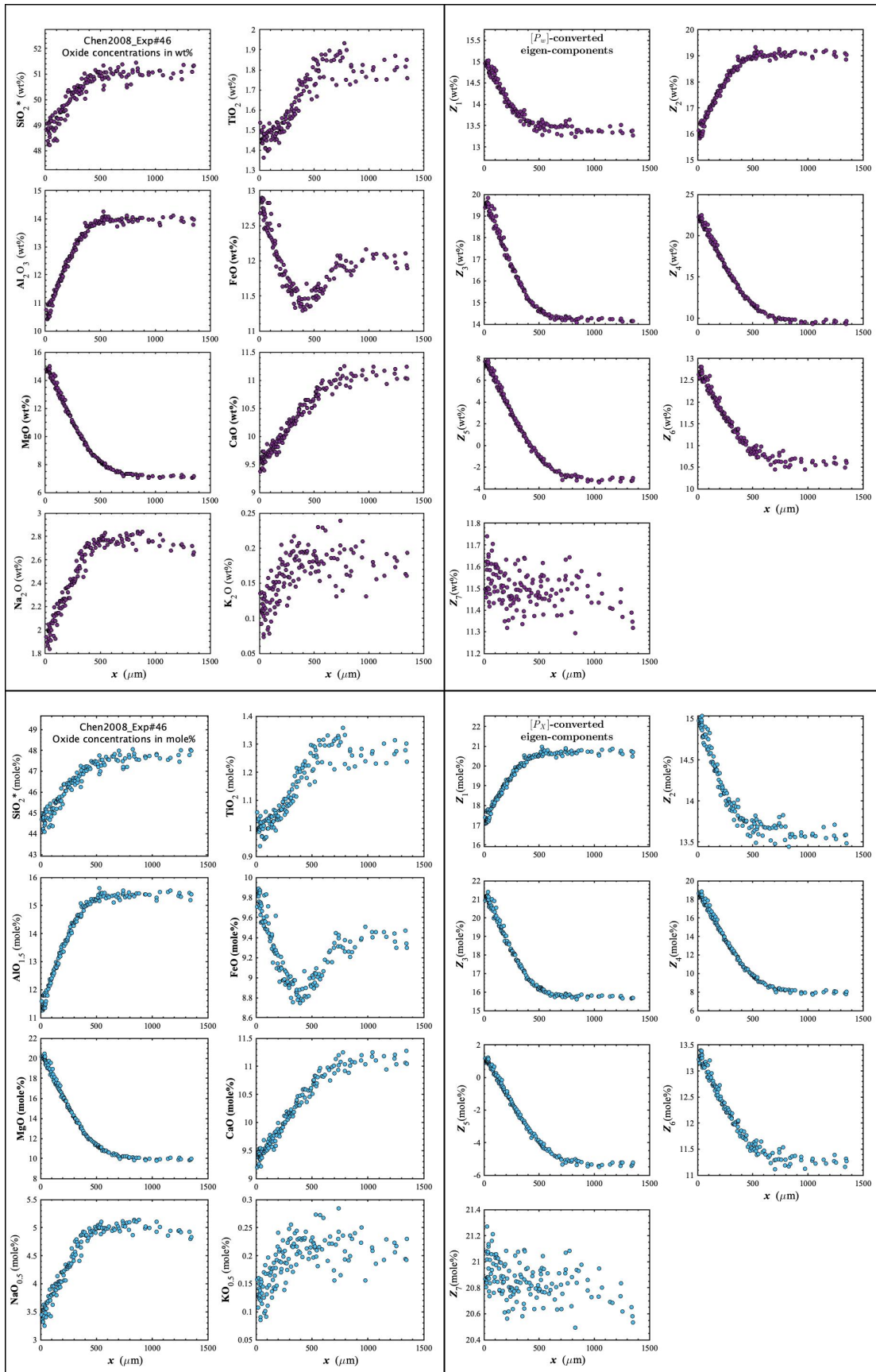
161

Figure D42. Concentration profiles of oxide components in wt% (upper left panel), oxide components in mole% (lower left panel), [P_w]-converted eigen-components (upper right panel), and [P_X]-converted eigen-components (lower right panel) of Chen2008_Exp#24, which is an olivine dissolution experiment in basalt (Chen and Zhang, 2008).
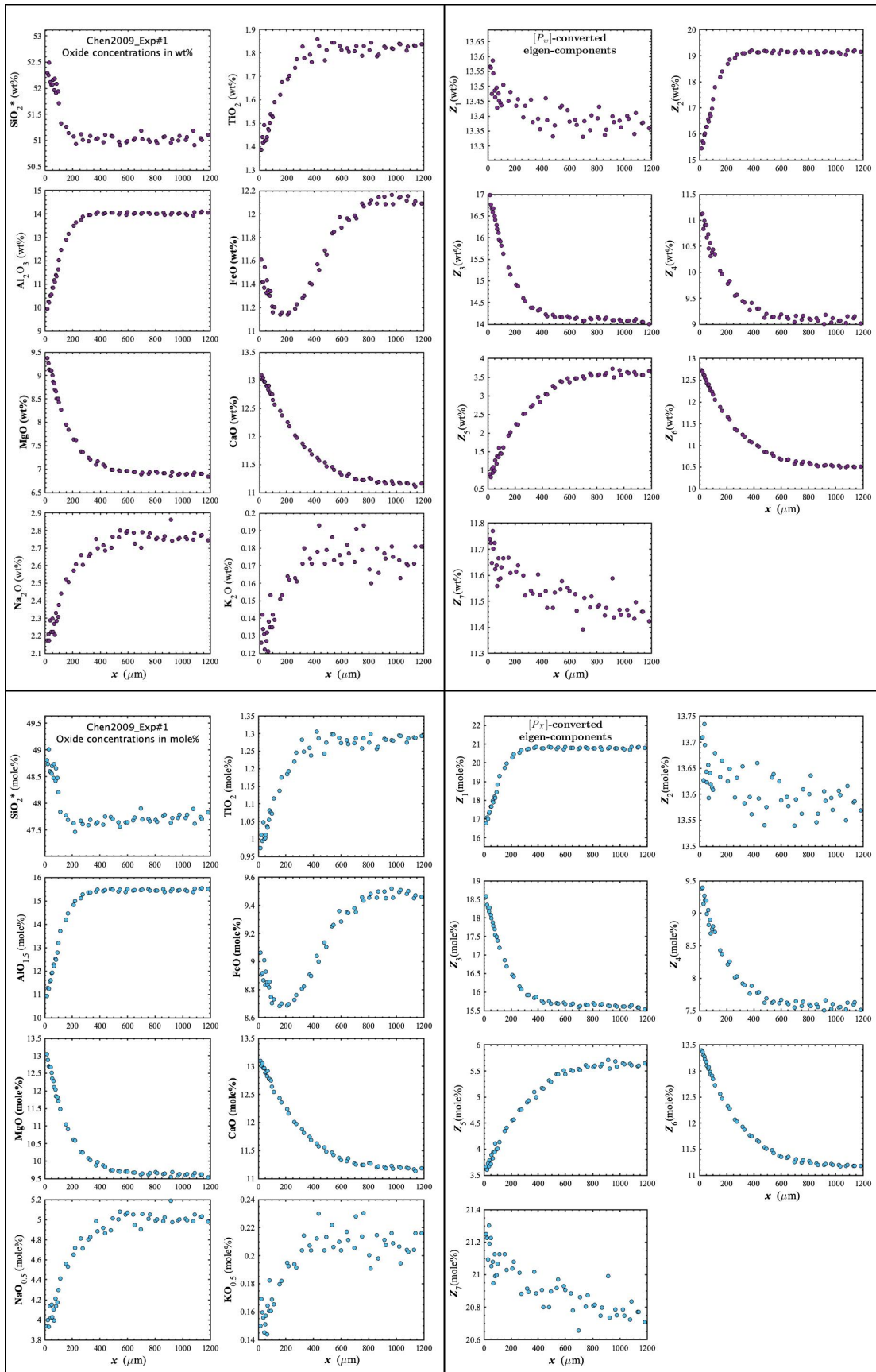
Figure D43. Concentration profiles of oxide components in wt% (upper left panel), oxide components in mole% (lower left panel), [P_w]-converted eigen-components (upper right panel), and [P_X]-converted eigen-components (lower right panel) of Chen2008_Exp#25, which is an olivine dissolution experiment in basalt (Chen and Zhang, 2008).
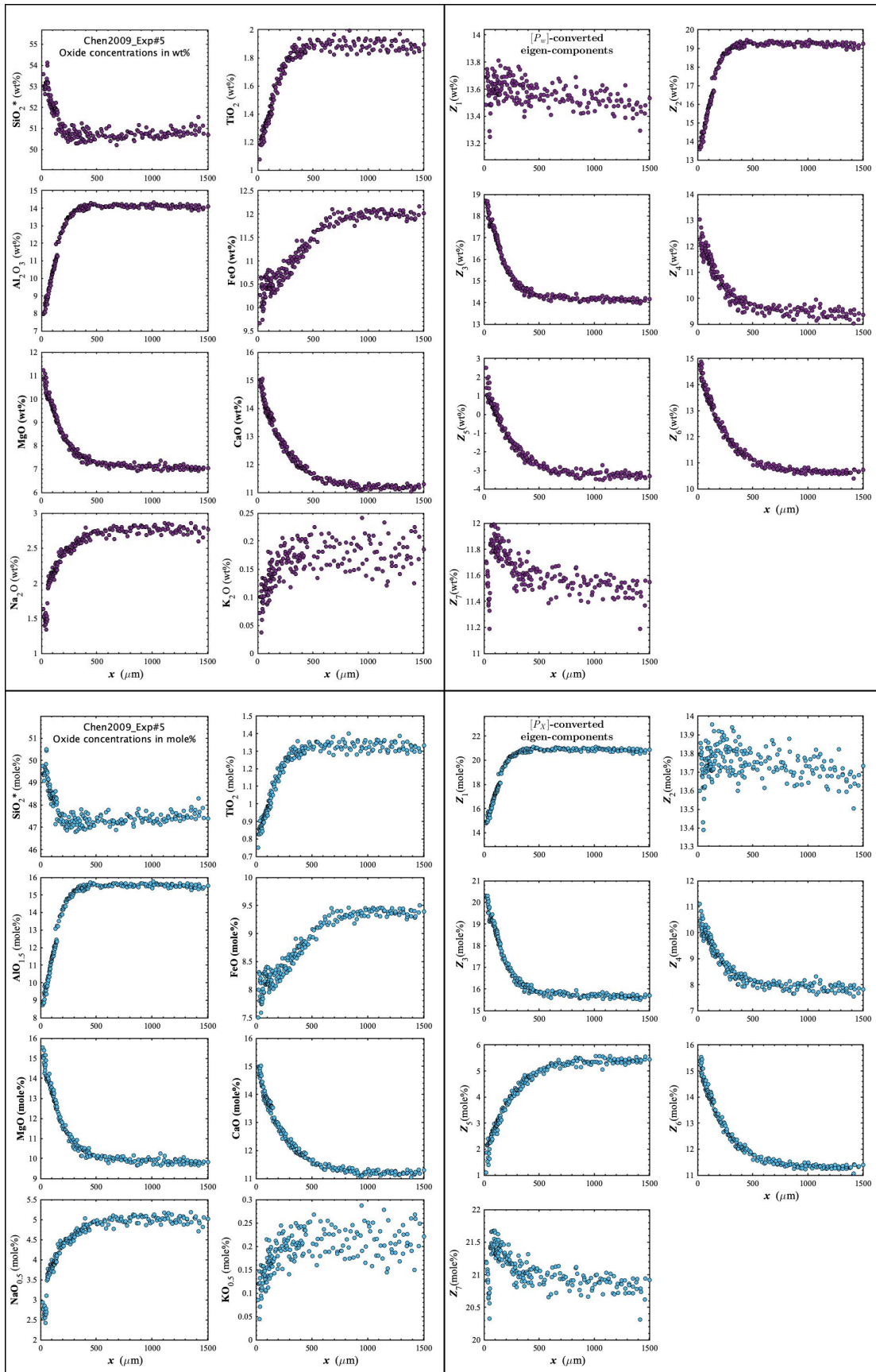
163

Figure D44. Concentration profiles of oxide components in wt% (upper left panel), oxide components in mole% (lower left panel), [P_w]-converted eigen-components (upper right panel), and [P_X]-converted eigen-components (lower right panel) of Chen2008_Exp#26, which is an olivine dissolution experiment in basalt (Chen and Zhang, 2008).
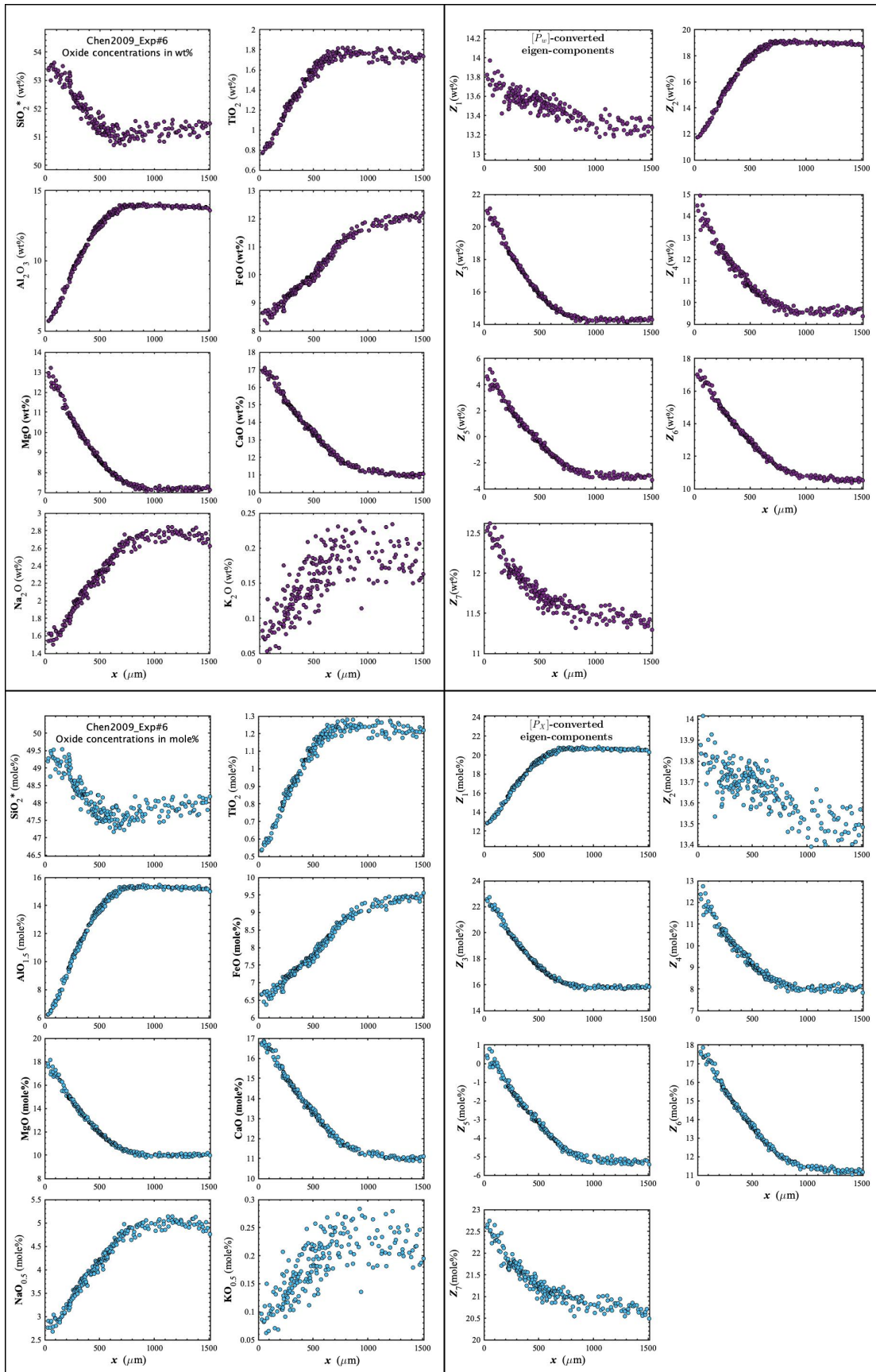
164

Figure D45. Concentration profiles of oxide components in wt% (upper left panel), oxide components in mole% (lower left panel), $[P_w]$-converted eigen-components (upper right panel), and $[P_X]$-converted eigen-components (lower right panel) of Chen2008_Exp#29, which is an olivine dissolution experiment in basalt (Chen and Zhang, 2008).
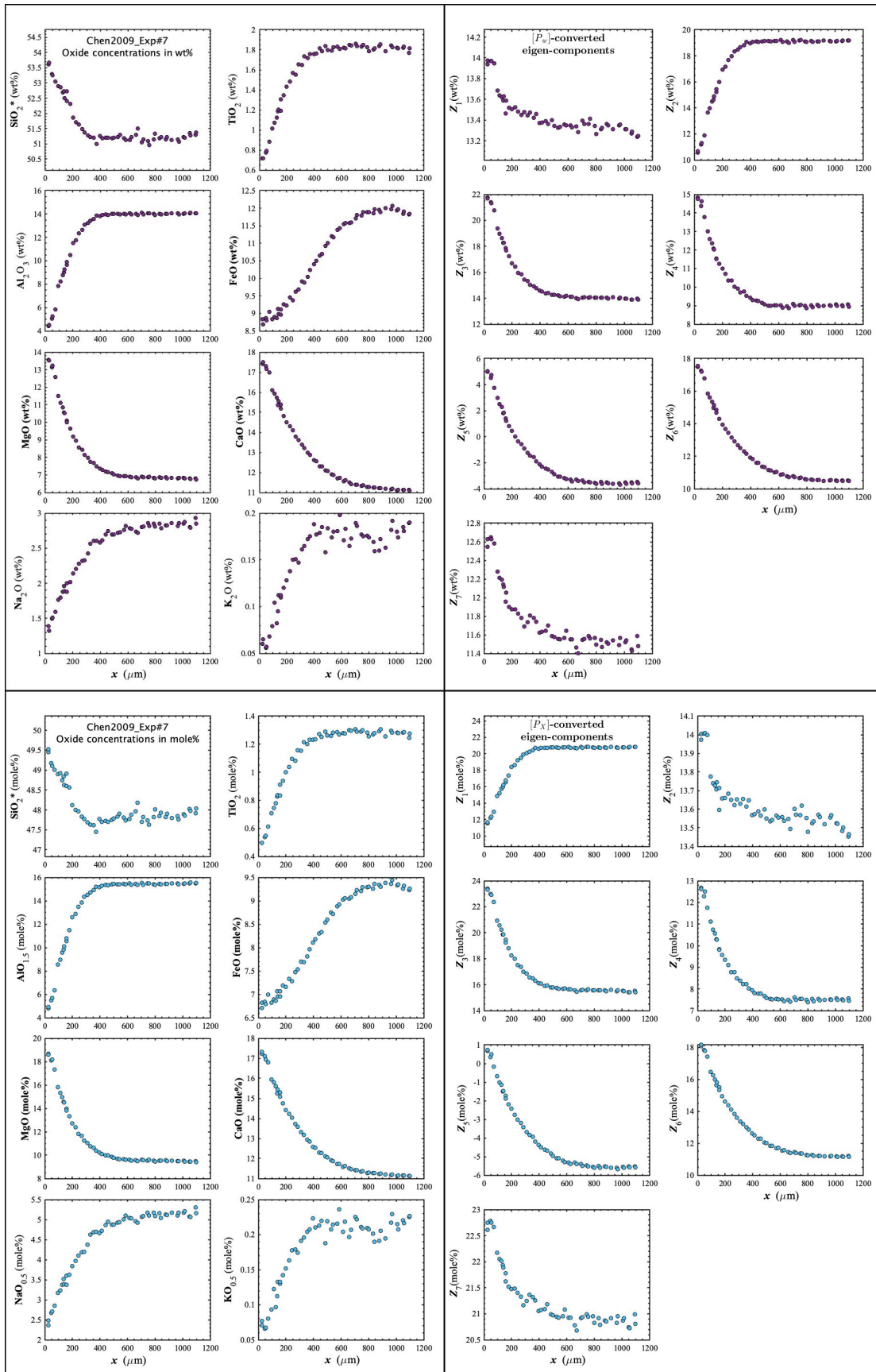
Figure D46. Concentration profiles of oxide components in wt% (upper left panel), oxide components in mole% (lower left panel), [P_w]-converted eigen-components (upper right panel), and [P_X]-converted eigen-components (lower right panel) of Chen2008_Exp#33, which is an olivine dissolution experiment in basalt (Chen and Zhang, 2008).

Figure D47. Concentration profiles of oxide components in wt% (upper left panel), oxide components in mole% (lower left panel), $[P_w]$-converted eigen-components (upper right panel), and $[P_X]$-converted eigen-components (lower right panel) of Chen2008_Exp#34, which is an olivine dissolution experiment in basalt (Chen and Zhang, 2008).
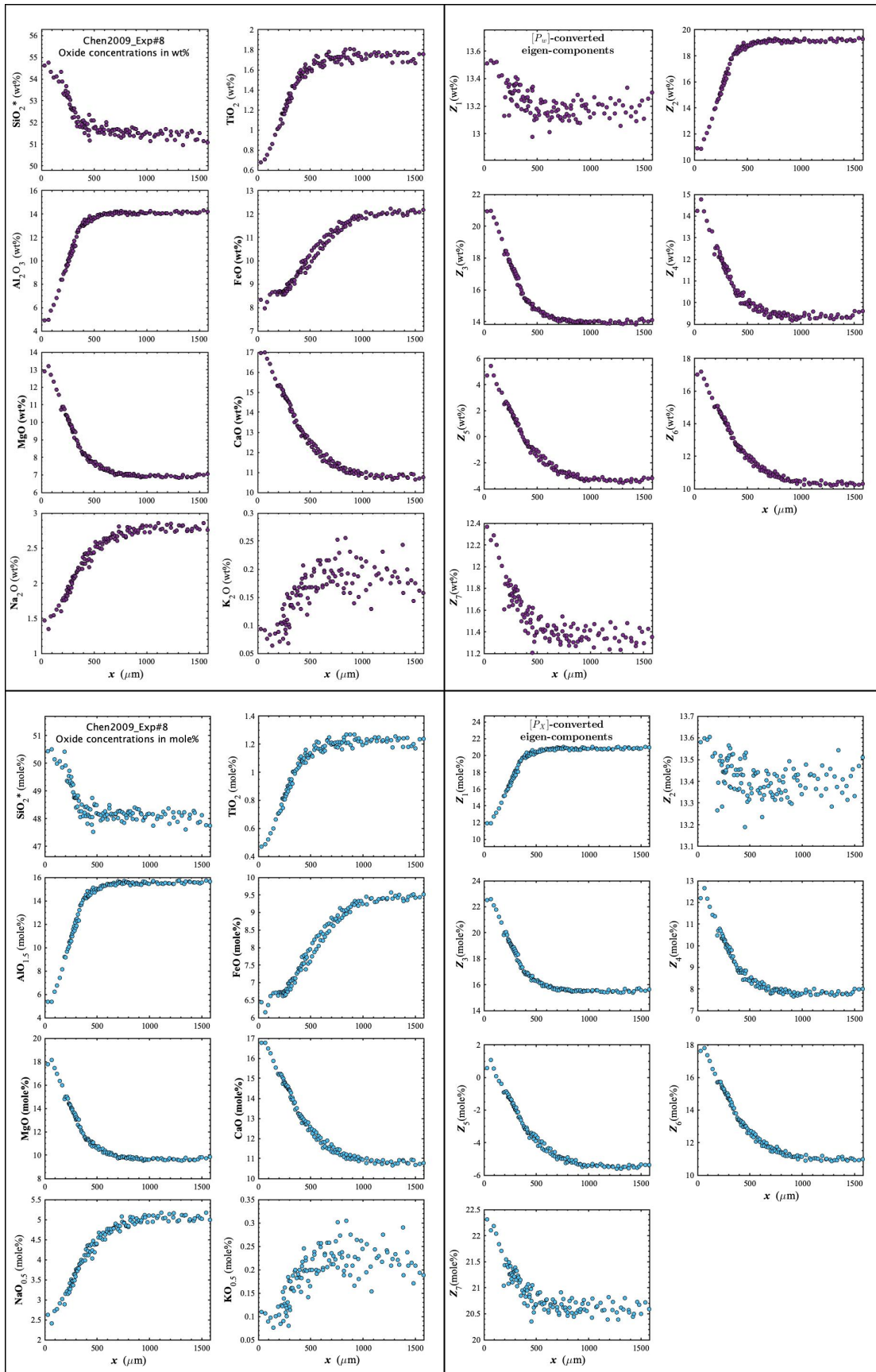
167

Figure D48. Concentration profiles of oxide components in wt% (upper left panel), oxide components in mole% (lower left panel), $[P_w]$-converted eigen-components (upper right panel), and $[P_X]$-converted eigen-components (lower right panel) of Chen2008_Exp#35, which is an olivine dissolution experiment in basalt (Chen and Zhang, 2008).
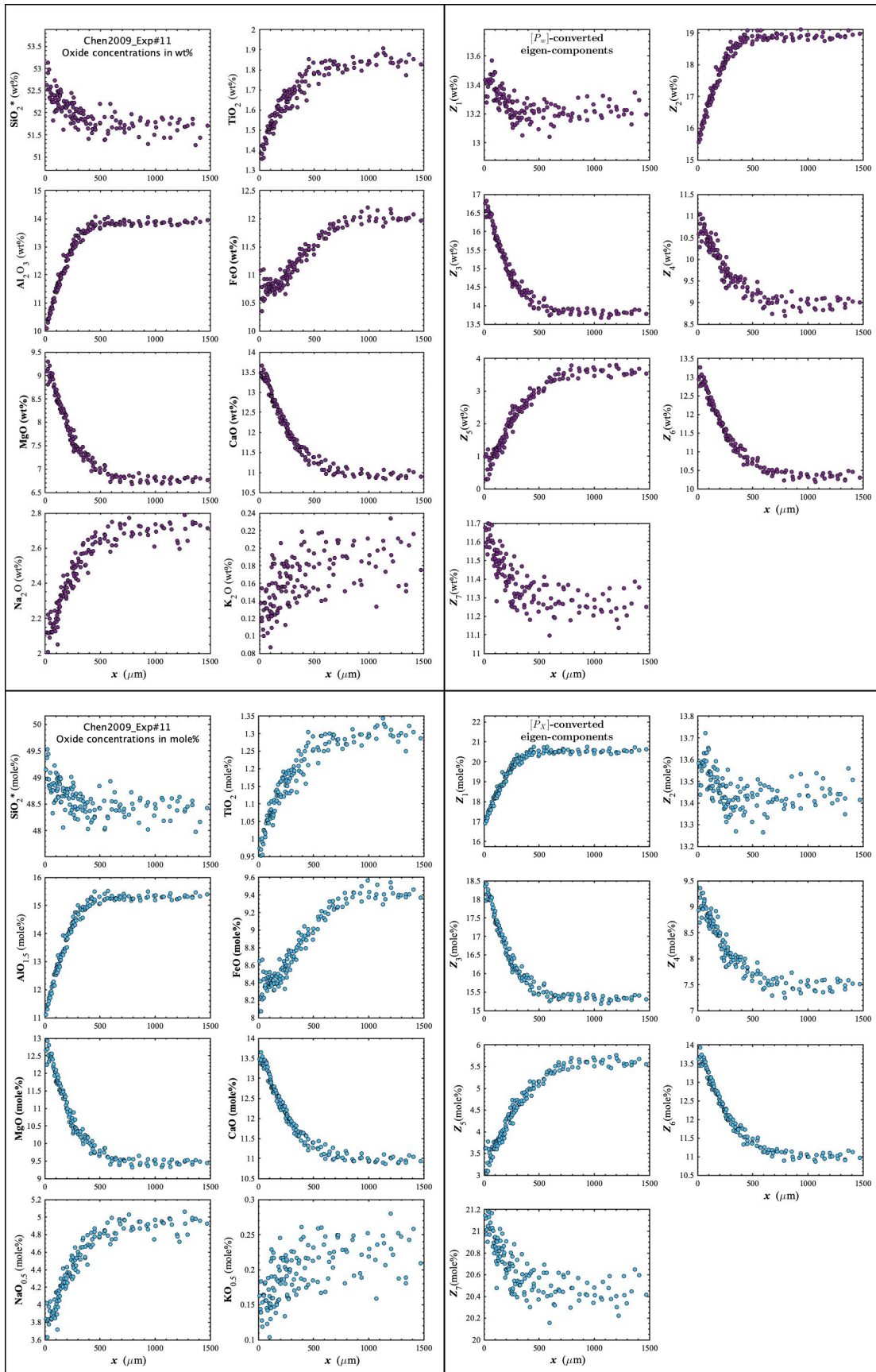
Figure D49. Concentration profiles of oxide components in wt% (upper left panel), oxide components in mole% (lower left panel), $[P_w]$-converted eigen-components (upper right panel), and $[P_X]$-converted eigen-components (lower right panel) of Chen2008_Exp#37, which is an olivine dissolution experiment in basalt (Chen and Zhang, 2008).
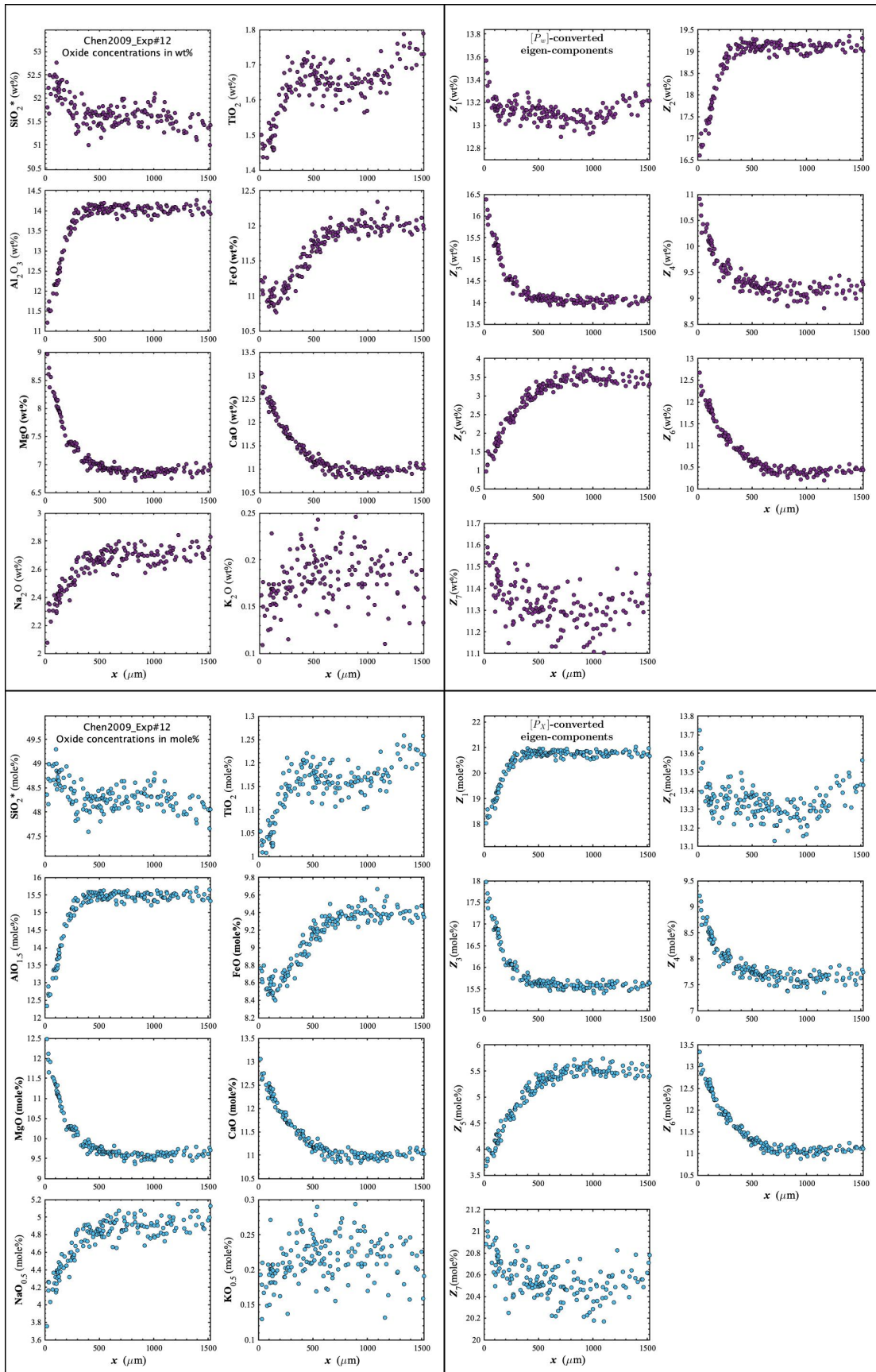
169

Figure D50. Concentration profiles of oxide components in wt% (upper left panel), oxide components in mole% (lower left panel), $[P_w]$-converted eigen-components (upper right panel), and $[P_X]$-converted eigen-components (lower right panel) of Chen2008_Exp#38, which is an olivine dissolution experiment in basalt (Chen and Zhang, 2008).
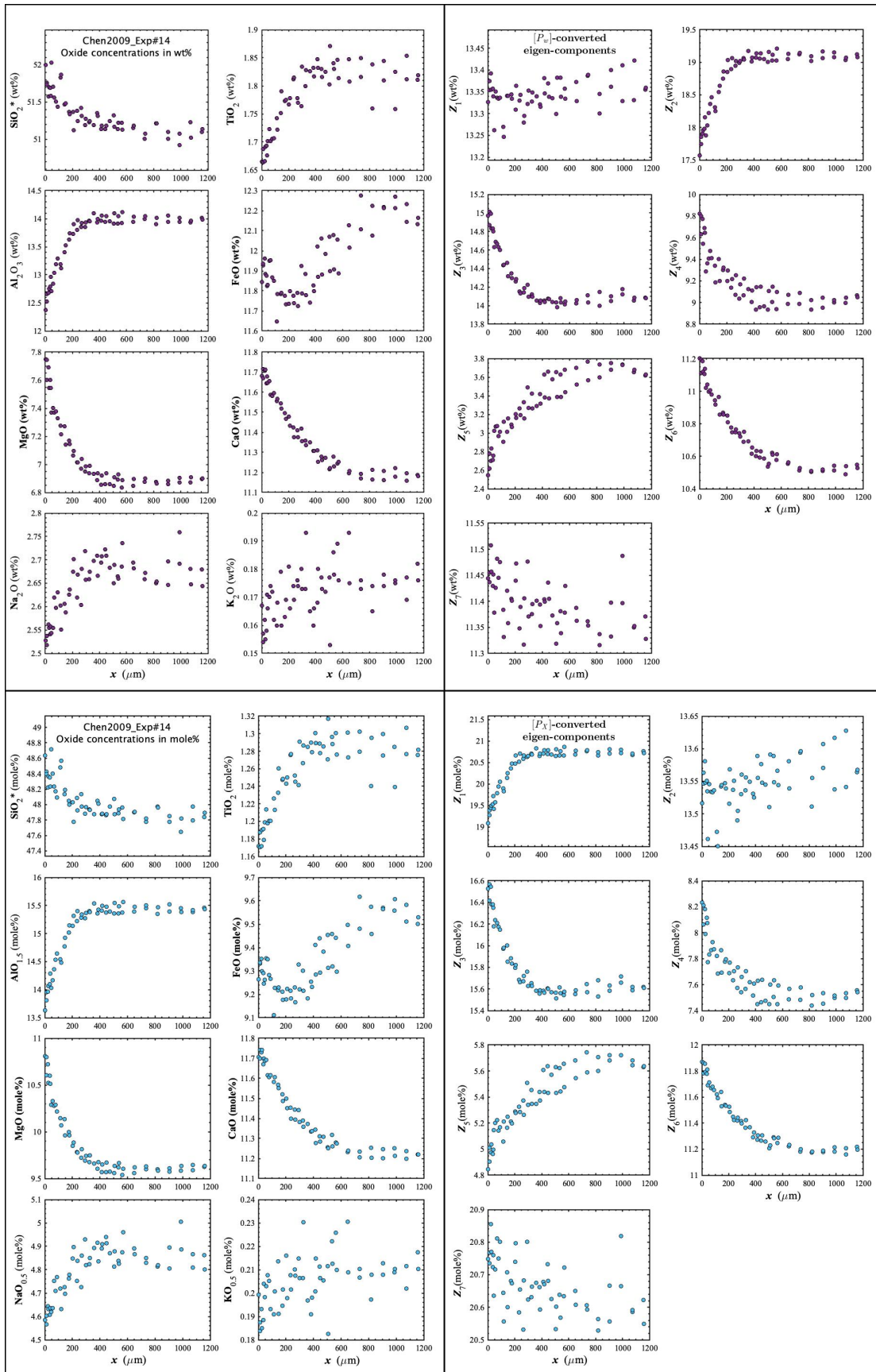
170

Figure D51. Concentration profiles of oxide components in wt% (upper left panel), oxide components in mole% (lower left panel), [P_w]-converted eigen-components (upper right panel), and [P_X]-converted eigen-components (lower right panel) of Chen2008_Exp#39, which is an olivine dissolution experiment in basalt (Chen and Zhang, 2008).
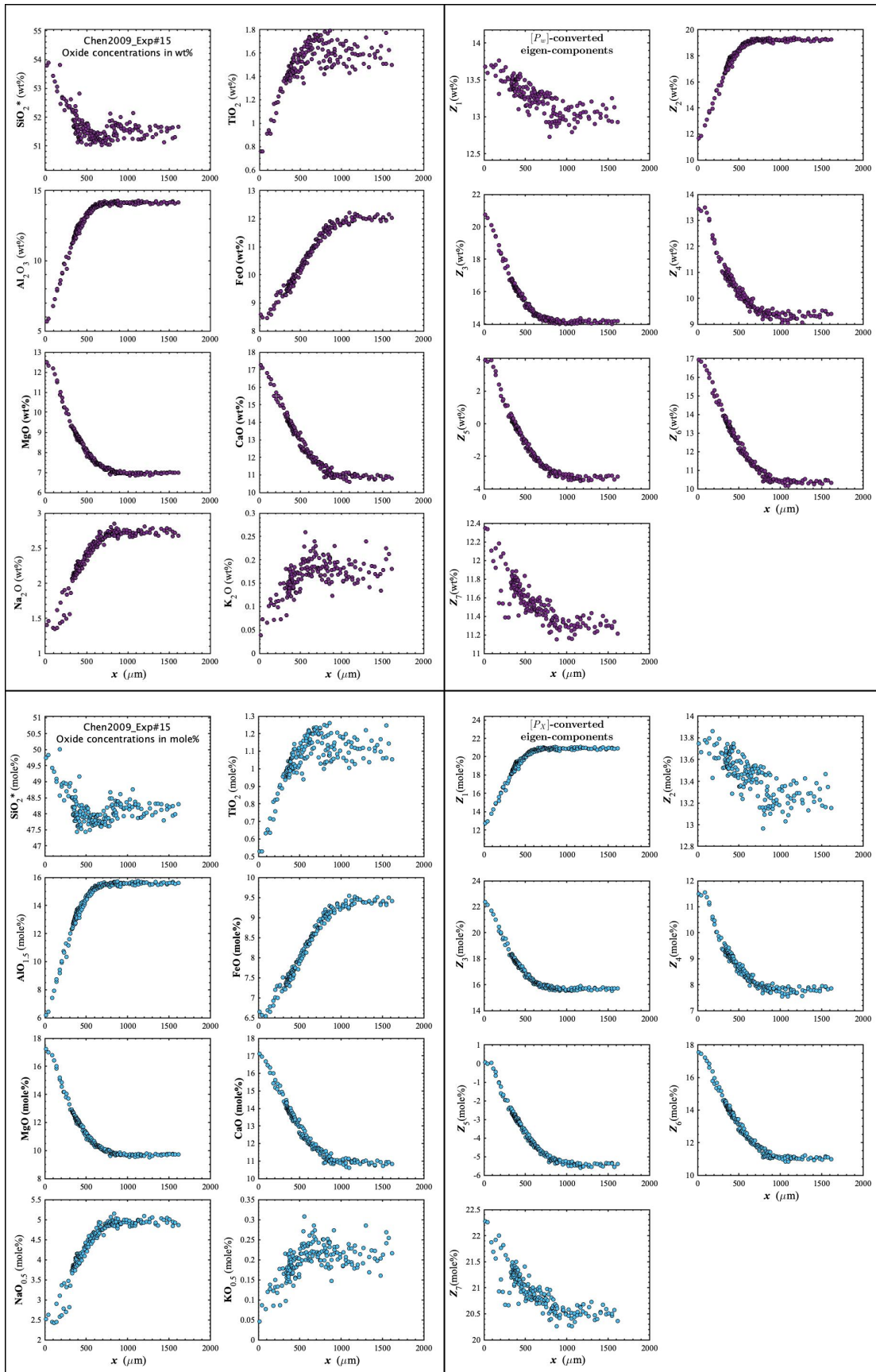
171

Figure D52. Concentration profiles of oxide components in wt% (upper left panel), oxide components in mole% (lower left panel), $[P_w]$-converted eigen-components (upper right panel), and $[P_X]$-converted eigen-components (lower right panel) of Chen2008_Exp#40, which is an olivine dissolution experiment in basalt (Chen and Zhang, 2008).
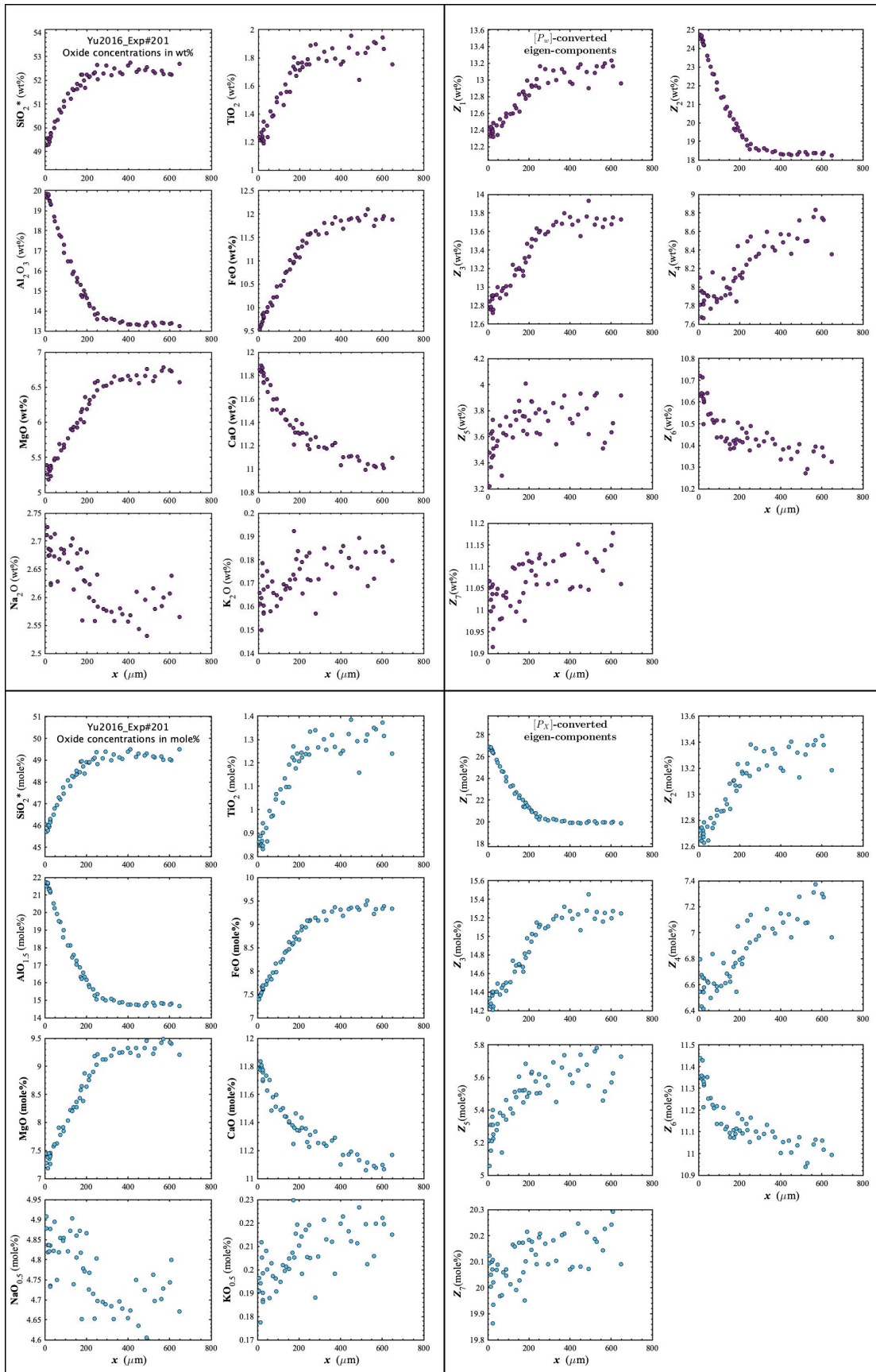
Figure D53. Concentration profiles of oxide components in wt% (upper left panel), oxide components in mole% (lower left panel), [P_w]-converted eigen-components (upper right panel), and [P_X]-converted eigen-components (lower right panel) of Chen2008_Exp#41, which is an olivine dissolution experiment in basalt (Chen and Zhang, 2008).
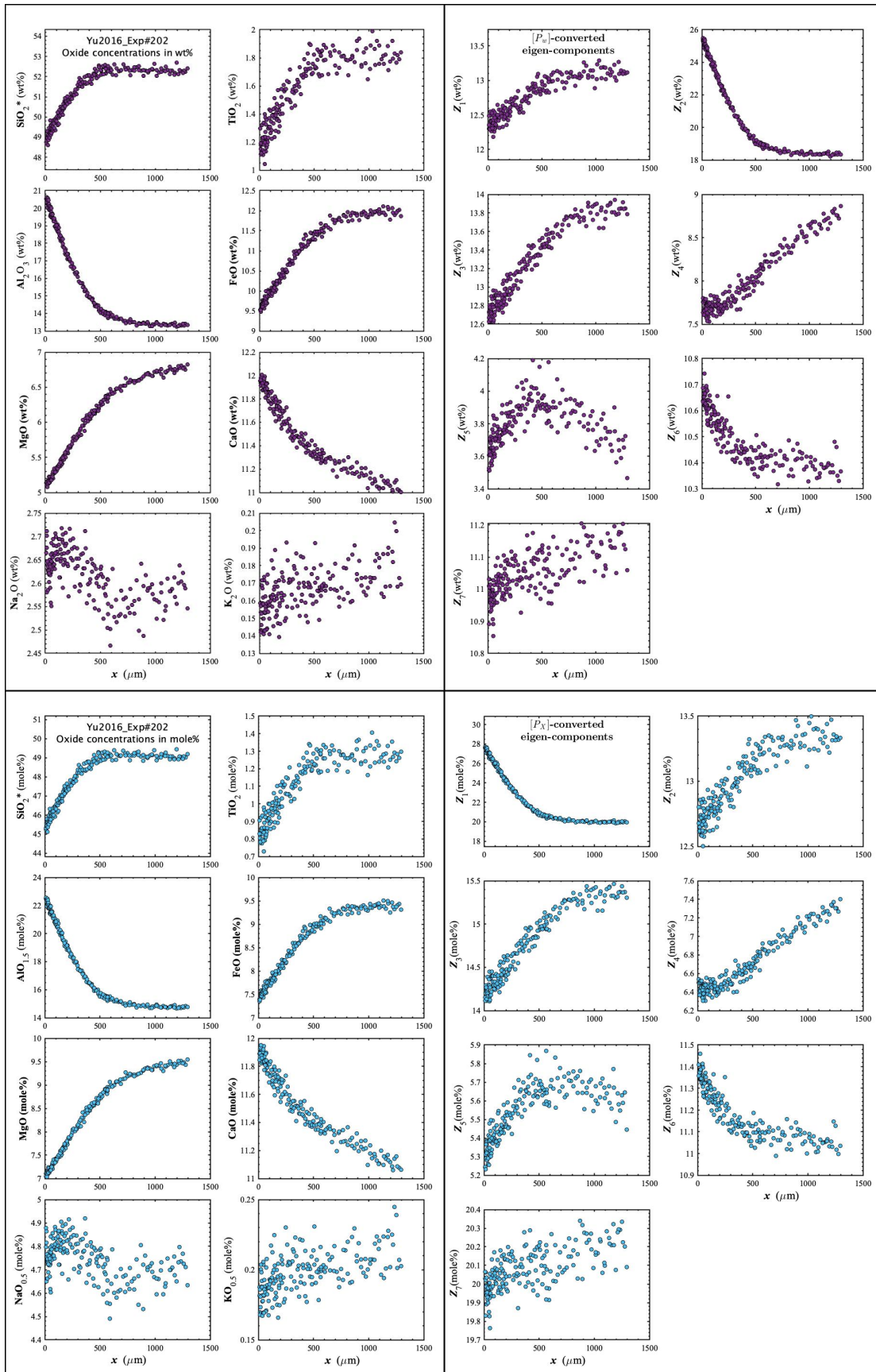
173

Figure D54. Concentration profiles of oxide components in wt% (upper left panel), oxide components in mole% (lower left panel), [P_W]-converted eigen-components (upper right panel), and [P_X]-converted eigen-components (lower right panel) of Chen2008_Exp#43, which is an olivine dissolution experiment in basalt (Chen and Zhang, 2008).

174

Figure D55. Concentration profiles of oxide components in wt% (upper left panel), oxide components in mole% (lower left panel), [P_w]-converted eigen-components (upper right panel), and [P_X]-converted eigen-components (lower right panel) of Chen2008_Exp#44, which is an olivine dissolution experiment in basalt (Chen and Zhang, 2008).
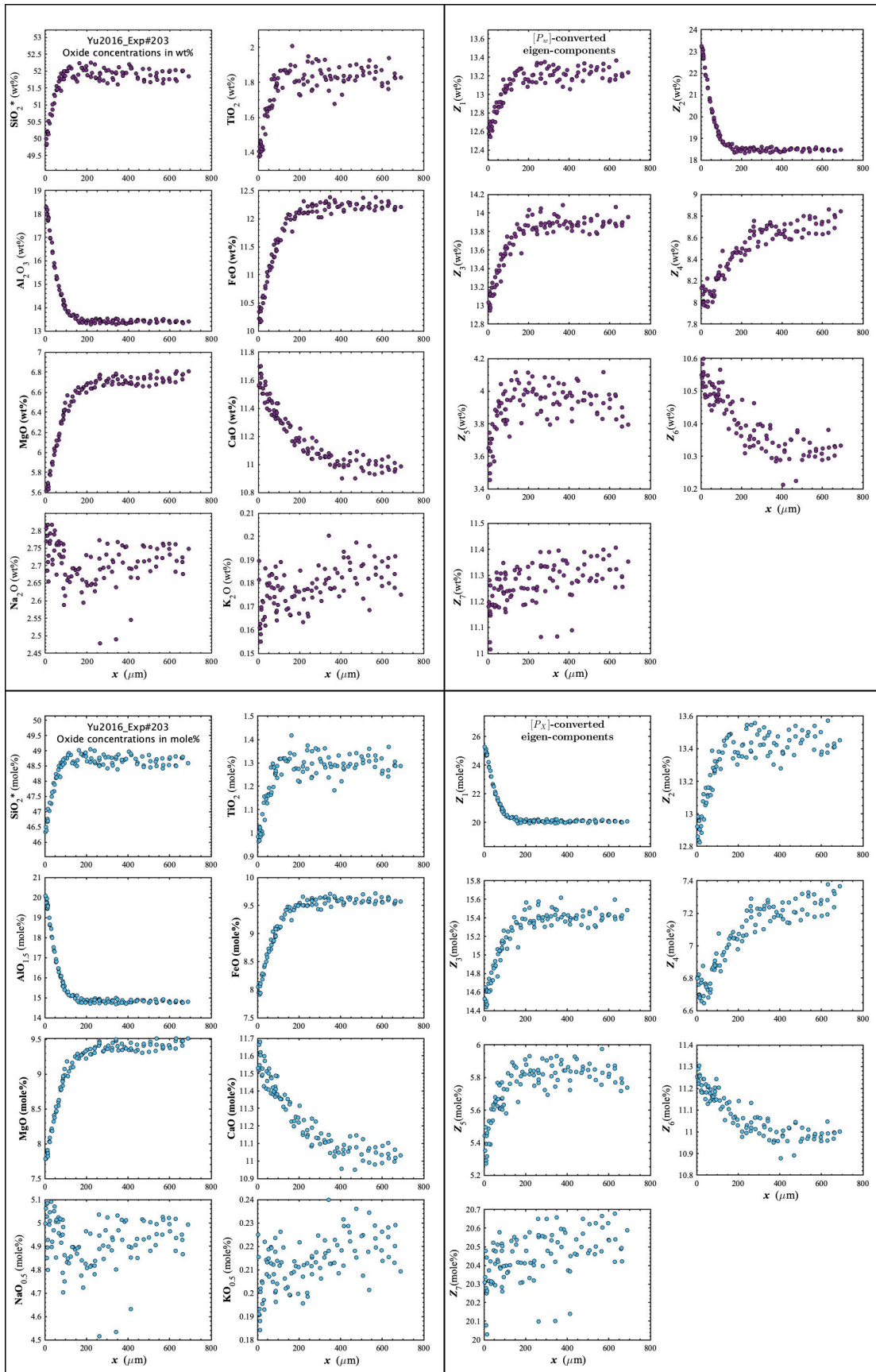
175

Figure D56. Concentration profiles of oxide components in wt% (upper left panel), oxide components in mole% (lower left panel), [P_w]-converted eigen-components (upper right panel), and [P_X]-converted eigen-components (lower right panel) of Chen2008_Exp#45, which is an olivine dissolution experiment in basalt (Chen and Zhang, 2008).
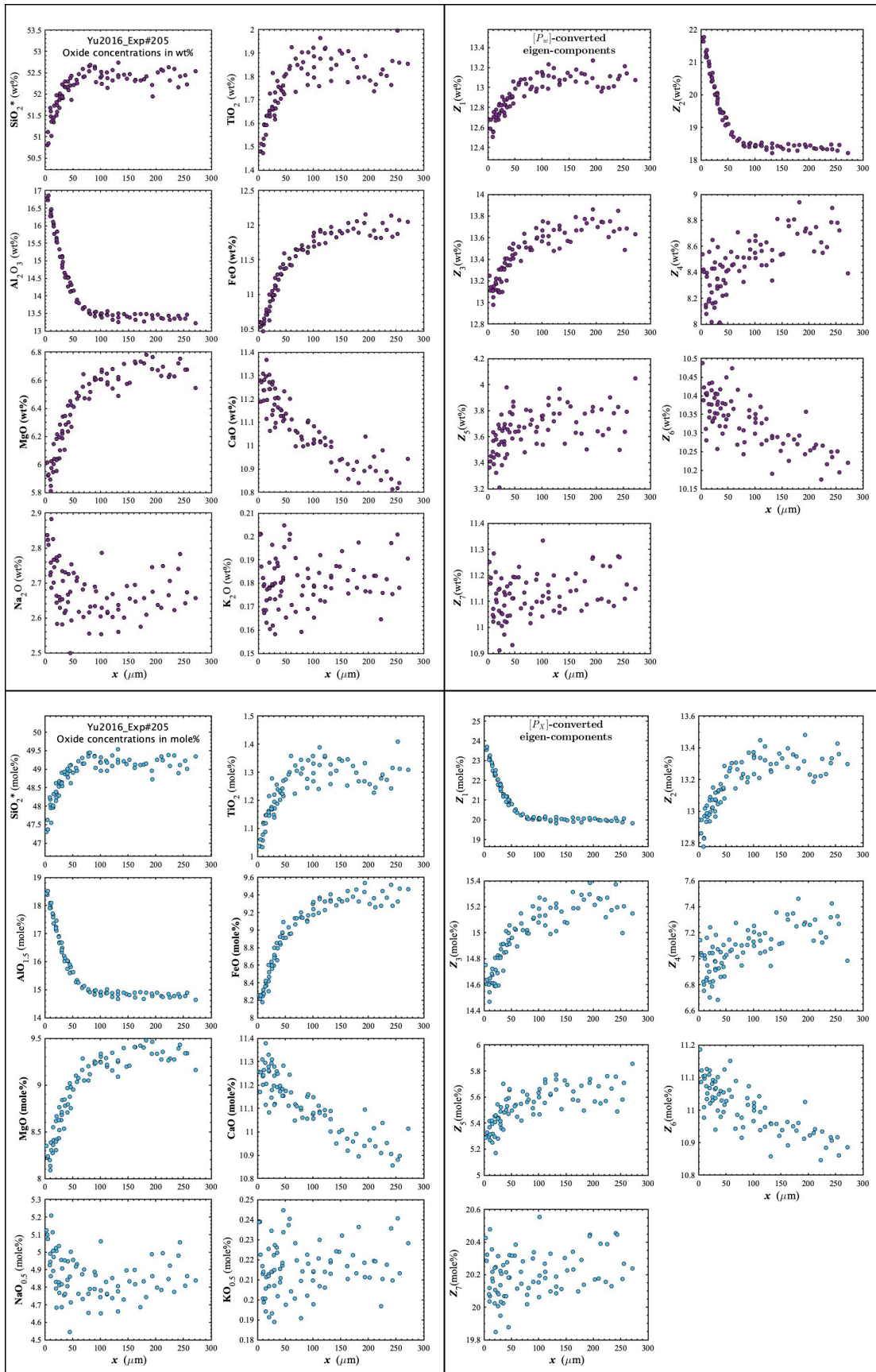
176

Figure D57. Concentration profiles of oxide components in wt% (upper left panel), oxide components in mole% (lower left panel), [P_w]-converted eigen-components (upper right panel), and [P_X]-converted eigen-components (lower right panel) of Chen2008_Exp#46, which is an olivine dissolution experiment in basalt (Chen and Zhang, 2008).
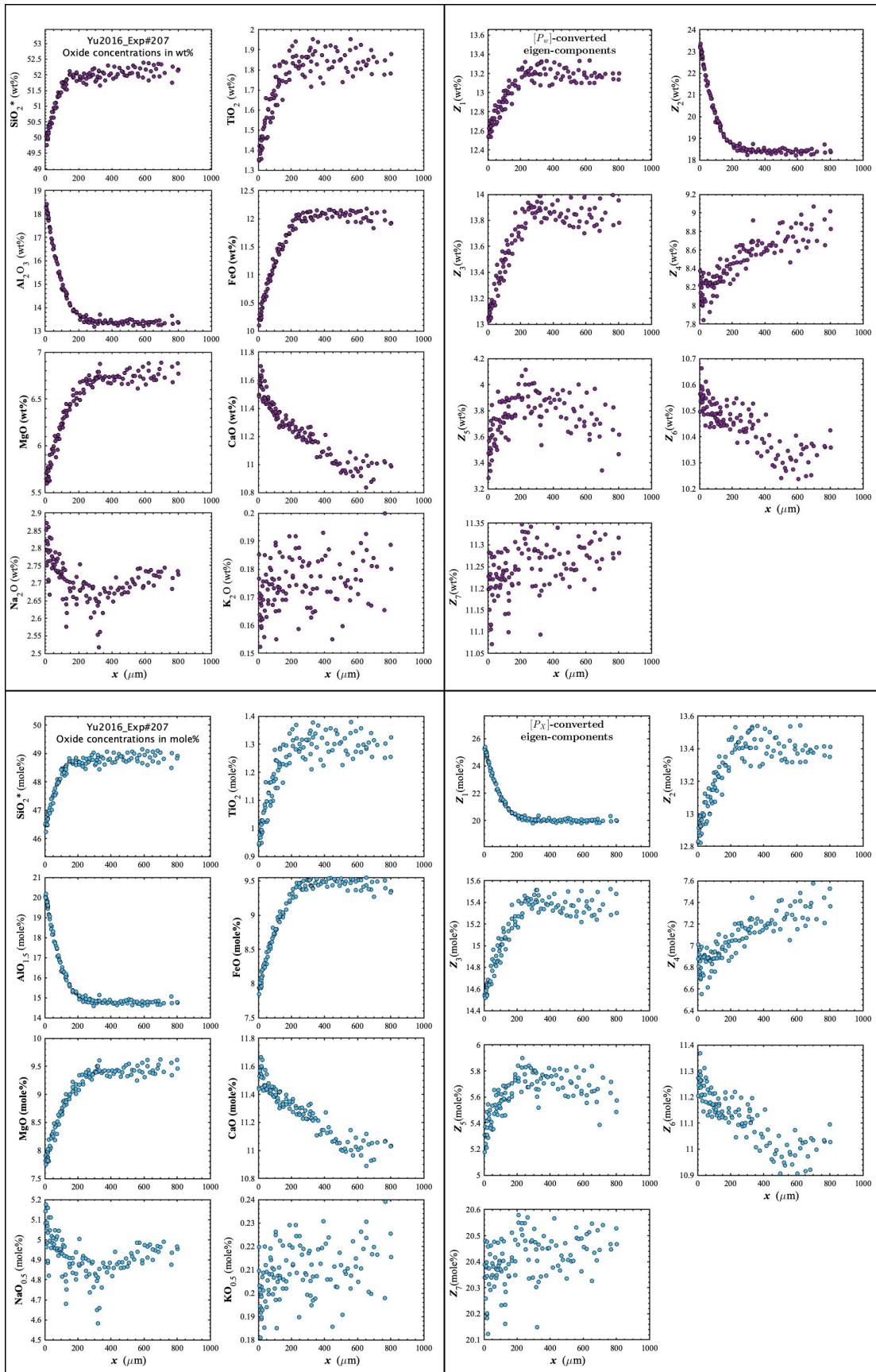
177

Figure D58. Concentration profiles of oxide components in wt% (upper left panel), oxide components in mole% (lower left panel), [P_w]-converted eigen-components (upper right panel), and [P_X]-converted eigen-components (lower right panel) of Chen2009_Exp#1, which is a clinopyroxene dissolution experiment in basalt (Chen and Zhang, 2009).
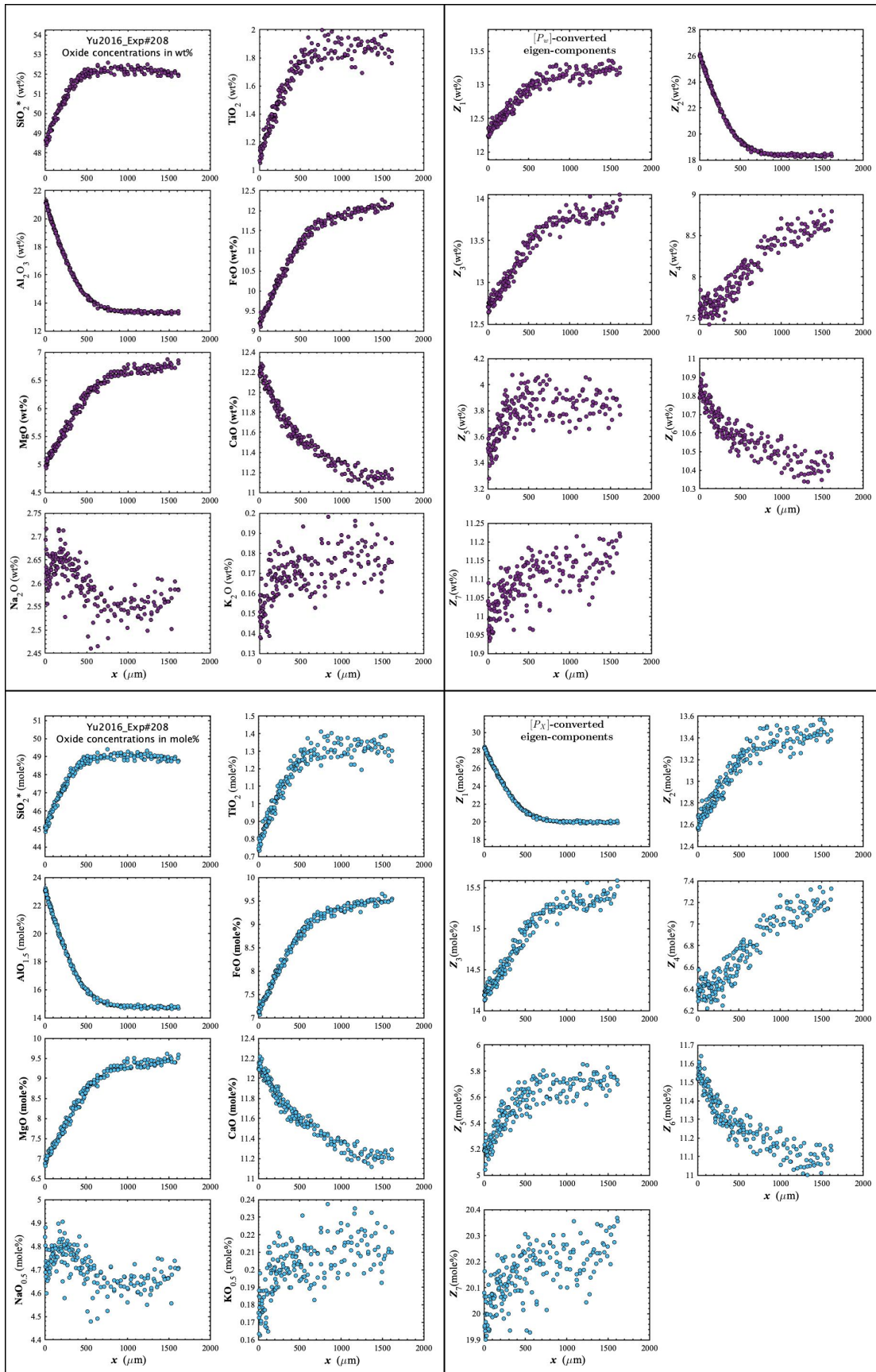
178

Figure D59. Concentration profiles of oxide components in wt% (upper left panel), oxide components in mole% (lower left panel), $[P_w]$-converted eigen-components (upper right panel), and $[P_X]$-converted eigen-components (lower right panel) of Chen2009_Exp#5, which is a clinopyroxene dissolution experiment in basalt (Chen and Zhang, 2009).
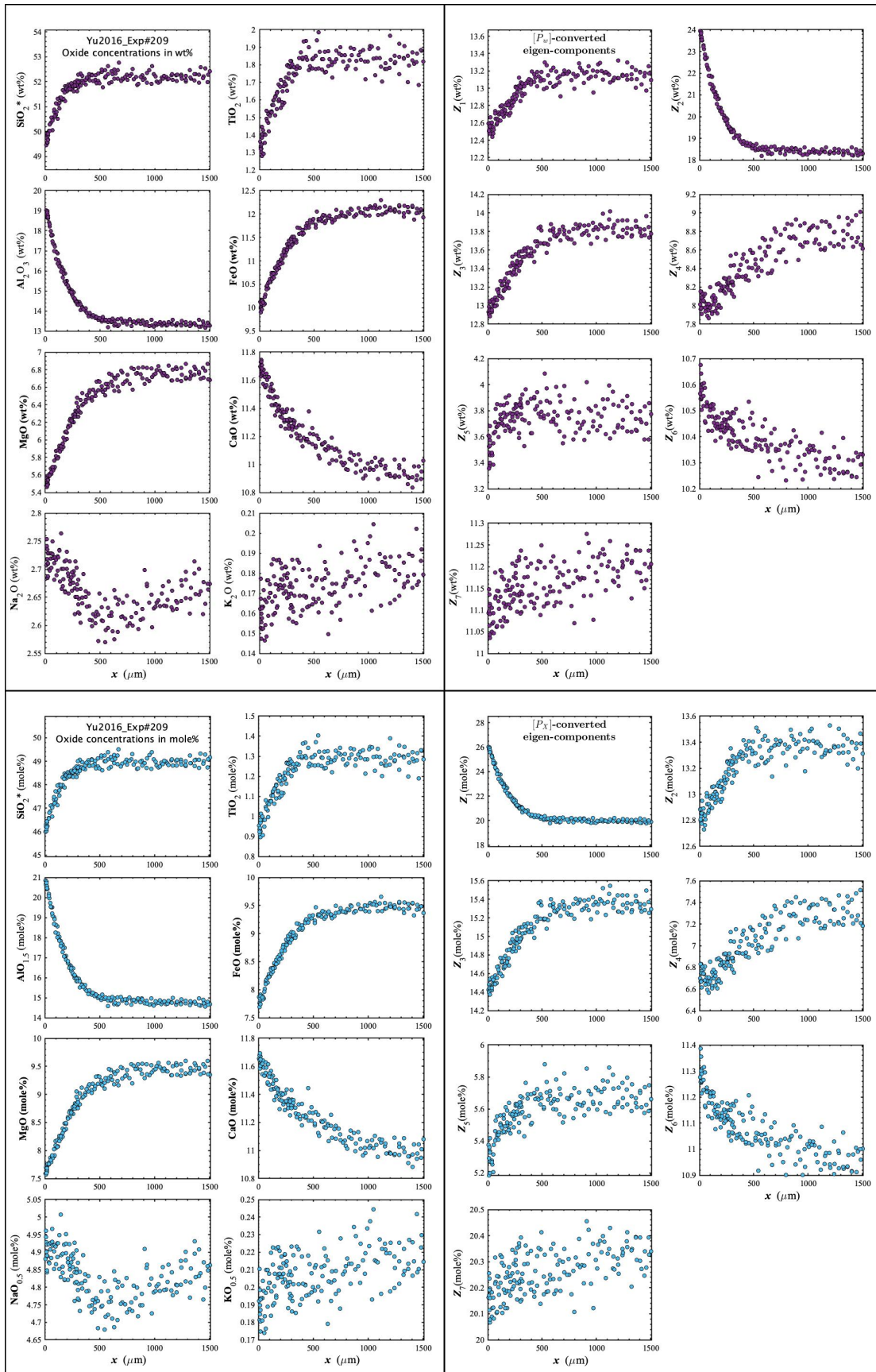
179

Figure D60. Concentration profiles of oxide components in wt% (upper left panel), oxide components in mole% (lower left panel), [P_w]-converted eigen-components (upper right panel), and [P_X]-converted eigen-components (lower right panel) of Chen2009_Exp#6, which is a clinopyroxene dissolution experiment in basalt (Chen and Zhang, 2009).
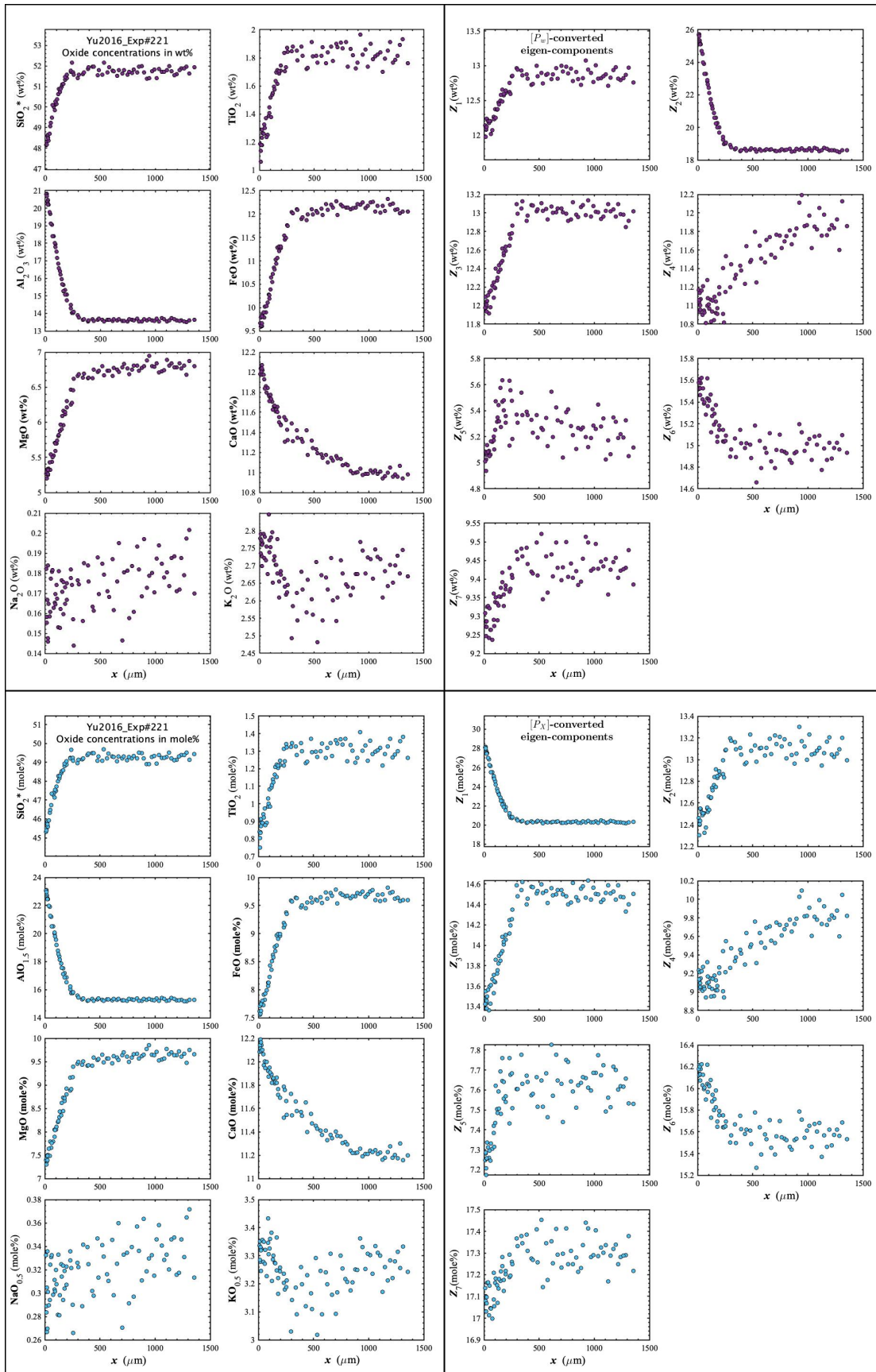
180

Figure D61. Concentration profiles of oxide components in wt% (upper left panel), oxide components in mole% (lower left panel), $[P_w]$-converted eigen-components (upper right panel), and $[P_X]$-converted eigen-components (lower right panel) of Chen2009_Exp#7, which is a clinopyroxene dissolution experiment in basalt (Chen and Zhang, 2009).
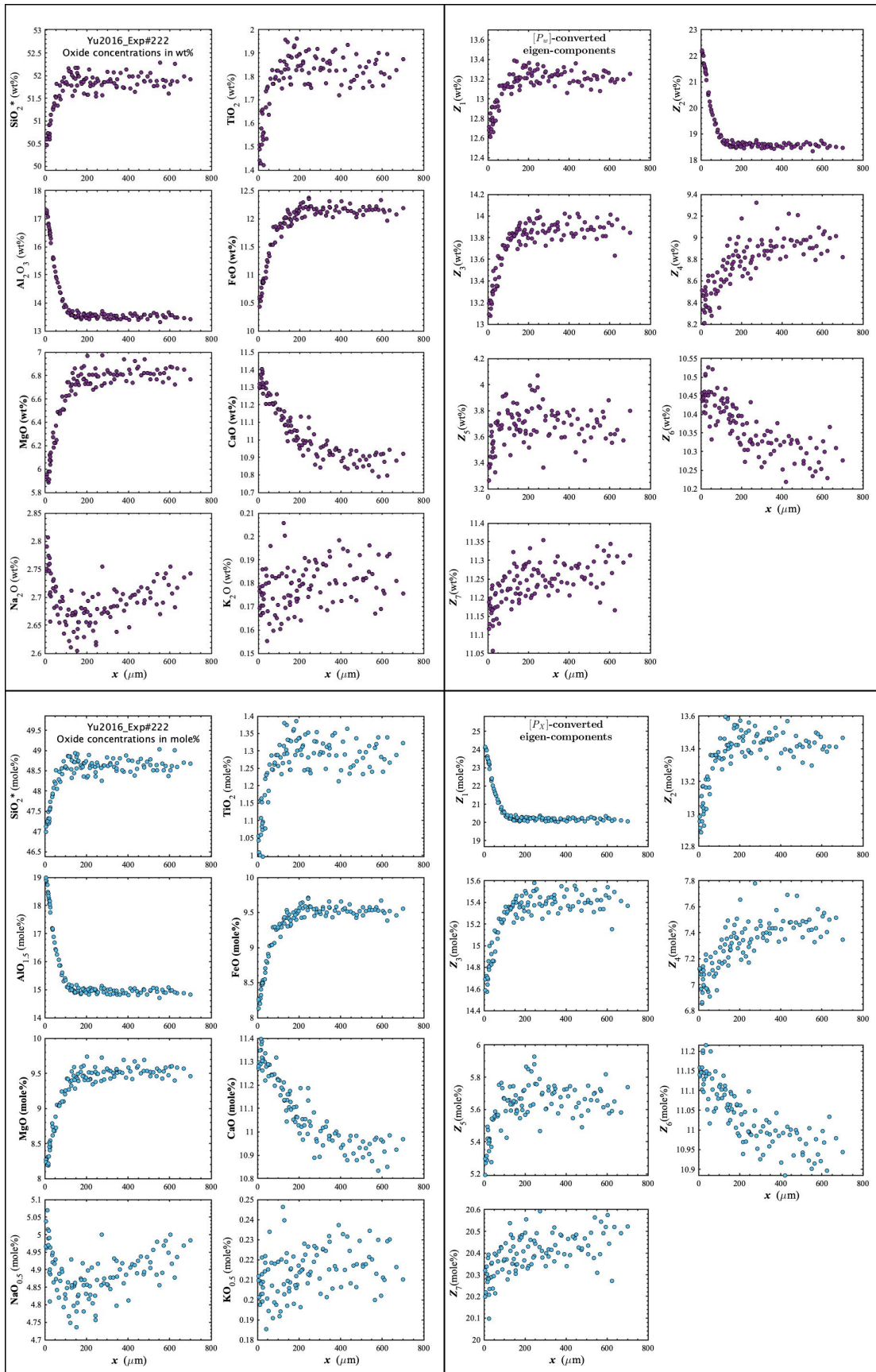
181

Figure D62. Concentration profiles of oxide components in wt% (upper left panel), oxide components in mole% (lower left panel), [P_w]-converted eigen-components (upper right panel), and [P_X]-converted eigen-components (lower right panel) of Chen2009_Exp#8, which is a clinopyroxene dissolution experiment in basalt (Chen and Zhang, 2009).
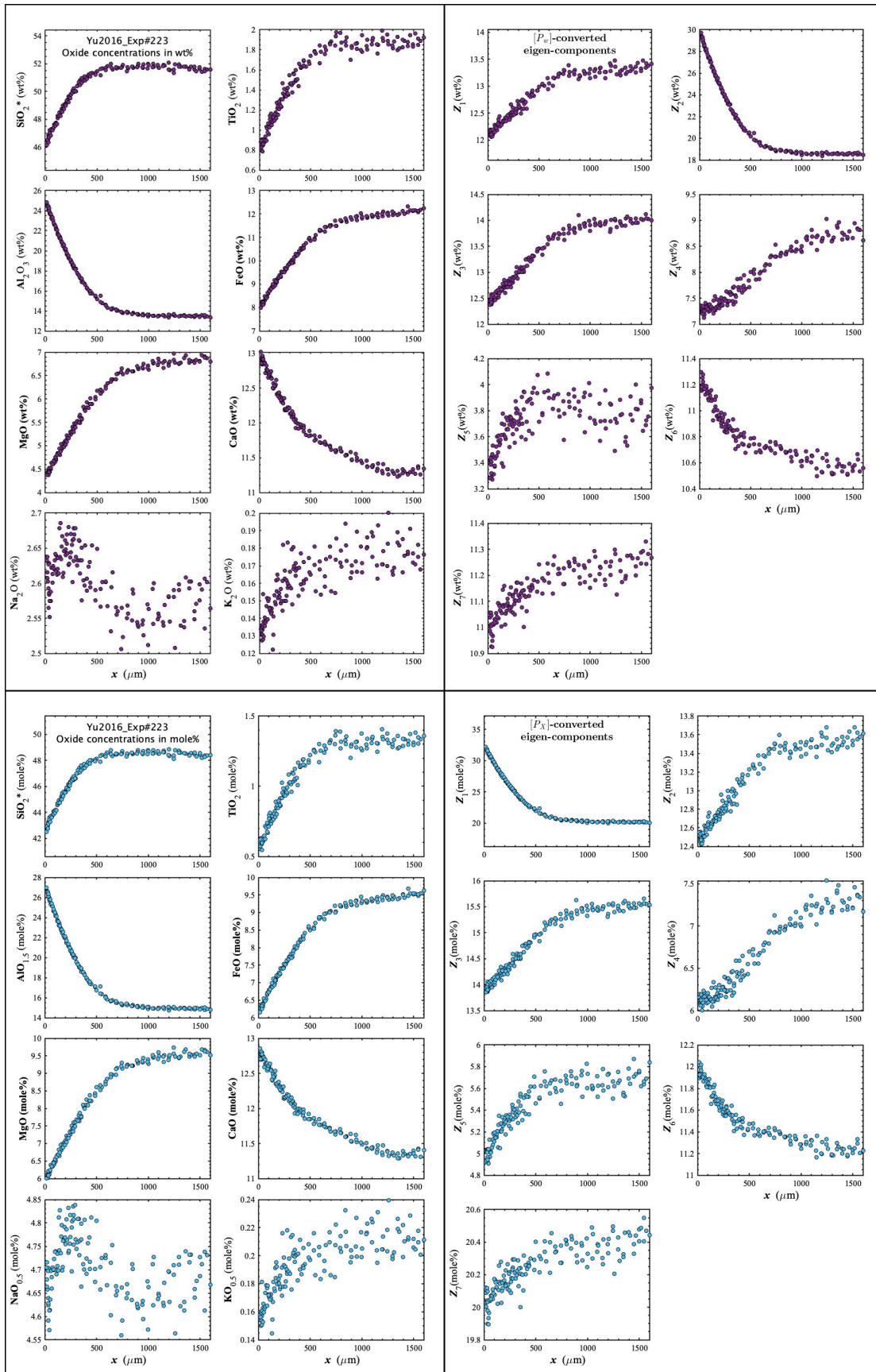
182

Figure D63. Concentration profiles of oxide components in wt% (upper left panel), oxide components in mole% (lower left panel), [P_w]-converted eigen-components (upper right panel), and [P_X]-converted eigen-components (lower right panel) of Chen2009_Exp#11, which is a clinopyroxene dissolution experiment in basalt (Chen and Zhang, 2009).

183

Figure D64. Concentration profiles of oxide components in wt% (upper left panel), oxide components in mole% (lower left panel), [P_w]-converted eigen-components (upper right panel), and [P_X]-converted eigen-components (lower right panel) of Chen2009_Exp#12, which is a clinopyroxene dissolution experiment in basalt (Chen and Zhang, 2009).
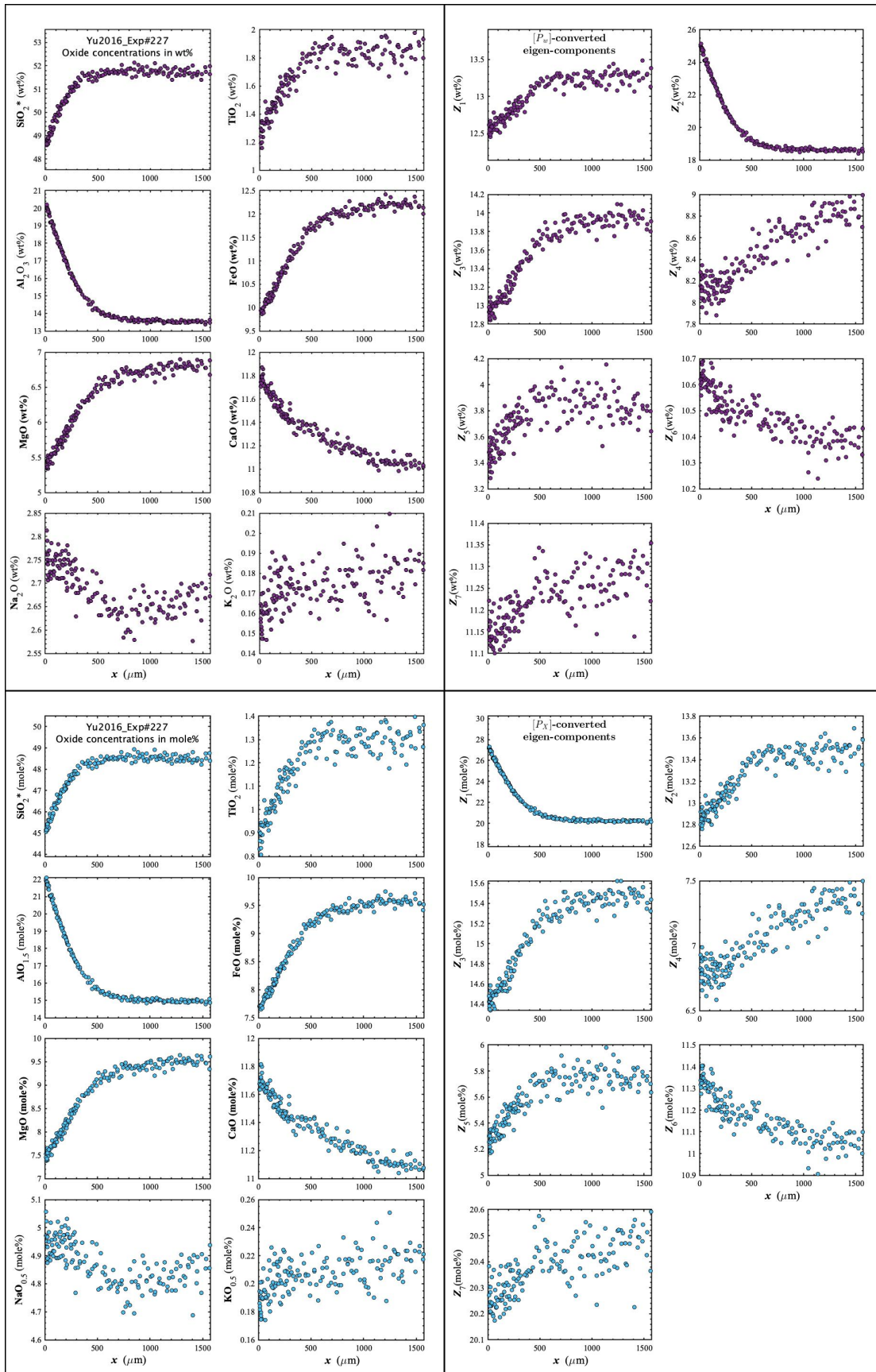
Figure D65. Concentration profiles of oxide components in wt% (upper left panel), oxide components in mole% (lower left panel), [P_w]-converted eigen-components (upper right panel), and [P_X]-converted eigen-components (lower right panel) of Chen2009_Exp#14, which is a clinopyroxene dissolution experiment in basalt (Chen and Zhang, 2009).
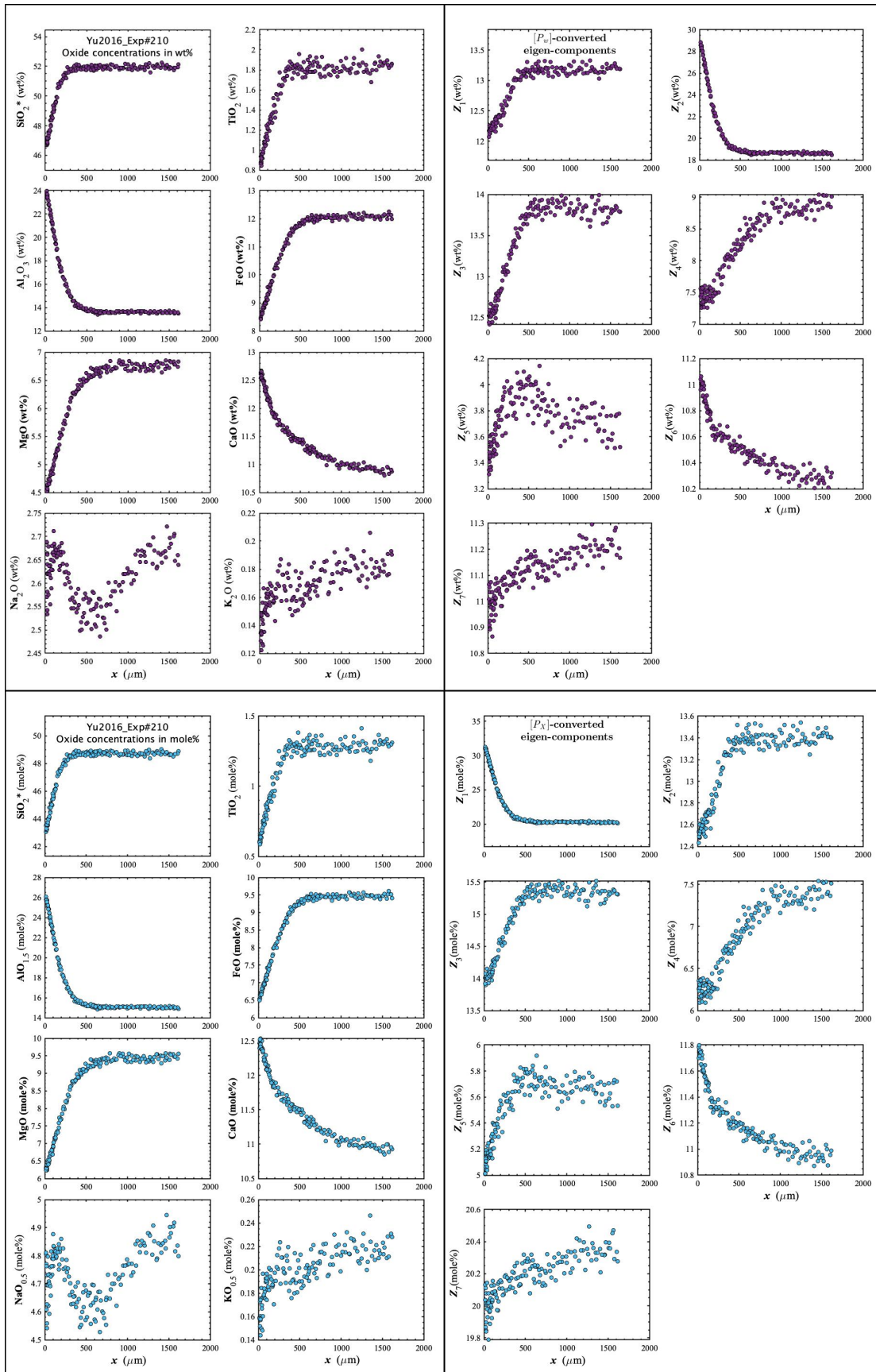
185

Figure D66. Concentration profiles of oxide components in wt% (upper left panel), oxide components in mole% (lower left panel), [P_w]-converted eigen-components (upper right panel), and [P_X]-converted eigen-components (lower right panel) of Chen2009_Exp#15, which is a clinopyroxene dissolution experiment in basalt (Chen and Zhang, 2009).

186

Figure D67. Concentration profiles of oxide components in wt% (upper left panel), oxide components in mole% (lower left panel), $[P_w]$-converted eigen-components (upper right panel), and $[P_X]$-converted eigen-components (lower right panel) of Yu2016_Exp#201, which is a plagioclase dissolution experiment in basalt (Yu et al., 2016).
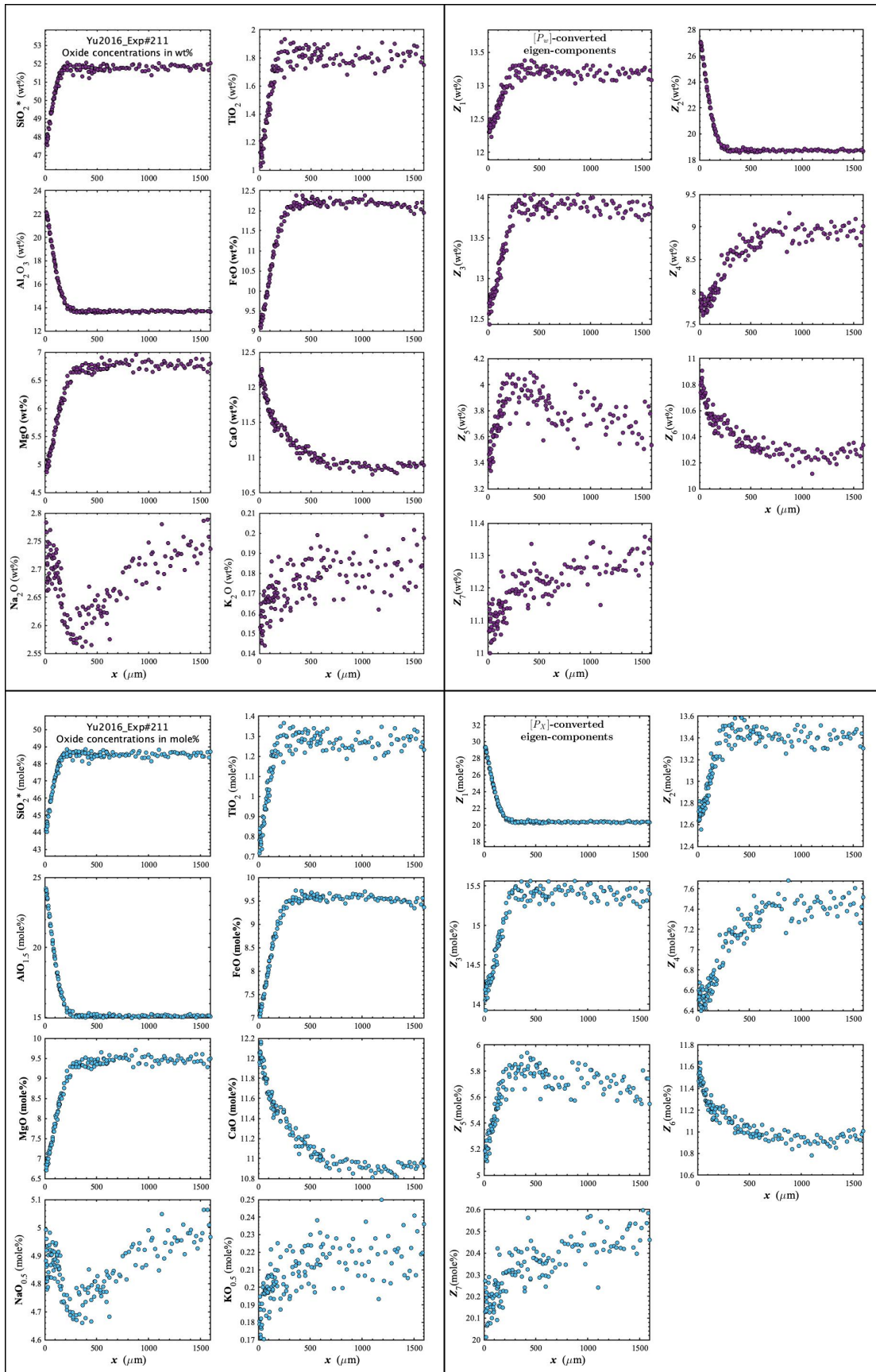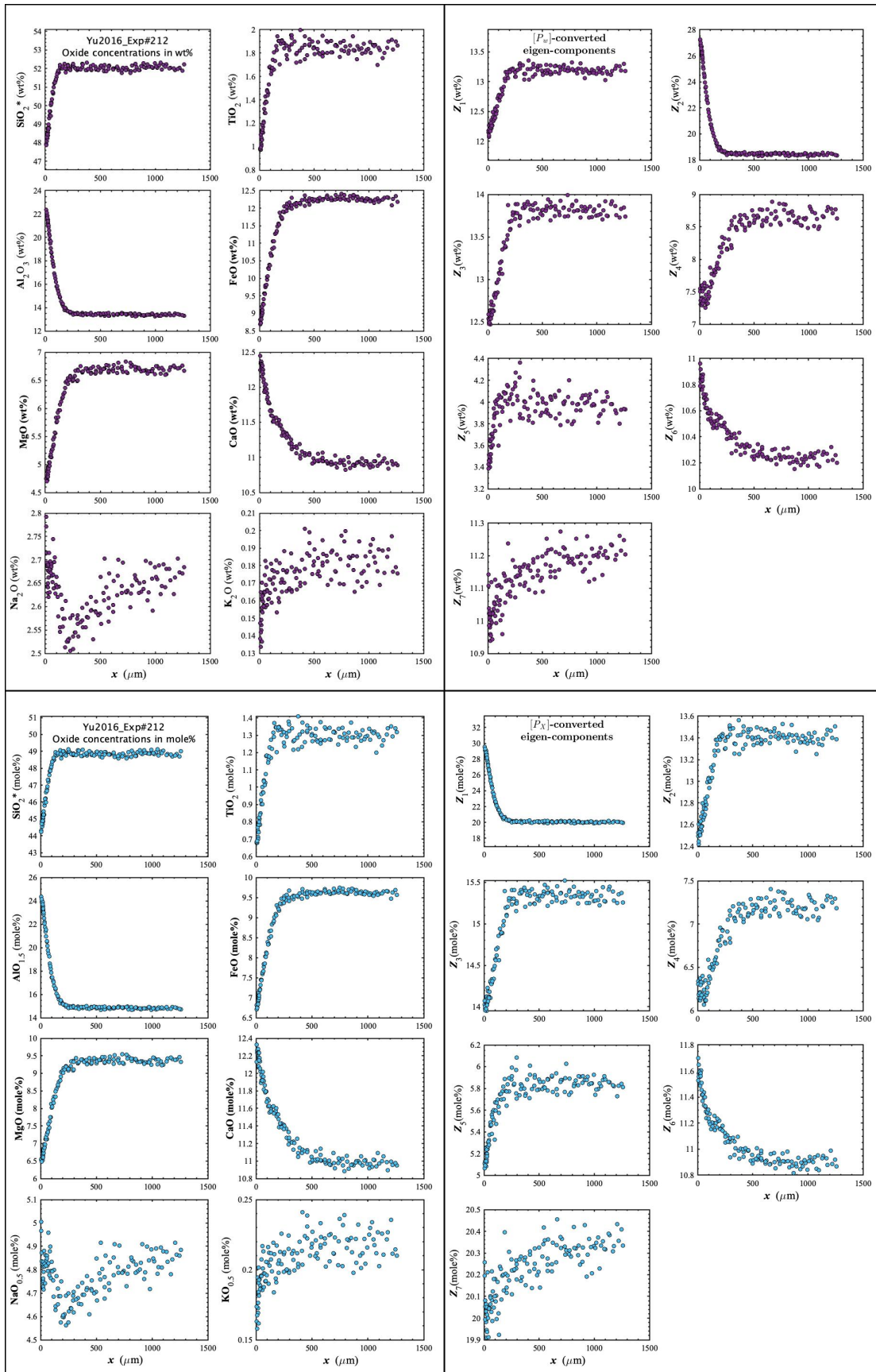
187

Figure D68. Concentration profiles of oxide components in wt% (upper left panel), oxide components in mole% (lower left panel), [P_w]-converted eigen-components (upper right panel), and [P_X]-converted eigen-components (lower right panel) of Yu2016_Exp#202, which is a plagioclase dissolution experiment in basalt (Yu et al., 2016).
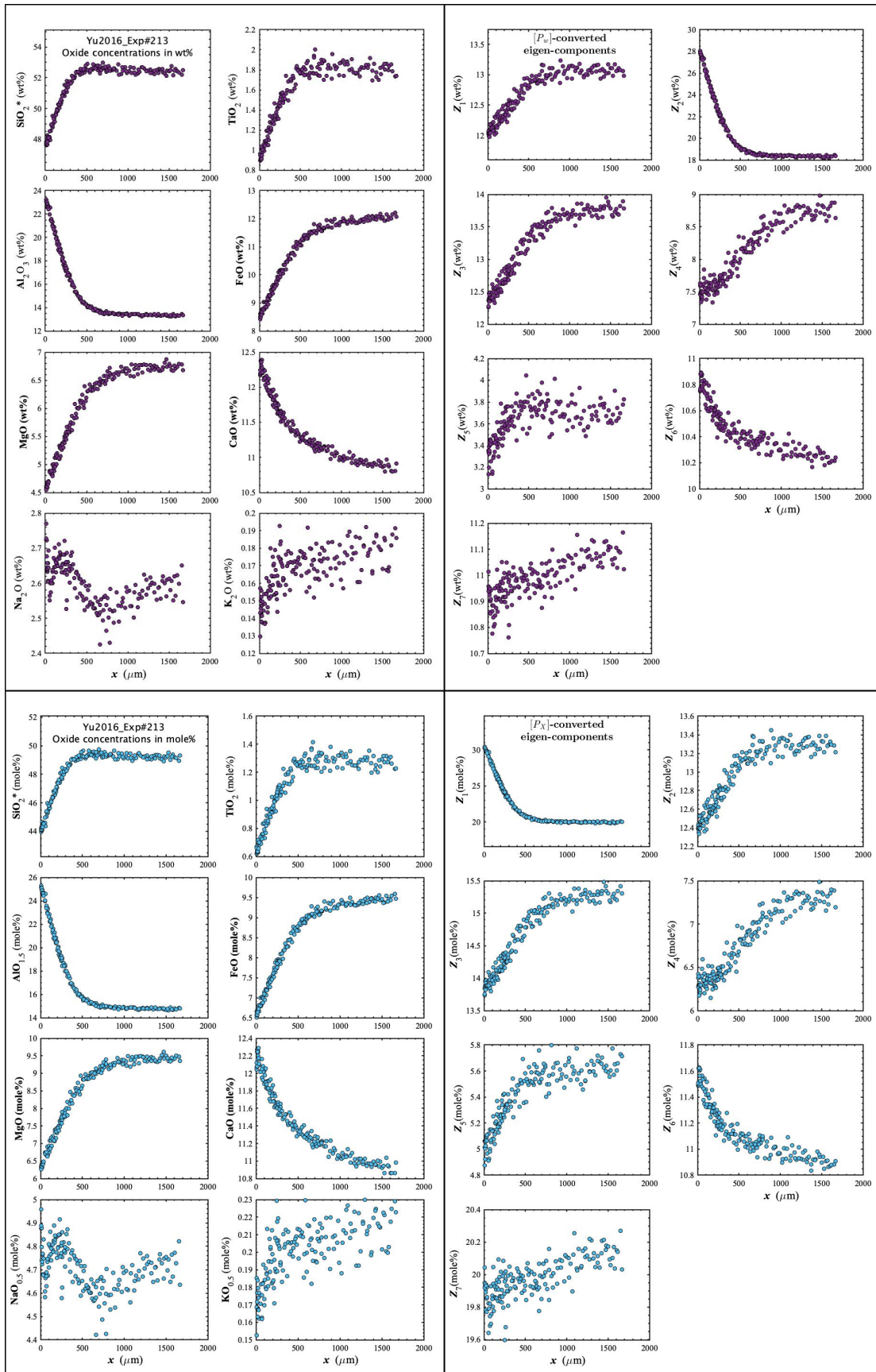
Figure D69. Concentration profiles of oxide components in wt% (upper left panel), oxide components in mole% (lower left panel), [P_w]-converted eigen-components (upper right panel), and [P_X]-converted eigen-components (lower right panel) of Yu2016_Exp#203, which is a plagioclase dissolution experiment in basalt (Yu et al., 2016).

Figure D70. Concentration profiles of oxide components in wt% (upper left panel), oxide components in mole% (lower left panel), [P_w]-converted eigen-components (upper right panel), and [P_X]-converted eigen-components (lower right panel) of Yu2016_Exp#205, which is a plagioclase dissolution experiment in basalt (Yu et al., 2016).
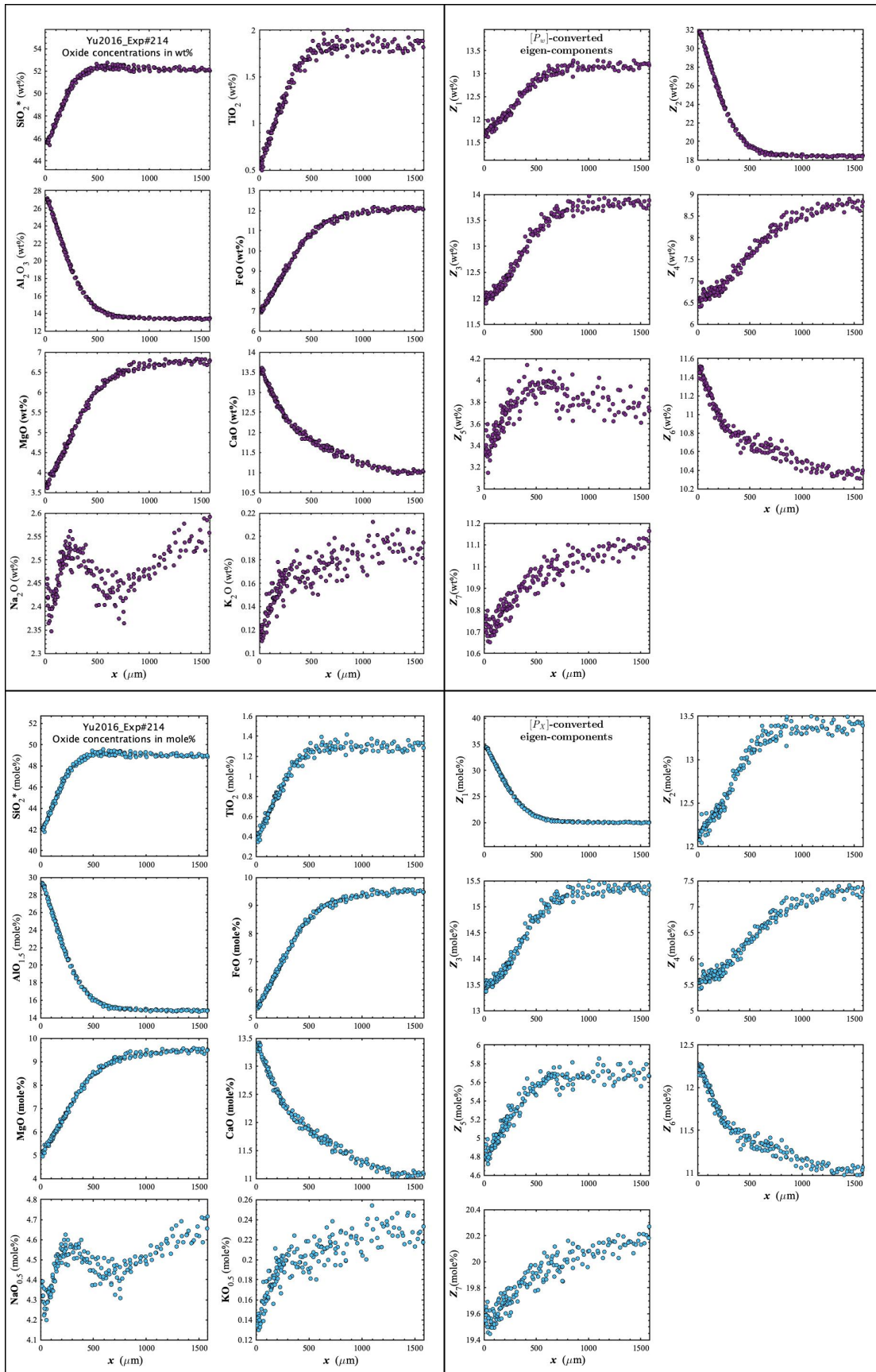
190

Figure D71. Concentration profiles of oxide components in wt% (upper left panel), oxide components in mole% (lower left panel), $[P_w]$-converted eigen-components (upper right panel), and $[P_X]$-converted eigen-components (lower right panel) of Yu2016_Exp#207, which is a plagioclase dissolution experiment in basalt (Yu et al., 2016).
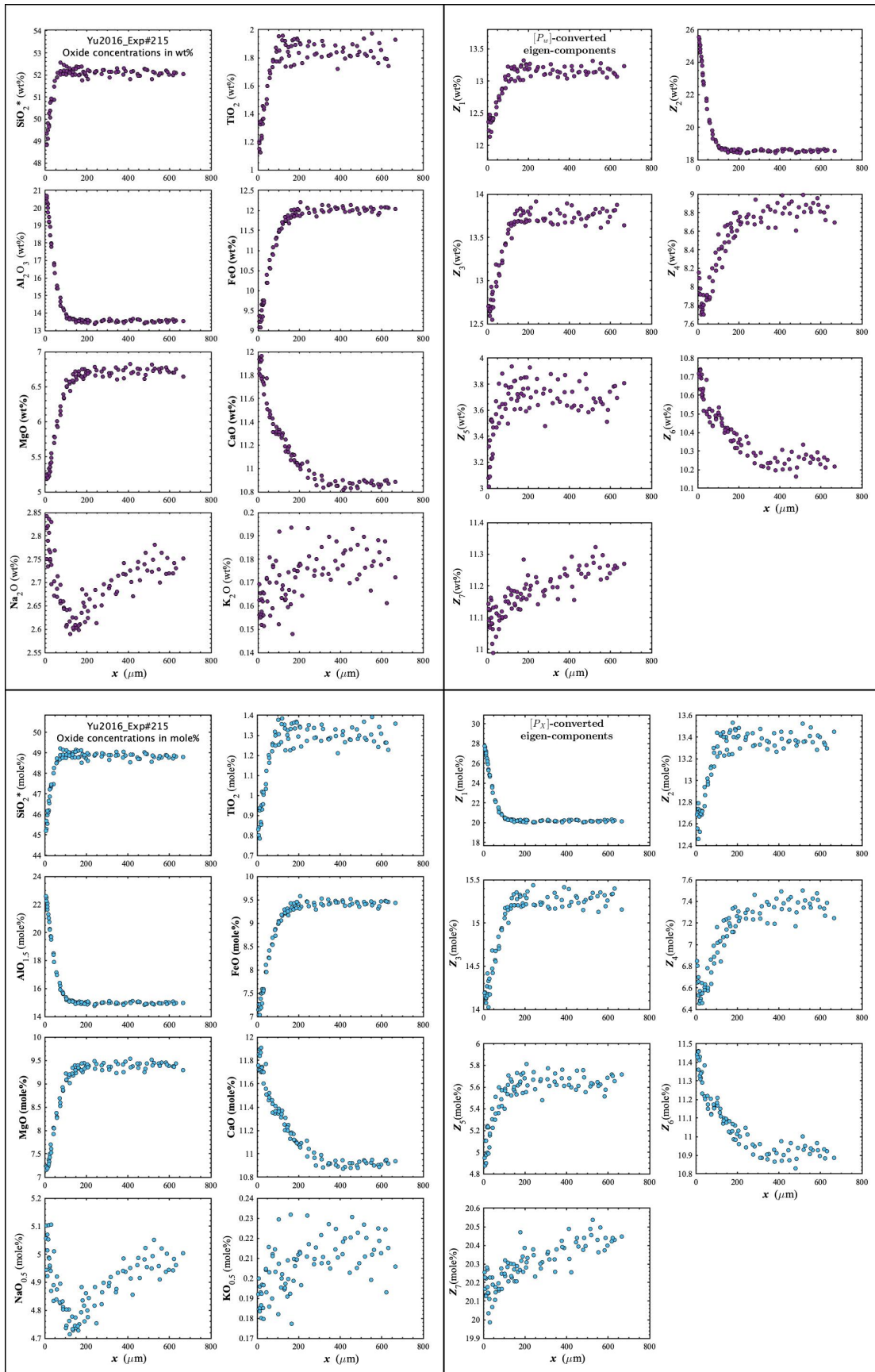
Figure D72. Concentration profiles of oxide components in wt% (upper left panel), oxide components in mole% (lower left panel), [P_w]-converted eigen-components (upper right panel), and [P_X]-converted eigen-components (lower right panel) of Yu2016_Exp#208, which is a plagioclase dissolution experiment in basalt (Yu et al., 2016).
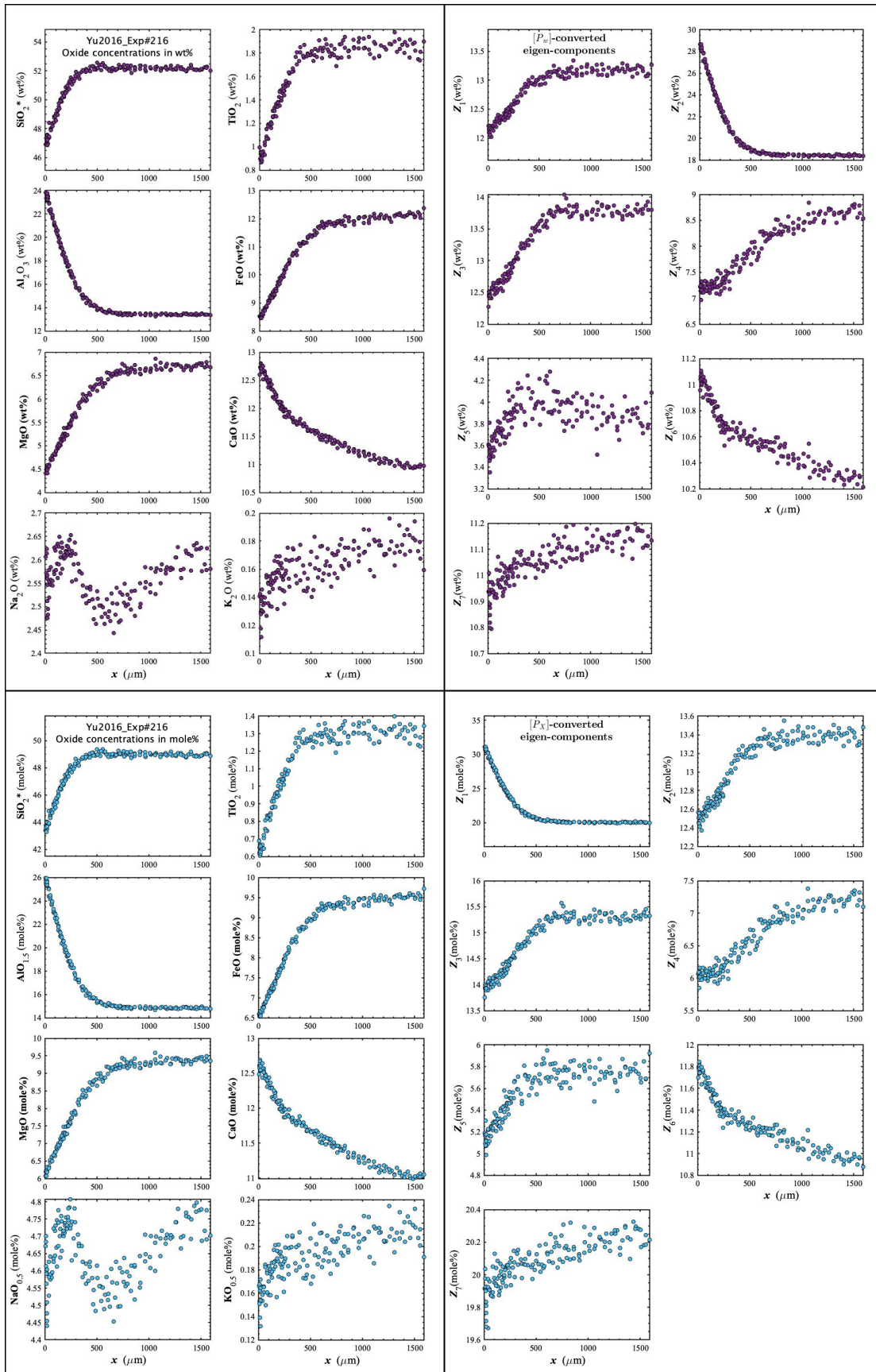
Figure D73. Concentration profiles of oxide components in wt% (upper left panel), oxide components in mole% (lower left panel), [P_w]-converted eigen-components (upper right panel), and [P_X]-converted eigen-components (lower right panel) of Yu2016_Exp#209, which is a plagioclase dissolution experiment in basalt (Yu et al., 2016).
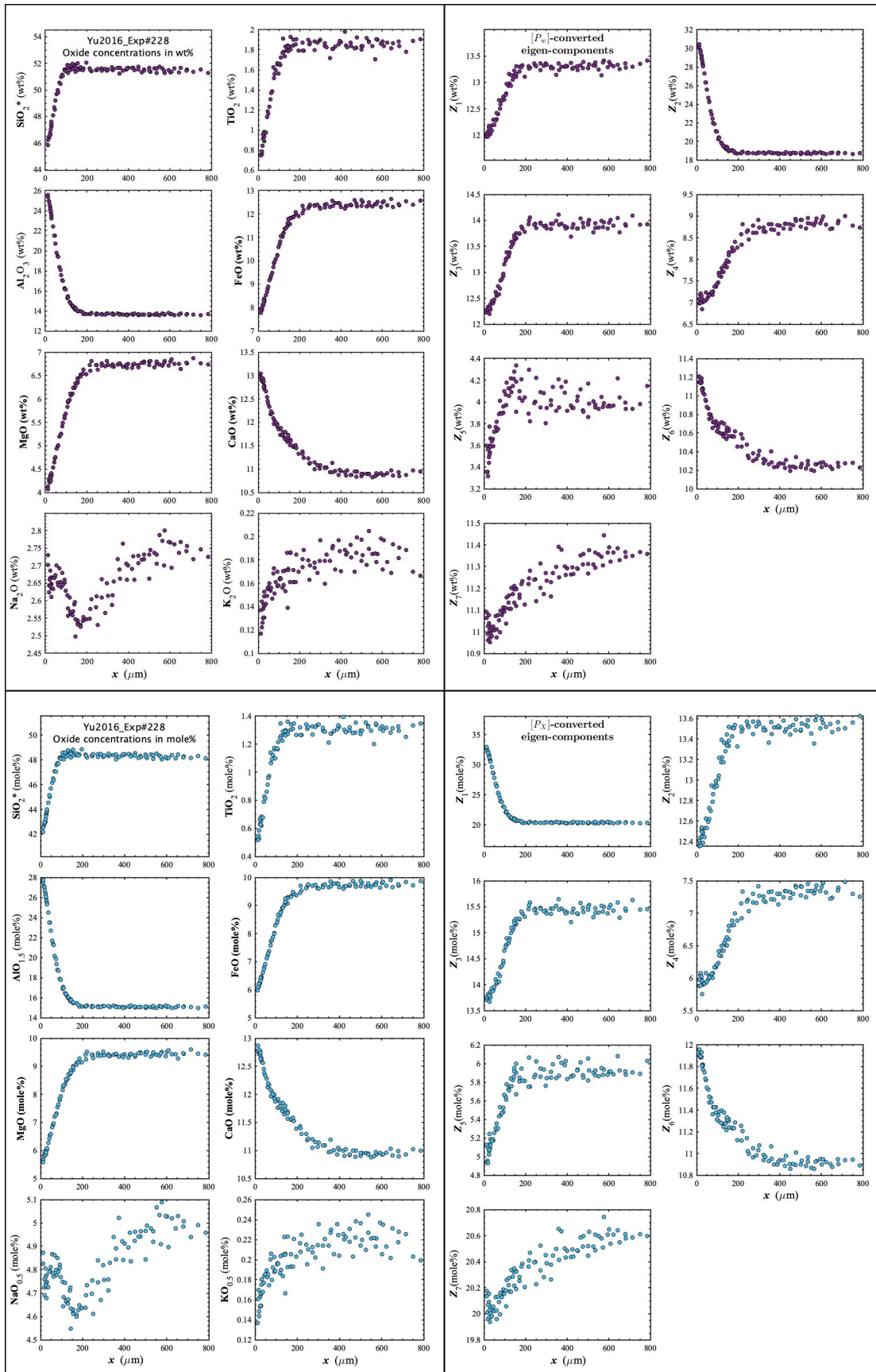
193

Figure D74. Concentration profiles of oxide components in wt% (upper left panel), oxide components in mole% (lower left panel), [P_w]-converted eigen-components (upper right panel), and [P_X]-converted eigen-components (lower right panel) of Yu2016_Exp#221, which is a plagioclase dissolution experiment in basalt (Yu et al., 2016).
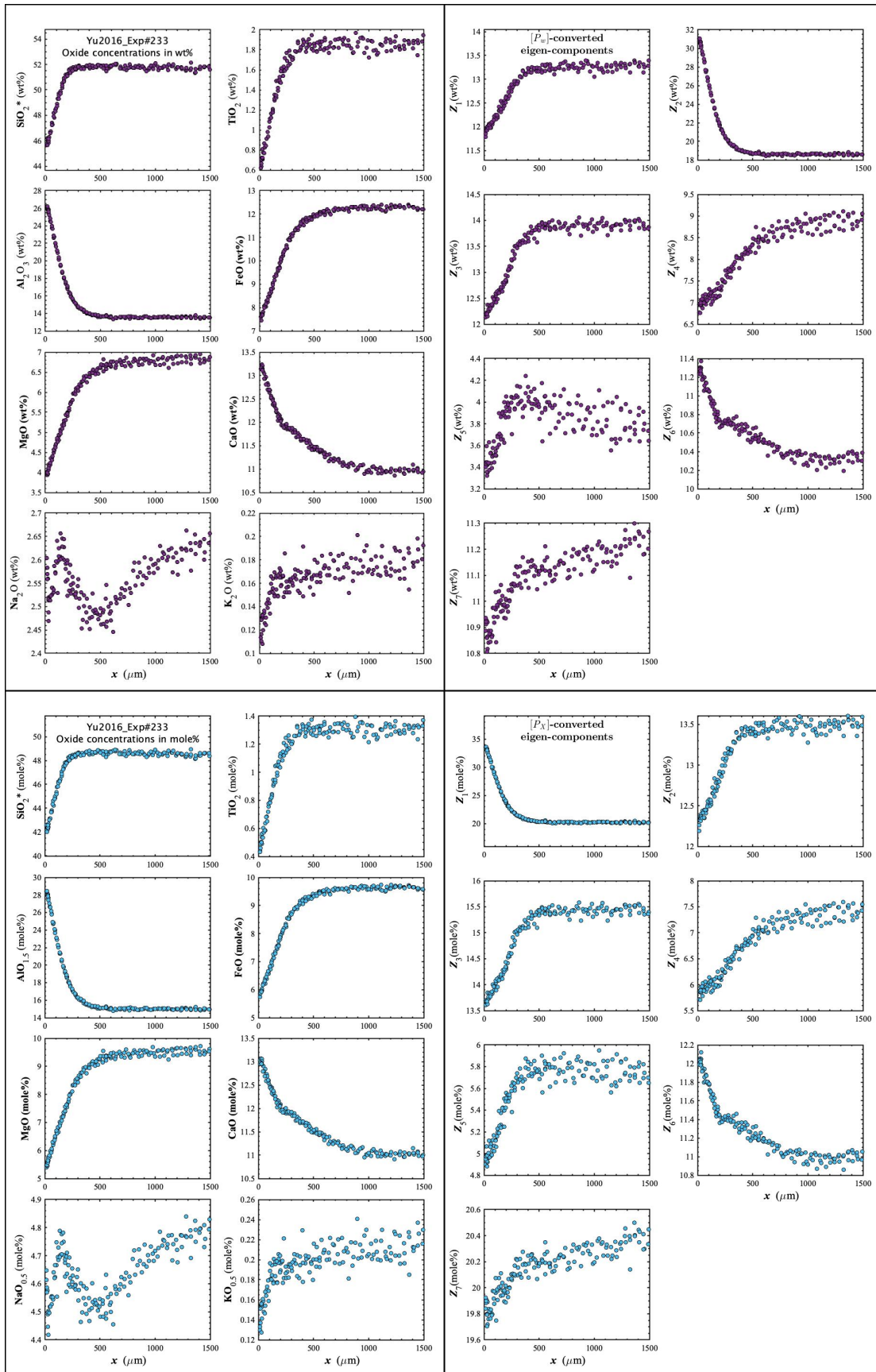
Figure D75. Concentration profiles of oxide components in wt% (upper left panel), oxide components in mole% (lower left panel), [P_w]-converted eigen-components (upper right panel), and [P_X]-converted eigen-components (lower right panel) of Yu2016_Exp#222, which is a plagioclase dissolution experiment in basalt (Yu et al., 2016).
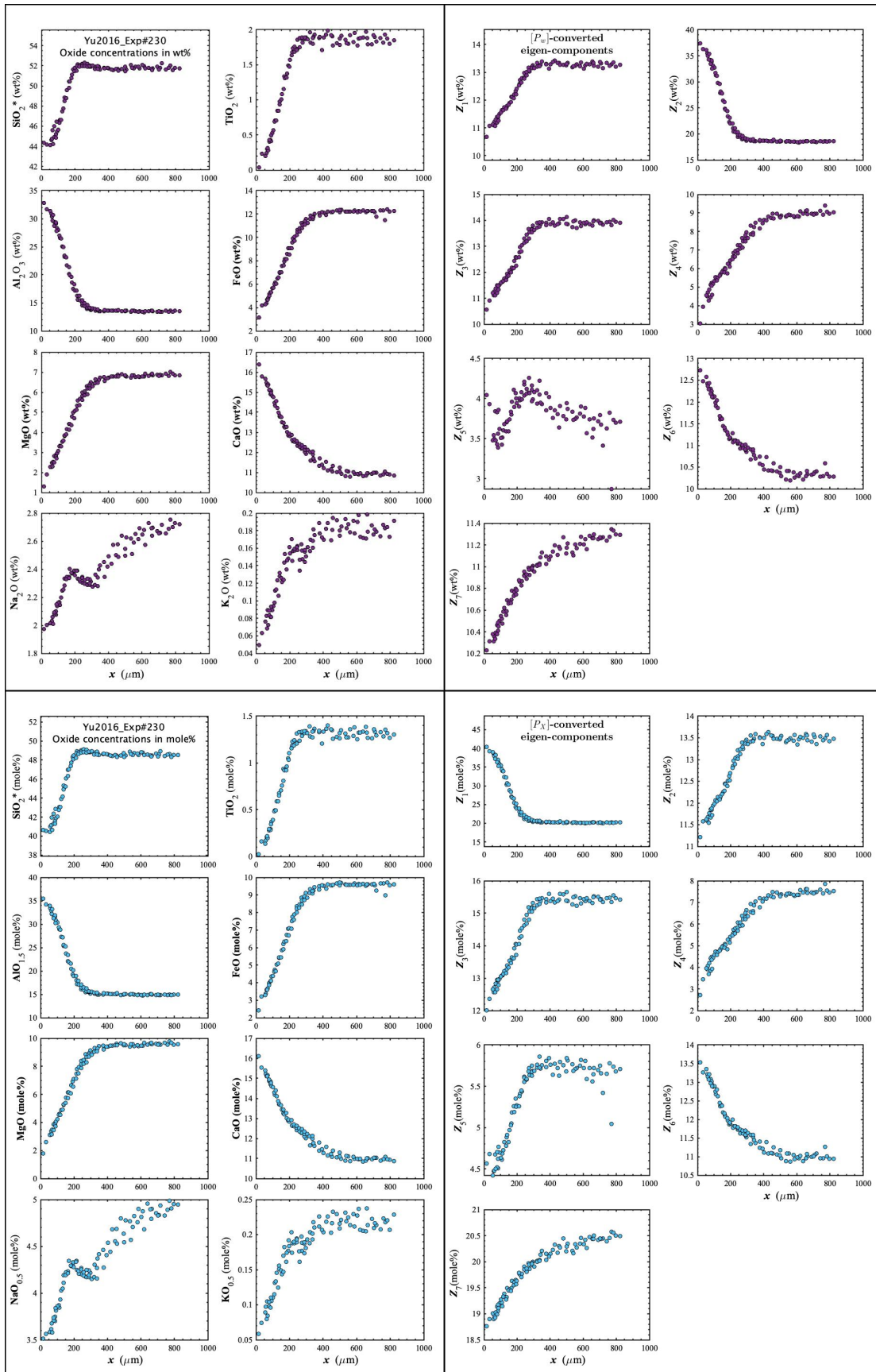
195

Figure D76. Concentration profiles of oxide components in wt% (upper left panel), oxide components in mole% (lower left panel), [P_w]-converted eigen-components (upper right panel), and [P_X]-converted eigen-components (lower right panel) of Yu2016_Exp#223, which is a plagioclase dissolution experiment in basalt (Yu et al., 2016).
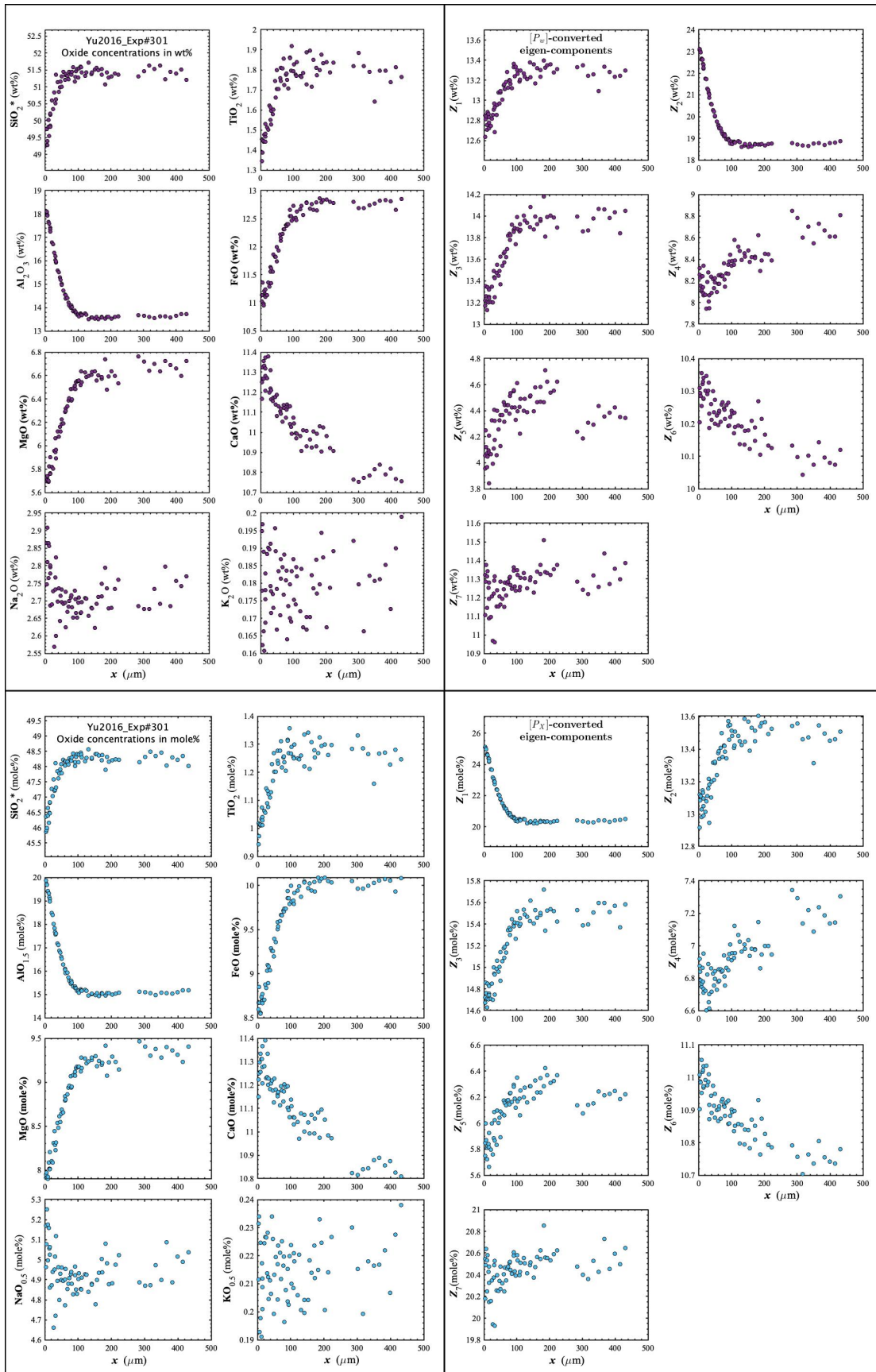
Figure D77. Concentration profiles of oxide components in wt% (upper left panel), oxide components in mole% (lower left panel), [P_w]-converted eigen-components (upper right panel), and [P_X]-converted eigen-components (lower right panel) of Yu2016_Exp#227, which is a plagioclase dissolution experiment in basalt (Yu et al., 2016).

197

Figure D78. Concentration profiles of oxide components in wt% (upper left panel), oxide components in mole% (lower left panel), $[P_w]$-converted eigen-components (upper right panel), and $[P_X]$-converted eigen-components (lower right panel) of Yu2016_Exp#210, which is a plagioclase dissolution experiment in basalt (Yu et al., 2016).
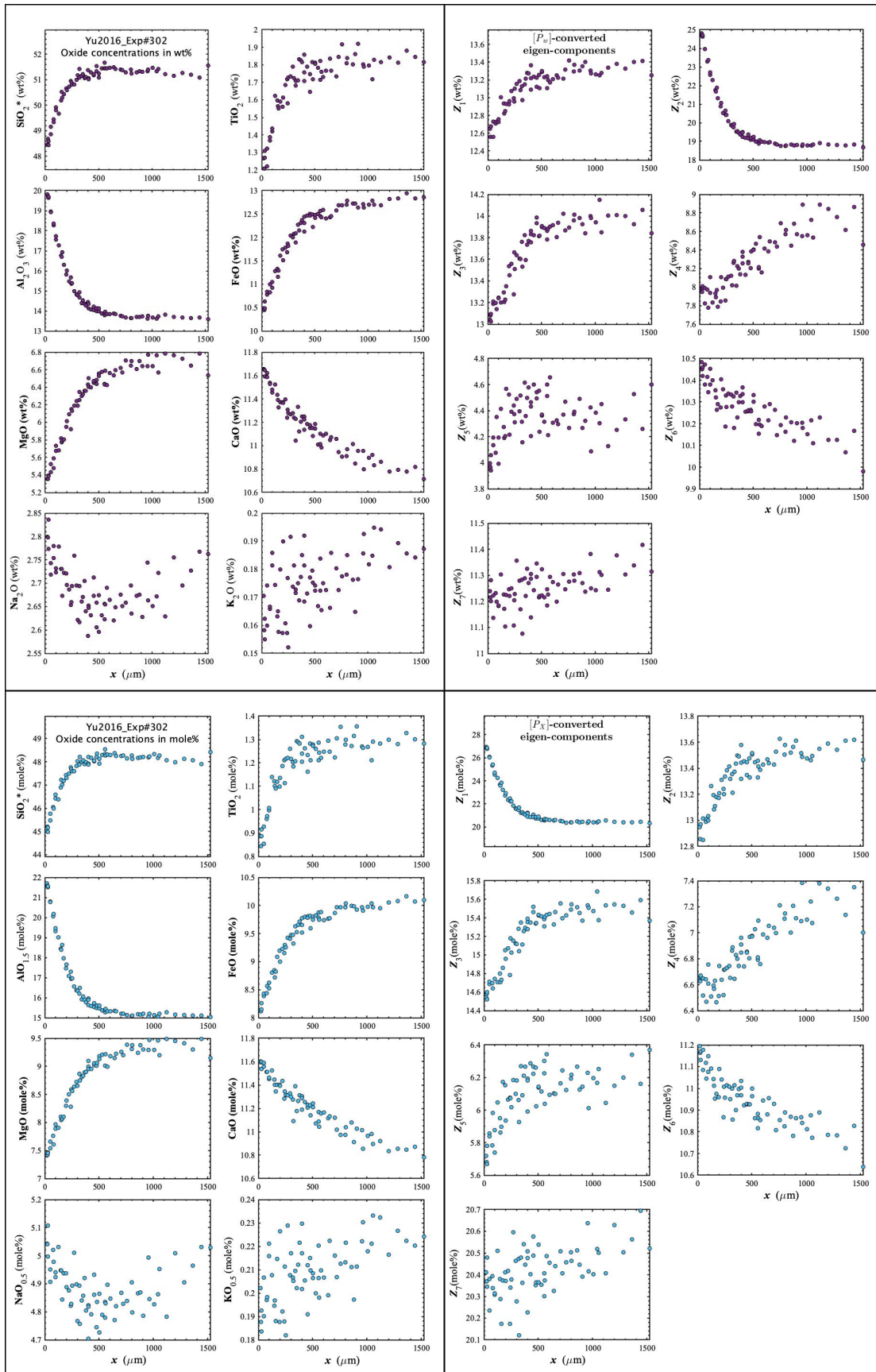
198

Figure D79. Concentration profiles of oxide components in wt% (upper left panel), oxide components in mole% (lower left panel), [P_w]-converted eigen-components (upper right panel), and [P_X]-converted eigen-components (lower right panel) of Yu2016_Exp#211, which is a plagioclase dissolution experiment in basalt (Yu et al., 2016).
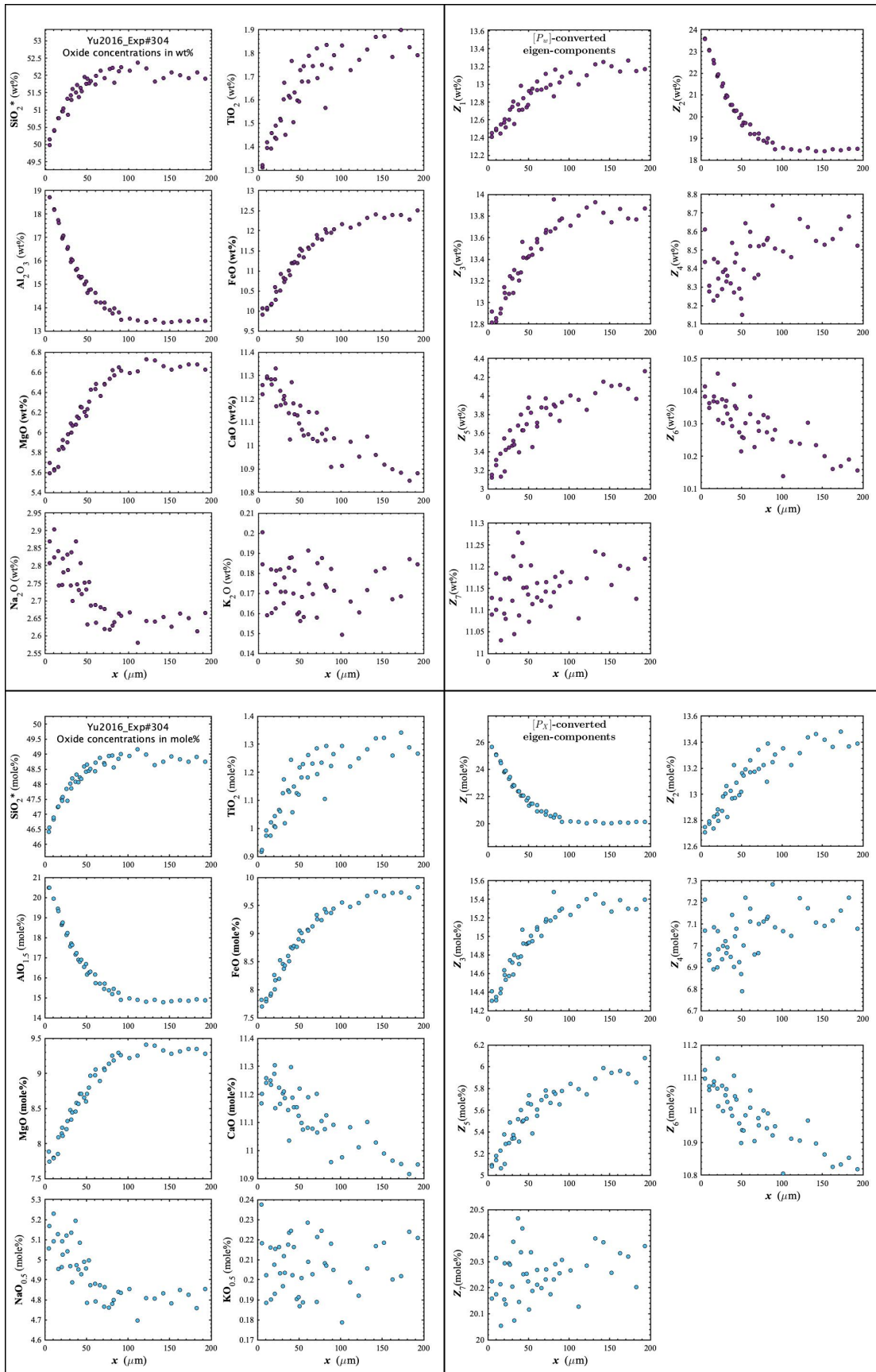
199

Figure D80. Concentration profiles of oxide components in wt% (upper left panel), oxide components in mole% (lower left panel), [P_w]-converted eigen-components (upper right panel), and [P_X]-converted eigen-components (lower right panel) of Yu2016_Exp#212, which is a plagioclase dissolution experiment in basalt (Yu et al., 2016).
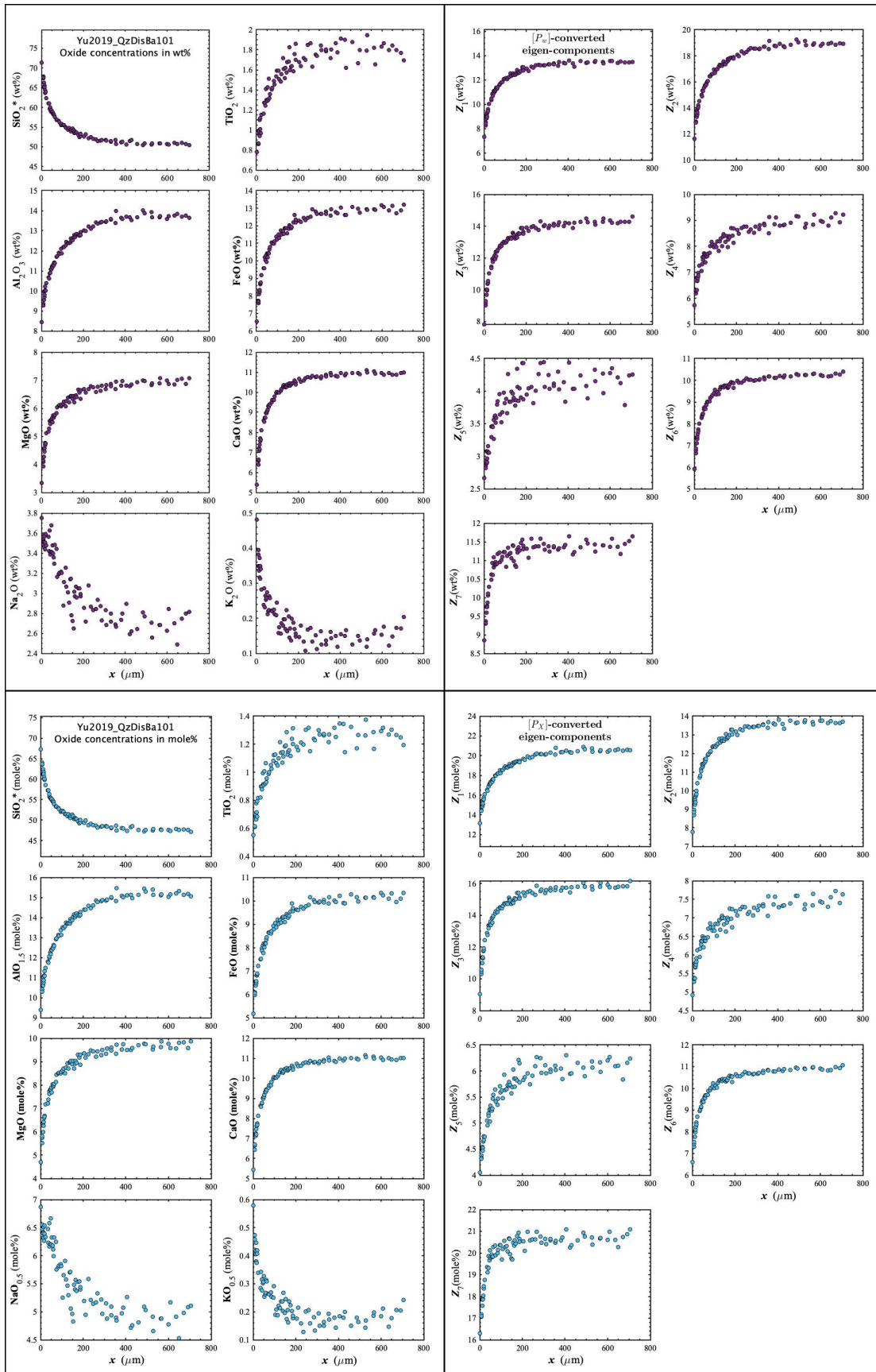
Figure D81. Concentration profiles of oxide components in wt% (upper left panel), oxide components in mole% (lower left panel), [P_w]-converted eigen-components (upper right panel), and [P_X]-converted eigen-components (lower right panel) of Yu2016_Exp#213, which is a plagioclase dissolution experiment in basalt (Yu et al., 2016).
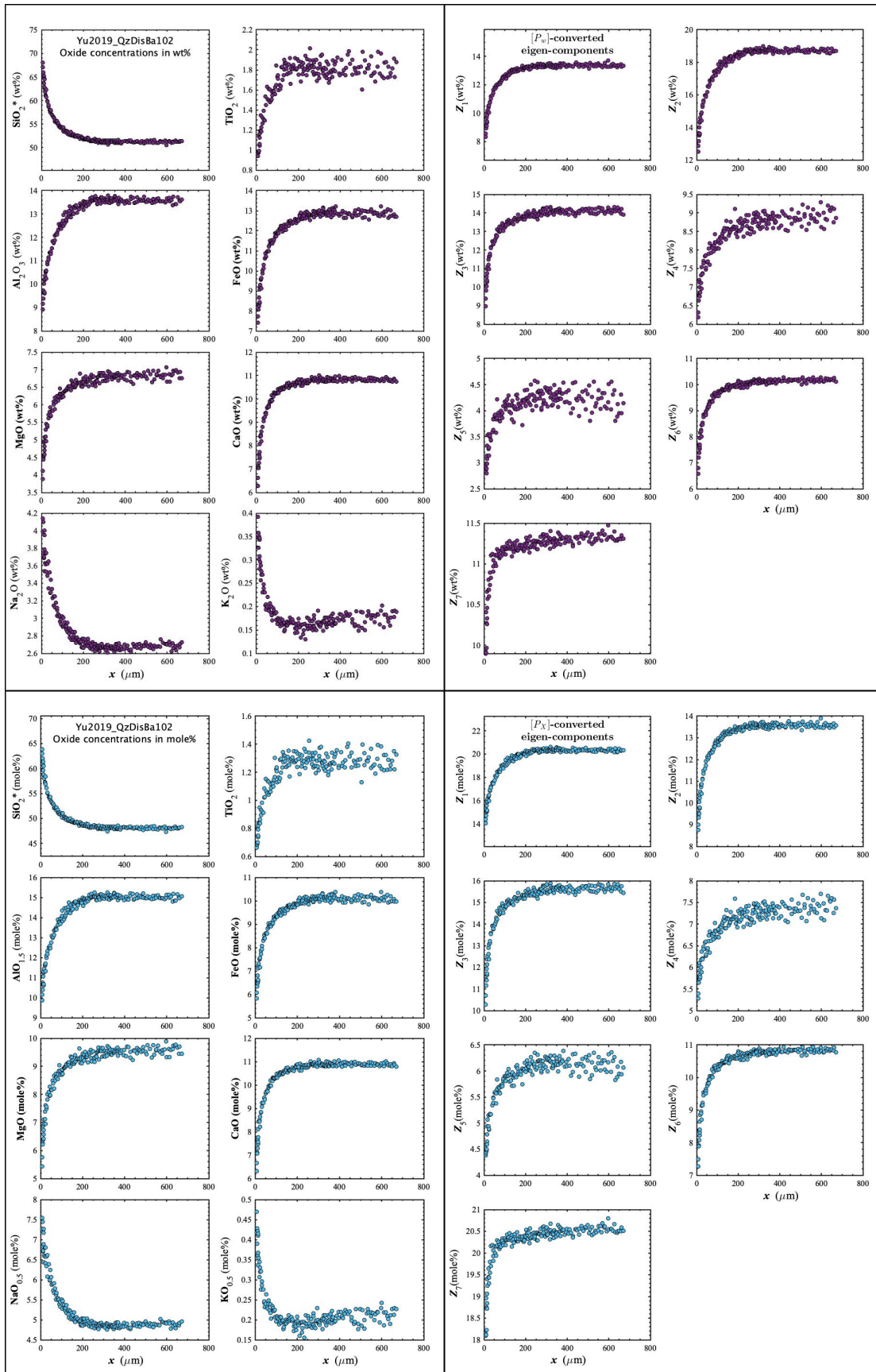
Figure D82. Concentration profiles of oxide components in wt% (upper left panel), oxide components in mole% (lower left panel), [P_w]-converted eigen-components (upper right panel), and [P_X]-converted eigen-components (lower right panel) of Yu2016_Exp#214, which is a plagioclase dissolution experiment in basalt (Yu et al., 2016).
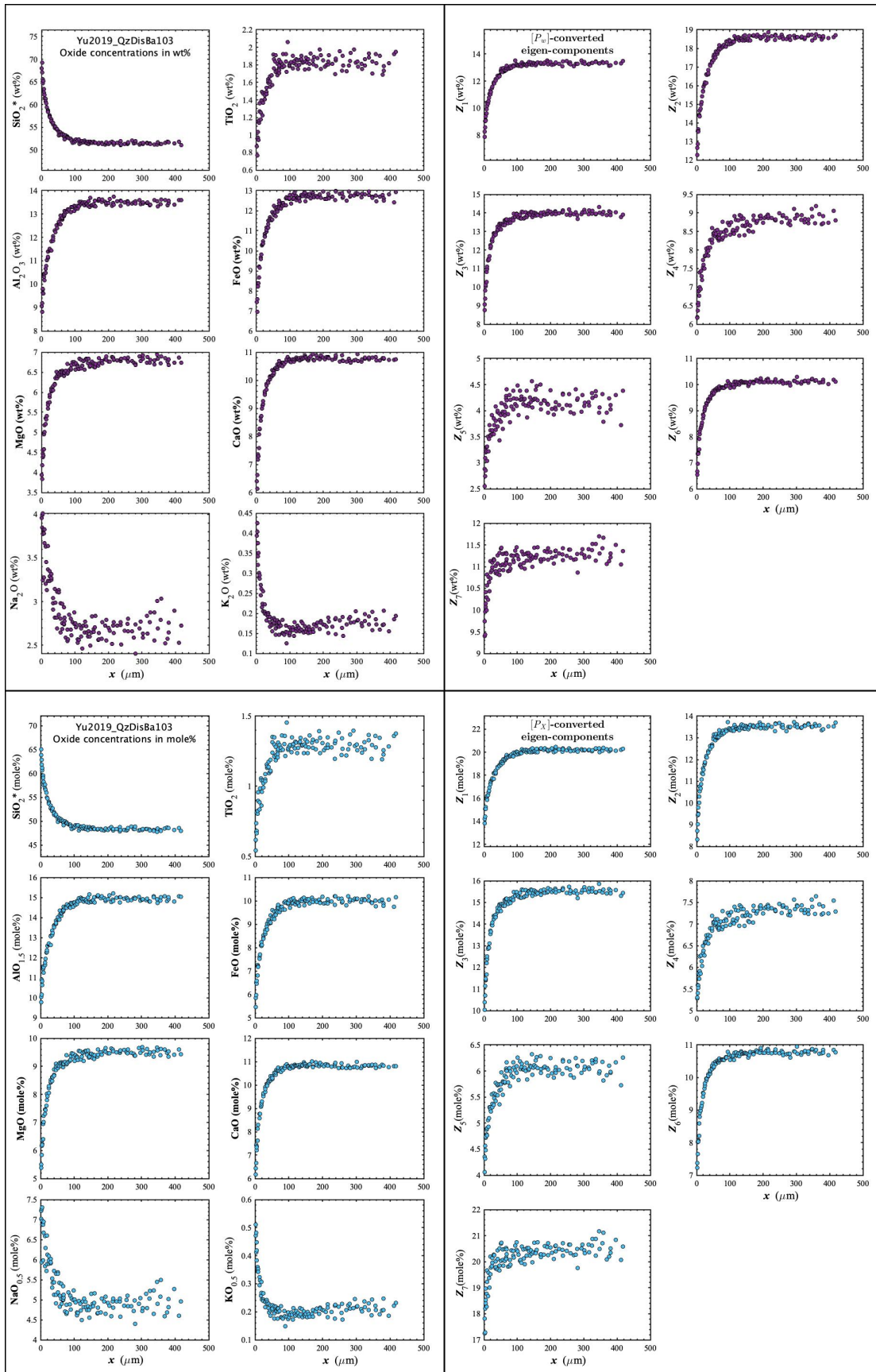
Figure D83. Concentration profiles of oxide components in wt% (upper left panel), oxide components in mole% (lower left panel), [P_w]-converted eigen-components (upper right panel), and [P_X]-converted eigen-components (lower right panel) of Yu2016_Exp#215, which is a plagioclase dissolution experiment in basalt (Yu et al., 2016).
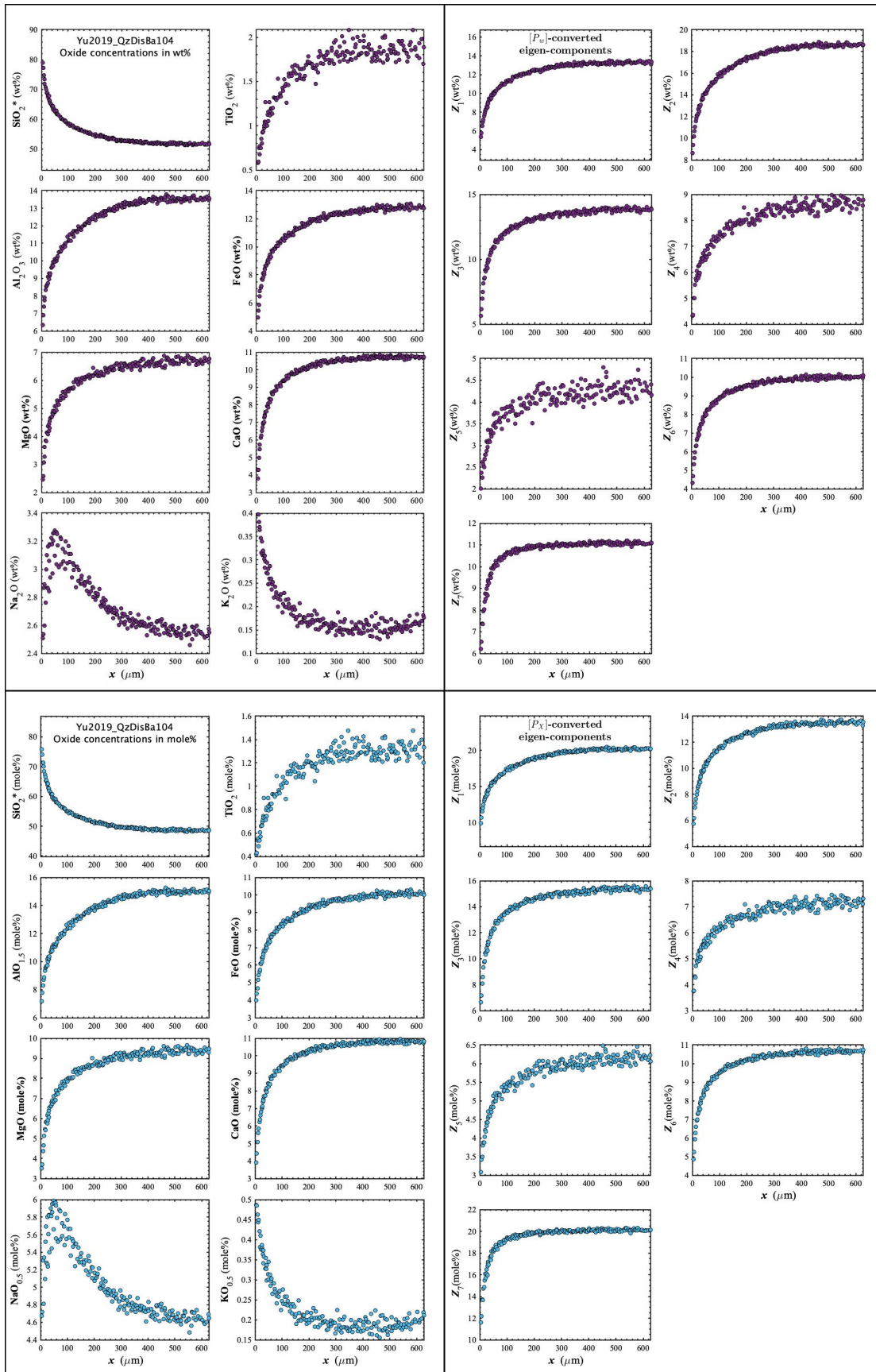
Figure D84. Concentration profiles of oxide components in wt% (upper left panel), oxide components in mole% (lower left panel), $[P_w]$-converted eigen-components (upper right panel), and $[P_X]$-converted eigen-components (lower right panel) of Yu2016_Exp#216, which is a plagioclase dissolution experiment in basalt (Yu et al., 2016).
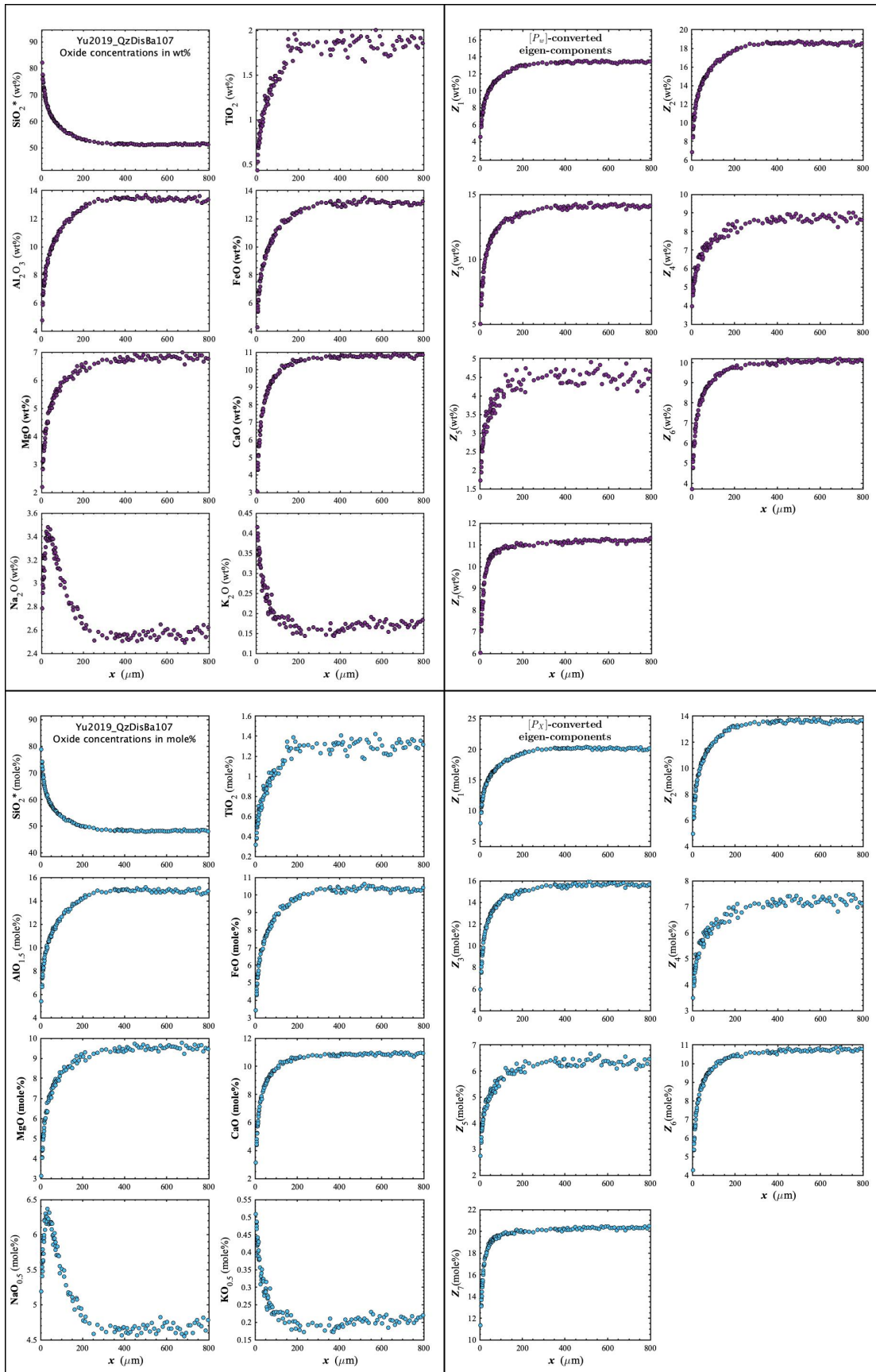
Figure D85. Concentration profiles of oxide components in wt% (upper left panel), oxide components in mole% (lower left panel), [P_w]-converted eigen-components (upper right panel), and [P_X]-converted eigen-components (lower right panel) of Yu2016_Exp#228, which is a plagioclase dissolution experiment in basalt (Yu et al., 2016).
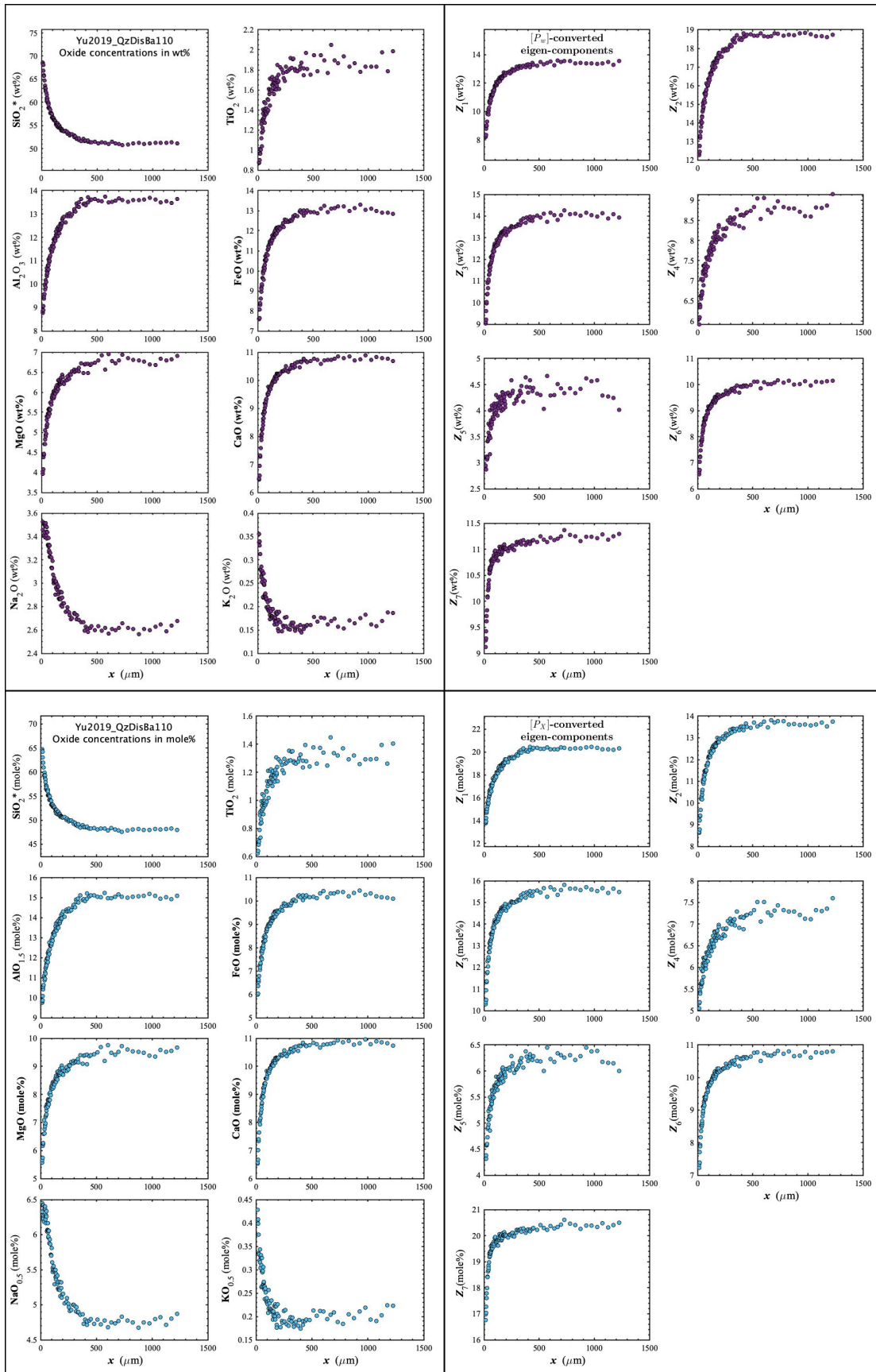
Figure D86. Concentration profiles of oxide components in wt% (upper left panel), oxide components in mole% (lower left panel), $[P_w]$-converted eigen-components (upper right panel), and $[P_X]$-converted eigen-components (lower right panel) of Yu2016_Exp#233, which is a plagioclase dissolution experiment in basalt (Yu et al., 2016).
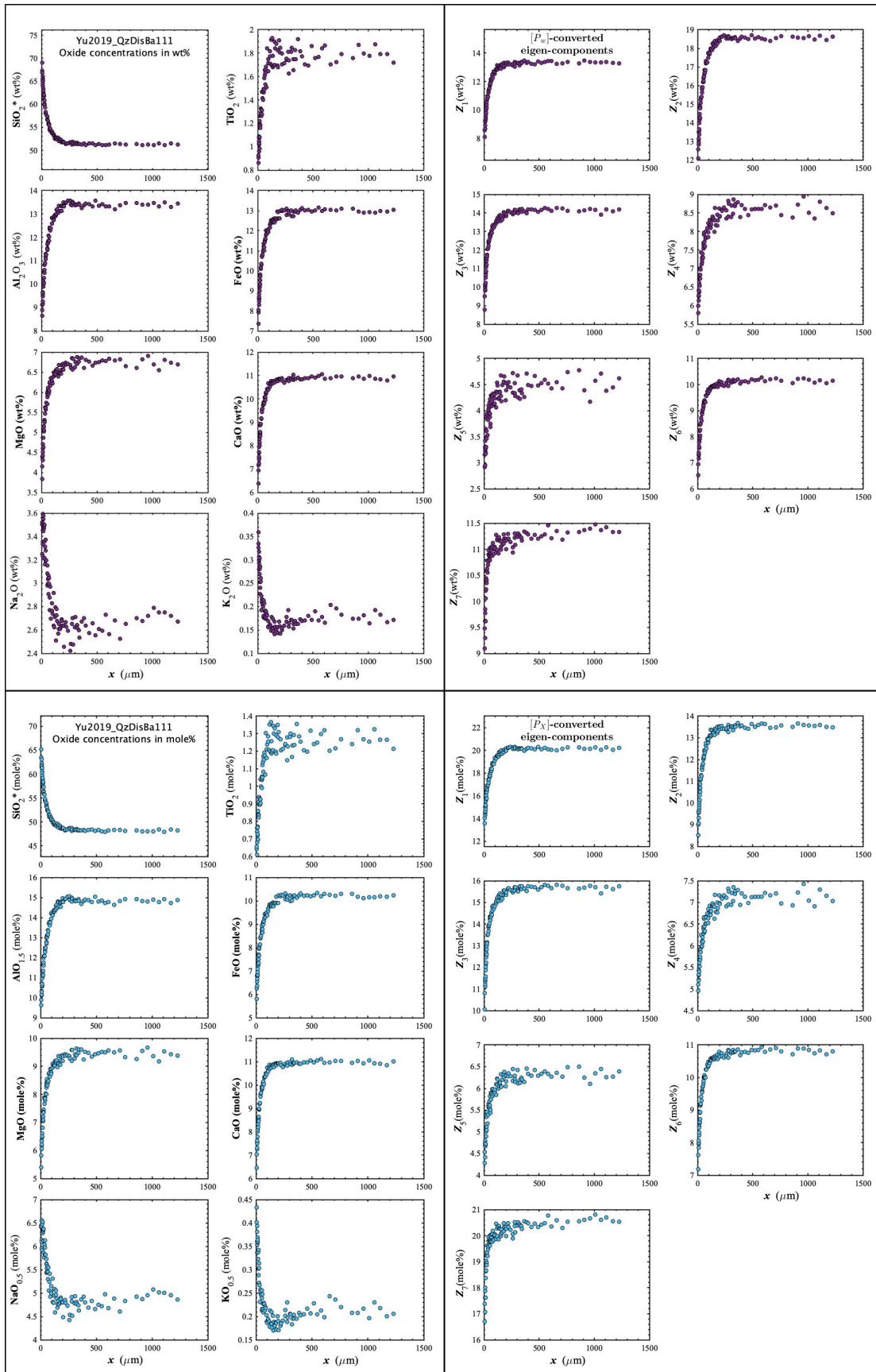
Figure D87. Concentration profiles of oxide components in wt% (upper left panel), oxide components in mole% (lower left panel), $[P_w]$-converted eigen-components (upper right panel), and $[P_X]$-converted eigen-components (lower right panel) of Yu2016_Exp#230, which is a plagioclase dissolution experiment in basalt (Yu et al., 2016).

207

Figure D88. Concentration profiles of oxide components in wt% (upper left panel), oxide components in mole% (lower left panel), $[P_w]$-converted eigen-components (upper right panel), and $[P_X]$-converted eigen-components (lower right panel) of Yu2016_Exp#301, which is a plagioclase dissolution experiment in basalt (Yu et al., 2016).
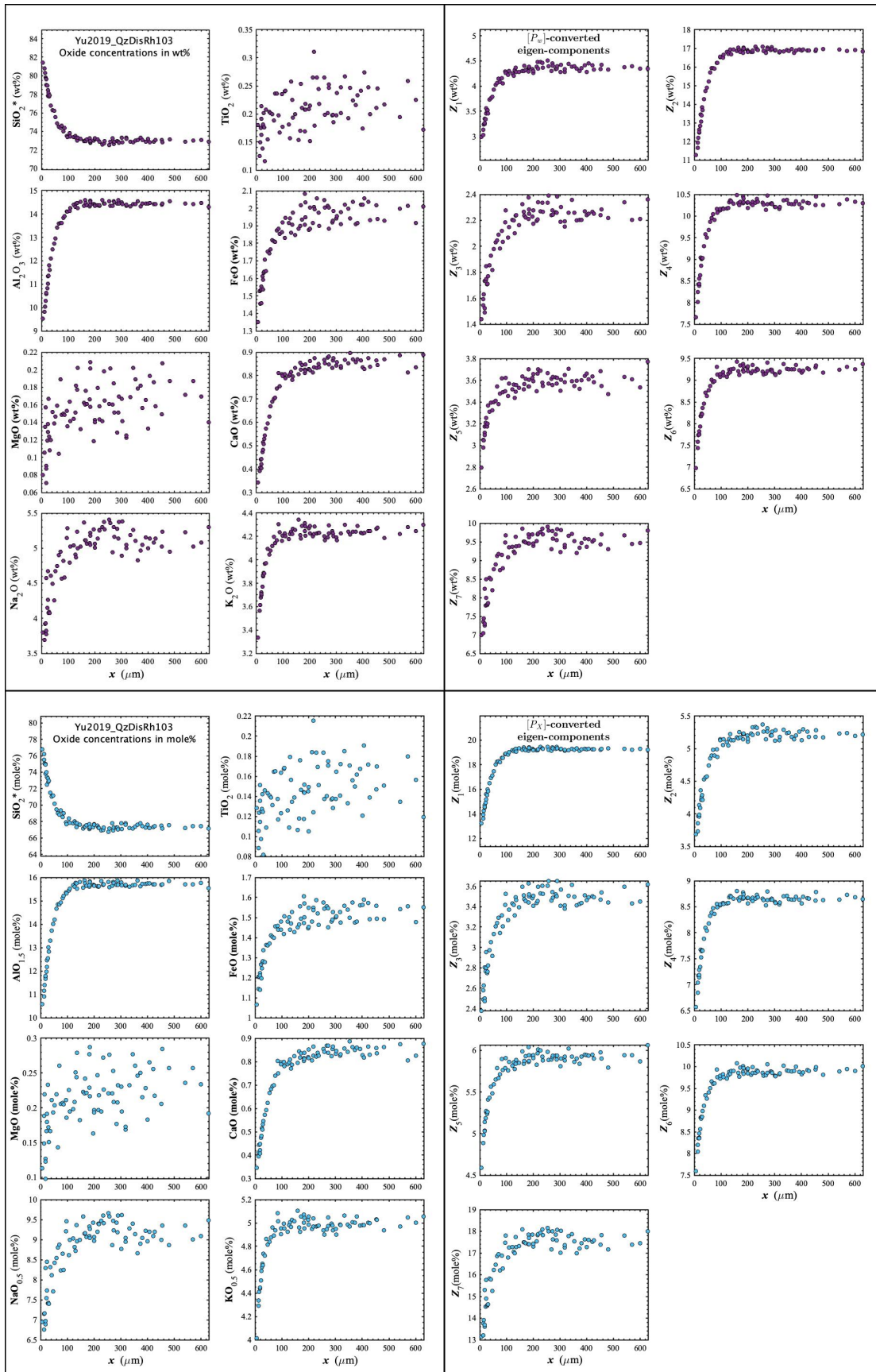
Figure D89. Concentration profiles of oxide components in wt% (upper left panel), oxide components in mole% (lower left panel), [P_w]-converted eigen-components (upper right panel), and [P_X]-converted eigen-components (lower right panel) of Yu2016_Exp#302, which is a plagioclase dissolution experiment in basalt (Yu et al., 2016).
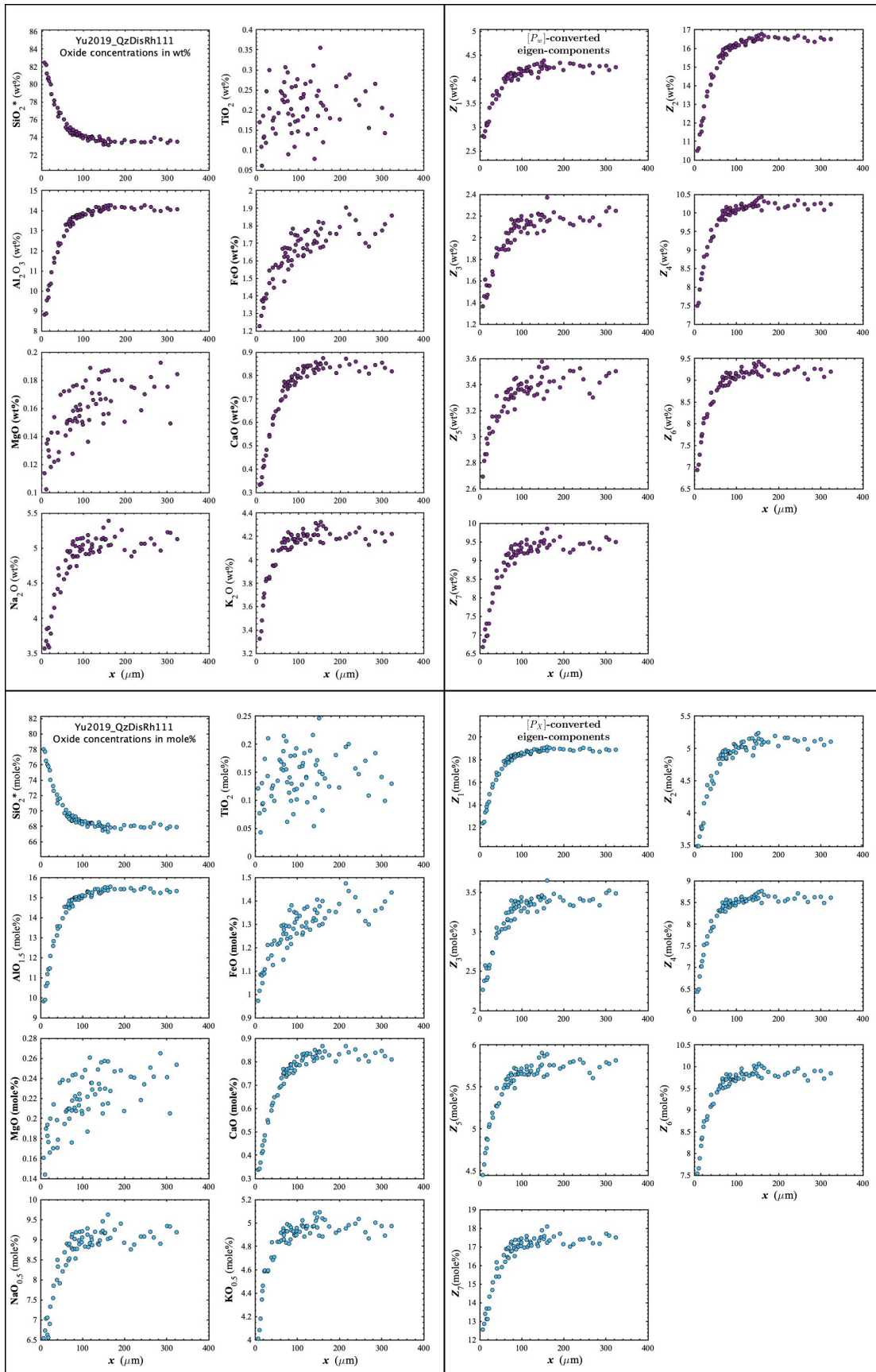
Figure D90. Concentration profiles of oxide components in wt% (upper left panel), oxide components in mole% (lower left panel), [P_w]-converted eigen-components (upper right panel), and [P_X]-converted eigen-components (lower right panel) of Yu2016_Exp#304, which is a plagioclase dissolution experiment in basalt (Yu et al., 2016).
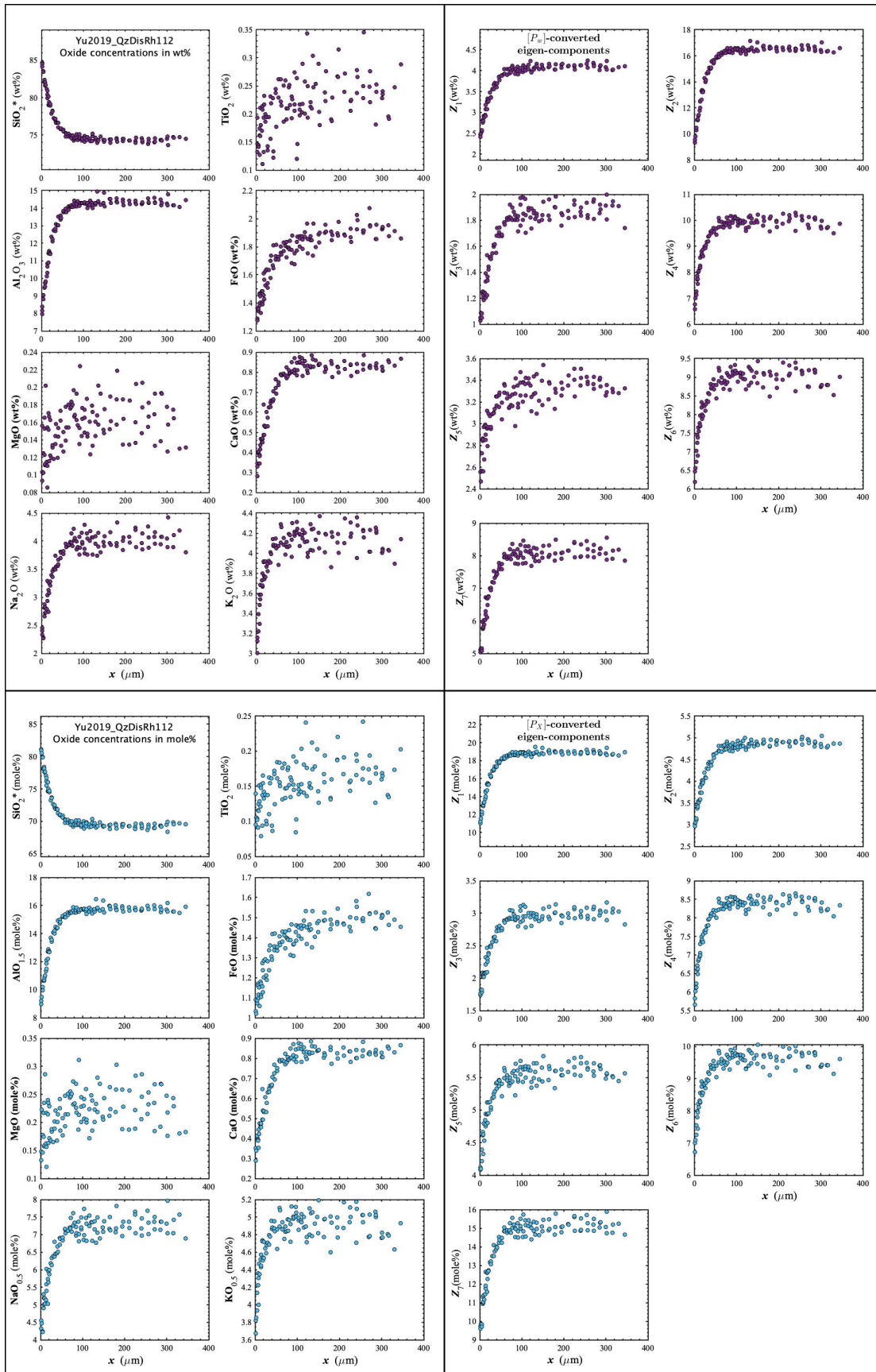
Figure D91. Concentration profiles of oxide components in wt% (upper left panel), oxide components in mole% (lower left panel), $[P_w]$-converted eigen-components (upper right panel), and $[P_X]$-converted eigen-components (lower right panel) of Yu2019_QzDisBa#101, which is a quartz dissolution experiment in basalt (Yu et al., 2019).
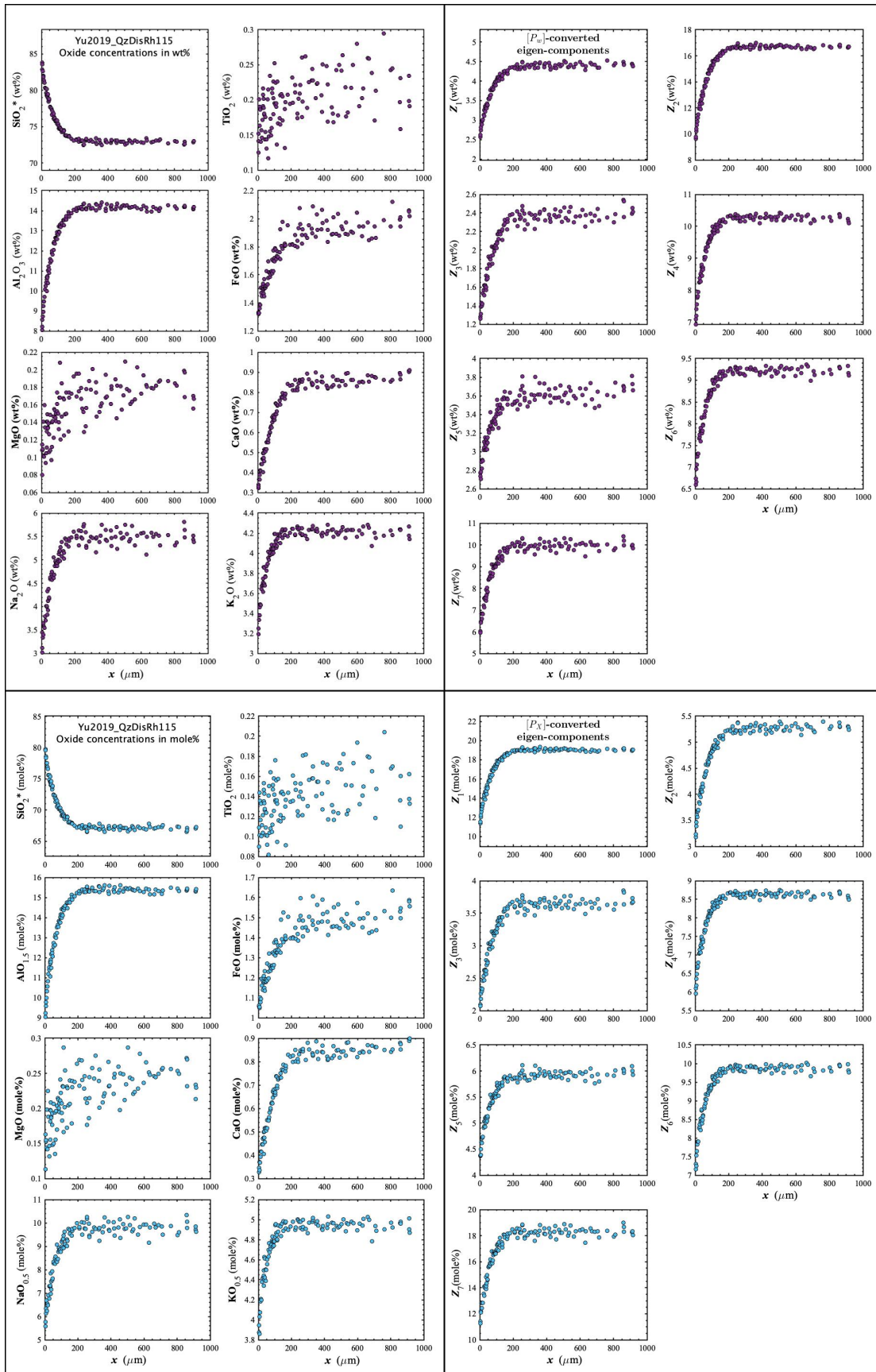
Figure D92. Concentration profiles of oxide components in wt% (upper left panel), oxide components in mole% (lower left panel), $[P_w]$-converted eigen-components (upper right panel), and $[P_X]$-converted eigen-components (lower right panel) of Yu2019_QzDisBa#102, which is a quartz dissolution experiment in basalt (Yu et al., 2019).
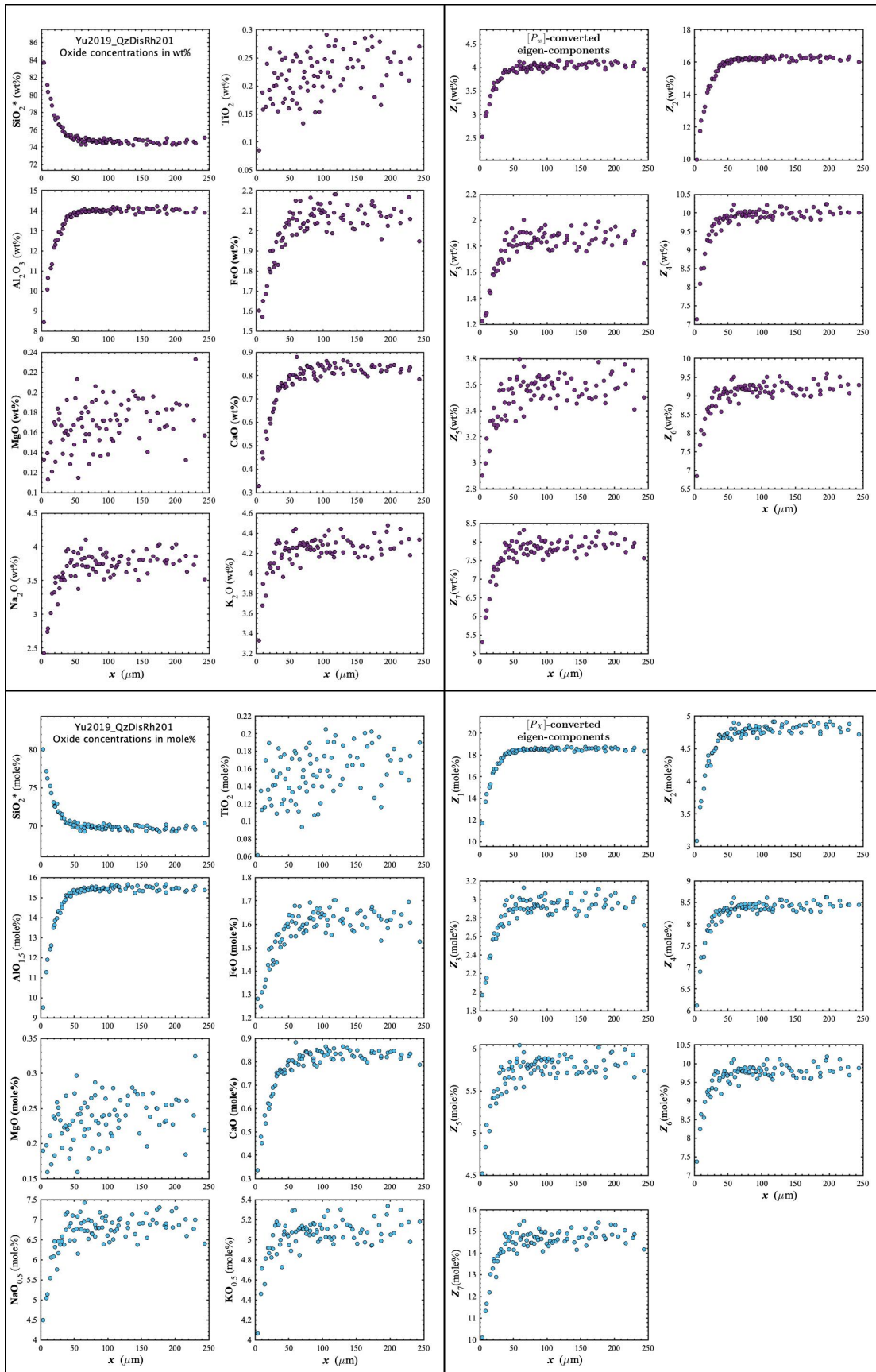
212

Figure D93. Concentration profiles of oxide components in wt% (upper left panel), oxide components in mole% (lower left panel), [P_w]-converted eigen-components (upper right panel), and [P_X]-converted eigen-components (lower right panel) of Yu2019_QzDisBa#103, which is a quartz dissolution experiment in basalt (Yu et al., 2019).
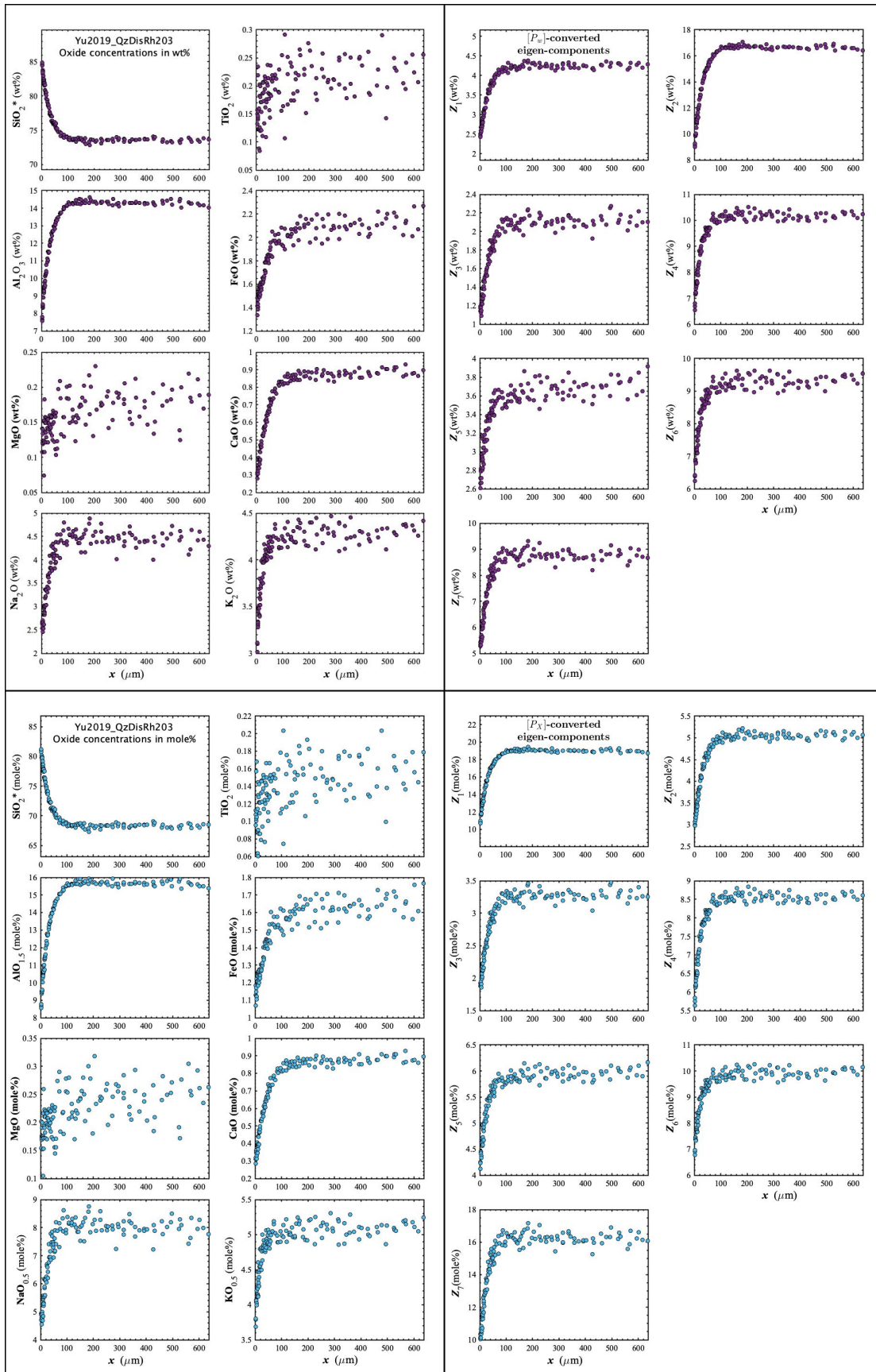
213

Figure D94. Concentration profiles of oxide components in wt% (upper left panel), oxide components in mole% (lower left panel), $[P_w]$-converted eigen-components (upper right panel), and $[P_X]$-converted eigen-components (lower right panel) of Yu2019_QzDisBa#104, which is a quartz dissolution experiment in basalt (Yu et al., 2019).
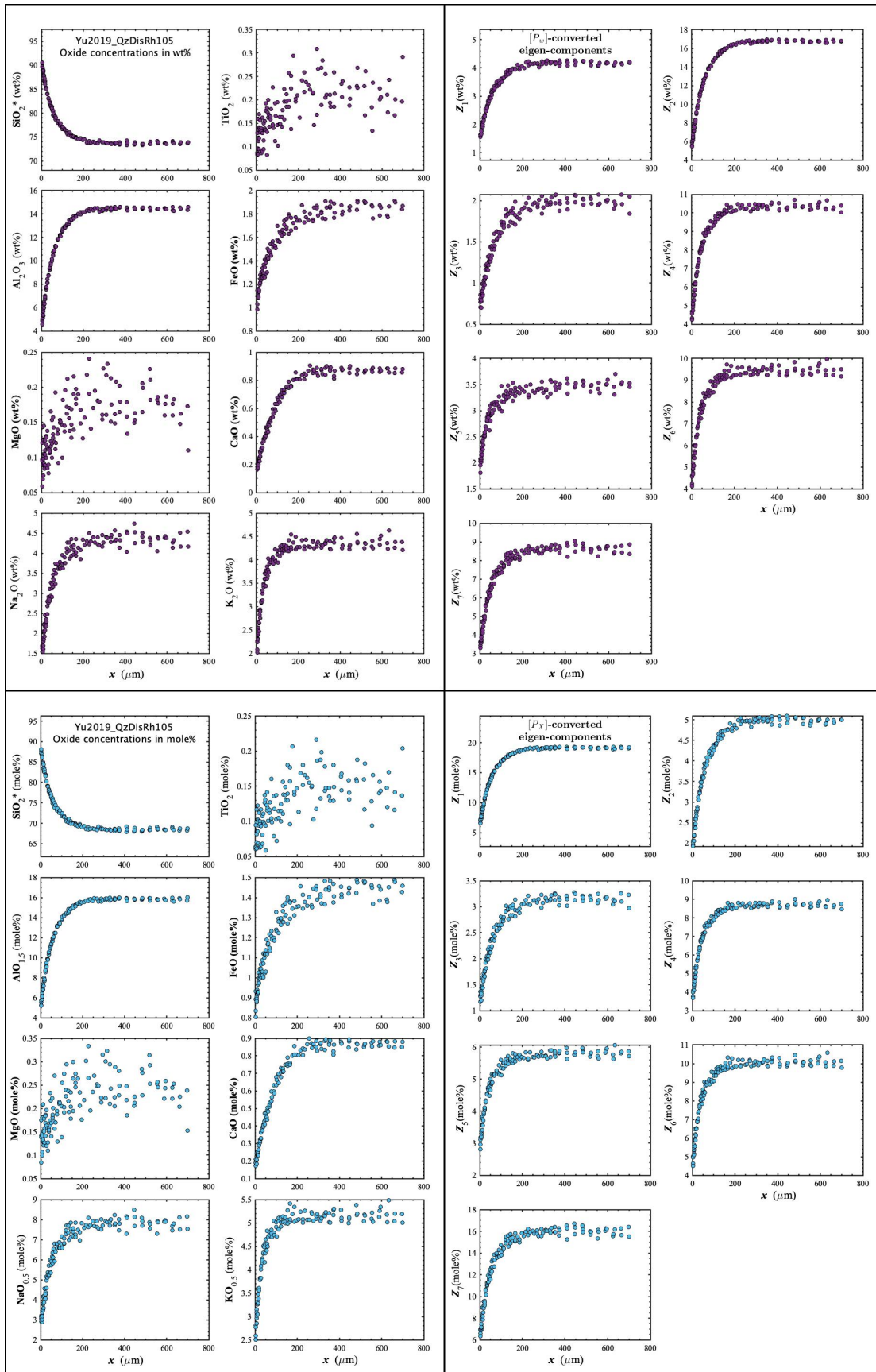
Figure D95. Concentration profiles of oxide components in wt% (upper left panel), oxide components in mole% (lower left panel), [P_w]-converted eigen-components (upper right panel), and [P_X]-converted eigen-components (lower right panel) of Yu2019_QzDisBa#107, which is a quartz dissolution experiment in basalt (Yu et al., 2019).

Figure D96. Concentration profiles of oxide components in wt% (upper left panel), oxide components in mole% (lower left panel), [P_w]-converted eigen-components (upper right panel), and [P_X]-converted eigen-components (lower right panel) of Yu2019_QzDisBa#110, which is a quartz dissolution experiment in basalt (Yu et al., 2019).
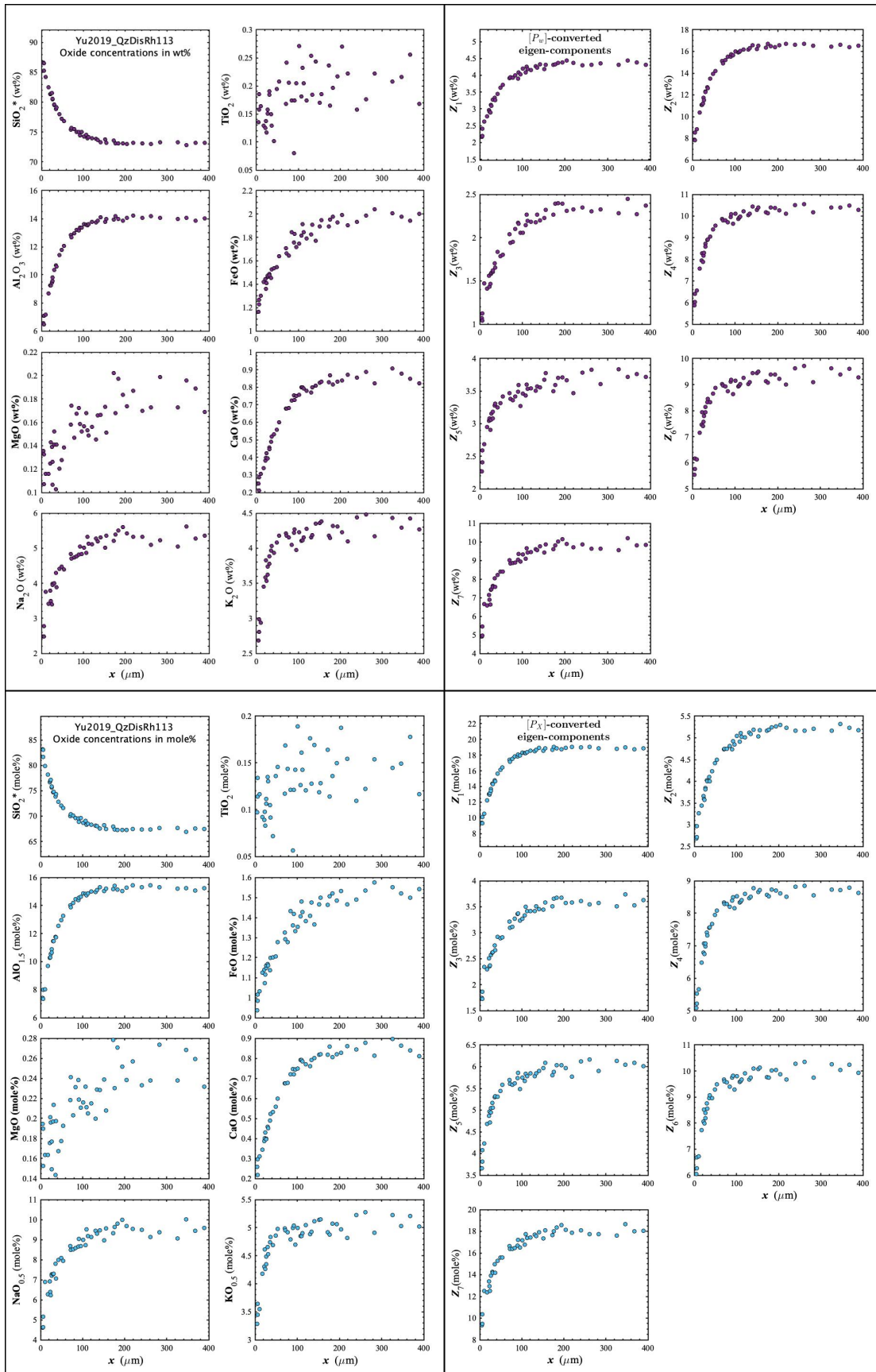
216

Figure D97. Concentration profiles of oxide components in wt% (upper left panel), oxide components in mole% (lower left panel), $[P_w]$-converted eigen-components (upper right panel), and $[P_X]$-converted eigen-components (lower right panel) of Yu2019_QzDisBa#111, which is a quartz dissolution experiment in basalt (Yu et al., 2019).

217

Figure D98. Concentration profiles of oxide components in wt% (upper left panel), oxide components in mole% (lower left panel), [P_w]-converted eigen-components (upper right panel), and [P_X]-converted eigen-components (lower right panel) of Yu2019_QzDisRh#103, which is a quartz dissolution experiment in rhyolite (Yu et al., 2019).
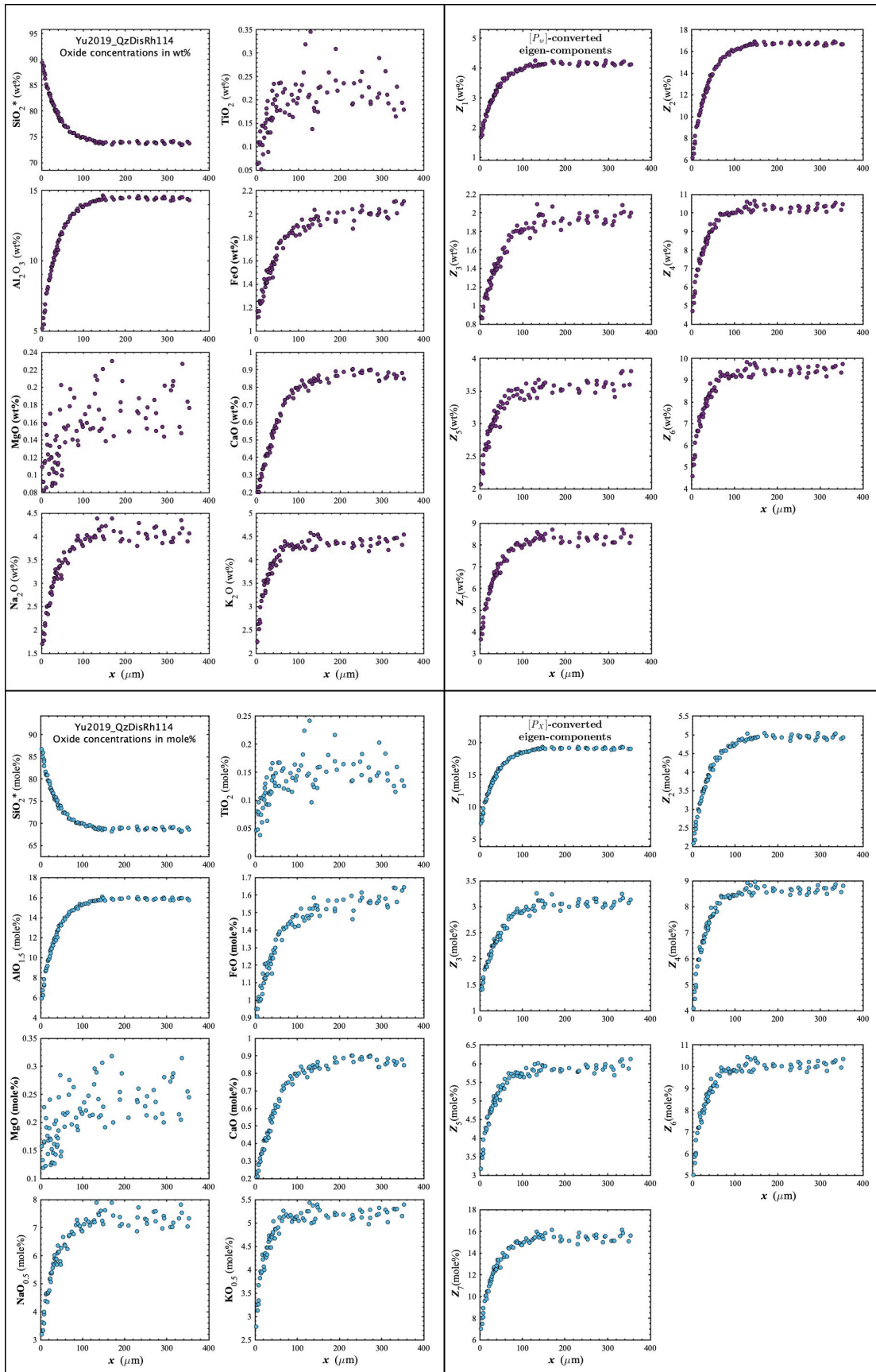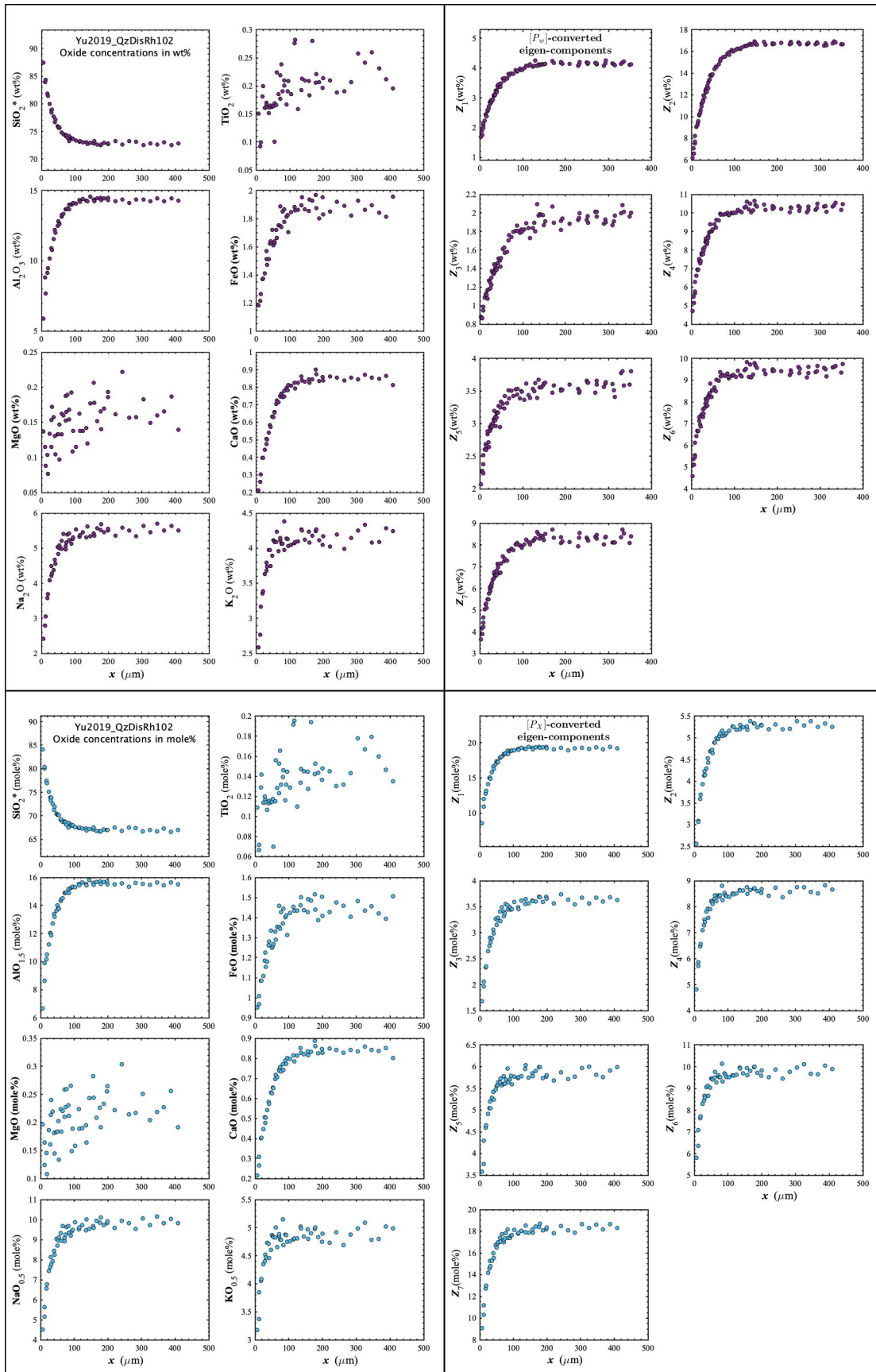
218

Figure D99. Concentration profiles of oxide components in wt% (upper left panel), oxide components in mole% (lower left panel), [P_w]-converted eigen-components (upper right panel), and [P_X]-converted eigen-components (lower right panel) of Yu2019_QzDisRh#111, which is a quartz dissolution experiment in rhyolite (Yu et al., 2019).
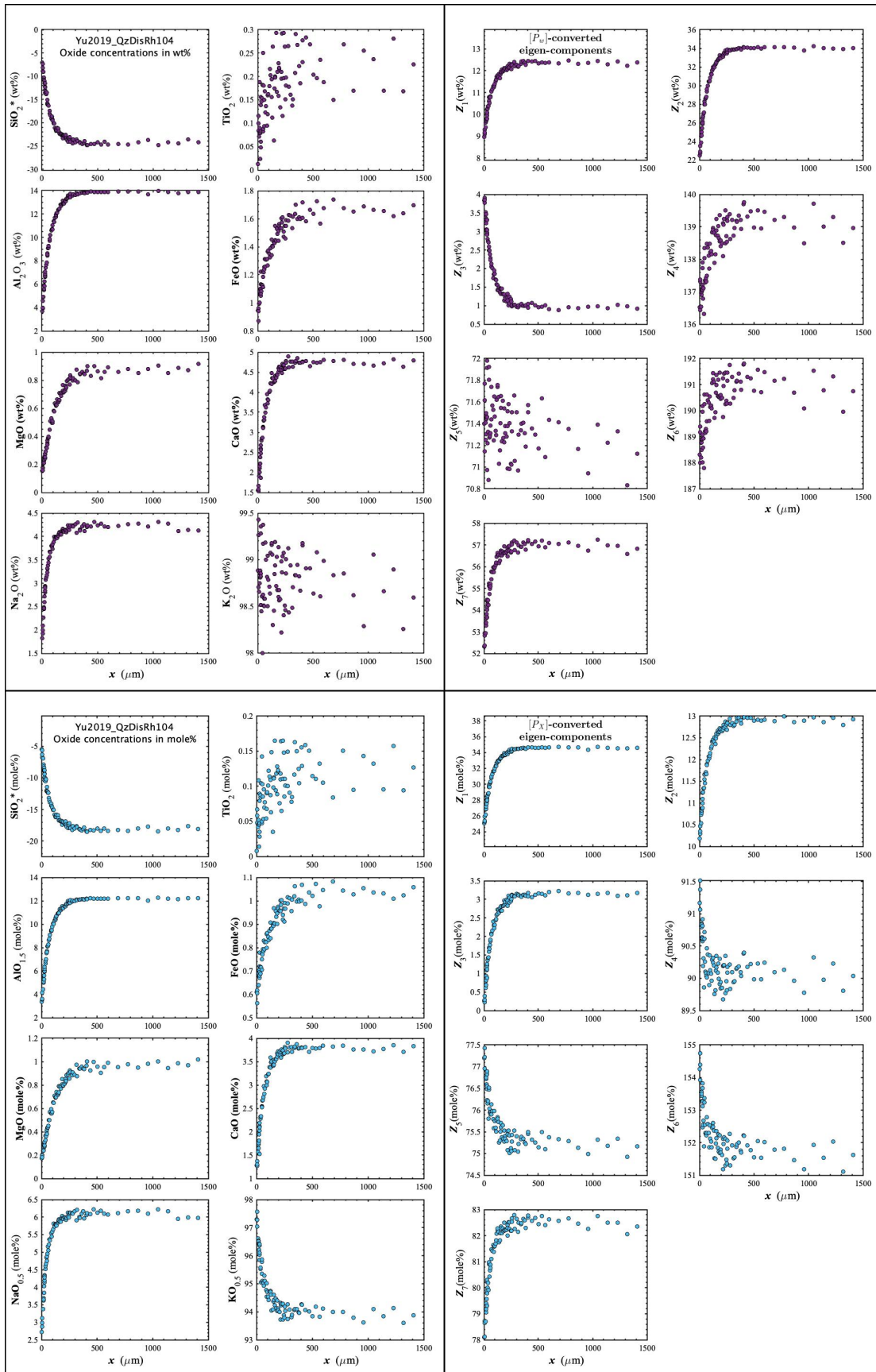
219

Figure D100. Concentration profiles of oxide components in wt% (upper left panel), oxide components in mole% (lower left panel), [P_w]-converted eigen-components (upper right panel), and [P_X]-converted eigen-components (lower right panel) of Yu2019_QzDisRh#112, which is a quartz dissolution experiment in rhyolite (Yu et al., 2019).

Figure D101. Concentration profiles of oxide components in wt% (upper left panel), oxide components in mole% (lower left panel), $[P_w]$-converted eigen-components (upper right panel), and $[P_X]$-converted eigen-components (lower right panel) of Yu2019_QzDisRh#115, which is a quartz dissolution experiment in rhyolite (Yu et al., 2019).
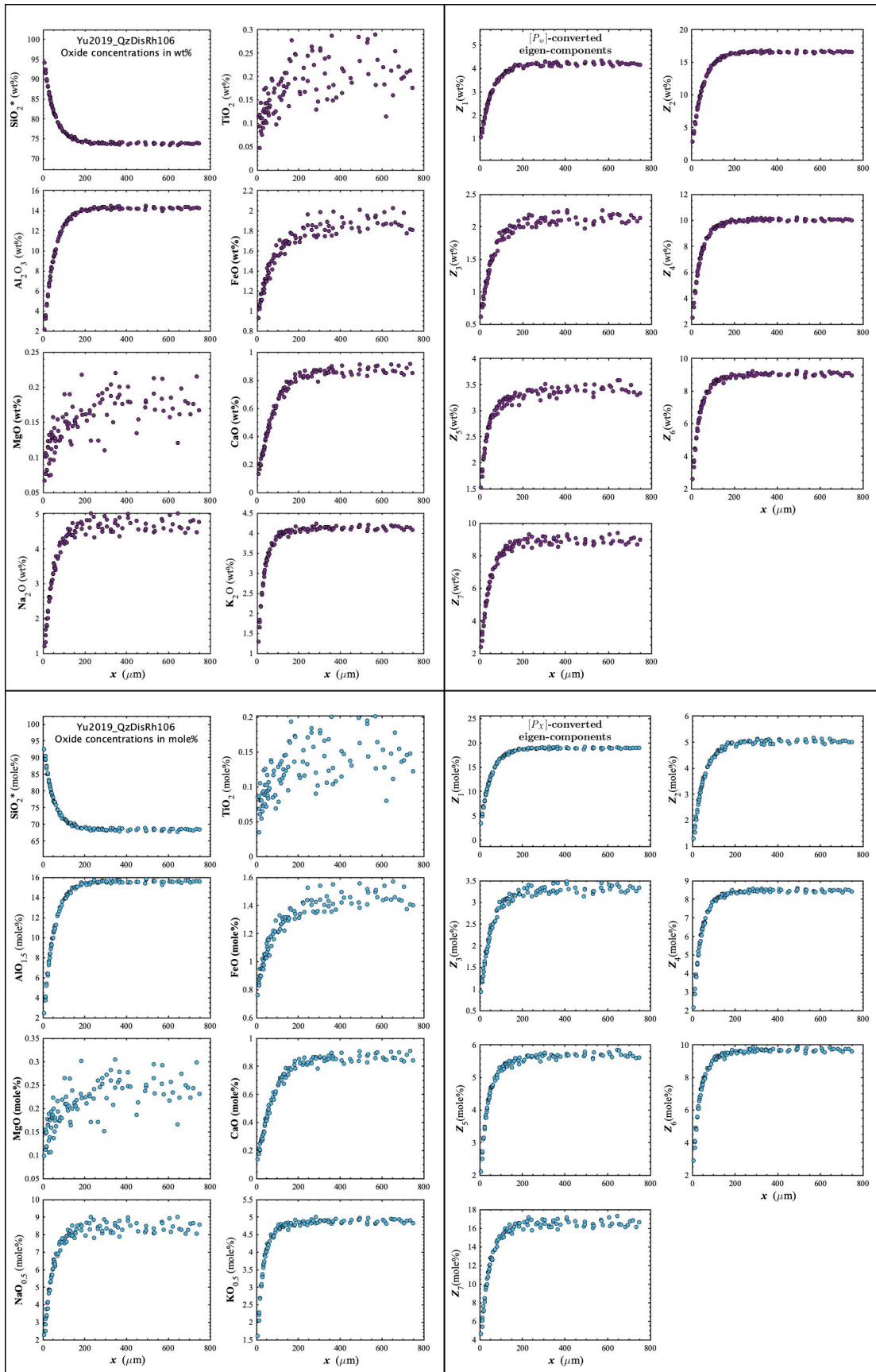
221

Figure D102. Concentration profiles of oxide components in wt% (upper left panel), oxide components in mole% (lower left panel), $[P_w]$-converted eigen-components (upper right panel), and $[P_X]$-converted eigen-components (lower right panel) of Yu2019_QzDisRh#201, which is a quartz dissolution experiment in rhyolite (Yu et al., 2019).
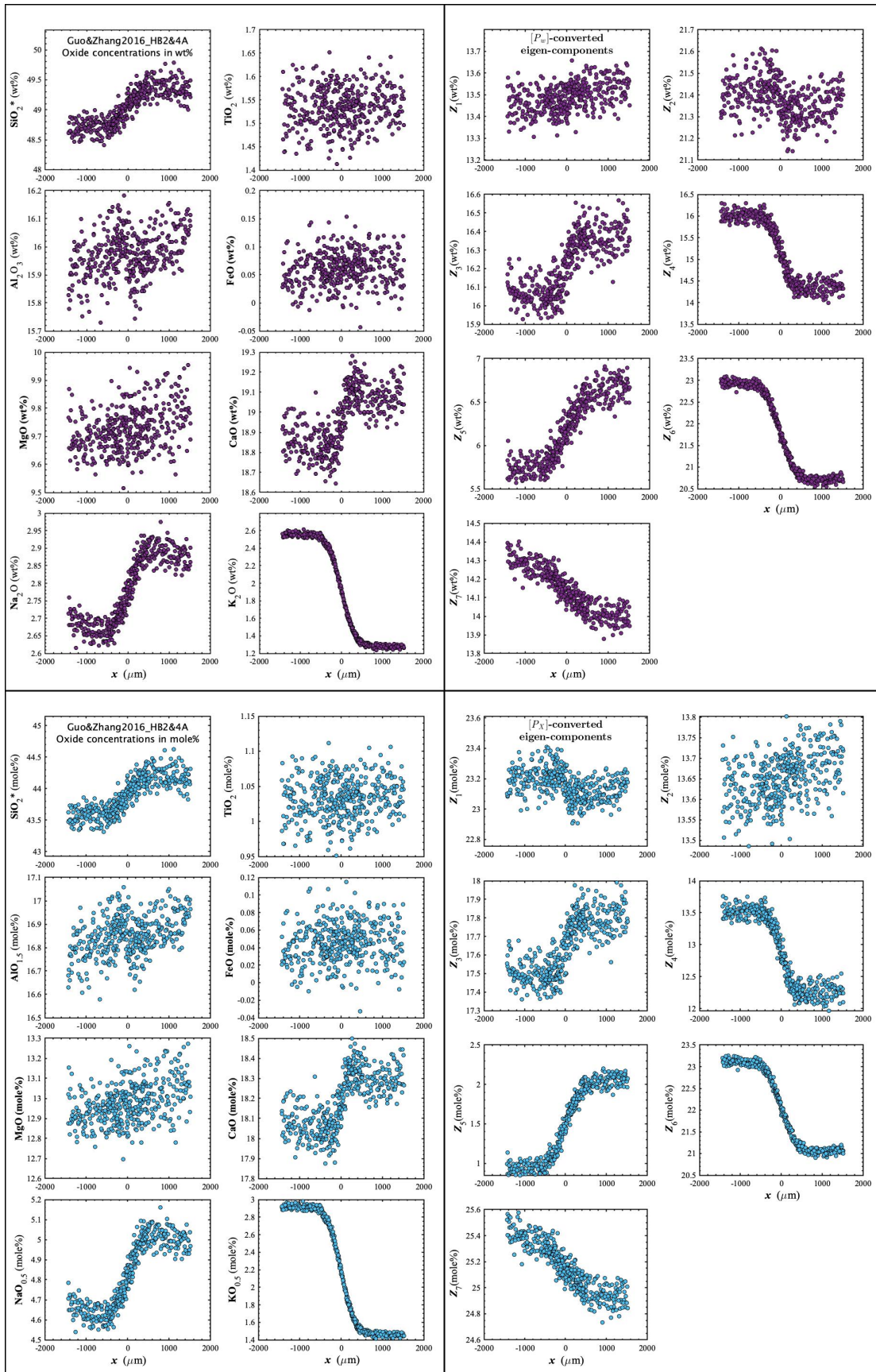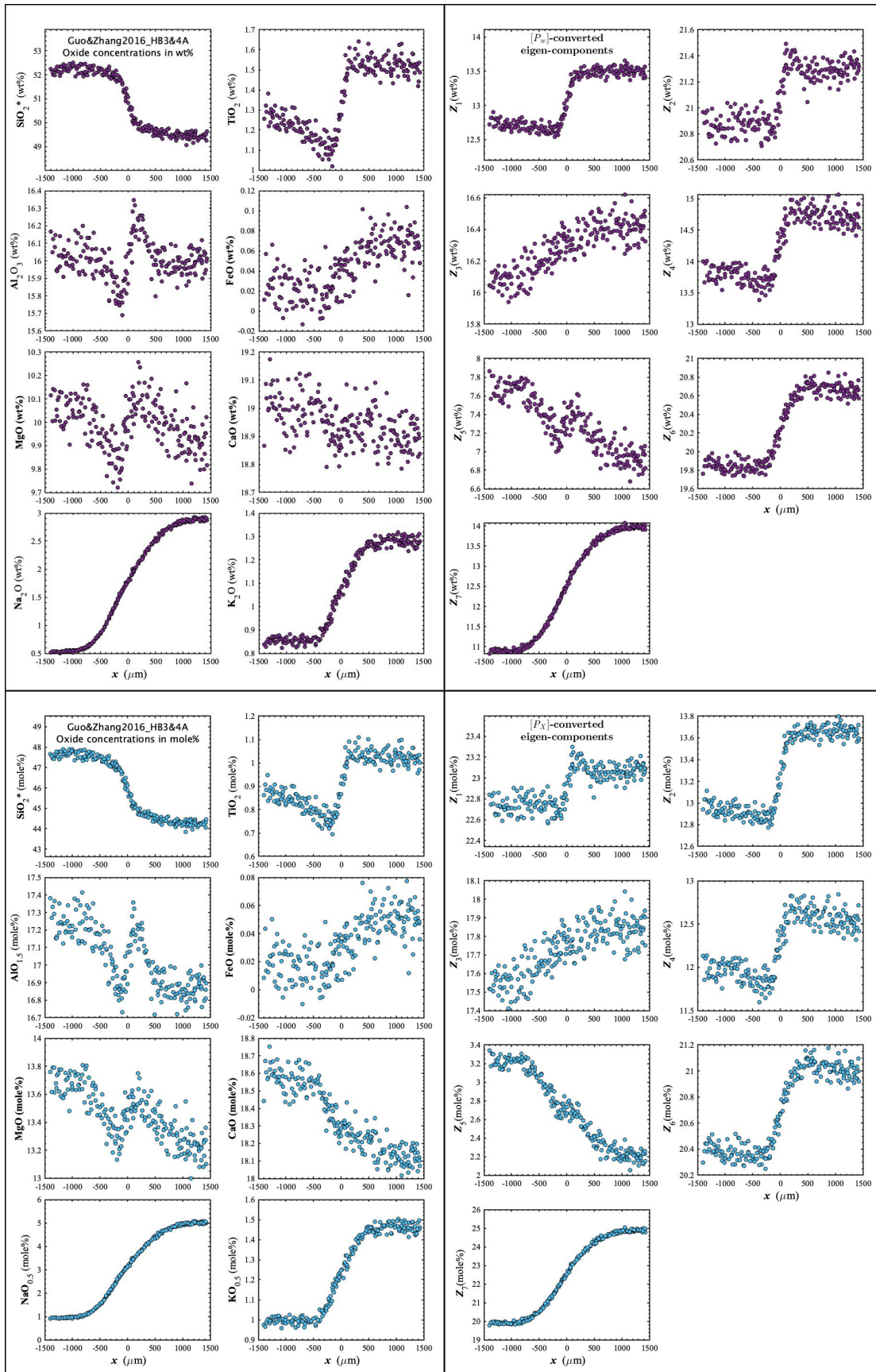
Figure D103. Concentration profiles of oxide components in wt% (upper left panel), oxide components in mole% (lower left panel), [P_w]-converted eigen-components (upper right panel), and [P_X]-converted eigen-components (lower right panel) of Yu2019_QzDisRh#203, which is a quartz dissolution experiment in rhyolite (Yu et al., 2019).

223

Figure D104. Concentration profiles of oxide components in wt% (upper left panel), oxide components in mole% (lower left panel), [P_w]-converted eigen-components (upper right panel), and [P_X]-converted eigen-components (lower right panel) of Yu2019_QzDisRh#105, which is a quartz dissolution experiment in rhyolite (Yu et al., 2019).
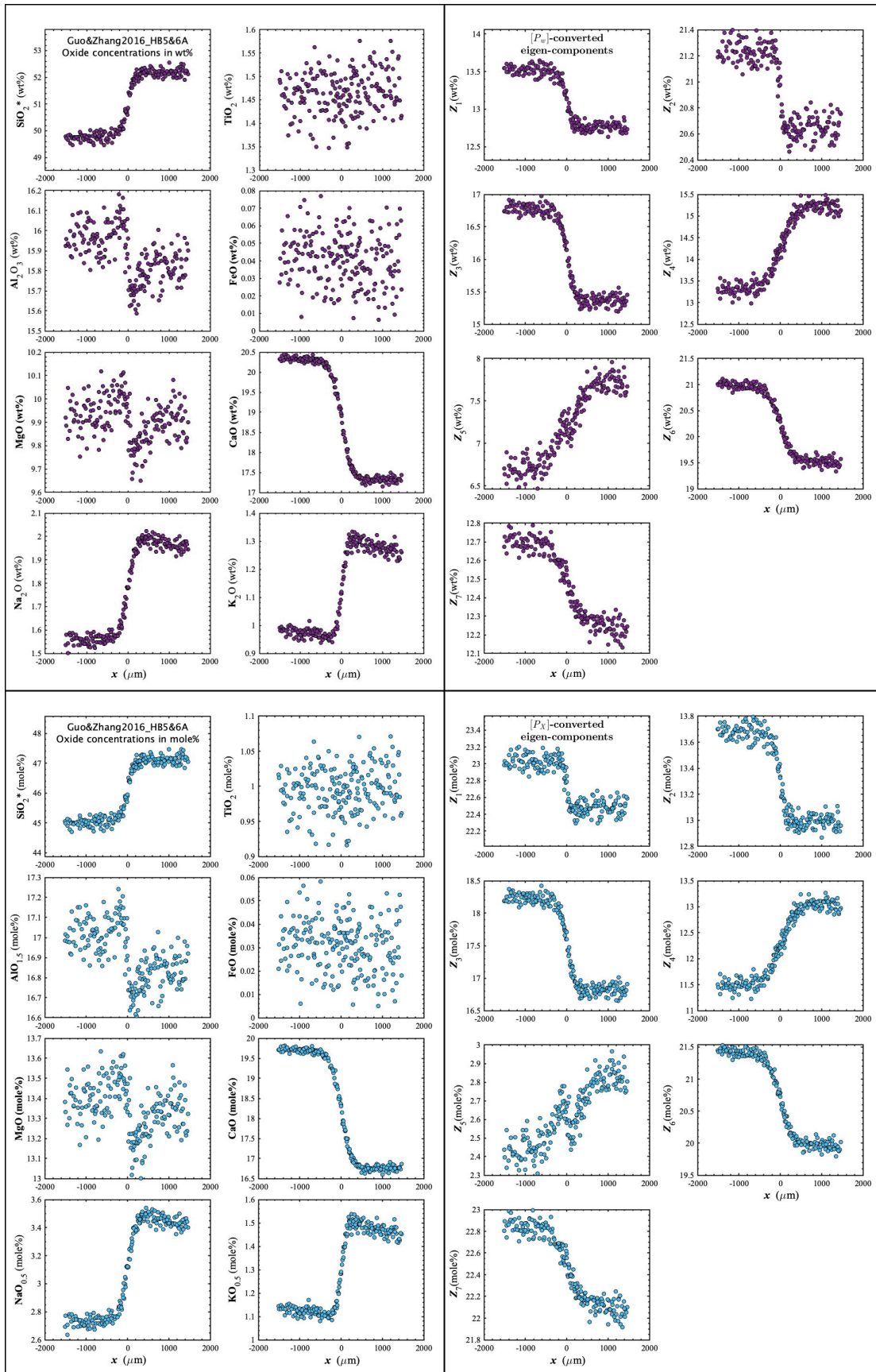
Figure D105. Concentration profiles of oxide components in wt% (upper left panel), oxide components in mole% (lower left panel), $[P_w]$-converted eigen-components (upper right panel), and $[P_X]$-converted eigen-components (lower right panel) of Yu2019_QzDisRh#113, which is a quartz dissolution experiment in rhyolite (Yu et al., 2019).
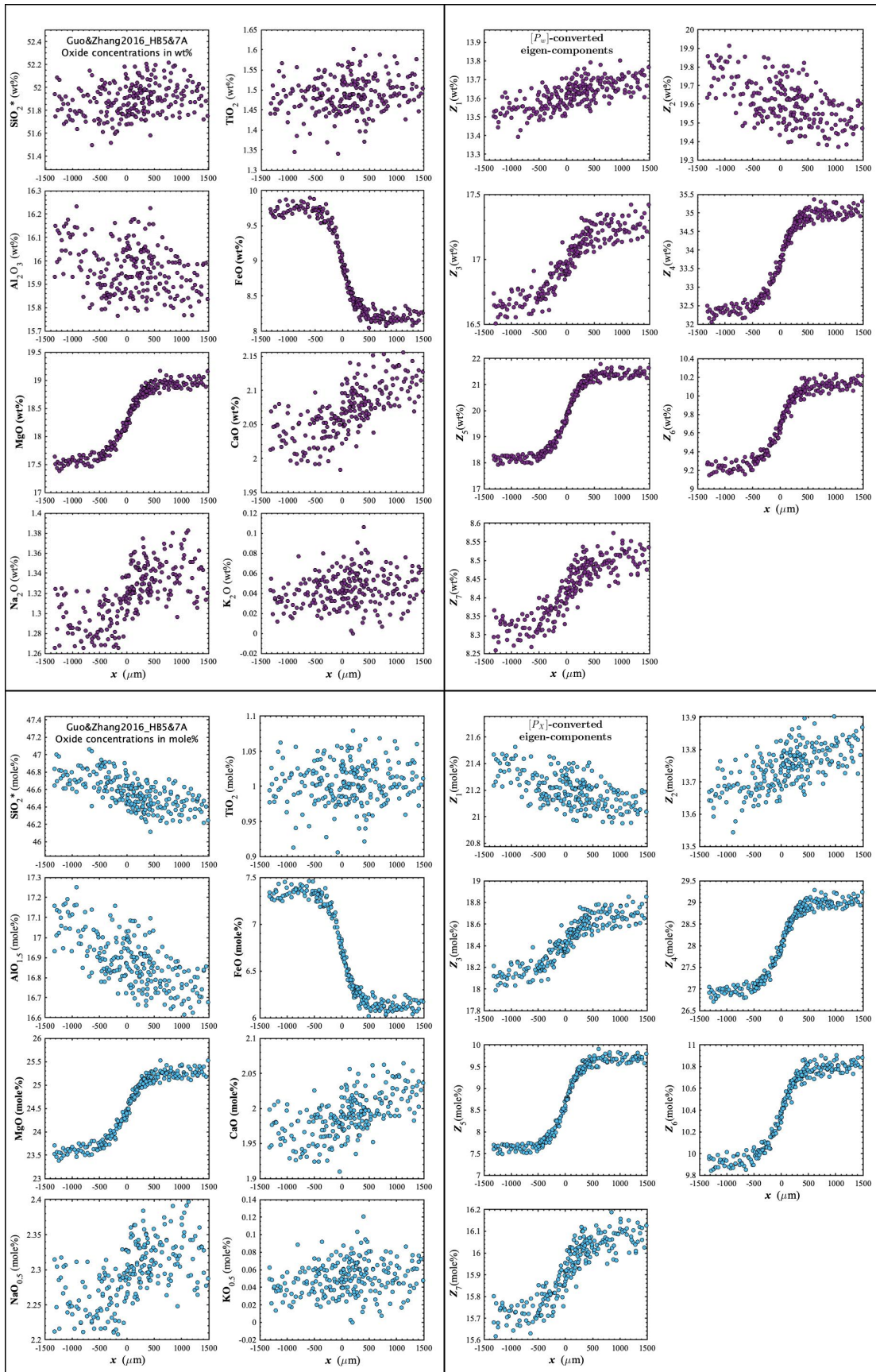
225

Figure D106. Concentration profiles of oxide components in wt% (upper left panel), oxide components in mole% (lower left panel), [P_w]-converted eigen-components (upper right panel), and [P_X]-converted eigen-components (lower right panel) of Yu2019_QzDisRh#114, which is a quartz dissolution experiment in rhyolite (Yu et al., 2019).
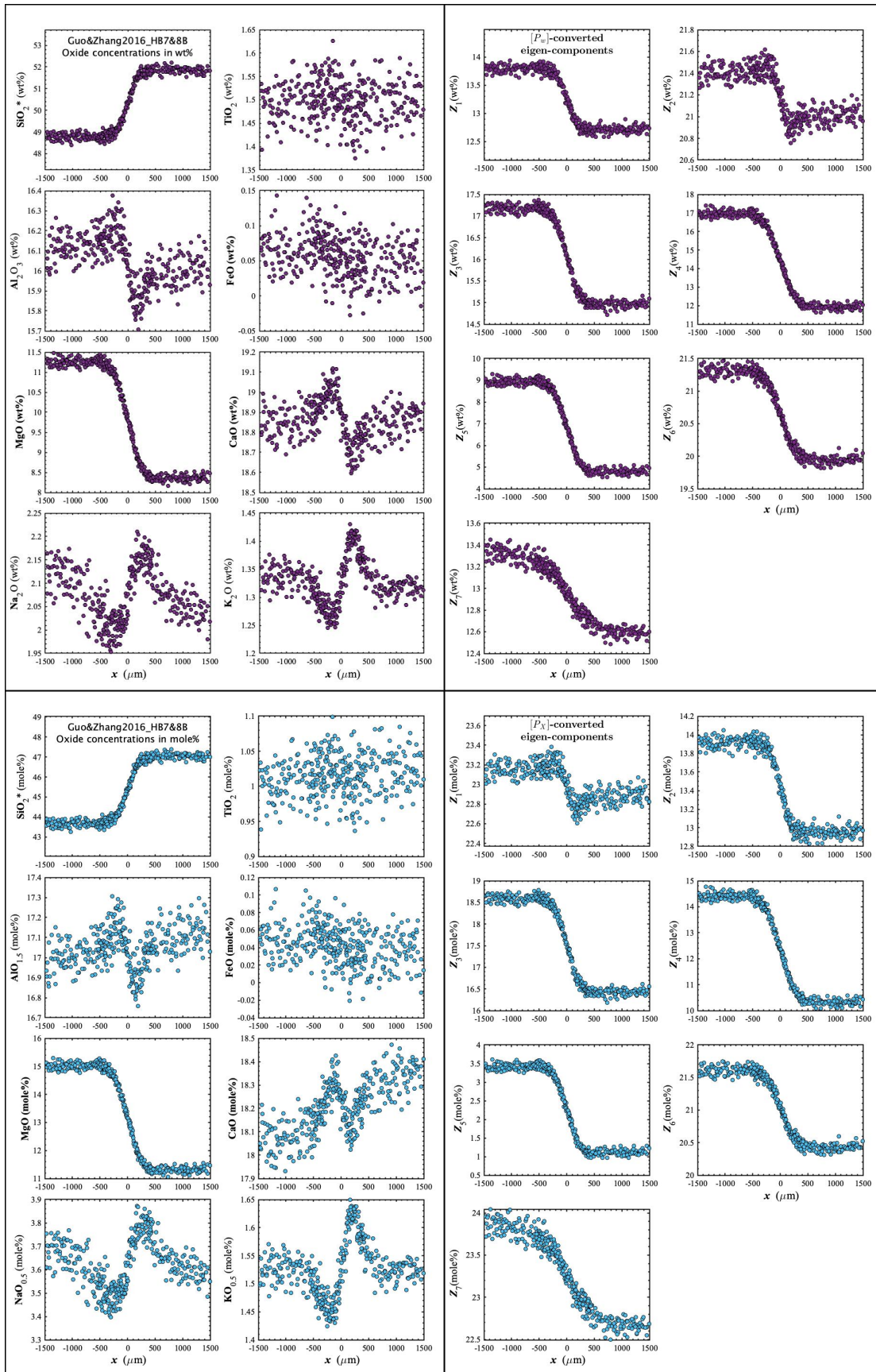
226

Figure D107. Concentration profiles of oxide components in wt% (upper left panel), oxide components in mole% (lower left panel), [P_w]-converted eigen-components (upper right panel), and [P_X]-converted eigen-components (lower right panel) of Yu2019_QzDisRh#102, which is a quartz dissolution experiment in rhyolite (Yu et al., 2019).
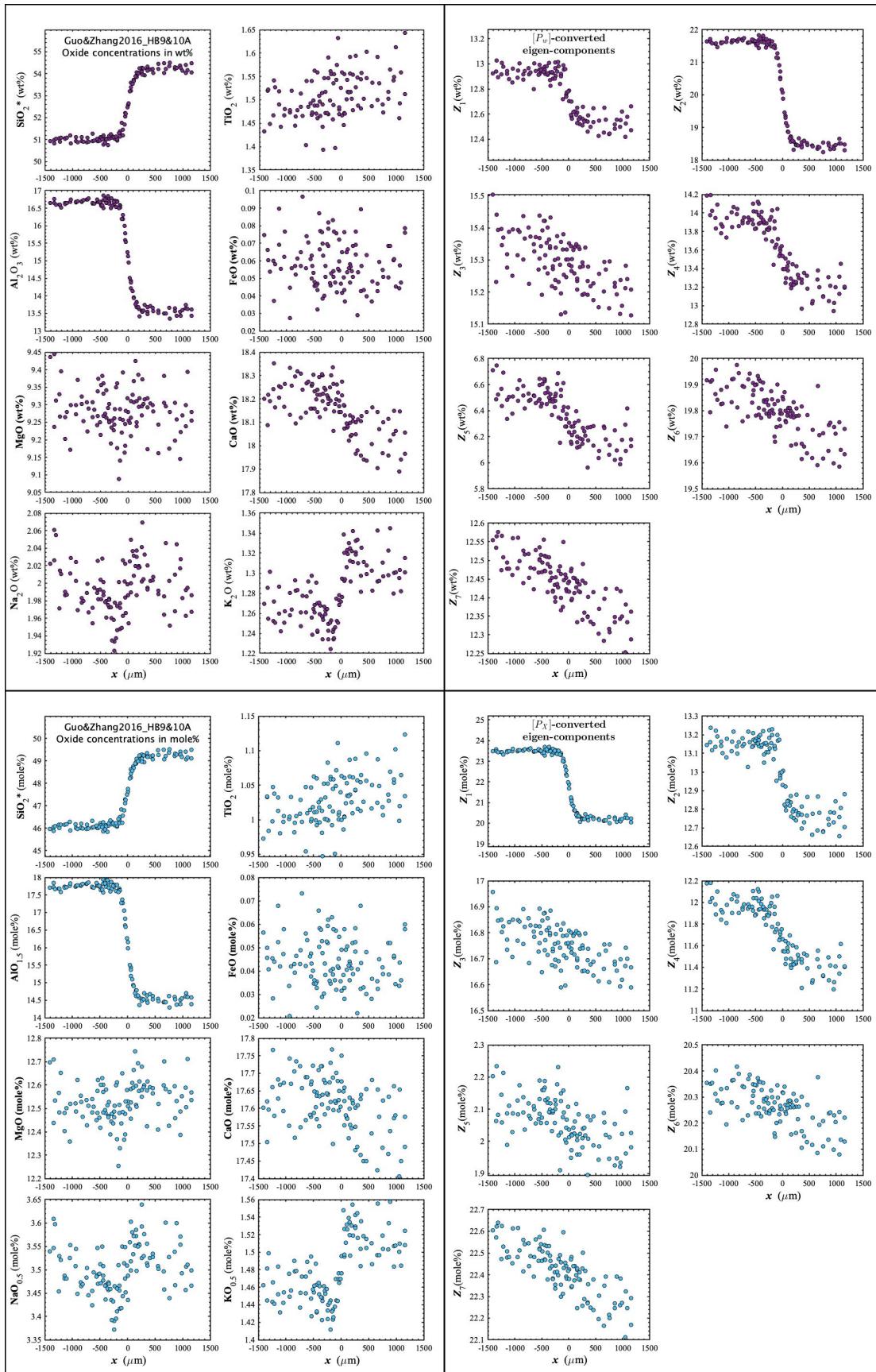
Figure D108. Concentration profiles of oxide components in wt% (upper left panel), oxide components in mole% (lower left panel), [P_w]-converted eigen-components (upper right panel), and [P_X]-converted eigen-components (lower right panel) of Yu2019_QzDisRh#104, which is a quartz dissolution experiment in rhyolite (Yu et al., 2019).

Figure D109. Concentration profiles of oxide components in wt% (upper left panel), oxide components in mole% (lower left panel), $[P_w]$-converted eigen-components (upper right panel), and $[P_X]$-converted eigen-components (lower right panel) of Yu2019_QzDisRh#106, which is a quartz dissolution experiment in rhyolite (Yu et al., 2019).

Figure D110. Concentration profiles of oxide components in wt% (upper left panel), oxide components in mole% (lower left panel), [P_w]-converted eigen-components (upper right panel), and [P_X]-converted eigen-components (lower right panel) of Guo&Zhang2016_HB2&4A, which is a diffusion couple experiment in haplo-basalt (Guo and Zhang, 2016).
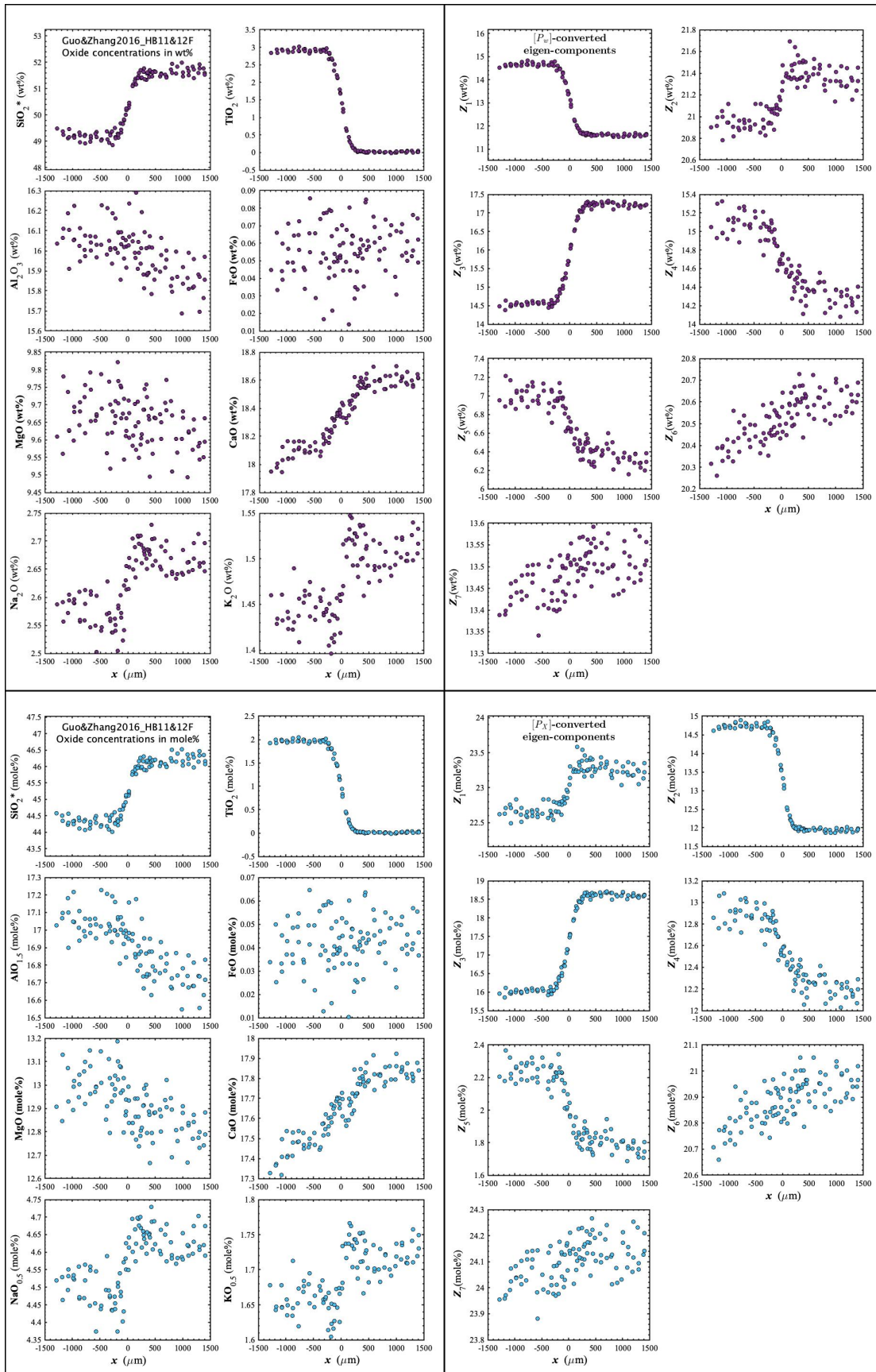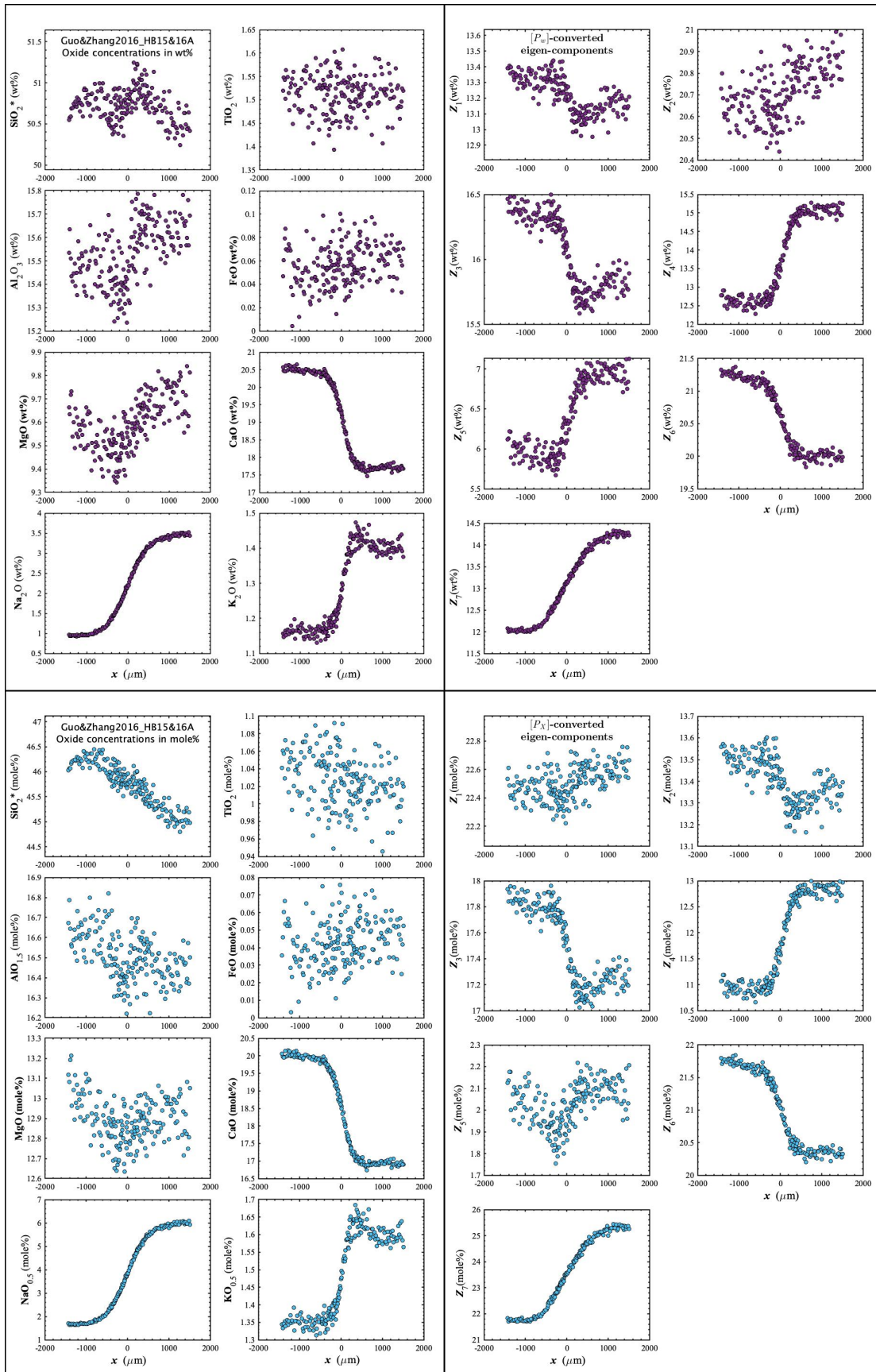
230

Figure D111. Concentration profiles of oxide components in wt% (upper left panel), oxide components in mole% (lower left panel), [P_w]-converted eigen-components (upper right panel), and [P_X]-converted eigen-components (lower right panel) of Guo&Zhang2016_HB3&4A, which is a diffusion couple experiment in haplo-basalt (Guo and Zhang, 2016).
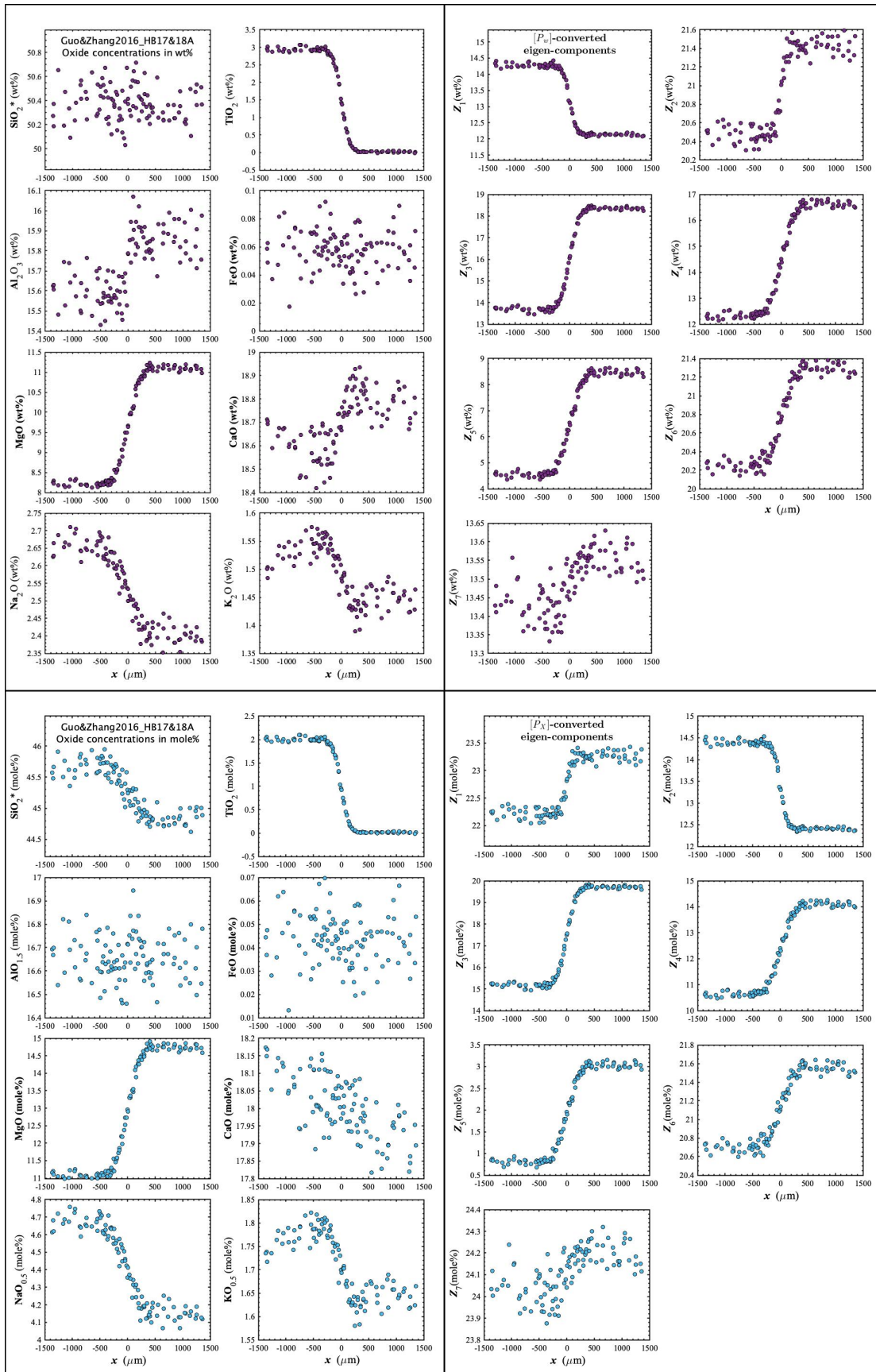
Figure D112. Concentration profiles of oxide components in wt% (upper left panel), oxide components in mole% (lower left panel), [P_w]-converted eigen-components (upper right panel), and [P_X]-converted eigen-components (lower right panel) of Guo&Zhang2016_HB5&6A, which is a diffusion couple experiment in haplo-basalt (Guo and Zhang, 2016).
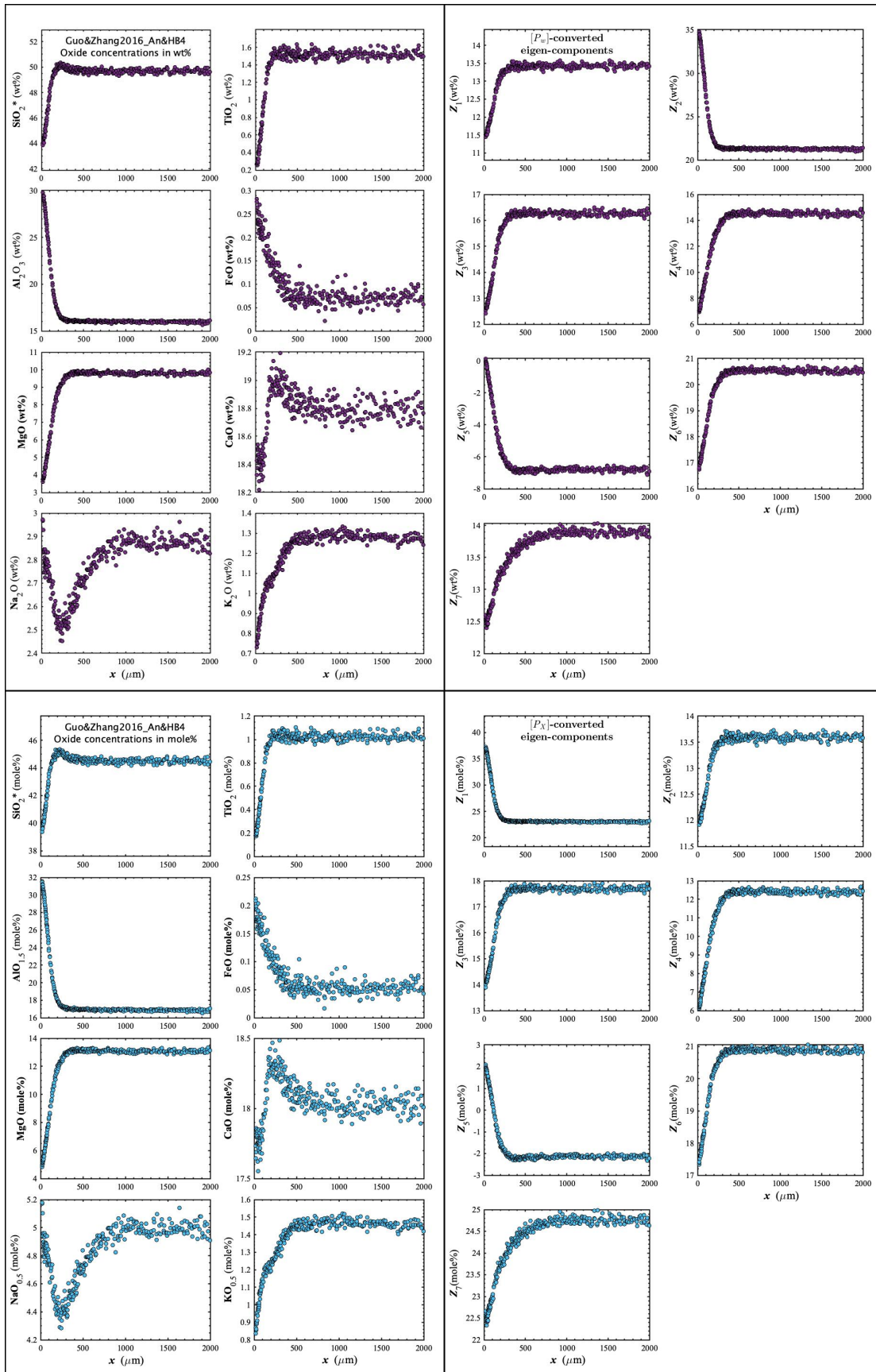
232

Figure D113. Concentration profiles of oxide components in wt% (upper left panel), oxide components in mole% (lower left panel), [P_w]-converted eigen-components (upper right panel), and [P_X]-converted eigen-components (lower right panel) of Guo&Zhang2016_HB5&7A, which is a diffusion couple experiment in haplo-basalt (Guo and Zhang, 2016).
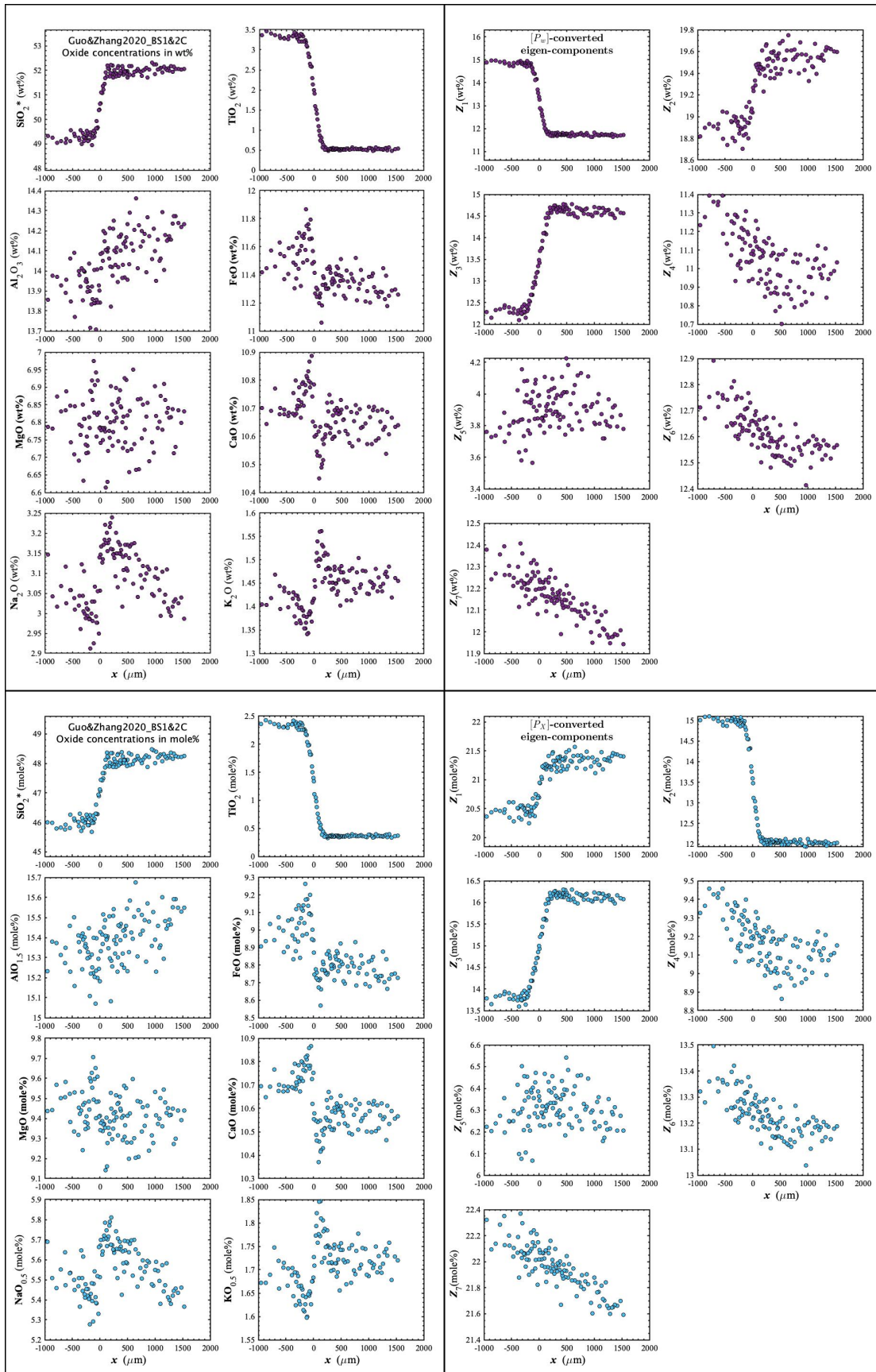
233

Figure D114. Concentration profiles of oxide components in wt% (upper left panel), oxide components in mole% (lower left panel), $[P_w]$-converted eigen-components (upper right panel), and $[P_X]$-converted eigen-components (lower right panel) of Guo&Zhang2016_HB7&8B, which is a diffusion couple experiment in haplo-basalt (Guo and Zhang, 2016).
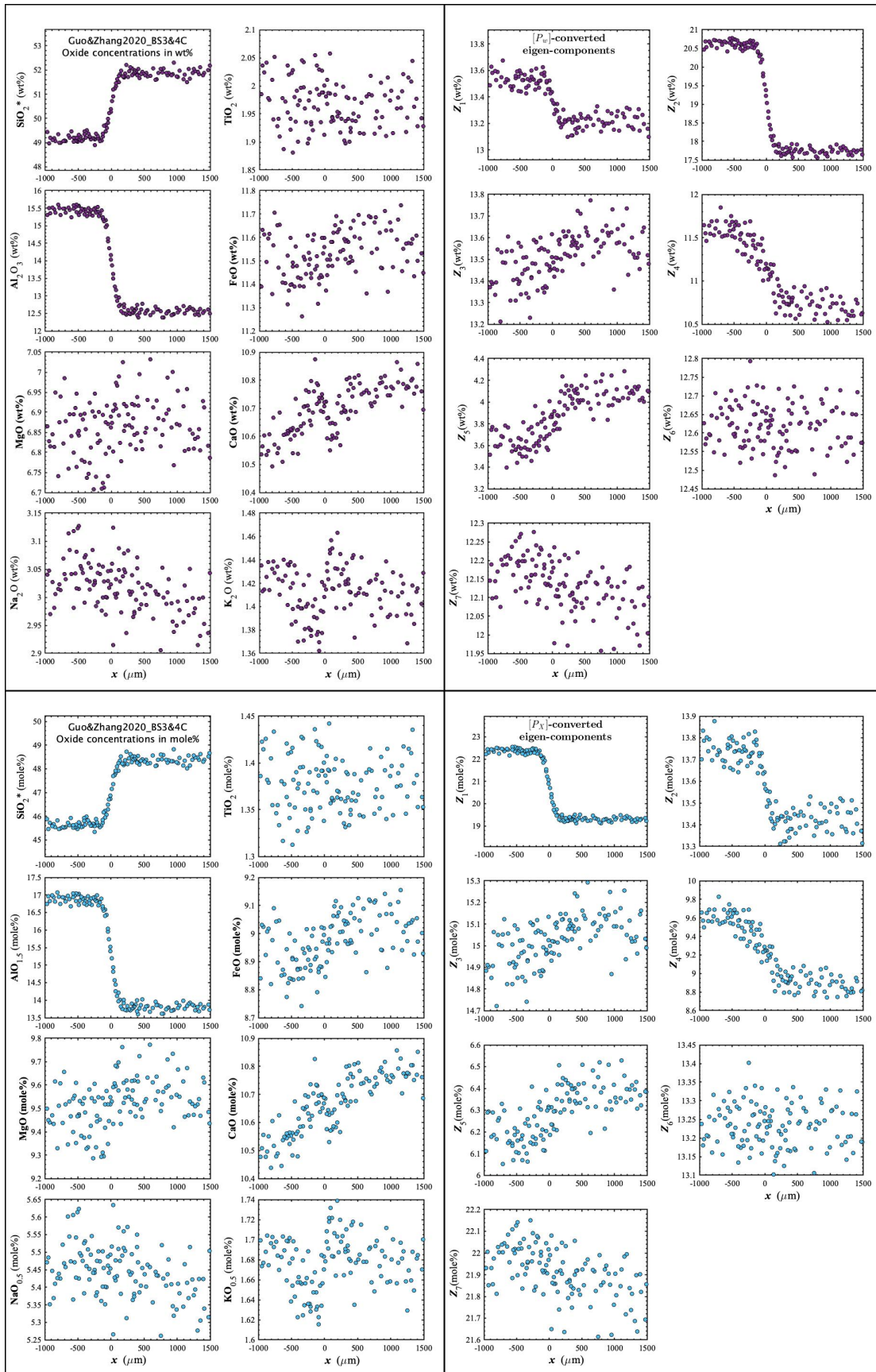
Figure D115. Concentration profiles of oxide components in wt% (upper left panel), oxide components in mole% (lower left panel), [P_w]-converted eigen-components (upper right panel), and [P_X]-converted eigen-components (lower right panel) of Guo&Zhang2016_HB9&10A, which is a diffusion couple experiment in haplo-basalt (Guo and Zhang, 2016).
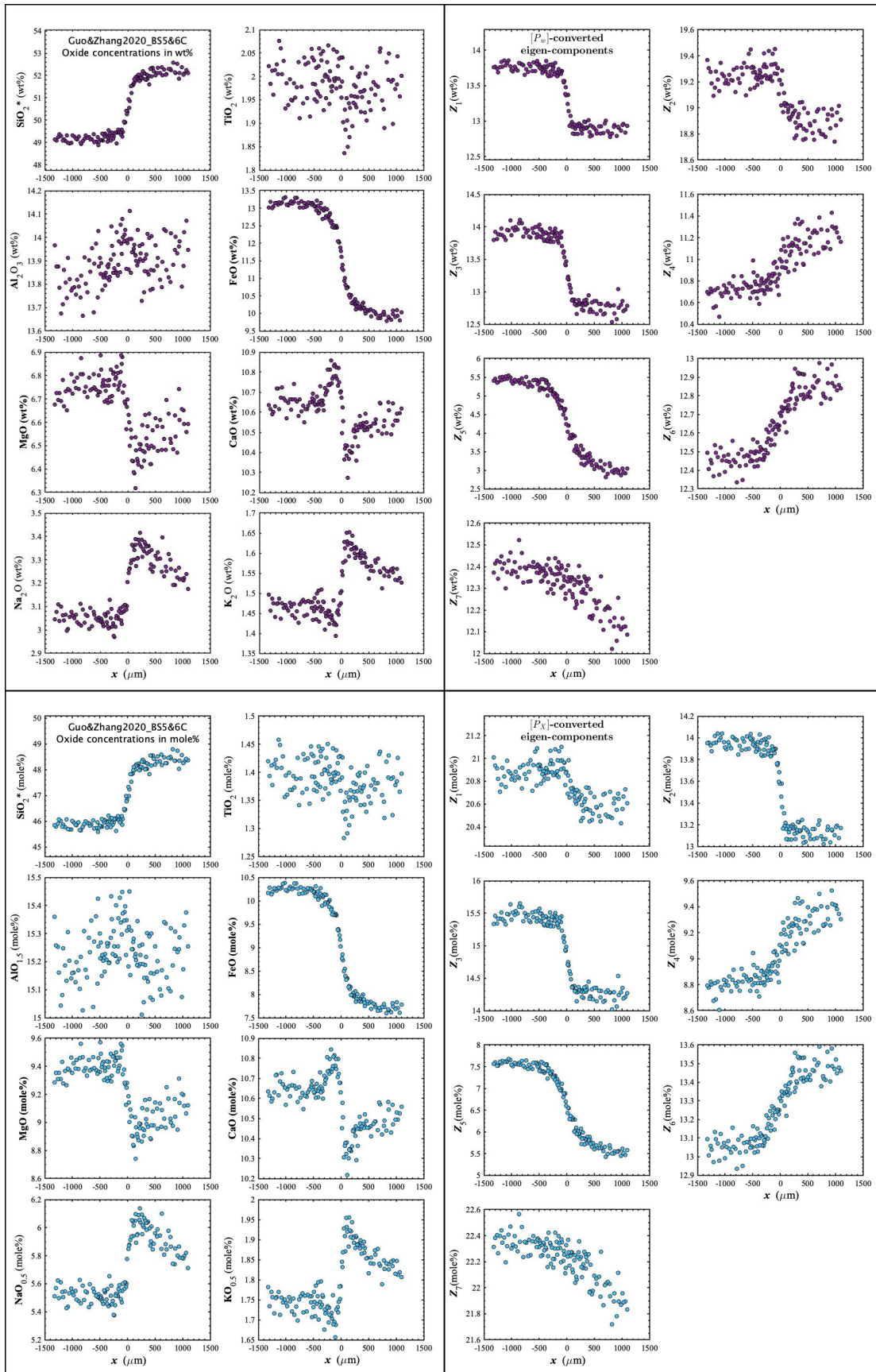
Figure D116. Concentration profiles of oxide components in wt% (upper left panel), oxide components in mole% (lower left panel), [P_w]-converted eigen-components (upper right panel), and [P_X]-converted eigen-components (lower right panel) of Guo&Zhang2016_HB11&12F, which is a diffusion couple experiment in haplo-basalt (Guo and Zhang, 2016).
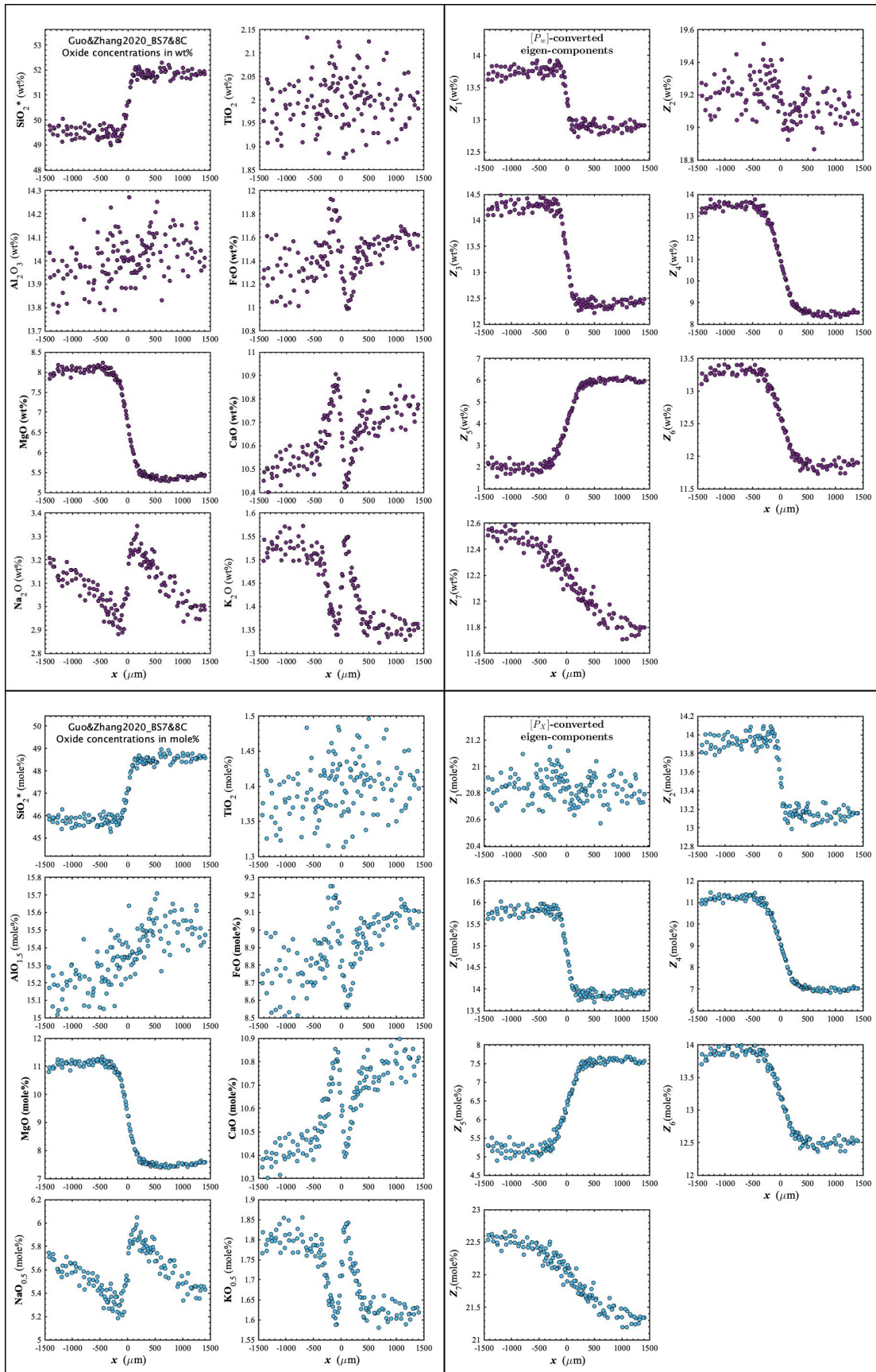
236

Figure D117. Concentration profiles of oxide components in wt% (upper left panel), oxide components in mole% (lower left panel), $[P_w]$-converted eigen-components (upper right panel), and $[P_X]$-converted eigen-components (lower right panel) of Guo&Zhang2016_HB15&16A, which is a diffusion couple experiment in haplo-basalt (Guo and Zhang, 2016).
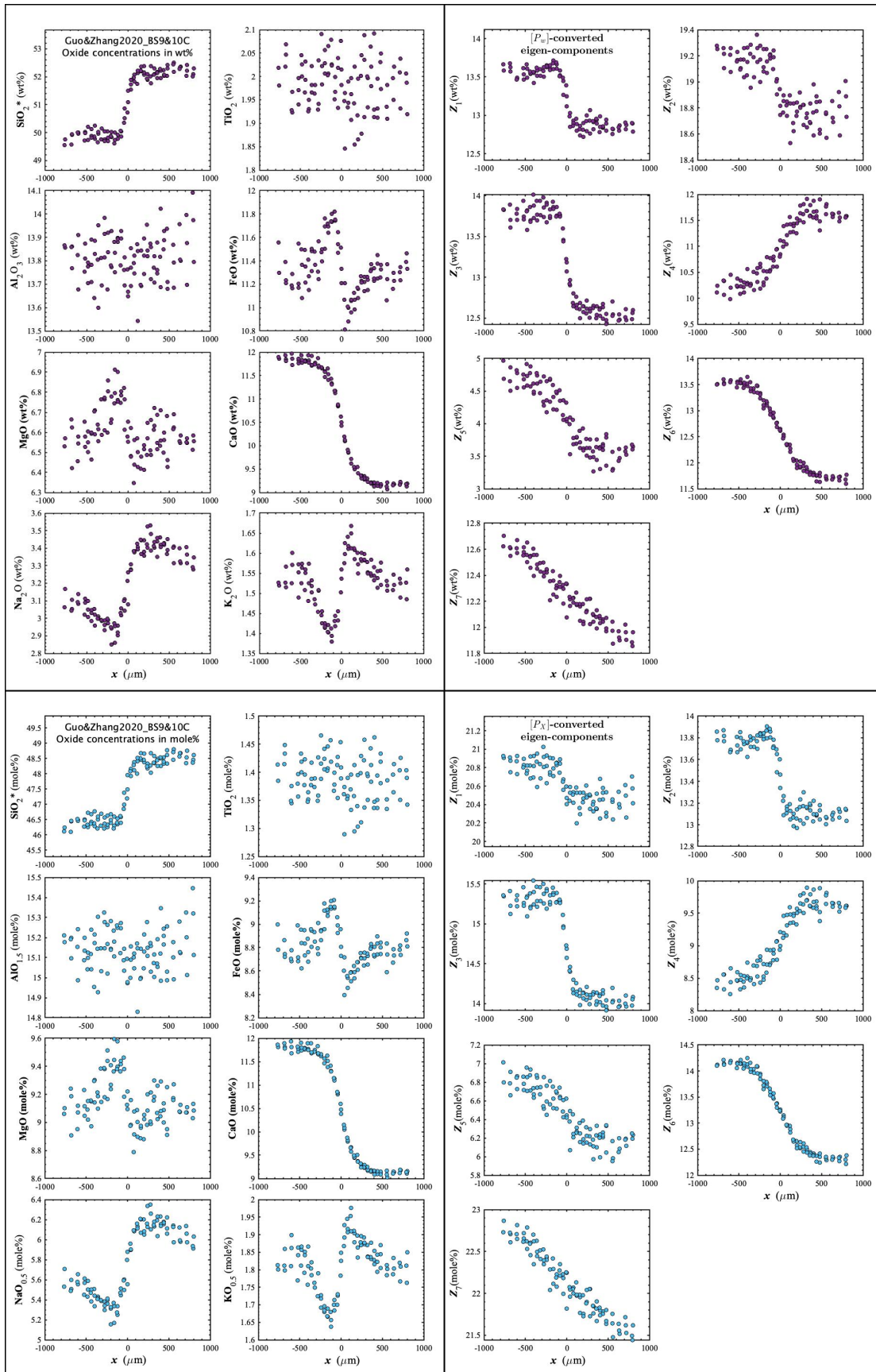
237

Figure D118. Concentration profiles of oxide components in wt% (upper left panel), oxide components in mole% (lower left panel), [P_w]-converted eigen-components (upper right panel), and [P_X]-converted eigen-components (lower right panel) of Guo&Zhang2016_HB17&18A, which is a diffusion couple experiment in haplo-basalt (Guo and Zhang, 2016).
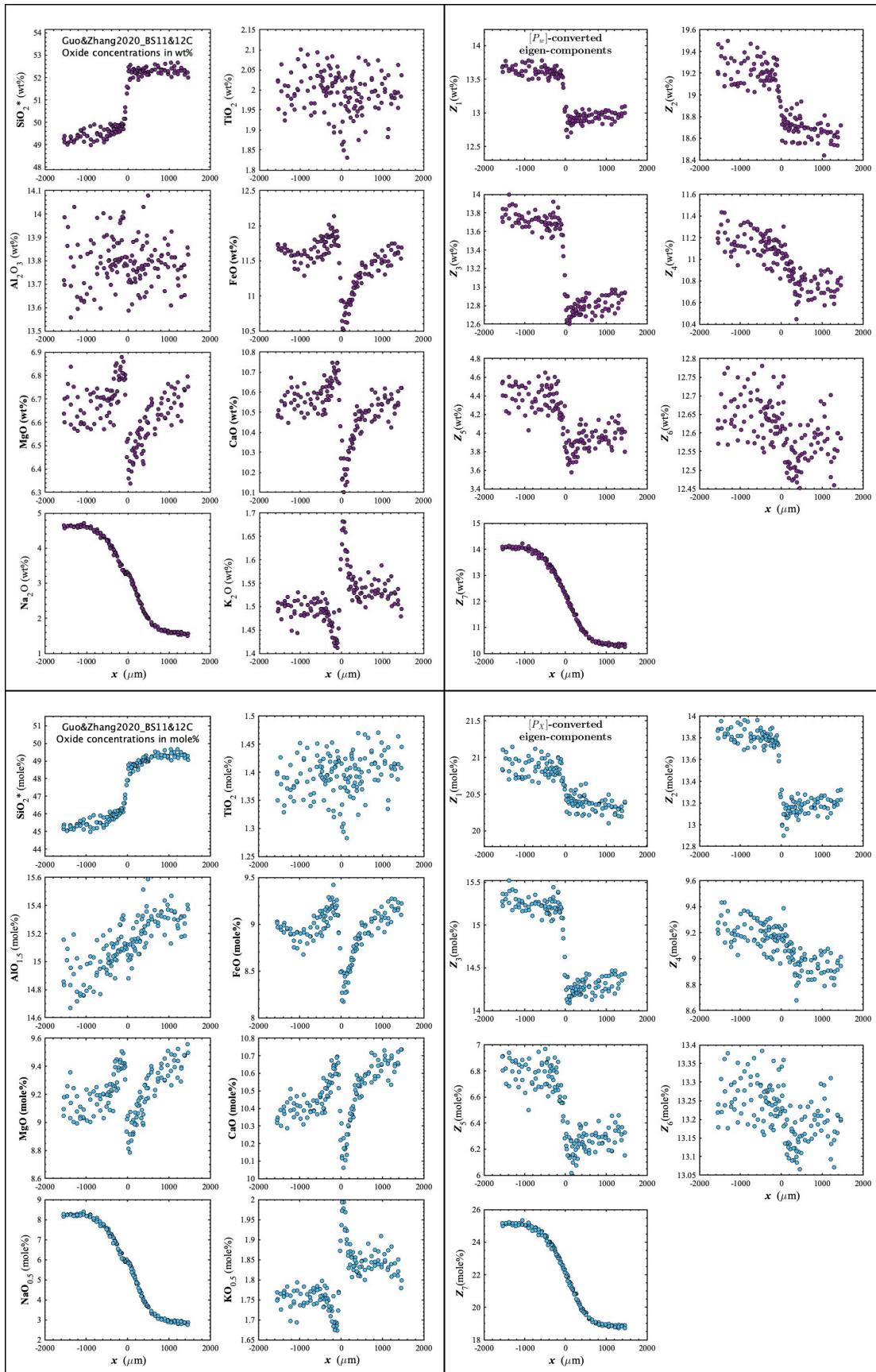
238

Figure D119. Concentration profiles of oxide components in wt% (upper left panel), oxide components in mole% (lower left panel), $[P_w]$-converted eigen-components (upper right panel), and $[P_X]$-converted eigen-components (lower right panel) of Guo&Zhang2016_An&HB4, which is an anorthite dissolution experiment in haplo-basalt (Guo and Zhang, 2016).

Figure D120. Concentration profiles of oxide components in wt% (upper left panel), oxide components in mole% (lower left panel), [P_w]-converted eigen-components (upper right panel), and [P_X]-converted eigen-components (lower right panel) of Guo&Zhang2020_BS1&2C, which is a diffusion couple experiment in basalt (Guo and Zhang, 2020).

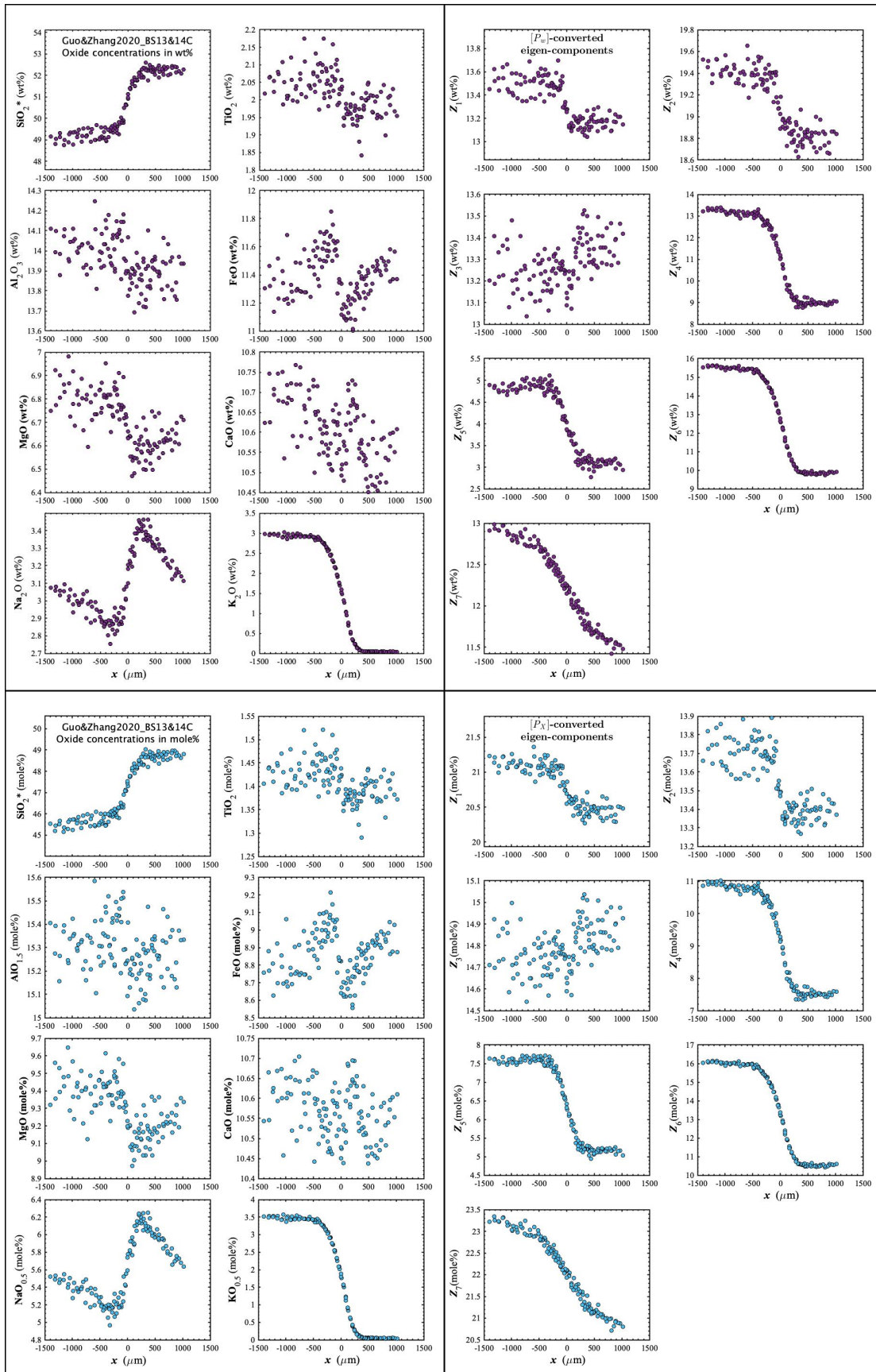**Figure D121.** Concentration profiles of oxide components in wt% (upper left panel), oxide components in mole% (lower left panel), $[P_W]$-converted eigen-components (upper right panel), and $[P_X]$-converted eigen-components (lower right panel) of Guo&Zhang2020_BS3&4C, which is a diffusion couple experiment in basalt (Guo and Zhang, 2020).
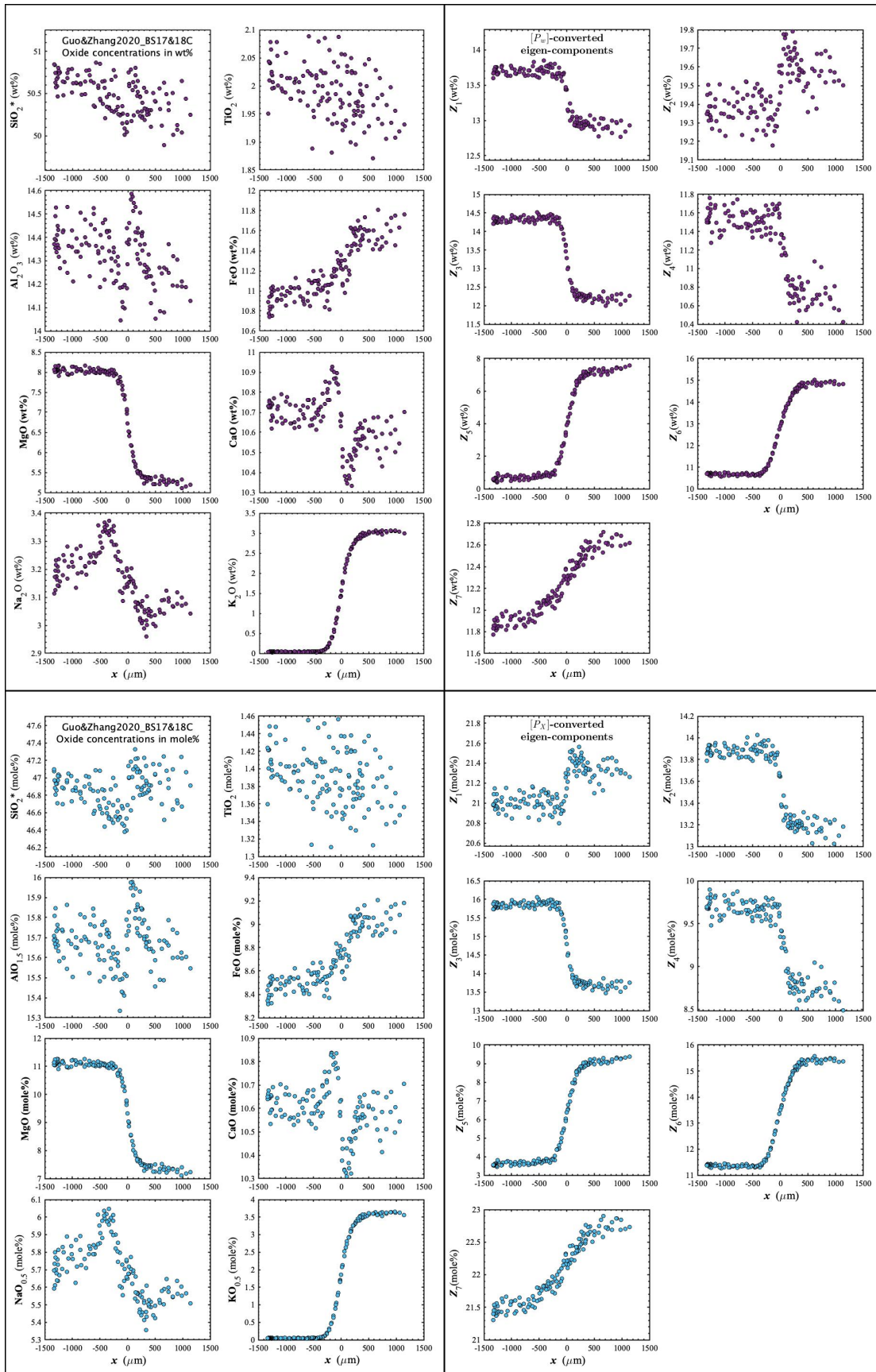
Figure D122. Concentration profiles of oxide components in wt% (upper left panel), oxide components in mole% (lower left panel), $[P_w]$-converted eigen-components (upper right panel), and $[P_X]$-converted eigen-components (lower right panel) of Guo&Zhang2020_BS5&6C, which is a diffusion couple experiment in basalt (Guo and Zhang, 2020).
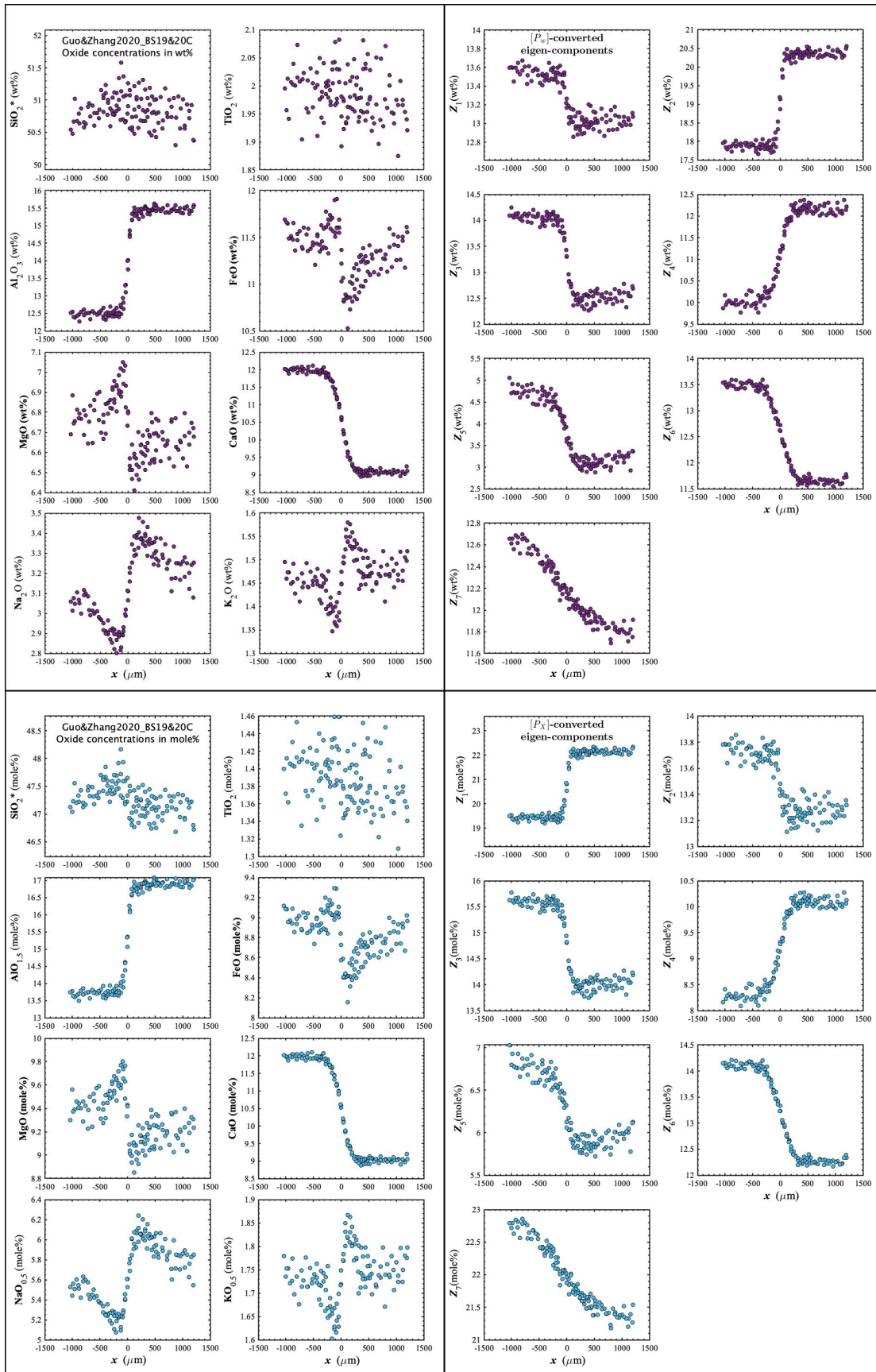
Figure D123. Concentration profiles of oxide components in wt% (upper left panel), oxide components in mole% (lower left panel), [P_w]-converted eigen-components (upper right panel), and [P_X]-converted eigen-components (lower right panel) of Guo&Zhang2020_BS7&8C, which is a diffusion couple experiment in basalt (Guo and Zhang, 2020).

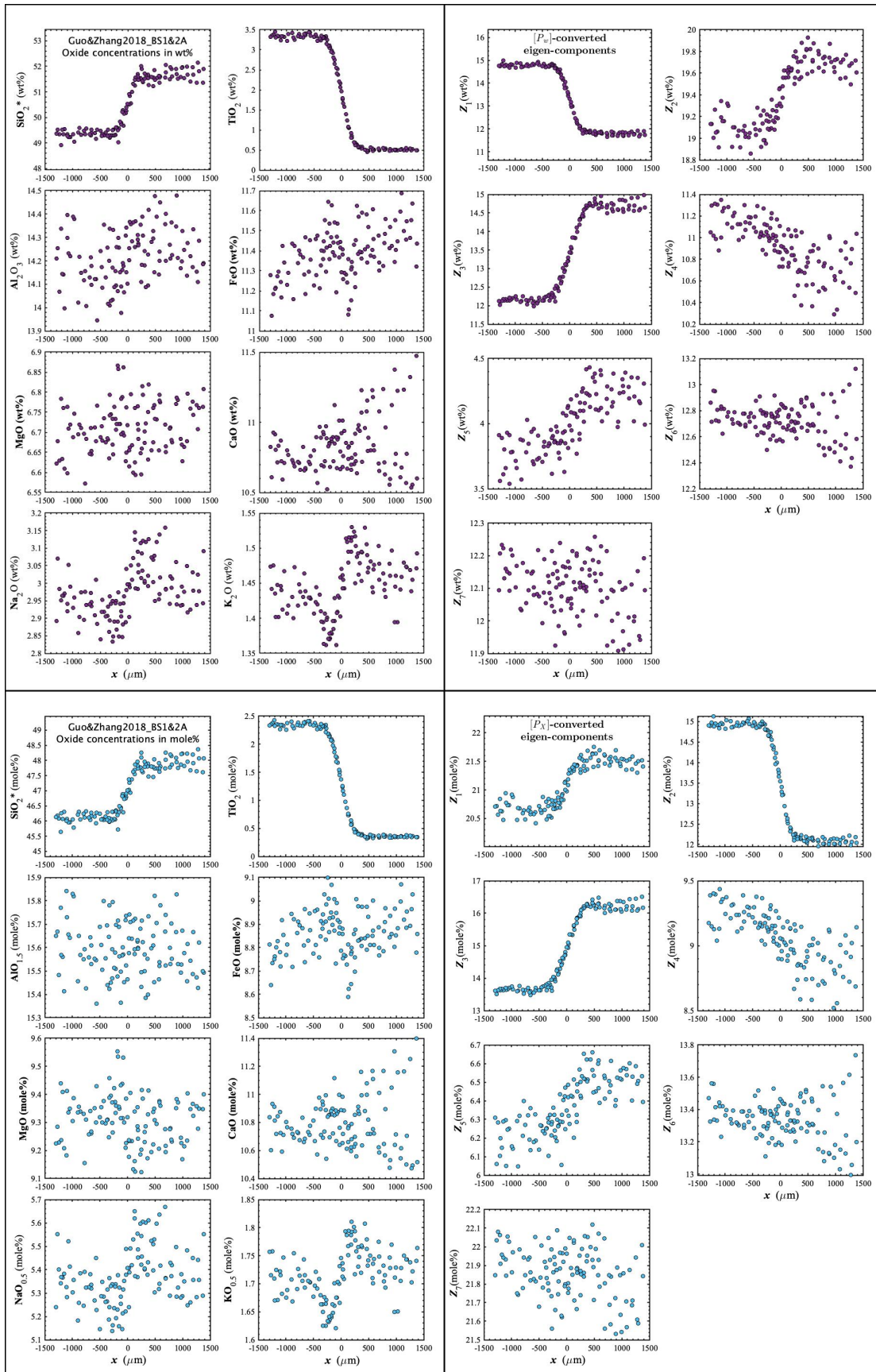**Figure D124.** Concentration profiles of oxide components in wt% (upper left panel), oxide components in mole% (lower left panel), [P_w]-converted eigen-components (upper right panel), and [P_X]-converted eigen-components (lower right panel) of Guo&Zhang2020_BS9&10C, which is a diffusion couple experiment in basalt (Guo and Zhang, 2020).
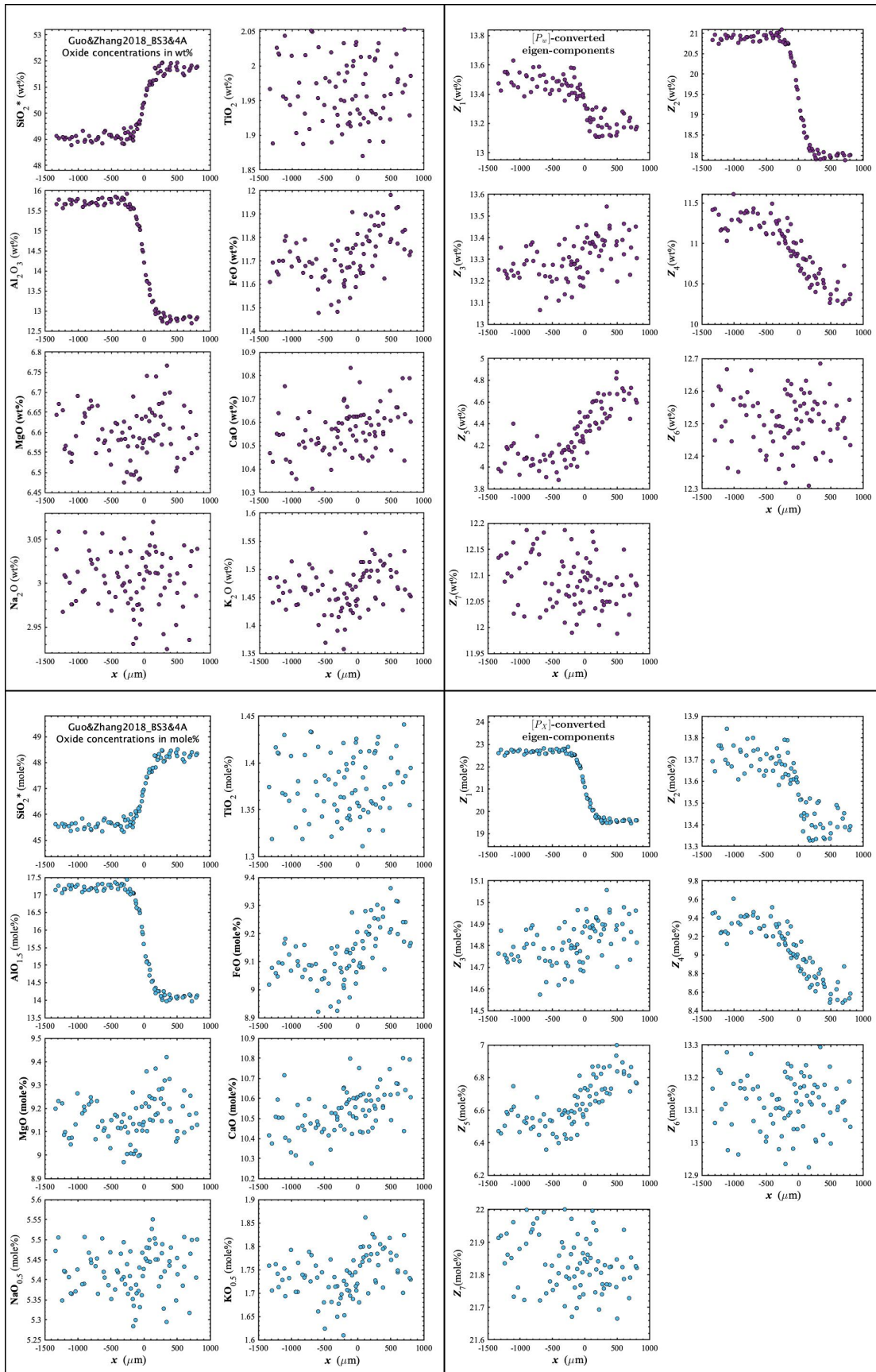
244

Figure D125. Concentration profiles of oxide components in wt% (upper left panel), oxide components in mole% (lower left panel), [P_w]-converted eigen-components (upper right panel), and [P_X]-converted eigen-components (lower right panel) of Guo&Zhang2020_BS11&12C, which is a diffusion couple experiment in basalt (Guo and Zhang, 2020).
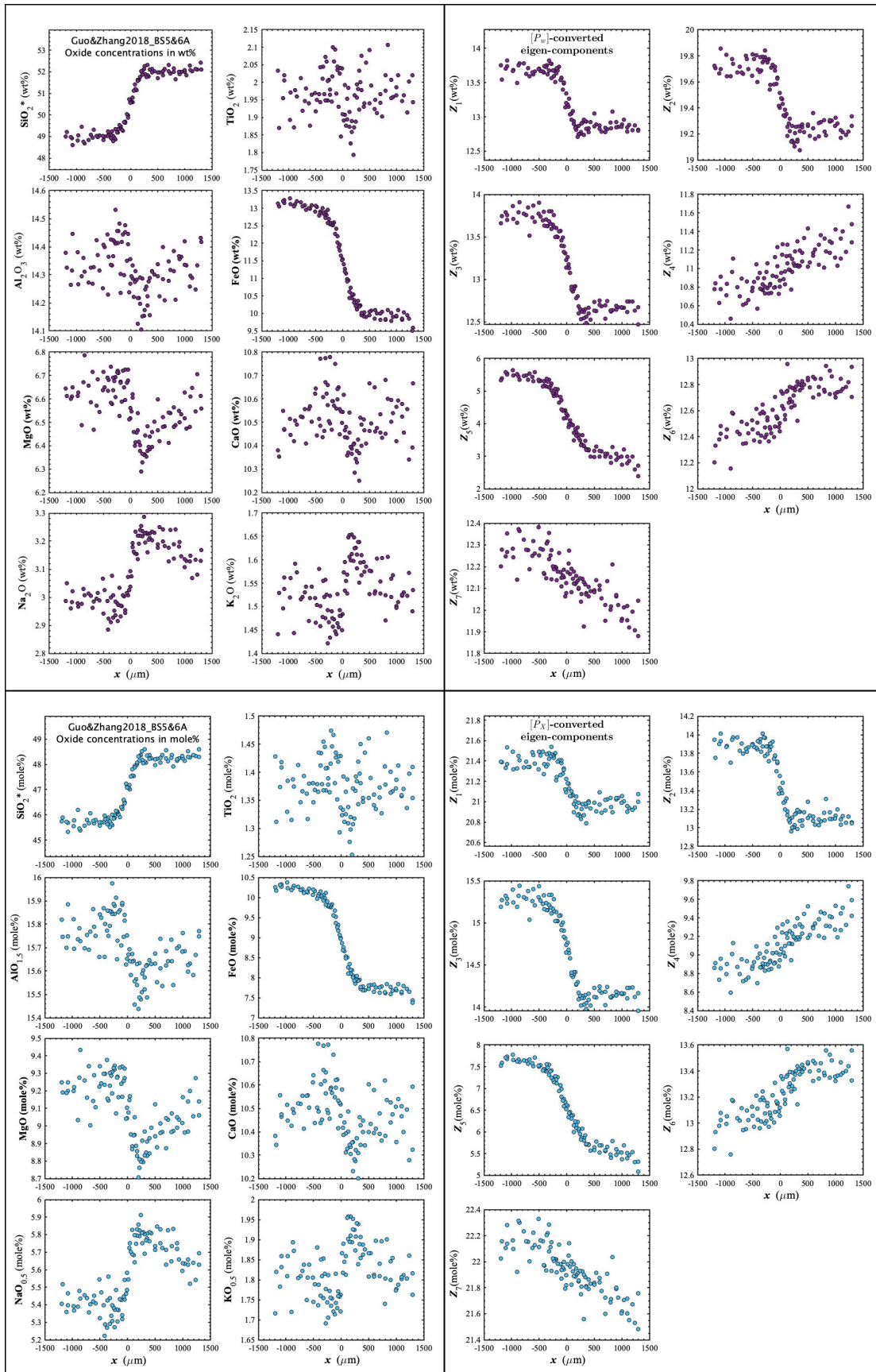
245

Figure D126. Concentration profiles of oxide components in wt% (upper left panel), oxide components in mole% (lower left panel), [P_w]-converted eigen-components (upper right panel), and [P_X]-converted eigen-components (lower right panel) of Guo&Zhang2020_BS13&14C, which is a diffusion couple experiment in basalt (Guo and Zhang, 2020).
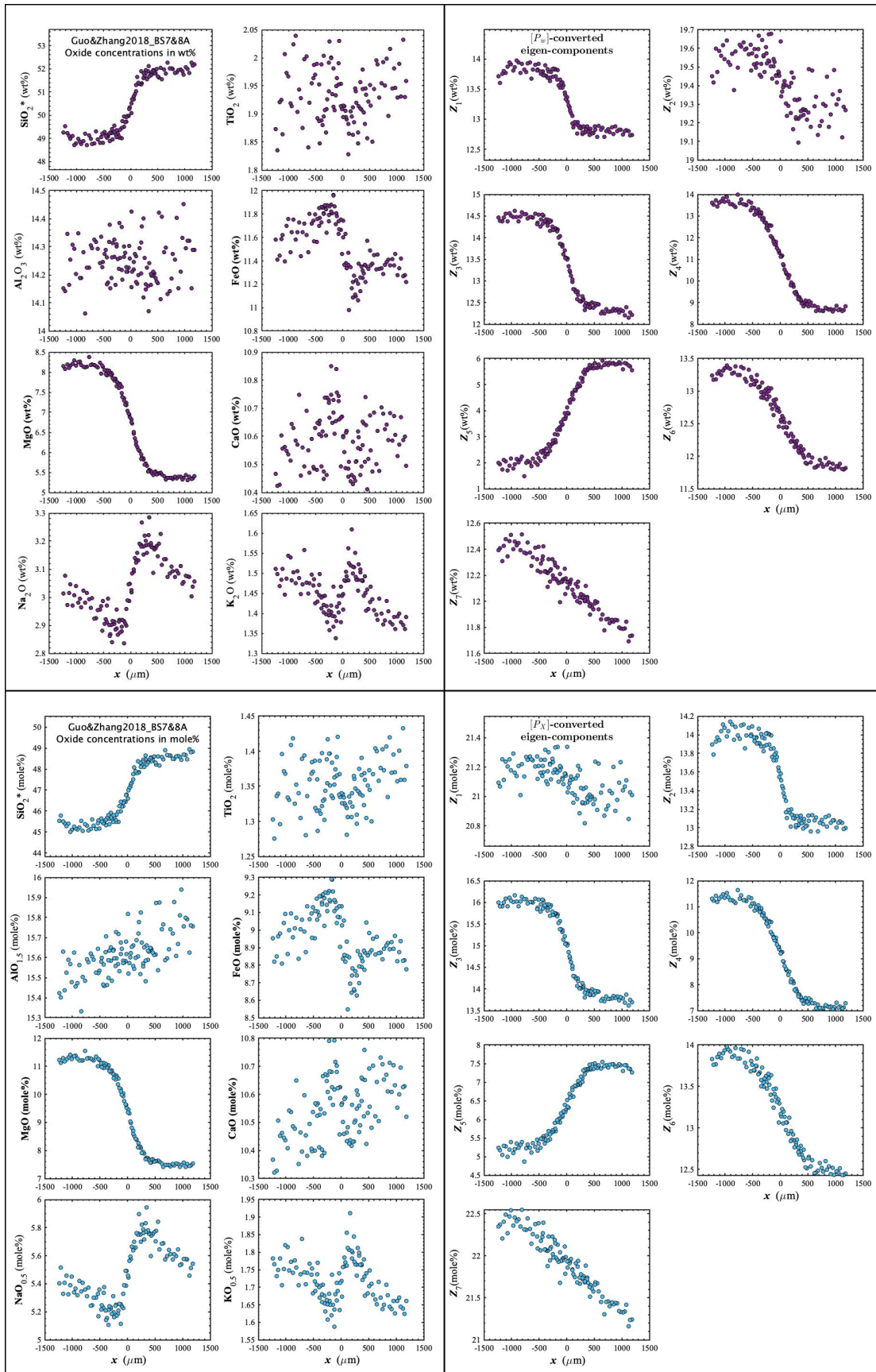
246

Figure D127. Concentration profiles of oxide components in wt% (upper left panel), oxide components in mole% (lower left panel), $[P_w]$-converted eigen-components (upper right panel), and $[P_X]$-converted eigen-components (lower right panel) of Guo&Zhang2020_BS17&18C, which is a diffusion couple experiment in basalt (Guo and Zhang, 2020).
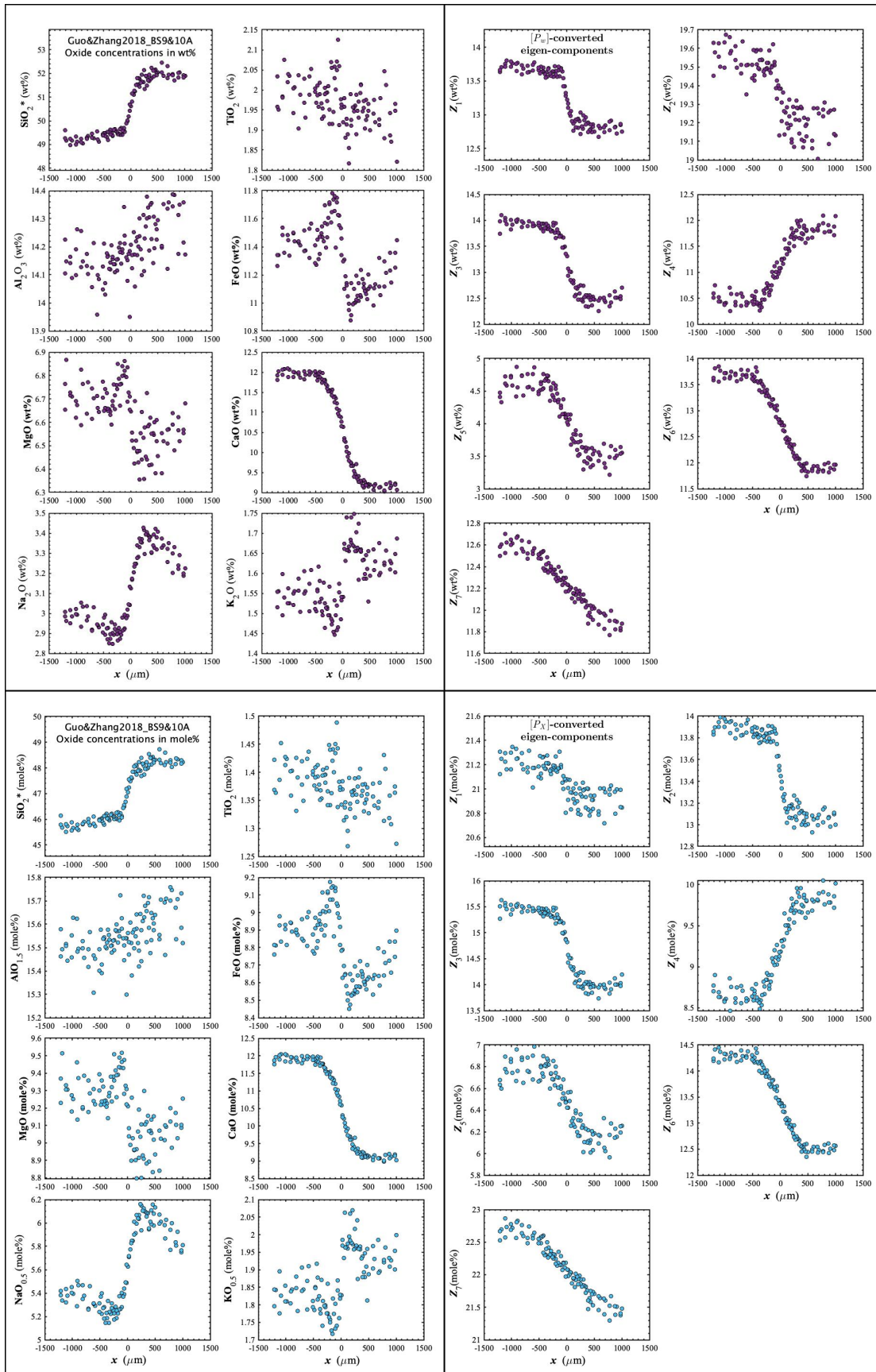
Figure D128. Concentration profiles of oxide components in wt% (upper left panel), oxide components in mole% (lower left panel), $[P_w]$-converted eigen-components (upper right panel), and $[P_X]$-converted eigen-components (lower right panel) of Guo&Zhang2020_BS19&20C, which is a diffusion couple experiment in basalt (Guo and Zhang, 2020).

248

Figure D129. Concentration profiles of oxide components in wt% (upper left panel), oxide components in mole% (lower left panel), [P_w]-converted eigen-components (upper right panel), and [P_X]-converted eigen-components (lower right panel) of Guo&Zhang2018_BS1&2A, which is a diffusion couple experiment in basalt (Guo and Zhang, 2018).
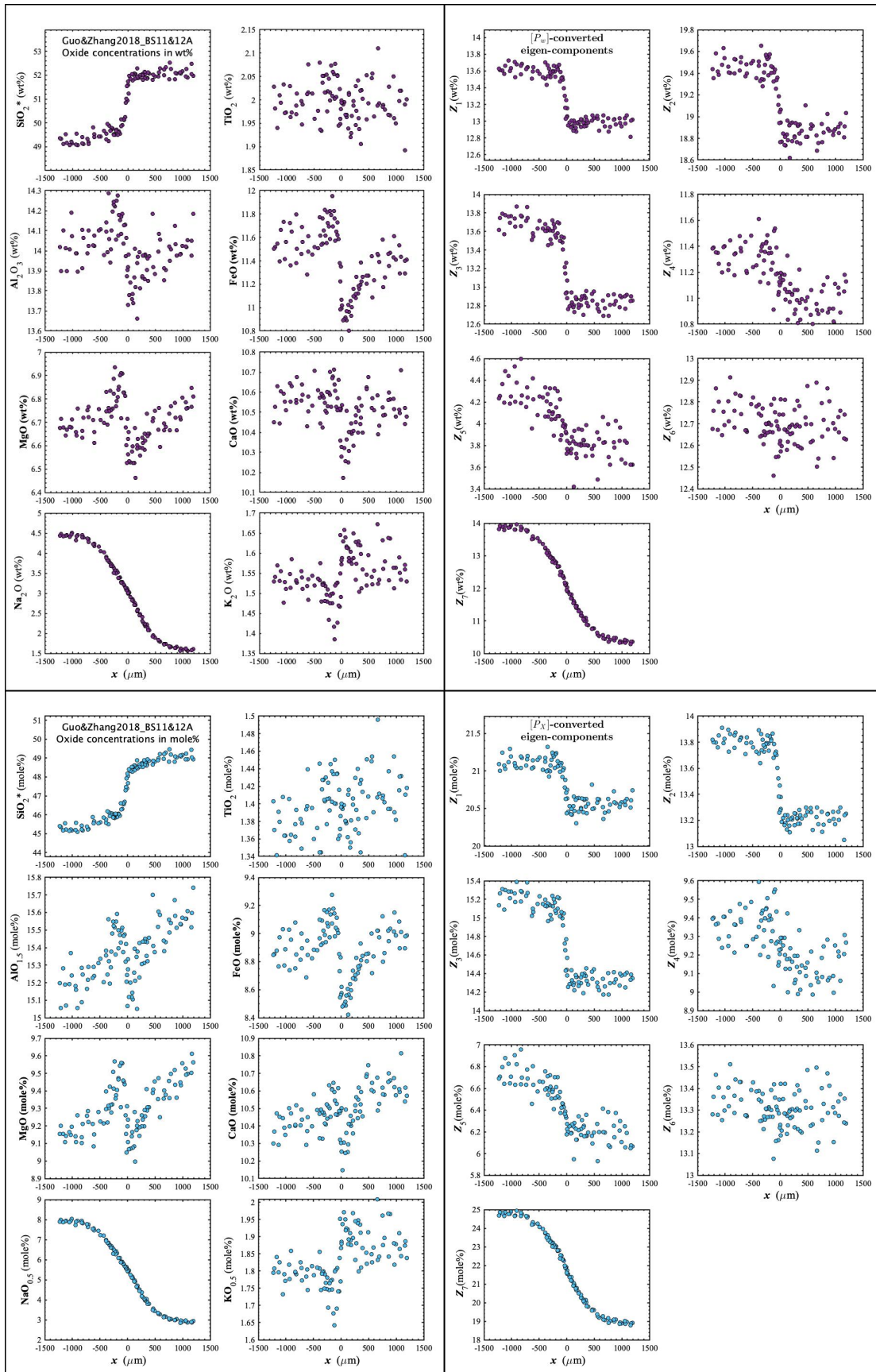
Figure D130. Concentration profiles of oxide components in wt% (upper left panel), oxide components in mole% (lower left panel), [P_w]-converted eigen-components (upper right panel), and [P_X]-converted eigen-components (lower right panel) of Guo&Zhang2018_BS3&4A, which is a diffusion couple experiment in basalt (Guo and Zhang, 2018).
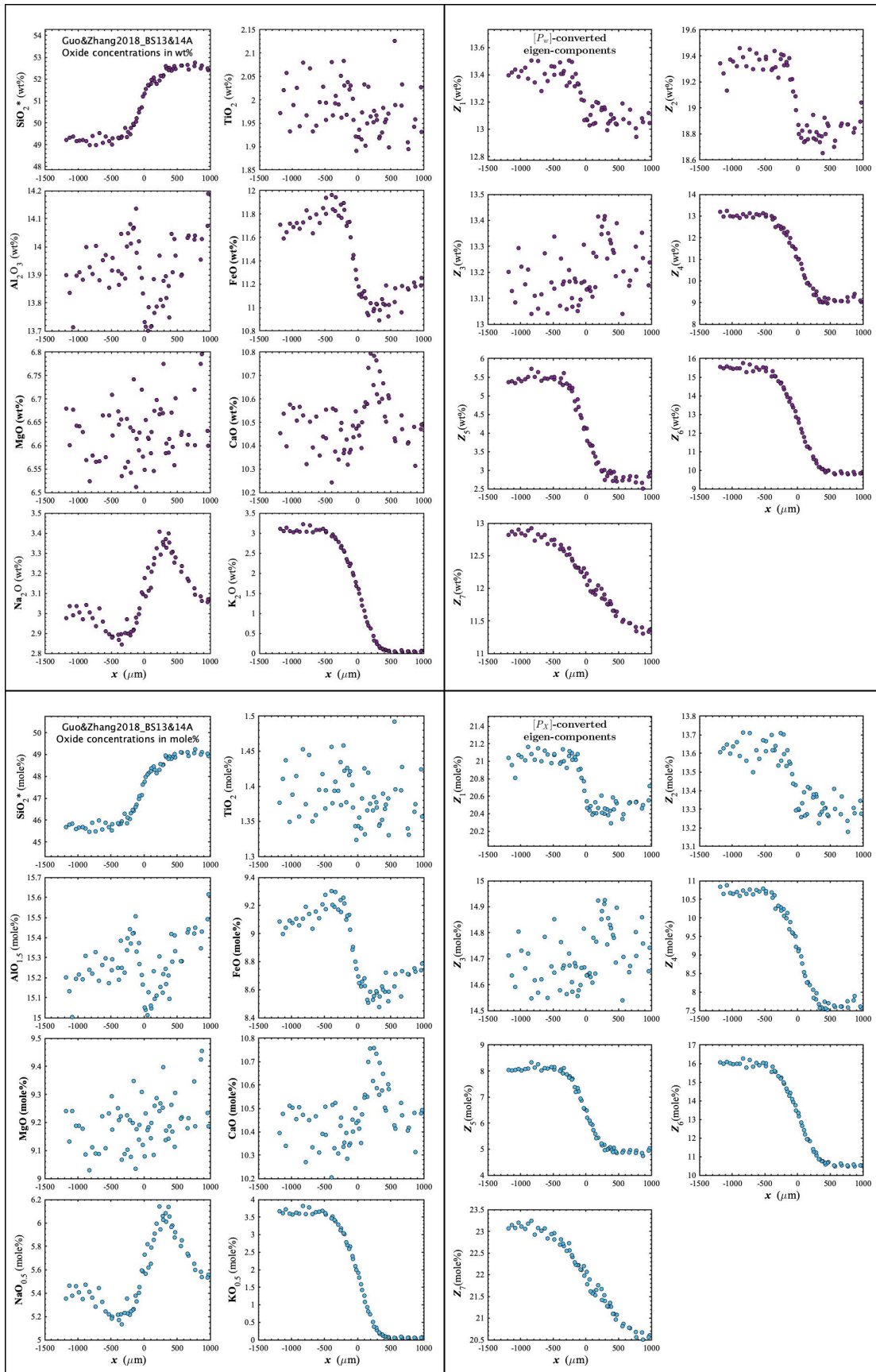
250

Figure D131. Concentration profiles of oxide components in wt% (upper left panel), oxide components in mole% (lower left panel), $[P_w]$-converted eigen-components (upper right panel), and $[P_X]$-converted eigen-components (lower right panel) of Guo&Zhang2018_BS5&6A, which is a diffusion couple experiment in basalt (Guo and Zhang, 2018).
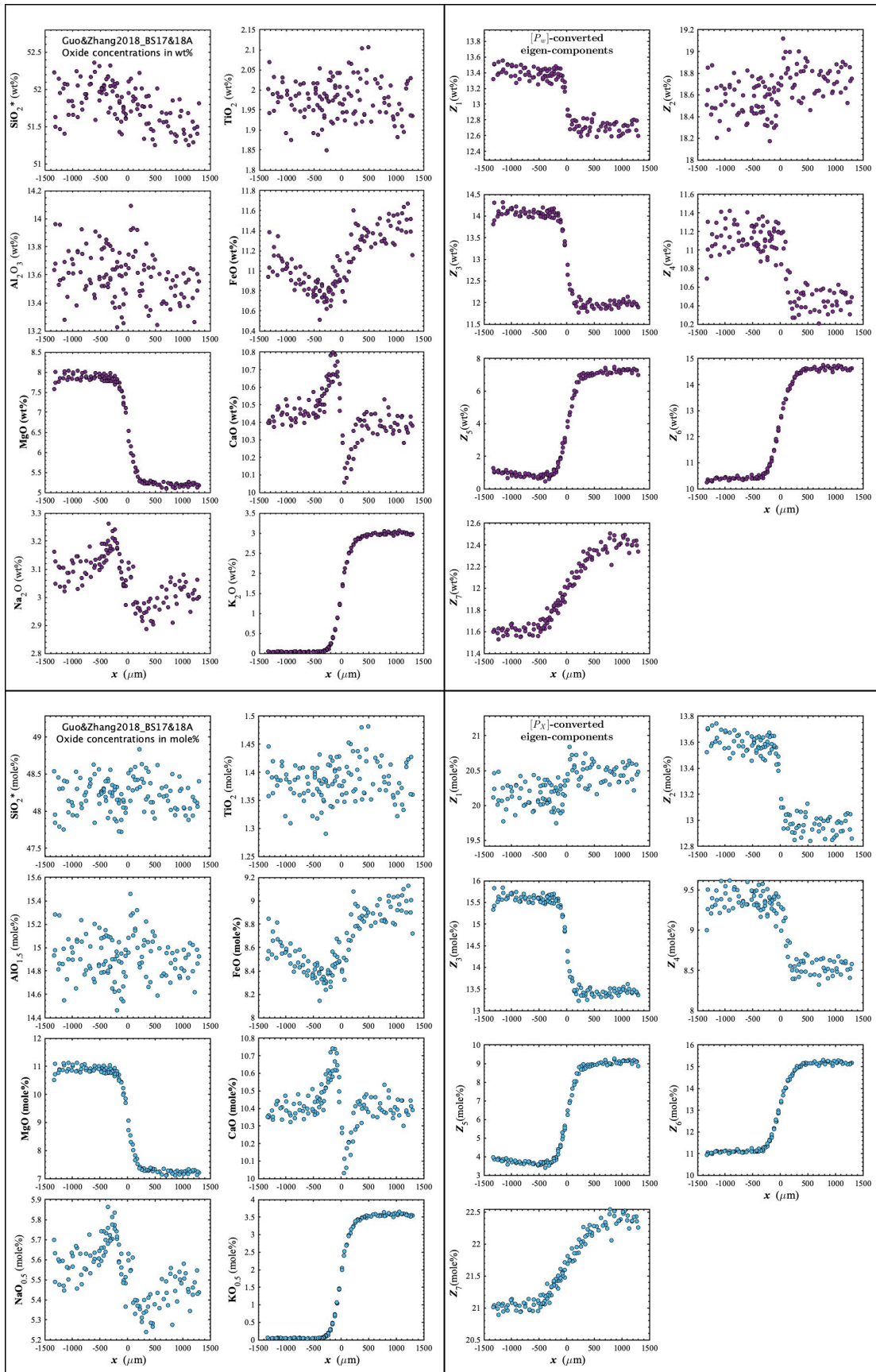
251

Figure D132. Concentration profiles of oxide components in wt% (upper left panel), oxide components in mole% (lower left panel), $[P_w]$-converted eigen-components (upper right panel), and $[P_X]$-converted eigen-components (lower right panel) of Guo&Zhang2018_BS7&8A, which is a diffusion couple experiment in basalt (Guo and Zhang, 2018).
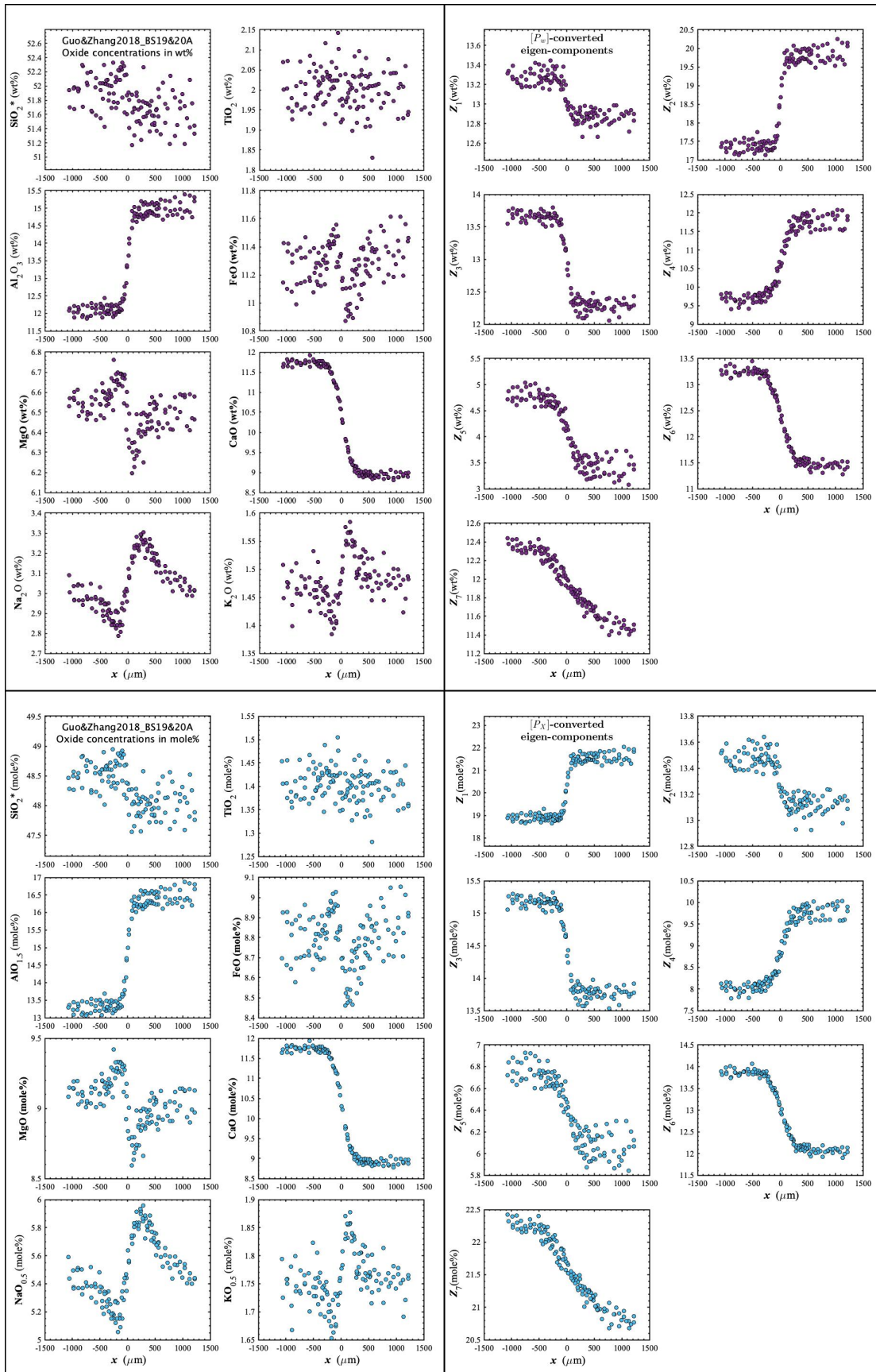
252

Figure D133. Concentration profiles of oxide components in wt% (upper left panel), oxide components in mole% (lower left panel), [P_w]-converted eigen-components (upper right panel), and [P_X]-converted eigen-components (lower right panel) of Guo&Zhang2018_BS9&10A, which is a diffusion couple experiment in basalt (Guo and Zhang, 2018).

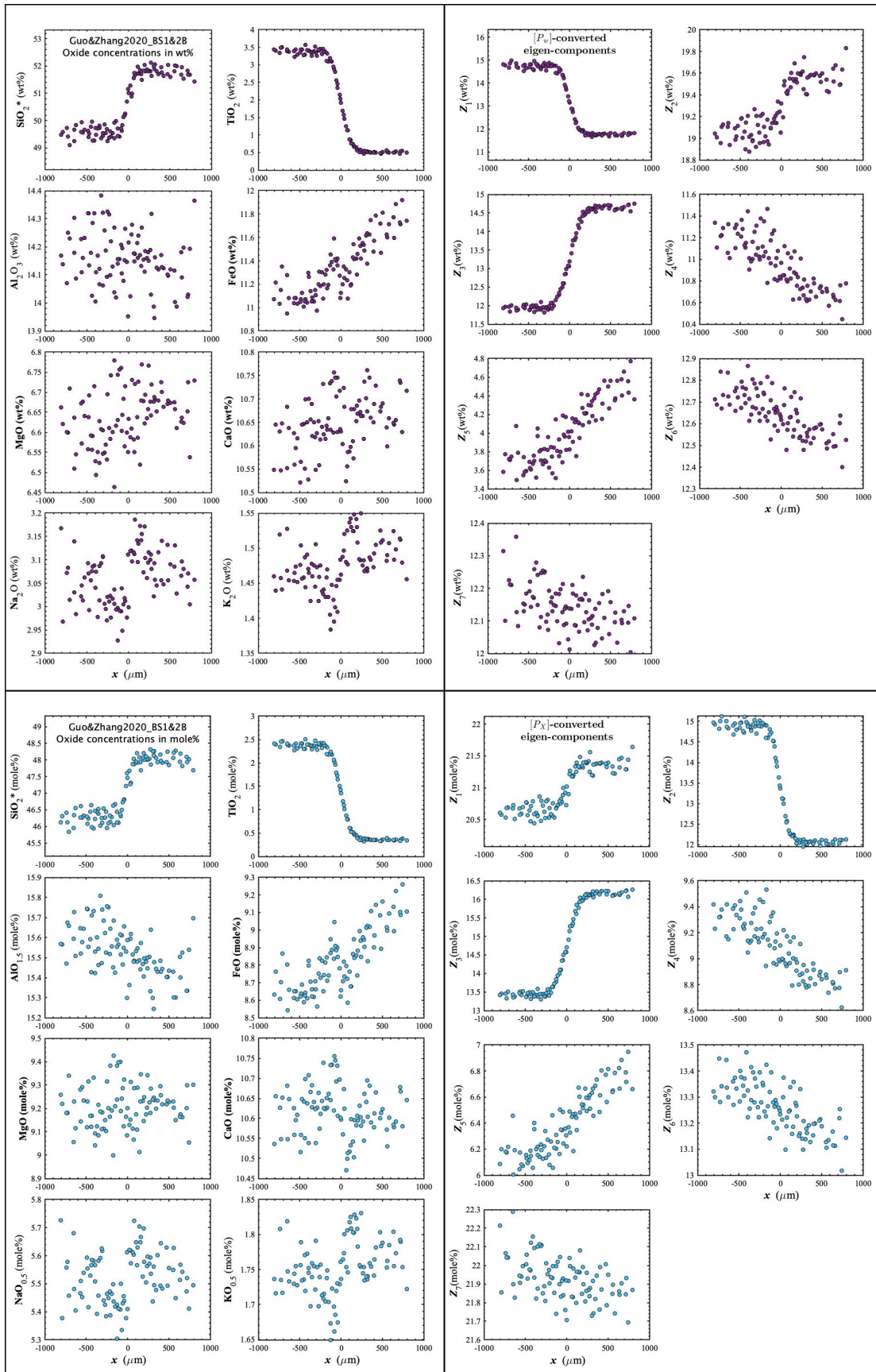253

Figure D134. Concentration profiles of oxide components in wt% (upper left panel), oxide components in mole% (lower left panel), [P_w]-converted eigen-components (upper right panel), and [P_X]-converted eigen-components (lower right panel) of Guo&Zhang2018_BS11&12A, which is a diffusion couple experiment in basalt (Guo and Zhang, 2018).
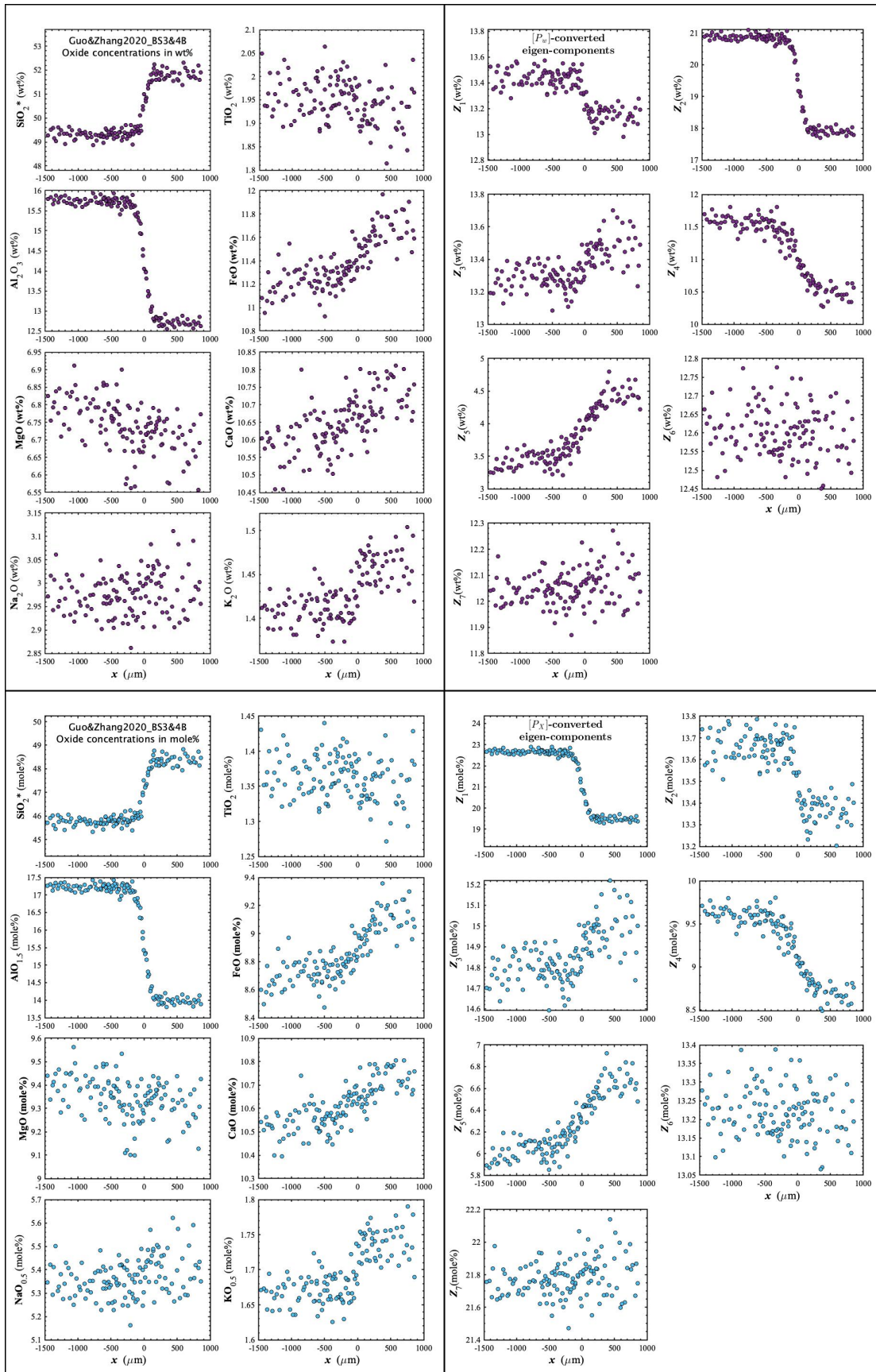
Figure D135. Concentration profiles of oxide components in wt% (upper left panel), oxide components in mole% (lower left panel), [P_w]-converted eigen-components (upper right panel), and [P_X]-converted eigen-components (lower right panel) of Guo&Zhang2018_BS13&14A, which is a diffusion couple experiment in basalt (Guo and Zhang, 2018).
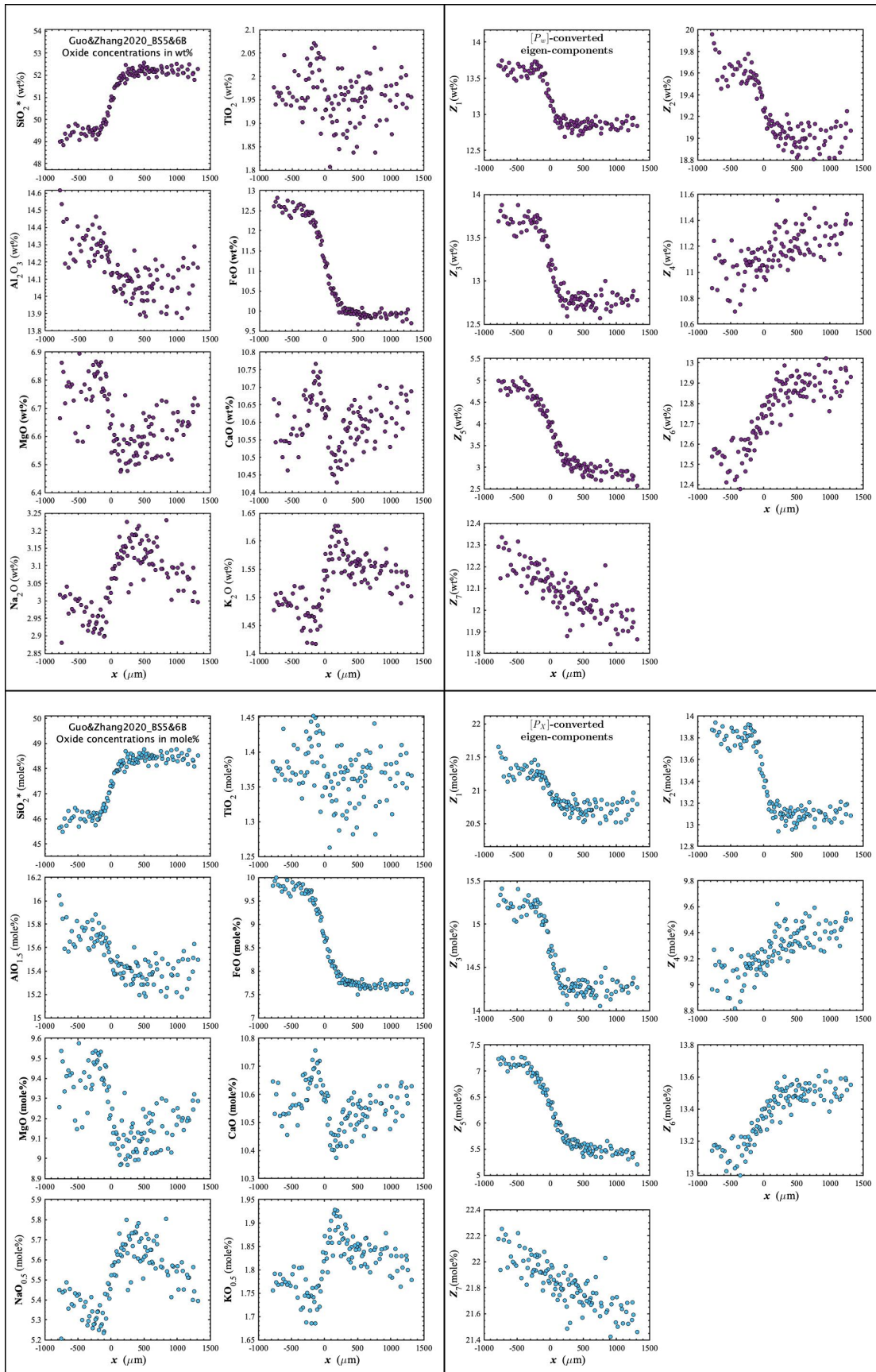
255

Figure D136. Concentration profiles of oxide components in wt% (upper left panel), oxide components in mole% (lower left panel), [P_w]-converted eigen-components (upper right panel), and [P_X]-converted eigen-components (lower right panel) of Guo&Zhang2018_BS17&18A, which is a diffusion couple experiment in basalt (Guo and Zhang, 2018).

256

Figure D137. Concentration profiles of oxide components in wt% (upper left panel), oxide components in mole% (lower left panel), [P_w]-converted eigen-components (upper right panel), and [P_X]-converted eigen-components (lower right panel) of Guo&Zhang2018_BS19&20A, which is a diffusion couple experiment in basalt (Guo and Zhang, 2018).

257

Figure D138. Concentration profiles of oxide components in wt% (upper left panel), oxide components in mole% (lower left panel), [P_w]-converted eigen-components (upper right panel), and [P_X]-converted eigen-components (lower right panel) of Guo&Zhang2020_BS1&2B, which is a diffusion couple experiment in basalt (Guo and Zhang, 2020).
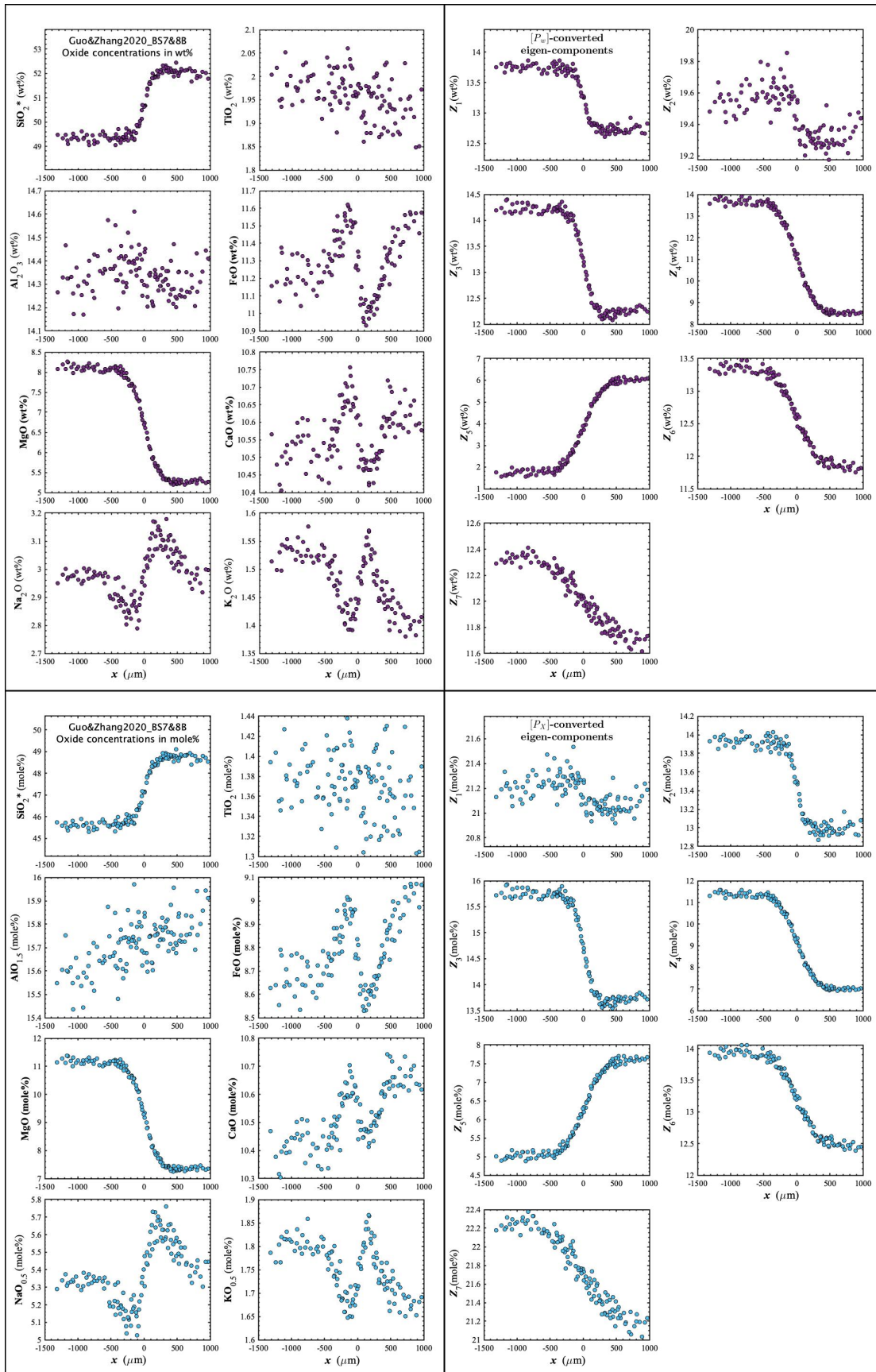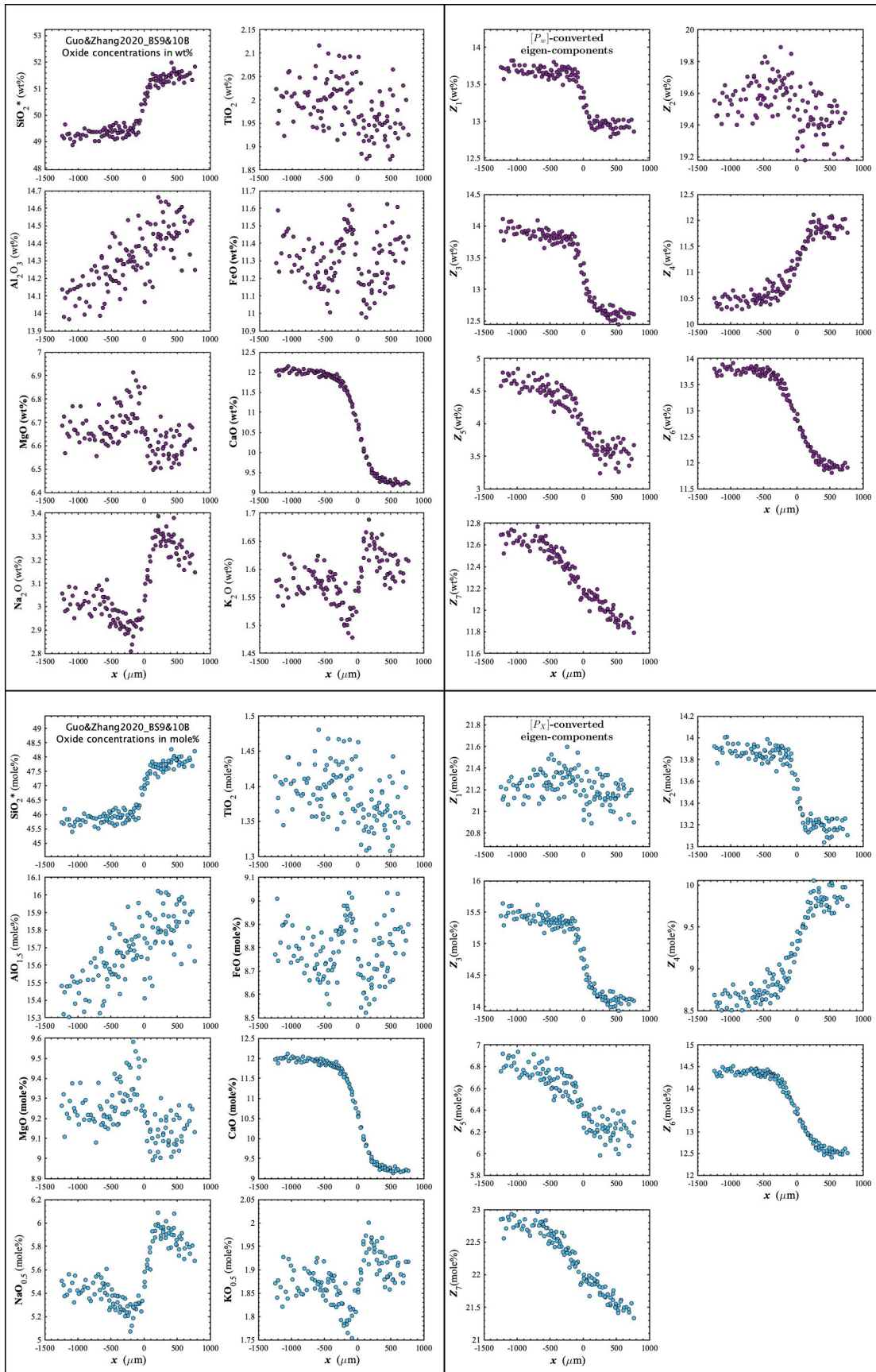
258

Figure D139. Concentration profiles of oxide components in wt% (upper left panel), oxide components in mole% (lower left panel), $[P_w]$-converted eigen-components (upper right panel), and $[P_X]$-converted eigen-components (lower right panel) of Guo&Zhang2020_BS3&4B, which is a diffusion couple experiment in basalt (Guo and Zhang, 2020).
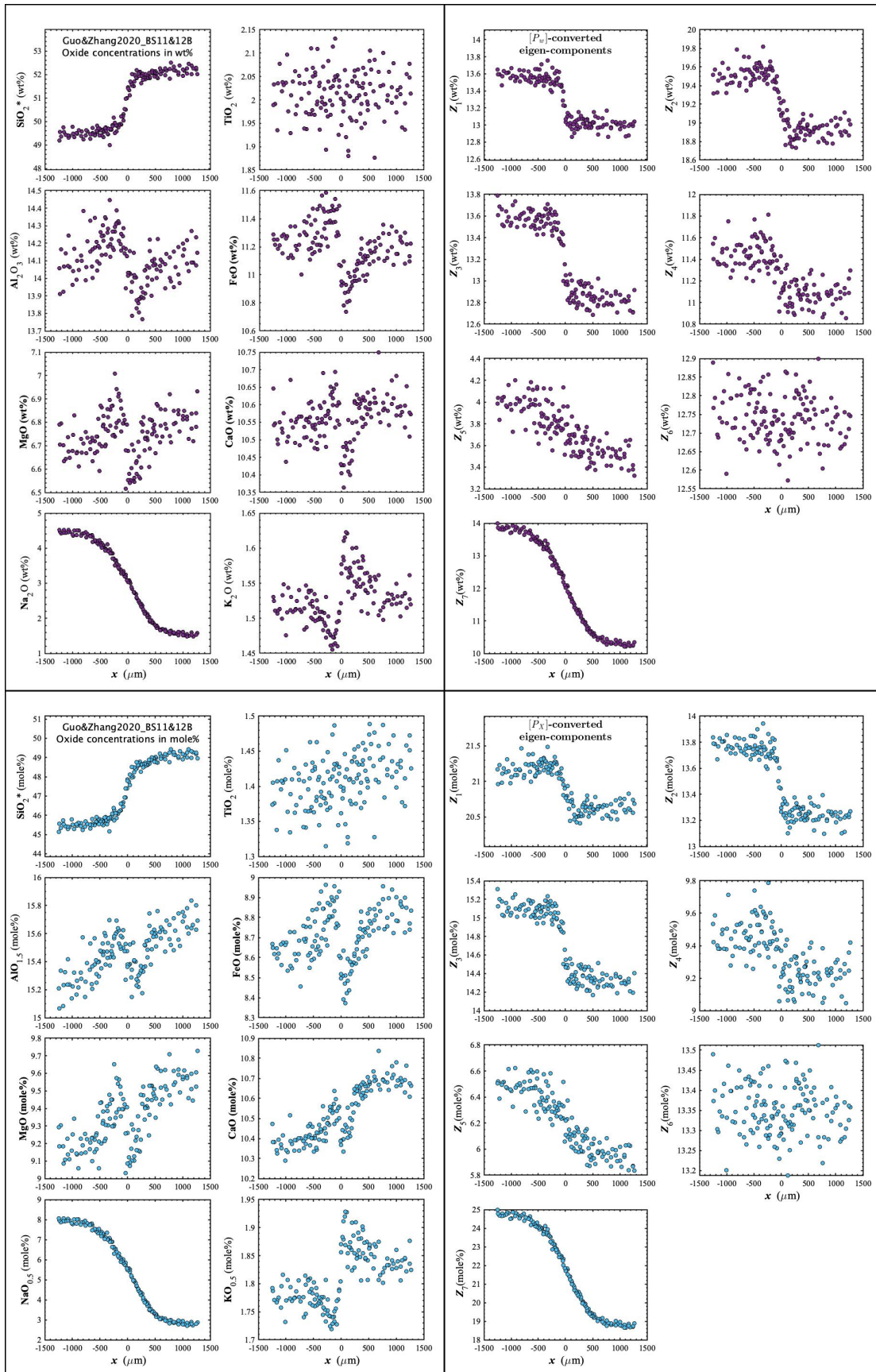
Figure D140. Concentration profiles of oxide components in wt% (upper left panel), oxide components in mole% (lower left panel), [P_w]-converted eigen-components (upper right panel), and [P_X]-converted eigen-components (lower right panel) of Guo&Zhang2020_BS5&6B, which is a diffusion couple experiment in basalt (Guo and Zhang, 2020).

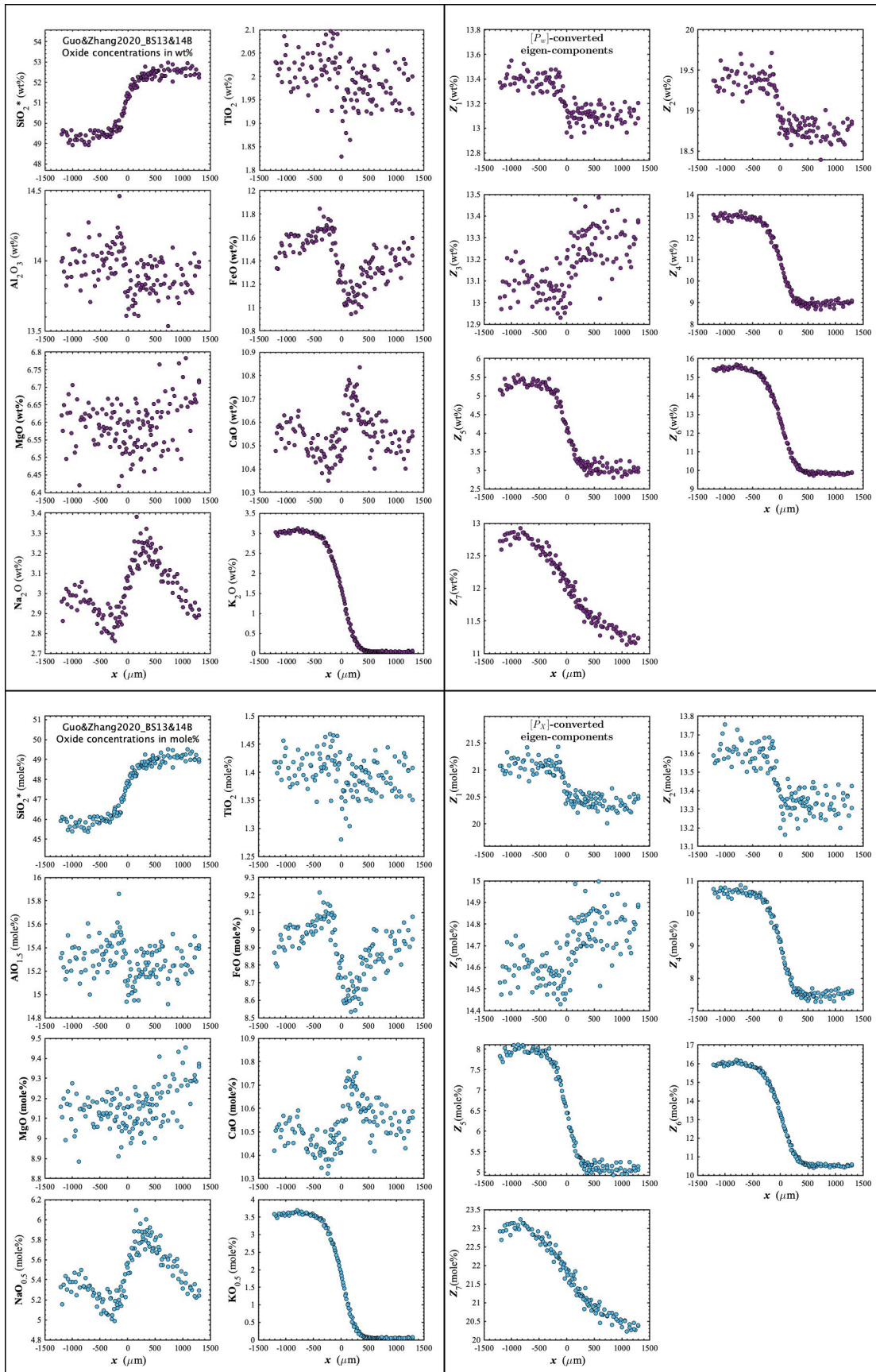**Figure D141.** Concentration profiles of oxide components in wt% (upper left panel), oxide components in mole% (lower left panel), [P_w]-converted eigen-components (upper right panel), and [P_X]-converted eigen-components (lower right panel) of Guo&Zhang2020_BS7&8B, which is a diffusion couple experiment in basalt (Guo and Zhang, 2020).
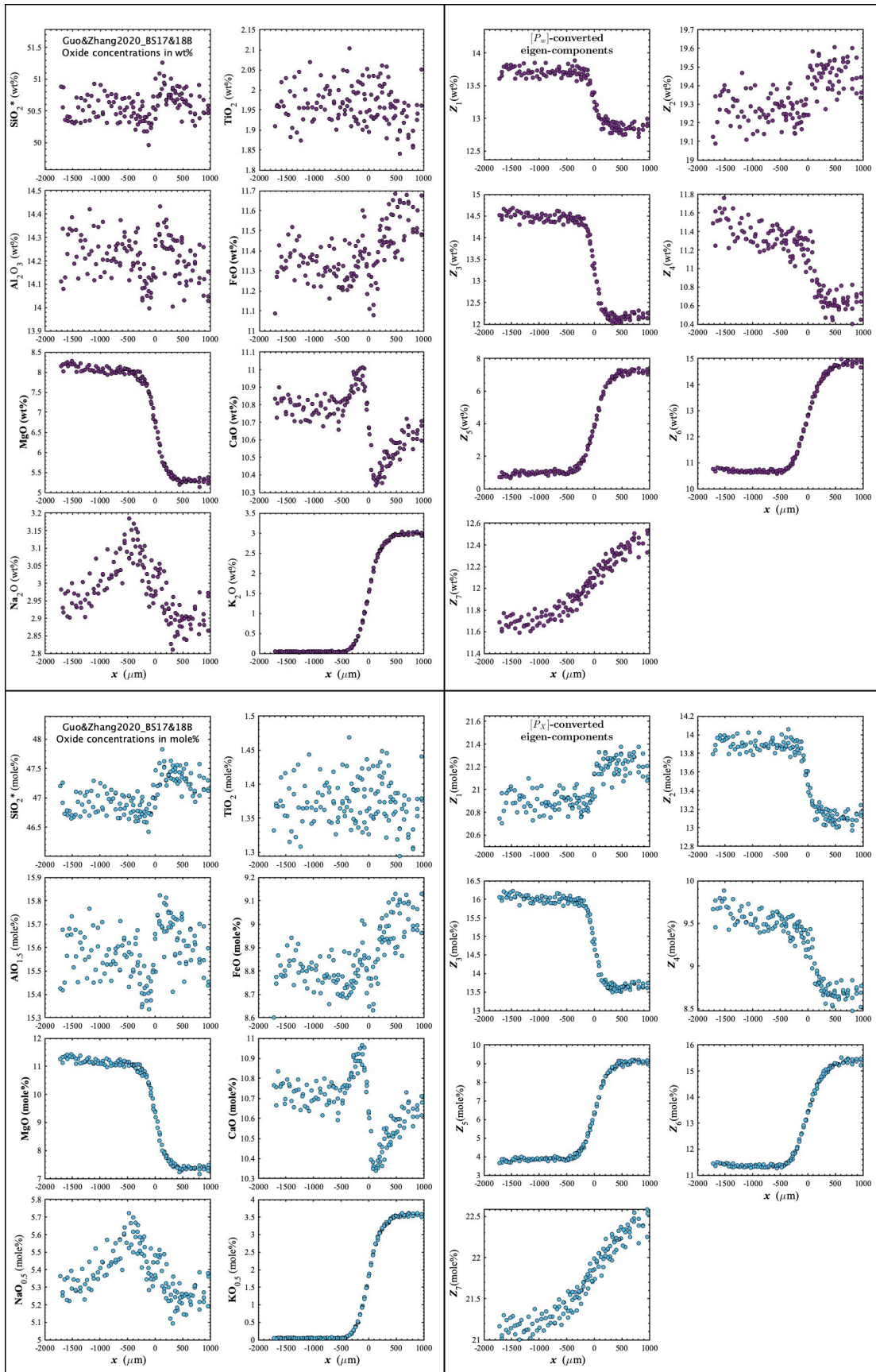
Figure D142. Concentration profiles of oxide components in wt% (upper left panel), oxide components in mole% (lower left panel), $[P_w]$-converted eigen-components (upper right panel), and $[P_X]$-converted eigen-components (lower right panel) of Guo&Zhang2020_BS9&10B, which is a diffusion couple experiment in basalt (Guo and Zhang, 2020).

Figure D143. Concentration profiles of oxide components in wt% (upper left panel), oxide components in mole% (lower left panel), [P_w]-converted eigen-components (upper right panel), and [P_X]-converted eigen-components (lower right panel) of Guo&Zhang2020_BS11&12B, which is a diffusion couple experiment in basalt (Guo and Zhang, 2020).
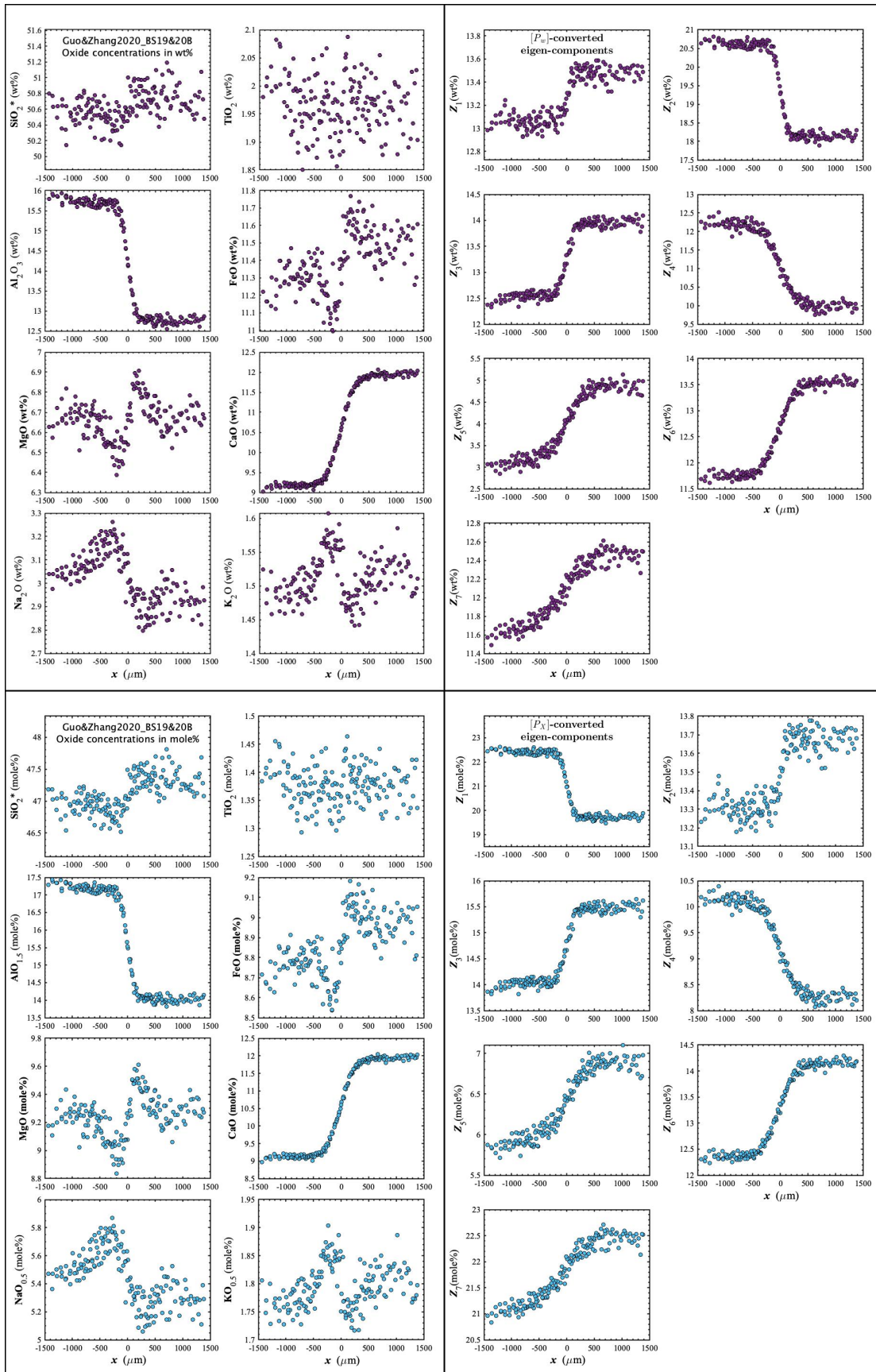
263

Figure D144. Concentration profiles of oxide components in wt% (upper left panel), oxide components in mole% (lower left panel), [P_w]-converted eigen-components (upper right panel), and [P_X]-converted eigen-components (lower right panel) of Guo&Zhang2020_BS13&14B, which is a diffusion couple experiment in basalt (Guo and Zhang, 2020).
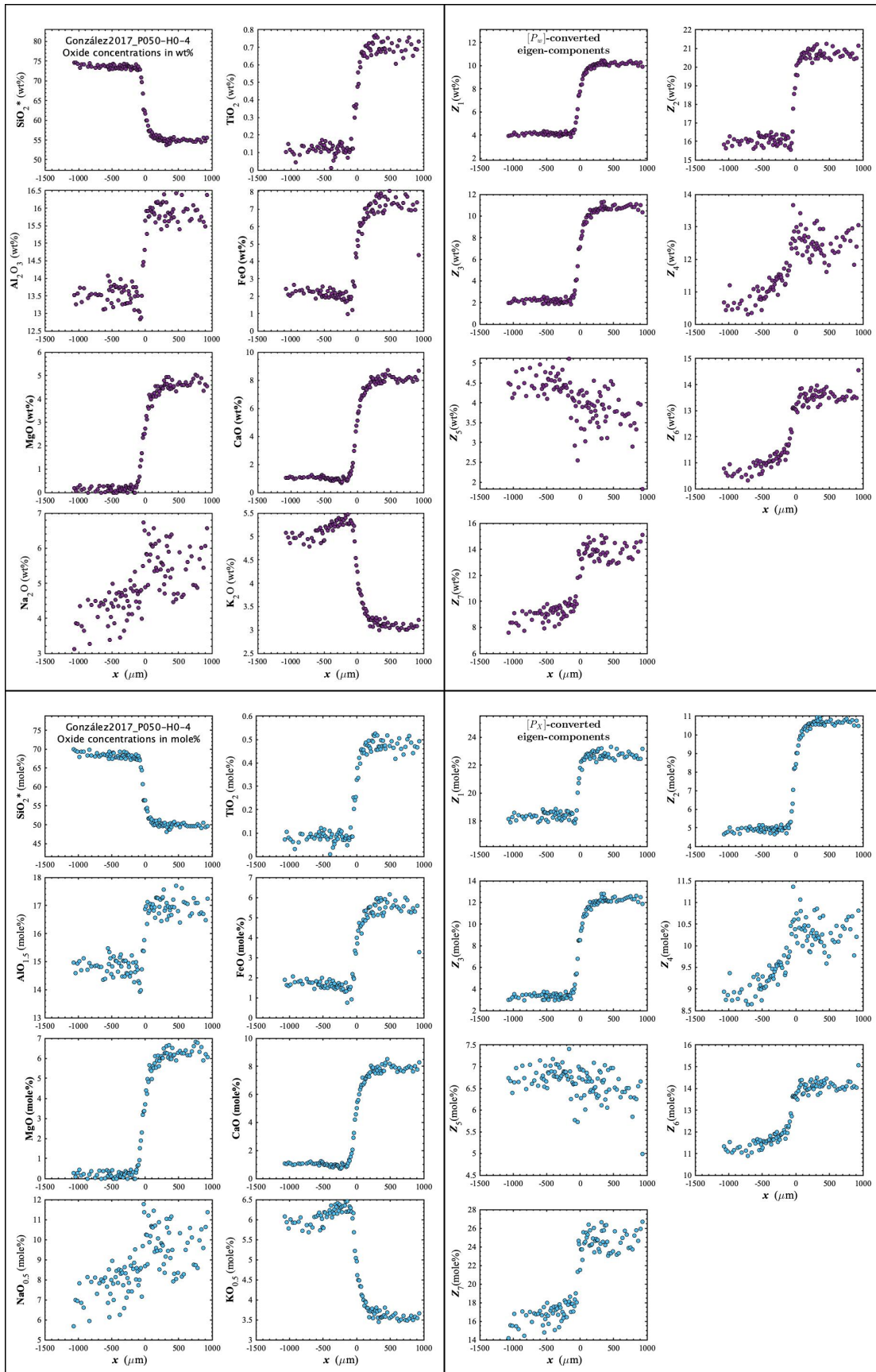
Figure D145. Concentration profiles of oxide components in wt% (upper left panel), oxide components in mole% (lower left panel), [P_w]-converted eigen-components (upper right panel), and [P_X]-converted eigen-components (lower right panel) of Guo&Zhang2020_BS17&18B, which is a diffusion couple experiment in basalt (Guo and Zhang, 2020).
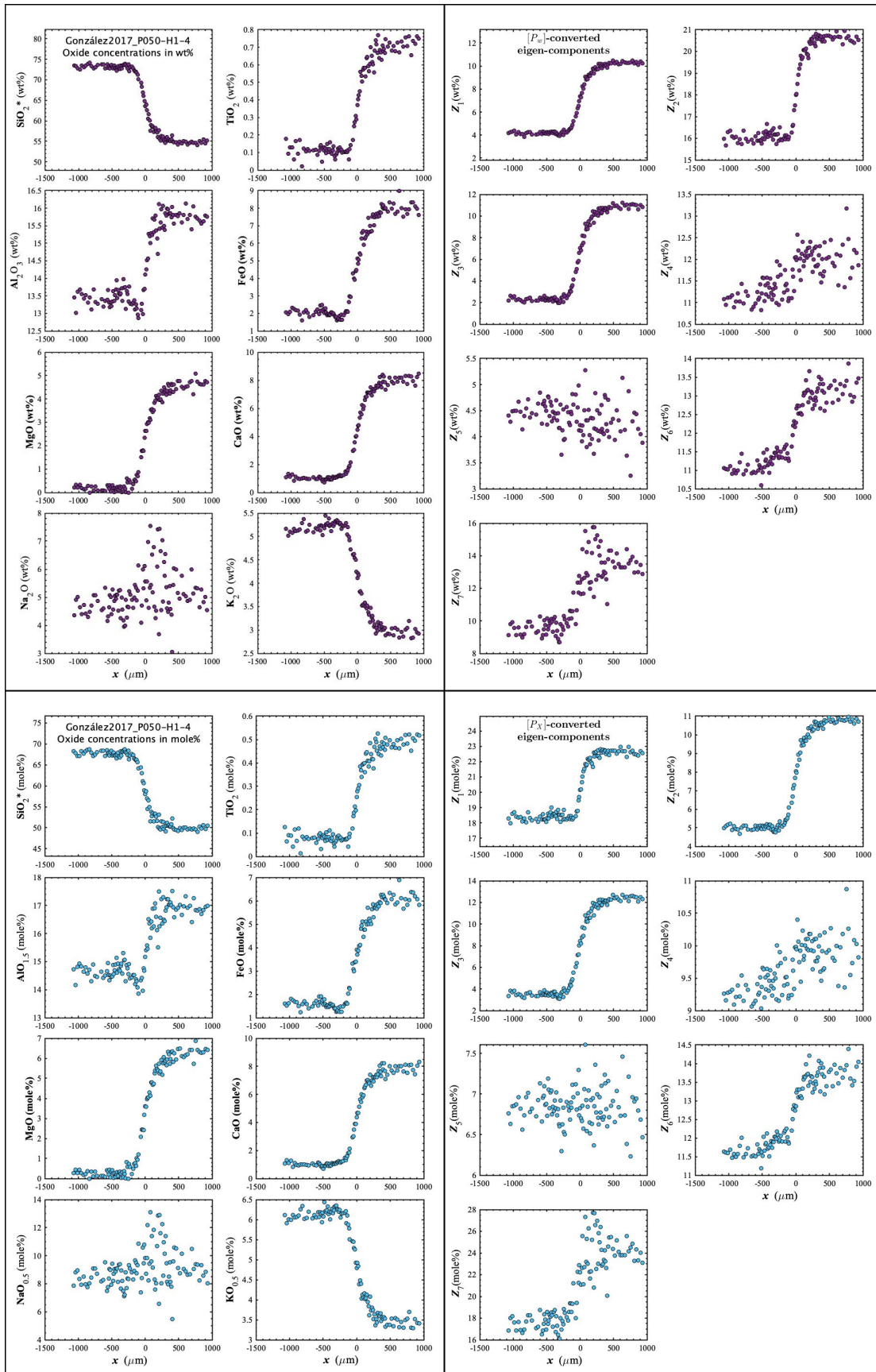
Figure D146. Concentration profiles of oxide components in wt% (upper left panel), oxide components in mole% (lower left panel), [P_w]-converted eigen-components (upper right panel), and [P_X]-converted eigen-components (lower right panel) of Guo&Zhang2020_BS19&20B, which is a diffusion couple experiment in basalt (Guo and Zhang, 2020).

266

Figure D147. Concentration profiles of oxide components in wt% (upper left panel), oxide components in mole% (lower left panel), [P_w]-converted eigen-components (upper right panel), and [P_X]-converted eigen-components (lower right panel) of González2017_P050-H0-4, which is a diffusion couple experiment between natural shoshonite and a high-K rhyolite (González - Garcia et al., 2017).
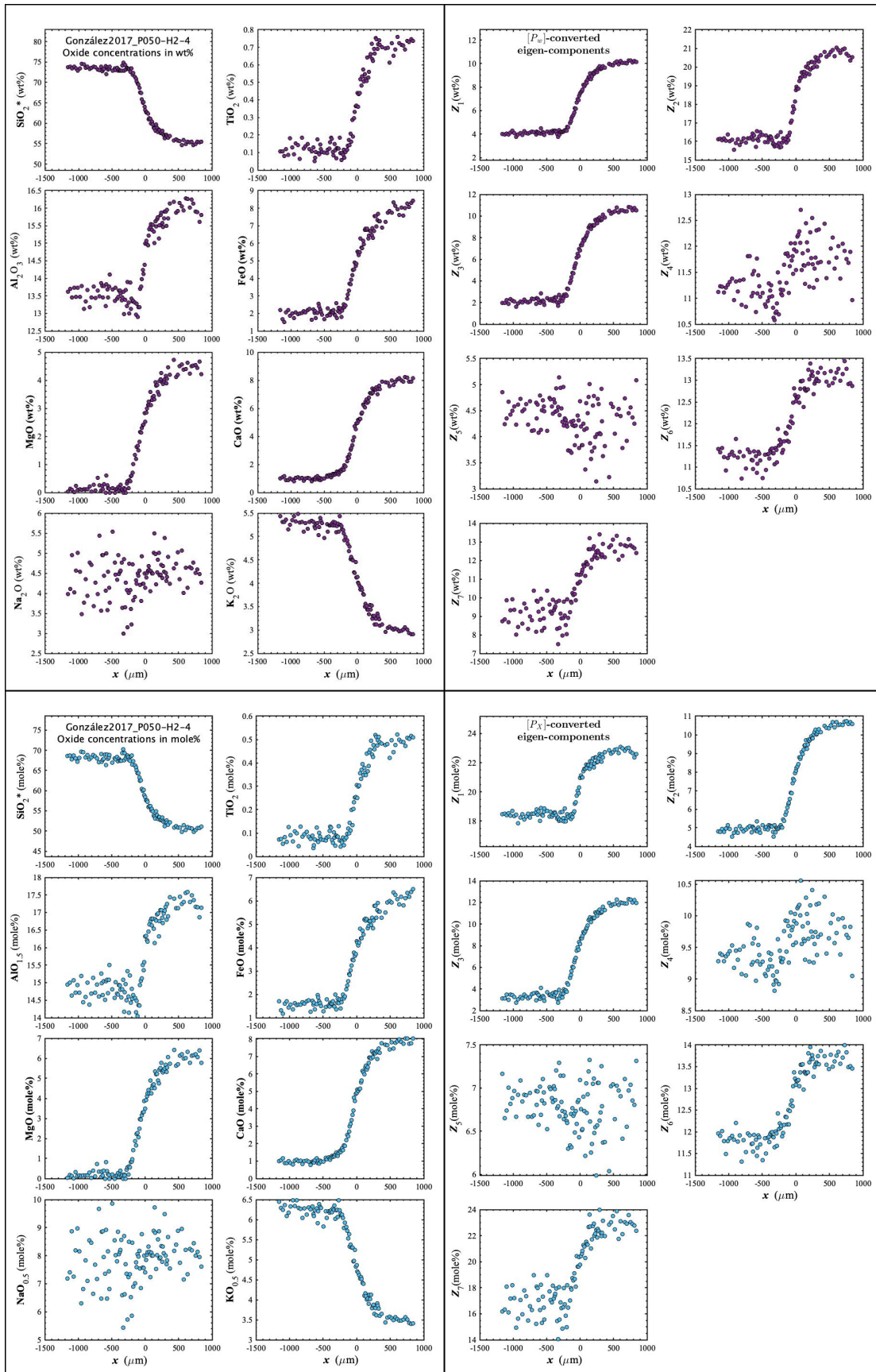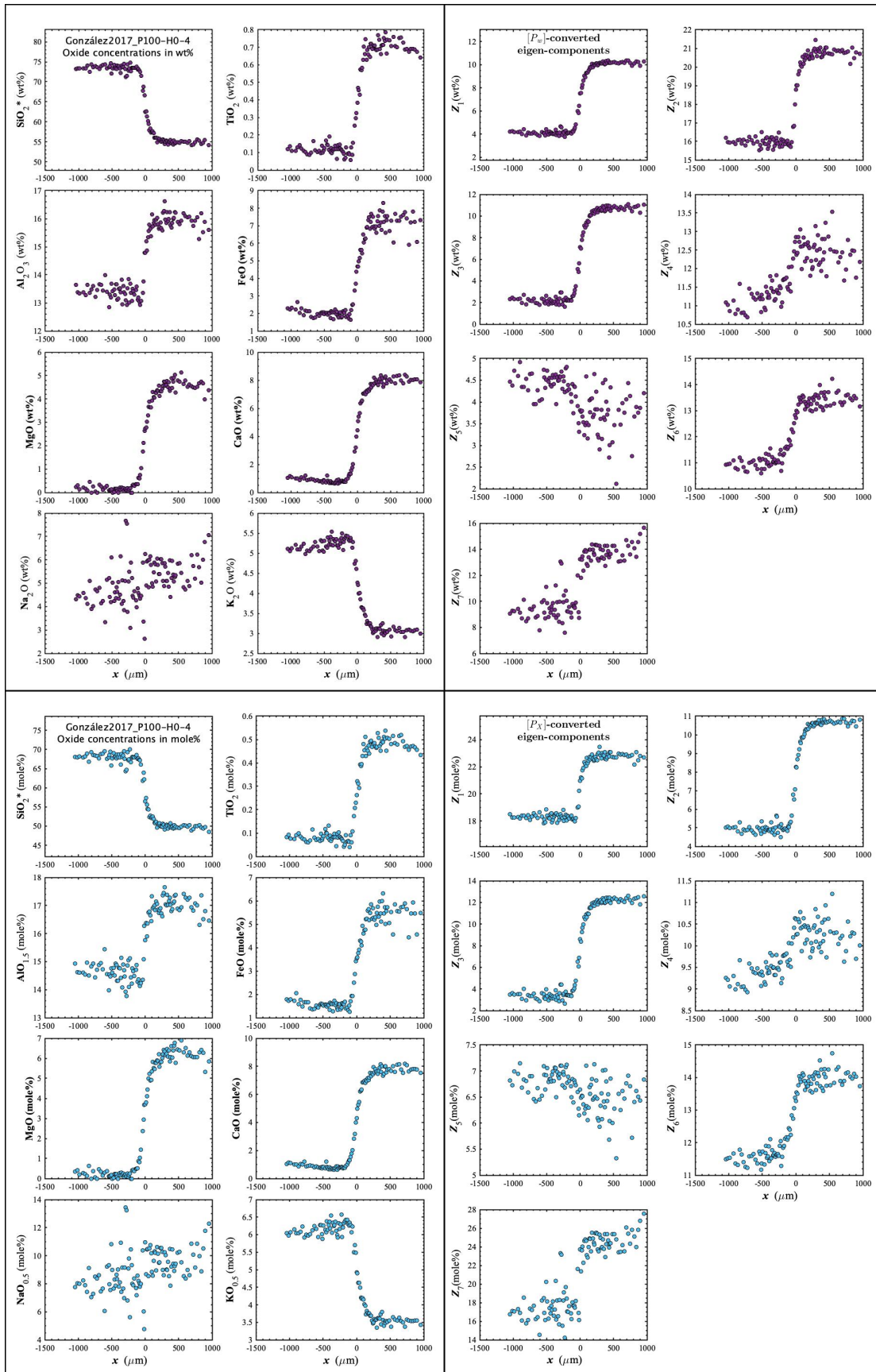
267

Figure D148. Concentration profiles of oxide components in wt% (upper left panel), oxide components in mole% (lower left panel), [P_w]-converted eigen-components (upper right panel), and [P_X]-converted eigen-components (lower right panel) of González2017_P050-H1-4, which is a diffusion couple experiment between natural shoshonite and a high-K rhyolite (González - Garcia et al., 2017).
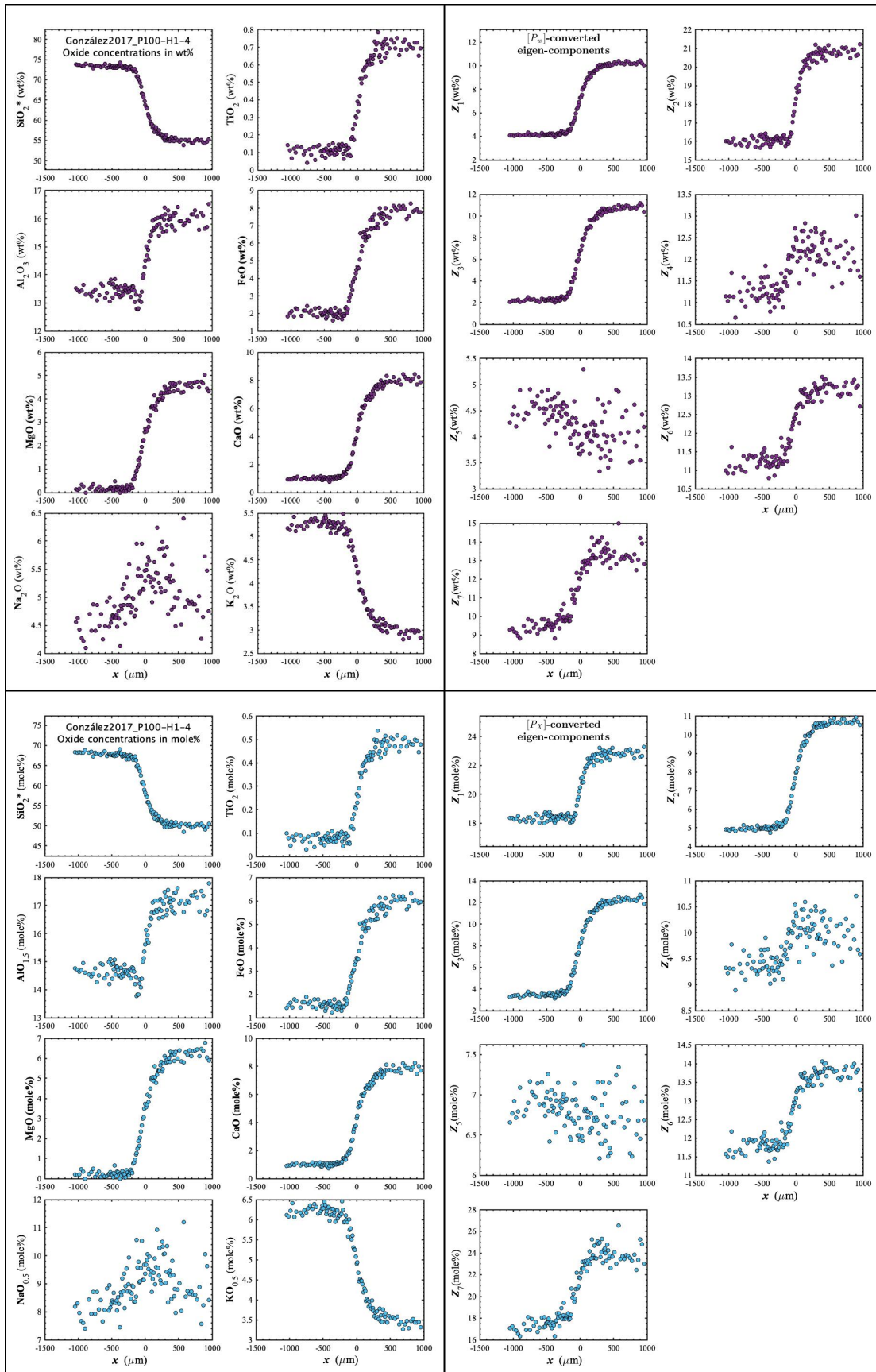
Figure D149. Concentration profiles of oxide components in wt% (upper left panel), oxide components in mole% (lower left panel), $[P_w]$-converted eigen-components (upper right panel), and $[P_X]$-converted eigen-components (lower right panel) of González2017_P050-H2-4, which is a diffusion couple experiment between natural shoshonite and a high-K rhyolite (González - Garcia et al., 2017).

269

Figure D150. Concentration profiles of oxide components in wt% (upper left panel), oxide components in mole% (lower left panel), [P_w]-converted eigen-components (upper right panel), and [P_X]-converted eigen-components (lower right panel) of González2017_P100-H0-4, which is a diffusion couple experiment between natural shoshonite and a high-K rhyolite (González - Garcia et al., 2017).
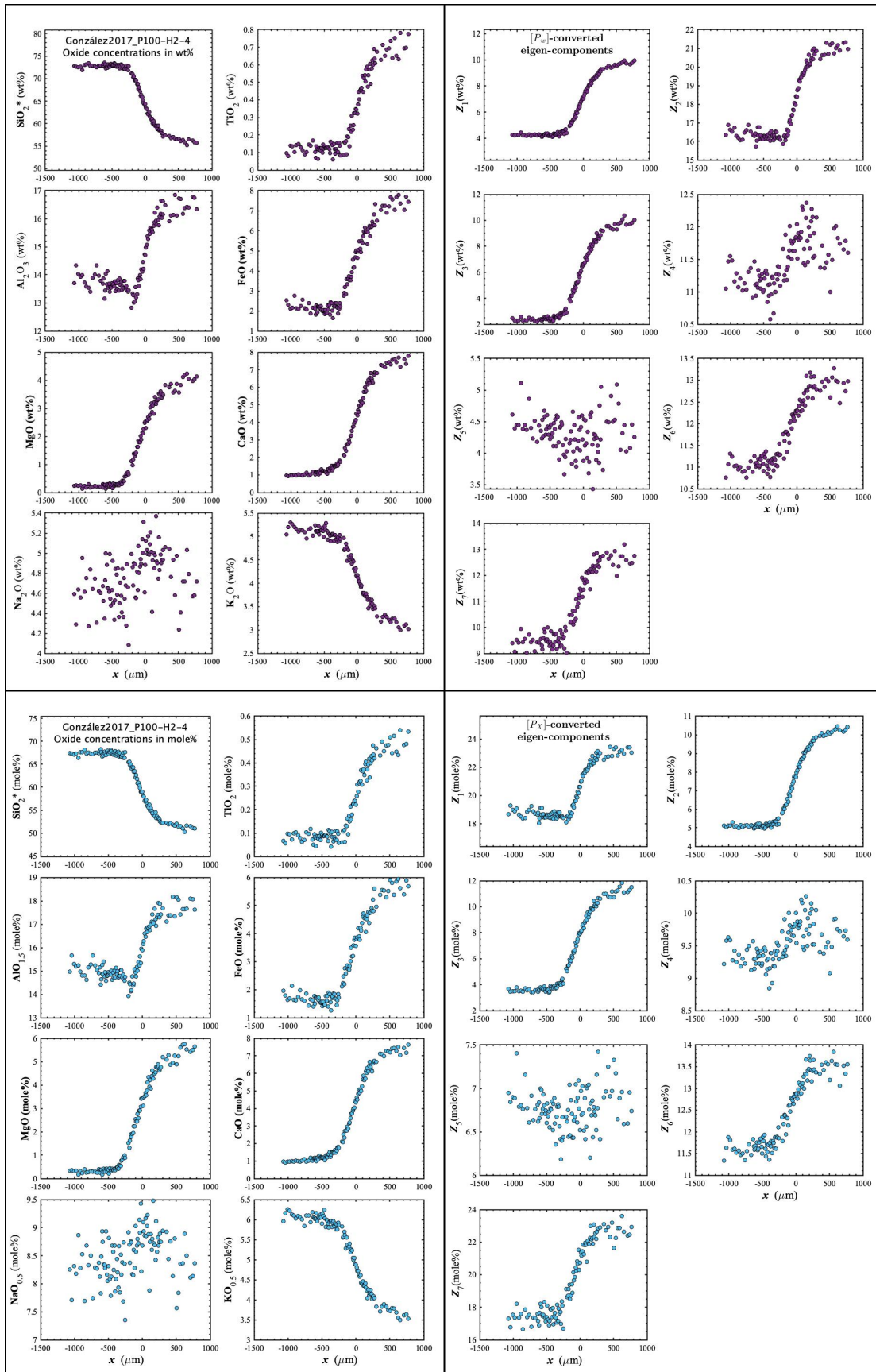
270

Figure D151. Concentration profiles of oxide components in wt% (upper left panel), oxide components in mole% (lower left panel), [P_w]-converted eigen-components (upper right panel), and [P_X]-converted eigen-components (lower right panel) of González2017_P100-H1-4, which is a diffusion couple experiment between natural shoshonite and a high-K rhyolite (González - Garcia et al., 2017).
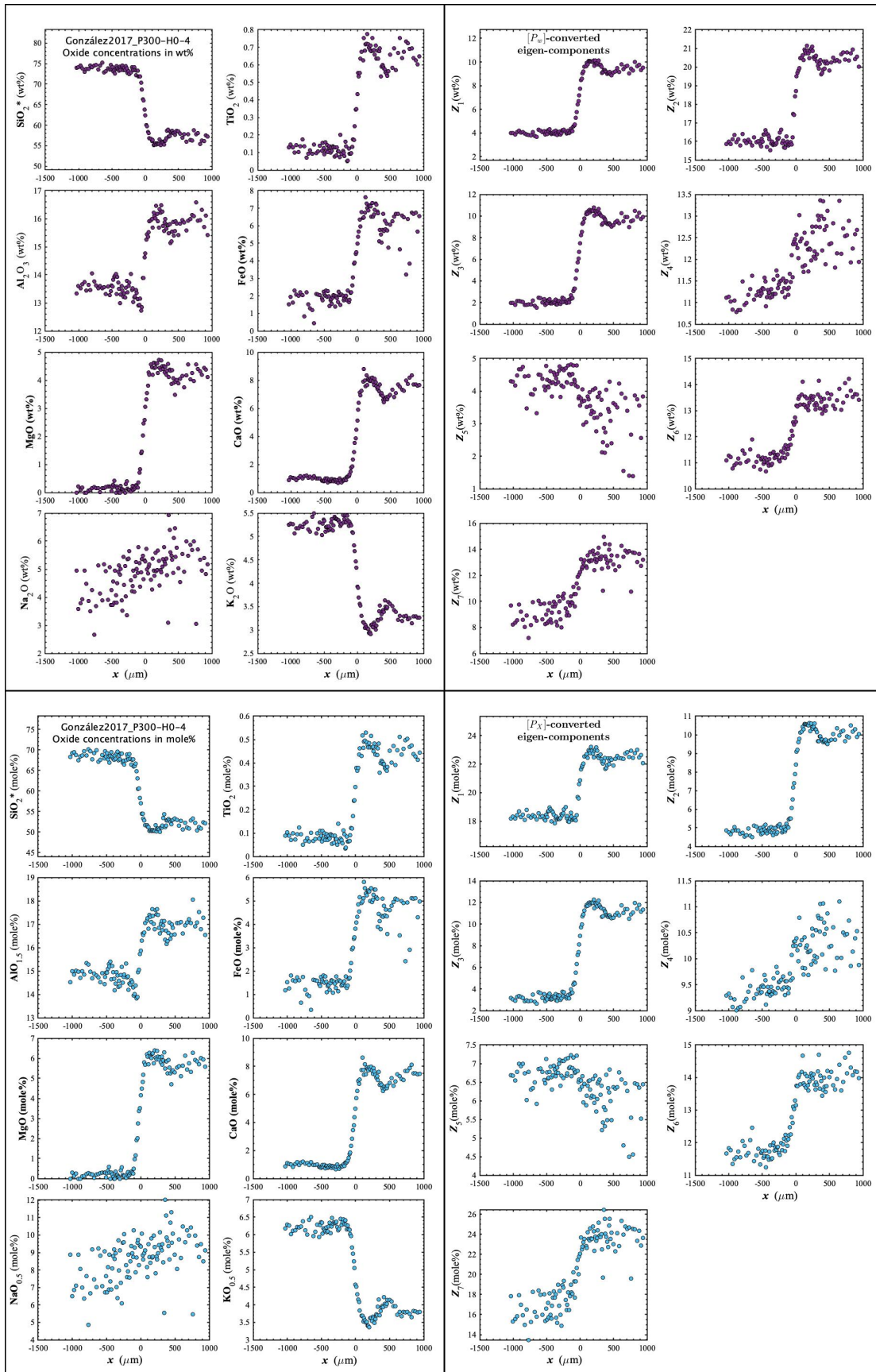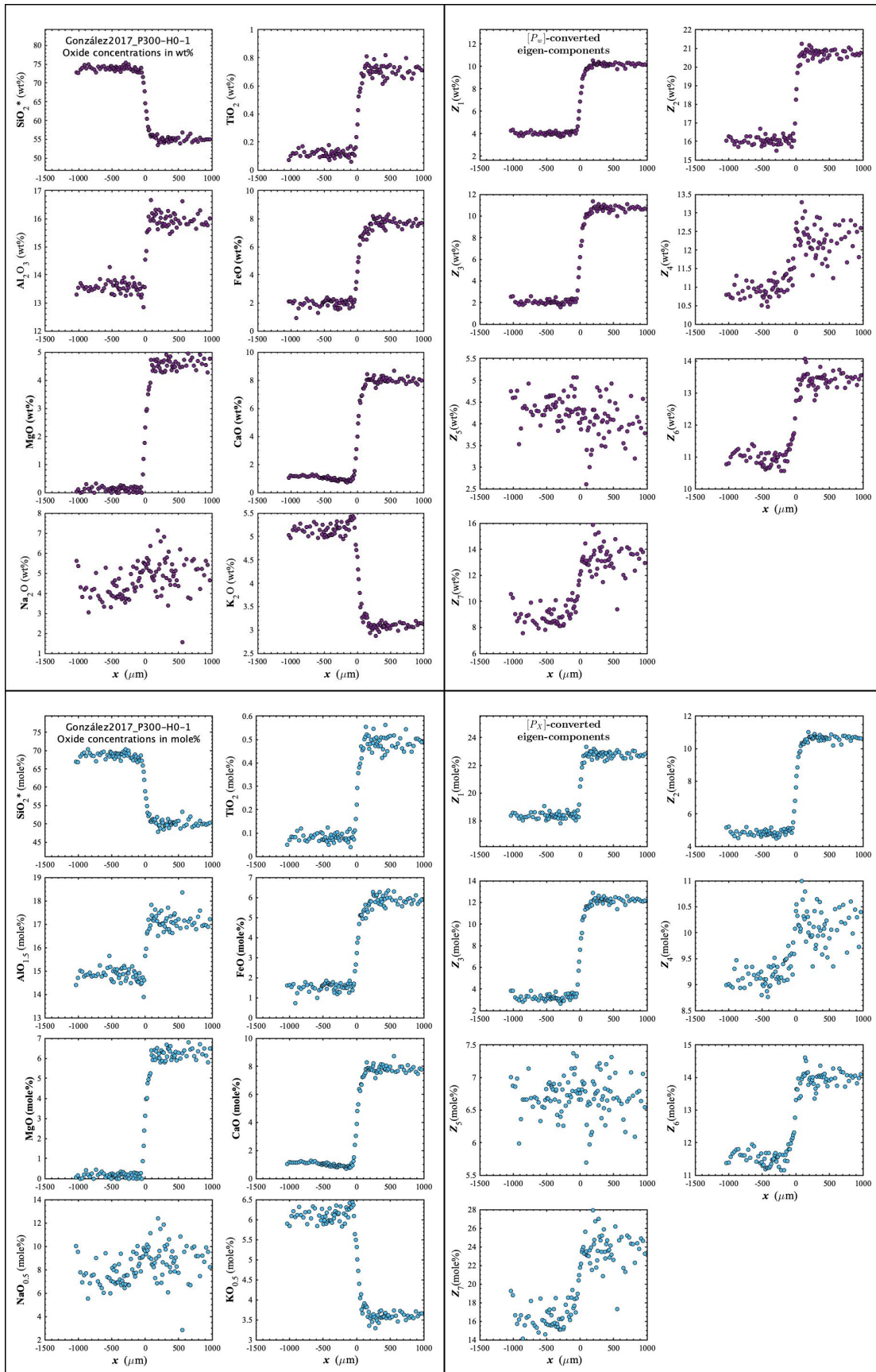
271

Figure D152. Concentration profiles of oxide components in wt% (upper left panel), oxide components in mole% (lower left panel), [P_w]-converted eigen-components (upper right panel), and [P_X]-converted eigen-components (lower right panel) of González2017_P100-H2-4, which is a diffusion couple experiment between natural shoshonite and a high-K rhyolite (González - Garcia et al., 2017).

272

Figure D153. Concentration profiles of oxide components in wt% (upper left panel), oxide components in mole% (lower left panel), [P_w]-converted eigen-components (upper right panel), and [P_X]-converted eigen-components (lower right panel) of González2017_P300-H0-4, which is a diffusion couple experiment between natural shoshonite and a high-K rhyolite (González - Garcia et al., 2017).
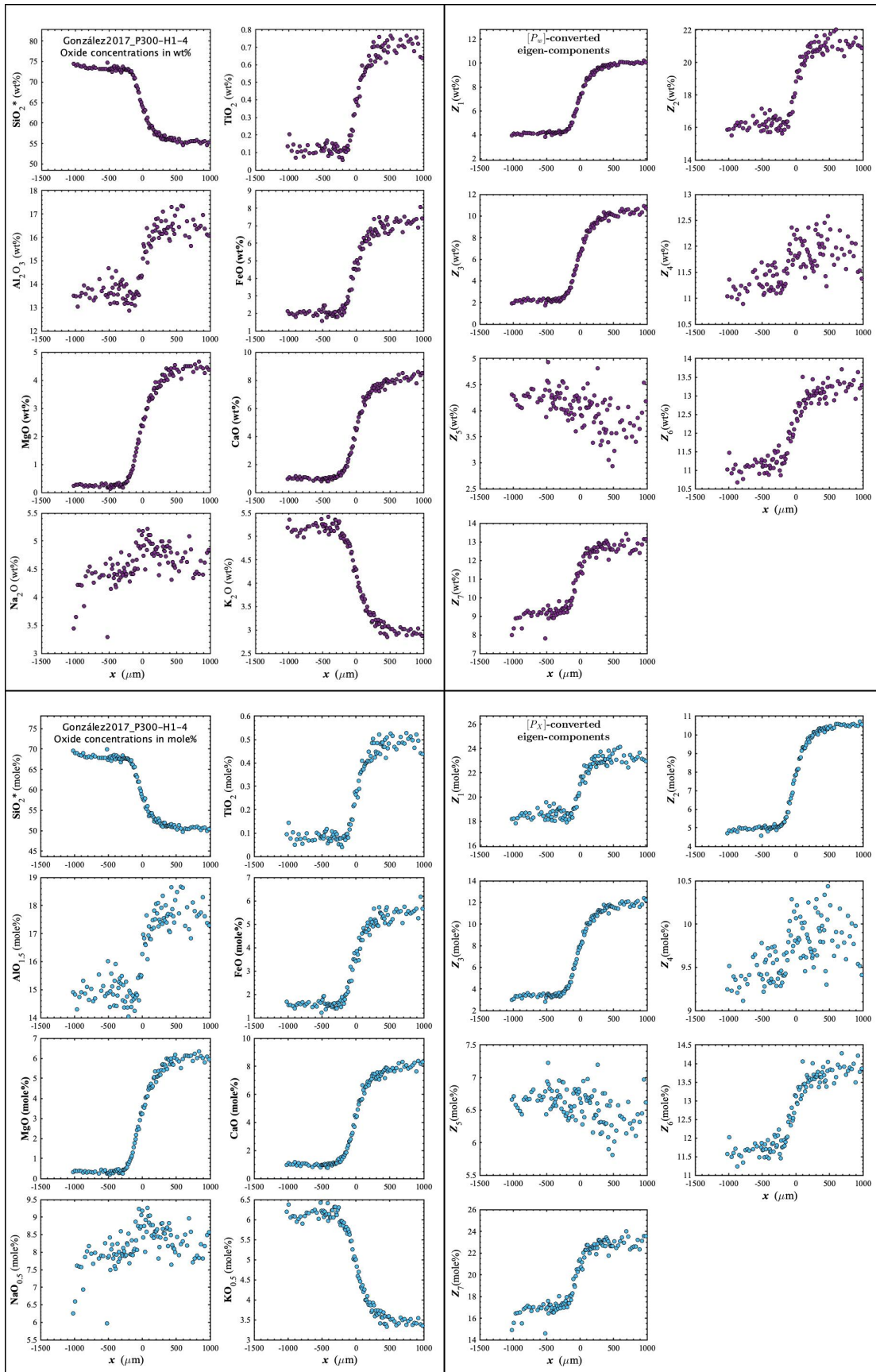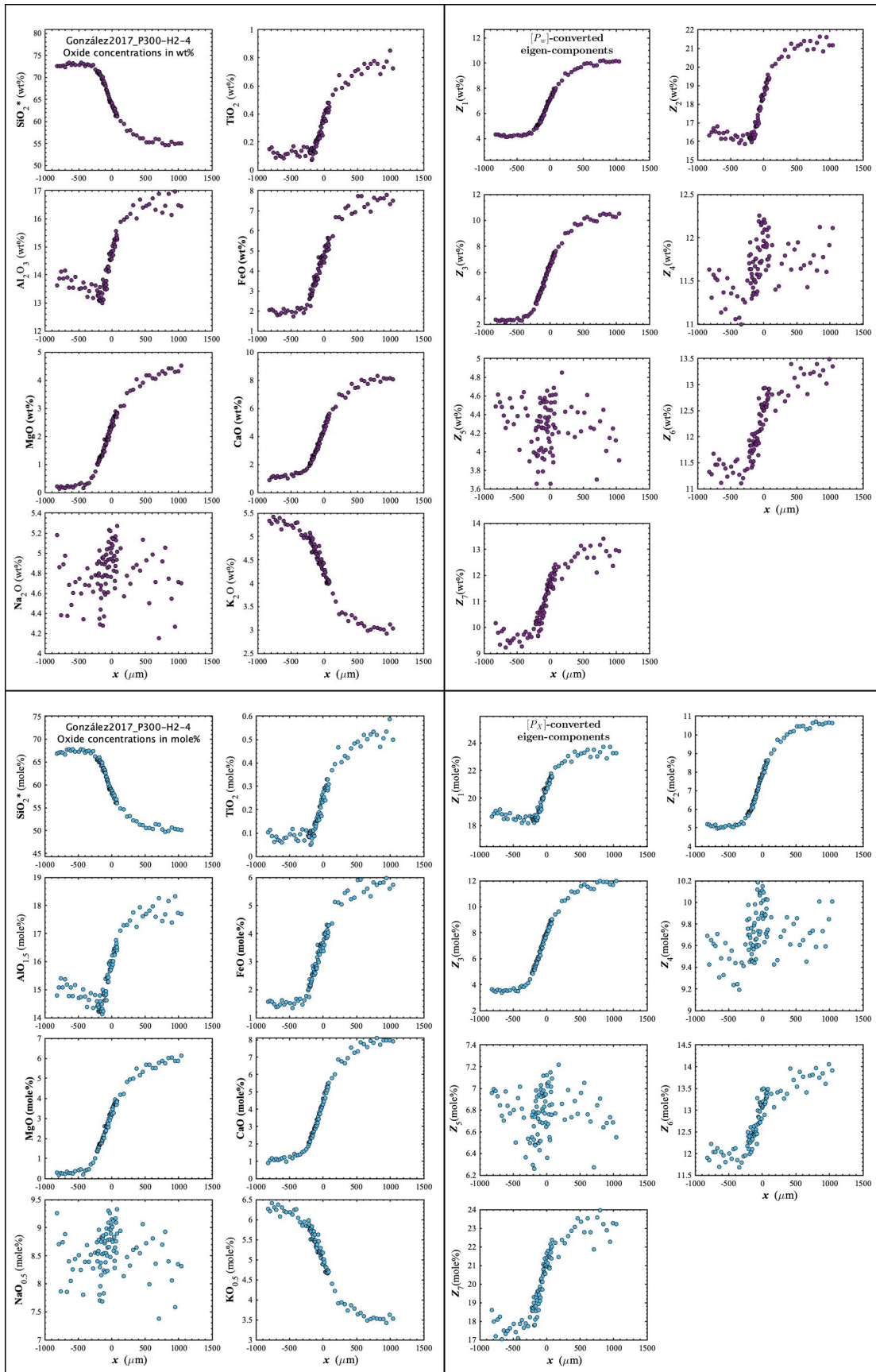
273

Figure D154. Concentration profiles of oxide components in wt% (upper left panel), oxide components in mole% (lower left panel), [P_w]-converted eigen-components (upper right panel), and [P_X]-converted eigen-components (lower right panel) of González2017_P300-H0-1, which is a diffusion couple experiment between natural shoshonite and a high-K rhyolite (González - Garcia et al., 2017).

274

Figure D155. Concentration profiles of oxide components in wt% (upper left panel), oxide components in mole% (lower left panel), [P_w]-converted eigen-components (upper right panel), and [P_X]-converted eigen-components (lower right panel) of González2017_P300-H1-4, which is a diffusion couple experiment between natural shoshonite and a high-K rhyolite (González - Garcia et al., 2017).
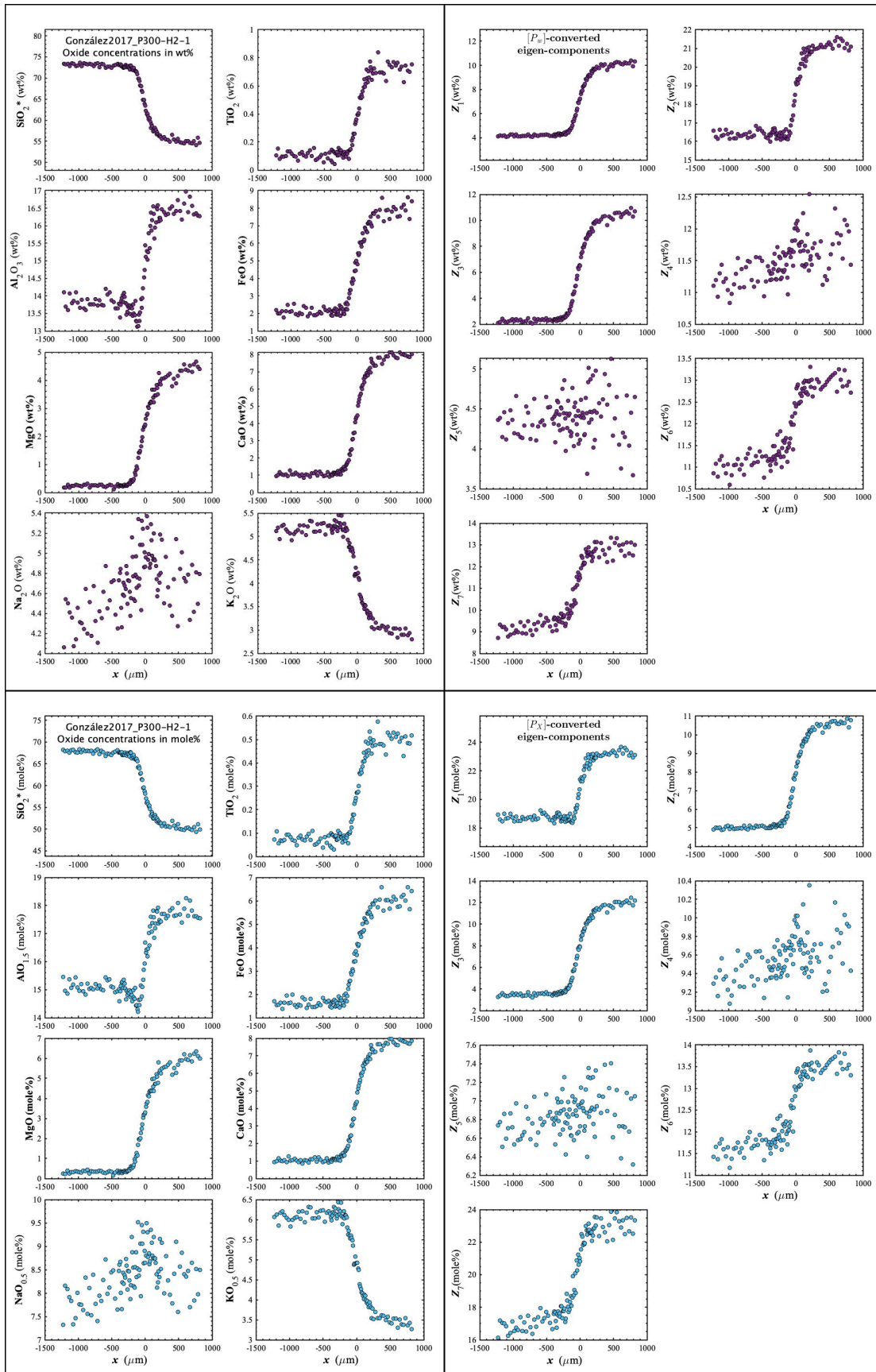
275

Figure D156. Concentration profiles of oxide components in wt% (upper left panel), oxide components in mole% (lower left panel), $[P_w]$-converted eigen-components (upper right panel), and $[P_X]$-converted eigen-components (lower right panel) of González2017_P300-H2-4, which is a diffusion couple experiment between natural shoshonite and a high-K rhyolite (González - Garcia et al., 2017).
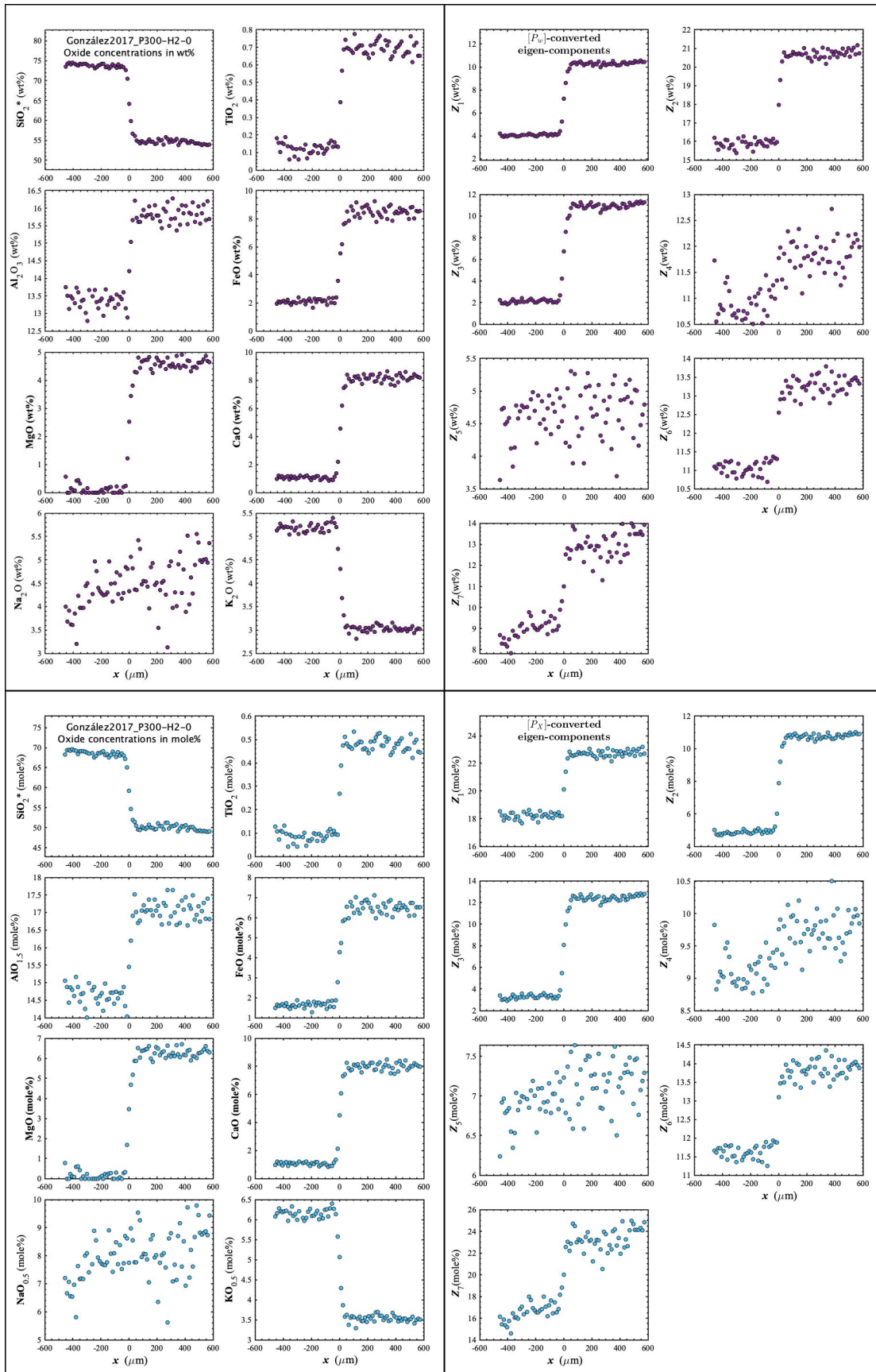
276

Figure D157. Concentration profiles of oxide components in wt% (upper left panel), oxide components in mole% (lower left panel), [P_w]-converted eigen-components (upper right panel), and [P_X]-converted eigen-components (lower right panel) of González2017_P300-H2-1, which is a diffusion couple experiment between natural shoshonite and a high-K rhyolite (González - Garcia et al., 2017).
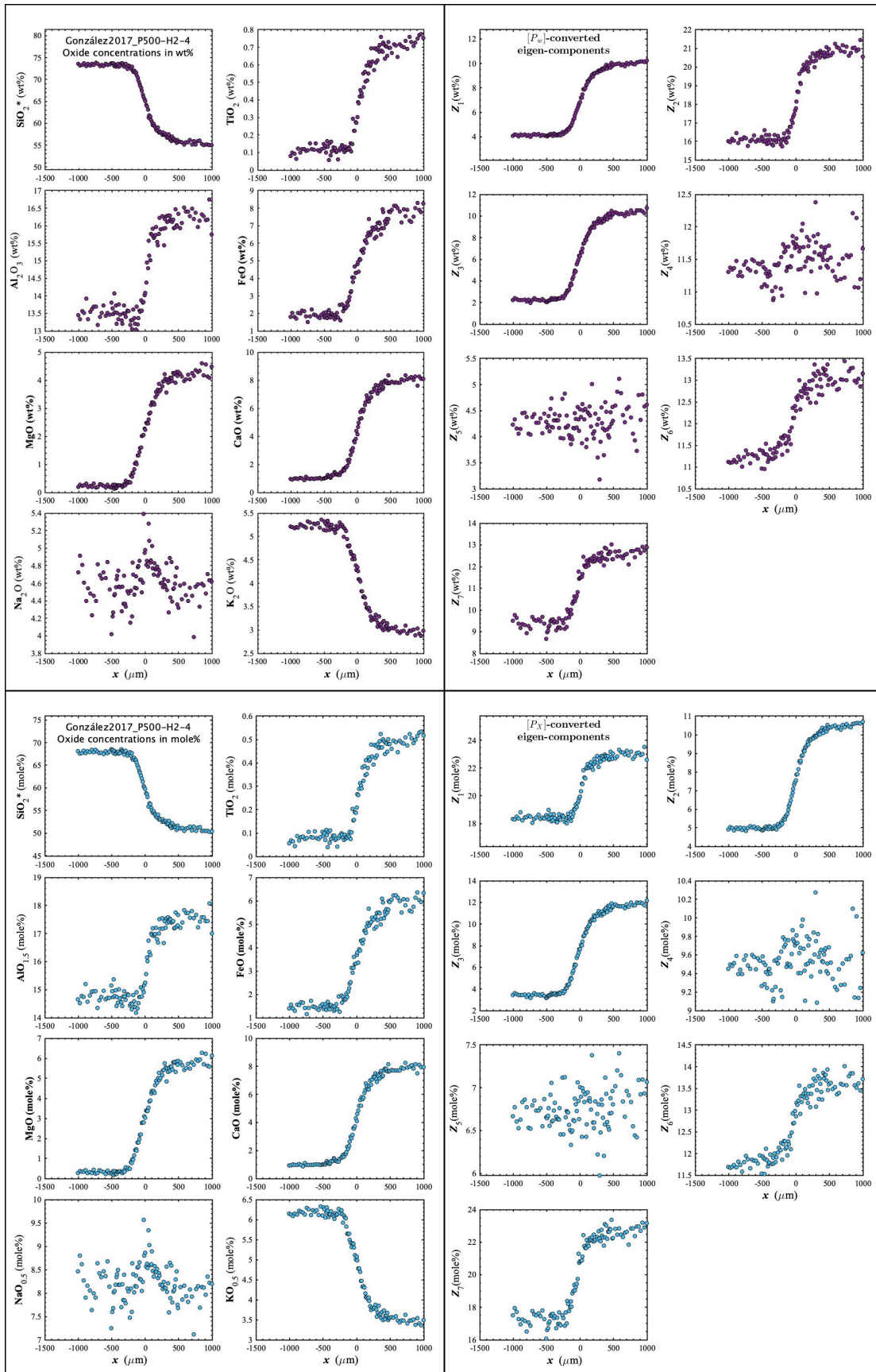
277

Figure D158. Concentration profiles of oxide components in wt% (upper left panel), oxide components in mole% (lower left panel), [P_w]-converted eigen-components (upper right panel), and [P_X]-converted eigen-components (lower right panel) of González2017_P300-H2-0, which is a diffusion couple experiment between natural shoshonite and a high-K rhyolite (González - Garcia et al., 2017).
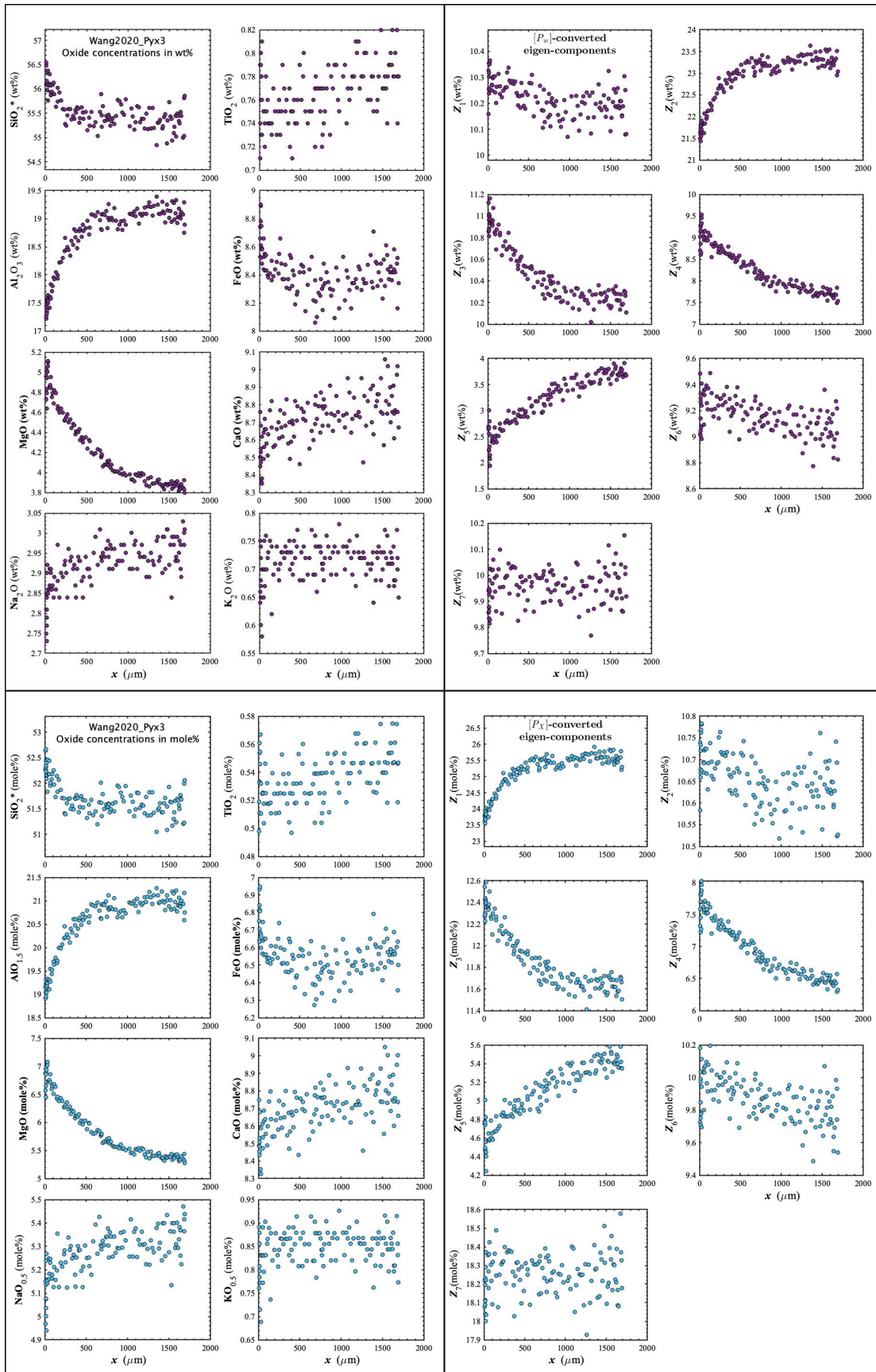
278

Figure D159. Concentration profiles of oxide components in wt% (upper left panel), oxide components in mole% (lower left panel), [P_w]-converted eigen-components (upper right panel), and [P_X]-converted eigen-components (lower right panel) of González2017_P500-H2-4, which is a diffusion couple experiment between natural shoshonite and a high-K rhyolite (González - Garcia et al., 2017).

279

Figure D160. Concentration profiles of oxide components in wt% (upper left panel), oxide components in mole% (lower left panel), [P_w]-converted eigen-components (upper right panel), and [P_X]-converted eigen-components (lower right panel) of Wang2020_Pyx3, which is a lherzolite dissolution experiment in basaltic andesite (Wang et al., 2020).
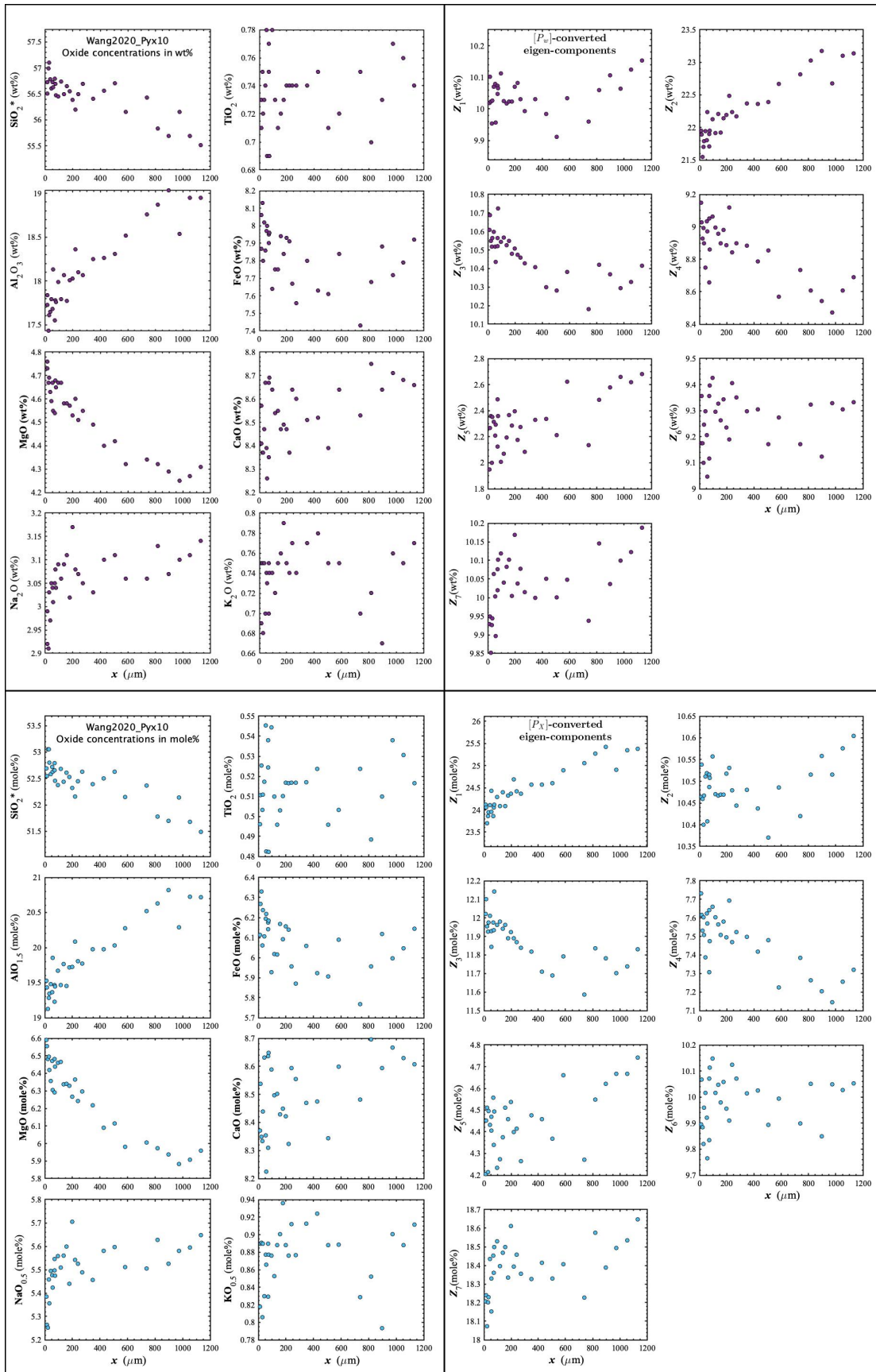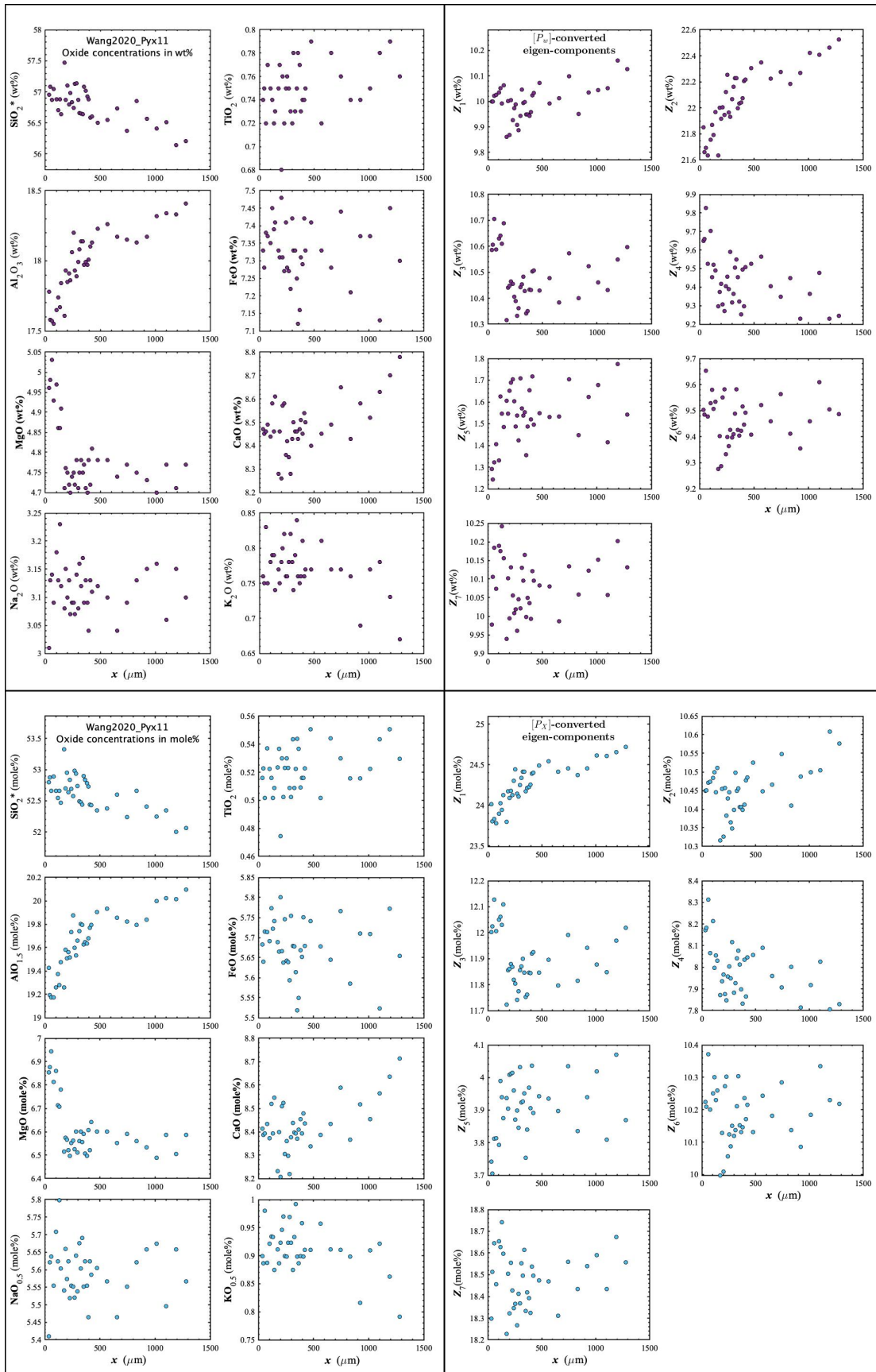
Figure D161. Concentration profiles of oxide components in wt% (upper left panel), oxide components in mole% (lower left panel), [P_w]-converted eigen-components (upper right panel), and [P_X]-converted eigen-components (lower right panel) of Wang2020_Pyx10, which is a lherzolite dissolution experiment in basaltic andesite (Wang et al., 2020).
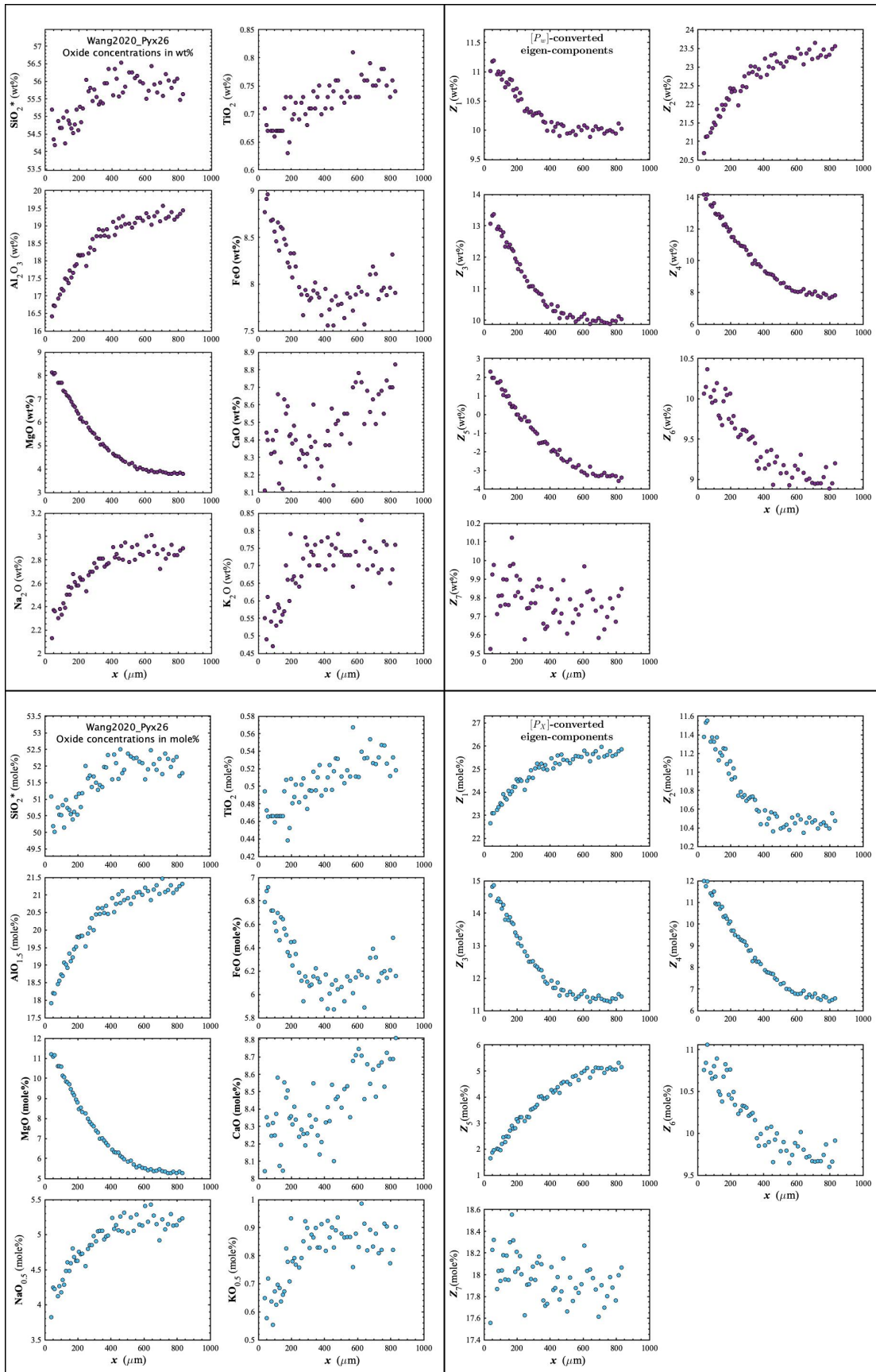
281

Figure D162. Concentration profiles of oxide components in wt% (upper left panel), oxide components in mole% (lower left panel), [P_w]-converted eigen-components (upper right panel), and [P_X]-converted eigen-components (lower right panel) of Wang2020_Pyx11, which is a lherzolite dissolution experiment in basaltic andesite (Wang et al., 2020).
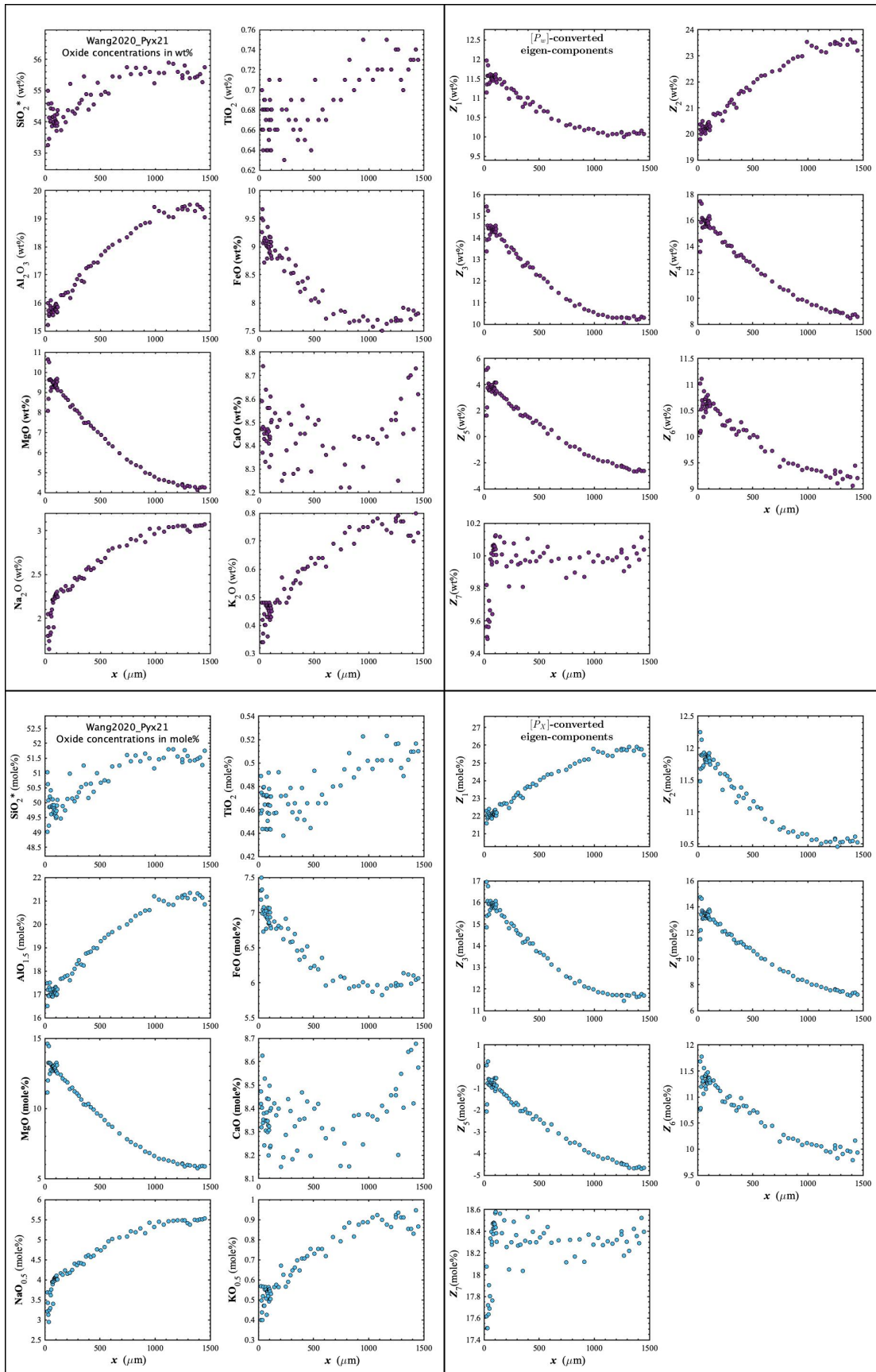
282

Figure D163. Concentration profiles of oxide components in wt% (upper left panel), oxide components in mole% (lower left panel), [P_w]-converted eigen-components (upper right panel), and [P_X]-converted eigen-components (lower right panel) of Wang2020_Pyx26, which is a lherzolite dissolution experiment in basaltic andesite (Wang et al., 2020).

283

Figure D164. Concentration profiles of oxide components in wt% (upper left panel), oxide components in mole% (lower left panel), $[P_w]$-converted eigen-components (upper right panel), and $[P_X]$-converted eigen-components (lower right panel) of Wang2020_Pyx21, which is a lherzolite dissolution experiment in basaltic andesite (Wang et al., 2020).
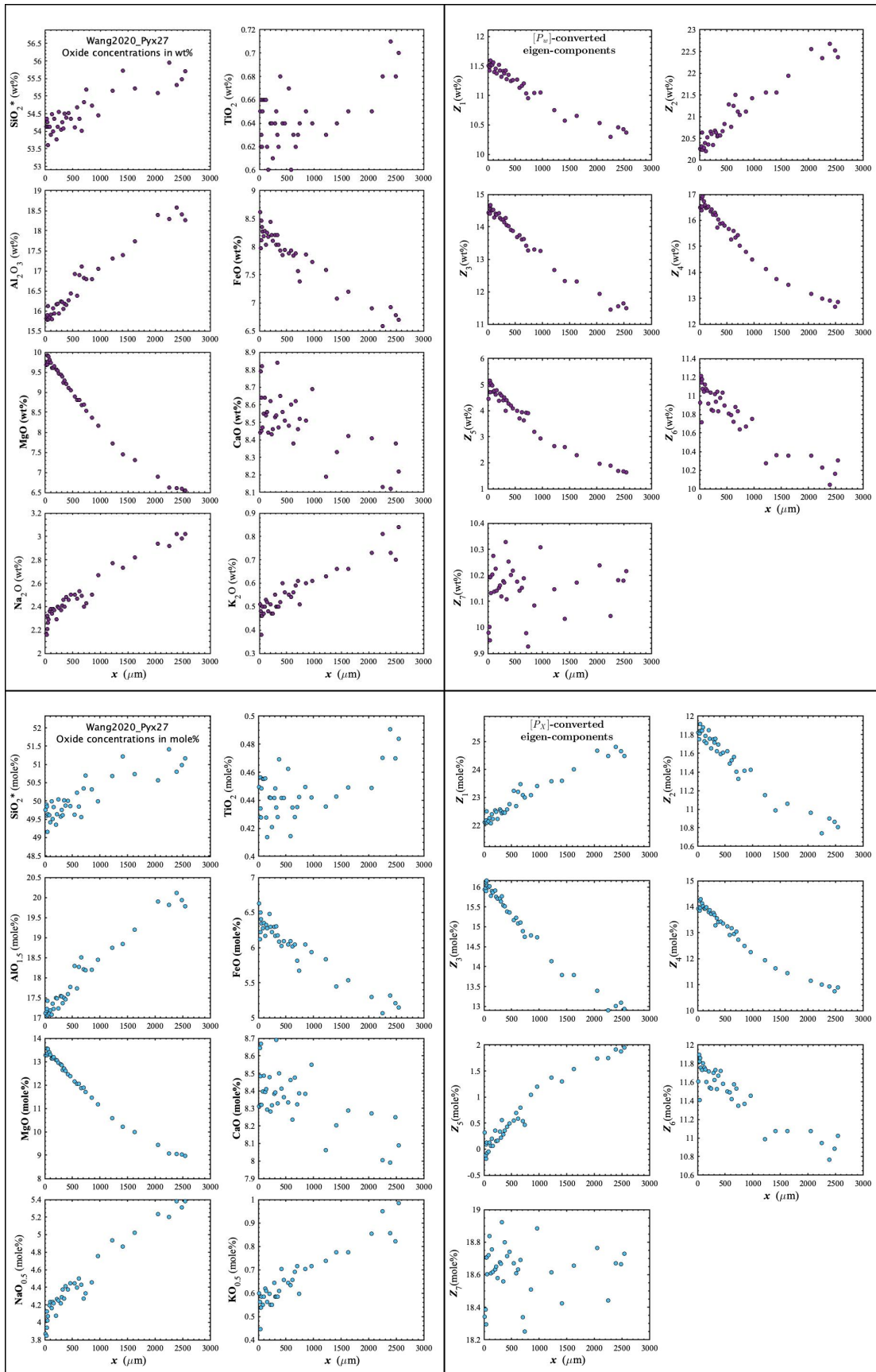
Figure D165. Concentration profiles of oxide components in wt% (upper left panel), oxide components in mole% (lower left panel), [P_w]-converted eigen-components (upper right panel), and [P_X]-converted eigen-components (lower right panel) of Wang2020_Pyx27, which is a lherzolite dissolution experiment in basaltic andesite (Wang et al., 2020).
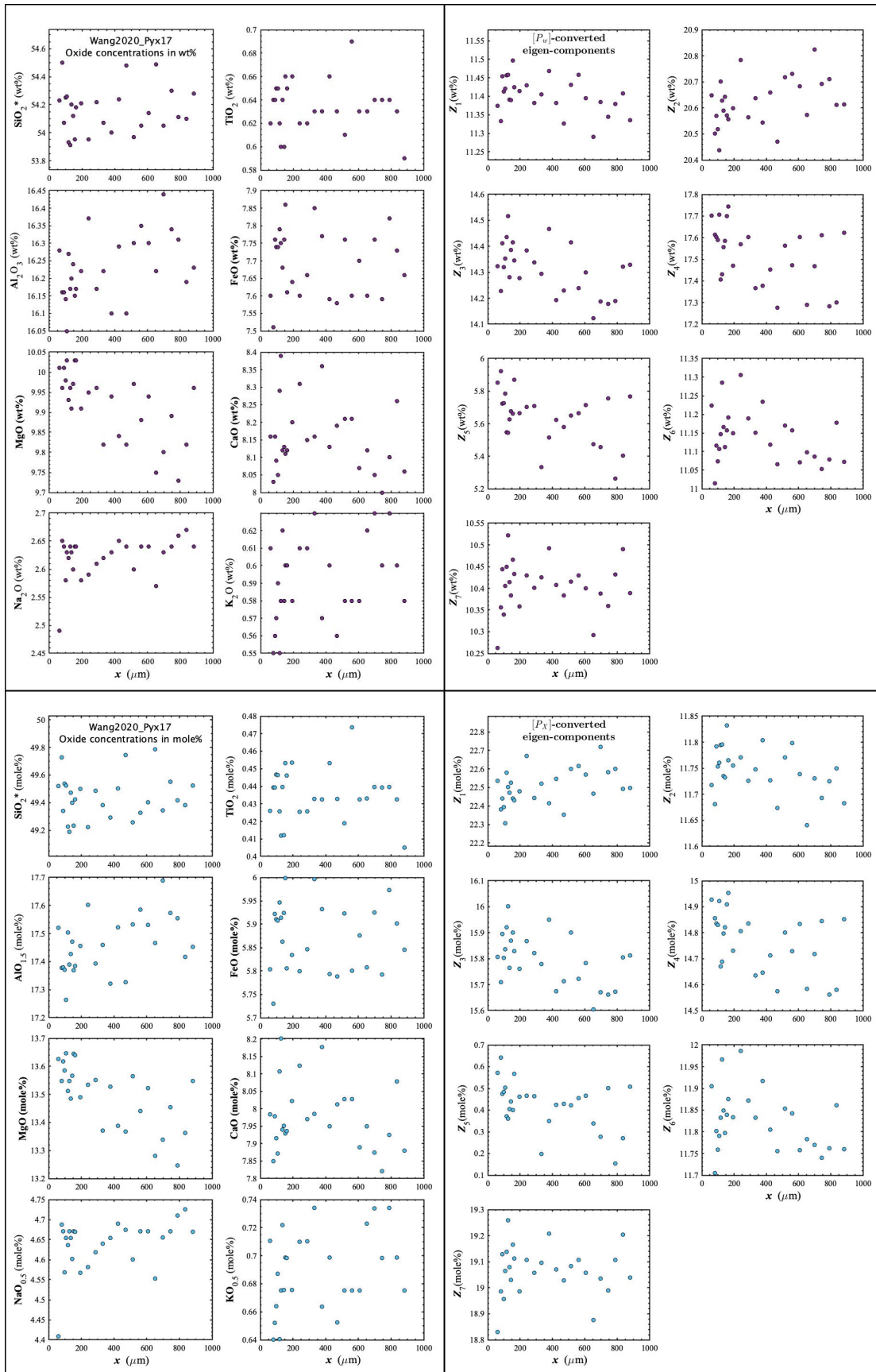
285

Figure D166. Concentration profiles of oxide components in wt% (upper left panel), oxide components in mole% (lower left panel), [P_w]-converted eigen-components (upper right panel), and [P_X]-converted eigen-components (lower right panel) of Wang2020_Pyx17, which is a lherzolite dissolution experiment in basaltic andesite (Wang et al., 2020).
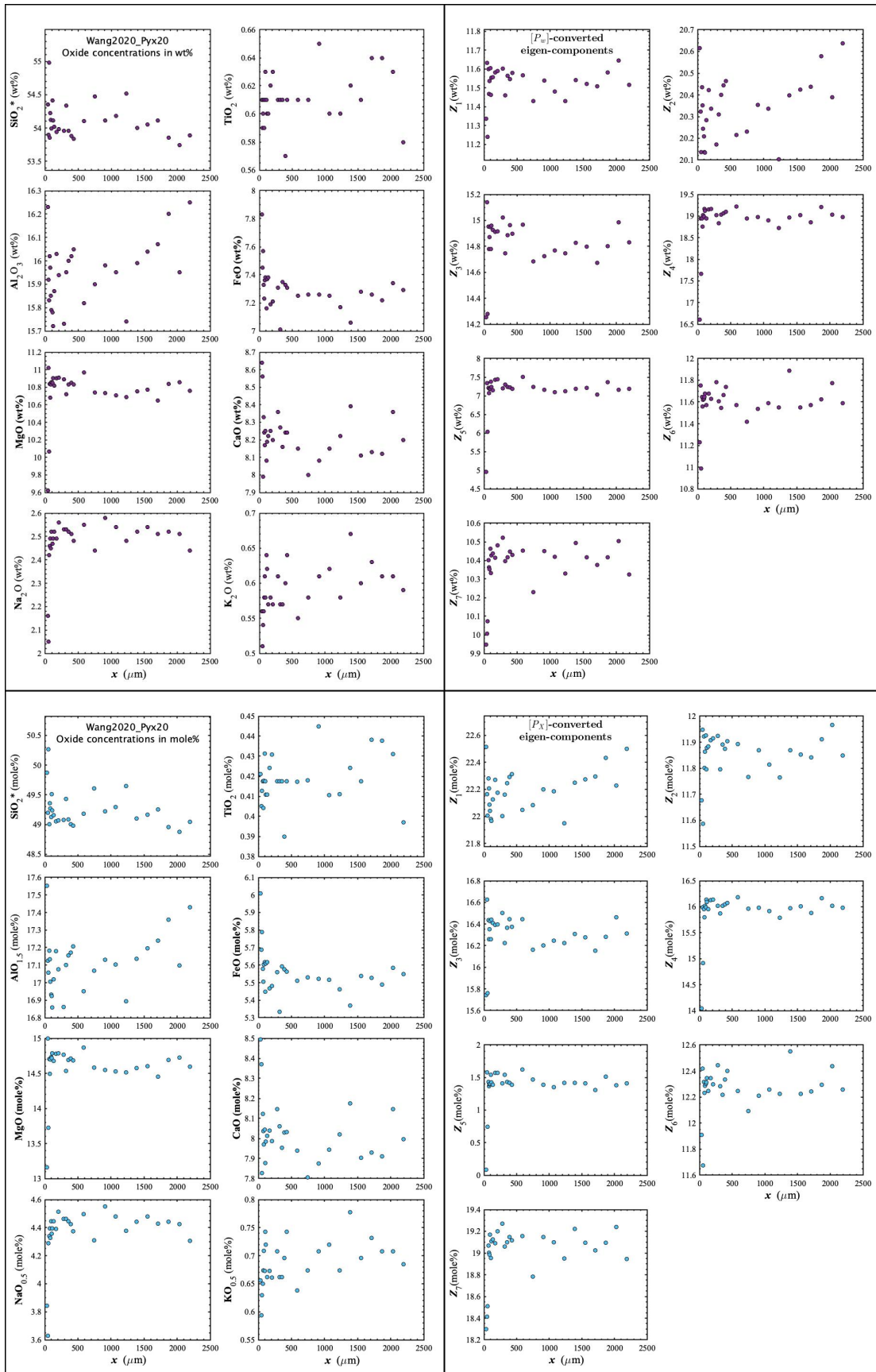
Figure D167. Concentration profiles of oxide components in wt% (upper left panel), oxide components in mole% (lower left panel), $[P_w]$-converted eigen-components (upper right panel), and $[P_X]$-converted eigen-components (lower right panel) of Wang2020_Pyx20, which is a lherzolite dissolution experiment in basaltic andesite (Wang et al., 2020).
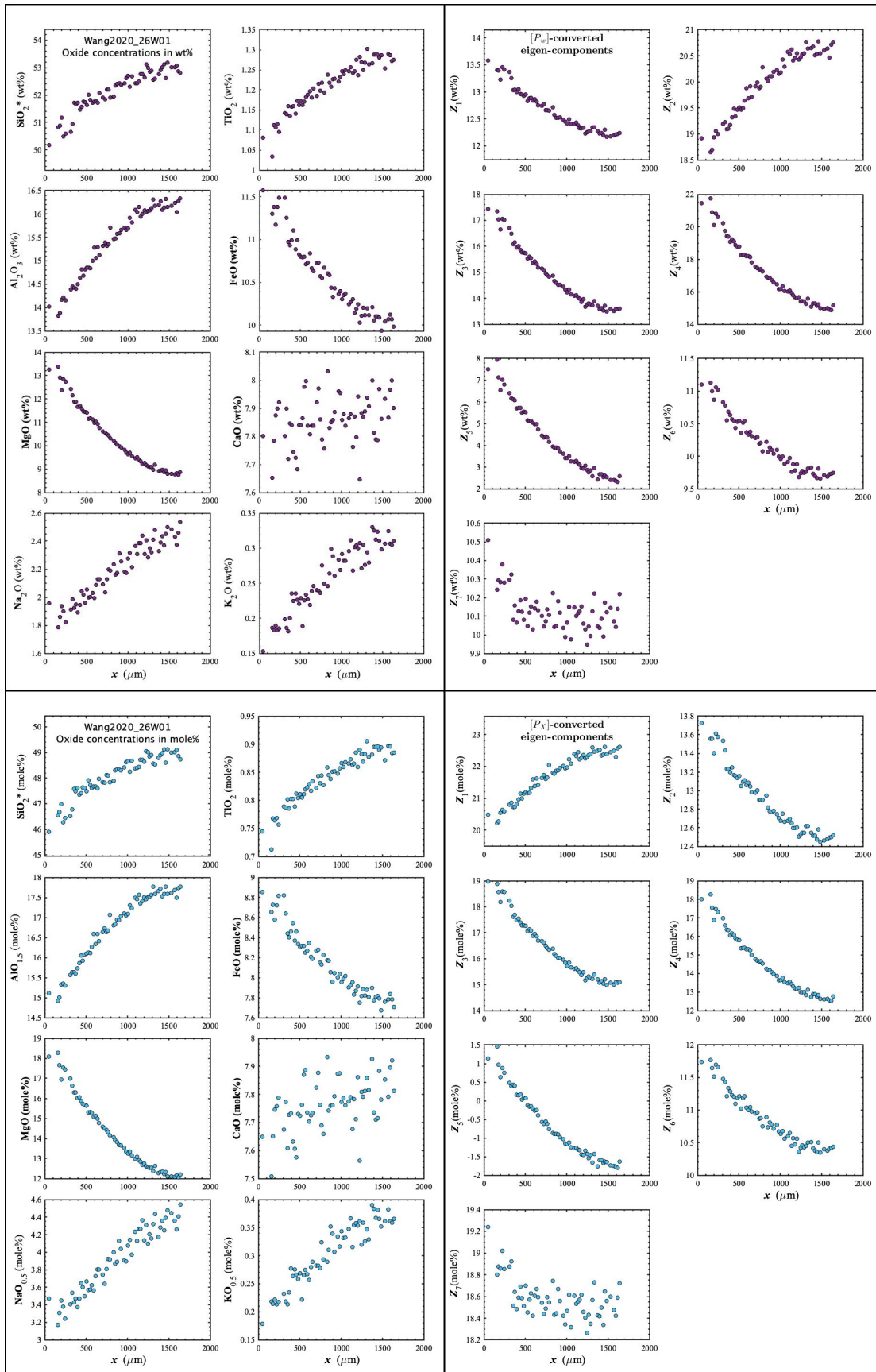
287

Figure D168. Concentration profiles of oxide components in wt% (upper left panel), oxide components in mole% (lower left panel), [P_w]-converted eigen-components (upper right panel), and [P_X]-converted eigen-components (lower right panel) of Wang2020_26W01, which is a lherzolite dissolution experiment in basaltic andesite (Wang et al., 2020).
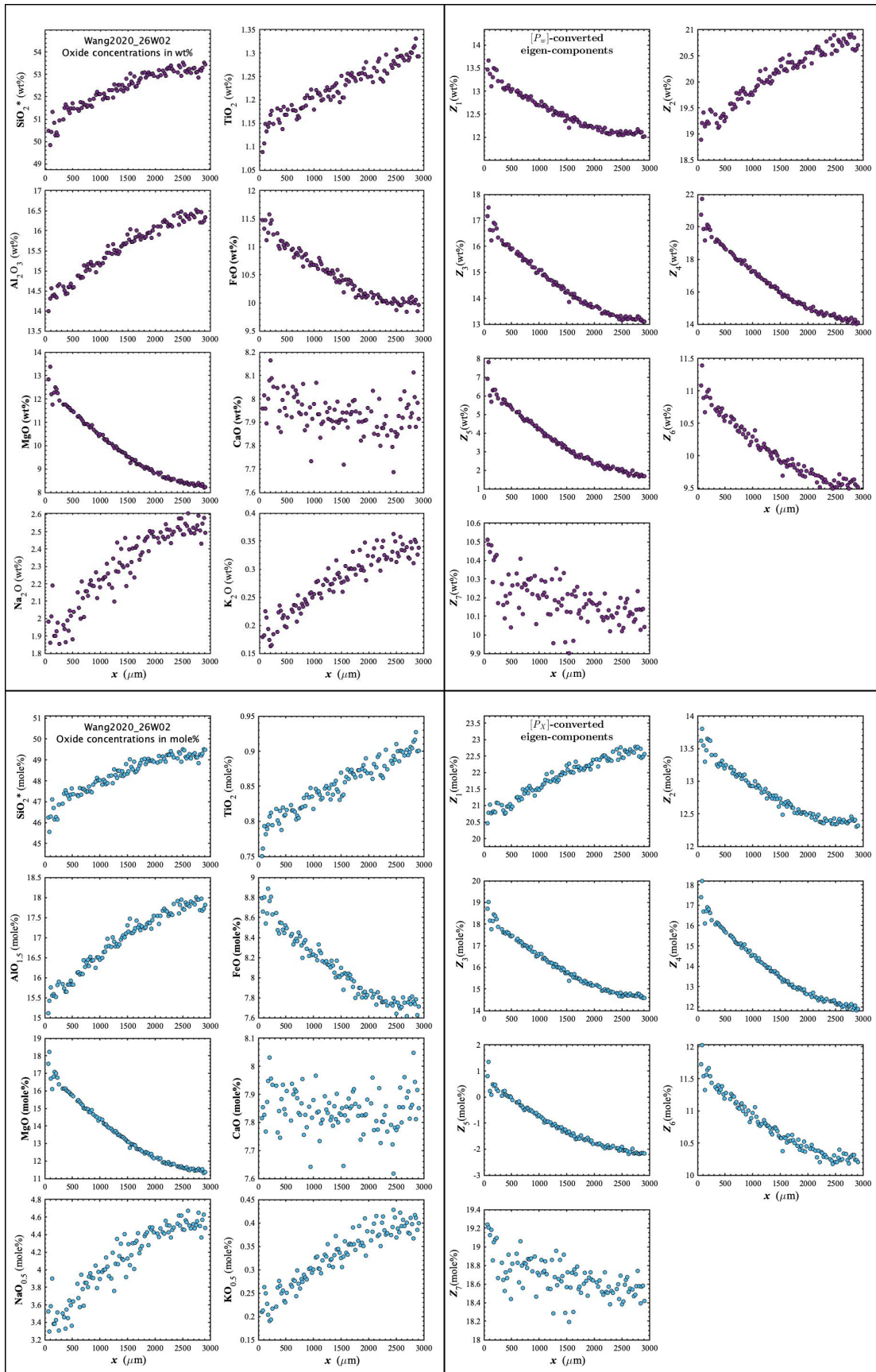
288

Figure D169. Concentration profiles of oxide components in wt% (upper left panel), oxide components in mole% (lower left panel), [P_w]-converted eigen-components (upper right panel), and [P_X]-converted eigen-components (lower right panel) of Wang2020_26W02, which is a lherzolite dissolution experiment in basaltic andesite (Wang et al., 2020).
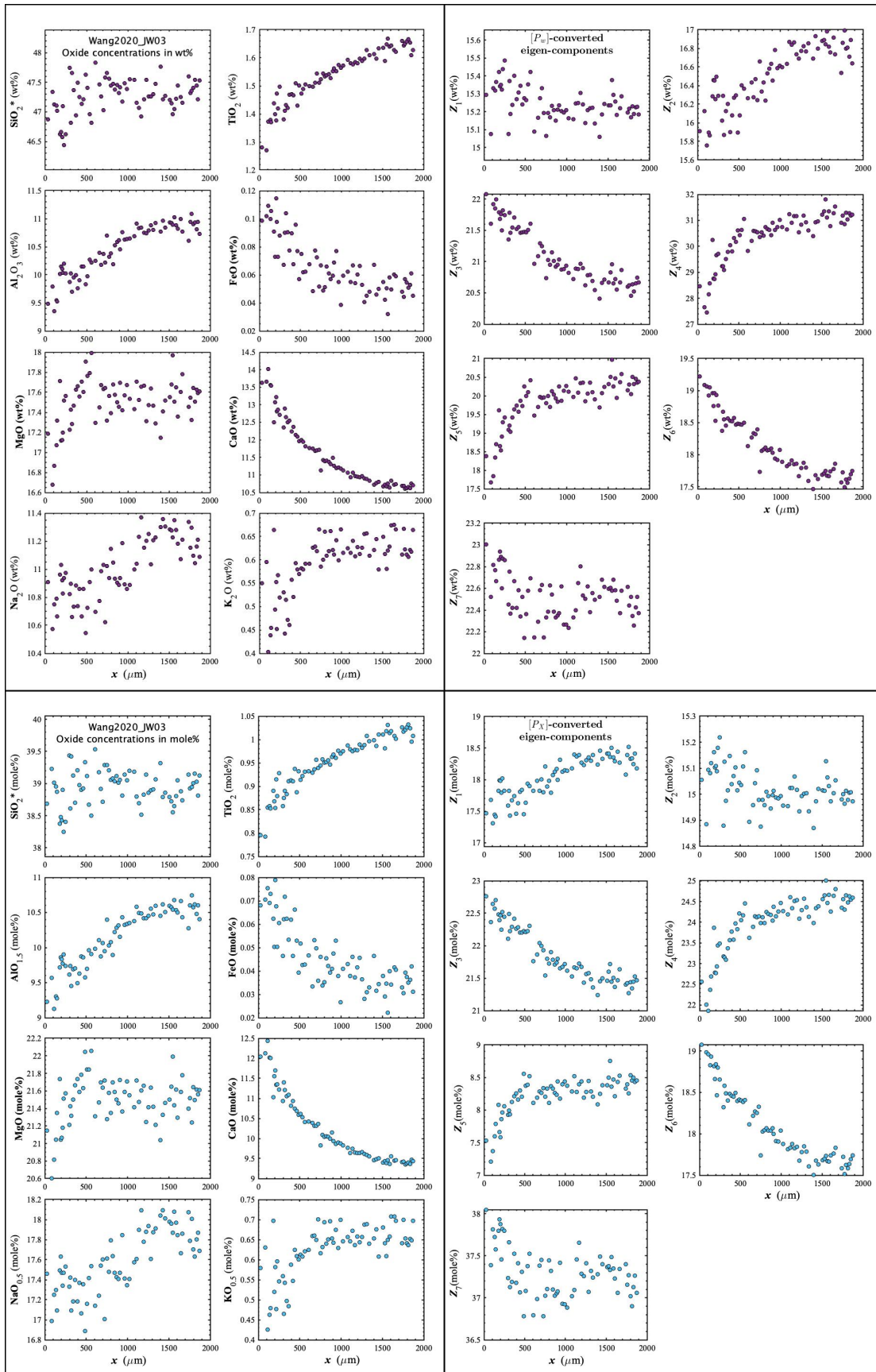
289

Figure D170. Concentration profiles of oxide components in wt% (upper left panel), oxide components in mole% (lower left panel), $[P_w]$-converted eigen-components (upper right panel), and $[P_X]$-converted eigen-components (lower right panel) of Wang2020_JW03, which is a lherzolite dissolution experiment in ferro-basalt (Wang et al., 2020).
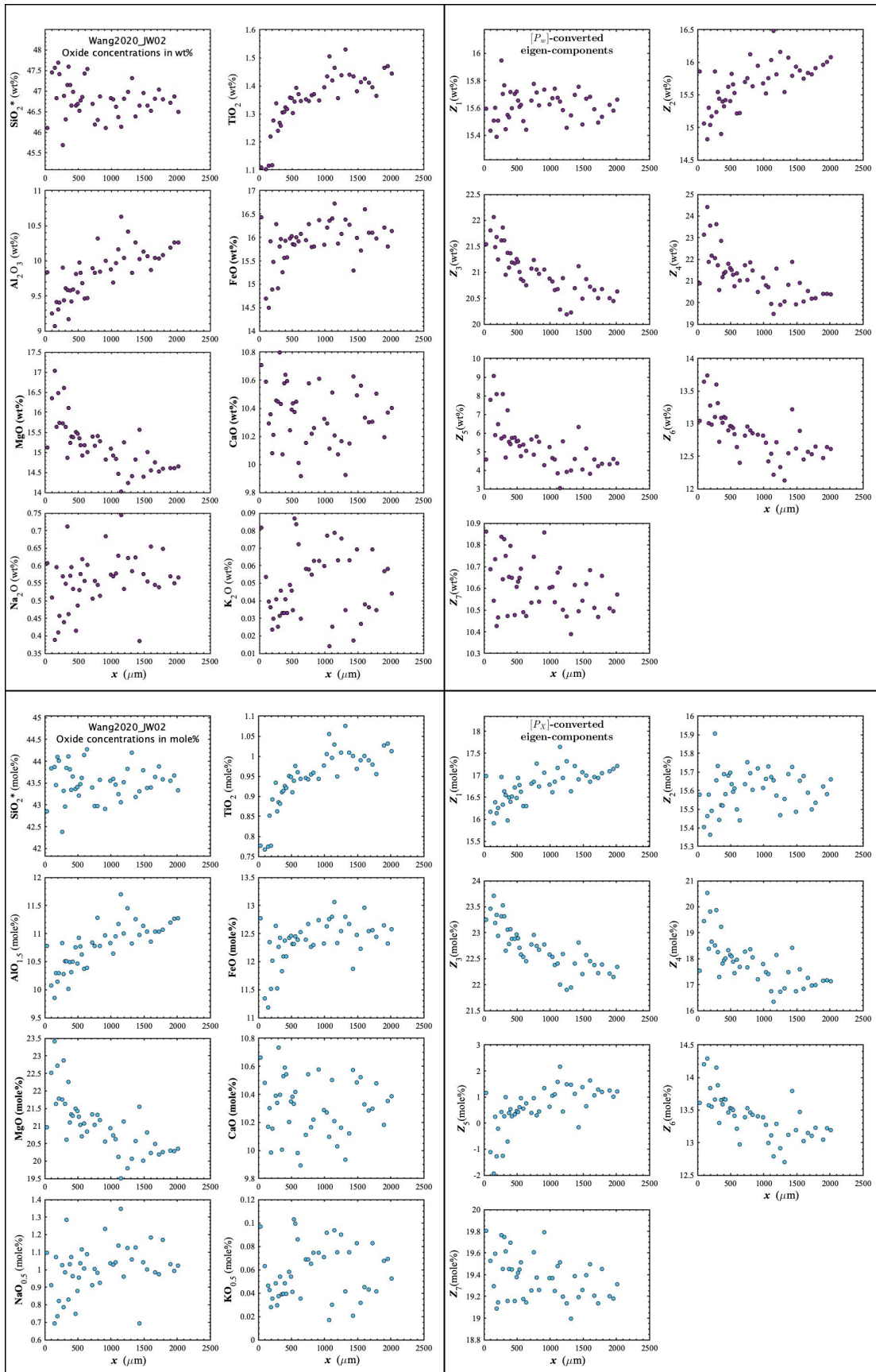
Figure D171. Concentration profiles of oxide components in wt% (upper left panel), oxide components in mole% (lower left panel), $[P_w]$-converted eigen-components (upper right panel), and $[P_X]$-converted eigen-components (lower right panel) of Wang2020_JW02, which is a lherzolite dissolution experiment in ferro-basalt (Wang et al., 2020).